NASA Conference Publication 10161

Sixth Annual Thermal and Fluids Analysis Workshop

Proceedings of a workshop
held at the Ohio Aerospace Institute, Brook Park, Ohio
cosponsored by NASA Lewis Research Center
and the Ohio Aerospace Institute
August 15–19, 1994

National Aeronautics and
Space Administration

Office of Management

**Scientific and Technical
Information Program**

1995

TABLE OF CONTENTS

N95-27346

EXTENSIONAL FLOW CONVECTING A REACTANT UNDERGOING A FIRST ORDER HOMOGENEOUS REACTION AND DIFFUSIONAL MASS TRANSFER FROM A SPHERE AT LOW TO INTERMEDIATE PECLET AND DAMKOHLER NUMBERS

N.Y. Shah and X.B. Reed, Jr.
University of Missouri-Rolla
Rolla, Missouri

SUMMARY

Forced convective diffusion-reaction is considered for viscous axisymmetric extensional convecting velocity in the neighborhood of a sphere. For Peclet numbers in the range $0.1 \leq Pe \leq 500$ and for Damkohler numbers increasing with increasing Pe but in the overall range $0.02 \leq Da \leq 10$, average and local Sherwood numbers have been computed. By introducing the eigenfunction expansion $c(r,\theta) = \sum c_n(r)P_n(\cos\theta)$ into the forced convective diffusion equation for the concentration of a chemical species undergoing a first order homogeneous reaction and by using properties of the Legendre functions $P_n(\cos\theta)$, the variable coefficient PDE can be reduced to a system of N+1 second order ODEs for the radial functions $c_n(r)$, n=0,1,2,...,N. The adaptive grid algorithm of Pereyra and Lentini can be used to solve the corresponding 2(N+1) first order differential equations as a two-point boundary value problem on $1 \leq r \leq r_\infty$. Convergence of the expansion for a specific value of N can thus be established and provides "spectral" behavior as well as the full concentration field $c(r,\theta)$.

INTRODUCTION

The prevalence of small often spherical or approximately spherical particles, bubbles, or droplets in atmospheric physics, chemical reaction engineering, combustion science, and environmental technology implies the small Reynolds number (Re << 1) assumed here. For concreteness a solid sphere is also assumed. Unlike the axisymmetric uniform streaming motion past a sphere (Stokes, 1851) that is a reasonable assumption in the neighborhood of sedimenting particles or those in fluidized beds, however, the flow field in neighborhood of most particles in other natural, industrial, and laboratory circumstances is neither uniform nor can it be assumed to be the so-called slip velocity characteristic of the ensemble average over all the particles in complex, even turbulent two phase flow such as occurs in stirred tanks, for instance.

We are interested in considering other physically realistic - and therefore necessarily more complicated - flow fields that would have another domain application. The ubiquitous spherical geometry and the mathematical simplicity of axisymmetry make the axisymmetric extensional flows (Re << 1) a natural candidate. The occurence of extensional flows, in particular of locally

axisymmmetric ones in the neighborhood of small spherical particles, bubbles, or drops, one of the basic building blocks in the rheology and flow of a wide variety of dispersions.

There are two axisymmetric extensional flow fields. The biaxial and uniaxial flows both have the same streamlines. However, the biaxial flow comes along the axes from $z = \pm\infty$ and approaches the poles of the sphere symmetrically, departing radially outwardly in the symmetry (x,y)-plane, whereas the uniaxial flow is oppositely directed and approaches radially symmetrically in the equatorial plane and departs along the $\pm z$ axes. Far from the sphere, the dimensionless Cartesian components of the velocity are $(U_x, U_y, U_z) = \pm(x, y, -2z)$, with $\pm$ referring throughout to biaxial and uniaxial, respectively.

For Re=0, all flow fields are at rest, and the Sherwood number is independent of the Peclet number and depends solely on the Damkohler number, i.e., $Sh=Sh(Da_{II})$. For $Re << 1$ but not identically zero, $Sh=Sh(Pe,Da_{II})$. Pe no more characterizes convection than Re characterizes the velocity field. Different velocity fields convect heat and mass differently, even if they have the same small non-zero Re and the same Pe. For Re=0, $Sh=1+\sqrt{Da_{II}}$, but for $Re << 1$, although the axisymmetric uniform streaming flow and the axisymmetric extensional flows all three have the same asymptote for Sh (viz., $1+\sqrt{Da_{II}}$) as $Pe \to 0$, for $Pe << 1$ but $Pe \neq 0$, the functional dependance upon Pe, Da_{II} will be different for the uniform flow, for the biaxial flow, and for the uniaxial flow, $Sh=Sh(Pe,Da_{II})$ will be different, even though Pe and Da_{II} are identical. What is more, the local mass transfer coefficients $Sh(\theta;Pe,Da_{II})$ will be even more different. For a uniform streaming flow at infinity, Pfeffer and his co-workers have studied homogeneous first order reactions for low Reynolds number convective diffusion (Rutland and Pfeffer, 1967), (Chen and Pfeffer, 1970)

We compare and contrast the results for convective diffusion-reaction for biaxial and uniaxial flows with one another and with those for the uniform streaming flow. Our emphasis, however, is on the theoretical approach, the mathematical calculations, and the use of the Pereyra-Lentini adaptive grid algorithm, above all on certain constraints and computational limitations that arise.

THEORETICAL APPROACH

Rather than directly attacking the forced convective diffusion/diffusion-reaction equation numerically as a variable coefficient partial differential equation in which the extensional velocity field introduces the known but complicated set of variable coefficients, we take another tack. We introduce the eigenfunction expansion

$$c(r,\theta) = \sum c_n(r)\ P_n(\cos\theta) \qquad (1)$$

with the $P_n(\cos\theta)$ being Legendre functions and the radial functions $c_n(r)$ are unknown. By utilizing properties of the $P_n(\mu)$, $\mu=\cos\theta$, we then reduce the single partial differential equation for $c(r,\theta)$ to a system of N+1 ordinary differential equations for the $c_n(r)$ and solve them numerically, as outlined in the next section.

The dimensionless forced convective diffusion-reaction equation investigated may be written

$$Pe\ \mathbf{U} \cdot \nabla c = \nabla^2 c - Da_{II}\ c\ , \qquad (2)$$

in which the second Damkohler number may be expressed in terms of the first,

$$Da_{II} = Da_I \, Pe \, , \tag{3}$$

and the Peclet number Pe for the extensional flow utilizes the characteristic velocity E a , in which E is the rate of strain at infinity and a is the radius of the solid sphere:

$$Pe = E\, a^2 / \mathcal{D} \, , \; Da_I = k / E \, , \; Da_{II} = k\, a^2 / \mathcal{D} \, . \tag{4}$$

The low Reynolds number axisymmetric extensional flow has two non-vanishing dimensionless velocity components

$$\begin{aligned} \mathcal{U}_r &= \pm \left(r - \frac{5}{2} r^{-2} + \frac{3}{2} r^{-4} \right) \left(1 - 3 \cos^2 \theta \right) , \\ \mathcal{U}_\theta &= \pm \left(r - r^{-4} \right) \left(1 - 3 \sin \theta \cos \theta \right) . \end{aligned} \tag{5}$$

The ± signs refer to the biaxial/uniaxial flows, respectively. The streamlines for the two are identical and are shown in Figure 1, with the flow being oppositely directed along the streamlines. The biaxial flow comes from infinity toward the poles and exits radially symmetrically in the equatorial plane. The axisymmetric extensional creeping flow was obtained by specialization of the solution to the creeping flow equation of Batchelor (1970) for a general linear rate of strain at infinity; see also Leal (1992) for the final result.

The partial differential equation to be solved,

$$Pe \left(\mathcal{U}_r(r,\theta) \, \frac{\partial c}{\partial r} + \frac{\mathcal{U}_\theta(r,\theta)}{r} \, \frac{\partial c}{\partial \theta} \right) = \nabla^2 c - Pe \, Da_I \, c \tag{6}$$

may be rewritten upon introducing the expansion (1) as

$$\begin{aligned} \sum_{n=0}^{\infty} \Bigg\{ \pm \Big[F(r) \, \frac{dc_n}{dr} (1 - 3\mu^2) \, P_n(\mu) + G(r) \, c_n(r) \, (3\mu) \, (n P_n(\mu) - n P_{n-1}(\mu)) \Big] \\ - \frac{1}{r^2} \frac{d}{dr} \left(r^2 \, \frac{dc_n}{dr} \right) \frac{n(n+1)}{r^2} \, c_n(r) - Da_{II} \, c_n(r) \Bigg\} = 0 \end{aligned} \tag{7}$$

in which,

$$\begin{aligned} F(r) &= \left(r - \frac{5}{2} r^{-2} + \frac{3}{2} r^{-4} \right) , \\ G(r) &= \left(1 - r^{-5} \right) . \end{aligned} \tag{8}$$

In order to reduce this to a system of ordinary differential equations by utilizing the orthogonality of the $P_n(\mu)$, we must first reduce all the θ-dependent coefficients to Legendre polynomials. To accomplish this we use both algebraic and differential recurrence relations for them (Abramowitz and Stegun, 1965) , the former repeatedly as required. Ultimately, the convection terms may be written as

$$\sum_{n=0}^{\infty} \pm \Bigg[\Bigg(F(r)\frac{dc_n}{dr} - 3\left\{F(r)\frac{dc_n}{dr} - nG(r)c_n(r)\right\}\left(\frac{1}{2n+1}\right) \left[\frac{(n+1)^2}{(2n+3)} + \frac{n^2}{(2n-1)}\right] - 3\frac{n^2}{(2n-1)}G(r)c_n(r)\Bigg) P_n(\mu) - 3\left\{F(r)\frac{dc_n}{dr} - nG(r)c_n(r)\right\}\left\{\frac{(n+1)(n+2)}{(2n+1)(2n+3)} P_{n+2}(\mu) + \frac{n(n-1)}{(2n-1)}\left[\frac{1}{(2n+1)} + G(r)c_n(r)\right]P_{n-2}(\mu)\right\} \tag{9}$$

The remaining terms of the equation need not be rewritten. Upon utilizing the orthogonality of the $P_n(\mu)$ and solving for the second derivatives, we obtain for the general n ($n \neq 0,1$),

$$\frac{d^2c_n}{dr^2} = \pm Pe\Bigg[F(r)\frac{dc_n}{dr} - \frac{3}{(2n+1)}\left(\frac{(k+1)^2}{(2n+3)} + \frac{n^2}{(2n-1)}\right) -3\frac{n(n-1)}{(2n-1)(2n-3)}\left(F(r)\frac{dc_{n-2}}{dr} - (n-2)G(r)c_{n-2}(r)\right) -3\frac{(n+1)(n+2)}{(2n+3)(2n+5)}\left(F(r)\frac{dc_{n+2}}{dr} + (n+3)G(r)c_{n+2}(r)\right)\Bigg] - \frac{2}{r}\frac{dc_n}{dr} + \frac{n(n+1)}{r^2}c_n(r) + Da_{II}\ c_n(r) \tag{10}$$

In the computations and results, it is more informative to vary Pe and Da_I (called K in the program and figures).

The boundary conditions on $c(r,\theta)$ are

$$\begin{aligned} c(r,\theta) &= 1\ , \\ c(r\to\infty,\theta) &= 0\ , \end{aligned} \tag{11}$$

which imply

$$\begin{aligned} c_0(r=1) &= 1, \\ c_n(r=1) &= 0,\quad n \geq 1, \\ c_n(r\to\infty) &= 0,\quad n \geq 0. \end{aligned} \tag{12}$$

NUMERICAL ALGORITHM

The algorithm of Pereyra and Lentini (1978) as codified now in the IMSL subroutine DBVPFD was used. It is a robust program for solving two-point boundary value problems. In order to solve the ordinary differential equation system represented by (10)-(12), we first must terminate the infinite series (1) at $N < \infty$, and the spatial domain at $r_\infty < \infty$. The former leads to a finite system of second order equations for which $c_n(r) \equiv 0$ for $n < 0$, $n > N$. The latter leads to the modified boundary conditions

$$\begin{aligned} c_0(r=1) &= 1 \\ c_n(r=1) &= 0 \ , \quad n \geq 0 \\ c_n(r=r_\infty) &= 0 \ , \quad n \geq 0 \ . \end{aligned} \tag{13}$$

The results for $c_n(r;Pe,Da_I)$ will obviously depend upon N and r_∞. The latter (r_∞) is a parameter that can be varied in the program. The former (N) must be selected before the program can be run, but once selected (as conservatively as possible), convergence of the series can be established. The other crucial computational parameters in the subroutine are the initial and maximum number of mesh points (NINIT, MXGRID).

Finally, the system of N+1 second order equations must be converted in the usual way to a system of 2(N+1) first order equations in order to employ the IMSL subroutine:

$$\begin{aligned} c_0(r) &\rightarrow y_1(x) \\ c_1(r) &\rightarrow y_2(x) \\ &\vdots \\ c_{N-1}(r) &\rightarrow y_{\frac{NEQNS}{2}-1}(x) \\ c_N(r) &\rightarrow y_{\frac{NEQNS}{2}}(x) \\ \frac{dc_0}{dr}(r) &= \frac{dy_1}{dx}(x) \rightarrow y_{\frac{NEQNS}{2}+1}(x) \\ \frac{dc_1}{dr}(r) &= \frac{dy_2}{dx}(x) \rightarrow y_{\frac{NEQNS}{2}+2}(x) \\ &\vdots \\ \frac{dc_n}{dr}(r) &= \frac{dy_{n+1}}{dx}(x) \rightarrow y_{\frac{NEQNS}{2}+n+1}(x) \\ &\vdots \\ \frac{dc_{N-1}}{dr}(r) &= \frac{dy_{\frac{NEQNS}{2}-1}}{dx}(x) \rightarrow y_{NEQNS-1}(x) \\ \frac{dc_N}{dr}(r) &= \frac{dy_{\frac{NEQNS}{2}}}{dx}(x) \rightarrow y_{NEQNS}(x) \end{aligned} \tag{14}$$

RESULTS AND DISCUSSION

For a practicing engineer and for many engineering and other scientists and mathematicians, the principal goal of such an investigation would be a relation between the average Sherwood number (the dimensionless mass transfer coefficient) Sh and the physicochemical parameters, viz., $Sh(Pe;Da_I)$. Of some practical interest is also the local Sherwood number, which for an axisymmetric convecting velocity would be expressible as $Sh(\theta;Pe,Da_I)$, the integral of which, when carried out over the surface of the sphere, yields the average Sherwood number Sh. The magnitude of the local Sherwood number is the normal derivative of the concentration field $c(r,\theta)$ at the sphere surface, $\partial\, c/\partial\, r\ (r,\theta)|_{r-1}$. Although the concentration field $c(r,\theta)$ in other approaches to the forced convective diffusion-reaction problem would be the object of the numerical research, it generally receives short schrift as being of little practical interest. In multiparticle systems, the extent of the concentration fields non-negligible level for a single particle can for instance, be useful in assessing, or at least estimating, the minimum interparticle distance at which concentration fields of neighboring particles would affect one another.

We start our discussion, neither with $Sh(\theta;Pe,Da_I)$ nor with $c(\theta;Pe,Da_I)$, but with the object of our numerical study, the radial functions $c_n(r;Pe,Da_I)$, denoted as $c_n(r;Pe,K)$. In Figure 2a,b for r_∞ ($\equiv R$ in the notation employed throughout the paper) = 10 and Pe=5, K=1 we show the radial functions $c_n(r)$, for n=0,1,2,...,70 for a biaxial flow. Consistent with the reflection symmetry across the equatorial ($\theta=\pi/2$) plane, only the even radial modes are nonvanishing. The radial functions decrease in magnitude, and N=70 clearly produces a convergent series.

Biaxial

When the radial functions are multiplied respectively by their corresponding Legendre polynomials, the isocontour plot shown in the upper half of Figure 1 results. The biaxial velocity field produces the thin(ner) stagnation concentration boundary layer at the poles. The concentration wake then imbeds the equatorial plane symmetrically. There are, to emphasize the point, neither momentum boundary layers nor momentum wakes (Re << 1). At the same Pe, r_∞, and N, an increase of K from 1 to 2 reduces (Figure 3) the boundary layer a bit and the wake more, effects that are still more pronounced for K=5 (Pe=5) in Figure 4. For K=10 (Pe=5), all of the isocontours (0.1-0.9 in increments of 0.1) except for c=0.01 are spherically symmetric (Figure5), as far as is apparent to the naked eye (and undoubtedly a boon to theoreticians).

For an increase of Pe to 50, the K=2 (Figure 6) is of course dissimilar to that for Pe=5, but for K=5,10 similar remarks apply to the Pe=50 isocontours: there is one nonspherical isocontour for K=5 and none at K=10 (Plots not shown).

For a further increase to Pe=200 (Figure 7) the isocontours show a 2-d salient at K=1, which has become almost spherically symmetric at K=2 (Figure 8). For K=5 and 10 (Plots not shown) spherical symmetry reigns, the differences being solely the decreasing radii of the circles with increasing K.

The isocontour plot for Pe=500 and K=0.5 (Figure 9) is similar to that for Pe=200 and K=1 (Figure 7).

Uniaxial

The area of stagnation concentration boundary layer for uniaxial extensional creeping flow is centered on the stagnation velocity ring, the equator. The concentration wakes are two, stretching from the poles ($\theta=0,\pi$), qualitatively similar to the concentration wake on the downwind pole of a sphere in a uniform streaming flow at infinity. Such observations are rendered more faithfully in Figure 10 for Pe=5, K=5 than in words.

An increase from K=5 to 10 for the same Peclet number (Pe=5) brings about expected isocontours (Figure 11), as does an increase of Pe to 50 for K=5 (Figure 12) and for K=10 (Figure 13), by which values spherical isocontours result.

Local Sherwood Numbers

For fast reactions (Da_I=K=5,10), spherical isocontours were observed. An increase in the convection (i.e., in Pe) served to feed the reaction faster but did not further influence the spherical symmetry of the isocontours, once a Pe was reached at which they were spherical. This is nowhere more evident than for the biaxial flow in Figures 14a,b for K=5 and 10 respectively; Pe=5, 50, 200, 500. There are slight local maxima at $\theta=0,\pi$ and a slight local minimum at $\theta=\pi/2$. Increases in Pe lead to dramatic increases in the level of mass transfer rates without however appreciably affecting local values over the surface, relative to one another. The increase in Da_I from 5 to 10 increases the level of order 10 % for each Pe shown.

Absent reaction, biaxial convective diffusion produces a local Sherwood number that is peaked at $\theta=0,\pi$ and troughed around $\theta=\pi/2$. The clear minimum is reduced rapidly as the maxima increase with K (Figure 15a, Pe=5; Figure 15b, Pe=50; Figure 15c, Pe=200; Figure 15d, Pe=500).

For a uniaxial flow the convective diffusion problem without reaction produces a pronounced maximum at $\theta=\pi/2$ and minima at $\theta=0,\pi$, as expected (Figure 16a). Also as expected, the strong maximum is reduced relative to the minima with increasingly fast reaction (Figure 16a), an effect observed with higher Pe (Figure 16b,c).

Crossplots for K=5 and 10 for the several values of Pe in Figures 17a,b, emphasizing the weak θ-dependence of $Sh(\theta)$ for fast reactions.

Average Sherwood Number

Different velocity fields convect heat and mass differently, as is evident even for the two types of axisymmetric extensional flows. Concentration isocontours, other than those for very high Da_I, are different for biaxial and uniaxial flows.

For Pe=5, convective diffusion (K=0 in Tables 1,2) by uniaxial flow manifests a greater average mass transfer coefficient than by biaxial flow. Indeed, strictly speaking, for any value of Pe and K, $Sh(Pe_i, K_j)_{uni} > Sh(Pe_i, K_j)_{bi}$, as is evident from Tables 1 and 2.

Nonetheless, for Pe=5, K=1, Sh_{uni} is greater than Sh_{bi} by only 0.07; for K=2, by only 0.03; for K=5, by only 0.005. For Pe=50 and K=5, 10, $Sh_{uni} > Sh_{bi}$ only in the third decimal place, which also holds for the same K's, at Pe=200. For K=10, at Pe=500, they differ only in the fourth decimal place. Thus, from this limited set of results, Sh is virtually identical for uniaxial and biaxial flows for K=5,10 for $Pe \geq 50$. For smaller reaction rates and for smaller convection (smaller Pe), small but perceptible differences will arise between biaxial and uniaxial creeping flows, with the latter being the larger of the two.

BIBLIOGRAPHY

1. Stokes, G.G.: On the Effect of Internal Friction of Fluids on the Motion of Pendulums. Trans. Cambridge Phil. Soc., vol. 9, Part II, 1851, pp 8-106.
2. Rutland, L.; and Pfeffer, R.: Mass Transfer from a Single Sphere in Stokes' Flow with a Homogeneous Chemical Reaction. A.I.Ch.E. J., vol. 13, no. 1, Jan. 1967, pp 182-186.
3. Chen, W.C.; and Pfeffer, R.: Local and Over-All Mass Transfer Rates around Solid Spheres with

First-Order Homogeneous Chemical Reaction. Ind. Eng. Chem. Fundamentals, vol. 9, no. 1, Feb. 1970, pp 101-107.
4. Batchelor, G.K.: An Introduction to Fluid Dynamics. Cambridge, 1970
5. Leal, L.G.: Laminar Flow and Convective Transport Processes. Butterworth, 1992
6. Abramowitz, M.; and Stegun, I.A.: Handbook of Mathematical Functions. Dover 1965
7. Pereyra, Victor (1978), PASVA3: An adaptive finite-difference FORTRAN program for first order nonlinear boundary value problems, in Lecture Notes in Computer Science, 76, Springer-Verlag, Berlin, 67-88.

ACKNOWLEDGEMENTS

Computer runs for small values of Pe were run on the HP 9000 worksatations in the Computer Center of the University of Missouri - Rolla; the Director, David Dearth, and several of his colleagues have been helpful, but Gerry O'Brennan deserves special credit. Because of the local hardware limitations, we are especially indebted to John Gee and CRAY Research for access to EL92, with sufficient memory to run the larger memory and CPU intensive (higher Pe, N) jobs. Without the Mr. Gee's generous cooperation, we would not have been able to run Pe $\geq$ 50.

FIGURE 1

CONCENTRATION ISOCONTOURS

BIAXIAL FLOW WITH HOMOGENEOUS REACTION

PE=5 K=1 R=10 ORDER=1 L=70

LEVELS: 0.01, 0.1 TO 0.9 BY 0.1

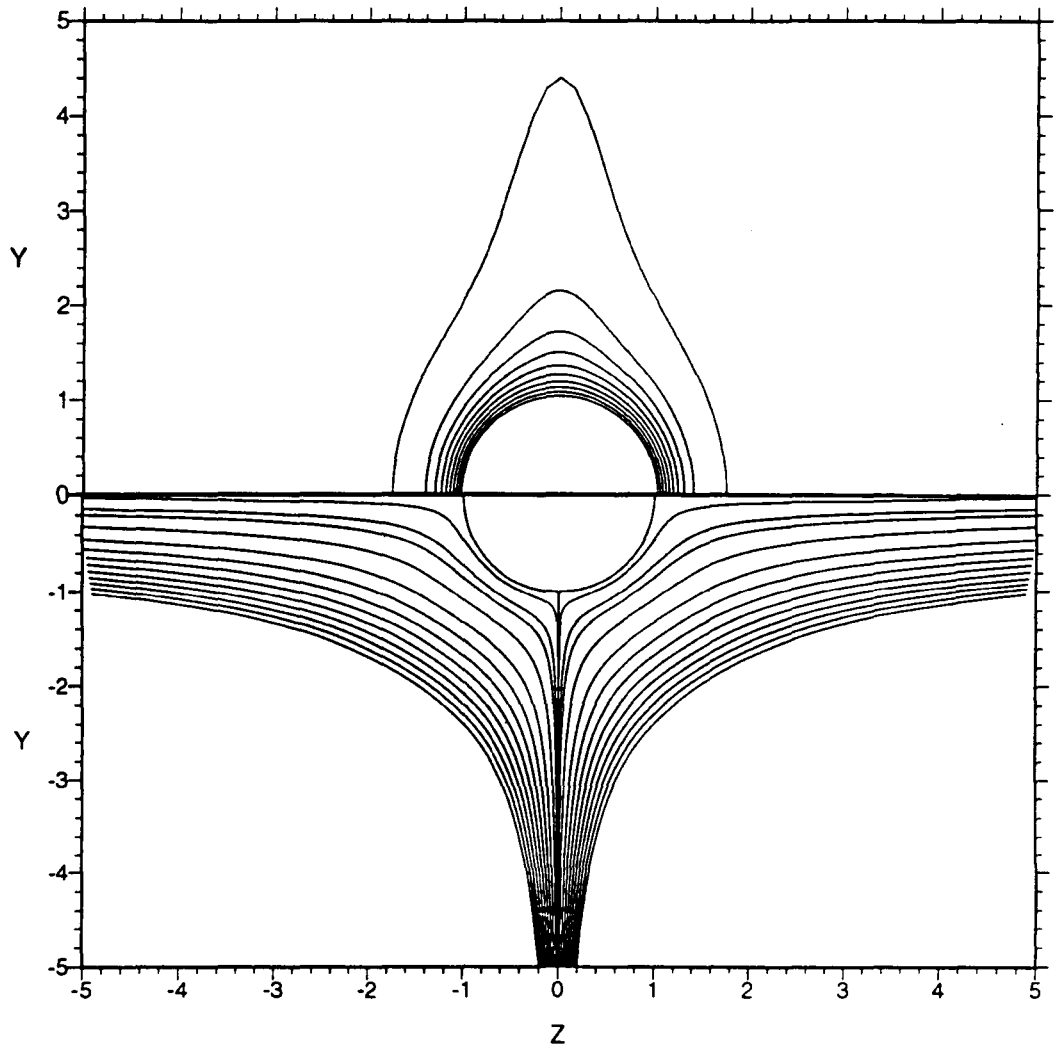

STREAM FUNCTION ISOCONTOURS

BIAXIAL AND UNIAXIAL EXTENSIONAL FLOW

LEVELS: +/- 0.01, +/- 0.1, -5 TO 5 BY 0.5

FIGURE 2a

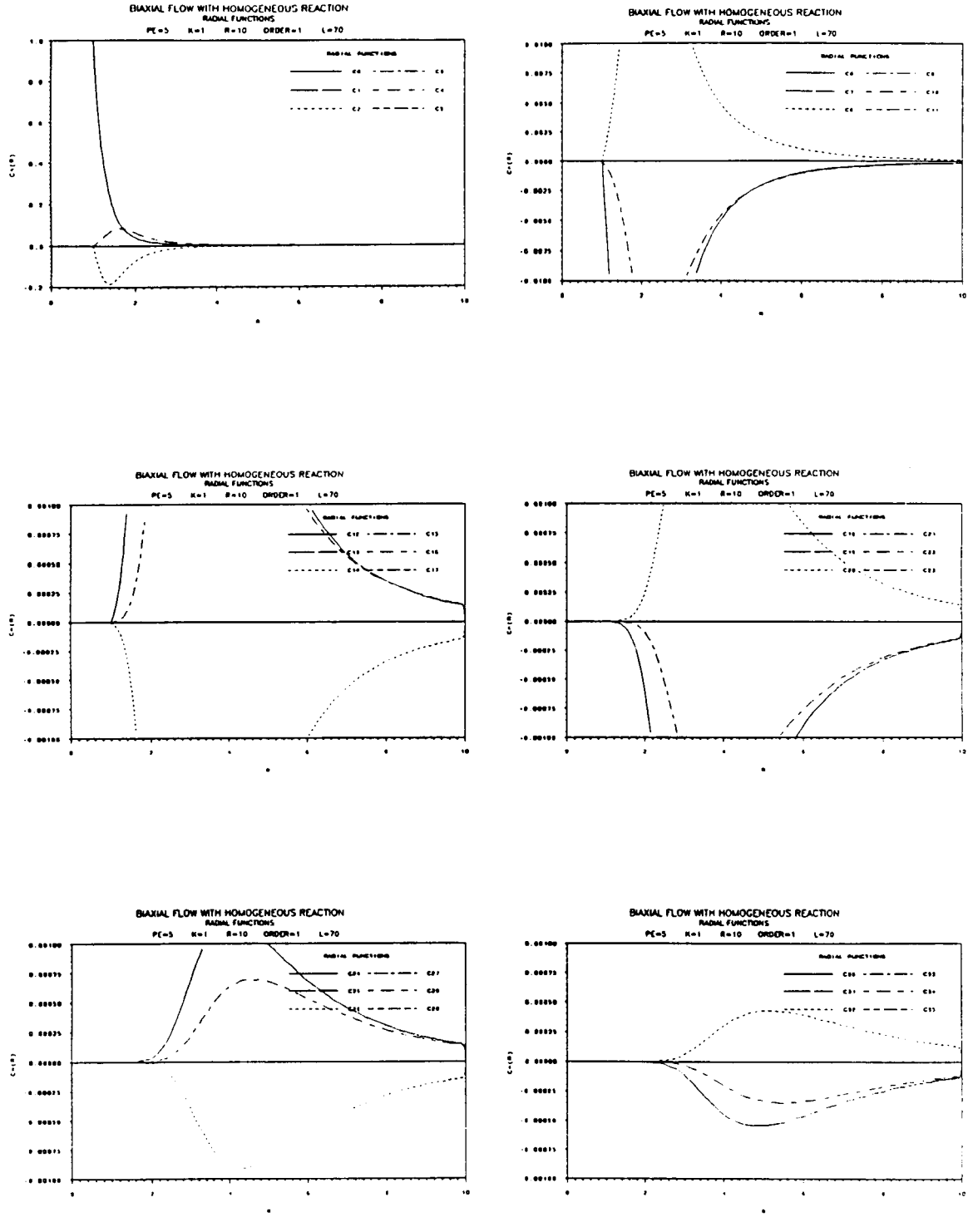
BIAXIAL FLOW WITH HOMOGENEOUS REACTION
RADIAL FUNCTIONS
PE=5 K=1 R=10 ORDER=1 L=70
RADIAL FUNCTIONS
C(R)
R

FIGURE 2b

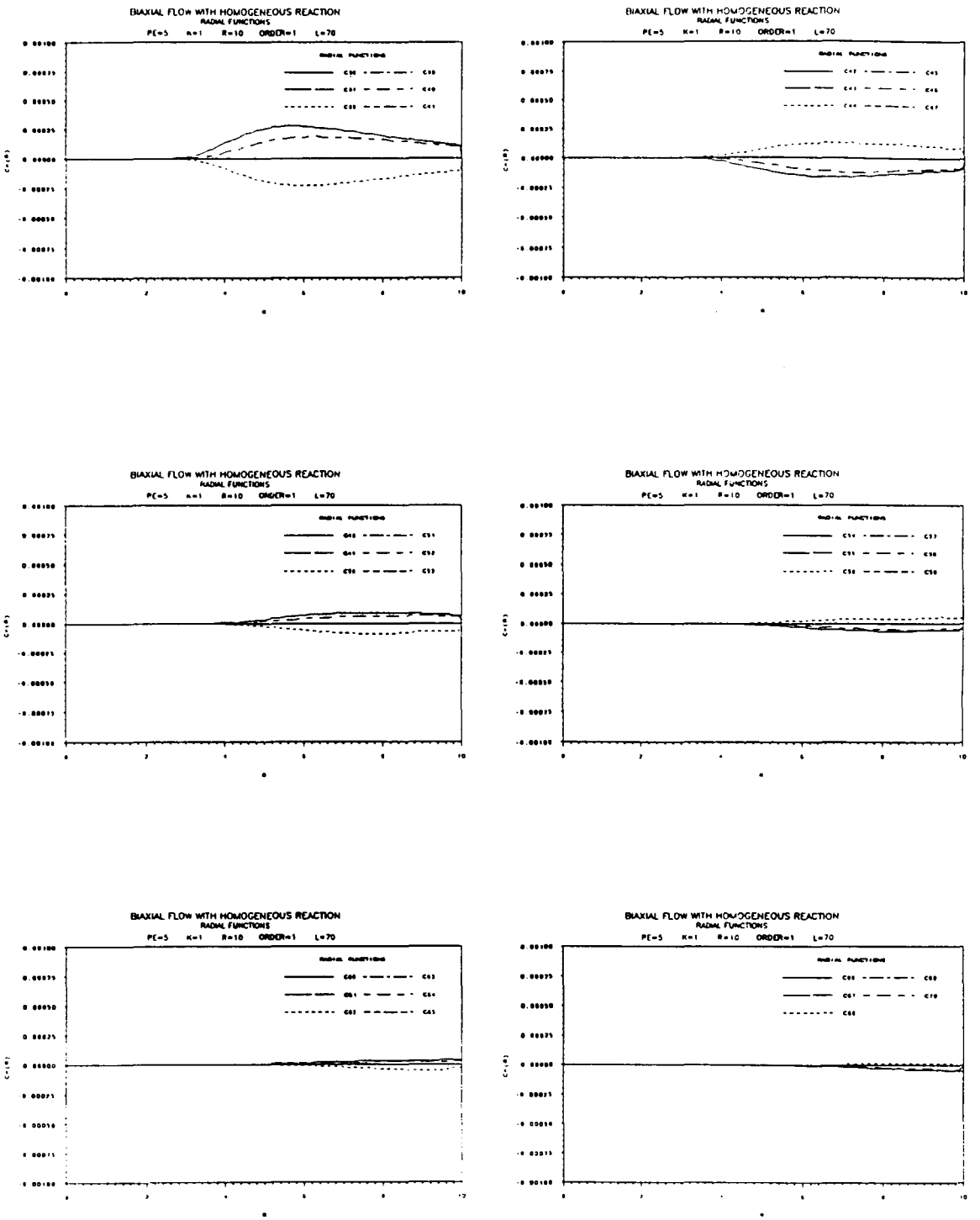

FIGURE 3

CONCENTRATION ISOCONTOURS

BIAXIAL FLOW WITH HOMOGENEOUS REACTION

PE=5.00 K=2.00 R=10.0 ORDER=1 L=70

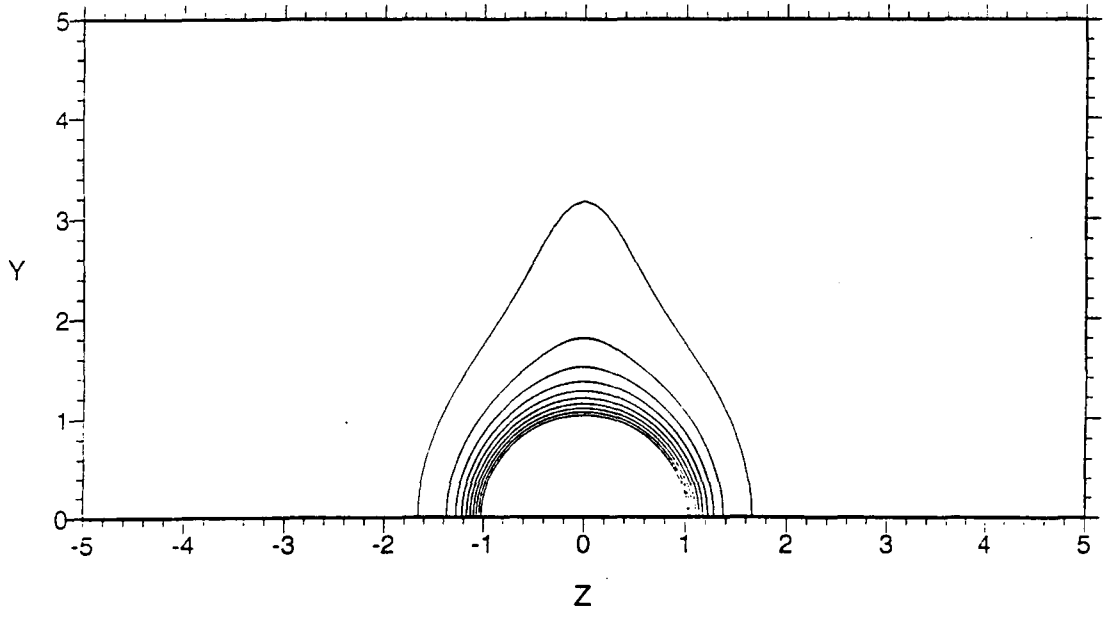

FIGURE 4

CONCENTRATION ISOCONTOURS

BIAXIAL FLOW WITH HOMOGENEOUS REACTION

PE=5.00 K=5.00 R=10.0 ORDER=1 L=70

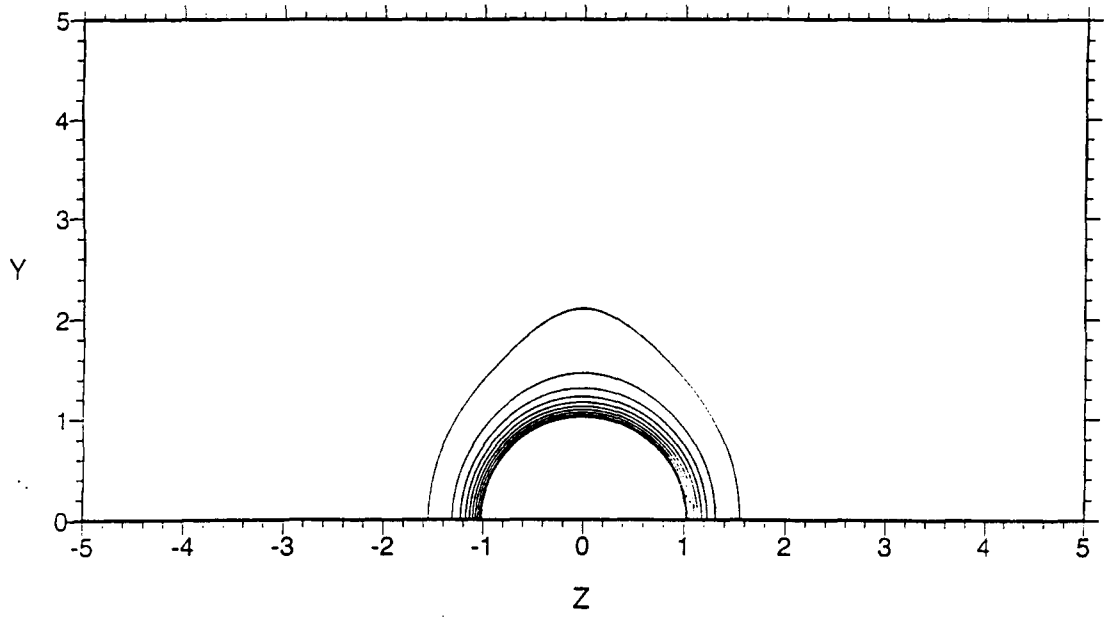

FIGURE 5

CONCENTRATION ISOCONTOURS

BIAXIAL FLOW WITH HOMOGENEOUS REACTION

PE=5.00 K=10.00 R=10.0 ORDER=1 L=70

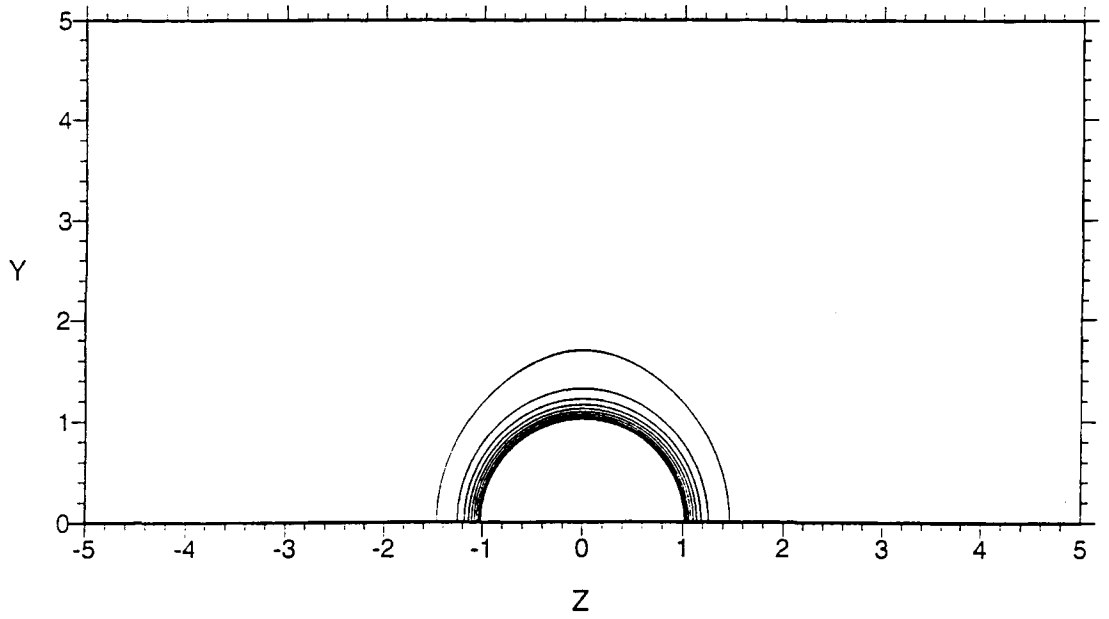

FIGURE 6

CONCENTRATION ISOCONTOURS

BIAXIAL FLOW WITH HOMOGENEOUS REACTION

PE=50.00 K=2.00 R=5.0 ORDER=1 L=70

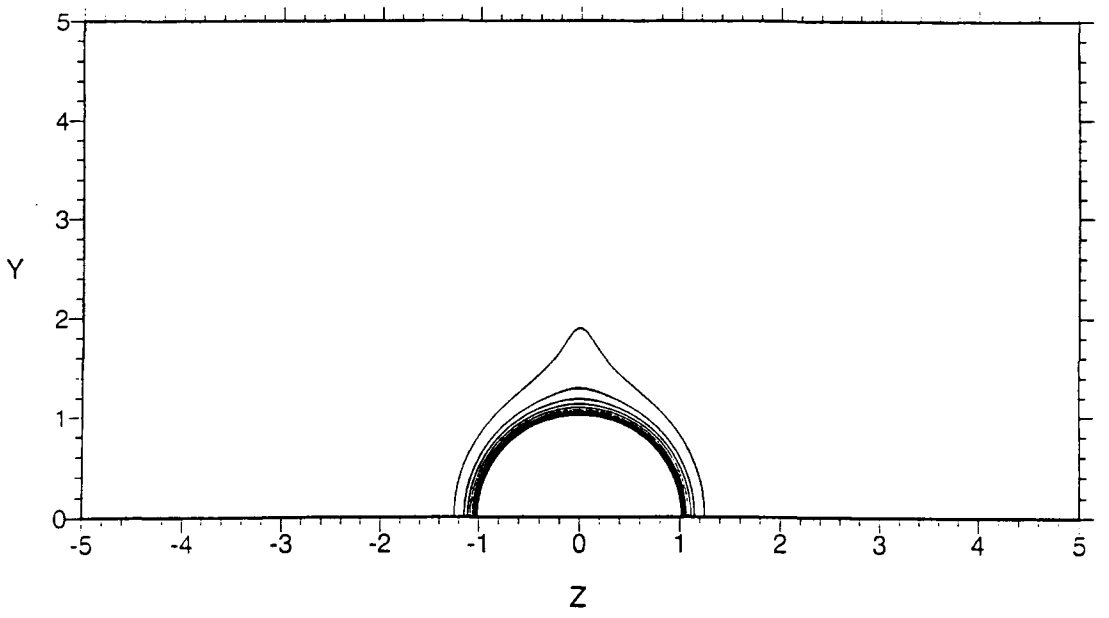

FIGURE 7

CONCENTRATION ISOCONTOURS

BIAXIAL FLOW WITH HOMOGENEOUS REACTION

PE=200.00 K=1.00 R=5.0 ORDER=1 L=70

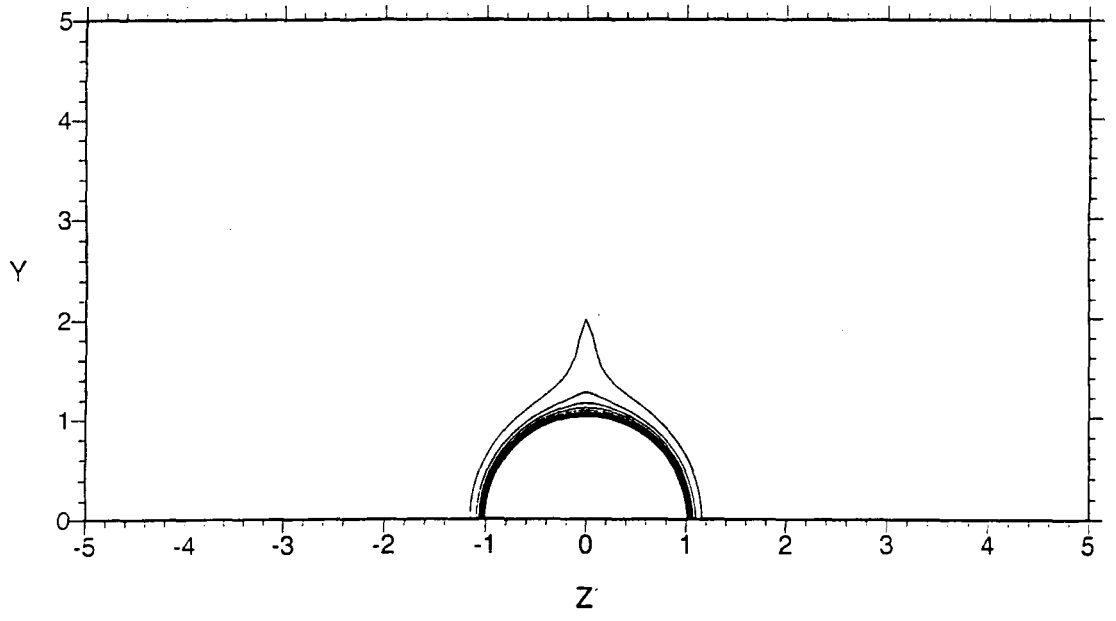

FIGURE 8

CONCENTRATION ISOCONTOURS

BIAXIAL FLOW WITH HOMOGENEOUS REACTION

PE=200.00 K=2.00 R=5.0 ORDER=1 L=70

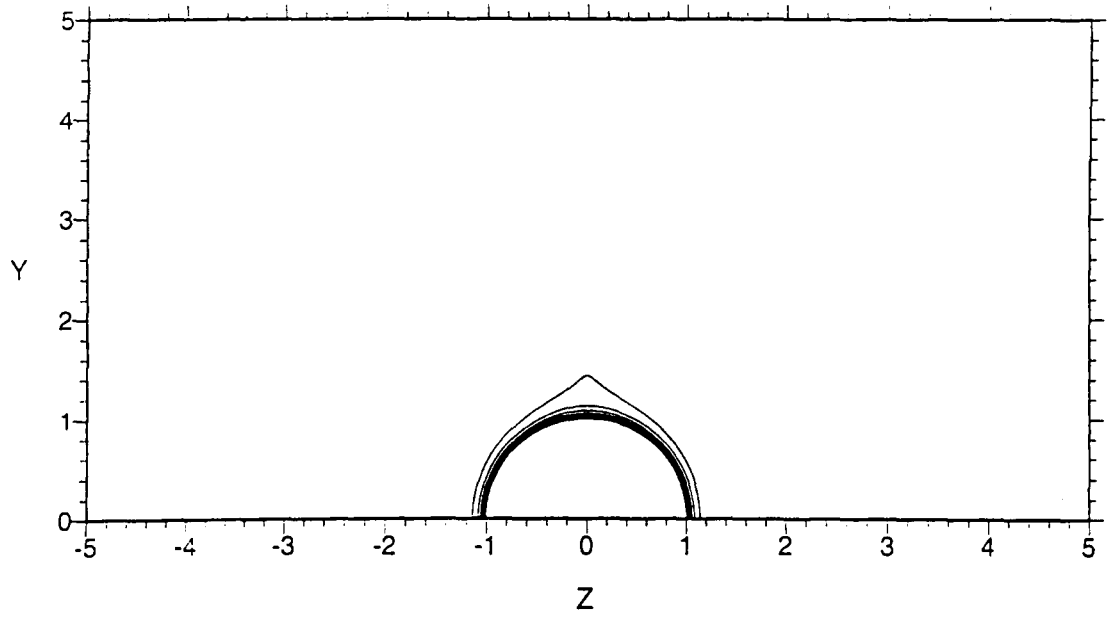

FIGURE 9

CONCENTRATION ISOCONTOURS

BIAXIAL FLOW WITH HOMOGENEOUS REACTION

PE=500.00 K=0.50 R=5.0 ORDER=1 L=70

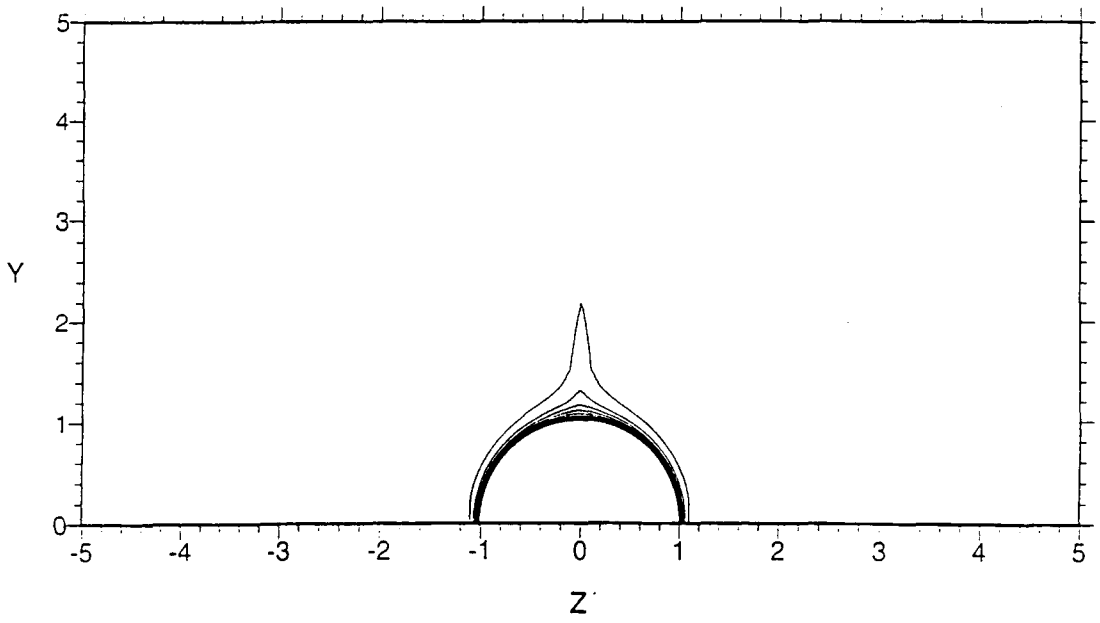

FIGURE 10

CONCENTRATION ISOCONTOURS

UNIAXIAL FLOW WITH HOMOGENEOUS REACTION

PE=5.00 K=5.00 R=10.0 ORDER=1 L=70

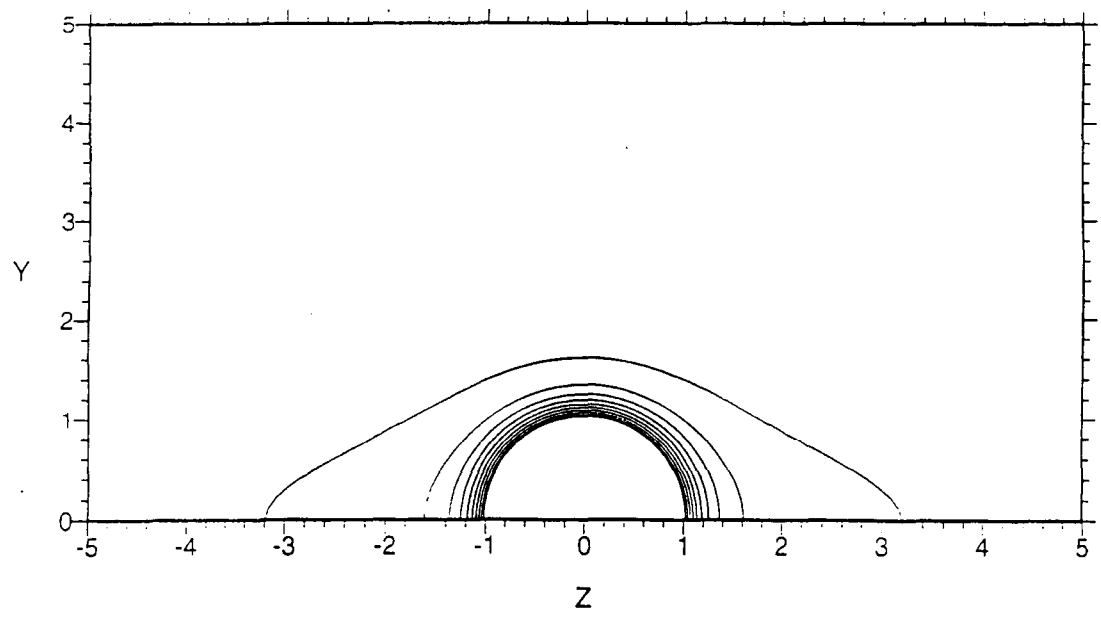

FIGURE 11

CONCENTRATION ISOCONTOURS

UNIAXIAL FLOW WITH HOMOGENEOUS REACTION

PE=5.00 K=10.00 R=10.0 ORDER=1 L=70

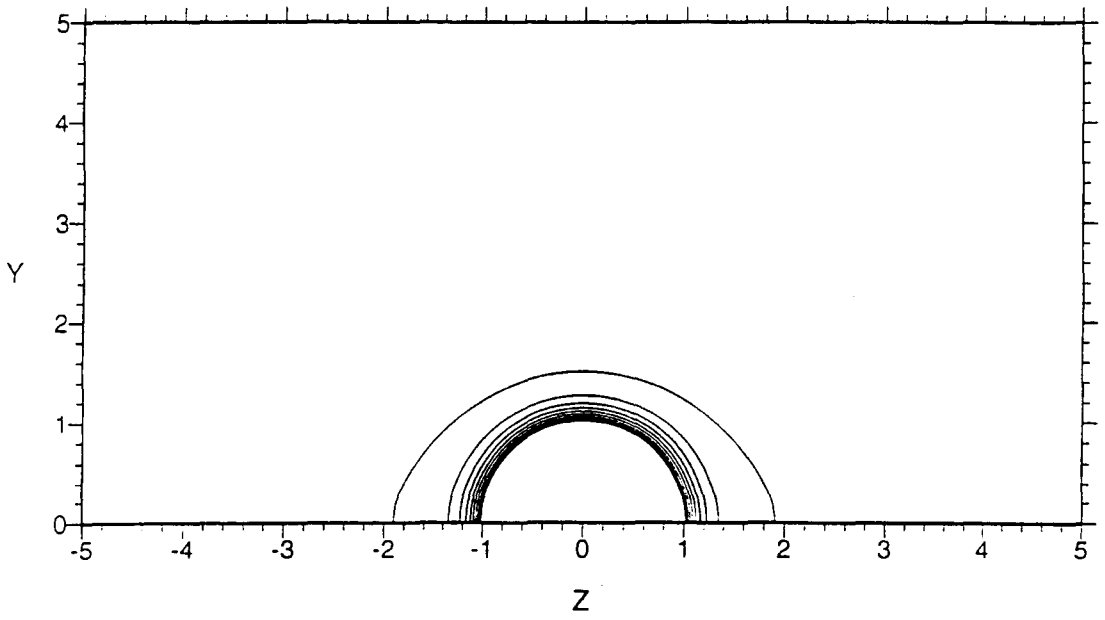

FIGURE 12

CONCENTRATION ISOCONTOURS

UNIAXIAL FLOW WITH HOMOGENEOUS REACTION

PE=50.00 K=5.00 R=5.0 ORDER=1 L=70

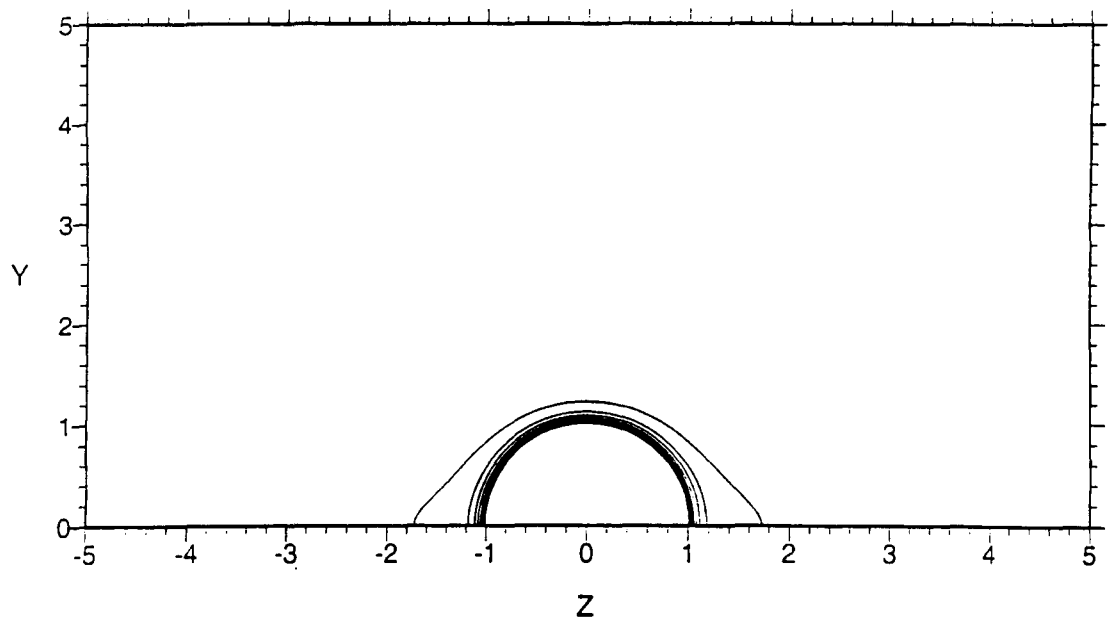

FIGURE 13

CONCENTRATION ISOCONTOURS

UNIAXIAL FLOW WITH HOMOGENEOUS REACTION

PE=50.00 K=10.00 R=5.0 ORDER=1 L=70

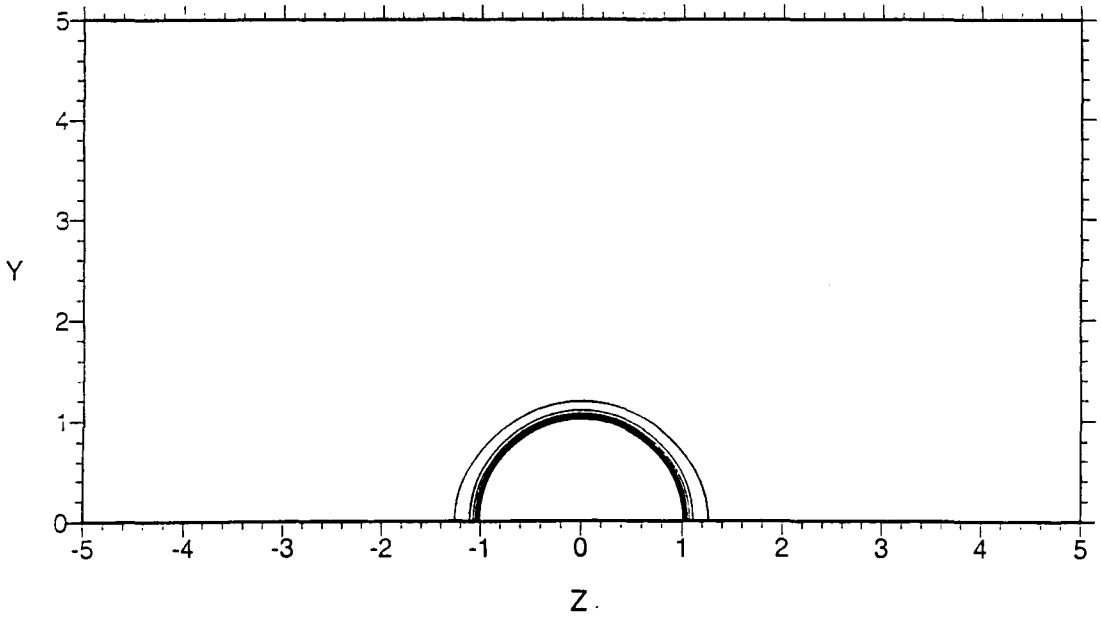

FIGURE 14a

BIAXIAL FLOW WITH HOMOGENEOUS REACTION

K=5; PE=5, 50, 200, 500

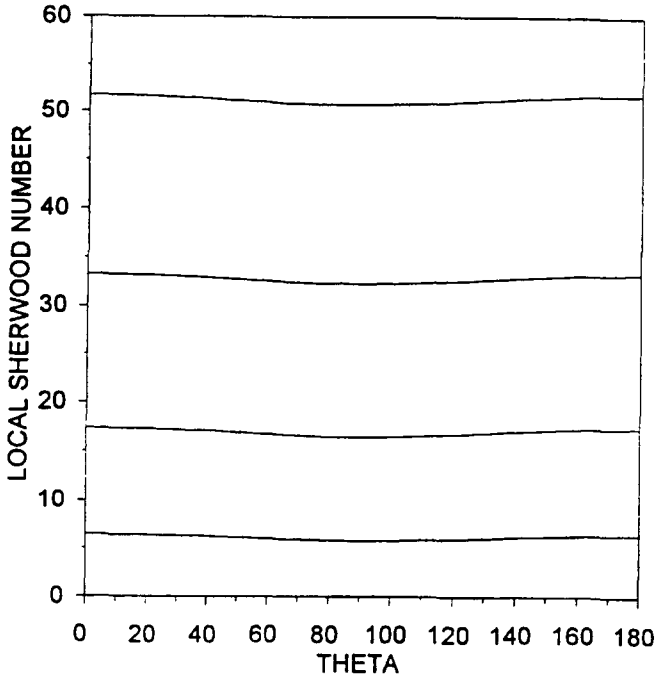

FIGURE 14b

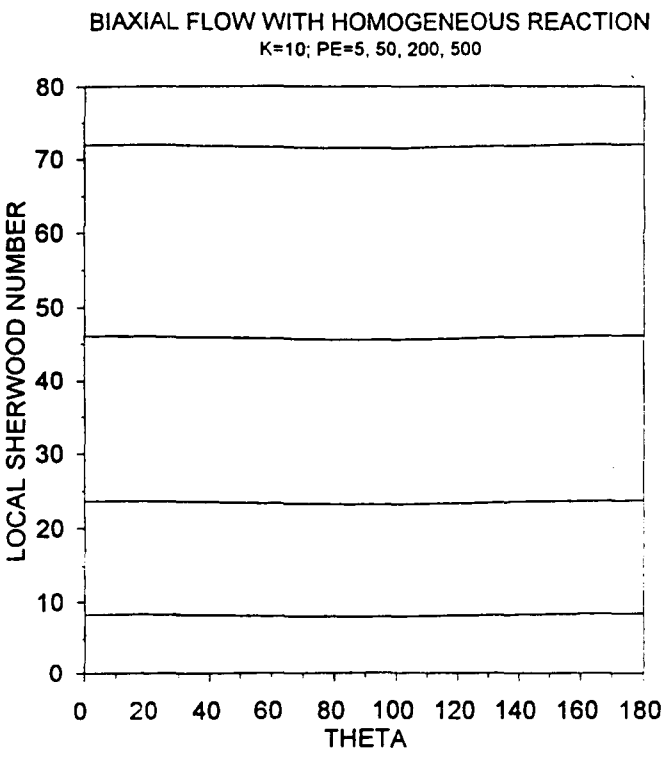

FIGURE 15a

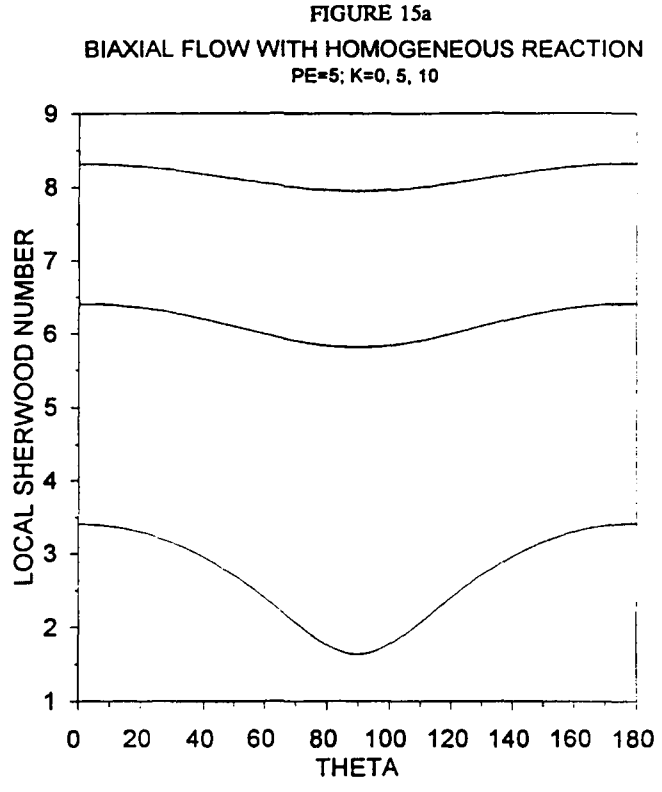

FIGURE 15b

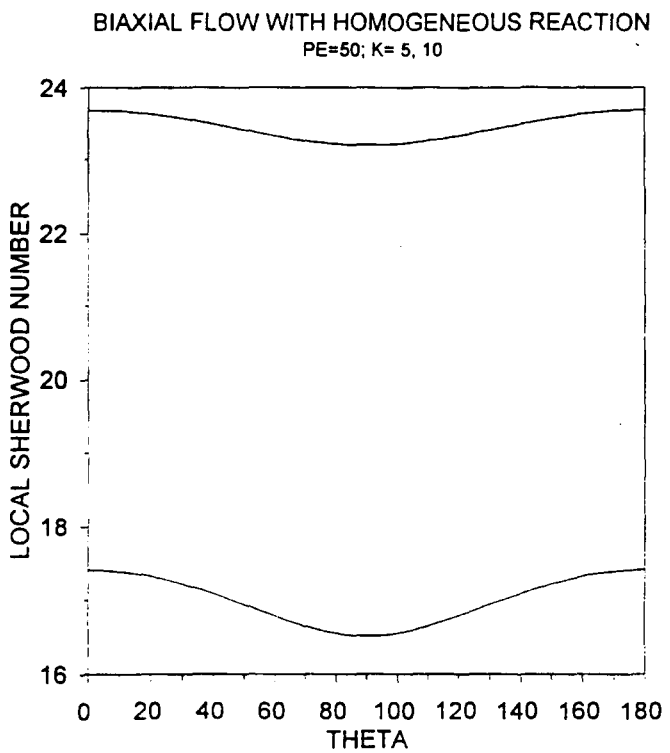

FIGURE 15c

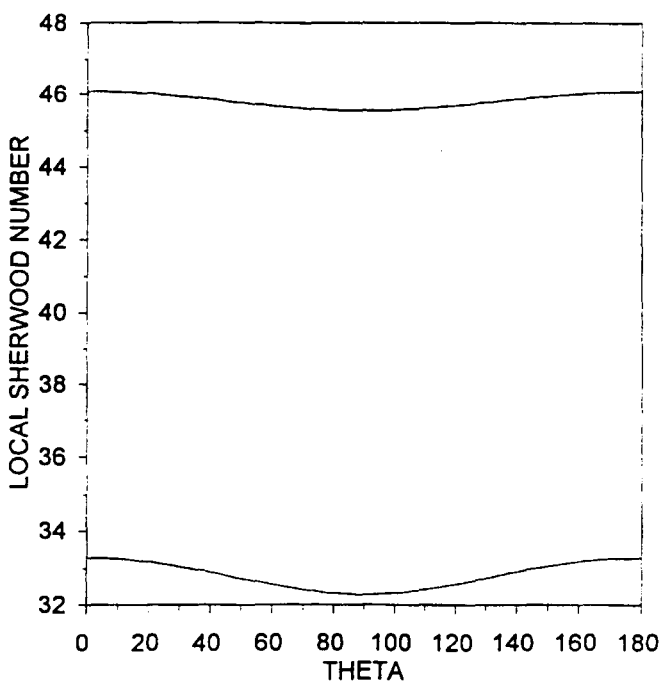

FIGURE 15d

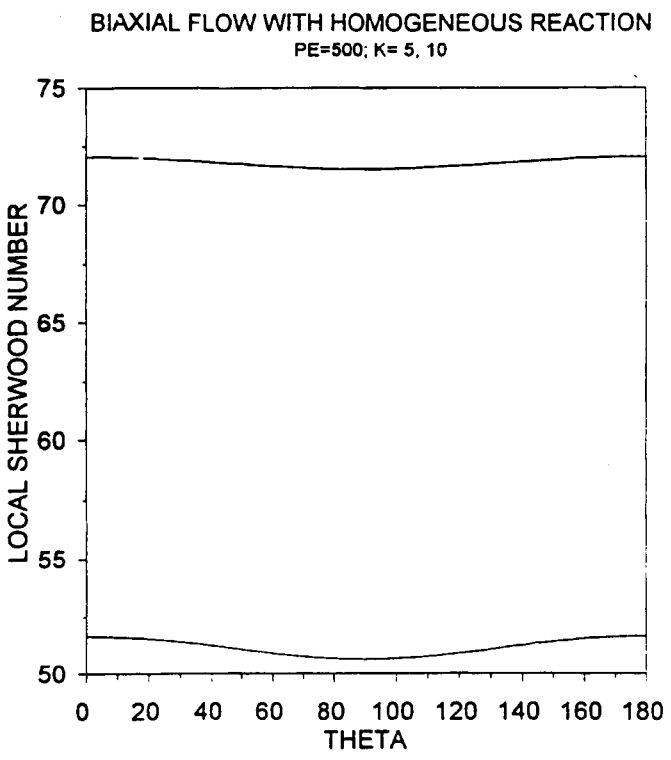

FIGURE 16a

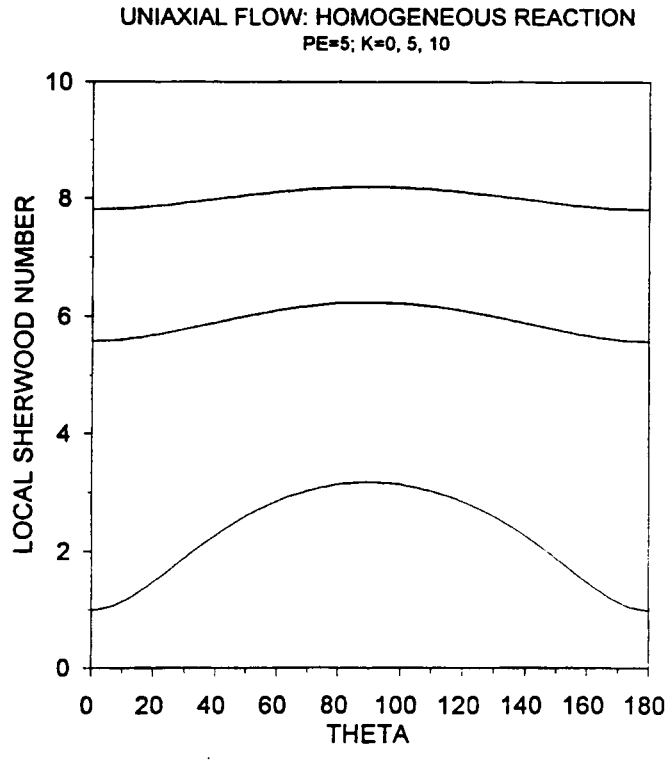

FIGURE 16b

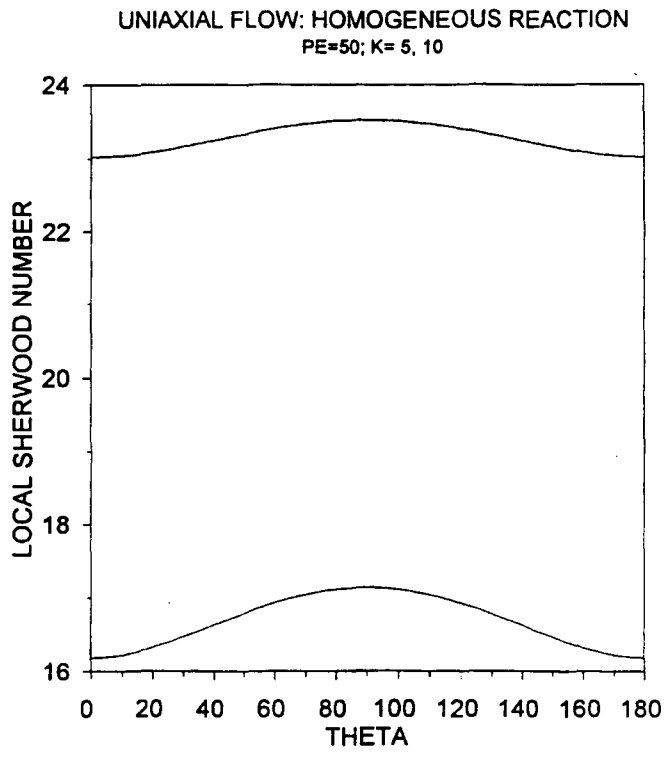

FIGURE 16c

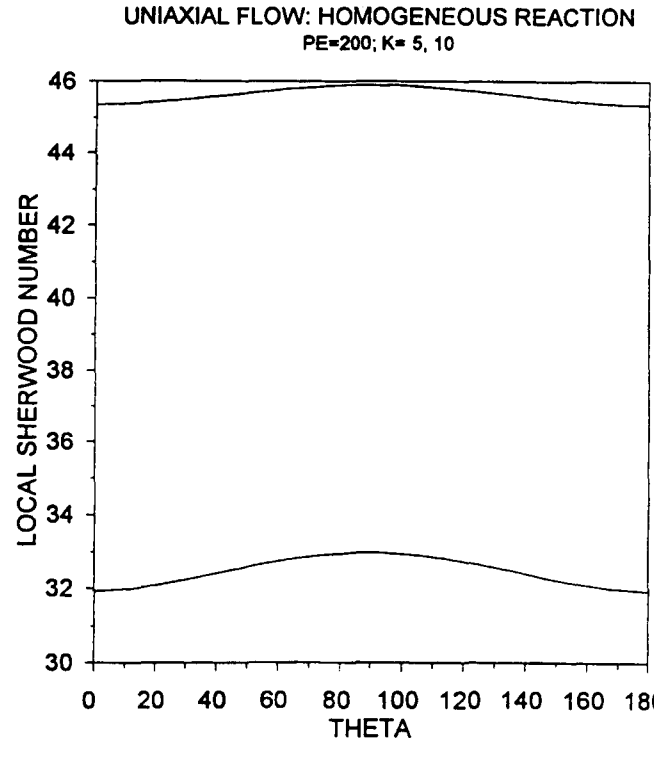

FIGURE 17a

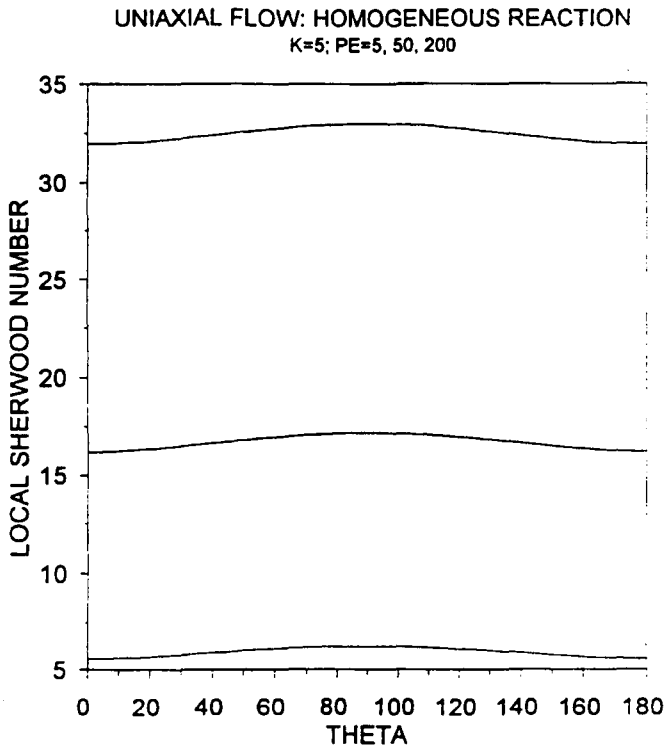

FIGURE 17b

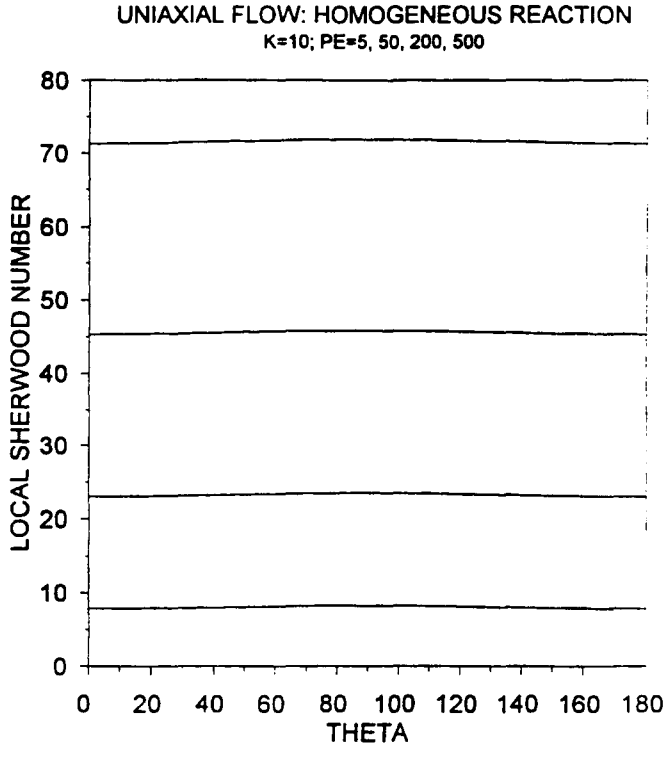

TABLE 1: Average Sherwood Numbers for Biaxial Flow

Pe	K	R	Avg. Sherwood N	NI	NM	NF	NE	N	TOL
5	0	10	2.4222332546	60	600	166	142	70	1E-06
5	1	10	3.4844020321	60	600	135	142	70	1E-06
5	2	10	4.2826214867	60	600	135	142	70	1E-06
5	5	10	6.0326632737	60	600	104	142	70	1E-06
5	10	10	8.0806645862	60	600	101	142	70	1E-06
50	5	5	16.8417150406	100	875	140	142	70	1E-06
50	10	5	23.3676877824	100	875	130	142	70	1E-06
200	5	5	32.6445658252	100	875	219	142	70	1E-06
200	10	5	45.7258627584	100	875	235	142	70	1E-06
500	5	5	51.0160617125	100	875	425	142	70	1E-06
500	10	5	71.7138264523	100	875	202	142	70	1E-06

TABLE 2: Average Sherwood Numbers for Uniaxial Flow

Pe	K	R	Avg. Sherwood N	NI	NM	NF	NE	N	TOL
5	0	10	2.6345022231	60	600	141	142	70	1E-06
5	1	10	3.5533852471	60	600	178	142	70	1E-06
5	2	10	4.3116939874	60	600	189	142	70	1E-06
5	5	10	6.0374513084	60	600	154	142	70	1E-06
5	10	10	8.0814290608	60	600	141	142	70	1E-06
50	5	5	16.8450206823	100	875	309	142	70	1E-06
50	10	5	23.3680425224	100	875	243	142	70	1E-06
200	5	5	32.6462378512	100	875	527	142	70	1E-06
200	10	5	45.7260072732	100	875	353	142	70	1E-06
500	10	5	71.7138969816	100	875	417	142	70	1E-06

NI Number of initial grid points, including the endpoints (NINIT)

NM Maximum number of grid points allowed (MXGRID)

NF Number of final grid points, including the endpoints (NFINAL)

NE Number of (first order) differential equations (NEQNS)

N Number of terms in the eigenfunction expansion

TOL Relative error control parameter

COMPUTATION OF THREE-DIMENSIONAL MIXED CONVECTIVE BOUNDARY LAYER FLOW

Prashant Gadepalli and Muhammad M. Rahman
Department of Mechanical Engineering
University of South Florida
Tampa, Florida

ABSTRACT

The paper presents the numerical solution of heat and mass transfer during cross-flow (orthogonal) mixed convection. In this class of flow, a buoyancy-driven transport in the vertical direction and a forced convective flow in the horizontal direction results in a three-dimensional boundary layer structure adjacent to the plate. The rates of heat and mass transfer are determined by a combined influence of the two transport processes. The equations for the conservation of mass, momentum, energy, and species concentration were solved along with appropriate boundary conditions to determine the distributions of velocity components, temperature, and concentration across the thickness of the boundary layer at different locations on the plate. Results were expressed in dimensionless form using Reynolds number, Richardson number for heat transfer, Richardson number for mass transfer, Prandtl number, and Schmidt number as parameters. It was found that the transport is dominated by buoyancy at smaller vertical locations and at larger distances away from the forced convection leading edge. Effects of forced convection appeared to be very strong at smaller horizontal distances from the leading edge. The cross-stream forced convection enhanced the rate of heat and mass transfer by a very significant amount.

INTRODUCTION

Heat and mass transfer under the combined influence of a vertical buoyant force and an externally-imposed horizontal flow occurs frequently in nature and has several technological applications as well. Some examples of such cross-flow mixed convection are: the cooling of electronic circuit boards by fans, heat transfer from vertical walls in buildings, heat loss mechanisms from solar collectors, mass transfer during a drying process, and wind-driven propagation of fire.

There have been a number of past studies devoted to the understanding of mixed convective heat and mass transfer. These include aiding, opposing, and cross flow situations. Lin et al. (ref.1) have studied the mixed convection problem of an isothermal horizontal plate moving in parallel or reversely to a free stream. They concluded that the heat transfer rate increases significantly with increase in buoyancy, and increase in the velocities of the plate and the free stream. Khouaja et al. (ref.2) studied mixed convection in slender vertical cylinders for power law variation in surface heat flux. They found that the local heat transfer rate increases with increasing Prandtl number, increasing curvature, and increasing value of power law exponent. A vertical flat plate was simulated as a limiting form of the cylinder and provided satisfactory results. Wickern (ref.3) studied mixed convection from an arbitrarily inclined semi-infinite flat plate for different inclination angles and for different Prandtl numbers. He found that for opposing buoyancy forces, singular as well as regular behavior can occur.

In a cross-flow situation, the transport is more complicated because of the three-dimensional nature of the boundary layer flow. In an early study, Young and Yang (ref.4) used a perturbation analysis and found that a weak cross-flow has very little effect on natural convection over a vertical flat surface. Eichorn and Hasan (ref.5) as well as Plumb (ref.6) have obtained similarity solutions for Falkner-Skan type three-dimensional mixed convection. But similarity exists only for certain power law surface

temperature distributions. Evans and Plumb (refs. 7, 8) extended the box scheme developed by Keller and Cebeci (ref.9) to three dimensions and obtained numerical solutions for mixed convection from an isothermal surface in a cross-flow. Rahman and Carey (refs. 10,11) examined the transient behavior of the flow that may precede the final steady state configuration. They looked at heat transfer from a vertical plate in a number of transient conditions. They found that under certain conditions, the local velocity and temperature fields overshoot before reaching the final steady-state configuration.

The present study explored the process of combined heat and mass transfer during cross-flow mixed convection. The three-dimensional cross-flow boundary layer flow was analyzed when buoyancy-driven flow and transport in the vertical direction was the same order of magnitude as the forced convection in the horizontal direction. Equations governing the conservation of mass, momentum, energy, and species concentration were solved numerically to predict velocity, temperature, and concentration distribution across the boundary layer and the variation of heat and mass transfer rate over the plate. A parametric study was performed to determine the effects of Reynolds, Richardson (Ri and Ri^*), Prandtl, and Schmidt numbers.

MATHEMATICAL MODEL

The schematic of the problem under consideration is shown in Figure 1. A vertical flat plate of finite length and height is placed in an extensive horizontal fluid stream. The surface of the plate is maintained at a constant temperature T_0 and the concentration of the diffusing medium at the surface remains constant at C_0. The ambient fluid is at a constant temperature T_∞ and has the diffusing species with a constant concentration C_∞. It is assumed that $T_0 > T_\infty$ and $C_0 > C_\infty$. The velocity of the fluid in the free stream far away from the plate remains constant at w_∞. A three-dimensional boundary layer flow develops adjacent to the plate due to the combined effects of the horizontal forced flow and buoyancy force due to temperature and concentration differences acting in the vertical direction. The characteristics of the mixed convective flow are determined by the relative magnitudes of the forced and buoyancy-driven flows.

The equations describing the conservation of mass, momentum, energy, and concentration inside the boundary layer for steady, incompressible, laminar flow, with constant fluid properties (Boussinesq approximation for buoyancy) are given by:

$$\frac{\partial u}{\partial x}+\frac{\partial v}{\partial y}+\frac{\partial w}{\partial z}=0 \qquad (1)$$

$$u\frac{\partial u}{\partial x}+v\frac{\partial u}{\partial y}+w\frac{\partial u}{\partial z}=\nu\frac{\partial^2 u}{\partial x^2}+g\beta\,(T-T_\infty)+g\beta^*\,(C-C_\infty) \qquad (2)$$

$$u\frac{\partial w}{\partial x}+v\frac{\partial w}{\partial y}+w\frac{\partial w}{\partial z}=\nu\frac{\partial^2 w}{\partial x^2} \qquad (3)$$

$$u\frac{\partial T}{\partial x}+v\frac{\partial T}{\partial y}+w\frac{\partial T}{\partial z}=\alpha\frac{\partial^2 T}{\partial x^2} \qquad (4)$$

$$u\frac{\partial C}{\partial x}+v\frac{\partial C}{\partial y}+w\frac{\partial C}{\partial z}=D\frac{\partial^2 C}{\partial x^2} \tag{5}$$

The boundary conditions are given by:

$$x = 0 : v = 0,\ w = 0,\ T = T_0,\ C = C_0 \tag{6}$$

$$x \to \infty : v = 0,\ w = w_\infty,\ T = T_\infty,\ C = C_\infty \tag{7}$$

$$y = 0 : v = 0,\ w = w_\infty,\ T = T_\infty,\ C = C_\infty \tag{8}$$

$$z = 0 : v = 0,\ w = w_\infty,\ T = T_\infty,\ C = C_\infty \tag{9}$$

It is convenient to define the following non-dimensional variables at this point.

$$\theta = \frac{T - T_\infty}{T_0 - T_\infty} \quad ; \quad \psi = \frac{C - C_\infty}{C_0 - C_\infty}$$

$$U = \frac{u}{w_\infty} \ , \quad V = \frac{v}{w_\infty} \ , \quad W = \frac{w}{w_\infty}$$

$$X = \frac{x}{L} \ , \quad Y = \frac{y}{L} \ , \quad Z = \frac{z}{L}$$

Using the above non-dimensionalized variables, the governing equations (1-5) can be expressed as:

$$\frac{\partial U}{\partial X}+\frac{\partial V}{\partial Y}+\frac{\partial W}{\partial Z}= 0 \tag{10}$$

$$U\frac{\partial V}{\partial X}+V\frac{\partial V}{\partial Y}+W\frac{\partial V}{\partial Z}=\frac{1}{Re}\frac{\partial^2 V}{\partial X^2}+Ri\theta+Ri^*\psi \tag{11}$$

$$U\frac{\partial W}{\partial X}+V\frac{\partial W}{\partial Y}+W\frac{\partial W}{\partial Z}=\frac{1}{Re}\frac{\partial^2 W}{\partial X^2} \tag{12}$$

$$U\frac{\partial\theta}{\partial X}+V\frac{\partial\theta}{\partial Y}+W\frac{\partial\theta}{\partial Z}=\frac{1}{Re.Pr}\frac{\partial^2\theta}{\partial X^2} \qquad (13)$$

$$U\frac{\partial\psi}{\partial X}+V\frac{\partial\psi}{\partial Y}+W\frac{\partial\psi}{\partial Z}=\frac{1}{Re.Sc}\frac{\partial^2\psi}{\partial X^2} \qquad (14)$$

And, the boundary conditions (6-10) are transformed to :

$$X = 0 : V = 0, \quad W = 0, \quad \theta = 1, \quad \psi = 1 \qquad (15)$$

$$X \to \infty : V = 0, \quad W = 1, \quad \theta = 0, \quad \psi = 0 \qquad (16)$$

$$Y = 0 : V = 0, \quad W = 1, \quad \theta = 0, \quad \psi = 0 \qquad (17)$$

$$Z = 0 : V = 0, \quad W = 1, \quad \theta = 0, \quad \psi = 0 \qquad (18)$$

The governing equations (10-14) contain the Reynolds number, Re, Prandtl number, Pr, Schmidt number, Sc, Richardson number, Ri, and Richardson number for mass transfer Ri^* as parameters. The relative magnitude of these parameters determines the characteristics of the flow. The effects of each of these parameters on the flow configuration has been studied during the course of the present investigation. The parameters were varied over the following range. Re = 10^3, 10^4, and 10^5; Pr = 0.7 and 7 (corresponding to air and water respectively); Sc = 0.6 and 580 (nominally for water vapor-air system and sodium chloride - water system); Ri = 1, 10, and 100; and Ri^*=1, 10 and 100.

COMPUTATIONAL PROCEDURE

The governing transport equations, along with the boundary conditions described in the previous section were solved numerically using the PHOENICS computer program. A Cartesian grid structure covering the entire boundary layer region was used for the computation. The distribution of cells in the computation domain was determined from a series of test runs with different number of cells in the x, y, and z directions. It was found that 60x20x20 cells are adequate for the present computation. The finite volume equations were derived by using the principles of conservation of mass, momentum, energy, and species concentration at each cell. The variables were stored in a staggered fashion where they made more physical sense for cell conservation. For each cell, the velocity components were stored at downstream boundaries, whereas all pressures and temperatures were stored at the cell center. The hybrid difference scheme demonstrated by Patankar (ref.12) was used to preserve the relative contribution of convection and diffusion to a cell from its neighbor in terms of cell Peclet number. The discretized equations were solved by using the SIMPLEST algorithm (ref.13). The convergence of the numerical solution was monitored by spot checking of field values during the course of the computation and by calculating and monitoring the sum of residuals for each equation. Iterations were continued until sum of residuals for each computational cell dropped below 10^{-7}. All equations had to be solved simultaneously because of the coupling of velocity, temperature, and concentration through the buoyancy terms.

RESULTS AND DISCUSSION

The numerical solution procedure described in the last section was used to compute the velocity components, and temperature and concentration distributions for different combinations of Reynolds number, Richardson number (Ri and Ri^*), Prandtl number, and Schmidt number. These results were used to predict Nusselt and Sherwood numbers which quantified the rates of heat and mass transfer. Figure 2 shows the variation of the vertical component of velocity across the thickness of the boundary layer for a combination of $Re = 10^3$, $Ri = 1$, $Ri^* = 0$, and $Pr = 0.7$. Physically, it corresponds to pure heat transfer from an isothermal vertical plate to air. The plot shows the velocity profile at four different locations on the plate. Of these four locations chosen, two were near the leading edge and the other two farther downstream (looking at both natural convection and forced flow directions). These were chosen to observe the increasing influence of the boundary layer growth. It is observed that, at all four locations, the vertical component of velocity has a bell shaped structure typical for natural convection with zero velocity at the wall as well as at the edge of the boundary layer. For any given value of Z (horizontal location), the magnitude of V increases with increasing Y (vertical location). This is because of the growth of buoyancy-induced boundary layer in the vertical direction of the plate. The effects of buoyancy becomes stronger with increase in vertical height. For any given Y, there is a very significant increase of buoyant flow with increase in the horizontal coordinate. The forced convection boundary layer develops in the horizontal direction. The effects of forced flow remains strong near the near edge of this boundary layer. As the fluid particles move downstream, their horizontal component of velocity decreases because of the viscous resistance from the wall. With increase in horizontal location, the effects of forced convection become weaker, and buoyancy becomes the more dominant transport mechanism.

Figure 3 shows the variation of horizontal component of velocity across the boundary layer. As expected, the horizontal component of velocity increases monotonically from zero to the free stream value with increase in X at locations on the plate. It may be noticed that at smaller values of Z, there is no significant change of W-velocity profile with vertical distance. This is because buoyancy is relatively weaker in that region. Further downstream in the horizontal direction, the magnitude of W-velocity decreases with Y because of a significant increase in buoyancy induced flow. The continuity has to be preserved at all locations of the flow. Therefore, a steeper variation of one velocity component results in a corresponding variation in the other velocity component. The distribution of temperature across the thickness of the boundary layer is demonstrated in Figure 4 for the same combination of parameters used in figures 2 and 3. Analogous to a two-dimensional boundary layer flow (for either natural or forced convection), the temperature decreases monotonically with X at all locations on the plate. The slope of the temperature curve at the wall is proportional to the rate of heat transfer from the wall. It may be noticed that heat transfer is larger near both forced and natural convection leading edges and increases as the boundary layer increases in thickness. Comparing with figure 3, it can be noticed that the thickness of the thermal boundary layer is somewhat larger because of the Prandtl number smaller than 1.

The effects of Reynolds and Prandtl number on the flow and heat transfer are demonstrated in figures 5 and 6. Figure 5 shows the variation of the vertical component of velocity across the boundary layer for a given plate location, for a number of combinations of Reynolds and Prandtl number. The corresponding plots for temperature distribution are shown in figure 6. It can be noticed that with increase in Reynolds number, the thickness of both velocity and thermal boundary layer decrease. The decrease in boundary layer thickness causes a slight increase for the peak of the vertical velocity even though the Richardson number is preserved constant. With increase in Reynolds number, the slope of the temperature curve at the wall also increases. This indicates a larger rate of heat transfer. The increase of heat transfer with fluid velocity is obviously expected. With increase of Prandtl number, both vertical component of velocity and boundary layer thickness decrease. The temperature curve becomes steeper showing an increase of heat transfer rate with Prandtl number.

The effects of the variation of Richardson number (Ri) is explored in figures 7 and 8. Richardson number indicates the ratio of buoyant force and the inertia due to forced convection. The usual definition of Richardson number is modified in the present study with the plate aspect ratio to account for different lengths and heights of the plate. For a given Reynolds number and aspect ratio, a higher Richardson number (Ri) implies a higher Grashof number (Gr_H), which in turn means a stronger natural convection component and smaller boundary layer thickness. This can be clearly seen in figure 7 where the vertical component of velocity is plotted for a number of combinations of Reynolds and Prandtl number. Comparing the peak values of V, it can be realized that a ten time increase in Ri results in more than 3 times increase in vertical velocity. Results for both Prandtl numbers confirm the same trend, but a larger Prandtl number results in a smaller boundary layer thickness and a smaller vertical velocity. In figure 8, it can be noticed that the temperature curve becomes steeper and the rate of heat transfer at the wall increases with increase in both Reynolds and Prandtl numbers.

The distribution of Nusselt number over the plate is demonstrated in figure 9, where the variation of Nusselt number with the horizontal coordinate is plotted for two different vertical locations. Results for both fluid systems (Pr=0.7 and 7) are shown in the figure. The Nusselt number is calculated here with the vertical height as the length scale. The plot therefore essentially demonstrates the variation of the actual heat transfer coefficient. In a cross-flow situation, both vertical and horizontal distances are useful length scales and can be used in the calculation of dimensionless parameters. The Nusselt number is maximum near the vertical leading edge, drops down very rapidly as one proceeds along Z and finally reaches a stable value at large values of Z. The magnitude of Nu for any given Reynolds number and vertical location is significantly higher for an higher Prandtl number. This is because of the smaller boundary layer thickness and steeper temperature profile at the wall. The effects of Reynolds number (strength of the forced flow) on Nusselt number is shown in figure 10. It can be noticed that the increase of Nusselt number with Reynolds number is very significant at all locations on the plate. Therefore, a reasonable cross-flow may very significantly alter the fluid flow and heat transfer scenario in an otherwise natural convection situation. Comparing with the magnitude of Nusselt number for pure natural convection flow, it was noticed that an order of magnitude increase in heat transfer was noticed at smaller Z-locations. The enhancement factor became smaller at larger values of horizontal coordinate.

Mass transfer from a vertical plate in the presence of a horizontal cross-flow was studied for two specific fluid systems. These are: the evaporation of water from a porous vertical wall which involves the diffusion of water vapor to ambient air; and the dissolution of sodium chloride into water. The Schmidt number for these diffusion processes under normal atmospheric pressure and temperature are 0.6 and 580, respectively. To illuminate the mass transfer process, the vertical wall containing the diffusing medium is assumed to be at the same temperature as the free stream. In addition Soret and Dufor effects are neglected. Therefore, Richardson number for heat transfer (Ri) is zero during these mass transfer processes. The buoyant force is created due to concentration difference and the corresponding Richardson number is labeled as Ri^*.

The variation of the vertical fluid velocity and the concentration of water vapor into air are shown in figures 11 and 12 for different locations of the plate. It is not surprising that the V distribution looks very similar to that in figure 2 and concentration distribution looks similar to that of temperature distribution presented in figure 3. This is because, in either case though the cause of the buoyancy force is different, the resulting effect is almost the same. Also, we are considering the case of $Ri^*=1$, which means that the buoyancy forces are about the same order of magnitude of the forced flow. Hence, even though the physics of the problem is totally different for heat transfer and for mass transfer, mathematically they are very similar. For locations near the vertical leading edge (smaller Z), forced convective flow predominates and there is not much change in the V or T profiles with Y. But as one proceeds further downstream, the natural convective effects begin to show up and the magnitude of the peak value of V increases. From figure 12, it can be seen that the concentration gradient is higher at

locations nearer the leading edge, thus implying that the rate of mass transfer is higher here.

The effects of Reynolds number on the vertical velocity and concentration profiles for a particular location in the plate is shown in figures 13 and 14. A larger Reynolds number decreases the boundary layer thickness and increases the slope of the concentration curve. Therefore, the rate of mass transfer increases. The effect of Schmidt number is very significant. It significantly enhances the rate of mass transfer. The vertical velocity for the dissolution of NaCl into water is much smaller in magnitude compared to the vertical velocity attained during diffusion of water vapor into air. The vertical velocity, V increases greatly with increase in Ri* (figure 15). This is due to the fact that for any given values of Reynolds number and any aspect ratio of the plate, Ri^* is directly proportional to Gr_H^*, which controls the buoyancy force. Increase in Ri* causes reduction of the thermal boundary layer thickness and results in steeper concentration profiles, suggesting a high diffusion rate of the species. Comparing the two fluid systems, the rate of mass transfer is larger for Nacl-H_2O system owing to much steeper concentration profile at the wall.

The Sherwood number (Sh) variation along the Z direction is plotted in figure 17 for different Y-locations for a fixed Re and Ri*. Results for both flow systems has been shown in this plot. Analogous to heat transfer, the mass transfer rate is largest near the leading edge for forced convection, diminishes monotonically with Z, and approaches a constant value at locations far away from the leading edge. The Sherwood number is higher for higher values of Y and increases significantly with Sc, thus stressing the importance of fluid properties in determining the mass transfer coefficient. The variation of Sh along the Z-direction for different values of Re, for Sc=0.6 and Sc=580 is shown in figure 18. It can be seen that increase in Reynolds number increases Sh significantly. This effect is more pronounced at locations near the forced convective leading edge. Therefore, the presence of a cross-flow may very significantly enhance the rate of mass transfer in practical diffusion processes.

CONCLUSIONS

The objective of the present analysis was to identify the relative importance of the free and forced mode of transport at different locations over a vertical flat plate in cross-flow and also to determine the influence of the different dimensionless parameters on the flow structure and on the rate of heat and mass transfer. It was found that forced convection dominates at locations near the vertical leading edge and natural convection attains importance at locations further downstream. The heat as well as mass transfer coefficients are higher at the leading edge owing to smaller thermal boundary layer thickness and steeper gradients of temperature and concentration. With increase in Reynolds number and/or Prandtl number, the boundary layer thickness became smaller and both heat and mass transfer coefficient increased. A larger Richardson number (Ri or Ri^*) resulted in larger buoyancy-induced transport. The combined effects of natural and forced convection resulted in much larger overall rate of heat and mass transfer.

NOMENCLATURE

A	Aspect ratio, ratio of the length of the plate to its height (L/H)
C	Mass concentration
D	Mass diffusivity
g	Acceleration due to gravity
G	Mass transfer coefficient
Gr_H	Grashof number for heat transfer, $g\beta H^3 (T_w - T_\infty/\nu^2$
Gr^*_H	Grashof number for mass transfer, $g\beta^* H^3 (C_0 - C_\infty/\nu^2$

h	Heat transfer coefficient
H	Height of the plate (in the y-direction)
k	Thermal conductivity
L	Length of the plate (in the z-direction)
Nu	Nusselt number, hy/k
Pr	Prandtl number
Re	Reynolds number, $w_\infty L/\nu$
Ri	Richardson number for heat transfer, $Gr_H A^3/ Re^2$
Ri^*	Richardson number for mass transfer, $Gr_H^* A^3/ Re^2$
Sc	Schmidt number
Sh	Sherwood number, $Gy/\varrho D$
T	Temperature
u	Velocity component in the x-direction
U	Dimensionless velocity component in the x-direction, u/w_∞
v	Velocity component in the y-direction
V	Dimensionless velocity component in the y-direction, v/w_∞
w	Velocity component in the z-direction
W	Dimensionless velocity component in the z-direction, w/w_∞
x	Normal coordinate
X	Dimensionless normal coordinate, x/L
y	Vertical coordinate
Y	Dimensionless vertical coordinate, y/L
z	Horizontal coordinate
Z	Dimensionless horizontal coordinate, z/L

Greek Symbols

α	Thermal diffusivity
β	Coefficient of thermal expansion
β^*	Volume expansion coefficient for concentration
ν	Kinematic viscosity
θ	Dimensionless temperature, $(T- T_\infty) / (T_0 - T_\infty)$
ψ	Dimensionless concentration, $(C - C_\infty) / (C_0 - C_\infty)$
ϱ	Density

Subscripts

0	Plate-fluid interface
∞	Free-stream condition

REFERENCES

1. Lin, H.T.: Wu, K.Y.; and Hoh, H.L.: Mixed Convection from an Isothermal Horizontal Plate Moving in Parallel or Reversely to a Free Stream. Int. J. Heat Mass Transfer., vol.36, no.14,1993, pp. 3547-3554.

2. Khouaja, H.; Chen, T.S., and Armaly, B.F.: Mixed Convection Along Slender Vertical Cylinders with Variable Surface Heat Flux. Int. J. Heat Mass Transfer., vol.34, no.1, 1991, pp. 315-319.
3. Wickern, G.: Mixed Convection From an Arbitrarily Inclined Semi-Infinite Flat Plate. Int. J. Heat Mass Transfer., vol.34, 1991, pp. 1935-1957.
4. Young, R.J.; and Yang, K.T.: Effect of Small Cross-Flow and Surface Temperature Variation of Laminar Free Convection Along a Vertical Plate., ASME J. of Applied Mechanics, vol. 30, 1963, pp. 252-256.
5. Eichhorn, R.; and Hasan, M.M.: Mixed Convection About a Vertical Surface in Cross-Flow: A Similarity Solution., ASME J. of Heat Transfer, vol. 102, 1980, pp. 775-777.
6. Plumb, O.A.: The Effect of Crossflow on Natural Convection from Vertical Heated Surfaces. ASME paper no. 80-HT-71, 1980.
7. Evans, G.H.; and Plumb, O.A.: Laminar Mixed Convection from a Vertical Heated Surface in a Cross-Flow. ASME J. of Heat Transfer., vol.104, 1982, pp. 554-558.
8. Evans, G.H.; and Plumb, O.A.: Numerical and Approximate Numerical Solution to a Three-Dimensional Mixed Convection Boundary Layer Flow. Numerical Heat Transfer, vol. 5, 1982, pp. 287-298.
9. Keller, H.B.; Cebeci, T.: Accurate Numerical Methods for Boundary Layers, I. Two-Dimensional Laminar Flows. Proc. 2nd Int. Conference on Numerical Methods in Fluid Dynamics., Lecture Notes in Physics, vol. 8, Springer-Verlag, New York, 1971.
10. Rahman, M.M.; and Carey, V.P.: Transient Cross-Flow Mixed Convection Adjacent to an Isothermal Vertical Plate in Air. Proc. 8th Int. Heat Transfer Conf., San Fransisco, vol. 3, 1986, pp. 1439-1444.
11. Rahman, M.M.; and Carey, V.P.: Steady and Transient Mixed Convection Near a Vertical Uniformly Heated Surface Exposed to Horizontal Fluid Flow. Numerical Heat Transfer, vol. 19, 1986, pp. 327-347.
12. Patankar, S.V.: Numerical Heat Transfer and Fluid Flow. Hemisphere Publishing, Washington, D.C., 1980.
13. Spalding, D.B.: Mathematical Modeling of Fluid Mechanics, Heat Transfer and Chemical Reaction Processes. A Lecture Course, CFDU Report, HTS/80/1, Imperial College, London, 1980.

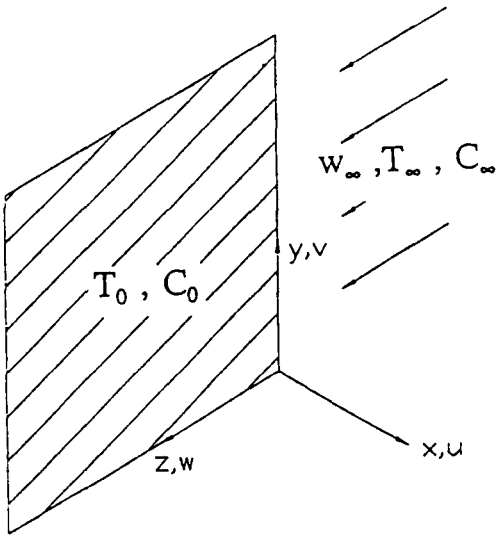

Figure 1. Schematic of the physical problem

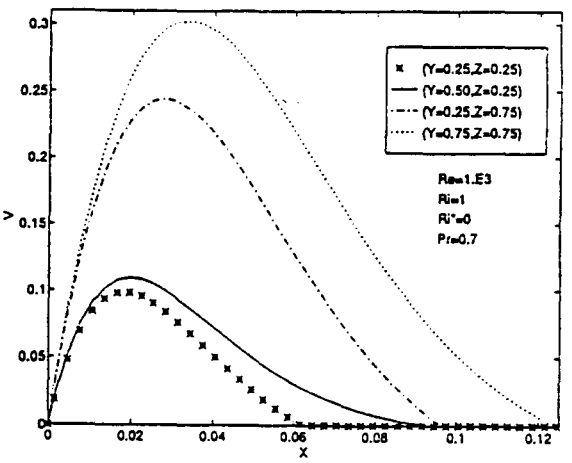

Figure 2. Vertical velocity profile at different locations on the plate

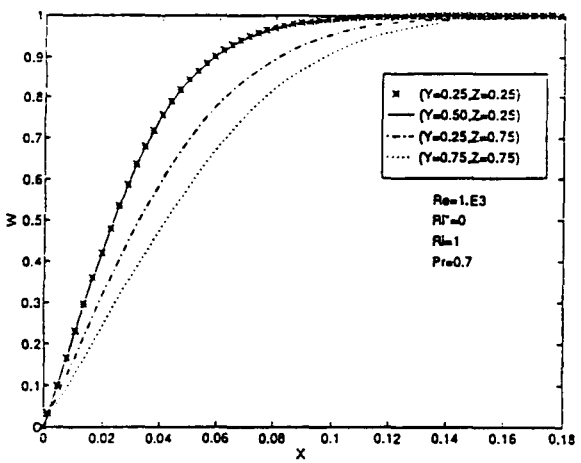

Figure 3. Horizontal velocity profile at different locations on the plate

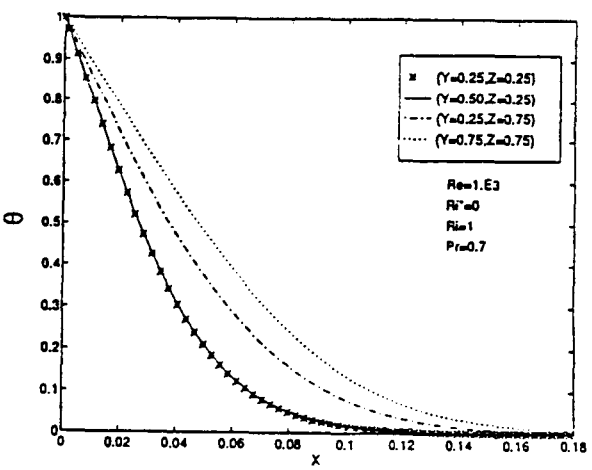

Figure 4. Temperature distribution at different locations on the plate

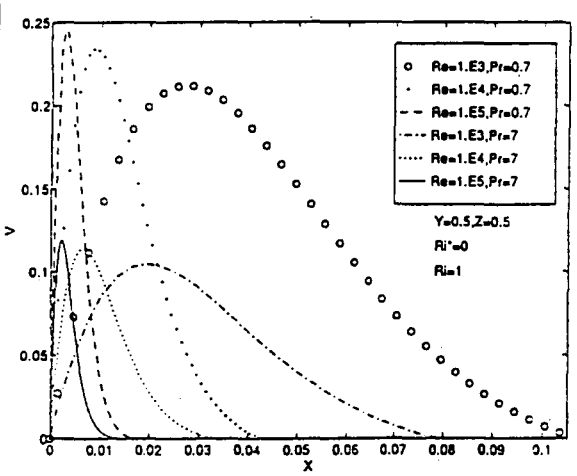

Figure 5. Vertical velocity profile at different Reynolds number

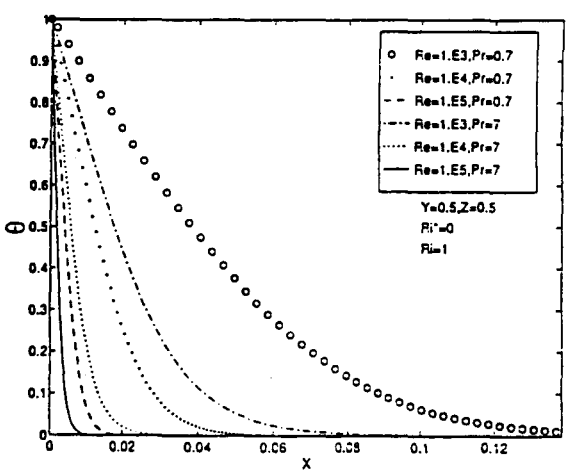

Figure 6. Temperature distribution at different Reynolds number

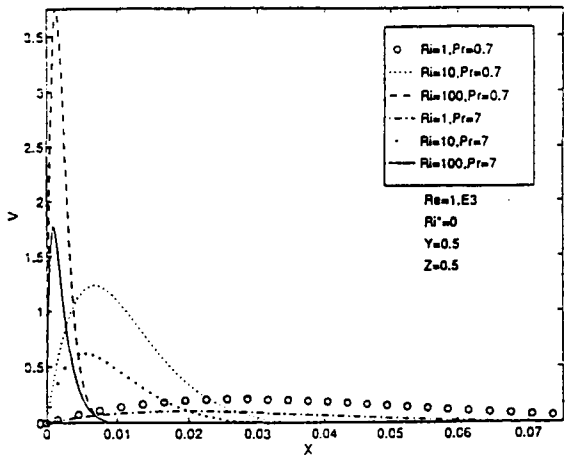

Figure 7. Vertical velocity profile at different Richardson number

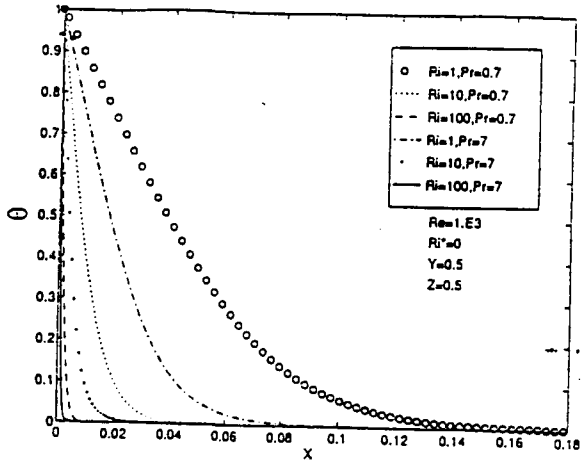

Figure 8. Temperature distribution at different Richardson number

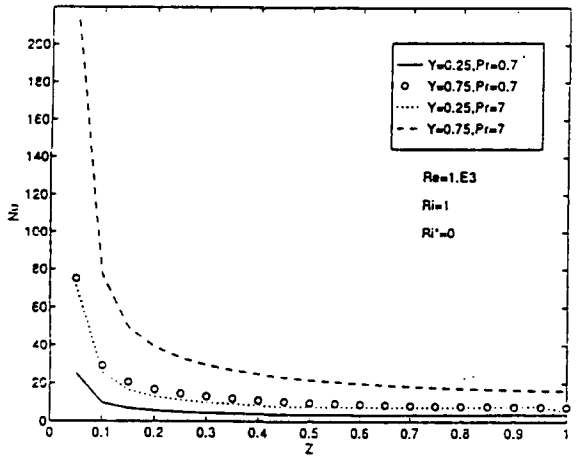

Figure 9. Nusselt number variation over the plate

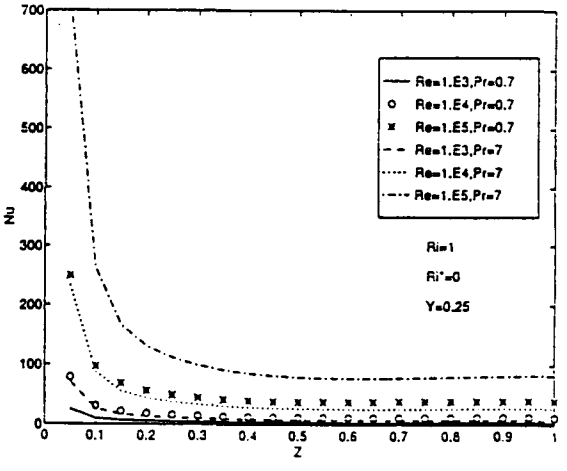

Figure 10. Nusselt number variation at different Reynolds number

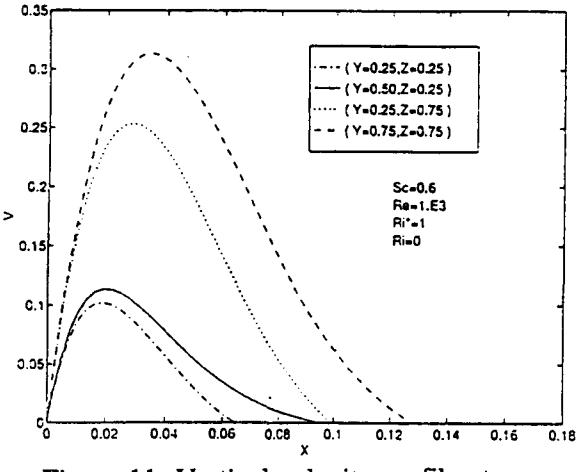

Figure 11. Vertical velocity profile at different locations on the plate

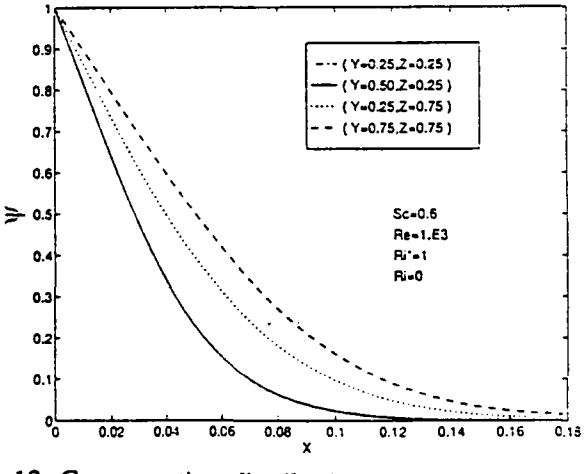

Figure 12. Concentration distribution at different locations on the plate

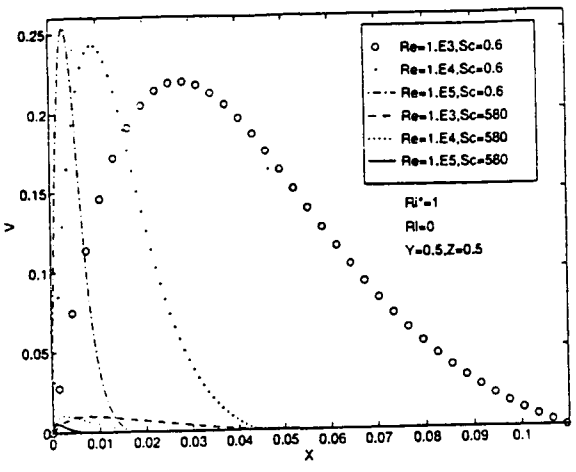

Figure 13. Vertical velocity profile at different Reynolds number

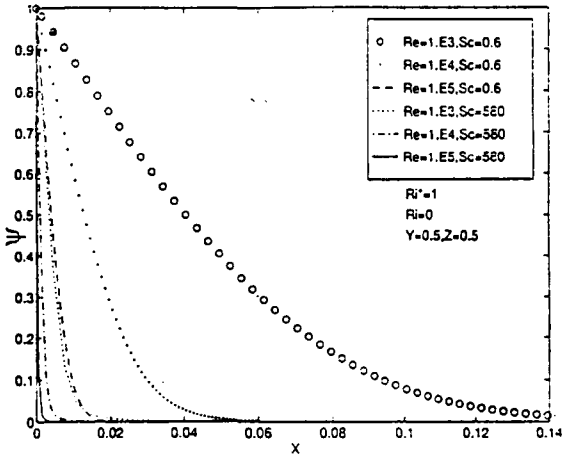

Figure 14. Concentration distribution at different Reynolds number

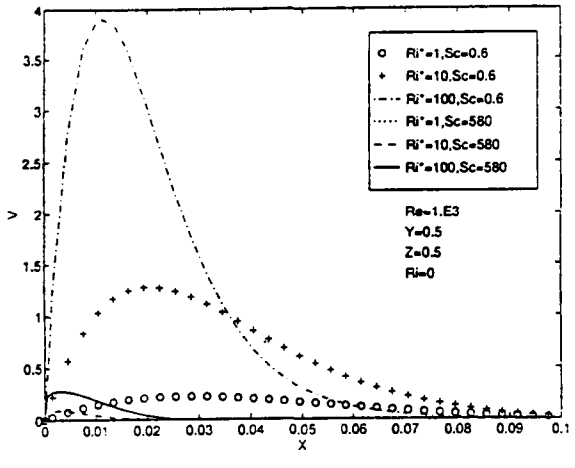

Figure 15. Vertical velocity profile at different Richardson number

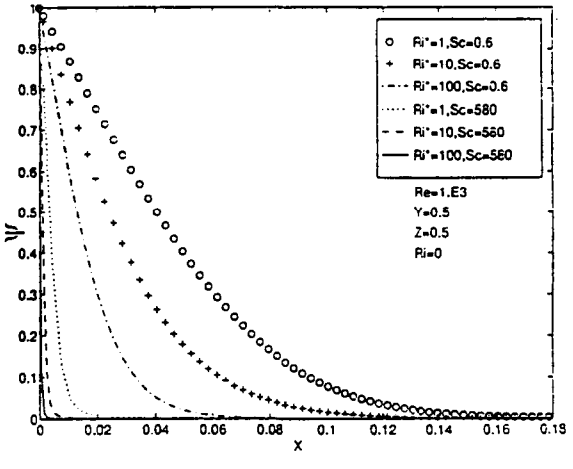

Figure 16. Concentration distribution at different Richardson number

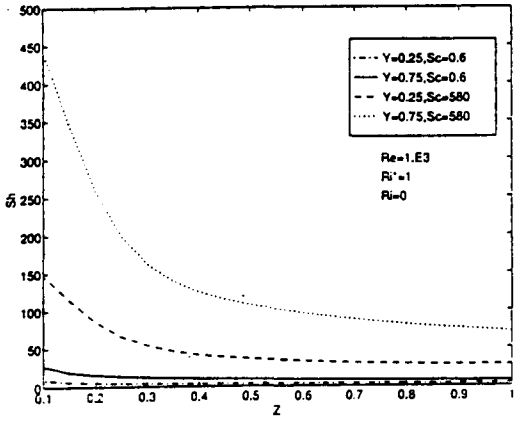

Figure 17. Sherwood number variation over the plate

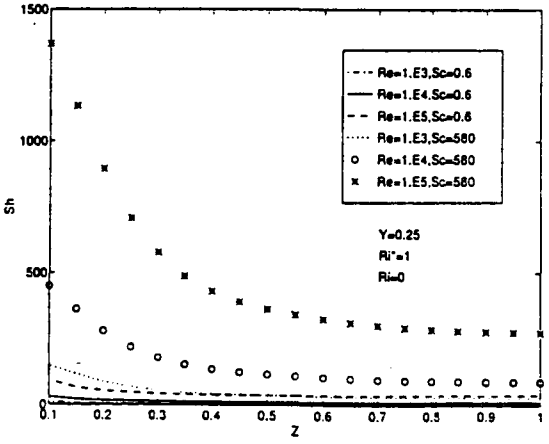

Figure 18. Sherwood number variation at different Reynolds number

ANALYSIS OF GAS ABSORPTION TO A THIN LIQUID FILM IN THE PRESENCE OF A ZERO-ORDER CHEMICAL REACTION

S. Rajagopalan and M.M. Rahman
Department of Mechanical Engineering
University of South Florida
Tampa, Florida

SUMMARY

The paper presents a detailed theoretical analysis of the process of gas absorption to a thin liquid film adjacent to a horizontal rotating disk. The film is formed by the impingement of a controlled liquid jet at the center of the disk and subsequent radial spreading of liquid along the disk. The chemical reaction between the gas and the liquid film can be expressed as a zero-order homogeneous reaction. The process was modeled by establishing equations for the conservation of mass, momentum, and species concentration and solving them analytically. A scaling analysis was used to determine dominant transport processes. Appropriate boundary conditions were used to solve these equations to develop expressions for the local concentration of gas across the thickness of the film and distributions of film height, bulk concentration, and Sherwood number along the radius of the disk. The partial differential equation for species concentration was solved using the separation of variables technique along with the Duhamel's theorem and the final analytical solution was expressed using confluent hypergeometric functions. Tables for eigenvalues and eigenfunctions are presented for a number of reaction rate constants. A parametric study was performed using Reynolds number, Ekman number, and dimensionless reaction rate as parameters.

At all radial locations, Sherwood number increased with Reynolds number (flow rate) as well as Ekman number (rate of rotation). The enhancement of mass transfer due to chemical reaction was found to be small when compared to the case of no reaction (pure absorption), but the enhancement factor was very significant when compared to pure absorption in a stagnant liquid film. The zero-order reaction processes considered in the present investigation included the absorption of oxygen in aqueous alkaline solutions of sodiumdithionite and rhodium complex catalyzed carbonylation of methanol. Present analytical results were compared to previous theoretical results for limiting conditions, and were found to have very good agreement.

INTRODUCTION

Mass transfer with chemical reactions into thin films has been the subject of many theoretical and experimental investigations. Understanding the process of gas absorption into thin films and its effect on the chemical kinetics of the associated reactions is very important in chemical process industries. Absorption of oxygen into thin films is important in medical engineering. Wetted wall columns are being extensively used in mass transfer studies. The present study presents a detailed theoretical analysis of gas absorption to a thin liquid film adjacent to a horizontal rotating disk. This kind of absorption process is useful in a microgravity environment where usual falling film columns cannot be established and the rate of transport can be enhanced by the introduction of fluid acceleration by an alternative approach such as rotation. In addition to its fundamental scientific contribution and possible application in space based chemical processes, the results of this research will be useful for the design of a spacecraft thermal management system using absorption heat pump.

In the past, there has been a number of studies on mass transfer to a falling liquid film. Olbrich and Wild [ref. 1] studied the diffusion from the free surface into a liquid film in laminar flow over a sphere, a cone and a cycloid of revolution. They used the Laplace transform technique to solve the governing differential equations followed by the application of the residue theorem. Gas absorption with zero-order reaction for a liquid moving in a plug flow was studied by Astarita and Marrucci [ref. 2] Riazi and Faghri [ref. 3] analyzed the gas absorption in a laminar falling film with zero-order reactions. The differential equations were solved by the method of separation of variables, and the subsequent solution was given using an infinite series of hypergeometric functions. They also presented the enhancement factor when compared to the absorption rates in a stagnant liquid film found from a simple penetration model. A simplified form of the enhancement factor was derived for specific conditions.

The overall reaction rate in a gas-liquid reaction is controlled by the physical mass transfer rate and/or by the chemical reaction rate. Two models are generally used to describe the transfer mechanism, viz., the film model and the penetration model. The film model postulates a stagnant film at the surface of the liquid next to the gas . While the rest of the liquid is kept uniform in composition, the gas diffuses into the film by molecular diffusion alone. The penetration theory assumes that after some time the interface is renewed by fresh liquid and fresh gas. The elements of gas and liquid leaving the interface are more or less saturated with the absorbed component. Of the two theories, the film model is the simplest and is applied most frequently. Landau [ref. 4] studied the simultaneous interphase mass transfer and a zero-order reaction using the film model. He gave analytical solutions for three regimes of the absorption process, viz., low rates of absorption when the reaction goes to completion in the film, higher rates of absorption when it goes to completion in the bulk and, at still higher rates of absorption when it does not go to completion. Van de Vusse [ref. 5] derived expressions for the overall reaction rate for mass transfer with chemical reactions. He used both the film theory and the penetration theory. He showed that at high transfer rates the overall reaction rate approaches the chemical reaction rate. The effect of chemical reaction on the bulk-phase concentration was studied by Nagy and Ujhidy [ref. 6]. They gave a mathematical model to calculate the bulk-phase concentrations in the entire finite reaction rate regime in case of both irreversible and reversible reactions. Analyses of mass transfer in hemodialysers for laminar blood flow and homogeneous dialysate was done by Cooney, Kim and Davis [ref. 7]. The solutions were obtained in terms of confluent hypergeometric functions. They also discussed the application of their mathematical model to systems used in clinical practice.

Mass transfer to a thin film adjacent to a rotating disk surface was studied by Rahman and Faghri [ref. 8]. They gave analytical and numerical solutions to the problem. The analytical solution was obtained using the method of separation of variables and hypergeometric functions. Sherwood numbers and bulk concentration were calculated for different values of Reynolds and Ekman numbers and then the results were compared with that of the numerical finite difference solution. They found that significant enhancement of absorption rate can be obtained when the angular velocity of the rotating disk is increased. Their problem involved pure absorption with no chemical reaction.

Several experimental investigations have also been done to study effect of chemical reactions on mass transfer into a thin liquid film. Jhaveri and Sharma [ref. 9] studied the absorption of oxygen in aqueous alkaline solution of sodium diothionite. The reaction was found to be first order with respect to diothionite concentration below 0.08 g mol/l. and second order with respect to diothionite concentration above 0.08 g mol/l. The reaction was found to be zero order with respect to oxygen for all other diothionite concentrations. Roberts and Danckwerts [ref. 10] studied the kinetics of carbon dioxide absorption in alkaline solutions. They devised a method to eliminate the "stagnant film" end effect on wetted-wall columns. The catalytic effect of arsenite ions on the reaction between carbon dioxide and water was measured. Autocatalytic oxidation of Cyclohexane was investigated by Suresh et al [ref. 11]. The behavior of the reaction was found to be complex arising from the fact that the reaction was autocatalytic and the reaction was zero order in oxygen over the entire absorption range. Astarita [ref. 12]

studied the absorption of carbon dioxide into hydroxide solutions and in carbonate- bicarbonate buffer solutions. The absorption rates were measured for a packed tower column. The kinetics of the absorption of Carbon dioxide in monoethanolamine solutions at short contact times was studied by Clarke [ref. 13]. The rates of absorption of carbon dioxide at contact times of 3 and 20 ms and at gas pressures of 1 and 0.1 atm. was measured. He observed that the heat of reaction influences the rate of absorption. The effect of interfacial turbulence during the absorption of carbon dioxide into monoethanolamine was studied by Brian et al [ref. 14]. They discussed the discrepancies between the theoretical considerations and the available experimental data. They stated that this could be due to the interfacial turbulence driven by surface tension gradients. They found that the use of actual physical mass transfer coefficient during the reaction improves the agreement between the penetration theory model and experimental data. Hjortkjaer and Jension [ref. 15] investigated the kinetics of the Rhodium complex catalyzed carbonylation of methanol. The reaction was investigated at carbon mono-oxide pressures between 1 and 50 atm and in the temperature range of 150 - 225 °C. The reaction was discerned to be zero-order with respect to the reactants, and first order with respect to the catalyst and promoter. The activation energy was found to be 14.7 kcal/gmol.

Although a significant number of research has been done on mass transfer into thin liquid films with simultaneous chemical reactions, especially with respect to falling liquid films, very few work has been done on mass transfer into thin liquid films adjacent to a rotating disk. The present study gives a detailed theoretical analysis of gas absorption into a thin liquid film over a rotating disk in the presence of a zero-order chemical reaction. A theoretical model is developed and the effects of Reynolds number, Ekman number and dimensionless reaction rate are studied.

MATHEMATICAL MODEL

The flow of a thin film adjacent to a horizontal rotating disk is considered in the present study. The system is schematically shown in Figure 1. The film is formed by the impingement of a controlled liquid jet at the center of the disk. The disk rotates about its axis with a constant angular velocity ω. The liquid film enters the gas medium at a radial location $r=r_{in}$. A coordinate system attached to the free surface (Figure 1) is used for the analysis. The following assumptions are made to simplify the problem.

(1) $v \ll u$ or w and $\partial/\partial y \gg \partial/\partial r$. These assumptions are valid since the thickness of the film is much smaller than the radius of the disk.

(2) For a very thin liquid layer there is no significant hydrostatic pressure variation. The pressure everywhere in the film is equal to the ambient pressure.

(3) The gravitational body force is negligible when compared to the centrifugal force even for a moderate rate of rotation.

(4) $w \ll u$ and $u=\omega r$. These assumptions are valid only at a large rate of rotation, and become more appropriate at a larger radii.

Under these assumptions, the average velocity at any radial location can be calculated in a closed form and is given by

$$W=\frac{\omega^2 r\delta^2}{3\nu} \qquad (1)$$

The conservation of mass at any radial location gives

$$Q=2\pi rW\delta \tag{2}$$

From equation (1) and (2), the film thickness can be expressed as

$$\delta=\left(\frac{3\nu Q}{2\pi\omega^2 r^2}\right)^{1/3} \tag{3}$$

The above assumptions simplify the differential equation describing the conservation of gas concentration in the liquid stream. In the presence of a simultaneous zero-order chemical reaction occurring in the liquid phase, this equation is described by

$$v_r\frac{\partial C}{\partial r}=D\frac{\partial^2 C}{\partial z^2}-k \tag{4}$$

The appropriate boundary conditions to equation (4) are

$$r=r_{in}: \qquad C=0 \tag{5}$$

$$z=0: \qquad C=C^* \tag{6}$$

$$z=\delta: \qquad \frac{\partial C}{\partial z}=0 \tag{7}$$

Equation (4) can be written in a dimensionless form as follows

$$(1-Y^2)\frac{\partial \psi}{\partial X}=\frac{\partial^2 \psi}{\partial Y^2}-\alpha \tag{8}$$

where

$$X=B^{1/2}[\xi^{8/3}-1] \tag{9}$$

and

$$B=\frac{1}{(192)^{1/3}}Re_{in}^{-4/3}E_{in}^{-2/3}Sc^{-1} \tag{10}$$

Corresponding boundary conditions are given by

$$X=0 \quad and \quad 0 \le Y \le 1: \quad \psi = 0 \tag{11}$$

$$Y=0 \quad and \quad X>0: \quad \psi = 1 \tag{12}$$

$$Y=Y^* \quad and \quad X>0: \quad \frac{\partial \psi}{\partial Y} = 0 \tag{13}$$

where

$$\begin{aligned} Y^* &= 1 \qquad when \ \alpha \le 2 \\ &= \sqrt{\frac{2}{\alpha}} \qquad when \ \alpha \ge 2 \end{aligned} \tag{14}$$

In equation (14), $\alpha \le 2$ corresponds to the case when the maximum depth of penetration is equal to the film thickness.

$\alpha \ge 2$ corresponds to the case when the maximum depth of penetration is less then the film thickness. In that situation, the boundary condition given by equation(13) should be changed to

$$Y=Y^* \quad and \quad X>0: \quad and \quad \frac{\partial \psi}{\partial Y} = 0 \tag{15}$$

Now α can also be written as,

$$\alpha = \frac{p}{\sqrt{X+B}} \tag{16}$$

where

$$p = \alpha_{in} \sqrt{B} \tag{17}$$

Hence, the equation (8) becomes

$$(1-Y^2)\frac{\partial \psi}{\partial X} = \frac{\partial^2 \psi}{\partial Y^2} - \frac{p}{\sqrt{X+B}} \tag{18}$$

The present system [Equations (18), (11-15)] has non-homogeneity in the differential equation which is a function of the variable X, and in the boundary condition which is a constant. The principle of separation of variables can be used to solve the corresponding problem with the non-homogenity in the differential equation being independent of the variable X. Then Duhamel's theorem [ref. 16] can be applied to obtain the actual solution.

Introducing the parameter τ in equation (18), the auxiliary problem can be taken as

$$(1-Y^2)\frac{\partial \phi}{\partial X}=\frac{\partial^2 \phi}{\partial Y^2}-\frac{p}{\sqrt{\tau+B}} \tag{19}$$

and the associated boundary conditions being

$$Y=0 \quad and \quad X>0: \quad \psi=1 \tag{20}$$

$$X=0 \quad and \quad 0\le Y\le 1: \quad \psi=0 \tag{21}$$

and, if $\alpha\le 2$

$$Y=Y^* \quad and \quad X>0: \quad \frac{\partial \psi}{\partial Y}=0 \tag{22}$$

or, if $\alpha\ge 2$

$$Y=Y^* \quad and \quad X>0: \quad \frac{\partial \psi}{\partial Y}=0 \quad and \quad \psi=0 \tag{23}$$

Equation (19) along with the boundary conditions (20-23) was solved using the method of separation of variables, thus obtaining the solution to the auxiliary problem as

$$\phi(X,Y,\tau)=\frac{p}{2\sqrt{\tau+B}}Y^2-\frac{p}{\sqrt{\tau+B}}Y\,Y^*+1-\sum_{n=1}^{\infty}C_n\lambda_n^{1/2}Y exp(-\lambda_n^2 X) \times \exp(-\lambda_n Y^2/2)M\left(\frac{3-\lambda_n}{4},\frac{5}{2},\lambda_n Y^2\right) \tag{24}$$

The eigen values, λ_n are given as roots of the following equation.

$$(1-\lambda Y^{*2})M\left(\frac{3-\lambda}{4},\frac{3}{2},\lambda Y^{*2}\right)+Y^{*2}\frac{\lambda(3-\lambda)}{3}M\left(\frac{7-\lambda}{4},\frac{5}{2},\lambda Y^{*2}\right) \tag{25}$$

The constant, C_n can be determined by using the orthogonal property of the eigen functions, and given as

$$C_n=\frac{\int_0^1\left(-\frac{p}{2\sqrt{\tau+B}}Y^2+\frac{p}{\sqrt{\tau+B}}YY^*-1\right)(1-Y^2)N_n(Y)dY}{\int_0^1(1-Y^2)N_n^2(Y)dY} \tag{26}$$

where, $N_n(y)$ are the eigen functions given by

$$N_n(Y)=\lambda_n^{1/2}Y\exp(-\lambda_nY^2/2)M\left(\frac{3-\lambda_n}{4},\frac{3}{2},\lambda_nY^2\right) \tag{27}$$

and M(a,b,c) is the confluent hypergeometric functions with arguments a,b and c [ref. 17].

The solution to the present auxiliary problem is similar to that obtained by Riazi and Faghri [ref. 3] for gas absorption in a falling liquid film in the presence of a zero order chemical reaction.

The Duhamel's theorem relates the solution of the auxiliary problem to the original problem and is given by

$$\psi(X,Y)=\frac{\partial}{\partial X}\int_{\tau=0}^{X}\phi(X-\tau,Y,\tau)d\tau \tag{28}$$

After performing the integration, we get the concentration profile as

$$\psi(X,Y)=\frac{\alpha}{2}Y^2-\alpha Y^*+1-\sum_{n=1}^{\infty}A_n\lambda_n^{1/2}Y\exp(-\lambda_nY^2/2)\exp(-\lambda_n^2X)\times M\left(\frac{3-\lambda_n}{4},\frac{3}{2},\lambda_nY^2\right) \tag{29}$$

where

$$A_n=\frac{\int_0^1\left(-\frac{\alpha}{2}Y^2+\alpha YY^*-1\right)(1-Y^2)N_n(Y)dY}{\int_0^1(1-Y^2)N_n^2(Y)dY} \tag{30}$$

The first fifteen values of λ_n and A_n are listed in Table 1. The eigen values λ_n were determined from equation (25) by using the bisection method and the corresponding integration constants, A_n were obtained from equation (30). The numerical integration was performed using Simpson' rule. Up to 32 digits were retained for all mathematical calculations though we list only eight digits after the decimal in table 1. This was required to overcome truncation errors during the computation of confluent hypergeometric functions which are periodic in nature.

The Sherwood number for gas absorption can be written as

$$Sh^* = \frac{-\frac{\partial \psi}{\partial Y}\Big|_{Y=0}}{1-\int_0^1 \psi dy} \tag{31}$$

After substituting for ψ from equation (29) into equation (31), the Sherwood number can be written as

$$Sh^* = \frac{\alpha Y^* + \sum_{n=1}^{\infty} A_n \exp(-\lambda_n^2 X)\lambda_n^{1/2}}{-\frac{\alpha}{6} + \frac{\alpha Y^*}{2} + \sum_{n=1}^{\infty} A_n \exp(-\lambda_n^2 X)\lambda_n^{1/2} \int_0^1 \exp(-\lambda_n Y^2/2) Y M\left(\frac{3-\lambda_n}{4}, \frac{3}{2}, \lambda_n\right)} \tag{32}$$

In order to get a better understanding of the change of absorption rate with the flow rate and the rate of rotation, Sherwood number without the film thickness, Sh was also calculated.The Sherwood number, Sh can be related to Sh^* by the relation

$$Sh = Sh^* \left(\frac{\nu^2}{3gr_{in}^3}\right)^{1/3} Re_{in}^{1/3}\ E_{in}^{-2/3}\ \xi^{2/3} \tag{33}$$

The influence of the chemical reaction can be evaluated by comparing the rate of gas absorption, G to the rate of gas absorption, G_∞^0 of an infinitely deep stagnant liquid with the same physical properties and with no chemical reaction. The ratio, G/G_∞^0 is known as the enhancement factor [ref. 3]. The the Enhancement Factor when compared to the case of physical absorption, E_∞ can be written as

$$E_\infty = \frac{Y^* \alpha X + \sum_{n=1}^{\infty} \frac{A_n}{\lambda_n^{3/4}} (1 - e^{-\lambda_n^2 X})}{\sqrt{\frac{4}{\pi} X}} \tag{34}$$

The influence in the chemical reaction can also be evaluated by comparing the absorption rate, G with the absorption rate, G_o, of the same flow system but in which the chemical reaction is absent. Thus the Enhancement Factor when compared to the case of no chemical reaction but the same flow system, E_o is given by

$$E_0 = \frac{Y^* \alpha X + \sum_{n=1}^{\infty} \frac{A_n}{\lambda_n^{3/4}} (1 - e^{-\lambda_n^2 X})}{\sum_{n=1}^{\infty} \frac{A_n}{\lambda_n^{3/4}} (1 - e^{-\lambda_n^2 X})} \qquad (35)$$

RESULTS AND DISCUSSION

The mathematical model developed in the previous section was used to calculate the mass transfer rates and enhancement factors for some specific flow rates and rates of rotation. The flow system that was considered in the present investigation is shown in figure 1. The fluid enters the gas medium at a radial location $r=r_{in}$ and is dispersed along the radial direction. The gas is absorbed and reacts with the fluid in zero-order simultaneously and the absorbed gas is transported downstream with the flow. It is assumed that the mass of the gas absorbed is negligible compared to the mass of the liquid. The flow remains laminar throughout the physical domain considered in the present investigation. The important dimensionless parameters are: the radial location X, the normal coordinate Y, the concentration Ψ, the Reynolds number Re, the Ekman number E and the reaction parameter α.

The thickness of the liquid film is given by equation (3). As can be seen from the equation, the thickness decreases monotonically with the radius. The thickness depends on the fluid flow rate and the rotational speed. At larger radii, the flow is driven by the centrifugal force. The effects of inertial force are significant only at smaller radii. The present study did not consider the development region near the center of the disk. For a small Ekman number (large rate of rotation), the flow is primarily driven by centrifugal force even at small radial locations. The film height can greatly influence the rate of absorption. Under a very fast reaction, a low diffusion rate, or when the thickness of the film is large, the penetration depth remains smaller than the film thickness($\alpha \geq 2$) at the entire flow domain. Under a slow reaction, a very thin film, or a high diffusion rate, the penetration depth becomes equal to the film thickness ($\alpha \leq 2$) after the film has travelled some distance downstream.

The analytical solutions for dimensionless concentration and Sherwood number (dimensionless mass transfer rate) are given by equation (29) and equation (32), respectively.These equations represent the solution as a series of confluent hypergeometric functions, and are valid for any given reaction rate. The solution for the first fifteen sets of eigenvalues (λ_n) and the coefficients (C_n) are presented in Table 1 for different values of α. The eigen values were obtained as roots of equation (25). The bisection method was used to calculate the eigenvalues. Simpson's rule was used to perform the numerical integration with 5000 intervals. In all numerical computations, 32 digits were retained after the decimal to accurately calculate the values of hypergeometric functions. The values in Table 1 were compared with those presented by Riazi and Faghri [ref. 3] for gas absorption to a falling film with zero order chemical reaction and Olbrich and Wild [ref. 1] and Rahman and Faghri [ref. 10] for the case of $\alpha=0$ (absorption with no chemical reaction). The present results differed slightly from those of Riazi and Faghri [ref. 3]. The difference becomes larger at higher eigen values. It was found that the discrepancy is due to truncation errors in the calculations of Riazi and Faghri [ref. 3] who used double precision arithmetic for their calculations. The results in this paper appears to be more accurate as up to 32 significant digits were used for the calculations and the eigen values and the integration coefficients agree exactly with that of Olbrich and Wild[ref. 1] and Rahman and Faghri[ref. 10] for the limiting case of $\alpha=0$. The eigen values calculated from the equation (25) are independent of α when $\alpha \leq 2$ but it depends on α when $\alpha \geq 2$ (since

$Y^*=\sqrt{(2/\alpha)}$ when $\alpha \geq 2$). It may be noted that for any given flow rate and speed of rotation, the dimensionless reaction parameter α, varies with the radial location as it is dependent on the local film thickness.

The concentration profile at different radial locations for $\alpha=0.1$ and $\alpha=2$ are shown in figures 2 and 3 respectively. In both these graphs, it can be seen that the concentration increases in the downstream direction at all locations across the thickness of the film. As the liquid film moves downstream, the gas diffuses in and reacts with the film. At values of α less then or equal to 2, the gas can penetrate the entire film thickness. When α is larger then 2, the penetration can extend only through a part of the film thickness. It can be seen in figure 2 that at $\alpha=0.1$, the gas penetrates the entire film thickness when X is larger than 0.05. At larger values of X, the concentration increases all across the film thickness, until at about 0.7, the concentration profile reaches a fully-developed condition. The concentration profile does not change as the film moves further downstream. This profile is shown as $X=\infty$ in the plots. In figure 3, it can be noticed that at $\alpha=2$, the gas penetrates only through the part of the film thickness and part of the liquid remains pure. The penetration depth becomes larger and larger as the film moves downstream, and in the fully developed condition, it just touches the solid wall. The fully-developed concentration profile for different values of α is demonstrated in figure 4. It can be clearly seen from the graph that the reaction goes to completion within a part of the film when $\alpha \geq 2$. As α increases, the fully developed concentration decreases for any particular radial location.

Figures 5 and 6 shows the variation of Sherwood number (Sh and Sh^*) along the radius of the disk for different values of Ekman number. In these plots, both Reynolds number and the chemical reaction rate are preserved constant. In figure 5, it can be noticed that the Sherwood number decreases downstream monotonically. As the Ekman number becomes smaller, the Sh^* also becomes smaller. This is due to the fact that at smaller Ekman number (i.e. at larger rotational speed) the film thickness also becomes smaller. To single out the variation of mass transfer rate with the rotational speed of the disk, Sh is plotted in figure 6. As expected, the Sherwood number increases with a decrease in Ekman number as the actual mass transfer coefficient increases with the increase in rotational speed. The effect of Reynolds number on Sherwood number can be seen in figures 7 and 8. In these plots, the Ekman number and the chemical reaction rate are kept constant. From figure 7 it can be seen that an increase in Reynolds number causes an increase in Sh^*. This is true, since an increase in the flow rate can cause an increase in the mass transfer rate. Figure 8 shows the variation of the Sherwood number (Sh) with the radius at different Reynolds number. It can be noticed that the Sherwood number, Sh decreases monotonically with the radius. For flow over a rotating disk, at smaller radii the flow is dominated by the inertial force and at larger radii, it is dominated by the centrifugal force. Figures 9 and 10 show the variation of the bulk concentration with the radial location, ξ at different values of Ekman and Reynolds numbers. As expected, in both these plots, the bulk concentration increases with the radial location at all values of Reynolds and Ekman numbers.

The effect of reaction rate is shown in figures 11 and 12. The figures show the variation of the Sherwood number and the bulk concentration with the radius for two different chemical reactions. These are the reaction of oxygen with the aqueous alkaline solution of sodium dithionite ($K=6.4\times10^2$) and the carbonylation of methanol ($K=1.42\times10^6$). Figure 11 shows the variation of Sherwood Number Sh^* along the radius for the two chemical reaction rates considered. The Sherwood number, Sh^* decreases with an increase in rate constant k for both the flow systems considered. When the rate constant is larger, an increase in the mass transfer coefficient might be expected for a given set of fluid properties. But the dimensionless parameter α also depends upon the diffusion rate, D and the solubility of the gas in the liquid, C^*. Thus for a given film thickness, the mass transfer coefficient depends upon the quantity $k/(C^*D)$. Therefore, when two different gas liquid reactions (zero-order) are considered, it would be appropriate to consider the variation of the parameters with respect to the ratio of the quantity k/C^*D. When this quantity is larger, the gas absorption rate increases. This is consistent with the trend seen in

figure 11. The quality k/C^*D for the reaction of sodium dithionite with oxygen is 8.95×10^7 and for the carbonylation reaction it is 5.5×10^7 m^{-2}. Figure 12 shows the variation of bulk concentration with radius for the two different reactions considered in the study. The bulk concentration shows an increase with an increase in the reaction rate.

The enhancement factors (equations 34 and 35) were calculated for different values of X and different combinations of reaction reate, Reynolds number, and Ekman number. It was found that E_∞ is the maximum near the entrance and reduces rapidly with the radius. The larger enhancement near the entrance may be attributed to the smaller concentration boundary layer thickness in that region.

CONCLUSIONS

An analytical solution for the process of gas absorption to a thin film liquid film adjacent to a horizontal rotating disk in the presence of a zero order chemical reaction is presented. The analysis yielded closed form solutions in terms of a series of confluent hypergeometric functions. It was found that the gas can penetrate all across the thickness of the film only if the dimensionless reaction rate α is less than or equal to 2. For $\alpha>2$, the penetration depth can be only a part of the film thickness. It was also observed that the concentration profile attains a fully developed condition at approximately X=0.7. The rate of mass transfer increased with flow rate as well as with the rate of rotation. The chemical reaction influenced the rate of gas absorption at the free surface. The mass transfer coefficient increased with increase in k/C^*D. The enhancement factor was found to be very significant when compared to absorption in a stagnant liquid film.

NOMENCLATURE

A_n	integration coefficient for n th eigen value (equation 30)
B	constant defined by equation (10)
C	Concentration of dissolved gas in the liquid [kmol m^{-3}]
C^*	Concentration of the dissolved gas at the interface [kmol m^{-3}]
C_n	integration coefficient for n th eigen value (equation 26)
D	liquid phase diffusion coefficient [m^2 s^{-1}]
E	Ekman number, $\nu/\omega r^2$
E_0	enhancement factor for the case of no chemical reaction
E_∞	enhancement factor for the case of infinitely deep stagnant liquid
G	gas absorption rate [kg m^{-2} s^{-1}]
G_0	gas absorption rate when the chemical reaction is absent [kg m^{-2} s^{-1}]
G_∞^0	gas absorption rate without chemical reaction in an infinitely deep stagnant liquid [kg m^{-2} s^{-1}]
k	zero-order reaction rate constant [kmol m^{-3} s^{-1}]
m	dimensionless gas absorption rate
m_0	dimensionless gas absorption rate when the chemical reaction is absent
M	confluent hypergeometric function
p	constant defined by equation (17)
Q	volumetric flow rate [m^3 s^{-1}]
r	radial coordinate [m]
Re	Reynolds number, $W\delta/\nu$
Sc	Schimdt number, ν/D
Sh	Sherwood number, $[G(\nu^2/g)^{1/3}]/\rho D$

Sh^*	Sherwood number in terms of the film height, $G\delta/\rho D$
u	velocity in the angular direction [m s^{-1}]
v	velocity in the normal direction [m s^{-1}]
w	velocity in the radial flow direction [m s^{-1}]
W	average velocity along the radius [m s^{-1}]
X	dimensionless coordinate in the radial direction
Y	dimensionless coordinate normal to the plate, z/δ
z	coordinate normal to the plate [m]

Greek symbols

α	dimenesionless reaction parameter, $k\delta^2/C^*D$
δ	film thickness [m]
θ	angular coordinate [rad]
λ	eigen value
ν	kinematic viscosity [m^2 s^{-1}]
ξ	dimesionless radial coordinate, r/r_{in}
ρ	density of the liquid [kg m^{-3}]
τ	parameter introduced in the auxiliary problem
Φ	solution of the auxiliary problem given by equation (24)
ψ	dimensionless concentration, C/C^*
ω	angular velocity [rad s^{-1}]

Subscripts

in	condition at entrance
ave	average value across the film thickness
b	mixed-mean (bulk) condition

REFERENCES

1. Olbrich, W.E.; and Wild, J.D.: Diffusion from the Free Surface into a Liquid Film in Laminar Flow over Defined Shapes. Chem. Engg. Sci., vol. 24, 1969, pp. 25-32.
2. Astarita, G.; and Marrucci, G.: Gas Absorption with Zero-Order Chemical Reaction. I. & EC Fund., vol. 2, no. 1, 1963, pp. 4-7.
3. Riazi, M.; and Faghri, A.: Gas Absorption with First-Order Chemical Reaction. AIChE JL., vol.31, 1985, pp. 1967-1972.
4. Landau, J.: Absorption Accompanied by a Zero-Order Reaction. Canad. Jl. Chem. Engg., vol. 68, 1990, pp. 599-607.
5. Van de Vusse, J.G.: Mass Transfer with Chemical Reaction. Chem. Engg. Sci., vol. 16, 1961, pp. 21-30.
6. Nagy., E.; and Ujhidy A.: Model of the Effect of Chemical Reaction On Bulk Concentrations. AIChE Jl., vol. 35, no. 9, 1989, pp. 1564-1568.
7. Conney, D.O., Kim, S.S.; and Davis, E.J.: Analysis of Mass Transfer in Hemodialysers for Laminar Blood and Homogeneous dialystate. Chem. Engg. Sci., vol. 29, 1974, pp. 1731-1738.
8. Rahman, M.M.; and Faghri, A.: Gas Absorption and Solid Dissolution in a Thin Liquid Film on a Rotating Disk. Int. Jl. Heat and Mass Tran., vol. 36,no. 1, 1993, pp. 189-199.

9. Jhaveri, A.S.; and Sharma, M.M.: Absorption of Aqueous Solutions of Sodium Dithionite. Chem. Engg. Sci., vol. 23, 1968, pp. 1-8.
10. Roberts, D.; and Danckwerts, P.V.: Absorption in alkaline Solutions-I Transient Absorption Rates and Catalysis by Arsenite. Chem. Engg. Sci., vol. 17, 1962, pp. 961-969.
11. Suresh, A.K., Sridhar, T.; and Potter, O.E.: Autocatalytic oxidation of Cyclohexane - Mass Transfer and Chemical Reaction. AIChE Jl., vol. 34, no. 1, 1988, pp. 81-93.
12. Astarita, G.: Absorption of Carbon dioxide into Alkaline Solutions in Packed Towers. I & EC Fund., vol. 3, no. 4, 1963, pp. 294,297.
13. Clarke, J.K.A.: Kinetics of Absorption of Carbon dioxide in Momoethanolamine. Solutions at Short Contact Times. I & EC Fund. vol. 3, no. 3, 1964, pp. 239-245.
14. Brian, P.L.T., Vivian, J.E.; and Matiatos, D.C.: Interfacial Turbulence during the Absorption of Carbon Dioxide into monoethanolamine. AIChE Jl. vol. 13, no. 1, 1967, pp. 28-36.
15. Hjortkjaer, J.; and Erren. W.J.: Rhodium Complex Catalyzed Methanol Carbonylation. Ind. Engg. Chem. Prod. Res. Dev. vol 15, no. 1, 1976, pp. 46-49.
16.Ozisik, M.N.: Heat conduction. Wiley, 1980.
17. Abarmowitz, M.; and Stengun. I.A.: Handbook of Mathematical Functions with Formulas, Graphs and Mathematical Tables. National Bureau of Standards, Department of Commerce, Washington DC, 1972.

TABLE 1. Eigen values and Integration Coefficients

No	λ_n	C_n			α=3		α=4	
		α=0	α=0.1	α=2	λ_n	C_n	λ_n	C_n
1	2.26311053	1.79238360	1.72977244	0.54016045	2.38906211	0.41660402	2.59139039	0.36164776
2	6.29768520	1.02469014	1.02672555	1.06539830	6.74541597	0.93826498	7.42019229	0.87219849
3	10.30772681	0.79631238	0.79386970	0.74745885	11.11656887	0.72127416	12.28077919	0.72237188
4	14.31279359	0.67455957	0.67511830	0.68573409	15.49931414	0.63800582	17.15401771	0.64786122
5	18.31592741	0.59583217	0.59511046	0.58139800	19.88870854	0.57066555	22.03297228	0.51668786
6	22.31808871	0.53954469	0.53980138	0.56467864	24.28213765	0.52485522	26.91492866	0.51736060
7	26.31968463	0.49671455	0.49637764	0.48997642	28.67816743	0.48388371	31.79863869	0.42056847
8	30.32091973	0.46270665	0.46285379	0.46564935	33.07595966	0.45403568	36.68345574	0.44504888
9	34.32190893	0.43485365	0.43466002	0.43098101	37.47499588	0.41836349	41.56901374	0.39960741
10	38.32272219	0.41149648	0.41159178	0.41340251	41.87493997	0.40073456	46.45509083	0.35605761
11	42.32340476	0.39154207	0.39141699	0.38903440	46.27556533	0.36863628	51.34154512	0.37809093
12	46.32398727	0.37423651	0.37430322	0.37557063	50.67671399	0.36209288	56.22828181	0.31925983
13	50.32449129	0.35904110	0.35895337	0.35728658	55.07827279	0.33499816	61.11523525	0.34052013
14	54.32493248	0.34555884	0.34560810	0.34654405	59.48015860	0.33538518	66.00235857	0.31814302
15	58.32532250	0.33349027	0.33342546	0.32106149	63.88230912	0.31361091	7088961745	0.28518091

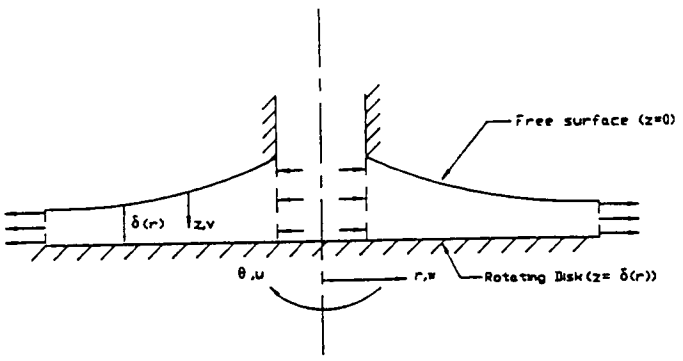

Figure 1 Schematic diagram of the flow system

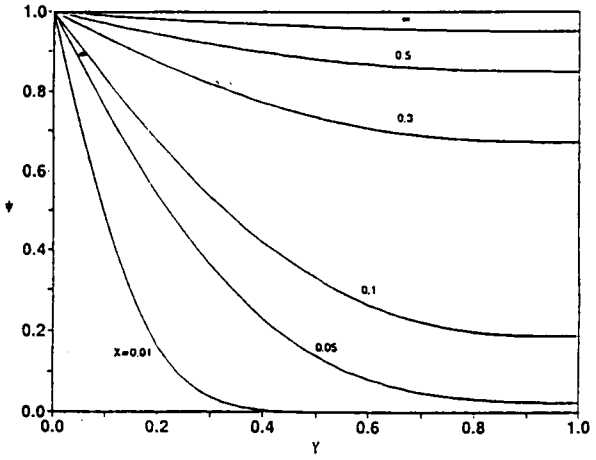

Figure 2 Concentration profile for α=0.1

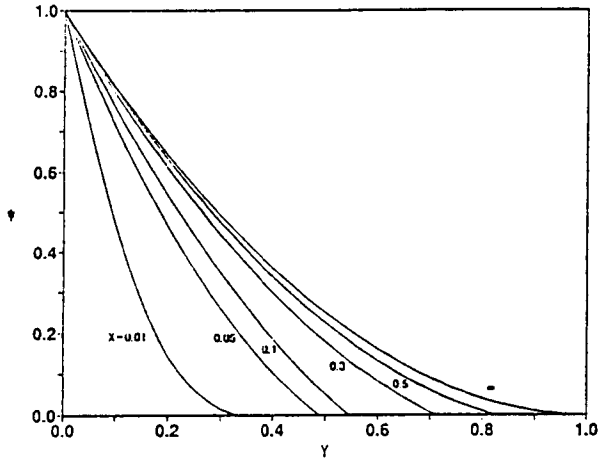

Figure 3 Concentration profile for α=2

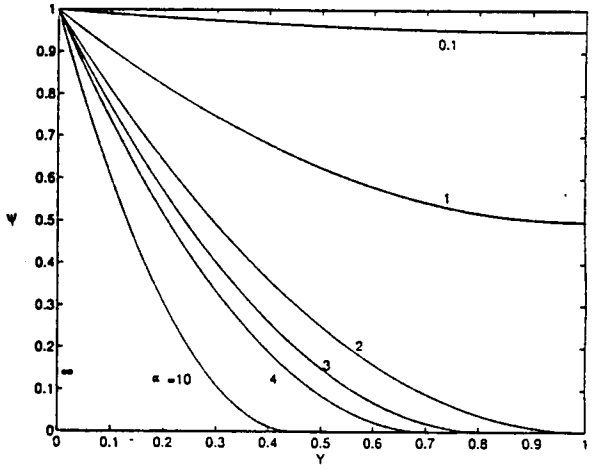

Figure 4 Fully-developed concentration distribution at different values of α

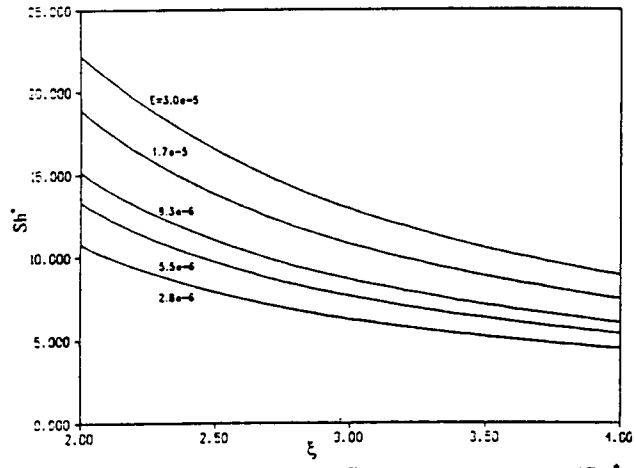

Figure 5 Variation of Sherwood number (Sh*) for Re=520 and k=142.5

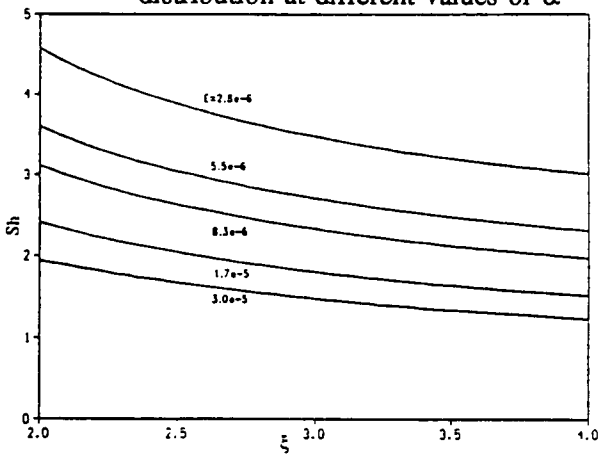

Figure 6 Variation of Sherwood number (Sh) for Re=520 and k=142.5

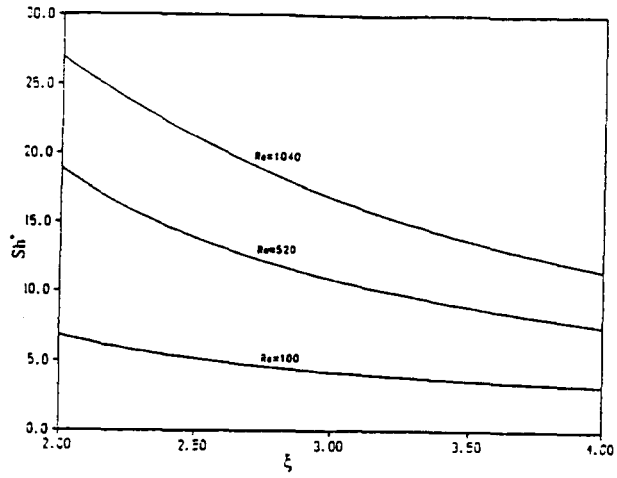

Figure 7 Variation of Sherwodd number (Sh^*) for $E=1.7x10^{-5}$ and k=142.5

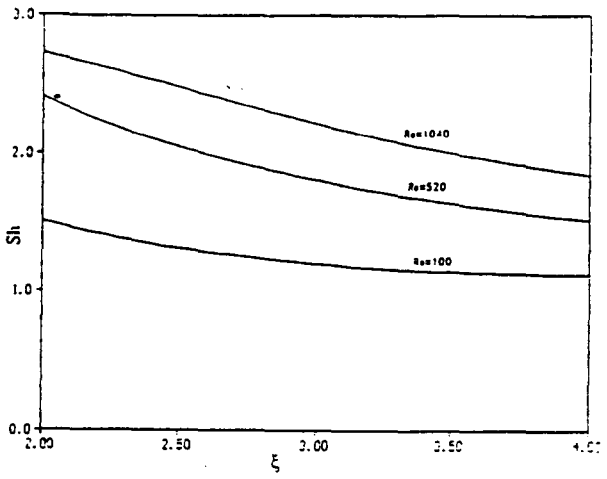

Figure 8 Variation of Sherwood number (Sh) for $E=1.7x10^{-5}$ and k=142.5

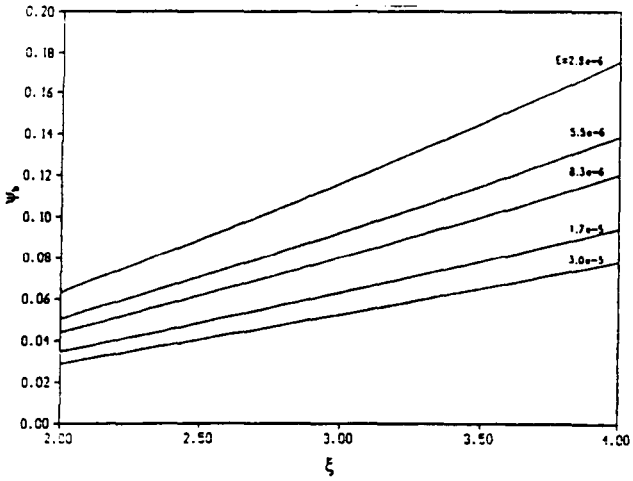

Figure 9 Variation of mixed-mean concentration for Re=520 and k=142.5

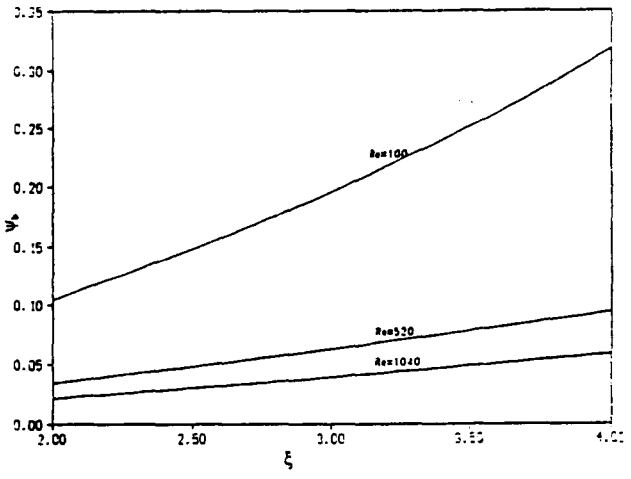

Figure 10 Variation mixed-mean concentration for $E=1.7x10^{-5}$ and k=142.5

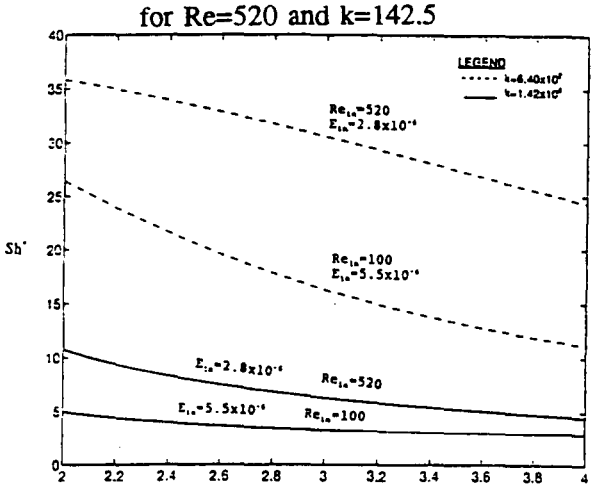

Figure 11 Comparison of Sherwood number (Sh^*) variation for different flow systems

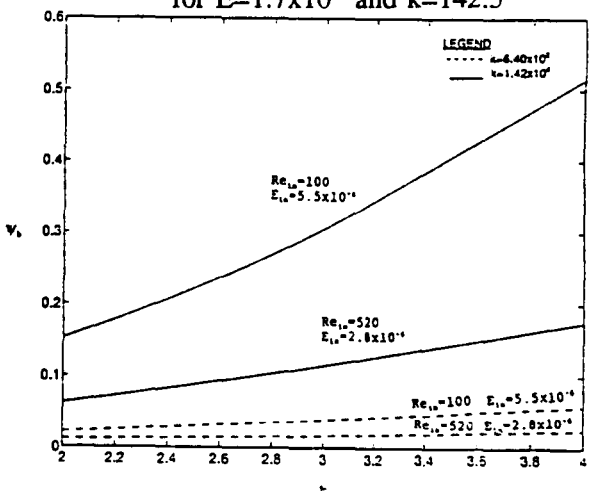

Figure 12 Comparison of mixed-mean concentration for different flow systems

FEATURES AND APPLICATIONS OF THE GROOVE ANALYSIS PROGRAM (GAP)

Tu M. Nguyen
OAO Corporation
Lanham, Maryland

Jentung Ku
NASA Goddard Space Flight Center
Greenbelt, Maryland

and

Patrick J. Brennan
OAO Corporation
Lanham, Maryland

SUMMARY

An IBM Personal Computer (PC) version of the Groove Analysis Program (GAP) was developed to predict the steady state heat transport capability of an axially grooved heat pipe for a specified groove geometry and working fluid. In the model, the capillary limit is determined by the numerical solution of the differential equation for momentum conservation with the appropriate boundary conditions. This governing equation accounts for the hydrodynamic losses due to friction in liquid and vapor flows and due to liquid/vapor shear interaction. Back-pumping in both 0-g and 1-g is accounted for in the boundary condition at the condenser end. Slug formation in 0-g and puddle flow in 1-g are also considered in the model. At the user's discretion, the code will perform the analysis for various fluid inventories (undercharge, nominal charge, overcharge, or a fixed fluid charge) and heat pipe elevations. GAP will also calculate the minimum required heat pipe wall thickness for pressure containment at design temperatures that are greater than or lower than the critical temperature of the working fluid.

This paper discusses the theory behind the development of the GAP model. It also presents the many useful and powerful capabilities of the model. Furthermore, a correlation of flight test performance data and the predictions using GAP is presented and discussed.

NOMENCLATURE

A	Cross-sectional area
g	Gravitational constant
K	Permeability
N	Number of grooves
P	Pressure
Q	Axial heat flow
QL	Heat transport capability at capillary limit
R	Meniscus radius
Re	Reynolds number
R_i	Groove root radius
R_r	Groove root corner radius
R_t	Groove tip corner radius
R_v	Vapor core radius
T_s	Pseudo-land thickness
WP	Wetted perimeter
W_g	Groove width
x	Axial location
γ	Angle to define groove geometry in Figure 1
δ	Angle to define groove geometry in Figure 1

θ	Angle to define groove geometry in Figure 1
ξ	Groove land taper angle
θ_c	Contact angle
λ	Heat of vaporization
μ	Dynamic Viscosity
ν	Kinematic Viscosity
ϕ	Groove aspect ratio (half groove width/groove depth)
Ψ	Function defined in equation (5) or (6)
ρ	Density
ω	Angular velocity
σ	Surface tension

Subscripts

l	Liquid
v	Vapor
vl	Vapor/Liquid
x	Axial direction

ACRONYMS

ATS	Applications Technology Satellite
CRYOHP	Cryogenic Heat Pipe Experiment
GAP	Groove Analysis Program
HPP	Heat Pipe Performance Experiment
NASA	National Aeronautics and Space Administration
PC	Personal Computer
RPM	Revolutions Per Minute

INTRODUCTION

In recent years, spacecraft size and power requirements have increased, along with a corresponding demand for more efficient waste heat rejection. The design of heat pipe-based spacecraft thermal management systems requires a clear understanding of the thermal performance and working fluid behavior of heat pipes in microgravity. On Earth, the strong gravitational field dominates the capillary forces developed in the heat pipe wick. However, in the absence of gravity, the surface tension forces within the wick are the heat transport's limiting factor. One method of predicting 0-g performance is by extrapolating ground test data, but the presence of a liquid puddle in the condenser can make this technique unreliable. This is particularly true with axially grooved ammonia heat pipes at the high end of their operating temperature range and with most cryogenic fluids because of their low surface tensions.

The principal microgravity application of heat pipe technology is cooling electronics packages in spacecraft and satellites. Commercial telecommunication spacecraft alone are utilizing more than two thousand heat pipes annually for high power thermal management. The majority of these pipes are aluminum/ammonia axially grooved tubing because of their simplicity and high reliability. It has been very apparent that there is a need to accurately predict the microgravity performance characteristics of a heat pipe to minimize the penalties associated with over-design. One problem that often arises is how to use ground test data to predict microgravity thermal performance of a heat pipe. In space, the heat

pipes can also be exposed to a wide range of temperatures, and the expansion and contraction of the working fluid can lead to excess or insufficient fluid inventories. During a cold startup scenario, a heat pipe containing the correct fluid charge for nominal operating temperatures may be undercharged due to liquid contraction. One common method of preventing this condition is to overcharge the heat pipe by 5 percent or more. At higher operating temperatures this leads to excess fluid that could form a thick film over the condenser wick, or a liquid slug, either of which will result in decreased heat rejection efficiency and higher operating temperatures. Also, as a result of limited heat pipe performance flight data, thermal systems engineers currently must specify heat pipes with large performance margins to compensate for possible degradations and uncertainties in heat transport capacity, therein incurring volume and weight penalties.

Therefore, a design tool is needed to assist the thermal engineers in designing an axially grooved heat pipe for a particular space application. This design tool must be accurate in predicting the thermal performance of a heat pipe at any operating condition and also be easy to use. This IBM PC version of GAP was designed to accomplish both requirements.

MATHEMATICAL FORMULATION

An IBM PC version of the GAP model was developed to predict the steady state heat transport capacity of an axially grooved heat pipe for a specified groove geometry and working fluid. An example of the geometry applicable to GAP is the divergent groove shown in Figure 1. A full description of the model is contained in the user's manual (Reference 1).

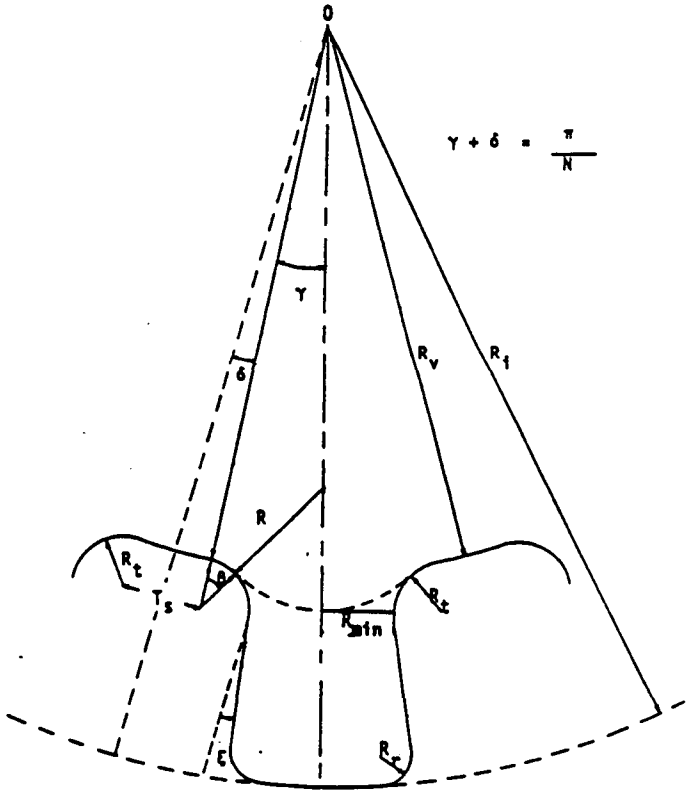

Figure 1. Divergent Groove Geometry

In the model, the capillary limit of the heat pipe is determined by the numerical solution of the differential equation for momentum conservation with the appropriate boundary conditions. This governing equation accounts for the hydrodynamic losses due to friction in the liquid and vapor flows and due to liquid/vapor shear interaction. Back-pumping which is the capillary force that develops at the condenser end in both 1-g and 0-g is accounted for in the condenser boundary condition. Slug formation in 0-g and puddle flow in 1-g are also considered in the model. At the user's discretion, the code will perform the analysis for various heat pipe elevations and fluid inventories, including both undercharged and overcharged conditions. GAP will also calculate the minimum heat pipe wall thickness required for pressure containment at design temperatures that are greater than or lower than the critical temperature of the working fluid.

The capillary pumping limit is the transport limit generally experienced in 0-g heat pipe operation. Sonic and vapor limits are typically encountered in 1-g applications with very high axial heat fluxes or when operating near the melting point. The viscous limit becomes important if the pipe is very long and is operated at lower temperature range of the working fluid. The capillary limit occurs when the capillary pumping head can no longer sustain the hydrodynamic losses. In the operation of an axial groove heat pipe, as heat is applied to the evaporator and is removed from the condenser, fluid flows develop within the heat pipe. The vapor flows to the condenser end and the liquid in the grooves is pumped back to the evaporator. In addition to the viscous pressure drops due to the vapor and liquid flows, there is an additional pressure drop due to shearing at the liquid/vapor interface. For steady state operation, the sum of all these pressure drops and those of body forces must be balanced by the capillary pumping force developed by the groove opening, i.e.

$$\Delta P_{x,capillary} = \Delta P_{x,v} + \Delta P_{x,l} + \Delta P_{x,vl} + \sum \Delta P_{x,body} \tag{1}$$

This constitutes the basic hydrodynamic governing equation for an axially grooved heat pipe. A differential form of this equation can be derived by making the following assumptions:

(1) One dimensional laminar liquid flows in the axial groove and one dimensional laminar or turbulent vapor flow in the inner core of the heat pipe;
(2) The groove depth is small compared to its wicking height, thus the hydrostatic loss associated with the groove depth is negligible;
(3) Identical grooves with uniform groove properties for each groove over the entire length; and
(4) Uniform heat transfer in the evaporator and condenser.

The governing equations are thus:

- Laminar vapor flow ($Re_v < 2000$)

$$\frac{\sigma Cos\theta_c}{R^2}\frac{dR}{dx} = \rho_l g Sin\beta + \left[\frac{8\mu_v}{\rho_v A_v R_v^2} + \frac{\mu_l}{KA_l\rho_l}\left(1+\frac{\phi^2}{3}\psi_x\right)\right]\frac{Q(x)}{\lambda} \tag{2}$$

- Turbulent vapor flow ($Re_v > 2000$)

$$\frac{\sigma Cos\theta_c}{R^2}\frac{dR}{dx} = \rho_l g Sin\beta + \frac{0.06558\mu_v^{0.25}}{\rho_v A_v^{1.75} R_v^{1.25}}\left(\frac{Q(x)}{\lambda}\right)^{1.75} + \frac{\mu_l}{KA_l\rho_l}\left(1+\frac{\phi^2}{3}\psi_x\right)\frac{Q(x)}{\lambda} \qquad (3)$$

where the groove aspect ratio ϕ, defined as the ratio of half the groove width to the groove depth, can be written as

$$\phi = \frac{(R_v+R_t)\ Sin\gamma\ -\ R_t}{R_i-R_v} \qquad (4)$$

and the parameter ψ_x which accounts for liquid/vapor shear (Reference 2) is defined as

- Laminar vapor flow

$$\psi_x = \frac{4(R_i-R_v)}{R_v}\frac{\nu_v}{\nu_l}\frac{A_{l,x}}{A_v} \qquad (5)$$

- Turbulent vapor flow

$$\psi_x = 0.03279\frac{R_i-R_v}{R_v^{0.25}}\frac{A_{l,x}}{A_v^{1.75}}\frac{\mu_v^{0.25}}{\rho_v\nu_l}\left(\frac{Q(x)}{\lambda}\right)^{0.75} \qquad (6)$$

The left hand side of equation (2) or (3) represents the capillary pumping. The right hand side represents the following pressure losses:

(1) The first term is the hydrostatic loss;
(2) The second term is the viscous vapor loss; and
(3) The third term is the liquid flow loss which combines both the viscous loss and the liquid/vapor shear interaction. The magnitude of the shear loss relative to the viscous liquid loss is $\phi^2\psi_x/3$. The factor 1/3 in this term is recommended in Reference 3 for grooves that have groove depths larger than groove widths, which is usually the case for axially grooved heat pipes.

Equations (2) and (3) are solved by using a fourth order Runge-Kutta integration method. The variables include working fluid properties, axial groove geometries, and heat pipe dimensions. The boundary conditions and heat distribution are also required to completely specify the problem. The integration of expression (2) or (3) yields the local meniscus radius required to support the local pressure drop in each groove. The integration process starts from the evaporator end with a minimum meniscus radius specified as half the groove width and proceeds to the condenser end. This process is normally repeated many times with the heat transport rate continuously updated until the boundary condition at the condenser end is satisfied. The liquid flow analysis conducted in Reference 2 demonstrated that the maximum transport is obtained when the meniscus radius at the upstream end of the evaporator is a minimum. Therefore, the boundary condition at the evaporator end for both 0-g and 1-g environments

for all fluid charge conditions is

$$@\ x = 0 \qquad R = R_{min} = \frac{W_g}{2} \tag{7}$$

where R_{min} for the axial groove geometry is shown in Figure 1.

At the condenser end, e.g. x = L, the boundary condition depends on the fluid charge condition and the gravitational environment. For nominal charge and overcharge, the meniscus radius is set to a maximum value to obtain the highest capillary pumping in the grooves. In 0-g, the excess liquid will form a slug in the vapor core at the condenser end. Two radii of curvature both equal to half the vapor core diameter define the minimum energy condition at the slug's liquid/vapor interface. Mass continuity between the liquid slug and the liquid in the grooves in turn dictates an equivalent groove radius in the condenser. In the code, the meniscus radius at the condenser end is set at half the vapor core radius to model this condition

$$For\ 0\text{-}g,\quad @\ x = L \qquad R = R_{max} = \frac{R_v}{2} \tag{8}$$

In 1-g, when there is excess liquid in the pipe, a puddle will form at the condenser end. Beyond the puddle, if preferential drainage is neglected, only one radius of curvature exists in the groove. This liquid/vapor interface extends from the tip of one fin to the tip of the adjacent fin and its maximum value is equal to the vapor core radius, i.e.

$$For\ 1\text{-}g,\quad @\ x = L \qquad R = R_{max} = R_v \tag{9}$$

For undercharge condition, the meniscus radius at the condenser end is incremented gradually from R_{min} up to R_{max} until the specified fluid charge is found. Thus, depending on the amount of undercharge and the gravitational environment, the actual meniscus radius at the condenser end will be between R_{min} and the value shown in equation (8) or (9).

The program estimates the maximum transport using a closed form solution for liquid losses only. It then uses an incremental heat load based on this value and solves the differential equation to determine the axial variation of the meniscus. Once this is known, the corresponding liquid and vapor inventories are calculated. Repeating this solution procedure will then yield the maximum transport that can be obtained as a function of fluid inventory up to the nominal charge condition.

FEATURES IN GAP

The IBM PC version of this GAP code is a menu-driven computer program designed for user friendliness and flexibility not only in the data input but also in the code operation and in the processing of the output data. The general flow chart of the code is shown in Figure 2. The code is written in standard FORTRAN 77 and assembly language. It is designed to operate with an IBM PC or compatible system that employs an 80286, 80386, or 80486 microprocessor with an appropriate coprocessor. The present code has been intended to be interactive and user-friendly. It can be installed into a PC in a few minutes and with the interactive data input feature, the user can run the code immediately to get the results. Other special features of the code include:

- Multiple runs for various heat pipe elevations and over a wide range of temperatures are readily achieved;
- A comprehensive data base that contains the properties of 24 heat pipe working fluids is included with the code. A listing of these working fluids and their corresponding range of operating temperatures are included in Table 1;
- For pressure containment, the minimum required heat pipe wall thickness can be determined for specified factors of safety; and
- At the user's discretion, the desired output data is written to a plot file which can be imported to most spreadsheet or graphic software programs for fast quality plotting.

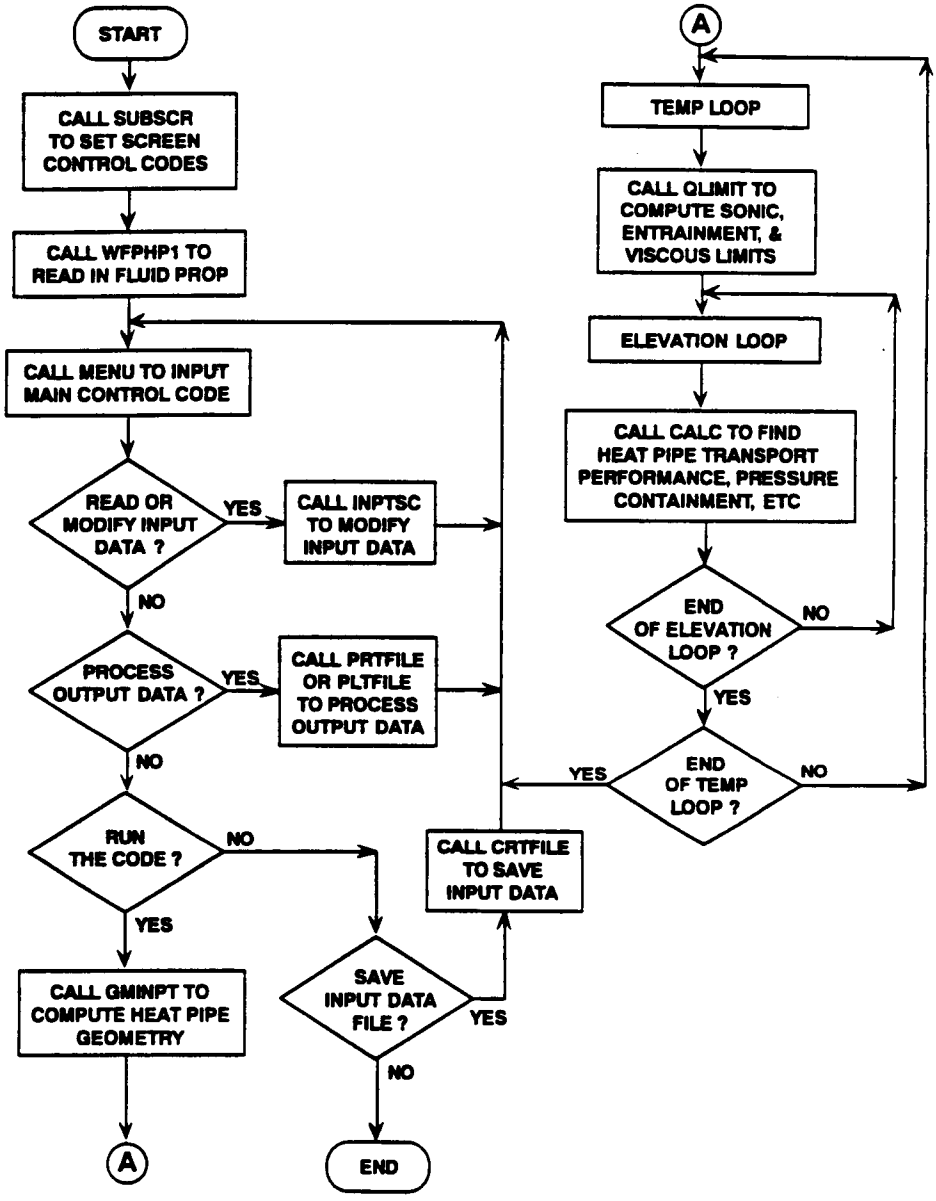

Figure 2. GAP General Flowchart

Table 1. Heat Pipe Working Fluids in GAP

Working Fluid	Temperature Range (K)	Working Fluid	Temperature Range (K)
Acetone	250 to 474	Freon 21	213 to 449
Ammonia	200 to 404	Freon 113	293 to 368
Argon	85 to 149	Heptane	273 to 472
Benzene	270 to 559	Lithium	500 to 2099
Butane	260 to 349	Mercury	280 to 1069
Cesium	400 to 1499	Methane	91 to 189
Dowtherm-A	373 to 669	Methanol	273 to 502
Dowtherm-E	283 to 609	Nitrogen	65 to 124
Ethane	100 to 304	Oxygen	55 to 154
Freon 11	293 to 412	Potassium	400 to 1799
Freon 13	163 to 292	Sodium	400 to 1499
Freon 14	130 to 221	Water	273 to 642

FLIGHT DATA CORRELATIONS

The GAP code was used to predict the heat transport capacity of the axially grooved heat pipes employed in the Heat Pipe Performance (HPP) (References 4 and 5) and the Cryogenic Heat Pipe (CRYOHP) (Reference 6) flight experiments. The results were obtained by running the code to predict 0-g performance for each pipe with a nominal charge at various operating temperatures. These results were then correlated with the flight test data to assess the accuracy of the code. The following sections discuss the GAP predicted performance and the associated correlations with flight data for these pipes.

HPP Freon 113/Aluminum Heat Pipe

This heat pipe utilizes a rectangular groove geometry with its measured groove geometry shown in Table 2. The detail of the HPP experiment design is discussed in References 4 and 5. The GAP predicted 0-g steady state heat transport capacity of the pipe as a function of the operating temperature range of interest is shown in Figure 3. At 58°C, the pipe is expected to transport about 23 watts before dry-out occurs. This power level is in excellent agreement with the actual 24 watts obtained in flight. It should be noted that these pipes were charged for operation at 40°C and have a 4.9% overcharge at 58°C. This charge is based on the accounting for meniscus recession.

The prediction of the heat transport capacity of a heat pipe subjected to adverse spin was determined in the following manner. First, the maximum transport under a no spin condition was obtained from GAP. Then, this value was used in the following expression to determine the heat transport capacity of a heat pipe under adverse spin as:

$$QL = (QL)_{max}\left[1 - \frac{1}{4}\frac{\rho_l W_g}{\sigma}\omega^2\left(R_c^2 - R_e^2\right)\right] \qquad (10)$$

Table 2. HPP Freon 113/Aluminum Heat Pipe Design Summary

Groove Cross Section	Rectangular Form
Number of Grooves	40
Outer Diameter (inch, mm)	0.499, 12.675
Inner Diameter (inch, mm)	0.437, 11.10
Vapor Core Diameter (inch, mm)	0.364, 9.246
Fin Tip Corner Radius (inch, mm)	0.00428, 0.1087
Groove Root Corner Radius (inch, mm)	0.00409, 0.1039
Pseudo-land Tip Thickness (inch, mm)	0.00638, 0.1621
Groove Land Taper Angle (radian)	0.047
Groove Width (inch, mm)	0.0143, 0.3635
Wetted Perimeter (1 Groove) (inch, mm)	0.0909, 2.308
Total Groove Area (inch^2, mm^2)	0.0222, 14.31
Evaporator Length (inch, mm)	4.0, 101.6
Transport Section Length (inch, mm)	0.0, 0.0
Condenser Length (inch, mm)	12.76, 324.1

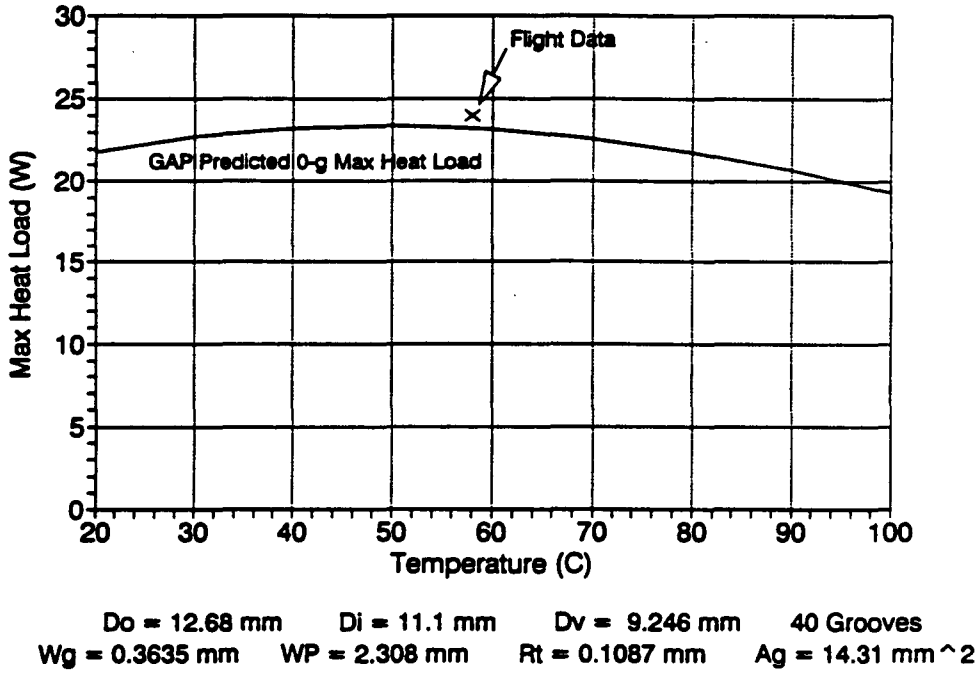

Figure 3. HPP Freon Heat Pipe 0-g Transport Capability vs. Temperature

where QL = transport capacity of the heat pipe experiencing adverse spin
$(QL)_{max}$ = maximum transport capacity under no spin condition
ρ_l = density of the liquid phase
ω = angular velocity
σ = surface tension
R_c = linear distance from the center of rotation to the end of the condenser section
R_e = linear distance from the center of rotation to the end of the evaporator section
W_g = groove width

With this procedure, the maximum heat load for the pipe at 32°C versus adverse spin rate is computed. The data indicates that at a spin rate of about 6 RPM, the pipe can transport a maximum power of 6 watts. This result is in good agreement with the flight data which showed that dry-out for the pipe occurred between 6 and 8 RPM with 6 watts applied.

HPP Water/Copper Heat Pipe

This heat pipe utilizes a rectangular groove geometry. Table 3 provides the groove measurement of this pipe. The GAP code was used to predict the 0-g steady state heat transport capacity of the pipe as a function of the operating temperature range as shown in Figure 4. Note that at 50°C, the curve seems to have a discontinuity. This is the point at which the vapor flow in the pipe is predicted to transition from a laminar to a turbulent flow regime. The pressure losses due to vapor flow and vapor-liquid shear in turbulent flow are higher than those in laminar flow; and thus, the slope of the heat transport curve decreases slightly. With the same procedure used for the freon heat pipe, the heat transport capacity of this water heat pipe at 72°C was predicted as a function of adverse spin and it is shown in Figure 5. From this Figure, one would expect a pipe transporting about 40 watts to dry out at about 10.4 RPM. This turns out to be the case in flight where the measured dry-outs were obtained between 10 to 12 RPM.

Table 3. HPP Water/Copper Heat Pipe Design Summary

Groove Cross Section	Rectangular Form
Number of Grooves	25
Outer Diameter (inch, mm)	0.497, 12.631
Inner Diameter (inch, mm)	0.454, 11.521
Vapor Core Diameter (inch, mm)	0.375, 9.535
Fin Tip Corner Radius (inch, mm)	0.00464, 0.1178
Groove Root Corner Radius (inch, mm)	0.01462, 0.3713
Pseudo-land Tip Thickness (inch, mm)	0.00391, 0.09934
Groove Land Taper Angle (radian)	0.08155
Groove Width (inch, mm)	0.0351, 0.8915
Wetted Perimeter (1 Groove) (inch, mm)	0.1092, 2.775
Total Groove Area ($inch^2$, mm^2)	0.0335, 21.622
Evaporator Length (inch, mm)	4.0, 101.6
Transport Section Length (inch, mm)	0.0, 0.0
Condenser Length (inch, mm)	12.76, 324.1

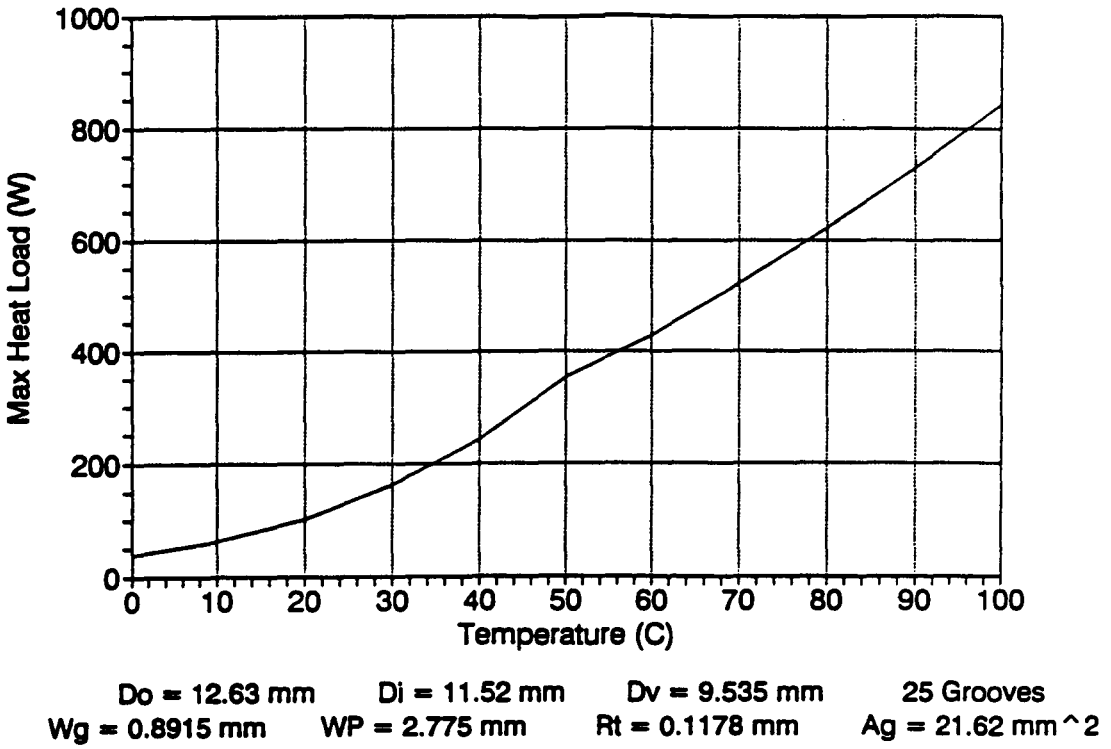

Figure 4. HPP Water Heat Pipe 0-g Transport Capability vs. Temperature

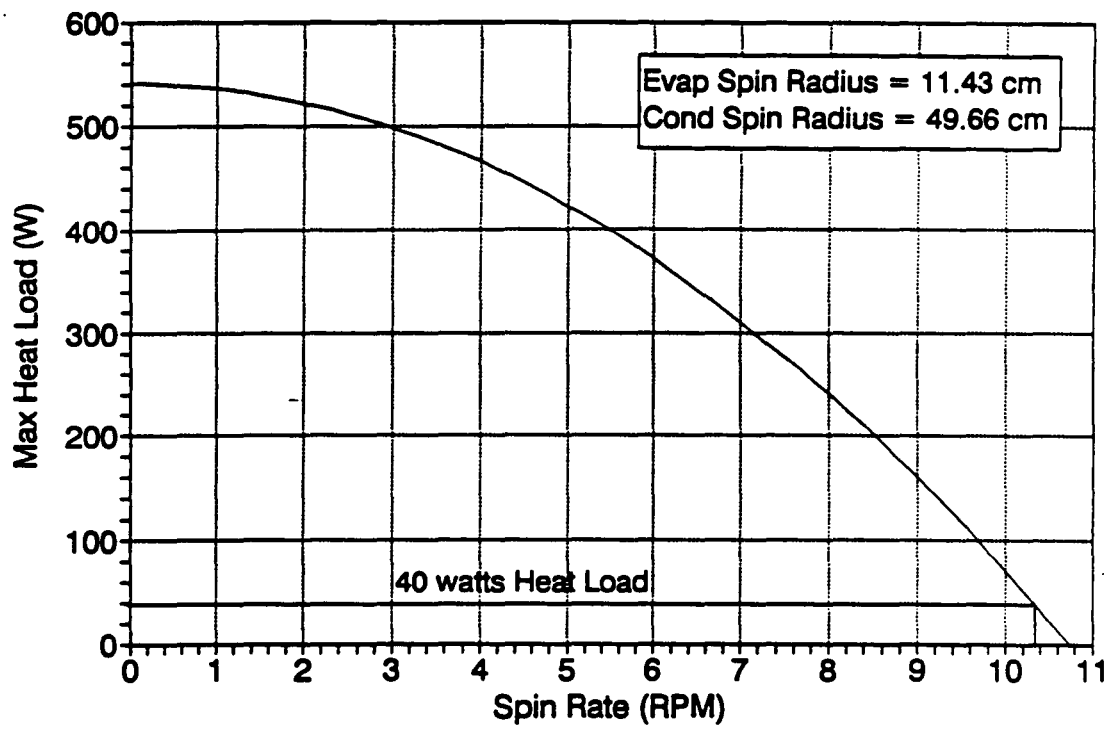

Figure 5. HPP Water Heat Pipe 0-g Transport @ 72°C vs. Adverse Spin Rate

TRW Cryogenic Heat Pipe (CRYOHP)

This heat pipe has oxygen working fluid and employs a rectangular groove geometry with relatively shallow grooves ($\sim$0.8 mm deep) as shown in Table 4. This design was intentionally degraded so that its heat transport capacity could be tested within the limits of the CRYOHP's cooling capacity ($\sim$5 watts at 80 K). The CRYOHP experiment design and component test results are discussed in Reference 7.

The 0-g steady state heat transport capacity of the heat pipe predicted by GAP is shown in Figure 6 with the flight and ground test data. Flight data points are the actual electrical heater power applied to the evaporator. The GAP predictions include a 0.8 watt parasitic heat leak from the surrounding environment to the heat pipe. This heat leak was determined from ground and flight data transients (Reference 6). The GAP predictions are in good agreement with the flight test data. GAP correctly predicted the fully dry-out heat load at 69 K and under-predicted the values at 92 K and 102 K by approximately 0.5 watt. The applied power increments for the TRW pipe are 0.5 watt and therefore there is up to a 0.5 watt uncertainty when full dry-out occurs.

Also shown in Figure 6 is the 1-g performance at 82 K that was extrapolated from the component tilt test results presented in Reference 7. At this temperature, the pipe was predicted to be over-filled as listed in Table 5. The nominal charge required at 82 K as predicted by GAP is 8.54 grams. If the grooves were filled without any meniscus recession, the charge would increase by 1.05 grams or 12.2% above the nominal charge with recession. In addition to the amount associated with meniscus recession and based on the actual 10.3 grams charge, there is an additional 0.71 gram or 8.4% of further overcharge at 82 K. The 0-g slug length at 82 K for this overcharge condition is 3.63 cm. The GAP predicted performance at 82 K for a 1-g horizontal test condition was obtained with this overcharge (i.e. 1.76 grams excess) and is plotted in Figure 6. Note that in this 1-g analysis, the same 0.8 watt parasitic heat leak to the pipe was assumed. This theoretical data point is only 0.3 watt lower than the extrapolated ground-test data point.

Table 4. TRW CRYOHP Heat Pipe Design Summary

Groove Cross Section	Rectangular Form
Number of Grooves	17
Outer Diameter (inch, mm)	0.442, 11.224
Inner Diameter (inch, mm)	0.349, 8.872
Vapor Core Diameter (inch, mm)	0.2865, 7.277
Fin Tip Corner Radius (inch, mm)	0.004, 0.1016
Groove Root Corner Radius (inch, mm)	0.00508, 0.1291
Pseudo-land Tip Thickness (inch, mm)	0.02887, 0.7334
Groove Land Taper Angle (radian)	0.1685
Groove Width (inch, mm)	0.0175, 0.445
Wetted Perimeter (1 Groove) (inch, mm)	0.0822, 2.089
Total Groove Area ($inch^2$, mm^2)	0.0094, 6.065
Evaporator Length (inch, mm)	6.0, 152.4
Transport Section Length (inch, mm)	40.8, 1015.24
Condenser Length (inch, mm)	6.0, 152.4
Fluid Charge (gr)	10.3

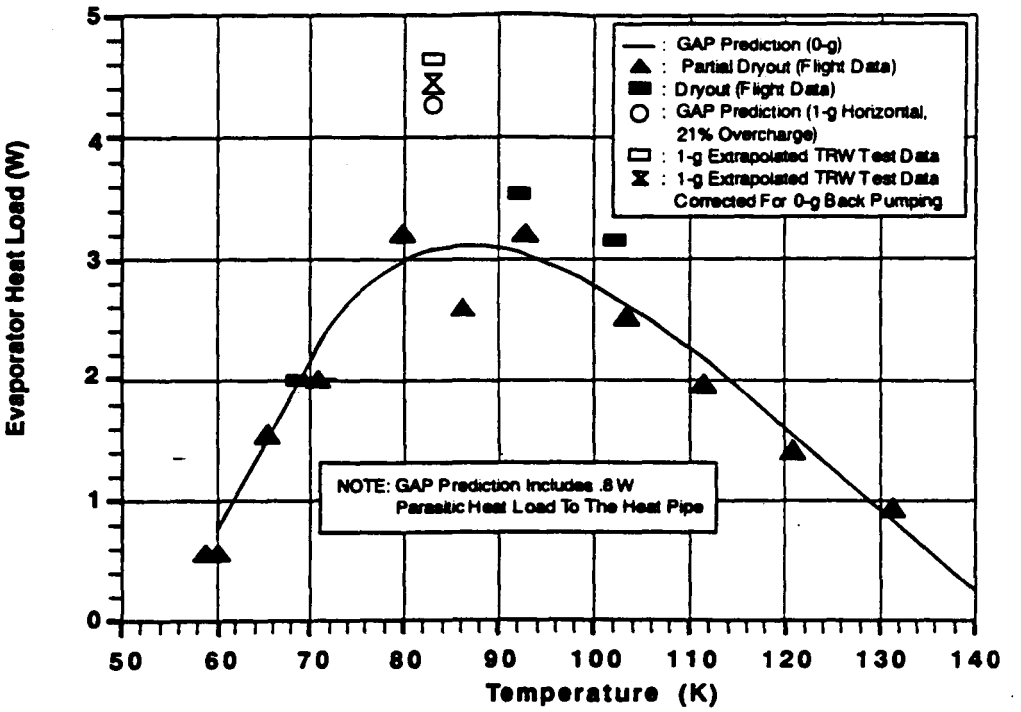

"AS-FABRICATED" GROOVE DIMENSIONS FOR GAP PREDICTIONS:
D_O = 11.22 mm D_I = 8.872 mm D_V = 7.277 mm 17 Grooves
W_g = 0.445 mm WP = 2.089 mm R_c = 0.1016 mm A_g = 6.065 mm^2

Figure 6. TRW CRYOHP Heat Pipe Transport Capability vs. Temperature

Table 5. TRW CRYOHP Heat Pipe Fluid Charge Conditions
Actual Charge = 10.3 gr

Operating Temperature (K)	GAP Computed Nominal Charge (gr)	Percentage Charge (Actual/GAP Nominal)
60	8.93	115.34
70	8.71	118.23
80	8.58	120.11
90	8.40	122.62
100	8.29	124.24
110	8.45	121.89
120	9.05	113.86
130	10.16	101.36
140	12.17	84.61
150	18.06	57.02

Hughes Aircraft Cryogenic Heat Pipe (CRYOHP)

This heat pipe also utilizes oxygen with the conventional ATS rectangular groove geometry (Reference 8). Design details of the heat pipe and the groove geometry obtained from a shadowgraph measurement are listed in Table 6. The oxygen charge for this heat pipe is 33.7 grams.

The GAP predicted 0-g steady state transport capability of this heat pipe is shown in Figure 7 versus operating temperature. Flight and thermal vacuum test data are also included in this figure. The GAP predictions include a 1.1 watt uniform parasitic heat leak to the heat pipe from the surroundings (Reference 6). In general, the flight data is in good agreement with the GAP prediction. A partial dry-out is the best measure of a heat pipe's capillary transport limit and these data points correlate almost exactly over the test temperature range of 100 to 140 K. The model tends to under-predict the dry-out condition by almost 5 watts at 128 K. This data point was obtained under transient condition because of inadequate cooling, and transient performance is not an accurate measure of the transport limit.

Also shown in Figure 7 is the 1-g performance at 85 K that was extrapolated from the component tilt tests in Reference 8. At this temperature, the Hughes heat pipe was predicted to be slightly over-filled by just 0.1 gram. Fluid charge conditions at other temperatures were predicted by GAP and are listed in Table 7. Again the performance of this heat pipe at 85 K for a 1-g horizontal position with a 1.14 watt parasitic heat leak to the pipe was predicted and is included in Figure 7. This single GAP data point is approximately 1.5 watts lower than the extrapolated ground-test data. The small difference is, however, well within the accuracy of the groove measurements and the experimental error.

Table 6. Hughes Aircraft CRYOHP Heat Pipe Design Summary

Groove Cross Section	Rectangular Form
Number of Grooves	27
Outer Diameter (inch, mm)	0.627, 15.914
Inner Diameter (inch, mm)	0.429, 10.897
Vapor Core Diameter (inch, mm)	0.334, 8.484
Fin Tip Corner Radius (inch, mm)	0.0064, 0.1623
Groove Root Corner Radius (inch, mm)	0.00625, 0.1588
Pseudo-land Tip Thickness (inch, mm)	0.00159, 0.0403
Groove Land Taper Angle (radian)	0.0546
Groove Width (inch, mm)	0.0259, 0.658
Wetted Perimeter (1 Groove) (inch, mm)	0.1281, 3.253
Total Groove Area ($inch^2$, mm^2)	0.036, 23.226
Evaporator Length (inch, mm)	6.0, 152.4
Transport Section Length (inch, mm)	42.8, 1065.2
Condenser Length (inch, mm)	6.0, 152.4

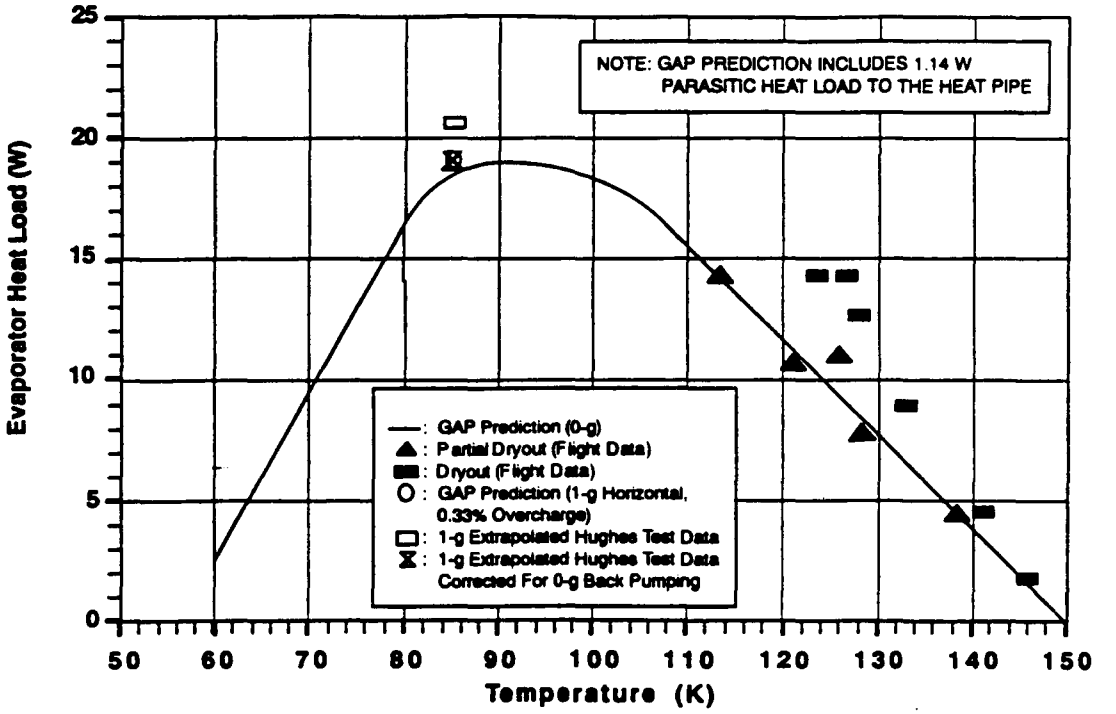

"AS-FABRICATED" GROOVE DIMENSIONS FOR GAP PREDICTIONS:

D_O = 15.91 mm D_I = 10.90 mm D_V = 8.487 mm 27 Grooves

W_g = 0.658 mm WP = 3.253 mm R_c = 0.1623 mm A_g = 23.23 mm^2

Figure 7. Hughes Aircraft CRYOHP Heat Pipe Transport Capability vs. Temperature

Table 7. Hughes Aircraft CRYOHP Heat Pipe Fluid Charge Conditions

Actual Charge = 33.7 gr

Operating Temperature (K)	GAP Computed Nominal Charge (gr)	Percentage Charge (Actual/GAP Nominal)
60	35.69	94.42
70	34.78	96.89
80	33.79	99.73
90	32.99	102.15
100	31.68	106.38
110	30.73	109.66
120	30.57	110.24
130	31.20	108.01
140	32.39	104.04
150	36.66	91.93

CONCLUSIONS

An IBM PC model of GAP was developed to predict the steady state thermal performance of an axially grooved heat pipe operating in 1-g or microgravity environment. The model is user-friendly and easy to use. It has been shown to accurately predict the transport capability of axially grooved heat pipes. For the HPP flight experiment, static dryout limits of the aluminum/freon pipes in microgravity were obtained and are in excellent agreement with the analytical predictions by the model. The transport limits of the freon and water pipes under adverse spin also correlate well with the predictions by the GAP model. For further verification, the computer model was applied to predict the transport limits of two aluminum/oxygen pipes flown in the CRYOHP experiment. These predictions are also in excellent agreement with the test data over a wide range of operating temperatures.

In support of the on-going Heat Pipe Performance Reflight (HPP-2) project and with the recommendations by several users, the current GAP model is being upgraded to accommodate the actual boundary conditions of an axially grooved heat pipe utilized in most applications. The following features have been planned for this new version:

- Boiling limit will be included in the calculation of transport limits. Heat diffusion in the heat pipe wall will be accounted for in this calculation. Therefore, thermal conductivity of the heat pipe wall is an important parameter and will be correlated with the evaporator temperature;
- Asymmetric heating and cooling of the evaporator and condenser, respectively, will be considered in the computation of maximum heat transport capability. In most practical applications, the heat pipe is embedded inside a panel, which results in non-uniform heating or cooling of the evaporator or condenser, respectively. In these cases, the heat pipe exhibit lower heat transport capability because of local dry-out in the grooves; and
- Multiple sections of evaporator, transport, and condenser will also be included in the model. This feature is critical to account for distributed heat loads along a heat pipe in many applications.

REFERENCES

1. Nguyen, T. M., "User's Manual for Groove Analysis Program (GAP) IBM PC Version 1.0," OAO Corporation, February 1994.
2. Kroliczek, E. J. and Jen, H., "Axially Grooved Heat Pipe Study," Summary Report, BK012-1009, B&K Engineering, Incorporated, June 1977.
3. Hufschmidt, E. et al. "The Shearing Effect of Vapor Flow on Laminar Liquid Flow in Capillaries of Heat Pipe," NASA TT-F-16601, October 1975.
4. Heat Pipe Performance Experiment (HPP) Final Report, Fleishman, G. L. and Grier, K. D., Hughes Aircraft Company, Electron Dynamics Division, June 1993.
5. Buchko, M. T., Brennan, P. J., and Nguyen, T. M., "Flight and Ground Test Data Analysis for the Heat Pipe Performance (HPP) Experiment," SAE Paper Number 941300, June 1994.
6. Brennan, P. J., Thienel, L., Swanson, T., and Morgan, M., "Flight Data for the Cryogenic Heat Pipe (CRYOHP) Experiment," AIAA Paper Number 93-2735, July 1993.
7. Antoniuk, D. and Pohner, J., "Development of an Oxygen Axial Groove Heat Pipe for A Microgravity Flight Experiment," AIAA Paper Number 91-1357, June 1991.
8. Fleishman, G. L., Chiang, T. C., and Ruff, R. D., "Oxygen Heat Pipe 0-g Performance Evaluation Based on 1-g Tests," AIAA Paper Number 91-1358, June 1991.

VALIDATION OF THE SINDA/FLUINT CODE USING SEVERAL ANALYTICAL SOLUTIONS

John R. Keller
Lockheed Engineering and Sciences Company
Houston, Texas

ABSTRACT

The Systems Improved Numerical Differencing Analyzer and Fluid Integrator (SINDA/FLUINT) code has often been used to determine the transient and steady-state response of various thermal and fluid flow networks. While this code is an often used design and analysis tool, the validation of this program has been limited to a few simple studies.

For the current study, the SINDA/FLUINT code was compared to four different analytical solutions. The thermal analyzer portion of the code (conduction and radiative heat transfer, SINDA portion) was first compared to two separate solutions. The first comparison examined a semi-infinite slab with a periodic surface temperature boundary condition. Next, a small, uniform temperature object (lumped capacitance) was allowed to radiate to a fixed temperature sink. The fluid portion of the code (FLUINT) was also compared to two different analytical solutions. The first study examined a tank filling process by an ideal gas in which there is both control volume work and heat transfer. The final comparison considered the flow in a pipe joining two infinite reservoirs of pressure. The results of all these studies showed that for the situations examined here, the SINDA/FLUINT code was able to match the results of the analytical solutions.

INTRODUCTION

The Systems Improved Numerical Differencing Analyzer and Fluid Integrator (SINDA/FLUINT) program has often been used to determine the transient hydrodynamic and thermal response of various thermal and fluid networks. For example, the Space Station Freedom's (SSF) Active Thermal Control System (ATCS) [1] and airlock [2], the Space Shuttle's ATCS [3], and the SSF's Lunar Transport Vehicle Hangar [4] have all been analyzed using this code. While this code has provided important results in the design and analysis of these and other space related hardware, the validation of this program has been limited.

The validation of any numerical code is important, since once a code has been verified for several test cases, a user will have confidence that the code can accurately predict the physical processes of other, more complex problems. In general, there are three main verification methods. The first method compares the predicted results with those of a previously validated code [5]. The second method uses experimental data to verify the model's predictions [6]. Finally, the predicted results can be compared to those of a closed form analytical solution [7].

To date, the SINDA/FLUINT code has been validated with three simple closed form solutions [8,9,10] and one relatively complex experimental comparison [11]. The three closed form solutions considered were the transient conduction in a semi-infinite slab [8], the filling and decompression of a rigid, adiabatic tank with an ideal gas [9], and the transient heat transfer associated with a single phase fluid flowing in a duct [10]. The experimental comparison examined the combined radiative, conductive, and convective heat rejection process associated with the operation of the Space Shuttle's ATCS during orbital conditions [11]. For all the tests cases considered, the predictions of the SINDA/FLUINT code were able to match the results of either the closed form solutions or the experimental data; however, the program has yet to be validated for more complex situations such as transient radiation, conduction or fluid flow phenomenon.

This paper details a validation study of the SINDA/FLUINT program for several simple situations. The code was validated by comparing its results with those of several closed form analytical solutions. The SINDA portion of the code was compared to two different analytical solutions, while the FLUINT portion of the code was also validated with two separate analytical solutions. The results of these studies showed that for the situations examined here, the code was able to accurately predict the heat transfer and fluid flow processes.

HEAT TRANSFER IN A SEMI-INFINITE SOLID

The SINDA portion of the code was first validated using the classical closed form solution for conduction heat transfer in a semi-infinite solid. For this test case, a periodic surface temperature boundary condition was considered. A schematic of this system and its associated boundary condition is shown in Figure 1.

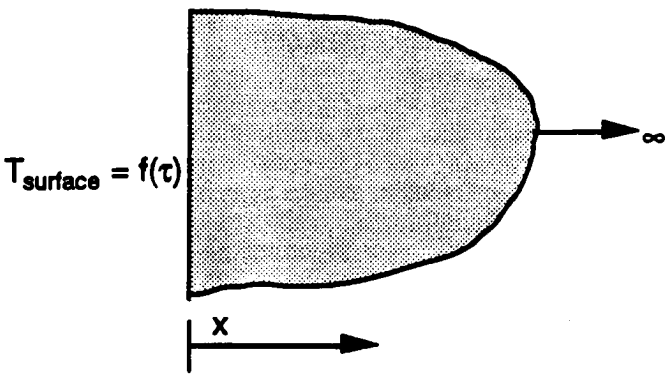

Figure 1 Schematic of a Semi-Infinite Solid.

The heat conduction in a semi-infinite solid, with no internal generation and constant thermophysical properties, is governed by the following differential equation,

$$\frac{\partial^2 T}{\partial x^2} = \frac{1}{\alpha}\frac{\partial T}{\partial \tau} \tag{1}$$

where the variables T, x, α, and τ are the temperature, distance, thermal diffusivity, and time, respectively. To reduce the complexity of the solution process, the temperature is replaced by a new variable, Θ, which is defined as

$$\Theta = T - T_i \tag{2}$$

where the subscript i denotes the initial condition. The new governing equation and the boundary conditions for this problem are

$$\frac{\partial^2 \Theta}{\partial x^2} = \frac{1}{\alpha}\frac{\partial \Theta}{\partial \tau} \tag{3}$$

$$\Theta(x,0) = 0 \tag{4}$$

$$\Theta(\infty,\tau) = 0 \tag{5}$$

$$\Theta(0,\tau) = \Theta_0 \cos\omega\tau \tag{6}$$

where Θ_0 and ω are the amplitude and frequency, respectively. To obtain a solution for equation (3), the separation of variables method must be used and for brevity will not be presented here. A detailed discussion of this solution procedure can be found in Reference 12. The solution to equation (3) with the appropriate boundary conditions is

$$\frac{\Theta(x,t)}{\Theta_0} = e^{-(\omega/2\alpha)^{1/2}x} \cos\left[\omega\tau - \left(\frac{\omega}{2\alpha}\right)^{1/2} x\right] \tag{7}$$

It is important to note that equation (7) is only valid for large values of time since there is a discontinuity at the initial conditions. In other words, equation (7) cannot accurately predict transient effects during the first increase of the solid's outer surface.

Once the analytical solution had been obtained for conduction in a semi-infinite solid, a SINDA model was built for the comparison study. A schematic of this SINDA model is shown in Figure 2. Here, a series of nodes with a height and depth of unity are placed together. The lengthwise spacing and thermophysical properties are input parameters and chosen in such a way that the computational process is simplified.

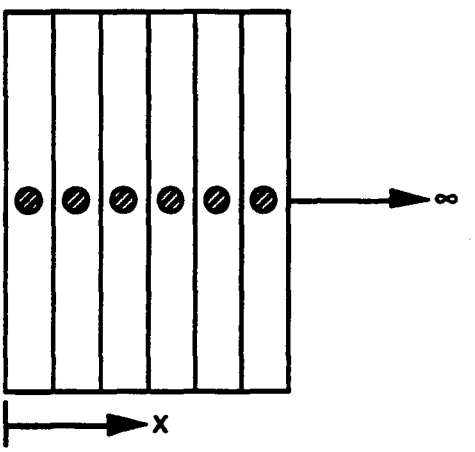

Figure 2 Schematic of the SINDA model.

Figure 3 shows the comparison between the results of the SINDA model and those of the analytical solution at different depths into the semi-infinite slab. As anticipated, the predictions show an exponential decay in the oscillating temperature as the depth into the solid increases. In addition, the predictions also show a phase shift in the oscillating temperatures and is associated with the time it takes the heat to be conducted into the solid. As is evident, for the parameters examined here, the predictions are nearly identical to those of the analytical solution. The greatest temperature difference between the results of the two solutions is less than 1.25 °F. Other conditions were also examined and a similar error was noted.

COOLING BY RADIATIVE HEAT TRANSFER

The SINDA portion of the code was next validated using a closed form solution of a simple radiative cooling process in which a warm object cools by thermal radiation to a cold sink. To simplify the analysis, the lumped capacitance method was employed and the object radiated to one source. In other words, the entire solid was at a uniform temperature, one cold sink was available and there was no reflected radiation. To further simplify the analysis, the radiating source was taken to be diffusive. Applying these assumptions, the heat loss, Q, at an instant in time is given by

$$Q = \varepsilon A \sigma [T^4 - T^4_{sink}] \tag{8}$$

where ε is the emissivity, A is the surface area, σ is the Stefan-Boltzmann constant, T is the object's lumped temperature, and T_{sink} is the radiative sink temperature. Rewriting equation (8) for transient conditions and using the lumped capacitance assumption yields

$$- \rho V C_p \frac{\partial T}{\partial \tau} = Q = \varepsilon A \sigma [T^4 - T^4_{sink}] \tag{9}$$

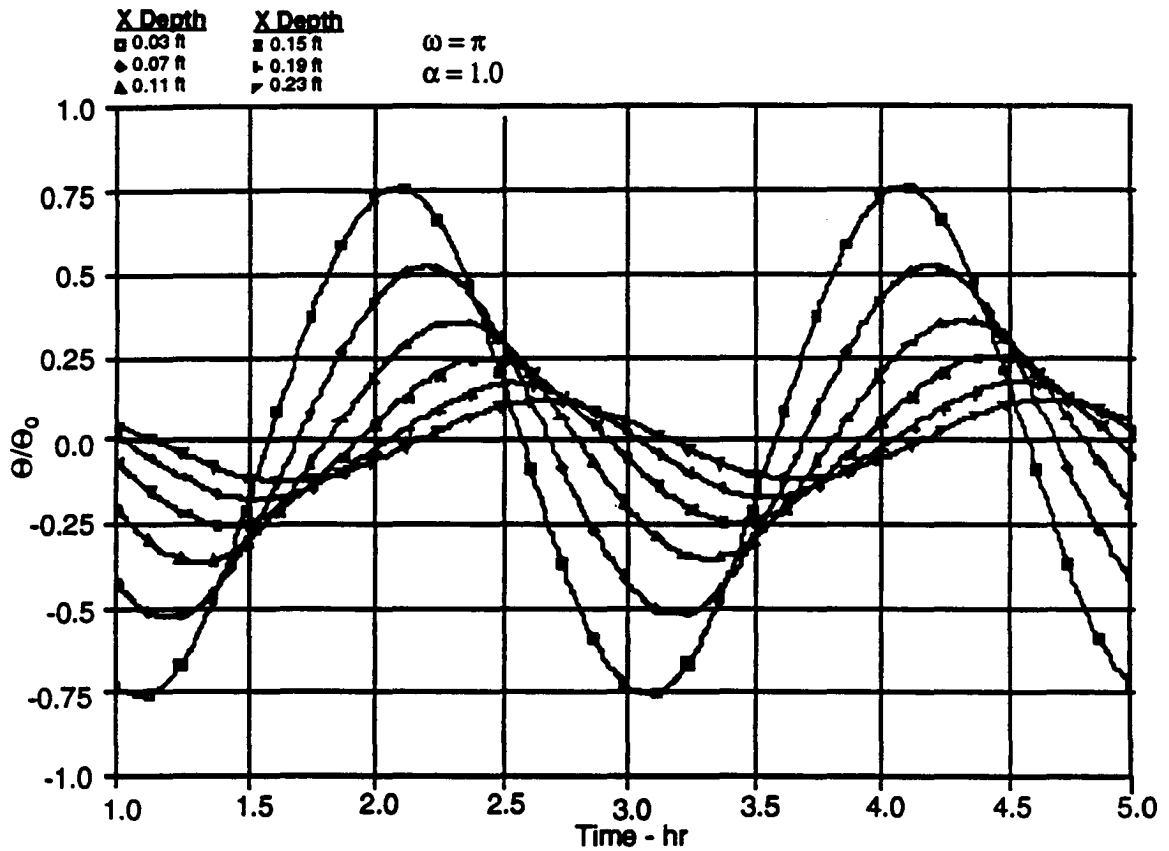

Figure 3 Temperature Response for Predicted (geometric shapes) and Analytical Solutions (solid lines).

where the new variables ρ, V, C_p, and τ represent the density, volume, the specific heat and time, respectively. Rearranging and integrating equation (9) yields,

$$-\int_{T=T_i}^{T=T_f} \frac{\partial T}{T^4 - T^4_{sink}} = \frac{\varepsilon A \sigma}{\rho V C_p} \int_0^{\tau} \partial\tau \qquad (10)$$

where T_i and T_f are the initial and final temperatures, respectively. Carrying out the integration on equation (10), yields equation (11)

$$\tau = \frac{\rho V C_p}{\varepsilon A \sigma}\left[\frac{1}{4T^3_{sink}} \ln\left\{\frac{(T_f + T_{sink})/(T_f - T_{sink})}{(T_i + T_{sink})/(T_i - T_{sink})}\right\} + \frac{1}{2T^3_{sink}}\left(\tan^{-1}\frac{T_f}{T_{sink}} - \tan^{-1}\frac{T_i}{T_{sink}}\right)\right] \qquad (11)$$

Equation (11) reveals that for a given initial temperature, the final temperature is governed by the time, τ, the sink temperature, T_{sink}, and the term, $\rho V C_p/\varepsilon A\sigma$, (capacitance divided by radiative conductance). These terms were varied during the verification process. For the present study, the sink temperature was held at either -100 °F, -200 °F or -400 °F, while the capacitance-conductance ratio was set at 0.25, 0.5, 1.0 and 4.0. For each simulation, the initial temperature was held at 70 °F and the object was allowed to cool for 10 hours.

The results from both the SINDA model and the analytical solution for all the above conditions are shown in Figure 4. As expected, the cooling process follows a typical exponential decay, and the higher capacitance (or lower radiative conductance) objects cool more slowly. As is evident, the SINDA generated results are in good agreement with those of the analytical solution, since the predicted results are nearly identical to those of the analytical solution. The greatest temperature difference between the results of the two solutions is less than 1.5 °F, which corresponds to an error based on absolute temperature of less than 0.5% .

FLOW BETWEEN TWO INFINITE RESERVIORS OF PRESSURE

When two infinite reservoirs of different pressure are connected by a circular duct, such as those shown in Figure 5, the flow rate between the two, neglecting any entrance effects, is related by the following expression,

$$\Delta P = \rho f \frac{L}{D}\frac{V^2}{2} \qquad (12)$$

where P is the pressure, ρ is the density of the working fluid, f is the friction factor, L is the length of the duct, D is the diameter of the duct, and V is the velocity of the fluid.

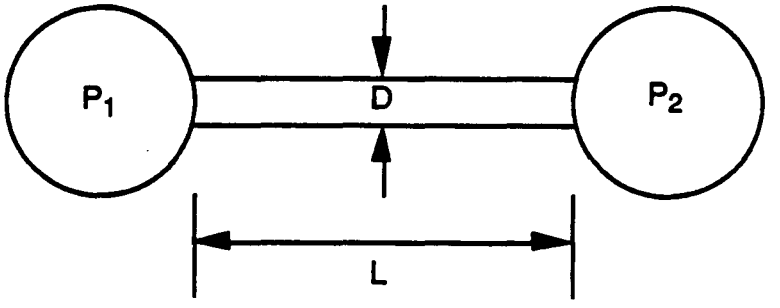

Figure 5 Schematic of the System.

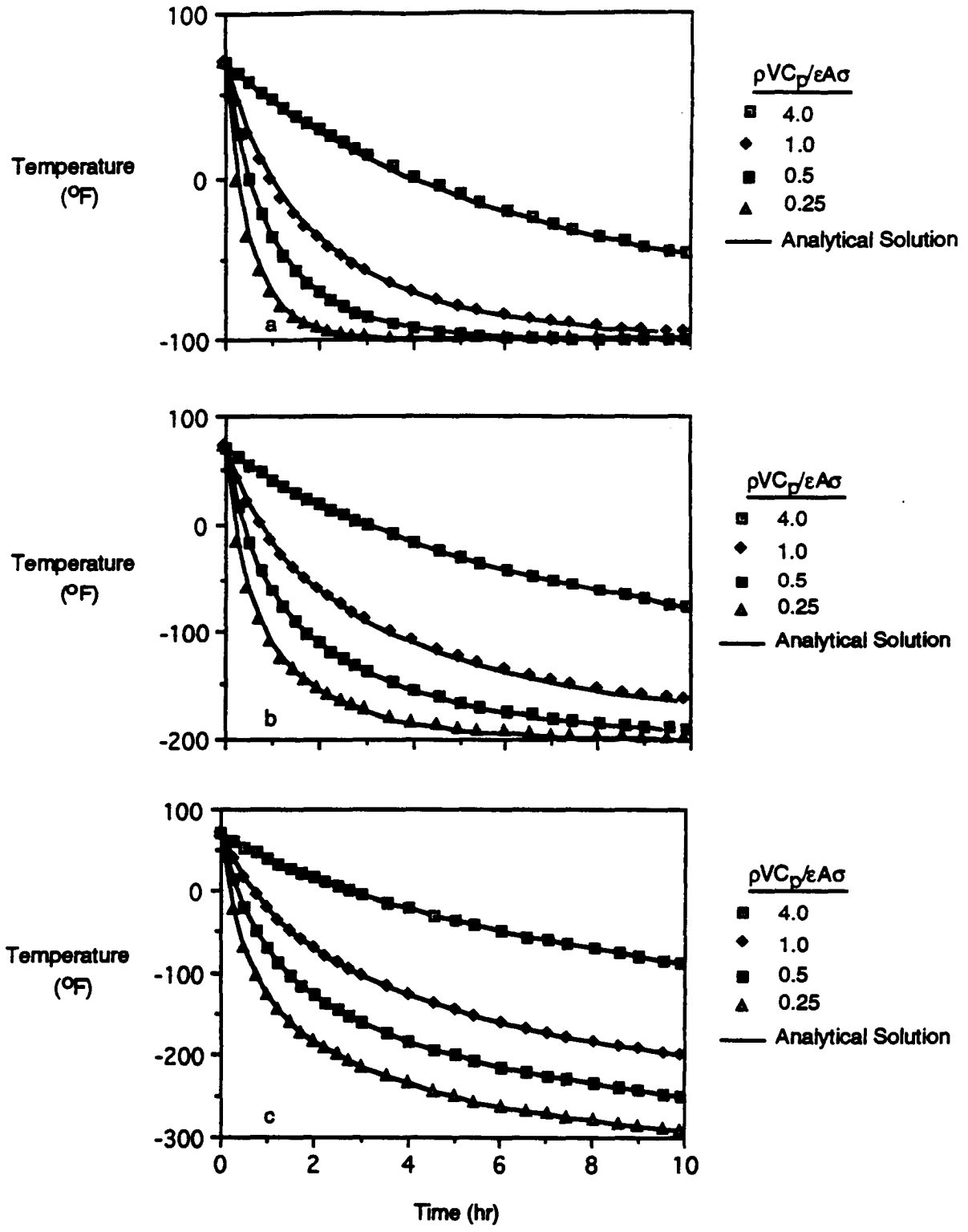

Figure 4 Predicted Temperature Response for Various Capacitance-Conductance Ratios for a) T_{sink} = -100 °F, b) T_{sink} = -200 °F, and c) T_{sink} = -400 °F.

The velocity of the fluid is related to the mass flow rate by

$$V = \dot{m}/\rho A \tag{13}$$

where m is the mass flow rate and A is the cross sectional area of the duct. The area of the duct is given by

$$A = \pi D^2/4 \tag{14}$$

Substituting equations (13) and (14) into equation (12) and rearranging yields

$$\Delta P = \frac{8 f \dot{m}^2 L}{\rho \pi^2 D^5} \tag{15}$$

Solving for the friction factor gives

$$f = \frac{\Delta P \rho \pi^2 D^5}{8 \dot{m}^2 L} \tag{16}$$

For laminar flow the friction factor is given by

$$f = 64/Re \tag{17}$$

where Re is the Reynolds number which is given by

$$Re = \frac{VD}{\nu} \tag{18}$$

where ν is the kinematic viscosity. For turbulent flow the friction factor is a function of the Reynolds number and the wall roughness ratio (e/D). The value of turbulent friction factors must be determined experimentally and can be found on the Moody chart [13]. Reviewing equations (12) through (16) shows that for a given fluid if the pressure difference, pipe diameter and length are fixed, the velocity can be determined, directly for laminar flow and iteratively for turbulent flow. As such, any numerical code that is developed correctly should be able to accurately predict fluid velocities when the other parameters are fixed.

For the system shown in Figure 5, a simple FLUINT model was developed. The duct was represented by the TUBE option so that internal pipe friction would be included in the model. The pressure source and sink were represented by plenums (PLEN in FLUINT) which maintained a constant pressure at the ends of the TUBE. A schematic of this FLUINT model is shown in Figure 6.

For the current study, the pressures of the PLENs, and the pipe length and diameter of the TUBE are fixed. The model is then run in a steady-state mode until a converged solution is obtained. Using this flow rate, the friction factor and Reynolds number were calculated (Equation (16) and (18)) and compared to the analytical solutions. If the FLUINT code is properly developed, the predictions should match the analytical solution or the Moody chart values.

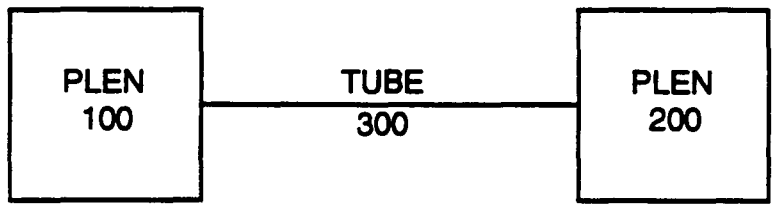

Figure 6 Schematic of the FLUINT Model.

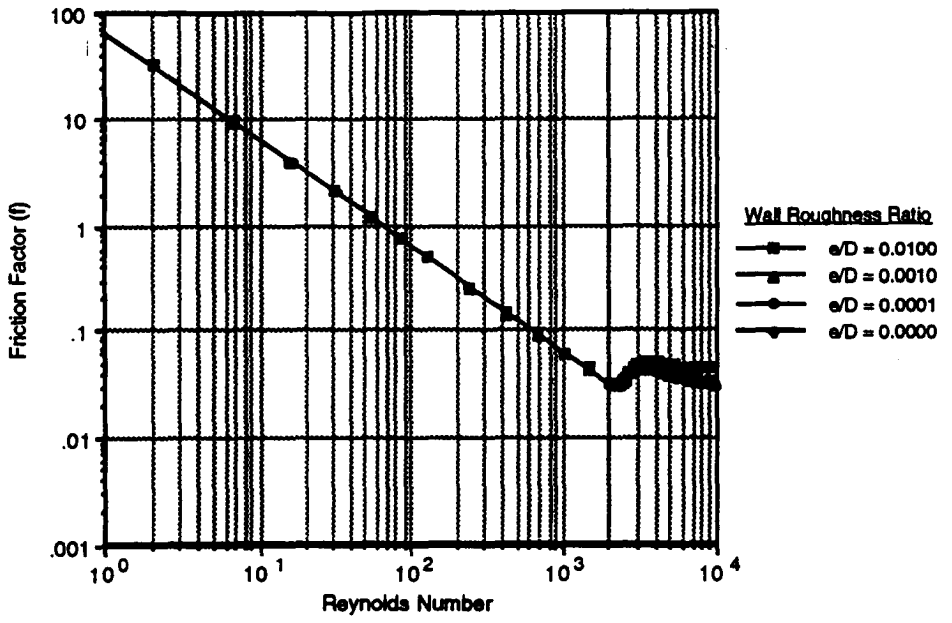

Figure 7 Predicted and Actual (Solid Line ——) Reynolds Number in the Laminar Region for Various Wall Roughness Ratios.

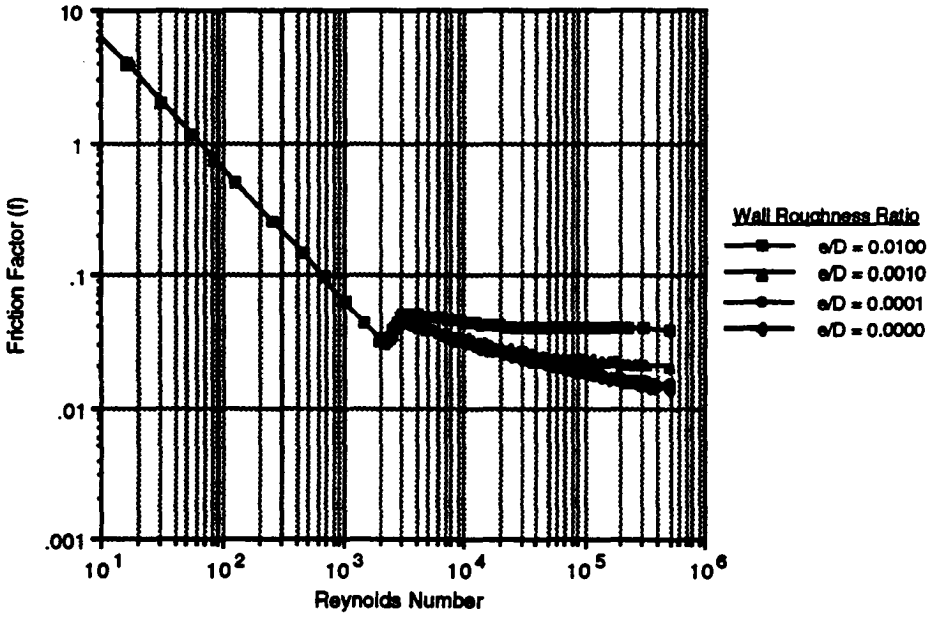

Figure 8 Predicted and Actual (Solid Line ——) Reynolds Number in the Turbulent Region for Various Wall Roughness Ratios.

The model was run over Reynolds numbers ranging from 1 to 10^6 for four different values of e/D and the predicted friction factors can be found in Figures 7 and 8. When laminar flow was considered (Figure 7), the friction factor was found to be independent of the wall roughness and a linear function of the Reynolds number. For this situation, the predicted FLUINT results are nearly identical (< 0.1%) to those of the analytical solution.

When the flow is turbulent (Re > 2300), the friction in the pipe is a function of the both the Reynolds number and the wall roughness. The greater the wall roughness, the great the friction factor. The predicted friction factors in the turbulent regime for various wall roughness ratios can be found in Figure 8. As is evident, the predicted friction factors agree with those taken from the Moody chart and also shows the dependence of the friction factor upon wall roughness after the laminar regime.

TANK FILLING WITH HEAT TRANSFER AND CONTROL VOLUME WORK

Development of the Analytical Solution

Many thermodynamic processes involve unsteady flow and are difficult to analyze; however, several processes, such as the filling of a closed container, can be approximated by a simplified model. These types of problems are known as uniform-state, uniform-flow (USUF) processes. The basic assumptions for this flow condition are as follows:

1) The thermodynamic state of the mass within the control volume may change with time, but at any instant of time the state is uniform throughout the entire control volume.

2) The thermodynamic state of the mass entering the control volume is constant with time.

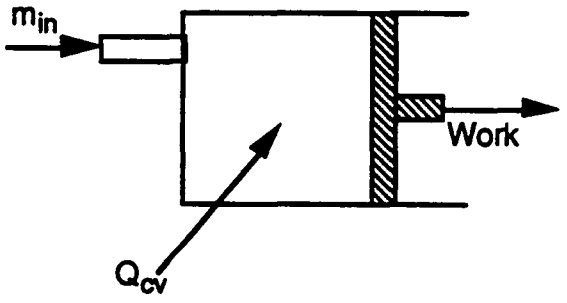

Figure 9 Schematic of the System.

Using these assumptions and Figure 9 as a guide, the first law [14] can be simplified for a tank filling scenario with heat transfer and control volume work. With no velocity or gravity potential terms, the first law for this tank filling process is,

$$m_{in}h_{in} = m_2u_2 - m_1u_1 + W_{cv} + Q_{cv} \quad (19)$$

where m is the mass, h is the enthalpy, u is the internal energy, W_{cv} is the total control volume work, and Q_{cv} is the total heat transfer. The subscripts in, 2, and 1 denote the inlet, final and initial states, respectively. From the continuity equation, the following relationship can also be developed.

$$m_{in} = m_2 - m_1 \quad (20)$$

Substituting equation (20) into equation (19), replacing the enthalpy with C_pT and the internal energy with C_vT (the assumption of constant specific heats) yields

$$(m_2 - m_1)C_pT_{in} = m_2C_vT_2 - m_1C_vT_1 + W_{cv} + Q_{cv} \tag{21}$$

where C_p, C_v and T are the constant pressure specific heat, the constant volume specific heat and temperature, respectively. Incorporating the ideal gas law (PV=RT) into equation (21) gives

$$\left(\frac{P_2V_2}{RT_2} - \frac{P_1V_1}{RT_1}\right)C_pT_{in} = \frac{P_2V_2}{RT_2}C_vT_2 - \frac{P_1V_1}{RT}C_vT_1 + W_{cv} + Q_{cv} \tag{22}$$

where P is the pressure, V is the volume, and R is the specific gas constant. Rearranging equation (22) produces

$$\left(\frac{P_2}{T_2} - \frac{P_1V_1}{T_1V_2}\right)C_pT_{in} = \left(P_2 - \frac{P_1V_1}{V_2}\right)C_v + \frac{W_{cv}R}{V_2} + \frac{Q_{cv}R}{V_2} \tag{23}$$

Dividing by the constant volume specific heat, C_v, and defining a new variable

$$\frac{V_1}{V_2} = \frac{1}{V_r} \tag{24}$$

equation (5) becomes,

$$\left(\frac{P_2}{T_2} - \frac{P_1}{T_1V_r}\right)kT_{in} = \left(P_2 - \frac{P_1}{V_r}\right) + \frac{W_{cv}R}{C_vV_2} + \frac{Q_{cv}R}{C_vV_2} \tag{25}$$

where k is the ratio of the specific heats. Rearranging equation (7) gives

$$\frac{P_2}{T_2} = \frac{P_2V_r - P_1}{kT_{in}V_r} + \frac{P_1}{T_1V_r} + \frac{W_{cv}R}{kT_{in}C_vV_2} + \frac{Q_{cv}R}{kT_{in}C_vV_2} \tag{26}$$

Solving for the final temperature gives,

$$T_2 = \frac{P_2}{\left(\frac{P_2V_r - P_1}{kT_{in}V_r} + \frac{P_1}{T_1V_r} + \frac{W_{cv}R}{kT_{in}C_vV_2} + \frac{Q_{cv}R}{kT_{in}C_vV_2}\right)} \tag{27}$$

Further simplification yields,

$$T_2 = \frac{kP_2T_1T_{in}V_r}{\left((P_2V_r - P_1)T_1 + kP_1T_{in} + \frac{W_{cv}RT_1}{C_vV_1} + \frac{Q_{cv}RT_1}{C_vV_2}\right)} \tag{28}$$

Reviewing equation (28) shows that when work or heat leaves the control volume, the final temperature will be reduced compared to a system in which these quantities are absent. It is also important to note that in the absence of work and heat transfer, equation (28) reduces to a common equation that is used to estimate final temperatures in rigid adiabatic containers [14].

In writing equation (28) it is assumed that the total work, W_{cv}, that occurs between the initial (1) and final (2) states is known or can be determined. In general, the work term is not constant and varies with both system pressure and volume. From thermodynamic relationships [14], the total control volume work is defined as

$$W_{cv} = \int_1^2 P dV \tag{29}$$

Typically, volume is related to the pressure by an arbitrary function.

$$V = f(P) \tag{30}$$

Similarly the pressure is related to the volume by the inverse function

$$P = f^{-1}(V) \tag{31}$$

Replacing the pressure term in equation (29) with equation (31) gives

$$W_{cv} = \int_1^2 f^{-1}(V)\, dV \tag{32}$$

For the present study, the function, f(P), was chosen so that the integral could easily be evaluated. The manipulation of the SINDA/FLUINT code to include control volume work will be discussed shortly in an upcoming section.

Development of the SINDA Model

Figure 10 shows a schematic of the FLUINT model that was used to validate the code. Here, a TANK is connected to a PLEN (PLENum) by an MFRSET (Mass Flow Rate SET). By using the TANK option, the first assumption for USUF processes (uniform state within the control volume) is met. The use of the PLEN ensures that the second USUF assumption of constant inlet properties is also maintained. To ensure that the working fluid is an ideal gas, an 8000 series fluid, using nitrogen as the working fluid, was developed and employed.

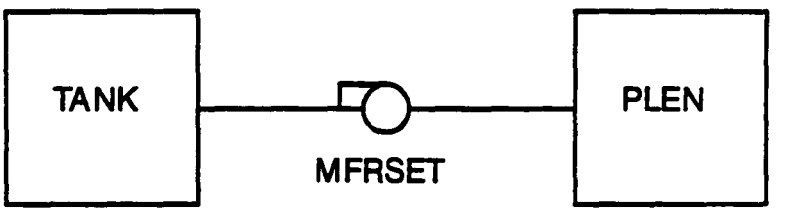

Figure 10 Schematic of the FLUINT Model.

While the SINDA/FLUINT program does not directly calculate (include) work terms for expanding (or contracting) control volumes, the code does calculate the thermal and hydraulic response of compliant (soft) TANKs. In the code, the compliance is defined as

$$COMP = \frac{1}{V}\frac{dV}{dP} \tag{33}$$

Therefore, if there is a function relating pressure and volume, an expanding control volume can be included in the FLUINT model, and by using equations (29) through (32), the control volume work can then be determined for the analytical solution.

Before the results are examined, it is important to first review the analytical solution. Equation (28) has been derived from a basic thermodynamic equation which was integrated over time. While the FLUINT code uses a rate based thermodynamic equation, the code integrates this equation over small discretized time intervals and the starting conditions at one time step are taken from the final conditions of the previous time step. This procedure employed by the FLUINT is the numerical equivalent of an integration. Since FLUINT has been developed using rate based

equations and the analytical solution uses overall heat transfer, one of the solution methods must be modified. To modify the heat transfer terms so that they can be included in the analytical solution, all that is required is that the FLUINT heat transfer term (QDOT in FLUINT) be multiplied by the total run time (TIMEN) and thus total heat transfer.

Results

The comparison study was conducted in several steps. First, the model considered situations where only heat transfer or the volume changed. The model was then run for situations in which there was both simultaneous heat transfer and control volume work. For all the cases examined, the initial pressure and temperature within the storage container was set to 100 psia and 70 °F, respectively, while the inlet temperature was held to 70 °F. The final pressure of the tank was limited to 1000 psia. The volume of the TANK was initially set to 0.5 ft^3. The results from these studies are summarized in Tables 1 through 4.

Figure 11 shows the predicted control volume temperature as a function of pressure for a variety of cooling rates with a fixed volume. As expected, the greater the heat loss, the lower the predicted temperature. In other words, a portion of the heat of compression is removed, resulting in lower predicted temperatures. More importantly, however, is to note that regardless of the heat transfer rate, the predictions are nearly identical to those of the analytical solution.

Figure 12 presents the analytical and predicted control volume temperature as a function of pressure for various heating rates. For these cases, the higher the heat addition, the higher the final volume temperature. Again, the predicted results are nearly identical to those of the analytical solution.

Figure 13 shows the predicted and analytical solution temperatures for the situation of an expandable control volume in which there is no heat transfer. Since a portion of the working fluid's energy must be used to produce work, the temperatures are lower then for the case in which the volume is fixed. For this situation too, the code was able to predict results nearly identical to those of the analytical solution.

Figure 14 presents the analytical and predicted temperatures for the conditions which include both control volume work and heat transfer. The volume is equal to the pressure multiplied by a constant. Depending on the situation examined, the predicted temperature was either greater (heating) or less (cooling) than the base case. As is evident, the code was able to match the results of the analytical solution.

SUMMARY AND CONCLUSIONS

This paper details a validation study of the SINDA/FLUINT program for several simple situations and focused on the major building blocks of the SINDA and FLUINT portions of the code. The code was validated by comparing its results with those of four closed form solutions. The thermal analyzer portion of the code (conduction and radiative heat transfer, SINDA portion) was first compared to two separate solutions. The first comparison examined a semi-infinite slab with a periodic surface temperature boundary condition. Next, a small, uniform temperature object (lumped capacitance) was allowed to radiate to a fixed temperature sink. The fluid portion of the code (FLUINT) was also compared to two different analytical solutions. The first study examined a tank filling process by an ideal gas in which there is both control volume work and heat transfer. The final comparison considered the flow in a pipe joining two infinite reservoirs of pressure. The results of all these studies showed that for the situations examined here, the SINDA/FLUINT code was able to match the results of the analytical solutions.

To date only one large scale SINDA/FLUINT model has been built and used to validate the FLUINT code [11] and the interaction between SINDA/FLUINT modeling components has yet to be examined. Therefore, future studies should be devoted to building large sized models which can be verified by either analytical solutions or experimental data.

Table 1 Predicted and Analytical Temperatures for Various Heat Loading Conditions.
Initial Conditions P_1 = 100 psia, T_1 = 70 °F, T_{in} = 70 °F, P_{final} = 1000 psia

SINDA/FLUINT T_{final} (°F)	Analytical T_{final} (°F)	Q (Btu/hr)	Volume Relationship
253.02	253.46	0.0	V=C
241.29	241.63	-500.0	V=C
229.58	229.75	-1000.0	V=C
193.65	193.64	-2500.0	V=C
132.69	132.30	-5000.0	V=C
5.77	5.05	-10000.0	V=C

Table 2 Predicted and Analytical Temperatures for Various Heat Loading Conditions.
Initial Conditions P_1 = 100 psia, T_1 = 70 °F, T_{in} = 70 °F, P_{final} = 1000 psia

SINDA/FLUINT T_{final} (°F)	Analytical T_{final} (°F)	Q (Btu/hr)	Volume Relationship
253.02	253.46	0.0	V=C
264.57	265.22	500.0	V=C
276.13	276.96	1000.0	V=C
310.59	311.76	2500.0	V=C
366.44	368.39	5000.0	V=C
473.25	476.80	10000.0	V=C

Table 3 Predicted and Analytical Temperatures for Volume Relationships
Initial Conditions P_1 = 100 psia, T_1 = 70 °F, T_{in} = 70 °F, P_{final} = 1000 psia

SINDA/FLUINT T_{final} (°F)	Analytical T_{final} (°F)	Q (Btu/hr)	Volume Relationship
253.02	253.46	0.0	V=C
156.12	157.01	0.0	V=CP
125.55	125.38	0.0	$V=CP^2$
189.30	189.66	0.0	$V=CP^{1/2}$

Table 4 Predicted and Analytical Temperatures for Various Heat Loading Conditions and Volume Relationships.
Initial Conditions P_1 = 100 psia, T_1 = 70 °F, T_{in} = 70 °F, P_{final} = 1000 psia

SINDA/FLUINT T_{final} (°F)	Analytical T_{final} (°F)	Q (Btu/hr)	Volume Relationship
156.12	157.01	0.0	V=CP
133.83	133.70	-1000.0	V=CP
180.19	180.29	1000.0	V=CP
40.84	40.21	-5000.0	V=CP
272.59	273.57	5000.0	V=CP

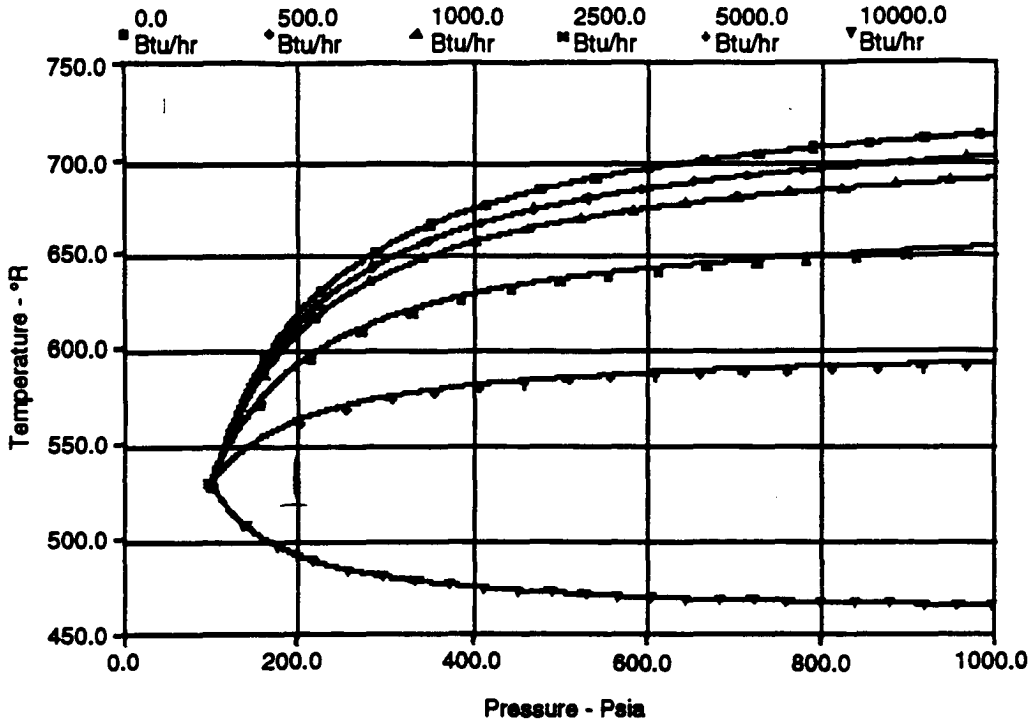

Figure 11 Predicted and Analytical (Solid Line ----) Temperature Response for Various Heat Losses and no Control Volume Work.

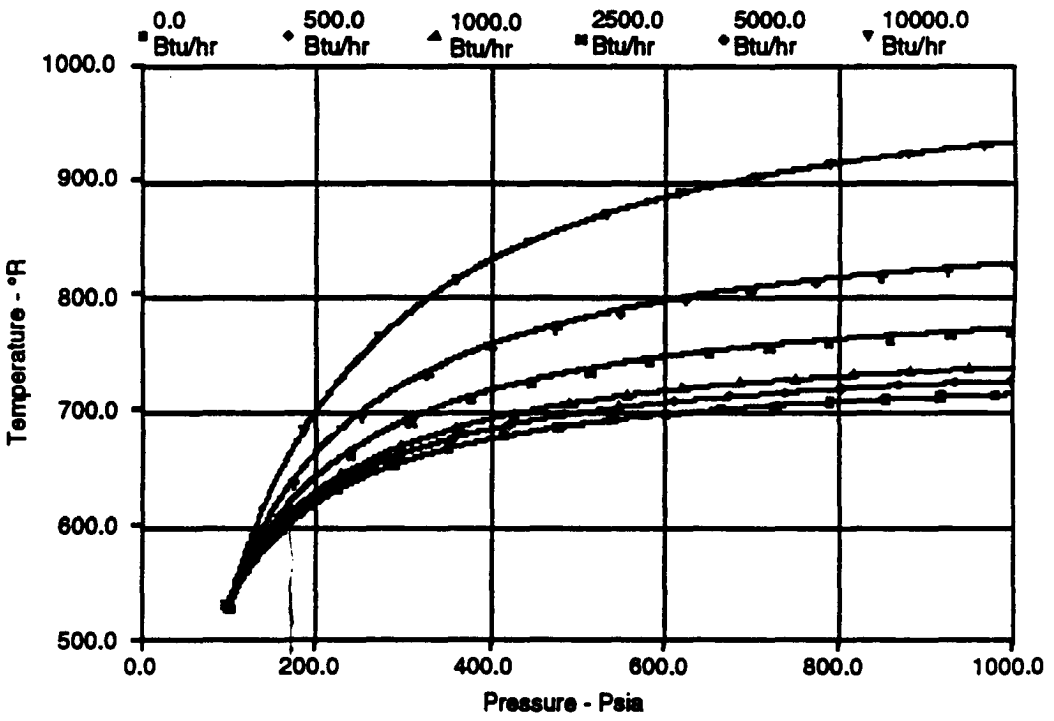

Figure 12 Predicted and Analytical (Solid Line ----) Temperature Response for Various Heating Rates and no Control Volume Work.

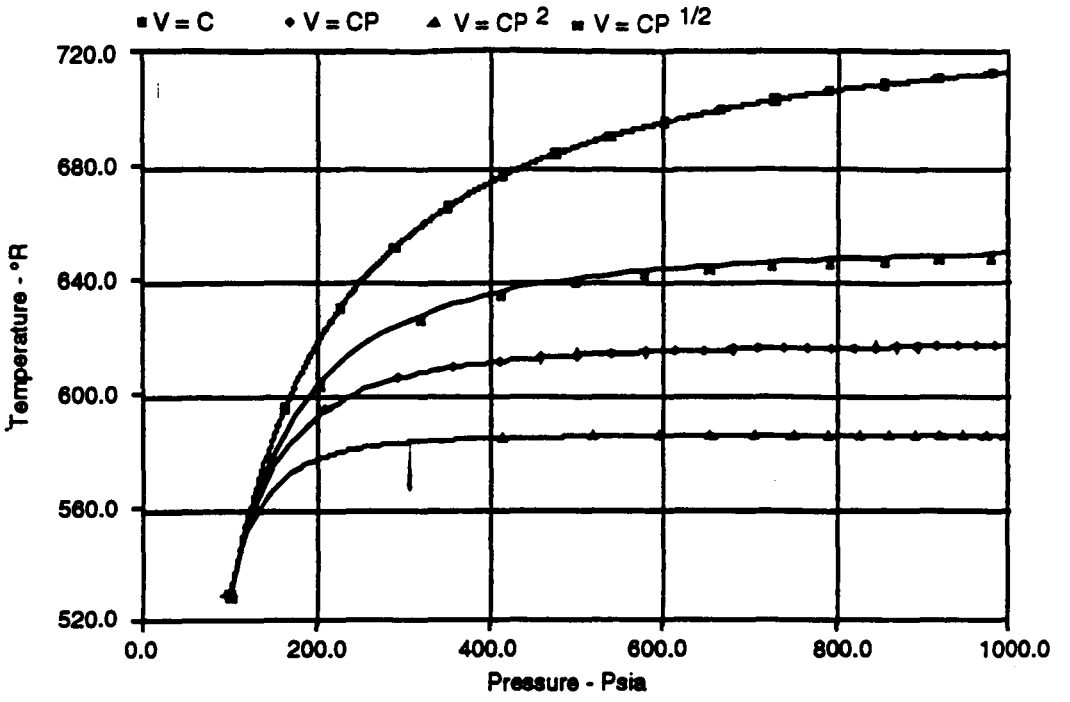

Figure 13 Predicted and Analytical (Solid Line ----) Temperature Response for Various Pressure-Volume Relationships and no Heat Transfer.

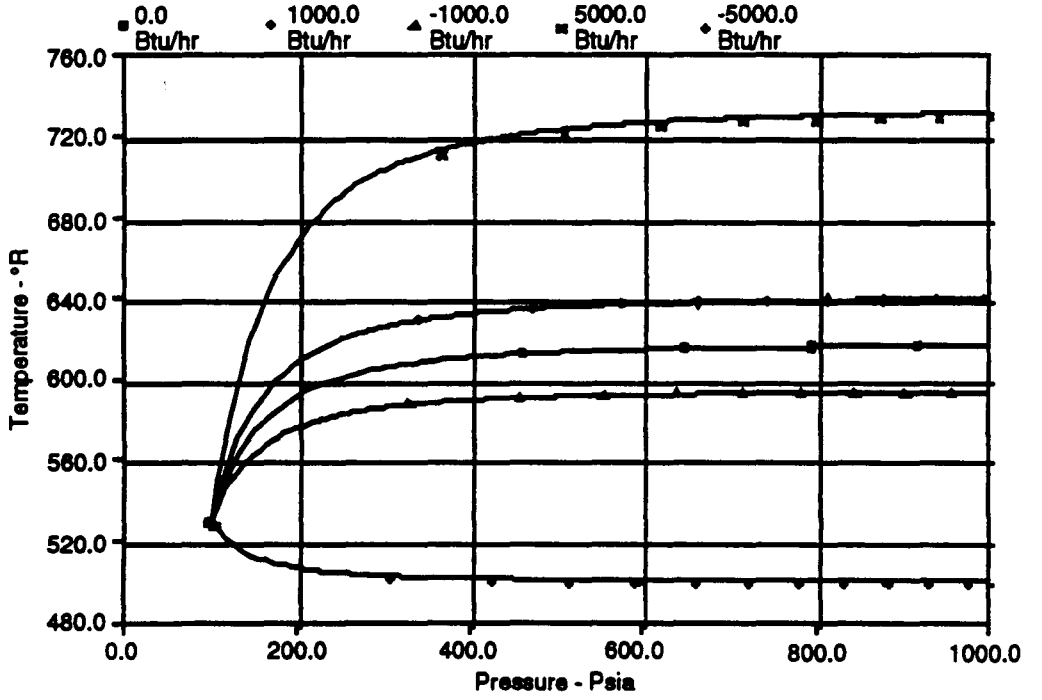

Figure 14 Predicted and Analytical (Solid Line ----) Temperature Response for Various Pressure-Volume Relationships and Heat Transfer.

REFERENCES

1) Andish, K.K., "SINDA85/FLUINT of the Boeing Thermal Bus System," LESC - 26930, CTSD - 0246, April 1989.

2) Keller, J.R., "Revised Predictions of Space Station Airlock Filling Using Updated SINDA85/FLUINT Models," LESC - 28137, March 1990.

3) Keller, J.R., "Conversion of the Space Shuttle Active Thermal Control System Models from SINDA/SINFLO to SINDA85/FLUINT," LESC - 27826, CTSD - 0504, December 1990.

4) Galate, J.W., Purvis, K.L., and Keller, J.R., "Lunar Transport Vehicle Hangar Thermal Environment Database," LMSC - 2EVA - EV - 078, October 1990.

5) De Vahl Davis, G., "Natural Convection of Air in a Square Cavity: A Bench Mark Numerical Solution," International Journal of Numerical Methods in Fluids, Vol 3., pp. 249-261, 1983.

6) Chapman, K.S., Johnson J.H., and Chiang, E.C., "The Enhancement and Validation of a Vehicle Engine Cooling Simulation for a Heavy Duty Diesel Truck," SAE Paper #88601, 1988.

7) Patanker, S.V., Numerical Heat Transfer and Fluid Flow, Hemisphere, Washington D.C., 1980.

8) Harris, R.S., "Verification of the SINDA85/FLUINT Program for Conduction Analysis," LESC - 28200, CTSD - 0614, March 1990

9) Keller, J.R., "WP II EVAS Hyperbaric Pressure Control - Final Report," LESC - 27928, January 1990.

10) Cullimore, B.A., "Applications of a General Thermal/Hydraulic Simulation Tool," AIAA paper, 1989.

11) Iovine, J.V., "SINDA85/FLUINT Benchmark Verification of Single Phase Fluid Flow in a Radiator System," LESC - 28156, March 1990.

12) Arpaci, V.S., Conduction Heat Transfer, Addison Wesley Publishing Co., Reading Massachusetts, 1966.

13) White, F.M., Fluid Mechanics, McGraw-Hill Book Company, New York, 1979.

14) Van Wylen, G.J., and Sonntag, R.E., Fundamentals of Classical Thermodynamics, 3rd Edition, John and Sons, New York,1986.

TRANSIENT STUDIES OF G-INDUCED CAPILLARY DRYOUT AND REWET

M.K. Reagan and W.J. Bowman
Department of Aeronautics and Astronautics
Air Force Institute of Technology
Wright Patterson Air Force Base, Ohio

SUMMARY

A transient, one-dimensional numerical code is developed to model the liquid motion in an axial groove with square cross section. Axial variation in liquid level, shear stress and heat transfer between the groove wall and the liquid, evaporation and transient body forces are accounted for in the model. Dryout and rewet of the groove are allowed; the front location is determined numerically using conservation of mass and linear extrapolation. Several numerical test results are presented and discussed.

INTRODUCTION

Heat pipe technology has been proposed for use in the aerospace environment as a means of cooling electronics on fighter aircraft or as a means of thermal management aboard space-based platforms (refs. 1-3). These environments are dynamic ones where time-varying body forces will primarily influence the motion of the working fluid within the wick structure of the heat pipe. While the magnitudes of the body forces in these two examples may be quite different, the effect on the working fluid in the wick is the same; namely, a bulk movement of the fluid towards either the evaporator or the condenser, depending on the magnitude and orientation of the body force. If the bulk motion of the fluid is towards the condenser, then dryout of the wick structure will be enhanced and heat pipe failure will result. The ability to correctly model liquid motion in a wick structure subject to transient body forces, then, is a necessary first step before heat pipe technology will be accepted as a means of thermal management in the aerospace industry.

Several attempts have been made to numerically model the liquid flow in a heat pipe wick. Two models repeatedly found in the literature are the Groove Analysis Program (GAP), developed by NASA (ref. 4) and a piston model developed by Beam (ref. 5). GAP is a steady-state formulation that is applicable only to grooved wick structures. Because it is steady-state, it does not account for the time-varying nature of body forces. It properly models the axial variation in radius of curvature; however, this radius of curvature is only allowed to vary from a minimum at the evaporator (equal to one-half the groove width) to a maximum at the condenser (equal to the radius of the vapor space). Because of this, dryout is never allowed to occur and therefore, it provides no capability to predict or model the dryout and rewet phenomena.

The piston model of Beam; however, is an unsteady formulation that does account for transient body forces. The wick is assumed to be entirely full up to the dryout front, past which no liquid may be present. The front is perpendicular to the axial direction, hence the reference to a piston. Because the

wick is assumed to be entirely full up to the front location, no recession of liquid and therefore, no radius of curvature, is allowed axially along the wet portion of the wick. In an actual heat pipe, recession of the liquid into the wick structure occurs continuously between the evaporator and condenser without causing dryout and always occurs as a precursor to dryout. Visual observations of Reagan (ref. 6) and Hawthorne (ref. 7) have verified this behavior. Because no liquid recession into the wick is allowed, the piston model predicts dryout earlier than actually occurs.

A limitation of both models is that neither attempts to describe the nature or behavior of the liquid front within the wick. In the GAP model, no liquid front is allowed to develop; the simulations are stopped when the capillary limit is reached. In the piston model, the front is treated like a piston with no attempt to describe what it actually looks like.

Additionally, both models assume that momentum changes in the liquid are negligible. This reduces the momentum equation to a form of Darcy flow, which models the pressure drop by equating the sum of pressure, shear and body force terms to zero and neglects any change in the liquid inertia. During steady-state behavior, the liquid velocity is small and hence, inertia effects are most likely negligible. The same conclusion cannot be deduced for the case of a transient body force environment. A new transient numerical model is therefore warranted.

THEORY

Several assumptions are made concerning the derivation of the governing equations. The wick is an axial groove with square cross section of constant width, w and depth, δ. One end of the groove can be tilted relative to the other end which provides the transient body force. No flooding of the groove is allowed and the pressure above the liquid in the groove is assumed constant and equal to ambient pressure, P_∞ .

The working liquid is ethanol and is assumed to be incompressible with density, $\rho = 785$ kg/m^3. Laminar flow within the groove is assumed at all times and kinetic and potential energy changes are assumed negligible with respect to changes in the internal energy. Free convection and radiation losses to the environment are also considered negligible with respect to the energy lost via evaporation.

Consider the control volume shown in Figure 1. This control volume encompasses the liquid only and not the groove structure. The liquid flow is from left to right and the meniscus level is assumed to vary linearly through the control volume. The equation of conservation of mass for this control volume, noting that $\rho\, dx$ is constant, yields

$$\frac{\partial A}{\partial t} + \frac{\partial (AV)}{\partial x} + \frac{\dot{m}_e}{\rho\, dx} = 0 \tag{1}$$

where A is the liquid cross-sectional flow area, V is the average liquid velocity and $\dot{m}_e$ is the evaporative mass flow rate for the differential control volume.

Figure 2 shows the same control volume with the appropriate forces (solid arrows) and momentum terms (dashed arrows). The groove with the liquid is tilted at an angle, ψ , around a center of rotation relative to the horizontal level and this angle is a function of time, which provides the transient body force, $\rho A g \sin\psi\, dx$ (g = gravitational constant). Momentum changes within the liquid, evaporative momentum flux, shear and capillary forces are all accounted for. The meniscus radius of curvature, R ,

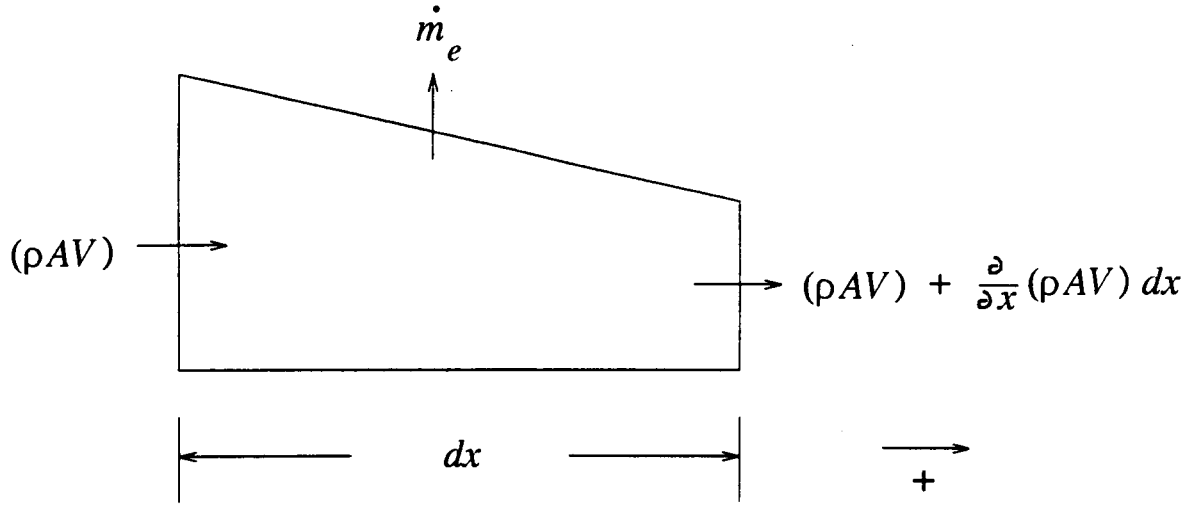

Figure 1. Control Volume for Conservation of Mass Analysis

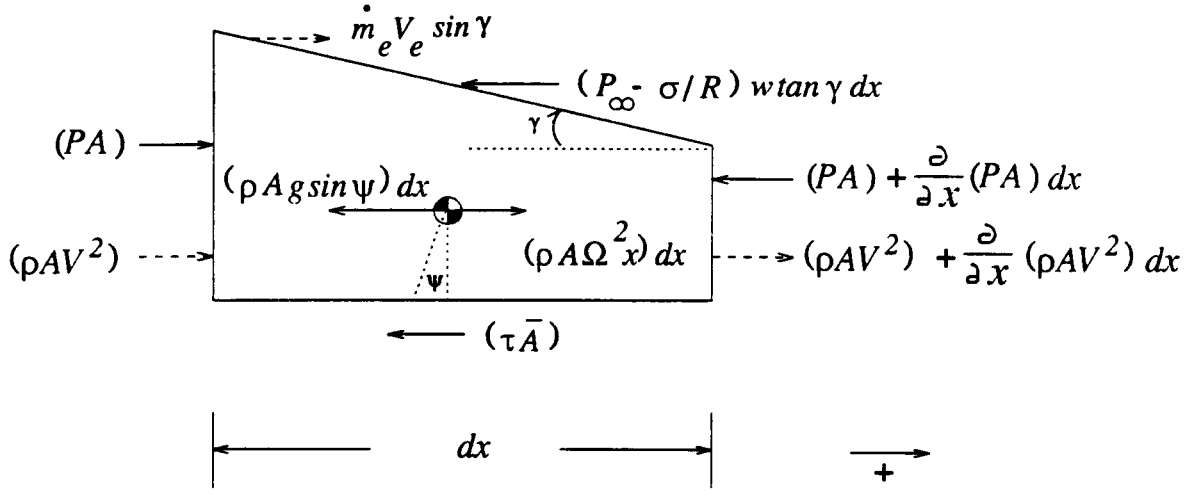

Figure 2. Control Volume for Conservation of Momentum Analysis

is a function of the liquid cross-sectional flow area and therefore can vary with axial location. The $(\rho A \Omega^2 x)dx$ term is a fictitious force term which accounts for the non-inertial reference frame of the governing equations. Applying conservation of momentum to this control volume yields

$$\frac{\partial(AV)}{\partial t} + \frac{\partial}{\partial x}(AV^2 + \frac{PA}{\rho}) = \frac{\dot{m}_e V_e \sin\gamma}{\rho dx} - Ag\sin\psi - \frac{\tau \bar{A}}{\rho dx} - \frac{1}{\rho}(P_\infty - \frac{\sigma}{R})w\tan\gamma + A\Omega^2 x \qquad (2)$$

where γ is the angle generated by the axial variation in meniscus level, V_e is the evaporative mass flux velocity, τ is the shear stress between the groove wall and liquid, $\bar{A}$ is the area over which the shear stress acts, σ is the surface tension coefficient and Ω is the angular rotation rate.

The average liquid pressure, P, at any axial location is assumed to be the ambient pressure minus the capillary pressure due to the curved interface, plus the pressure head due to the depth of liquid in the groove. The average depth of liquid in the groove, h, is approximated by $h = A/w$, and the average pressure head can be shown to be $\frac{1}{2}\rho g h \cos\psi$. The average liquid pressure then, is a function of the groove tilt angle, ψ, the cross-sectional flow area, A, and the meniscus radius of curvature, R.

This meniscus radius of curvature is a function of the liquid cross-sectional flow area and is assumed to behave as shown in Figure 3. When the groove is entirely full of liquid, there is no meniscus and the radius of curvature is infinite. As liquid evaporates or is moved by bulk motion, the meniscus recedes into the groove and R decreases from infinity until a hemispherical shape is formed. The radius of curvature at this condition is $R = w/2$. This hemispherical shape remains constant until the tangent to the meniscus is coincident with the bottom of the groove. As more liquid is removed by bulk motion or evaporation, the meniscus recedes further into the corners of the groove and the radius of curvature continues to decrease. This decrease is allowed to continue until the resulting liquid pressure is zero--a physical limitation. These three conditions (entirely full, initial hemisphere shape and tangent condition) allow a mathematical relationship between the cross-sectional flow area and the radius of curvature to be derived. Details of this derivation are found in Reference 6.

The shear stress between the groove wall and the liquid, τ, is modeled using

$$\tau = \frac{f\rho V^2}{2} \qquad (3)$$

where the friction coefficient, f, is determined using rectangular tube flow data from Shah (ref. 8) and modified for channel flow according to Chi (ref. 9). The remaining quantities in Eqn (2) (evaporative mass flux, groove tilt angle and angular rotation) are assumed to be known or measurable quantities.

The energy equation for this system is derived using the control volume in Figure 4. The total energy per unit mass is approximated by the internal energy, $E \approx e = c_p T$, where c_p is the liquid specific heat and T is the bulk liquid temperature. The energy influx, Q_{in}, is modeled using Newton's Law $Q_{in} = h_{in} A_{in}(T_g - T)$, where A_{in} is the groove wall area across which the heat energy travels, T_g is the groove wall temperature which is assumed known or measurable, and h_{in} is the transfer coefficient. This coefficient was calculated using

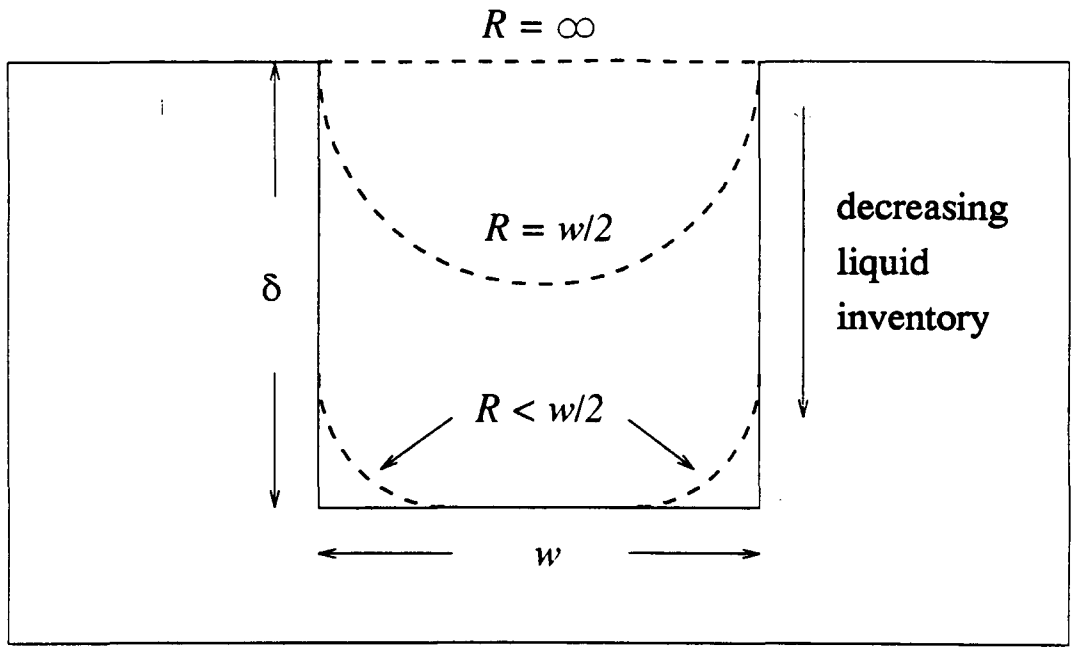

Figure 3. Meniscus Behavior in a Square Groove

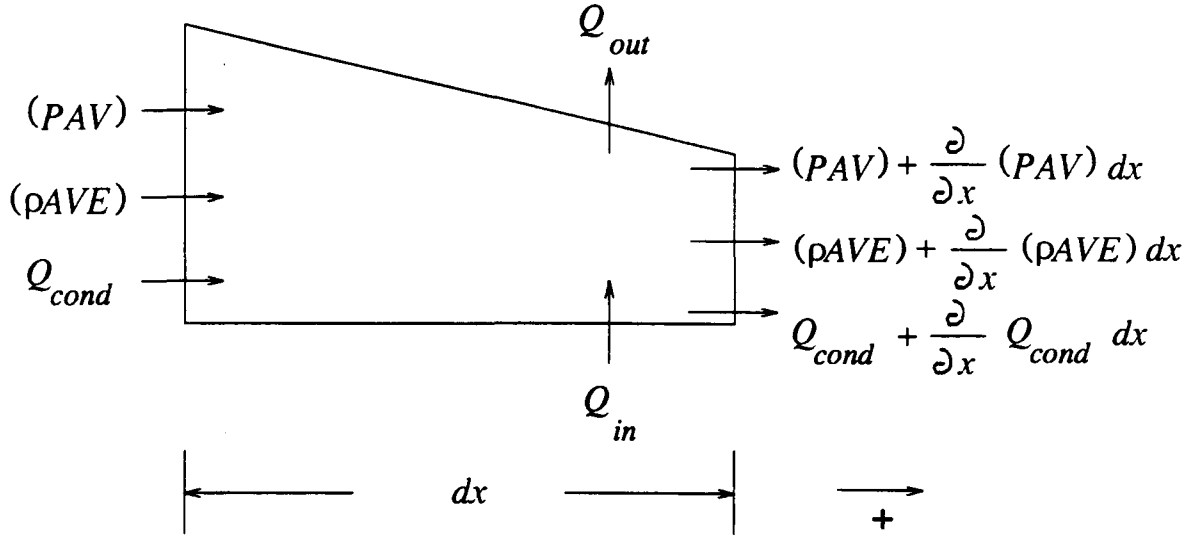

Figure 4. Control Volume for Conservation of Energy Analysis

$$h_{in} = \frac{Nu\,k}{D_h} \tag{4}$$

where Nu is the Nusselt Number, k is the liquid thermal conductivity and D_h is the hydraulic diameter. Nu was determined using convection correlations for constant surface heat flux (ref. 10), laminar tube flow and corrected for channel flow similar to the method used for the friction coefficient (see ref. 6 for more information).

The energy outflow, Q_{out}, is determined using $Q_{out} = \dot{m}_e \lambda$, where λ is the latent heat of vaporization. Q_{cond} is the rate of energy conducted axially through the control volume and was calculated using Fourier's Conduction Law. Applying these definitions, the energy equation for this control volume is written as

$$\frac{\partial}{\partial t}(AE) + \frac{\partial}{\partial x}\left(AV\left[E + \frac{P}{\rho}\right]\right) = \frac{(Q_{in} - Q_{out})}{\rho\,dx} - \frac{1}{\rho}\frac{\partial Q_{cond}}{\partial x} \tag{5}$$

Eqns (1), (2) and (5) form the set of governing equations for the new model. The pressure-area and radius-area relationships discussed previously provide closure for the system. The temporal derivative terms are grouped into a 3 x 1 matrix, $\bar{U}$, and the spatial derivative terms are grouped into a 3 x 1 matrix, $\bar{E}$. The remaining terms are combined into a source term, $\bar{S}$ and the resulting system is written as

$$\bar{U}_t + \bar{E}_x = \bar{S} \tag{6}$$

where the subscripts t and x refer to time and space derivatives respectively. Eqn (6) is non-dimensionalized and integrated using a first order accurate, explicit Roe scheme. Details of the solution methodology are found in Reference 6.

BOUNDARY CONDITIONS

The integration is performed on a one-dimensional grid, GRID1, that is I nodes wide as shown in Figure 5. Node 1 lies on the left boundary; this node is also the center of rotation of the groove. As such, it always contains liquid and because of the physical boundary, the velocity is always zero. The grid extends to I nodes, some or all of which have liquid in them, depending on the dryout/rewet front location. Node *nb* refers to the last wet node and is only equal to node I if the groove is fully wet. The grid remains fixed to the groove structure and does not move with the liquid.

At time level n, the total mass of liquid in the groove, m_r, is known. At time level n+1, assuming mass loss only by evaporation, the total mass of liquid in the groove is

$$m_g^{n+1} = m_g^n - \sum_{i=2}^{nb} \dot{m}_e \Delta t \tag{7}$$

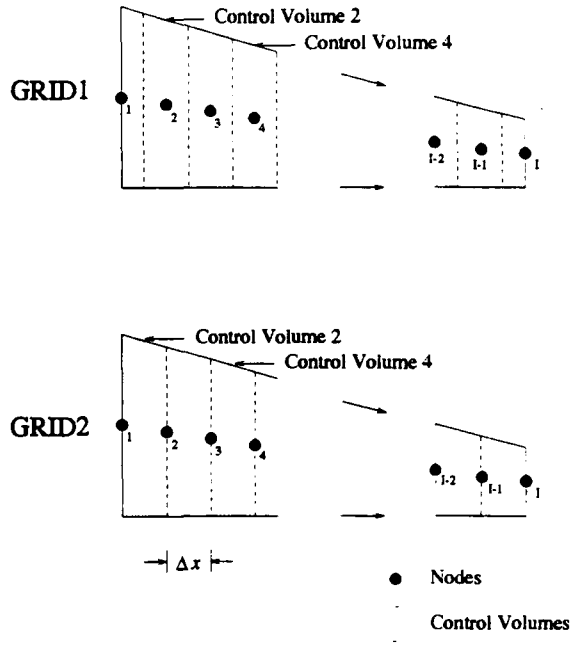

Figure 5. Numerical Grid Definitions

A second grid, GRID2, is used to update the boundary conditions and is also shown in Figure 5. The mass within any control volume using this grid is found using

$$m_i^n = \tfrac{1}{2}\rho\Delta x(A_i^n + A_{i-1}^n) \tag{8}$$

and the internal mass, m_{int}, is calculated by summing m_i^n between volumes 3 and nb. Applying the principle of conservation of mass to the leftmost control volume of GRID2 yields the area of node 1 as

$$m_2^{n+1} = m_2^n - \Delta t(\dot{m}_2^n + \dot{m}_e^n)$$

$$\Rightarrow A_1^{n+1} = \frac{2m_2^{n+1}}{\rho dx} - A_2^{n+1} \tag{9}$$

The velocity at node 1 is zero because of the physical boundary and the temperature is updated assuming an adiabatic end condition.

The remaining mass in the groove, m_r, at time level n+1 is found by subtracting the internal mass and the mass at node 2 calculated in Eqn (9) above from the predicted mass at time level n+1 (Eqn (7))

$$m_r^{n+1} = m_g^{n+1} - m_{int}^{n+1} - m_2^{n+1} \tag{10}$$

If the groove is not in a state of dryout, then m_r occupies control volume I and the area at node I is found by a simple average of the areas at nodes I and I-1. The velocity at node I is identically zero and the temperature is updated assuming an adiabatic end condition.

If, however, the groove is in a state of dryout or rewet, then a front exists and m_r occupies some specified volume extending beyond node *nb*. Several possibilities exist regarding the distribution of liquid extending beyond this node. Two of the more obvious are seen in Figure 6. The first order approximation fills a right triangle with the remaining mass, while the second order approximation attempts to match the remaining mass to a parabola with a specified slope at the front location. Higher order matches are also possible. For this work, the first order approximation is used.

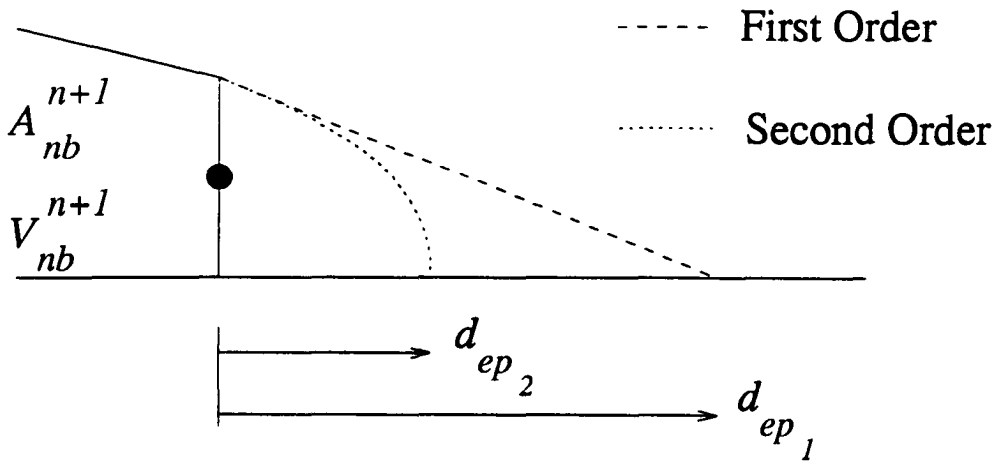

Figure 6. Sample Front Approximations

Defining the location in the groove where the cross-sectional flow area goes to zero as the extinction point, *ep*, then the distance between node *nb* and the extinction point is

$$d_{ep} = \frac{2m_r^{n+1}}{\rho A_{nb}^{n+1}} \tag{11}$$

This length can extend to one or to several nodes beyond node *nb* or it may not even extend to node *nb*+1 depending on the magnitude of m_r. Regardless, the boundary conditions at the extinction point are defined by the following relationships

Figure 8 shows the results of a ten second real time computer run. This is a three-dimensional plot of the non-dimensional area distribution in the groove, A^* , as a function of non-dimensional time, t^* , and non-dimensional axial groove location, x^* . Each axis runs from a minimum value of zero to a maximum value of one. The perspective of the liquid distribution is from an observer positioned on the groove. According to the figure, the area distribution does not vary with time from its initial level value of 0.5 (one-half full); the steady-state condition.

Test Two--Steady Body Force

This test was accomplished similarly to the first test; the only difference being in the initial groove angle and liquid distribution. The groove is set at an initial angle of, $\psi_{init} = \tan^{-1}(\delta/L_{\infty})$, and the initial distribution of liquid is such that $A^* = 1$ at the left end of the groove ($x^* = 0$) and $A^* = 0$ at the right end ($x^* = 1$) with a linear distribution in between, as shown in Figure 9. This provides the same volume of liquid used in the first test. In the absence of any capillary or body forces, there should be no tendency for the liquid to change from this position, which is the steady-state solution for the initial conditions.

Figure 10 shows the results of a ten second real time computer run and reveals no change from the initial distribution described above. This result demonstrates that the hydrostatic and atmospheric pressure forces, along with the body force, are modeled properly and coded correctly.

Test Three--Steady Body Force With Motion

It was necessary to determine if the code could predict the correct steady-state solution for an initial condition other than steady-state. To demonstrate this behavior, a setup identical to test two was used with the initial liquid distribution similar to that of test one and is shown in Figure 11. From this initial condition, the liquid should begin to flow towards the left end of the groove ($x^* = 0$) and reach the steady-state conditions of test two.

Figure 12 shows the results of a ten second real time computer run. Note that as time progresses, A^* increases at $x^* = 0$ and decreases at $x^* = 1$. This shows bulk liquid motion towards $x^* = 0$, and at $t^* = 1$, steady-state conditions are achieved. This test demonstrates that the code predicts the correct steady-state solution for a non steady-state initial condition.

Test Four--Steady Body and Capillary Forces

This test was performed to determine if the capillary force was modeled and coded properly. The initial conditions for this experiment are seen in Figure 13. The groove tilt angle was similar to test three and the liquid distribution was the same as test two. In the absence of the capillary force, it was seen in test two that the liquid had no tendency to move. However, if the capillary force is now considered, the liquid should have a tendency to move towards $x^* = 1$ since the liquid in that end has receded further into the groove and the capillary influence should be greatest.

Figure 14 shows the results from this study. With the capillary force present, the liquid does indeed move towards $x^* = 1$ as seen by the increase in A^* at $x^* = 1$ and a corresponding decrease in A^* at the other end of the groove, $x^* = 0$. The liquid approaches a steady-state distribution different from the steady-state condition seen in Figure 10. This is due to the inclusion of the capillary force.

$$A_{ep} = 0$$

$$\left|\frac{\partial A}{\partial x}\right|_{ep} = \frac{-\rho\left(A_{nb}^{n+1}\right)^2}{2m_r^{n+1}} \tag{12}$$

If d_{ep} is less than Δx, then m_r is not sufficient to extend the triangular profile to the node nb+1. In this case, the area, velocity and temperature distributions of the liquid are completely defined and no further calculations are required.

If, however, d_{ep} is greater than Δx, then the remaining mass is sufficient to extend the profile to node nb+1. In this case, A_{nb+1}^{n+1} is calculated using the area at node nb and the slope from Eqn (12). Applying conservation of mass on the control volume between nodes nb and nb+1 yields the velocity as

$$V_{nb+1}^{n+1} = \frac{(AV)_{nb}^{n+1} - \left(\frac{\partial \forall}{\partial t}\right)_{nb+1} - \frac{\dot{m}_e}{\rho}}{A_{nb+1}^{n+1}} \tag{13}$$

where $\forall$ is the volume of the differential element. A first order approximation to the volume derivative term is used and the evaporation term is evaluated at the temperature of node nb at time level n+1. The temperature is updated assuming no axial conduction.

After the area, velocity and temperatures are updated, the mass in the new control volume is calculated and subtracted from m_r and a new m_r is established. Node nb+1 is renumbered as node nb and a new value of d_{ep} is calculated and established. The procedure described above is repeated until this new value of d_{ep} is less than Δx .

NUMERICAL TEST PARAMETERS AND RESULTS

Several numerical experiments were performed with the new model to establish confidence in its ability to model the flow of liquid in a heated capillary structure subject to transient body forces. Since no comparisons to physical data are made, absolute accuracy of the results is not considered important. However, correct trends need to be demonstrated as well as the ability to numerically model the formation of a front in the groove structure.

Test One--No Body Force

The purpose of this test was to demonstrate that liquid in a groove that is initially level and remains level should have no tendency to move. The test setup is shown in Figure 7. The groove, shown by the dotted line in the figure, is a square channel. The width, w , and depth, δ , are 1.5875 mm, where the width dimension is into the page. The groove length, L_∞ , is 0.254 m, the liquid is ethanol and the capillary force and evaporation are neglected. In this test, the groove is maintained at the ambient temperature, $T = 295K$, and is not allowed to rotate. The initial area distribution is such that the groove is exactly one-half full. This is represented by the shaded area in the figure.

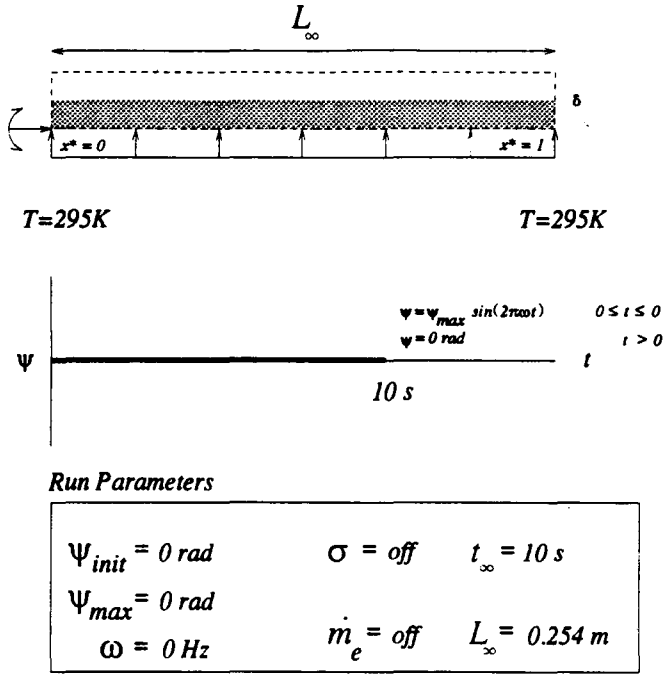

Run Parameters

$\Psi_{init} = 0$ rad	σ = off	$t_\infty = 10$ s
$\Psi_{max} = 0$ rad		
$\omega = 0$ Hz	$\dot{m}_e$ = off	$L_\infty = 0.254$ m

Figure 7. Numerical Test One Parameters

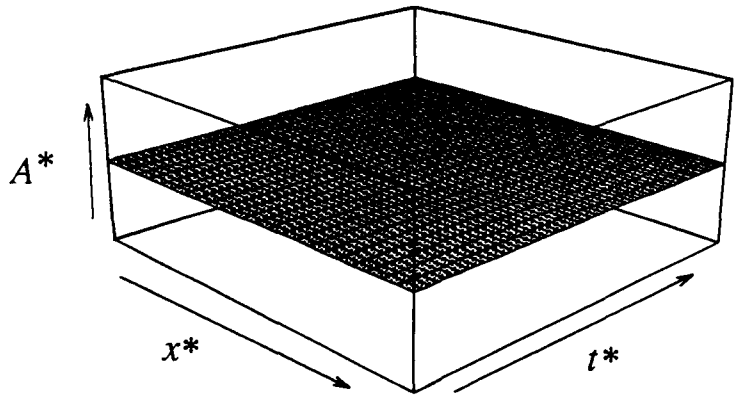

Figure 8. Numerical Test One Results

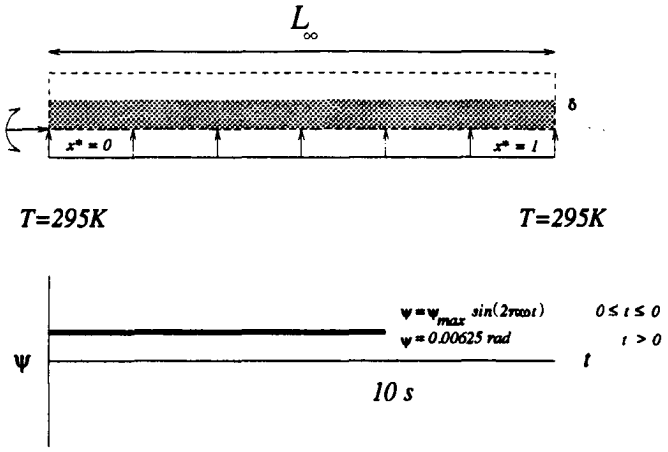

Run Parameters

$\Psi_{init} = 0.00625$ rad	σ = off	$t_\infty = 10$ s
$\Psi_{max} = 0$ rad		
$\omega = 0$ Hz	$\dot{m}_e$ = off	$L_\infty = 0.254$ m

Figure 11. Numerical Test Three Parameters

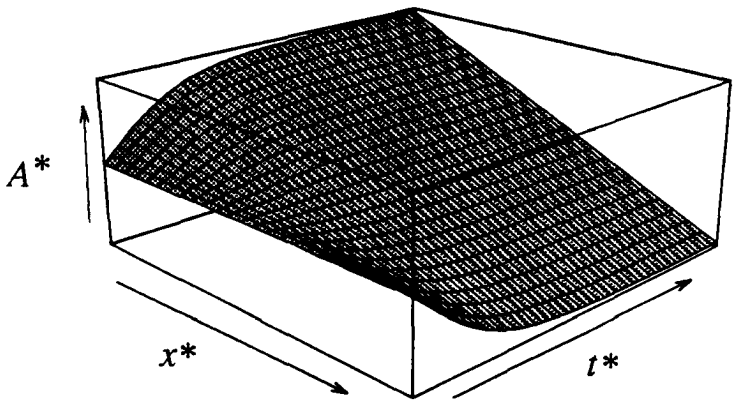

Figure 12. Numerical Test Three Results

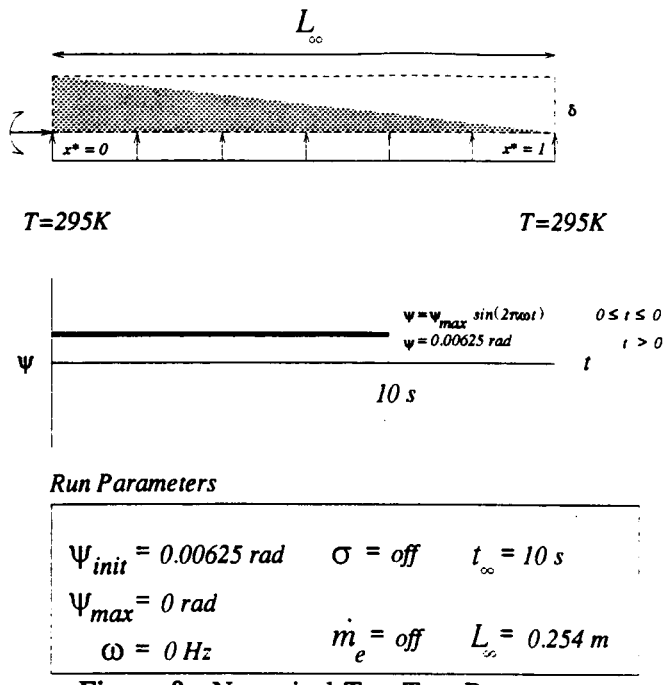

Run Parameters

$\Psi_{init} = 0.00625$ rad	σ = off	$t_\infty = 10$ s
$\Psi_{max} = 0$ rad		
$\omega = 0$ Hz	$\dot{m}_e$ = off	$L_\infty = 0.254$ m

Figure 9. Numerical Test Two Parameters

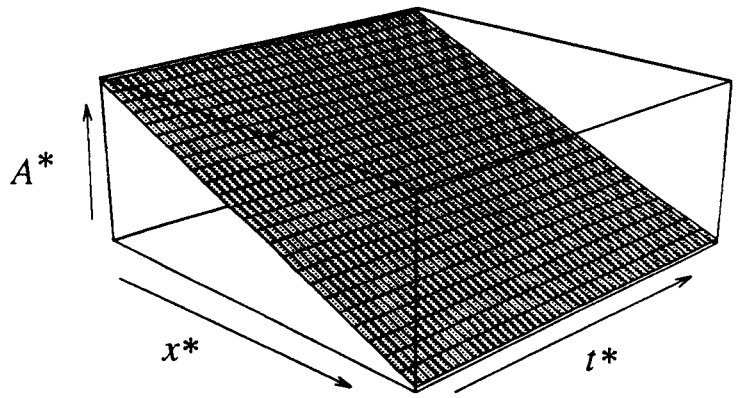

Figure 10. Numerical Test Two Results

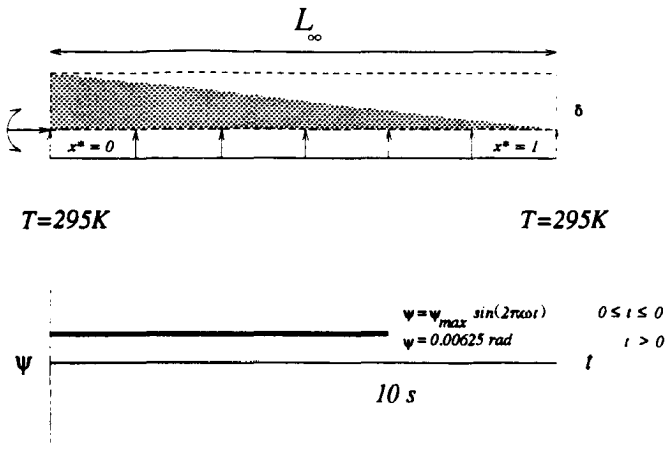

Run Parameters

$\Psi_{init} = 0.00625$ rad	σ = on	$t_\infty = 10$ s
$\Psi_{max} = 0$ rad		
$\omega = 0$ Hz	$\dot{m}_e$ = off	$L_\infty = 0.254$ m

Figure 13. Numerical Test Four Parameters

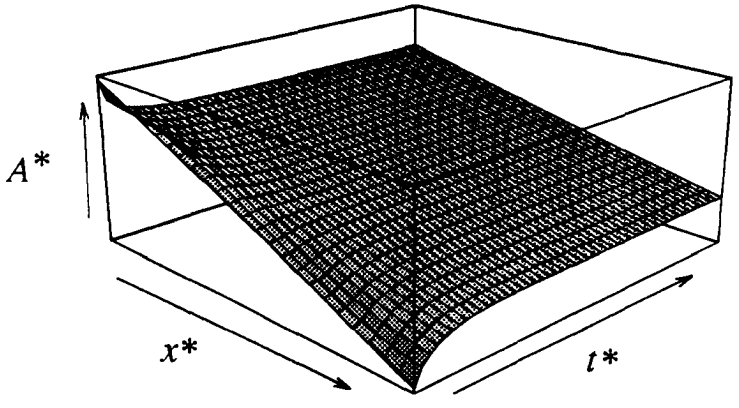

Figure 14. Numerical Test Four Results

The remaining three numerical experiments were performed with the capillary force and evaporation present. The goal of these remaining experiments was to determine the code's ability to model the liquid motion in the groove under transient body forces and external heating; two important parameters that were neglected in tests one through four. The magnitude and duration of the body forces and heating were sufficient to result in dryout in the groove: a phenomenon also not studied in tests one through four.

Test Five--Transient Body Force, No External Heating

This test was performed to determine if the code could capture the formation of a dryout front in a groove that was subject to a transient body force but no external heating. No external heating refers to no externally applied heat sources, such as a heater. It does not mean that no heat transfer takes place; in fact, heat transfer does occur in the form of evaporation.

In this test, the groove was initially at a level condition and one-third full of liquid. The groove was rotated through the schedule shown by the bold line in Figure 15. This schedule was

$$\psi = \psi_{max} \sin(2\pi\omega t) \qquad 0 \le t \le 5$$

$$\psi = 0 \qquad t > 5$$

with a maximum angle, ψ_{max} , of 0.0524 radians and a frequency of $\omega = 0.1$ Hz. This particular schedule was chosen after numerous numerical test runs because it resulted in a partial dryout of the groove followed by a rewet. The results of this test run are shown in Figure 16. As the transient body force is applied, the level of liquid at $x^* = 0$ increases and the level at $x^* = 1$ decreases, indicating bulk liquid motion towards $x^* = 0$. At approximately $t^* = 0.3$, the groove begins to dry out as noted by $A^* = 0$ at $x^* = 1$. As the tilt schedule reverses direction back towards the initial level condition, the liquid motion follows and the rewet is captured by the increase in A^* from its zero value. At $t^* = 1$, the liquid distribution in the groove is not level as steady-state conditions would dictate. The code was allowed to run for additional time and the liquid distribution did eventually reach a quasi-steady-state condition. This quasi-steady-state refers to the liquid level in the groove being uniform along its length but decreasing in time due to evaporation of the liquid. The time shown in Figure 16 was chosen to reveal details of the dryout and rewet. This experiment validated the code's ability to capture a dryout and rewet due solely to a transient body force.

Test Six--No Body Force, External Heating

This test was performed to determine if the code could capture the formation of a liquid front in a groove subjected to external heating but no transient body force. In this test, the groove was initially at a level condition and entirely full of liquid. The groove was kept level throughout the test as shown in Figure 17. The left end of the groove was maintained at $T = 295K$, while the right end was maintained at $T = 345K$, with a linear distribution of temperature between $x^* = 0$ and $x^* = 1$. A maximum temperature of 345 K was chosen to remain below the boiling point of ethanol. This test was carried out for 480 seconds. For the first 420 seconds, the temperature profile described above was used.

This was done to generate a dry region in the groove. Between 420 and 480 seconds, the temperature profile was reduced to a uniform temperature of $T = 295K$ to allow a rewet to occur.

The results of this experiment are seen in Figure 18. Several interesting trends are seen in this figure. First, the decrease in liquid volume between $t^* = 0$ and $t^* = 1$ is evident by the decrease in A^* along the groove. Note however, that the rate of decrease in A^* is greater at $x^* = 1$ than at $x^* = 0$. This is due to the elevated temperatures as x^* approaches one. Higher temperatures result in higher evaporation rates and a quicker depletion of liquid from the groove.

The second trend is the formation of a dryout front, $A^* = 0$, at approximately $t^* = 0.9$. At this point, the elevated temperature profile was reduced to the uniform profile and a rewet of the groove was noted. At $t^* = 1$ the liquid has not reached its quasi-steady-state condition. This test validated the code's ability to capture a dryout and rewet due solely to external heating.

Test Seven--Transient Body Force, External Heating

This numerical experiment was performed to determine the code's ability to capture a dryout and rewet in a groove subject to both transient body forces and external heating; similar to what was investigated in the physical experiments. The test setup is shown in Figure 19. The heating schedule of test six was combined with the tilt schedule of test five. The total run time for this experiment was ten seconds. This was done to compare the results to those of test five.

The results are seen in Figure 20. The same trends noted in Figure 16 are seen here; namely, the dryout of the groove at approximately $t^* = 0.3$ and the rewet following the groove rotation back to level. The primary difference between these two figures is in the rewet phase. In Figure 16 the rewet is seen by the rise in A^* at $x^* = 1$ between $t^* = 0.5$ and $t^* = 1$. The same region in Figure 20, however, shows a dryout condition; in fact, at $x^* = 1$, A^* is zero at $t^* = 1$, compared to $A^* = 0.045$ in Figure 16. This is due to the elevated temperatures and correspondingly increased evaporation rates.

Test Eight--Increased Frequency

An additional numerical study was performed to demonstrate the ability of the code to model the liquid flow in a heated capillary structure under a frequency and amplitude greater than those of tests one through seven. The code was run at the same conditions as numerical experiments one through seven, but the amplitude was allowed to vary between +0.0524 and -0.0524 radians. Additionally, a frequency of 1 Hz was used; one order of magnitude greater than the maximum frequency of the first seven numerical tests. Initial liquid distribution and temperature boundary conditions are shown in Figure 21.

The results of a sixty second run are shown in Figure 22. The sinusoidal motion of the liquid is evident. The overall volume of liquid in the groove is decreasing with time as evidenced by the maximum amplitude of the area peaks at $x^* = 0$ and $x^* = 1$ decreasing with time. No dryout is seen in the figure but this is only because the computer run was stopped before dryout occurred. The code appears to predict the correct trends in the liquid motion.

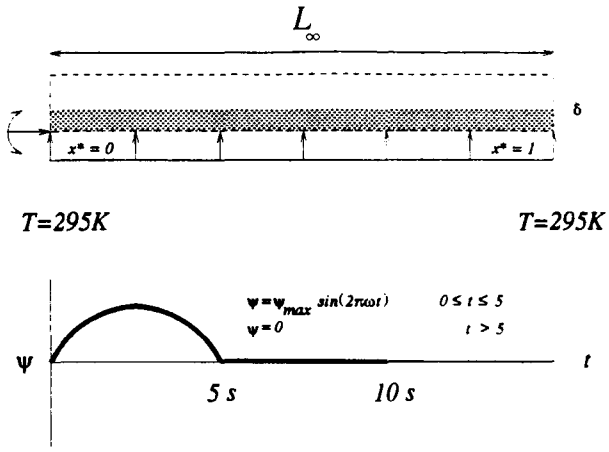

Run Parameters

Ψ_{init} = 0 rad	σ = on	t_∞ = 10 s
Ψ_{max} = 0.0524 rad		
ω = 0.1 Hz	$\dot{m}_e$ = on	L_∞ = 0.254 m

Figure 15. Numerical Test Five Parameters

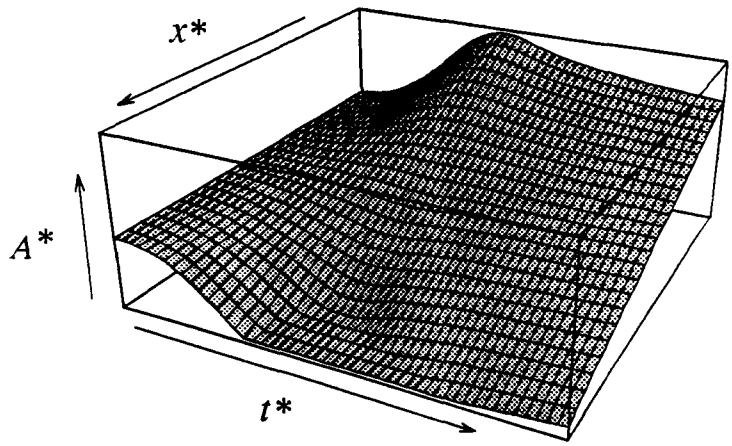

Figure 16. Numerical Test Five Results

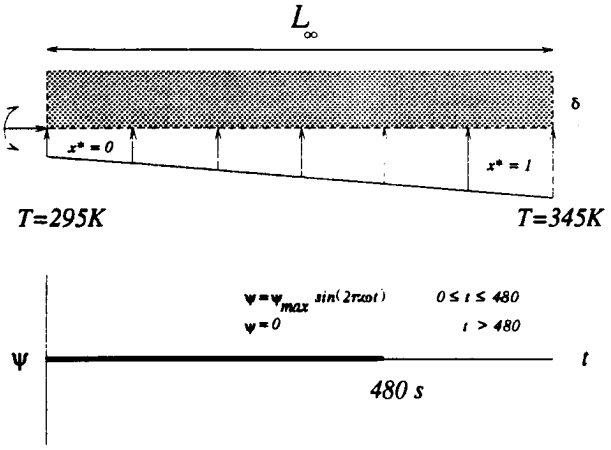

Run Parameters

$\psi_{init} = 0$ rad	σ = on	$t_\infty = 480$ s
$\psi_{max} = 0$ rad		
$\omega = 0$ Hz	$\dot{m}_e$ = on	$L_\infty = 0.254$ m

Figure 17. Numerical Test Six Parameters

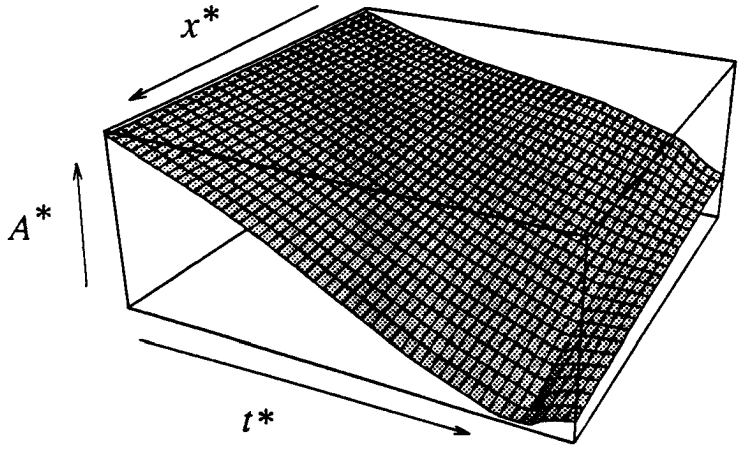

Figure 18. Numerical Test Six Results

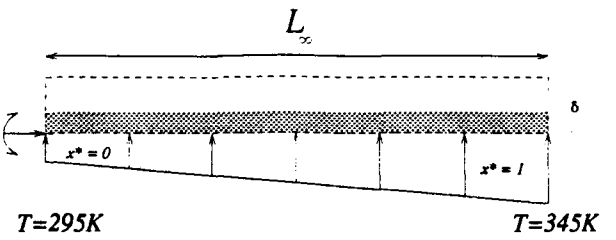

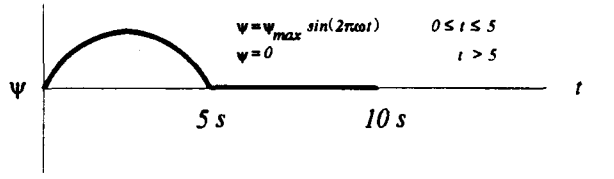

Run Parameters

Ψ_{init} = 0 rad	σ = on	t_∞ = 10 s
Ψ_{max} = 0.0524 rad		
ω = 0.1 Hz	$\dot{m}_e$ = on	L_∞ = 0.254 m

Figure 19. Numerical Test Seven Parameters

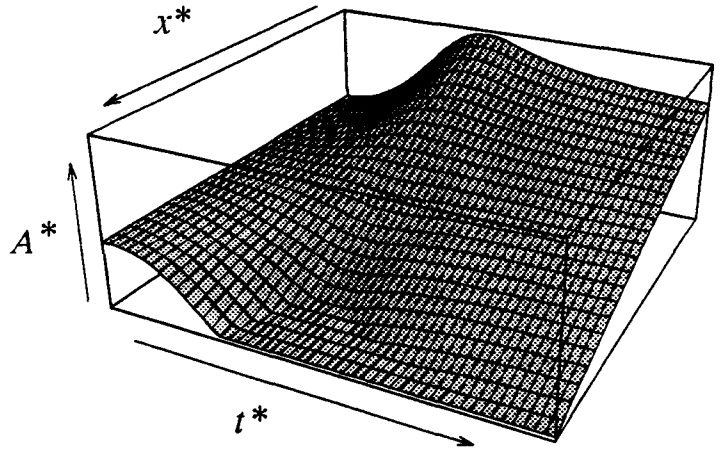

Figure 20. Numerical Test Seven Results

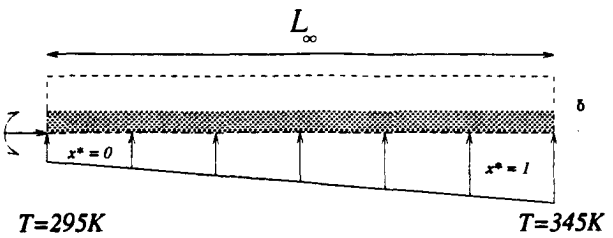

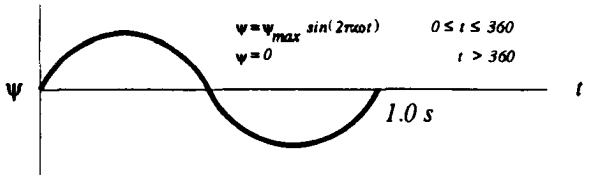

Run Parameters

$\psi_{init} = 0$ rad	σ = on	$t_\infty = 60$ s
$\psi_{max} = 0.0524$ rad		
$\omega = 1.0$ Hz	$\dot{m}_e$ = on	$L_\infty = 0.254$ m

Figure 21. Numerical Test Eight Parameters

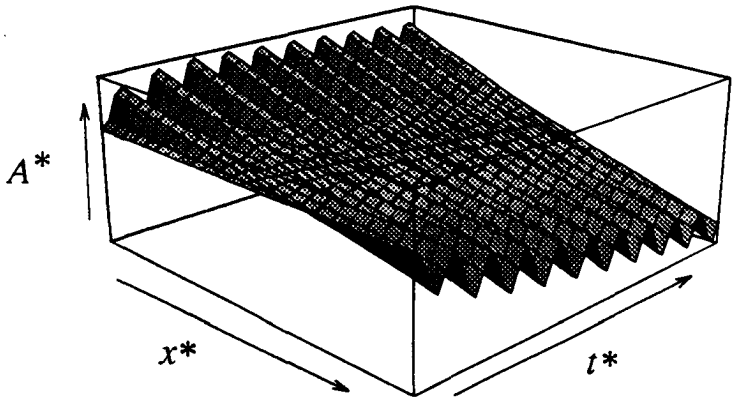

Figure 22. Numerical Test Eight Results

CONCLUSIONS AND RECOMMENDATIONS

A transient, one-dimensional numerical code has been developed which is capable of modeling the liquid motion in a grooved heat pipe wick structure subject to transient heat loads and body force effects. Simple numerical tests demonstrated its ability to predict the correct trends in axial variation of liquid inventory, to include both dryout and rewet, caused by asymmetric heating, transient body forces or a combination of both. It is recommended that experimental data be generated to compare with the results from this model to provide validation of the governing equations, simplifying assumptions and solution methodology.

REFERENCES

1. Peterson, G.P. "Heat Pipes in the Thermal Control of Electronic Components," *Proceedings of the 3rd International Heat Pipe Symposium*, Tsukuba City, Japan, Sep 1988.

2. Yerkes, K.L. and Hager, B.G., "Transient Response of Heat Pipes for Actuator Thermal Management," SAE Technical Paper Series 92-1024, Apr 1992.

3. Müller, R. "Analysis of the Liquid Distribution in Capillary Grooves of a SpacePlane Evaporation Cooler," *Proceedings of the 8th International Heat Pipe Conference*, Beijing, China, Sep 1992.

4. Jen, H. Summary Report for Axially Grooved Heat Pipe Study. contract NAS5-22562. Towson, Maryland: B & K Engineering, Inc., July 1979.

5. Beam, J.E. "Transient Heat Pipe Analysis," AIAA Paper 85-0936, Jun 1985.

6. Reagan, M.K. *Transient Body Force Effects on the Dryout and Rewet of a Heated Capillary Structure.* PhD Dissertation. Air Force Institute of Technology, Wright-Patterson AFB, OH, Apr 1994.

7. Hawthorne, Capt L.S. *Rewet Performance of a Rectangular Grooved Heat Pipe Wick After Gravitationally Induced Dryout.* MS Thesis. Air Force Institute of Technology, Wright-Patterson AFB OH, Dec 1993.

8. Shah, R.K. and London, A.L. "Laminar Flow Forced Convection in Ducts," Academic, New York, 1978, p. 190.

9. Chi, S.W. "Heat Pipe Theory and Practice," McGraw-Hill, Washington, 1976, pp. 40-41.

10. Kays, W.M. and Crawford, M.E. "Convective Heat and Mass Transfer," 2nd ed., McGraw-Hill, New York, 1987, p. 103.

ANALYSIS OF DEVELOPING LAMINAR FLOWS IN CIRCULAR PIPES USING A HIGHER-ORDER FINITE-DIFFERENCE TECHNIQUE

Ching L. Ko and Douglas E. Boddy
Oakland University
Rochester, Michigan

and

Herbert J. Gladden
NASA Lewis Research Center
Cleveland, Ohio

SUMMARY

A higher-order finite-difference technique is developed to calculate the developing-flow field of steady incompressible laminar flows in the entrance regions of circular pipes. Navier-Stokes equations governing the motion of such a flow field are solved by using this new finite-difference scheme. This new technique can increase the accuracy of the finite-difference approximation, while also providing the option of using unevenly spaced clustered nodes for computation such that relatively fine grids can be adopted for regions with large velocity gradients. The velocity profile at the entrance of the pipe is assumed to be uniform for the computation. The velocity distribution and the surface pressure drop of the developing flow then are calculated and compared to existing experimental measurements reported in the literature. Computational results obtained are found to be in good agreement with existing experimental correlations and therefore, the reliability of the new technique has been successfully tested.

INTRODUCTION

Due to the effect of viscous dissipation, velocity and pressure distributions in fluid flows normally vary non-uniformly. The flow velocity typically has a large spatial variation near a wall and a relatively small variation in a region far away from wall surfaces. To calculate flow characteristics, the classical finite-difference method discretizes the mathematical domain into uniform-size meshes. In order to obtain accurate results without resolving to using extremely fine meshes, the physical domain is preferable to be discretized into unenvenly spaced clustered nodes such that fine meshes can be adopted in regions with large velocity gradients and coarse meshes can be used in regions with small velocity gradients. As was discussed by Anderson et al (ref. 1), a physical domain discretized by using unevenly spaced clustered nodes can be transformed into a mathematical domain consisting of evenly spaced nodes by using the method of coordinate transformation such that the classical finite-difference technique can be applied. However, to find a proper mathematical function to transform coordinates of a physical domain discretized by using arbitrarily clustered nodes into new coordinates for a mathematical domain with uniformly spaced meshes is practically infeasible because of the complex nature of this type of transformation. In

addition,transformed governing equations for the mathematical domain can become highly transcendental because of the nonlinear behavior of fluid flows. Hence, it is highly desirable to develop a finite-difference technique which can be applied directly to a mathematical domain discretized by using arbitrarily spaced clustered nodes such that the transformation of governing equations can be avoided.

Several existing methods which utilize the classical finite-difference formulation to solve partial differential equations have been major tools in computational fluid mechanics. The conventional explicit method, Crank-Nicholson method, and the Box method of Keller (refs. 2 to 4) are major finite-difference techniques that have been widely used in computational fluid mechanics. However, theses methods are only second-order accurate and are not appropriate to be applied to cases with unevenly spaced clustered nodes without using the coordinate transformation technique. In view of these shortcomings, the objective of this work is to develop a fourth-order explicit finite-difference scheme such that clustered nodes can be directly used in a mathematical domain. In addition to having the capability of allowing untransformed governing equations be applied directly to unevenly spaced clustered nodes in a physical domain, this new technique determines the first four derivatives of dependent variables with respect to any independent variable consistently to the fourth-order accuracy. Therefore, it should be more accurate than the classical second-order finite difference method.

In order to test the reliability of the new explicit finite-difference technique, it is used to solve the flow-development problems of fluid flows in the entrance region of a circular tube as well as in the leading-edge region between parallel plates. The well known solutions of Couette flow and of plane Poiseuille flow are applicable to the fully developed regions of these problems. As were described by Sparrow et al (ref. 5), several analytical techniques such as linearized methods and boundary-layer approaches have also been developed to approximately model flows in the entrance regions of these two problems. Sparrow et al (ref. 5) used a linearized method to solve the developing flow problems for both cases. In addition, Bodoia and Osterle (ref. 6) also utilized the classical finite-difference method to solve these flow-development problems. However, they applied Prandtl's momentum equation for the boundary layer instead of Navier-Stokes equations to these problems. In order to properly model the actual developing process, the present analysis applies Navier-Stokes equations to the entire domain and utilizes an iterative sweeping technique to calculate nonlinear terms. Therfore, the present mathematical approach is different from any existing analyses.

HIGHER-ORDER FINITE-DIFFERENCE FORMULATION

Five different types of higher-order finite-difference formulations which allow the usage of clustered nodes can be developed by using Taylor's series expansion of functions up to the fourth-order accuracy. Nodal intervals for these five types of formulation, namely, the central difference, the partially forward difference, the fully forward difference, the partially backward difference, and the fully backward difference, are shown in Figure 1. All five types can be used for different nodes in the same domain and their selection for each node depends upon the distribution of unknown dependent variables surrounding the node under consideration. The first, the second, the third, and the fourth derivatives of a dependent variable with respect to an independent variable evaluated at this particular node (node i) can be expressed algebraically in terms of the nodal values of the same dependent variable associated with the five neighboring clustered nodes. The coefficients of these linear algebraic relationships can be calculated for any values of nodal intervals by solving four simultaneous linear algebraic equations relating to Taylor's series expansion. As an example, central-difference relationships for the case with uniform intervals ($h_1 = h_2 = h_3 = h_4 = h$) can be expressed as

$$\left[\frac{du}{dx}\right]_{x=x_i} = \frac{1}{12h}(u_{i-2} - 8u_{i-1} + 8u_{i+1} - u_{i+2}) \tag{1}$$

$$\left[\frac{d^2u}{dx^2}\right]_{x=x_i} = \frac{1}{12h^2}(-u_{i-2} + 16u_{i-1} - 30u_i + 16u_{i+1} - u_{i+2}) \tag{2}$$

$$\left[\frac{d^3u}{dx^3}\right]_{x=x_i} = \frac{1}{2h^3}(-u_{i-2} + 2u_{i-1} - 2u_{i+1} + u_{i+2}) \tag{3}$$

$$\left[\frac{d^4u}{dx^4}\right]_{x=x_i} = \frac{1}{h^4}(u_{i-2} - 4u_{i-1} + 6u_i - 4u_{i+1} + u_{i+2}) \tag{4}$$

where u_{i-2}, u_{i-1}, u_i, u_{i+1} and u_{i+2} are values of u evaluated at x_{i-2}, x_{i-1}, x_i, x_{i+1} and x_{i+2}, respectively.

FORMULATION OF THE PROBLEM

Two physical problems are considered to test the higher-order finite-difference technique. one is the axisymmetric developing incompressible laminar flow in a circular pipe and the other is the two-dimensional developing incompressible laminar flow between parallel plates. Flow velocity and the pressure at the inlet region are assumed to be uniform and the no-slip boundary conditions are imposed on all wall surfaces. By utilizing a switching constant m for both the two-dimensional problem (m = 0) and the axisymmetric problem (m = 1), governing equations for both problems in different regions can be expressed as follows:

(A) General Region of Fluid Flow $(0 < y^* < 1)$

(1) Continuity Equation

$$b\frac{\partial u^*}{\partial x^*} + \frac{mv^*}{y^*} + \frac{\partial v^*}{\partial y^*} = 0 \tag{5}$$

(2) Momentum Equations

$$bu^*\frac{\partial u^*}{\partial x^*} + v^*\frac{\partial u^*}{\partial y^*} = -ab\frac{\partial p^*}{\partial x^*} + \frac{b^2}{Re}\frac{\partial^2 u^*}{\partial x^{*2}} + \frac{m}{y^*Re}\frac{\partial u^*}{\partial y^*} + \frac{1}{Re}\frac{\partial^2 u^*}{\partial y^{*2}} \tag{6}$$

$$bu^*\frac{\partial v^*}{\partial x^*} + v^*\frac{\partial v^*}{\partial y^*} = -a\frac{\partial p^*}{\partial y^*} + \frac{b^2}{Re}\frac{\partial^2 v^*}{\partial x^{*2}} + \frac{m}{y^*Re}\frac{\partial v^*}{\partial y^*} - \frac{mv^*}{y^*Re} + \frac{1}{Re}\frac{\partial^2 v^*}{\partial y^{*2}} \tag{7}$$

(B) Centerline Region $(y^* = 0)$

(1) Continuity Equation

$$b\frac{\partial u^*}{\partial x^*} + (m+1)\frac{\partial v^*}{\partial y^*} = 0 \tag{8}$$

(2) Momentum Equations

$$bu^* \frac{\partial u^*}{\partial x^*} = -ab \frac{\partial p^*}{\partial x^*} + \frac{b^2}{Re} \frac{\partial^2 u^*}{\partial x^{*2}} + \frac{(1+m)}{Re} \frac{\partial^2 u^*}{\partial y^{*2}} \tag{9}$$

$$v^* = 0 \tag{10}$$

(C) Wall-Surface Region ($y^* = 1$)

(1) No-Slip Conditions

$$u^* = v^* = 0 \tag{11}$$

(2) Momentum Equation

$$ab \frac{\partial p^*}{\partial x^*} + a \frac{\partial p^*}{\partial y^*} = \frac{b^2}{Re} \frac{\partial^2 u^*}{\partial x^{*2}} + \frac{m}{y^* Re} \frac{\partial u^*}{\partial y^*} + \frac{1}{Re} \frac{\partial^2 u^*}{\partial y^{*2}} + \frac{b^2}{Re} \frac{\partial^2 v^*}{\partial x^{*2}} + \frac{m}{y^* Re} \frac{\partial v^*}{\partial y^*} - \frac{m v^*}{y^* Re} + \frac{1}{Re} \frac{\partial^2 v^*}{\partial y^{*2}} \tag{12}$$

where

$$b \equiv \frac{H}{L}, \qquad x^* \equiv \frac{x}{L}, \qquad y^* \equiv \frac{y}{H}, \qquad u^* \equiv \frac{u}{U_\infty}, \qquad v^* \equiv \frac{v}{U_\infty}, \qquad p^* \equiv \frac{p}{p_\infty},$$

$$a \equiv \frac{p_\infty}{\rho U_\infty^2}, \qquad Re \equiv \frac{\rho H U_\infty}{\mu}.$$

Here, x and y are either the Cartesian coordinates in the longitudinal and the transverse directions for the parallel-plate problem or the cylindrical coordinates in the axial and the radial directions for the circular-pipe problem. The origins of these coordinate systems are located at the flow inlets. The x axis is located either at the centerline of the parallel planes for the two-dimensional problem or at the center of the pipe for the axisymmetric problem. The flow domain in the x and y directions are denoted as L and H, respectively. Hence, H represents either the half distance between two parallel planes or the radius of the circular pipe. The axial velocity and the pressure at the inlet are specified as U_∞ and p_∞, respectively. Velocity components in the x and the y directions as well as the pressure, the density, and the viscosity of the flow are denoted as u, v, p, ρ, and μ, respectively. The x-momentum equation applied at $x = 0$ (centerline region) is derived by applying L'Hospital rule to the Navier-Stokes equation. In addition, equation (12) is obtained by combining both the x and the y components of the momentum equations such that the number of unknowns can be identical to the number of equations at each surface node.

Governing equations for the entire domain, equations (5-12), are discretized in the y^* direction by using the present higher-order finite-difference technique to adapt to unevenly spaced clustered nodes. However, they are discretized in the x^* direction by applying the classical finite-difference formulation to evenly spaced nodes such that an iterative sweeping technique can be used to calculate nonlinear terms. The initial value of a nonlinear term associated with a given node can be estimted by using values of terms evaluated at upstream nodes at the same y^* location such that governing equations can be solved line by line from the upstream to the downstream by using the classical backward difference formulation in the x^* direction. To reduce the inaccuracy due to this approximation, results calculated for each line are iterated to a convergent value before the

next marching sequence of the sweeping process is undertaken. To start the process, the first two lines have to be solved simultaneously by using the central difference for the first line and the backward difference for the second line in the x^* direction. For all subsequent sweeping calculations, only one line of nodes are involved in the process.

NUMERICAL RESULTS

The normalized domains for both the parallel-plate and the circular pipe problems are discretized by dividing the domain in the x^* direction into 30 evenly spaced intervals and the domain in the y^* direction into 20 uneven clustered intervals. These unevenly speced intervals in the y^* direction vary from 0.0025 at the wall to 0.1 at the centerline. Table 1 compares non-dimensional axial velocities of the circular pipe between those obtained by the present analysis and those measured by Nikuradse (ref. 7) as well as those calculated by Sparrow et al (ref. 5). Table 2 shows the comparison of non-dimensional longitudinal velocities for the parallel-plate problem between those calculated by using the present technique and those determined by Sparrow et al as well as by Bodia and Osterle (refs. 5 and 6). Table 3 summarizes the comparison of the non-dimensional centerline pressure drop, $[2(p_\infty - p)]/(\rho U_\infty^2)$, of the pipe flow between those calculated by using the present analysis and the Schiller's experimental correlation reported by Prandtl and Tietjens (ref. 7). Results obtained by using the present technique are shown to be in good agreement with those determined by existing techniques. The non-dimensional entrance length of the circular pipe estimated by locating the cross section with its centerline velocity being 99% of the fully developed centerline velocity is found to be approximately equal to $x/(DRe_D) = 0.0593$ or $x/(HRe) = 0.237$ which is roughly consistent with the value of $x/(DRe_D) = 0.05$ suggested by Kays (ref. 8) or the value of $x/(HRe) = 0.26$ reported by Prandtl and Tietjens (ref. 7) for pipe flows.

CONCLUSIONS

A higher-order finite-difference technique which allows the usage of clustered nodes has been successfully developed. Numerical results obtained in the present analysis have also verified the reliability of this technique. Therefore, it can be a very useful tool in computational fluid mechanics because of its accuracy and the need to use unevenly spaced clustered nodes for modeling fluid flows.

REFERENCES

1. Anderson, D.A.; Tannehill, J.C.; and Pletcher, R.H.: Computational Fluid Mechanics and Heat Tansfer. Hemisphere, 1984.
2. Bradshaw, P.; Cebecci, T.; and Whitelaw, J.H.: Engineering Calculation Methods for Turbulent Flow, Academic Press, 1984.
3. Crank, J.; and Nicholson, P.: A Practical Method for Numerical Evaluation of Solutions of Partial-Differential Equations of the Heat-Conduction Type. Proc. Cambridge Phil. Soc., vol. 43, 1947, pp. 50-67.
4. Keller, H.B.: A New Difference Scheme for Parabolic Problems. Numerical Solutions of Partial Differential Equations. (edited by Bramble, J.) Academic Press, 1970.
5. Sparrow, E.M.; Lin, S.H.; and Laudgren, T.S.: Flow Development in the Hydrodynamic Entrance Region of Tubes and Ducts. Phys. Fluids, vol. 7, no. 3, Mar. 1964, pp. 338-347.
6. Bodoia, J.R.; and Osterle, J.F.: Finite Difference Analysis of Plane Poiseuille and Couette Flow Developments. Appl. Sci. Res. sec. A, vol. 10, 1961, pp. 265-276.
7. Prandtl, L; and Tietjens, O.G.: Applied Hydro- and Aeromechanics. Dover, 1957, p. 25.
8. Kays, W.M.: Convetive Heat and Mass Transfer. McGraw-Hills, 1966, p. 63.

(a) Fully Forward Difference

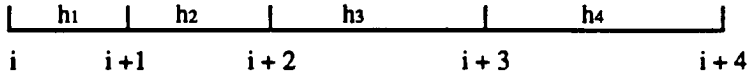

(b) Partially Forward Difference

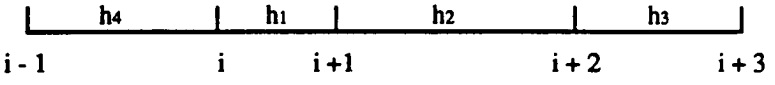

(c) Central Difference

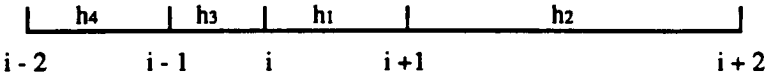

(d) Partially Backward Difference

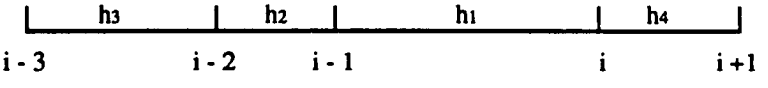

(e) Fully Backward Difference

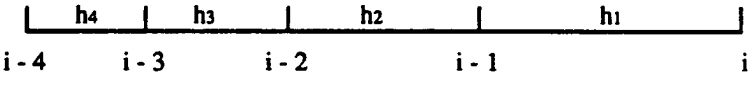

Figure 1. Higher-order finite-difference nodes

TABLE 1 - Comparison of the non-dimensional axial velocity (u/U_∞) of pipe flows

$\frac{x}{HRe}$	Present Analysis				Nikuradse's Expermental Measurement (ref.7)				Analysis by Sparrow et al (ref. 5)			
	y/H				y/H				y/H			
	0.0	0.4	0.8	0.9	0.0	0.4	0.8	0.9	0.0	0.4	0.8	0.9
0.01	1.34	1.32	0.99	0.63	1.30	1.32	1.12	0.71	1.32	1.31	1.00	0.59
0.02	1.44	1.41	0.92	0.53	1.43	1.44	0.95	0.58	1.44	1.42	0.92	0.51
0.03	1.53	1.48	0.87	0.48	1.53	1.53	0.89	0.52	1.53	1.49	0.87	0.47
0.04	1.60	1.52	0.84	0.46	1.60	1.58	0.86	0.50	1.60	1.53	0.84	0.45
0.05	1.66	1.56	0.81	0.44	1.66	1.60	0.83	0.48	1.66	1.57	0.81	0.44
0.10	1.84	1.63	0.76	0.40	1.83	1.65	0.77	0.41	1.85	1.63	0.76	0.40
0.20	1.97	1.67	0.73	0.38	1.97	1.67	0.72	0.38	1.97	1.67	0.72	0.38

TABLE 2 - Comparison of the non-dimensional axial velocity (u/U_∞) of flows between parallel plates

$\frac{x}{HRe}$	Present Analysis				Finite-Difference Calculation by Bodia and Osterle (ref. 6)				Calculation by Sparrow et al (ref. 5)			
	y/H				y/H				y/H			
	0.0	0.5	0.7	0.9	0.0	0.5	0.7	0.9	0.0	0.5	0.7	0.9
0.01	1.20	1.15	1.00	0.50	1.16	1.16	1.05	0.50	1.18	1.16	1.03	0.48
0.02	1.25	1.18	0.96	0.42	1.22	1.18	0.99	0.41	1.24	1.18	0.96	0.40
0.03	1.30	1.18	0.91	0.37	1.27	1.18	0.93	0.37	1.29	1.18	0.91	0.37
0.04	1.33	1.18	0.88	0.35	1.31	1.18	0.89	0.35	1.33	1.17	0.88	0.35
0.05	1.36	1.17	0.86	0.34	1.34	1.17	0.86	0.33	1.36	1.16	0.86	0.33
0.10	1.44	1.15	0.80	0.30	1.44	1.14	0.80	0.30	1.44	1.14	0.80	0.30
0.20	1.49	1.13	0.77	0.29	1.49	1.13	0.77	0.29	1.49	1.13	0.77	0.29

TABLE 3 - Comparison of the non-dimensional centerline pressure drop, $2(p_\infty - p)/\rho U_\infty^2$, of pipe flows.

$\frac{x}{HRe}$	Present Analysis	Schiller's Correlation (ref. 7)
0.01	0.89	0.66
0.02	1.21	1.03
0.03	1.49	1.27
0.04	1.74	1.48
0.05	1.96	1.80
0.10	2.94	2.68
0.12	3.30	3.18
0.16	3.98	3.70

A CASE STUDY OF VIEW-FACTOR RECTIFICATION PROCEDURES FOR DIFFUSE-GRAY RADIATION ENCLOSURE COMPUTATIONS

Robert P. Taylor and Rogelio Luck
Thermal & Fluid Dynamics Laboratory
Department of Mechanical Engineering
Mississippi State University
Mississippi State, Mississippi

ABSTRACT

The view factors which are used in diffuse-gray radiation enclosure calculations are often computed by approximate numerical integrations. These approximately calculated view factors will usually not satisfy the important physical constraints of reciprocity and closure. In this paper several view-factor rectification algorithms are reviewed and a rectification algorithm based on a least-squares numerical filtering scheme is proposed with both weighted and unweighted classes. A Monte-Carlo investigation is undertaken to study the propagation of view-factor and surface-area uncertainties into the heat transfer results of the diffuse-gray enclosure calculations. It is found that the weighted least-squares algorithm is vastly superior to the other rectification schemes for the reduction of the heat-flux sensitivities to view-factor uncertainties. In a sample problem, which has proven to be very sensitive to uncertainties in view factor, the heat transfer calculations with weighted least-squares rectified view factors are very good with an original view-factor matrix computed to only one-digit accuracy. All of the algorithms had roughly equivalent effects on the reduction in sensitivity to area uncertainty in this case study.

INTRODUCTION

It is general knowledge in the radiation heat transfer literature that the view factors in diffuse-gray radiation enclosure calculations should be computed in such a way that they satisfy the physical constraints of reciprocity and closure. For systems with a large number of surfaces, the only practical way to compute the view factors is by approximate numerical integrations. Monte-Carlo integration is a popular technique which is robust and has the added advantage of providing an estimate of the uncertainty in each calculation. These approximately computed view factors will only in the rarest of coincidences satisfy the reciprocity and closure constraints, and artificial means of enforcement must be adopted.

Most heat transfer textbooks adopt a naive enforcement. Only the view factors above the diagonal in the view-factor matrix are computed. The view factors below the diagonal are computed using reciprocity relationships, and the view factors along the diagonal are computed using closure. This technique is naive because it allows the view factors along the diagonal to be negative. Negative view factors are of course blatant physical impossibilities. Tsuyuki [1] presents a refined form of the naive enforcement which avoids negative view factors. van Leersum [2] presents an iterative approach which enforces closure and reciprocity on an approximate set of view factors and avoids negative instances.

It is often stated in the radiation heat transfer literature (Brewster [3] for example) that reciprocity and closure are required to avoid ill-conditioned matrixes in the linear equation set that results from the diffuse-gray enclosure analysis. Taylor et al. [4, 5] have demonstrated that diffuse-gray radiation enclosure problems can be very sensitive to errors in the view factors even when the coefficient matrixes are very well-conditioned with condition numbers of order 2 and 3. In their work, they found that the simultaneous enforcement of reciprocity and closure using the naive algorithm

described above will greatly reduce this sensitivity. Also, Taylor et al. demonstrated that enforcement of closure and reciprocity reduced the sensitivity of the heat-flux results to uncertainties in the surface areas.

This paper extends the previous work of Taylor et al. by considering more advanced reciprocity and closure enforcement algorithms and comparing the propagation of the view-factor errors and surface-area errors into computed heat-flux results of the diffuse-gray enclosure analysis for the different methods.

Four view-factor enclosure algorithms are discussed and compared

1) No enforcement--all view factors independently computed.
2) Naive enforcement.
3) van Leersum's enforcement.
4) Optimal enforcement.

The optimal enforcement algorithm uses a least-squares optimization which finds the minimum root-sum-square charge in the view factors which will simultaneously enforce reciprocity and closure. Nonnegativity conditions can also be included in the optimization algorithms.

The technique used for the comparison is a Monte-Carlo uncertainty analysis of a sample problem which has proven to be hypersensitive to errors in the view factors when reciprocity and closure are not enforced. The results are the distributions in computed surface heat fluxes for assumed uncertainty distributions of the original unrectified view factors and for assumed uncertainty distributions in surface areas.

DIFFUSE-GRAY ENCLOSURE FORMULATION

Radiation exchange between finite diffuse-gray areas which form an enclosure is discussed in almost all general heat transfer textbooks. Excellent detailed discussions can be found in any thermal radiation heat transfer textbook (Brewster [3] and Siegel and Howell [6], for example). The basic restrictions are that each surface have uniform temperature, uniform radiative properties which are diffuse and gray, and uniform radiosity. Boundary conditions for the k-th surface are expressed by specifying either the surface heat flux, q_k, or the surface temperature, t_k. Mixed boundary conditions cause no problem. If all of the surfaces with specified heat flux are considered first as surfaces 1 through M and the surfaces with specified temperatures numbered M + 1 through N, the following set of linear equations can be obtained for the radiosity values [4,5]

$$\left[I - \left(I - D_\epsilon^M\right) D_a^{-1} F^T D_a\right] q_o = b \tag{1}$$

where $\mathbf{D_a}$ is a diagonal matrix with areas as elements, $\mathbf{F}$ is the view factor matrix, D_ϵ^M is a diagonal matrix with zeros for elements in rows 1 through M and ϵ_k in rows k = M + 1 to N, b is a vector whose first M elements are q_k (k = 1,2,···,M) and whose last N-M elements are $\epsilon_k \sigma t_k^4$ (k = M+1,···,N), and $\mathbf{q_o}$ is the vector of radiosities.

Equation (1) is solved for the radiosities. If the result r is taken to be the vector whose first M elements are $\epsilon_k \sigma t_k^4$ (k = 1,2,···,M) and whose last N-M elements are q_k (k = M+1,···,N), the final equation is

$$r = \left[I - \left(I - D_\epsilon^{*M}\right) D_a^{-1} F^T D_a\right] q_o \tag{2}$$

where D_e^{*M} is the complement of D_e^M and has ϵ_k for the first M elements and zeros for the last N-M elements.

Usually at this stage of the development, the view-factor reciprocity relationship

$$F^T D_a = D_a F \tag{3}$$

is substituted into equations (1) and (2) to simplify the formulas. However, in this investigation, we are interested in cases where reciprocity is not strictly enforced. In that case, it is more appropriate to work with equations (1) and (2).

VIEW-FACTOR RECTIFICATION

Three view-factor rectification schemes are considered: 1) Naive, 2) Leersum's, and 3) least-squares optimum. For the least-squares optimum three subsets are considered: 1) unweighted without nonnegativity, 2) unweighted with nonnegativity, and 3) weighed with nonnegativity. Each of these procedures is discussed below.

Naive Rectification

For the naive rectification, the view factors above the main diagonal in the view-factor matrix, F, are retained and all others are discarded. The upper-triangular matrix containing these remaining view factors is designated as U and its transpose as U^T. Equation (3) can then be used to compute the missing view factors below the diagonal. If the lower-triangular matrix containing the view factors below the main diagonal calculated by reciprocity is designated L_N, equation (3) can be written as

$$L_N = D_a^{-1} U^T D_a \tag{4}$$

The rectified view-factor matrix excluding the diagonal is obtained by combining the lower- and upper-triangular matrixes

$$F_N = L_N + U \tag{5}$$

Next the diagonal elements are computed using the closure relation

$$f_{Nii} = 1 - \sum_{\substack{j=1 \\ j \neq i}}^{N} f_{Nij} \tag{6}$$

No attempt is made to ensure nonnegative view factors. The physically impossible negative view factors are naively accepted.

Leersum's Rectification

van Leersum (1989) has published an iterative scheme which can be considered a refinement of

the naive rectification. His method spreads the closure adjustments over all of the view factors and assures nonnegative view factors. His algorithm is given below.

1) For each row in the **F**, compute a correction factor based on closure

$$d_i = \left(1 - \sum_{k=1}^{N} f_{ik}\right) \Big/ m \tag{7}$$

where m is the number of nonzero view factors in row i.

2) For each nonzero view factor in row i, apply the correction

$$f_{Lik} = f_{ik} + d_i, \quad k = 1, \ldots, N \tag{8}$$

If any $f_{Lij} < 0$, decrease m by the number of negative values and recalculate d_i bypassing the view factors which made the previous f_{Lij} negative. Repeat this procedure until no negative view factors are obtained.

3) Enforce reciprocity by computing values for column i

$$f_{Lki} = \frac{a_i f_{Lik}}{a_k}, \quad k = 1, \ldots, N \tag{9}$$

4) Repeat this process in turn for each row.

5) Since the enforcement of reciprocity in 3) disturbs the closure forced in 1) and 2), repeat the entire process iteratively until the values of d_i are arbitrarily small.

The step-by-step enforcement of reciprocity in 3) over wrights all of the original view factors below the main diagonal; therefore, Leersum's procedure only considers the diagonal and upper triangular elements in the original view-factor matrix. Also, it is not clear why zero-valued view factors are considered to be exact and are not allowed to be modified.

Least-Squares Optimum

The least-squares optimization problem can be posed as the quadratic minimization of

$$y = \sum_{i=1}^{N} \sum_{j=1}^{N} w_{ij}(f_{oij} - f_{ij})^2 \tag{10}$$

subject to the closure and reciprocity equality constraints where the f_{ij}'s are the original approximately determined view factors, f_{oij}'s are the corrected view factors, and w_{ij}'s are the weights used when the view factors have unequal uncertainty. The closure and reciprocity constraints are

$$\sum_{j=1}^{N} f_{oij} = 1, \quad i = l, \ldots, N \tag{11}$$

$$a_j f_{oji} - a_i f_{oij} = 0 \quad i = 1, N - 1, j = i + 1, N \tag{12}$$

If nonnegativity is desired, the inequality constraints can be applied

$$f_{oij} \geq 0 \quad i = 1, \ldots, N, j = 1, \ldots, N \tag{13}$$

This problem can be readily solved using any number of nonlinear-programming techniques.

However, considerable insight can be gained and a computational formula can be derived if the problem is viewed from a geometric standpoint. First, the view factors are grouped into a column vector instead of a matrix. The view-factor matrix is stacked in row-major form; for example, the 2 $\times$ 2 view-factor matrix becomes

$$\boldsymbol{F} = \begin{bmatrix} f_{11} & f_{12} \\ f_{21} & f_{22} \end{bmatrix} \rightarrow \boldsymbol{f} = \begin{bmatrix} f_{11} \\ f_{12} \\ f_{21} \\ f_{22} \end{bmatrix} \tag{14}$$

Closure and reciprocity are enforced by applying the equality constraints (equations 11 and 12) to form a set of linear equations

$$\boldsymbol{R} \cdot \boldsymbol{f} = \boldsymbol{c} \tag{15}$$

The 2 $\times$ 2 system would yield, for example

$$\begin{bmatrix} 1 & 1 & 0 & 0 \\ 0 & 0 & 1 & 1 \\ 0 & a_1 & -a_2 & 0 \end{bmatrix} \begin{bmatrix} f_{11} \\ f_{12} \\ f_{21} \\ f_{22} \end{bmatrix} = \begin{bmatrix} 1 \\ 1 \\ 0 \end{bmatrix} \tag{16}$$

Equation (15) has N(N - 1)/2 degrees of freedom. The Naive rectification is obtained by specifying the N(N - 1)/2 view factors above the main diagonal and computing the remainder from equation (15). However, it is more desirable to use all of the N^2 view factors.

The solutions of equation (15) can be factored into two orthogonal subspaces--the rowspace and the nullspace. The rowspace component of the solution is computed using the expression (Strang [7])

$$\boldsymbol{f}_{row} = \boldsymbol{R}^T(\boldsymbol{R}\boldsymbol{R}^T)^{-1}\boldsymbol{c} \tag{17}$$

This vector is the particular solution of equation (15) which has the least norm. It is a unique and necessary component of all solutions of equation (15). The other component of the solution ($\mathbf{f} - \mathbf{f}_{row}$) should lie in the nullspace of the reciprocity and closure matrix R and can be expressed as a linear combination of basis vectors for the nullspace

$$(\boldsymbol{f} - \boldsymbol{f}_{row}) = \boldsymbol{N}_b\boldsymbol{x} \tag{18}$$

where N_b is the matrix whose columns form that basis and x contains the weights of the linear combination. However, if there are errors in the computed view factors, f, equations (18) will not be consistent, and we must resort to the least-squares solution [7]

$$x = \left(N_b^T N_b\right)^{-1} N_b^T (f - f_{row}) \tag{19}$$

The projection of ($f - f_{row}$) onto the nullspace, then, is the desired set of corrected view factors

$$f_{null} = N_b \left(N_b^T N_b\right)^{-1} N_b^T (f - f_{row}) \tag{20}$$

and the least-squares optimum set of view factors is

$$f_{opt} = f_{row} + f_{null} \tag{21}$$

When the data are not all equally reliable (usually the case for view factors), weighted least squares should be used for the solution of equations (18) [7]

$$f_{null}^w = N_b \left(N_b^T V^{-1} N_b\right)^{-1} N_b^T V^{-1} (f - f_{row}) \tag{22}$$

where V is the covariance matrix, and

$$f_{opt}^w = f_{row} + f_{null}^w \tag{23}$$

The view-factor rectifications computed using equations (21) and (23) do not enforce nonnegativity.

The least-squares optimum view-factor rectification obtained through equations (21) and (23) are exactly the same as those which would be obtained by solving the quadric minimization problem in equations (10), (11), and (12) without considering the nonnegativity constraints.

As discussed before the view factors must be nonnegative to be physically realistic; a negative view factor is meaningless. It is our opinion and experience that allowing slightly negative values in the rectified view-factor matrix does not seriously impact the fidelity of the heat transfer results. Certainly, the strict enforcement of reciprocity and closure has had a much stronger impact on our results.

A two-step procedure which is easy to implement and closely approximates the results of the nonlinear-programming solution with the nonnegativity constraints is to apply equations (21) or (23) and to assume that the equality in equations (13) would be enforced on all negative values. These view factors are set to zero and removed from consideration obtaining a reduced order problem, and the process is then repeated with the reduced set of data. This procedure has proven to give exactly the same set of rectified view factors as the nonlinear-programming solution in about 90% of the cases and only slightly different ones in the other 10% of the cases.

The rectification algorithm for the least-squares projection is as follows

1) Construct the closure and reciprocity matrix R.
2) Compute the row space component f_{row} using equation (17).
3) Construct the nullspace matrix N. (This can be constructed using standard routines).
4) Compute the nullspace least-squares projection using equation (20) or equation (22) for the

weighted case.

5) Compute the optimum rectified view factors using equation (21) or (23). View factors f_{opt} or f^{w}_{opt} now satisfy reciprocity and closure.

6) If nonnegativity is enforced, search f_{opt} or f^{w}_{opt} for negative entries, and set these to zero.

7) Remove all zero view factors from consideration. Remove the columns of matrix R corresponding to each diagonal zero element. For each off-diagonal zero reciprocal pair, remove the corresponding columns and reciprocity rows from the matrix R. The process is run a second time starting with step 2 and the reduced set of original view factors.

All of the rectification algorithms presented herein apply reciprocity using the best estimates of the areas in equation (15) as if the areas were known exactly. This is usually not a serious deficiency since the areas can usually be determined with low uncertainty. The authors are currently exploring procedures to properly weight the rectification procedure to account for area variance.

NUMERICAL EXAMPLES

The following problem from the heat transfer text by Incropera and Dewitt [8] is used as a basis of comparison of the different techniques in this paper.

13.62 A room (Figure 1) is represented by the following enclosure, where the ceiling (1) has an emissivity of 0.8 and is maintained at 40°C by embedded electrical heating elements. Heaters are also used to maintain the floor (2) of emissivity 0.9 at 50°C. The right wall (3) of emissivity 0.7 reaches a temperature of 15°C on a cold, winter day. The left wall (4) and end walls (5A, 5B) are very well insulated. To simplify the analysis, treat the two end walls as a single surface (5). Assuming the surfaces are diffuse-gray, find the net radiation heat transfer from each surface.

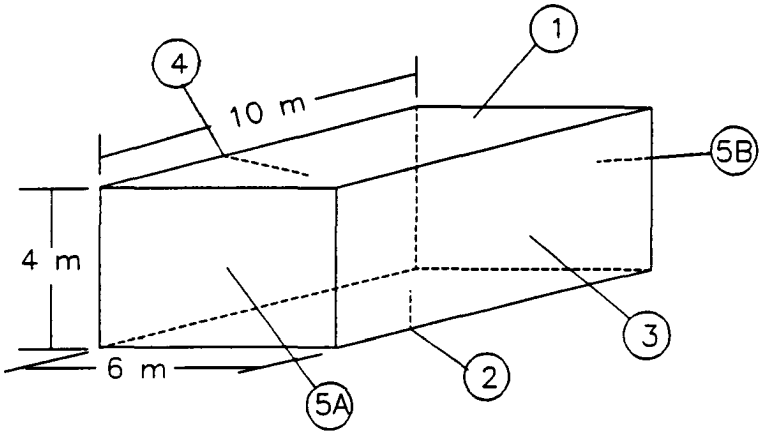

Figure 1. Schematic of a Room for the Example Problem.

This problem was the genesis of our interest in the subject of view-factor sensitivity and rectification. This problem was assigned in the second heat transfer course at Mississippi State University during the Fall 1992 term. Two students, Miguel and Simon, ignored the simplification and worked the problem as a six-sided enclosure. Miguel computed his view factors to four-digit accuracy and Simon to two-digit accuracy; they got radically different answers for the heat fluxes. An analysis of this problem and the cause for this hypersensivity are discussed in a previous publication (Taylor et al. [4]).

The view-factor matrix computed to four-digit accuracy is

$$F = \begin{bmatrix} 0.0 & 0.394 & 0.1921 & 0.1921 & 0.1109 & 0.1109 \\ 0.394 & 0.0 & 0.1921 & 0.1921 & 0.1109 & 0.1109 \\ 0.2881 & 0.2881 & 0.0 & 0.196 & 0.1139 & 0.1139 \\ 0.2881 & 0.2881 & 0.196 & 0.0 & 0.1139 & 0.1139 \\ 0.2774 & 0.2774 & 0.1898 & 0.1898 & 0.0 & 0.066 \\ 0.2774 & 0.2774 & 0.1898 & 0.1898 & 0.066 & 0.0 \end{bmatrix} \tag{24}$$

Seven different numerical experiments have been performed. In each case, the starting point was the view-factor matrix listed above. Random errors were then introduced by sampling a random-number generator which produced normally distributed values. The difference in each experiment resulted from the way that the variance of these random errors was assigned to the view factors. A thousand view-factor trials were conducted for each case. This was followed by a thousand trials where the areas were varied randomly. In all of the following, covariance terms are assumed to be negligible.

Equal Variance

The first numerical experiment considered the view factors to have equal variance with a view-factor standard deviation of 0.01 and the areas to be fixed. Table 1 gives mean values of the heat flux for several of the rectification schemes. Since the variances were all equal and the covariances were assumed to be zero, the weighted least-squares optimum scheme and the unweighted schemes are identical. The exact solution is computed using the view factors in equation (24) directly. Table 2 shows the standard deviations for the heat flux calculations and the root-mean-square average standard deviation for each treatment.

Table 1. Mean Heat-Flux Values for Equal View-Factor Variance Case.

	Least-Squares						
Surface	Not Nonneg.	N.L.P. Nonneg.	Nonneg.	Leersum	Naive	No Rectification	Exact
1	-3.6273	-3.6030	-3.6036	-3.6231	-3.6570	-3.9179	-3.6891
2	83.9532	83.7224	83.7249	83.7249	83.9429	83.9205	83.8721
3	-120.4888	-120.1792	-120.1820	-120.4798	-120.3951	-120.3969	-120.5353

Table 2. Standard Deviations in Heat Flux for Equal View-Factor Variance Case.

	Least-Squares					
Surface	Not Nonneg.	N.L.P. Nonneg.	Nonneg.	Leersum	Naive	No Rectification
1	0.4374	0.3449	0.3447	0.6364	1.0005	10.2714
2	0.5776	0.4394	0.4398	0.8416	1.5774	11.8809
3	0.7272	0.5138	0.5148	0.9571	2.2777	12.3575
rms-avg	0.5927	0.4382	0.4383	0.8225	1.7007	11.5379

From Table 1, all of the rectification schemes seem to have means which are roughly equal to the exact solution. Table 2 shows, however, that there is a large difference in the standard deviations of the calculated heat fluxes. For surface 1, the case of no rectification has a standard deviation which is almost an order of magnitude larger than the rectified values. Figure 2 shows histograms of surface-3 heat-flux distributions for each rectification scheme and for no rectification.

The tables and figure reveal that all of the rectifications are effective for this problem. The nonnegative least-squares procedures are about twice as effective in reducing errors in the heat flux calculations as Leersum's rectification which in turn is about twice as effective as the Naive rectification. Among the least-squares, the nonnegative projection scheme and the nonlinear-programming scheme yield almost identical results as expected, and the least-squares without nonnegativity has very slightly larger errors in heat flux than its nonnegative counter parts.

Next, the view factors were set at the values given in equation (24) and the areas were varied using a standard deviation of 1% for each area. Table 3 gives the standard deviations for the heat-flux calculations and the rms average standard deviation for each treatment.

Table 3. Standard Deviations in Heat Flux for the Area Variance Case with Equal View-Factor Variance.

	Least-Squares				
Surface	Not Nonneg.	Nonneg.	Leersum	Naive	No Rectification
1	0.4414	0.5132	0.4601	0.2285	4.641
2	0.5281	0.4678	0.4225	0.4928	4.377
3	0.3211	0.3334	0.4915	0.8307	4.461
rms-avg	0.4385	0.4447	0.4586	0.5730	4.794

The table shows that with no rectification the area uncertainties result in considerable uncertainties in the heat fluxes. However, when the view factors were rectified by enforcing closure and reciprocity these uncertainties in heat flux are reduced by an order of magnitude. All of the algorithms give about the same decrease in the sensitivity to area uncertainty for this case study.

Unequal Variance

Six cases were considered which contained unequal variance: 1) diagonal-dominated, 2) counter-diagonal-dominated, 3) row-dominated, 4) column-dominated, 5) upper-triangle-dominated, and 6) random variances. Depending on the location of the uncertainties in the view-factor matrix, the relative success of the rectification schemes with respect to the sensitivity to view-factor uncertainty is vastly different from that seen for equal variance.

For the diagonal-dominated case-study the view factors along the main diagonal are considered to have standard deviations which are 100 times as large as the off-diagonal view factors. The standard-deviation matrix corresponding to the view-factor matrix is

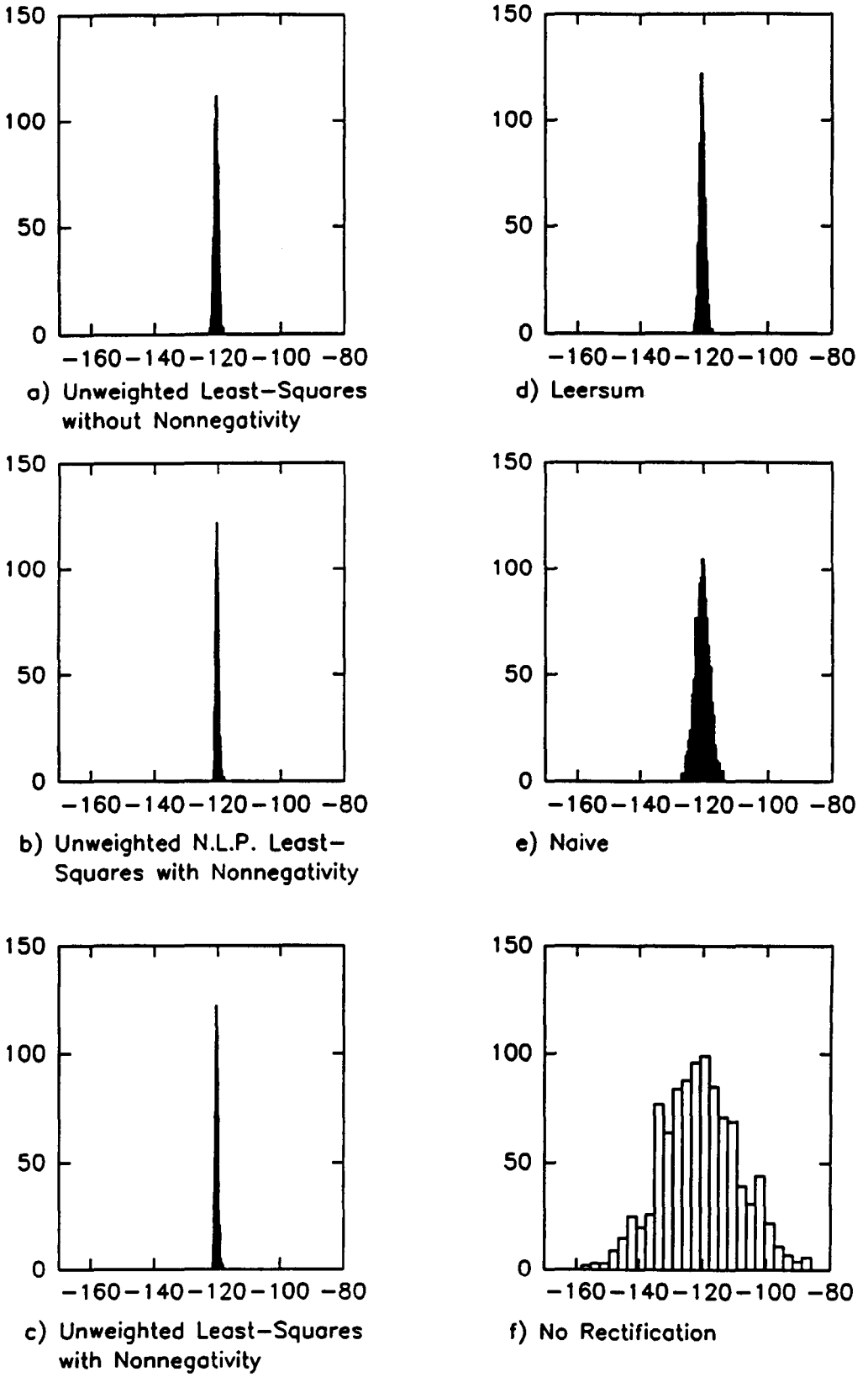

Figure 2. Histogram of Surface-3 Heat Flux [watts/m^2] for Equal Variance Case.

$$S = \begin{bmatrix} \mathbf{0.1000} & 0.0010 & 0.0010 & 0.0010 & 0.0010 & 0.0010 \\ 0.0010 & \mathbf{0.1000} & 0.0010 & 0.0010 & 0.0010 & 0.0010 \\ 0.0010 & 0.0010 & \mathbf{0.1000} & 0.0010 & 0.0010 & 0.0010 \\ 0.0010 & 0.0010 & 0.0010 & \mathbf{0.1000} & 0.0010 & 0.0010 \\ 0.0010 & 0.0010 & 0.0010 & 0.0010 & \mathbf{0.1000} & 0.0010 \\ 0.0010 & 0.0010 & 0.0010 & 0.0010 & 0.0010 & \mathbf{0.1000} \end{bmatrix} \quad (25)$$

Tables 4 and 5 show the mean and standard deviations of the heat fluxes for 1000 trials where the view factors in equation (24) were perturbed by values from a gaussian random number generator with standard deviations given by equation (25).

Table 4. Mean Heat-Flux Values for the Diagonal-Dominated View-Factor Variance Case.

	Nonnegative Least-Squares				
Surface	Unweighted	Weighted	Leersum	Naive	Exact
1	-3.4722	-3.6263	-3.4719	-3.6264	-3.6891
2	82.1136	83.8987	83.9797	83.9417	83.9417
3	-117.9622	-120.4087	-120.7616	-120.4729	-120.5353

Table 5. Standard Deviations in Heat Flux for the Diagonal-Dominated View-Factor Variance Case.

	Nonnegative Least-Squares			
Surface	Unweighted	Weighted	Leersum	Naive
1	1.7256	0.0468	3.5462	0.1029
2	2.3167	0.0623	5.1518	0.1584
3	3.3123	0.0912	6.4956	0.2284
rms-avg	2.5374	0.0693	5.2061	0.1711

The rectification schemes are the unweighted and weighted nonnegative least-squares projection methods, Leersum's method, and the Naive method. Figure 3 shows histograms for the heat-flux distributions for surface 3.

For this case study, Leersum's rectification is seen to be the least effective at reducing errors in the heat flux. The unweighted nonnegative least-squares projection is about twice as effective as Leersum's scheme, but the weighted nonnegative least-squares projection is an order of magnitude more effective. For this case, the Naive rectification is almost as good as the weighted least-squares projection.

Recall that the Naive rectification scheme lumps all of the corrections into the diagonal elements for closure enforcement while Leersum's scheme evenly distributes the corrections over all of the nonzero values. Therefore, when the view factor variance is mostly along the diagonal, we expect the Naive scheme to perform well and Leersum's to not perform well. When the variances are all equal, Leersum's is expected to perform well, as it did in the previous case study.

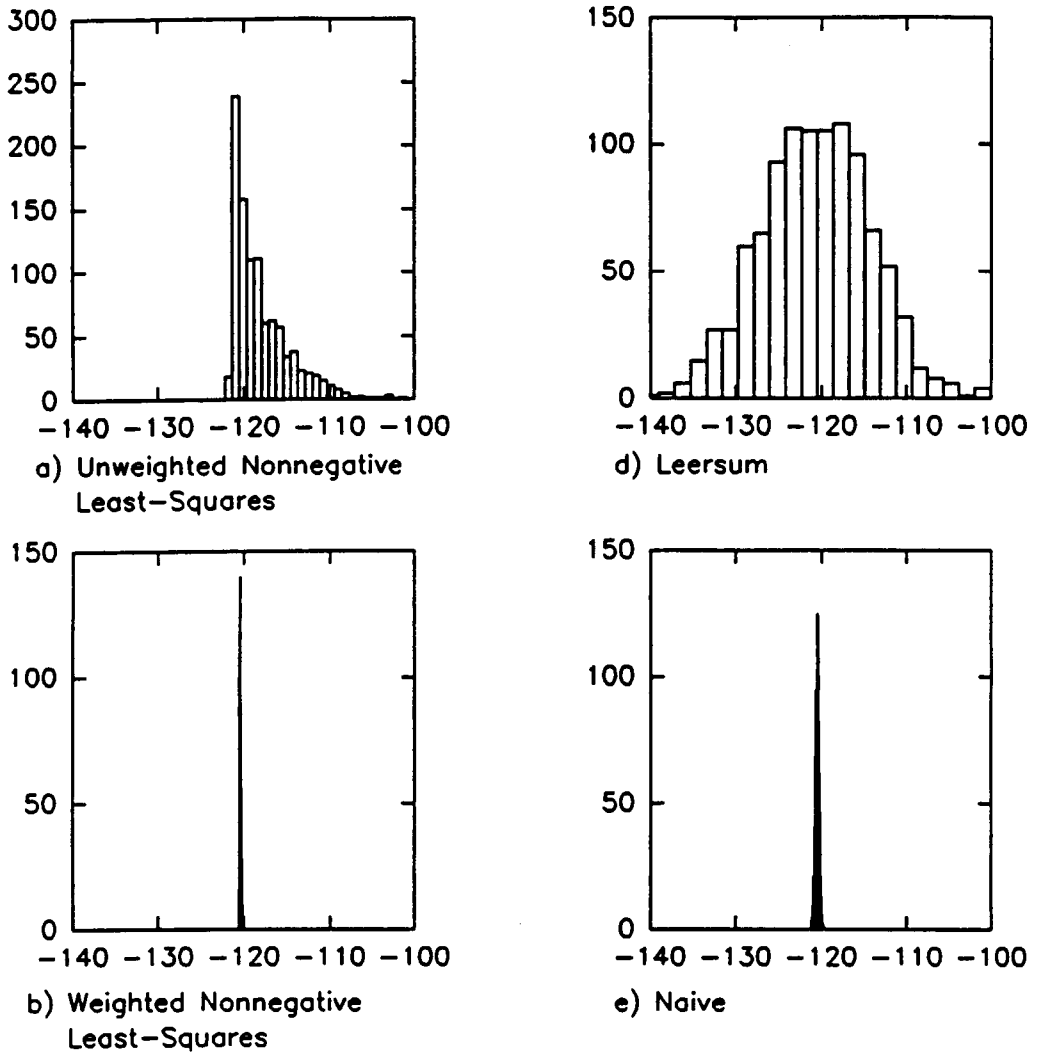

Figure 3. Histograms of Surface-3 Heat Flux [watts/m^2] for the Diagonal-Dominated Case.

Figure 3 shows that there is a considerable skew to the heat flux distributions for the nonnegative least-squares cases. It is believed that this is caused by the nonnegativity constraints. The diagonal elements of the view-factor matrix have nominal values which are zero; therefore, the Monte-Carlo procedure will produce many negative diagonal view factors that are then set to zero.

For the area uncertainties, a random perturbation is added to the view-factor matrix using a gaussian random-number generator with the standard deviations given above. The F-matrix is then frozen and the Monte-Carlo analysis is performed for the area uncertainties using a gaussian random-number generator and area standard deviations equal to 1% of each area. Table 6 shows the standard deviations for the resulting heat-flux calculations.

Table 6. Standard Deviations in Heat Flux for Area Variance with Diagonal-Dominated View-Factor Error.

Surface	Nonnegative Least-Squares Unweighted	Nonnegative Least-Squares Weighted	Leersum	Naive
1	0.4462	0.3718	0.4197	0.2298
2	0.5079	0.5679	0.3978	0.4840
3	0.3160	0.4742	0.5208	0.8534
rms-avg	0.4309	0.4781	0.4493	0.5818

As seen above, all of the rectification schemes have about the same effect on sensitivity to area uncertainty.

The same procedure is followed for the other unequal variance case studies. For all of the cases with regional dominance, the base view-factor standard deviation is 0.001, and the value in the dominate region is 0.1. For the counter-diagonal-dominated case, the larger values of standard deviation are obviously along the counter diagonal. For the row-dominated and column-dominated cases, the larger values are on the second row and second column respectively. For the upper-triangle-dominated case, the six elements in the upper-right corner have the larger values. For the random-variance case, the standard deviations were assigned randomly in the range 0-0.1.

Table 7 shows the mean heat flux values, and Table 8 shows the standard deviations of the heat fluxes for the various 1000 trial Monte-Carlo studies. The tables reveal that the weighted nonnegative

Table 7. Mean Heat-Flux Values for the Other Unequal View-Factor Variance Cases.

Surface	Nonnegative Least-Squares Unweighted	Nonnegative Least-Squares Weighted	Leersum	Naive	Exact
		Counter-Diagonal-Dominated View-Factor Variance			
1	-3.5645	-3.6229	-3.4449	-3.1886	-3.6891
2	82.2329	83.9206	83.0833	83.8364	83.8721
3	-119.5026	-120.4466	-120.4577	-120.4717	-120.5353
		Row-Dominated View-Factor Variance			
1	-2.7005	-3.6096	-2.6789	-1.7829	-3.6891
2	82.0741	83.9014	81.9244	79.4481	83.8721
3	-119.0604	-120.4378	-118.8689	-116.4979	-120.5353
		Column-Dominated View-Factor Variance			
1	-2.6462	-3.6033	-3.7737	-3.5184	-3.6891
2	81.8186	83.8880	83.7971	83.8305	83.8721
3	-118.7586	-120.4271	-120.0350	-120.4682	-120.5353
		Upper-Triangle-Dominated View-Factor Variance			
1	-3.5754	-3.6222	-3.3351	-3.3087	-3.6891
2	83.6157	83.9198	82.6190	80.2599	83.8721
3	-120.0605	-120.4450	-118.9259	-115.4267	-120.5353
		Random View-Factor Variance			
1	-3.2880	-3.2593	-3.3021	-2.0925	-3.6891
2	82.4014	82.7955	82.8567	80.3335	83.8721
3	-118.6701	-119.3044	-119.3318	-117.3613	-120.5353

least-squares projection scheme is vastly superior to the others. Overall its mean heat fluxes most closely agree with the exact values, and with the exception of the random-variance case, its standard deviation is one to four orders of magnitude smaller than those for the other schemes. For the random-variance case, the weighted least-squares scheme gives the best results, but the unweighted least-squares and Leersum's schemes also give good results since the uncertainties are more-or-less evenly distributed.

For some cases, the naive rectification scheme fails completely. Table 9 gives the range of computed heat fluxes for the naive rectification with the upper-triangle-dominated view-factor uncertainties. Clearly, any single heat-flux computation from this set is meaningless.

It should be noted that this is a terribly damaged view-factor matrix. For this case, the 95%-confidence uncertainty in view factor is approximately 0.1, or the view factors are considered to have approximately 1 digit accuracy. This would correspond to very crudely computed view factors. However, properly rectified cases yield very meaningful heat flux computations.

Table 10 gives the rms averaged heat flux standard deviations for the area uncertainty Monte-Carlo analysis. As seen before, all of the rectification schemes seem equally good at reducing the sensitivity of the heat flux calculations to the uncertainties in the areas for this case study.

Table 8. Standard Deviations in Heat Flux for the Other Unequal View-Factor Variance Cases.

	Nonnegative Least-Squares			
Surface	Unweighted	Weighted	Leersum	Naive
Counter-Diagonal-Dominated View-Factor Variance				
1	0.5277	0.0368	1.4061	3.4348
2	0.6197	0.0460	2.0133	5.2123
3	0.8957	0.0563	1.6163	6.2030
rms-avg	0.6988	0.0470	1.6973	5.0810
Row-Dominated View-Factor Variance				
1	1.7794	0.0477	3.6299	5.4372
2	2.7123	0.0630	7.0196	16.1912
3	2.5028	0.0618	5.8428	19.2367
rms-avg	2.3655	0.0579	5.6742	14.8523
Column-Dominated View-Factor Variance				
1	1.9819	0.0550	3.9047	5.1064
2	3.5176	0.0819	4.8266	5.2548
3	3.4125	0.0701	3.9496	0.3175
rms-avg	3.0521	0.0699	4.2482	4.2343
Upper-Triangle-Dominated View-Factor Variance				
1	0.2454	0.0353	2.0937	11.0725
2	0.3273	0.0438	1.9262	22.9427
3	0.4017	0.0535	2.2979	43.0558
rms-avg	0.3310	0.0448	2.1114	28.8835
Random View-Factor Variance				
1	2.6444	2.0461	4.7752	14.7834
2	2.6682	2.0091	6.1736	17.8497
3	2.4439	1.7696	5.3161	15.3694
rms-avg	2.5875	1.9454	5.4521	16.0560

Table 9. Range of Naive Heat-Flux Values for the Upper-Triangle-Dominated Variance Case.

Surface	1	2	3
max	38.9123	106.9031	991.5615
mean	-3.3087	80.2599	-115.4267
min	-281.7724	-389.7757	-205.6421

Table 10. Root-Mean-Square Averaged Standard Deviations in Heat Flux for Area Variance Cases with Other Unequal View-Factor Variance.

	Nonnegative Least-Squares			
View-Factor Variance Case	Unweighted	Weighted	Leersum	Naive
Counter-Diagonal	0.4397	0.4395	0.4605	0.5556
Row-Dominated	0.3916	0.4721	0.3570	0.4075
Column-Dominated	0.4071	0.4461	0.4417	0.5859
Upper-Triangle	0.4386	0.4432	0.4748	0.5556
Random	0.4243	0.4565	0.4355	0.5734

CONCLUSIONS

Several view-factor rectification schemes have been compared. Figure 4 summarizes the rms-averaged standard deviation results for heat flux when view-factor uncertainty is considered. The Naive scheme, where all of the corrections are placed in the diagonal elements of the view-factor matrix, has proven to be erratic and sometimes results in meaningless calculations. Leersum's iterative scheme is also erratic but, on average gives considerably better results than the Naive scheme. Leersum's scheme is most viable when the view factors have equal variance. The unweighted version of the nonnegative least-squares projection scheme is better behaved than either the Naive or Leersum's scheme; however, when the view-factor variance is not equally distributed, the unweighted nonnegative least-squares projection is consistently superior for all cases. In the cases where the variances were not equally distributed the weighted nonnegative least-squares projection gives heat-flux results which were orders of magnitude better than the other schemes.

The Naive scheme is not recommended. If no knowledge on the relative sizes of the view-factor variances is available, either Leersum's scheme or the unweighted nonnegative least-squares projection will take fairly crudely calculated view factors and compute meaningful heat transfer results. The least-squares projection is recommended since the computational tasks are roughly equivalent and it is about twice as effective. If information is available on the relative variance of the view factors (which is always the case for Monte-Carlo integrations), the weighted nonnegative least-squares projection should be used.

The weighted nonnegative least-squares projection can be thought of as a numerical filter for noisy view-factor data. In the examples given here, very good heat transfer calculations were made for cases with very crudely defined view-factor data (roughly 1 digit accuracy). View-factor calculations are the most computationally intensive part of many radiation enclosure problems. There is the possibility of considerable improvement in computational efficiency by combining this excellent filter with relatively crude computations of the view factor values. To properly make such a compromise, sensitivity estimates [5] of the heat transfer calculations would be required.

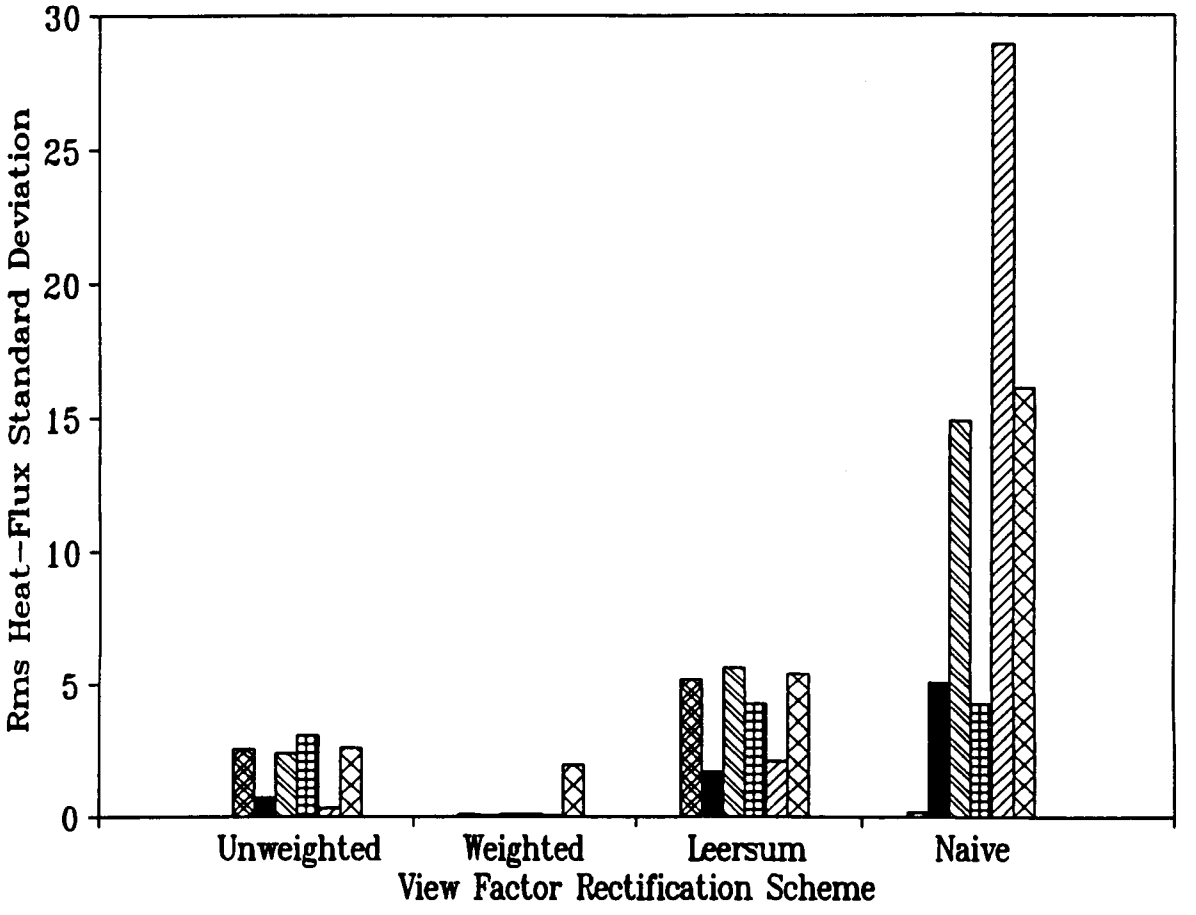

Figure 4. Summary of Surface-3 Standard Deviation Results for View-Factor Variance.

All of the schemes were roughly equal with regards to the propagation of uncertainties in the surface areas. When the view factors were rectified in this case study, the heat flux uncertainties were roughly an order of magnitude less than the case when no rectification was applied. The proper weighting procedure for the enforcement of reciprocity with uncertain areas is a topic of current research.

REFERENCES

1. Tsuyuki, G. T., 1992, "TRASYS Form Factor Matrix Normalization," Fourth Annual Thermal and Fluids Analysis Workshop, NASA Conference Publication 10106, pp. 71-82.
2. van Leersum, J., 1989, "A Method for Determining a Consistent Set of Radiation View Factors from a Set Generated by a Non-Exact Method," International Journal of Heat and Fluid Flow, Vol. 10, No. 1.
3. Brewster, M. Q., 1992, Radiative Heat Transfer, John Wiley & Sons, New York.
4. Taylor, R. P., Luck, R., Hodge, B. K., and Steele, W. G., 1993, "Uncertainty Analysis of Diffuse-Gray Radiation Enclosure Problems--A Hypersensitive Case Study," Fifth Annual Thermal & Fluids Analysis Workshop, NASA Conference Publication 10122, pp. 27-40.

5. Taylor, R. P., Luck, R., Hodge, B. K., and Steele, W. G., 1994, "Uncertainty Analysis of Diffuse-Gray Radiation Enclosure Problems," Paper AIAA-94-0132, American Institute of Aeronautics and Astronautics.
6. Siegel, R. and Howell, J. R., 1992, Thermal Radiation Heat Transfer, third edition, Hemisphere Publishing Co., Washington, DC.
7. Strang, G., 1980, Linear Algebra and Its Application, second edition, Academic Press, New York.
8. Incropera, F. P. and Dewitt, D. P., 1985, Fundamentals of Heat and Mass Transfer, John Wiley & Sons, New York.

CAE FOR THERMAL MANAGEMENT OF AEROSPACE ELECTRONIC BOARDS USING THE BETASOFT PROGRAM

Kimberly Bobish
Dynamic Soft Analysis, Inc.
Pittsburgh, Pennsylvania

SUMMARY

Aerospace electronic boards require special attention to thermal management due to constraints such as their need to be light, small, and maintain high power densities. Also, cooling is mainly through conductive and radiative modes with minor or negligible convective cooling. Due to these particular requirements, thermal design has become an integrated part of the electronic design process in order to avoid expensive repeat prototyping and to ensure high reliability.

To achieve high speed simulations, the BETAsoft code uses semi-empirical formulations and an advanced finite difference scheme that incorporates local adaptive grids. Detailed conduction, convection and radiation heat transfer is considered. Various benchmark verifications of the software simulation compared to infrared images typically prove to be within 10% of each other.

The thermal analysis of a sample avionic card in a natural convection environment is shown. Then, the individual effects of attaching metal screws to the casing, increasing radiative emissivities of the casing, increasing the conductance of the wedge lock, adding an aluminum core to the board, adding metal strips in board layers, inserting conduction pads under components, and adding heat sinks to components are demonstrated.

INTRODUCTION

With the trend of higher clock speeds and decreasing package sizes, the power density of electronic boards have increased continuously in the last two decades (1). Higher board power densities lead to higher component junction temperatures. Since the failure rates of junctions generally increase exponentially with their temperatures (2), thermal control thus becomes critical in achieving acceptable product reliability. Presently, more than half of electronic failures are due to thermal problems. Thermal management has has become an ever increasing concern of today's electronic designs.

Compared to the majority of electronic applications, those of the aerospace industry present unique thermal concerns due to their environment and resulting modes of heat transfer. Lower pressure leads to decreased convective flow and an increased need to effectively use conductive and radiative cooling. Furthermore, testing aerospace boards is usually difficult in terms of simulating the environment at reduced atmospheric pressures.

Due to the advances in numerical computations, thermal analysis software has become the best solution for electronic designers. Thermal software lowers design cost by

reducing the load of laborious prototyping tests. The thermal analysis results also provide far more detailed technical information than the tests which are limited by the instrumentation. Typically, software results include a temperature map and gradient of the entire board as well as the individual casing and junction temperatures of every part. Due to the speed software simulation, a significant amount of time is saved. This allows for further examination of alternatives and shortens the time to market. As a result, thermal analysis software is generally regarded as an integrated CAE tool with electronic CAD software today.

Among the thermal analysis tools, two types of software are available: general and specialized. Any general purposed heat transfer or CFD program can be used to simulate the thermal performance of electronic boards. This general software, however, suffers on the aspect of user friendliness. It is time consuming to set up a board or move a component using any general purpose finite element program. This, in turn, prohibits the effective analysis of a real board containing more than 20 components.

Specialized thermal software imports the board layout directly from CAD systems. User-friendly menus to allow for modifications of the board with only a couple key strokes and for quick and easy variation of the thermal environment. This allows for the setup time to shorten to a couple hours and with alternative results obtained in a only few minutes. Since thermal design generally requires an iterative process, this specialized software is the standard tool used in electronic designs today.

The objective of this paper is to describe a unique semi-empirical approach to thermal analysis which provides fast computation and high accuracy. This thermal software, BETAsoft-Board, is used to illustrate the applications of a typical aerospace board in terms of various parametric effects of design solutions and alternatives. Comparative advantages of these alternatives are discussed and the results of their combined used as design solutions are presented.

NUMERICAL MODELING

A straight forward approach of thermal analysis is to use the finite element scheme for conduction and the Navier-Stokes equations for convection. Although this is the approach used by many heat transfer programs, the obvious draw-back is the large memory requirement and substantial computational time involved. This excludes the use of PCs for sophisticated thermal designs.

A unique approach developed by Dynamic Soft Analysis, Inc. is the use of a modified finite difference scheme for conduction and semi-empirical based equations for convection. Significant effort has been devoted to this development. The end result is a fast yet accurate thermal analysis. Since the equations involved are numerous, only a brief summary of the modeling approach is described below.

Conduction:

Standard heat conduction equations are used in the computation (3). Finite difference grids with local properties are applied to the board. Along the board edges, heat transfer to wedge locks is implemented. Up to three physical board layers can be considered. The components interact with the board through the individual leads as well

as through the gap beneath a component. The board layers can be nonhomogeneous by specifying local regions of varying volumetric fractions of metal. Furthermore, the conductivities along the x and y directions of the board can be altered in localized regions of each layer.

Since the components can be set on either side and any location on the board, the modeling of conduction to the board is implemented through the use of locally refined adaptive grids. Only at the locations where grid refinement is needed, further grids are automatically generated. This scheme enhances the accuracy significantly while only slightly increasing the computational burden.

Convection:

Three dimensional flow effects and thermal fields are considered in the convective modeling. Although the experimental results and data correlations are well reported for 2 dimensional configurations (4), the consideration of detailed three dimensional effects takes substantial effort. Vast amounts of literature on various data and correlations were reviewed. It was found that frequent discrepancies appeared. As a result, a large amount of in-house wind tunnel tests using various boards from regular arrays to irregular arrays of components were conducted. Infrared results of components and boards were obtained to check with the existing correlations and to create a new set of correlations. To cover a large number of variations, more than 40 equations are employed.

For each component, the different heat transfer from each exposed side is calculated based upon its local flow and thermal environment. The convective heat loss from the leads is modelled. The effects of flow diversion, thermal boundary layer, heat sink fins, and adjacent boards or casings are also considered. Natural convection can be calculated. When there is forced convection, the combined convection is considered.

Radiation:

Radiation is very important in aerospace applications. The surface emissivities of individual components and of the boards can be assigned. The radiation between the components and the board underneath is precisely modeled in the computation. The radiation between a component and the opposite board is closely simulated. Lastly, the minor radiative interaction with adjacent components is approximated.

Integration:

Both the geometric configuration and thermal environment of the board are tightly integrated with other CAD and CAE programs. The BETAsoft-Board program interfaces with more than 20 different CAD placement programs to transfer the board layout directly into the board thermal analysis, saving a significant amount of set up time. The thermal environment of the board can be transferred from the BETAsoft-System program which determines the incoming air velocity and temperature as well as the spacing and conditions of adjacent boards. BETAsoft-Board solves for the detailed thermal environment of each individual component. This information can be transferred to the BETAsoft-Component program for an in-depth component packaging analysis.

Furthermore, the junction temperatures from the Board thermal analysis interface

to popular reliability analysis programs. This later allows for a very accurate reliability report.

RESULTS AND DISCUSSION

The BETAsoft-Board program has been in existence and under constant improvement for more than 7 years. Hundreds of leading companies worldwide use BETAsoft as an integral part of their design process. From the large number of comparisons with in-house and users' tests, an error range of within 10% has been generally observed. This includes computer mother boards, military backpacks, avionic boards, satellite boards, industrial control boards, etc. for a wide range of operational conditions. A typical infrared comparison is shown in Fig. 1 and data comparison in Table 1.

To illustrate thermal management techniques, an avionic board case is considered. The board layout has been automatically transferred from PCAD. As shown in Fig. 2, the transformer has a power of 3 watts; and the components along top edge of board and one near the bottom middle are 1 watt each. All of the remaining components are low power.

For this case, the environment conditions were an ambient temperature of 30°C and natural convection at .9 atmospheres of pressure. The objective of the present thermal design is to make sure all component casing temperatures are under 95°C to achieve the overall reliability requirements.

For this board in a natural convective environment, the casing temperatures of the transformer and 3rd component in at top are 184.6°C and 139.6°C, respectively. The computation time for this board is only 3 minutes on the PC platform and less than 1 minute on the workstation. The temperature contour is shown in Fig. 3 and the component temperatures are shown in Fig. 4. Some thermal design considerations to reduce the component casings in excess of 95°C are exercised in the following parametric studies:

Screws Attached to the Case:

A very common situation is the attachment of the board to the cold casing with screws. Five screws are used, each has a thermal resistance of 60°C/Watt. The sink temperature is at 30°C. The resulting temperature of the two components are 172.9 and 133.7°C respectively for the transformer and component CR25.

Surface Emissivities:

Since the board is hot and the case is cool (at 30°C), it is possible that the radiative heat loss can be increased by changing the inner casing emissivity from 0.05 (a bright metal) to 0.8 by applying an organic coating. The resulting temperature reduction is from 172.9°C to 125.0°C for the transformer and from 133.7 to 112.9°C for CR25.

As expected, surface emissivity plays an important role, especially for a hot board in a naturally convective environment. Plus, the change from .05 to .8 is a large magnitude for emissivity.

Wedge Lock Resistance:

The thermal resistance of the wedge lock can be varied. Changing the thermal resistance from 1 to .2 (°C inch/Watt) reduces the temperatures of the transformer from 125.0 to 123.7°C and CR25 from 112.9 to 108.5°C. There are some minor effects but they are not substantial for this range of resistance. Whether a wedge lock exists or not would have substantial effects.

Metal Core:

A very common approach is to add a metal core to the board. An aluminum metal core of .01" thickness has been applied to bring the heat from the hot components to the wedge lock. The results (with the new wedge lock resistance) show reduction of the temperatures of the transformer from 123.7 to 93.1°C and CR25 from 108.5 to 75.6°C. This appears to be a very effective means to cool the board.

Local Metal Strips:

For space applications, the weight of the board is very important. The aluminum core is effective but adds a lot of weight. An alternative is to use only strips of metal core to bring heat from the high power components to the wedge lock. The is done as shown in Fig. 5. The resulting temperature increases slightly from 93.1 to 99.9°C for the transformer and from 75.6 to 76.9°C for CR25. However, the weight of the strips are only 12% of the metal core.

Conduction pads:

Although the local board temperature has been reduced, the temperature of the hot components are still much higher than the board. This is because the high thermal resistance between the component and the board. This usually occurs when the component leads are few and thin while a gap exists underneath the component. This gap serves as a thermal resistance. To reduce this resistance, conduction pads (with conductivity .22 W/°C m) have been installed between the high power components and the board.

The resulting temperatures of the transformer and the CR25 are 84.7 and 61.2°C, respectively. Thus the addition of conduction pads have resulted in a significant temperature drop.

Heat Sink on Component:

The top row of 1 watt parts and the transformer are now within the desired range. However, the 1 watt part at the bottom edge is still well above the allowed value. A final resolution is the addition of a heat sink on top of this hot IC component. Since this part is located at the lower edge where it would be hard to be cooled with a metal strip to the top edge, a pin-fin heat sink is added to its top. As indicated by the manufacturer's catalog, this sink has a thermal resistance, Theta-sa, of value 6 °C/Watt at 3 ft/s air velocity and 3 °C/Watt at 10 ft/s velocity. The resulting temperature of this component is reduced from 107.6 to 69.9°C.

The overall temperature profile of the board is shown in Fig. 6. The resulting component temperatures are shown in Fig. 7. There are no parts beyond the desired values in the component map. The thermal design is now successful.

CONCLUSION

Aerospace electronic boards present special needs for thermal management. Although "general purpose" heat transfer programs may be used for thermal design, they typically are not user friendly and efficient since thermal is not their main function. "Specialized" thermal analysis software is effective because it is designed exactly for that one function. Also, the available integration to board layout, system thermal analysis, component thermal analysis, and reliability analysis software is an important consideration for concurrent engineering.

An unique approach using finite difference and semi-empirical formulations are demonstrated through the BETAsoft-Board program. This approach provides a fast computation while maintaining accurate solutions.

For aerospace thermal designs, the combined use of emissivities, wedge lock resistance, metal strips, conduction pads etc. allows for an effective thermal control which leads to high reliability of the products.

REFERENCES

1. Oktay, S.; Hannemann, R.; and Bar-Cohen, A.: "High Heat from a Small Package", Mechanical Engineering, March 1986, pp. 36-42.
2. MIL-HDBK-217, Naval Publications and Form Center, Philadelphia.
3. Carslaw, H.S.; and Jaeger, J.C.: Conduction of Heat in Solids, Oxford Press, 1967.
4. Moffat, R.J.; Arvizu, D.E.; and Ortega, A.: "Cooling Electronic Components: Forced Convection Experiments with an Air-Cooled Array", Heat Transfer in Electronic Equipment, ASME.HTD, Vol. 48, pp. 17-27, 1985.

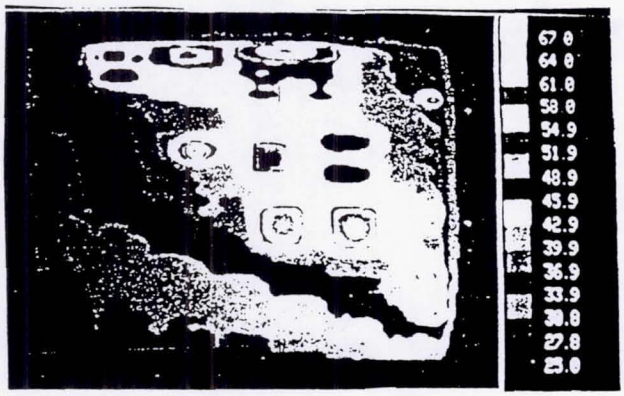

a. Infrared

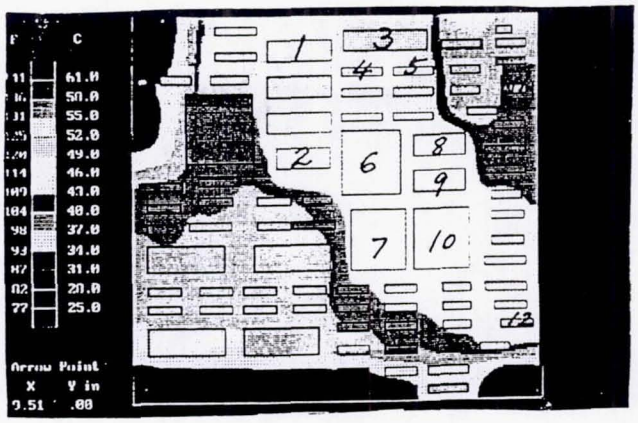

b. BETAsoft

Figure 1

Table 1

Component #	Infrared	BETAsoft
1	54.6	56.3
2	49	48.5
3	52.5	51.5
4	50.5	48.9
5	47.5	46.6
6	46.0	46.9
7	48.9	46.2
8	47.5	48.3
9	47.5	49.2
10	48.9	48.7
11	47.5	45.1
12	50.5	50.5

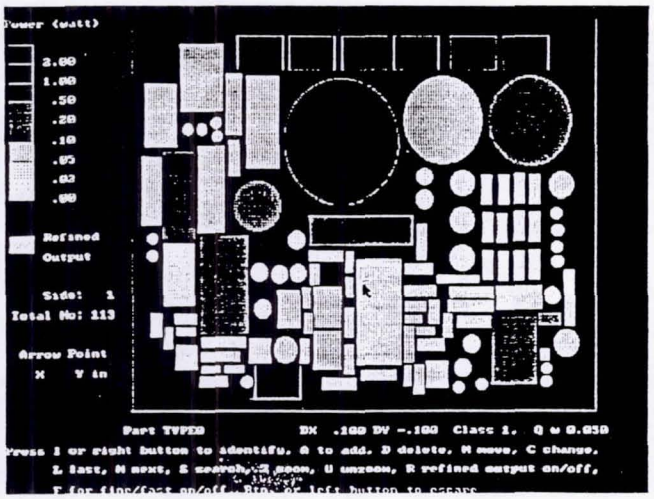

Figure 2

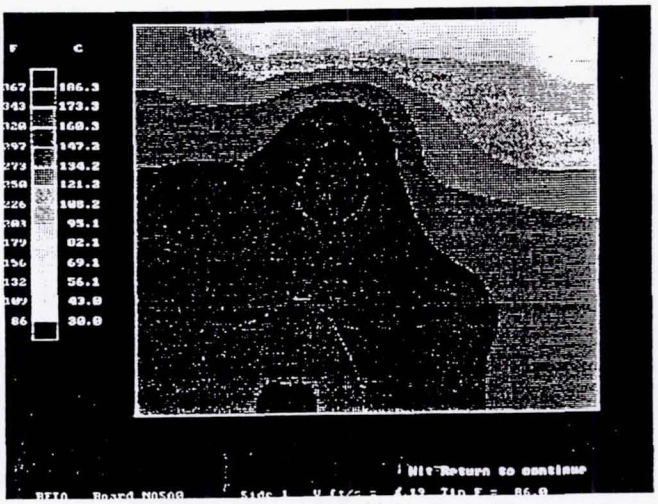

Figure 3

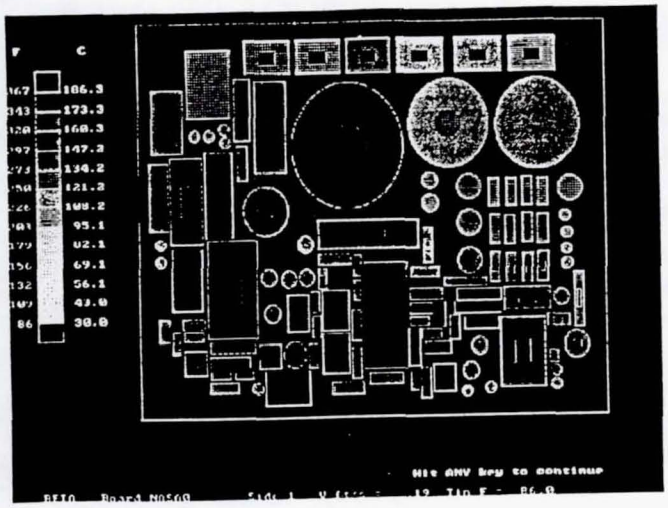

Figure 4

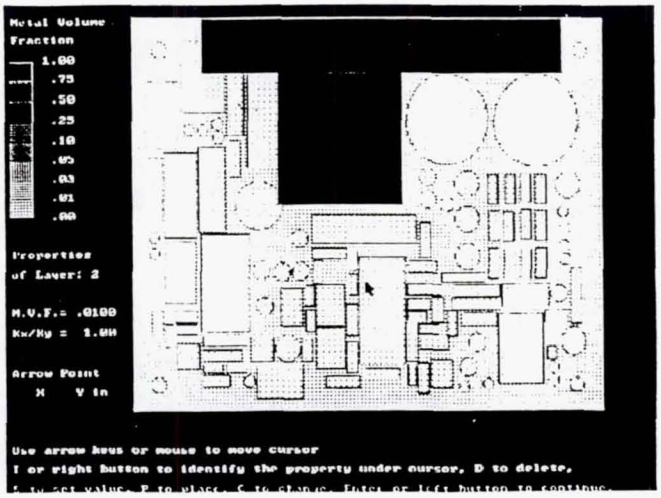

Figure 5

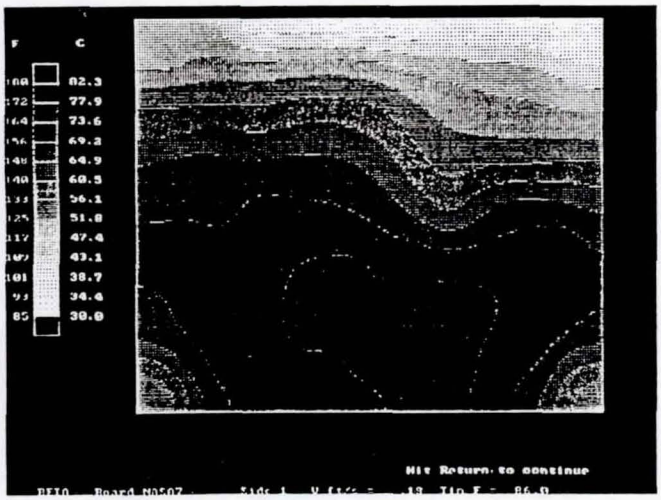

Figure 6

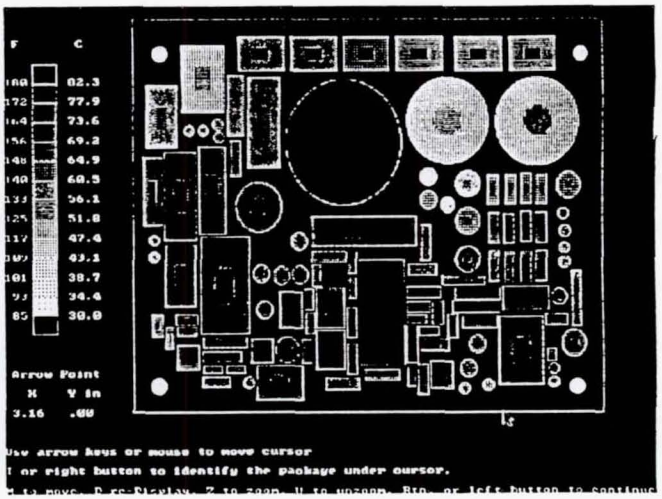

Figure 7

N95-27355

RTE—A COMPUTER CODE FOR ROCKET THERMAL EVALUATION

Mohammad H.N. Naraghi
Department of Mechanical Engineering
Manhattan College
Riverdale, New York

SUMMARY

The numerical model for a rocket thermal analysis code (RTE) is discussed. RTE is a comprehensive thermal analysis code for thermal analysis of regeneratively cooled rocket engines. The input to the code consists of the composition of fuel/oxidant mixture and flow rates, chamber pressure, coolant temperature and pressure, dimensions of the engine, materials and the number of nodes in different parts of the engine. The code allows for temperature variation in axial, radial and circumferential directions. By implementing an iterative scheme, it provides nodal temperature distribution, rates of heat transfer, hot gas and coolant thermal and transport properties. The fuel/oxidant mixture ratio can be varied along the thrust chamber. This feature allows the user to incorporate a non-equilibrium model or an energy release model for the hot-gas-side. The user has the option of bypassing the hot-gas-side calculations and directly inputting the gas-side fluxes. This feature is used to link RTE to a boundary layer module for the hot-gas-side heat flux calculations.

INTRODUCTION

Thermal analysis is an essential and integral part in the design of rocket engines. The need for thermal analysis is especially important in the reusable engines where an effective and efficient cooling system becomes a crucial factor in extending the engine life. In the new high pressure engines, such as chemical transfer vehicle engines, hot-gas temperature is very high (can reach 7000R at the throat). It is therefore essential to be able to estimate the wall temperature and ensure that the material can withstand such high temperature. Furthermore, an accurate thermal model enables an engine designer to modify the cooling channel configuration for the maximum cooling at high temperature areas.

The thermal phenomena in rocket engines involve interactions among a number of processes. including, combustion in the thrust chamber, expansion of hot-gases through the nozzle, heat transfer from hot-gases to the nozzle wall via convection and radiation, conduction in the wall, and convection to the cooling channel. Further complexities of the thermal analysis in rocket engines are due to three-dimensional geometry, coolant and hot gas heat transfer coefficient dependence on the pressure and wall temperature, unknown coolant pressure drop and properties, axial conduction of heat within the wall, and radiative heat transfer between gases and surfaces of the engine. A comprehensive thermal model must account for all of these items.

RTE [1] is a comprehensive rocket thermal analysis code that uses a number of existing codes and allows interaction among them via some iterative procedures. The code is based on the geometry of a typical regeneratively-cooled engine similar to that shown in Figure 1. It uses CET (Chemical Equilibrium with Transport Properties) [2] and GASP [3] for the

evaluation of hot-gas and coolant properties. The inputs to this code consist of the composition of fuel/oxidant mixtures and flow rates, chamber pressure. coolant entrance temperature and pressure, dimensions of the engine and materials in different parts of the engine, as well as the mesh generation data. This program allows temperature variations in axial, radial and circumferential directions, and by implementing an iterative scheme it provides temperature distributions, rates of heat transfer, and hot-gas and coolant thermal and transport properties. The fuel/oxidant mixture ratio can be varied along the thrust chamber. This feature allows the user to incorporate a nonequilibrium model or an energy release model for the hot-gas-side. The mixture ratio along the thrust chamber is calculated using ROCCID [4] (ROCket Combustor Interactive Design and Analysis Computer Program). ROCCID has been modified to take RTE input and make the mixture ratio variable along the thrust chamber. The user has the option of bypassing the hot-gas-side calculations and directly inputting gas side fluxes. This feature is used to link RTE to a boundary layer program for the hot-gas-side heat flux calculation. The procedure for linking RTE to a hot-gas side program. TDK [5] (Two-Dimensional Kinetics Nozzle Performance Computer Program) is described here.

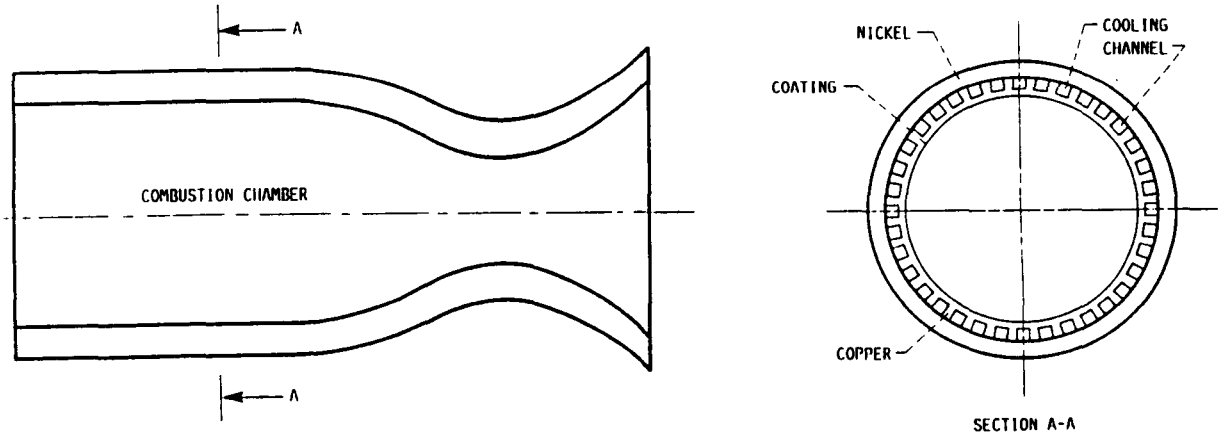

Figure 1. A Rocket Thrust Chamber and Nozzle

NUMERICAL MODEL

The numerical model of the RTE is based on the geometry of a typical regeneratively-cooled thrust chamber (shown in Figure 1). The wall can consist of three layers: a coating, the channel, and the closeout. These three layers can be different materials or the same material. The number of cooling channels in the wall are also specified by the user. For the numerical procedure, the rocket thrust chamber and nozzle are subdivided into a number of stations along the longitudinal direction, as shown in Figure 2. The thermodynamic and transport properties of the combustion gases are evaluated using the chemical equilibrium composition computer program developed by Gordon and McBride [2, 6] (CET, Chemical Equilibrium with Transport properties). The GASP (GAS Properties) [3] or WASP (Water And Steam Properties) [7] programs are implemented to obtain coolant thermodynamic and transport properties. Since the heat transfer coefficients of the hot-gas and coolant sides are related to

surface temperatures, an iterative procedure is used to evaluate heat transfer coefficients and adiabatic wall temperatures.

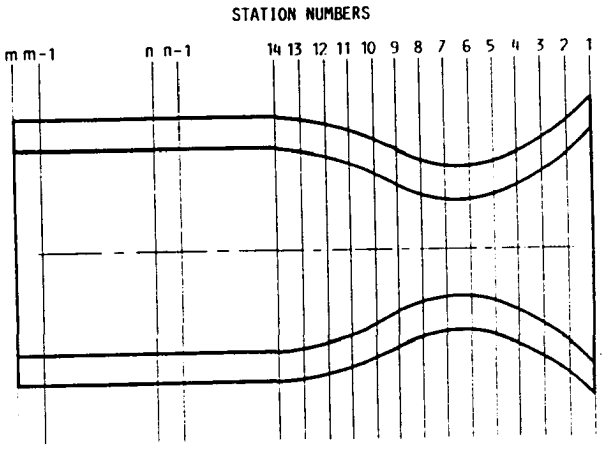

Figure 2. A Rocket Thrust Chamber Subdivided into a Number of Stations

The temperature distribution within the wall is determined via a three-dimensional finite difference scheme. In this method, finite difference grids are superimposed throughout the wall at different stations. The temperature of each node is then written in terms of temperatures of neighboring nodes (the four closest nodes at the same station and two nodes at the neighboring stations). The program marches axially from one station to another. At each station the Gauss-Siedel iterative method is used to obtain convergence for the temperature distribution along the radial and circumferential directions. When the axial march is completed, comparison is made between the results of the present march and that of the previous one to see if the convergence criteria in the axial direction has been met. If it is not met, the code starts again at the first station and makes another axial march. The process continues until convergence is achieved. A detailed description of this numerical model is outlined below.

First, the static pressures, temperatures, enthalpies and Mach numbers for the combustion gases are evaluated using the ROCKET subroutine from [2]. It should be noted that these properties are independent of wall temperature and only depend on the cross-sectional area of the nozzle, the propellant used and chamber pressure. Indeed, the heat transfer from hot gases to the chamber and nozzle wall will cause very little change in the gas temperature (the thermodynamic process dominates the transport process).

On the coolant side, the stagnation enthalpy and density at the entrance to the cooling channel are evaluated as functions of the coolant stagnation pressure and temperature ($i_{C0} = i_{C0}(P_{C0}, T_{C0})$ and $\rho_{C0} = \rho_{C0}(P_{C0}, T_{C0})$) using the GASP or WASP programs.

The model now begins its axial marches (passes) starting from the first station. At the first axial march an initial guess for the wall temperature distribution is made. For the next march, however, the results of temperature distribution for the previous march can be used as an initial guess. The hot gas and coolant adiabatic wall temperatures and wall properties can be evaluated at a given station based on the assumed wall temperature distribution using the properties computer codes [2, 6, 3, 7] for the combustion gases and the coolant. The reference enthalpy of the gas side, i_{GX_n} is given by [8]

$$i_{GX_n} = 0.5(i_{GW_n} + i_{GS_n}) + 0.180(i_{G0_n} - i_{GS_n}) \quad (1)$$

where i_{GW_n} is a function of gas static pressure P_{GS_n} and gas-side wall temperature T_{GW_n} and is evaluated using the program given in [2]. The gas-side adiabatic wall enthalpy, i_{GAW_n} is calculated using the following equation [8, 9]

$$i_{GAW_n} = i_{GS_n} + (Pr_{GX_n})^{1/3}(i_{G0_n} - i_{GS_n}) \quad (2)$$

where the gas reference Prandtl number Pr_{GX_n} is

$$Pr_{GX_n} = \frac{C_{pGX_n}\mu_{GX_n}}{k_{GX_n}} \quad (3)$$

C_{pGX_n}, μ_{GX_n} and k_{GX_n} are functions of P_{GS_n} and i_{GX_n}. Once the gas-side adiabatic wall temperature is determined, the wall adiabatic temperature is calculated via

$$T_{GAW_n} = f(P_{GS_n}, i_{GAW_n}) \quad (4)$$

and using the combustion codes [2, 6]. The hot-gas side heat transfer coefficient, h_{G_n} is given by [8]

$$h_{G_n} = \frac{C_{G_n}k_{GX_n}}{d_{G_n}} Re_{GX_n}^{0.8} Pr_{GX_n}^{0.3} \quad (5)$$

where C_{G_n} is the gas-side correlation coefficient given as input and the Reynolds number is defined by

$$Re_{GX_n} = \frac{4W_G}{\pi d_{G_n}\mu_{GX_n}} \frac{T_{GS_n}}{T_{GX_n}} \quad (6)$$

$$T_{GX_n} = f(P_{GS_n}, i_{GX_n}) \quad (7)$$

$$T_{GS_n} = f(P_{GS_n}, i_{GS_n}) \quad (8)$$

Once the hot-gas-side heat transfer coefficient is determined the wall heat flux can be evaluated via

$$q_n = h_{G_n}(T_{GAW_n} - T_{GW_n}) \quad (9)$$

or

$$q_n = \frac{h_{G_n}}{C_{pGX_n}}(i_{GAW_n} - i_{GW_n}) \quad (10)$$

The adiabatic wall temperature and gas-side heat transfer coefficient, calculated from equations (4) and (5), or wall heat flux calculated using equations (9) and (10) will be used in the conduction module to evaluate a revised wall temperature distribution. It should be noted that the formulation given by equations (5-10) yields an approximate value for the wall heat flux. To obtain a more accurate value for the wall heat flux a boundary layer model should be implemented. The procedure for interfacing a boundary layer module to the present model will be described later. Next, attention will be focused on calculating the coolant-side properties and heat transfer coefficient.

For the first station the coolant stagnation enthalpy, static pressure and static density are set equal to the stagnation enthalpy, pressure, and density at the entrance to the cooling channel (i.e., $i_{C0_1} = i_{C0}$, $P_{CS_1} = P_{C0}$ and $\rho_{CS_1} = \rho_{C0}$). For the other stations, the coolant stagnation enthalpy is calculated via

$$i_{C0_n} = i_{C0_{n-1}} + \frac{(q_n^{j-1} + q_{n-1})\Delta S_{n-1,n}}{2W_C} \tag{11}$$

where $\Delta S_{n-1,n}$ is the distance between two neighboring stations $n-1$ and n and q_n^{j-1} is the heat transferred per unit length of the cooling channel from the hot gases to the coolant at station n (calculated from the conduction subroutine at iteration $j-1$). For the first iteration at station n, q_n^{j-1} in equation (11) is not known; therefore the following equation is used to evaluate the stagnation enthalpy

$$i_{C0_n} = i_{C0_{n-1}} + \frac{q_{n-1}\Delta S_{n-1,n}}{W_C} \tag{12}$$

Note that q_{n-1} in equations (11) and (12) are the heat transfer per unit length of cooling channel at the previous station.

The coolant velocity is calculated from the following equation:

$$V_{CS_n} = \frac{W_C}{\rho_{CS_n} A_{C_n} N_n} \tag{13}$$

Note that ρ_{CS_n}, is set equal to ρ_{CO_n} for the first station, and for the other stations is evaluated using the GASP or WASP programs [3, 7] based on the static pressure and enthalpy at the previous iteration, i.e.,

$$\rho_{CS_n}^j = \rho(P_{CS_n}^{j-1}, i_{CS_n}^{j-1}) \tag{14}$$

At the first iteration, however, it is set equal to the static density of the previous station ($\rho_{CS_n}^1 = \rho_{CS_{n-1}}$).

Once the coolant velocity is determined, the static enthalpy can be calculated using the following equation:

$$i_{CS_n} = i_{C0_n} - \frac{V_{CS_n}^2}{2g_c J} \tag{15}$$

The coolant static and reference Reynolds numbers, respectively, are given by:

$$Re_{CS_n} = \frac{W_C d_{C_n}}{A_{C_n} N_n \mu_{CS_n}} \tag{16}$$

and

$$Re_{CX_n} = Re_{CS_n}\left(\frac{\rho_{CW_n}}{\rho_{CS_n}}\right)\left(\frac{\mu_{CS_n}}{\mu_{CW_n}}\right) \tag{17}$$

where μ_{CS_n} is a function of P_{CS_n} and i_{CS_n} and is calculated using the GASP program [3], or the WASP program [7] if the coolant is water. Note also that d_{C_n} is the coolant hydraulic diameter at station n. To employ a better value for the Reynolds number, an average Reynolds number between the entrance and exit to each station is evaluated, i.e.,

$$Re_{CS_{Avg.}} = 0.5(Re_{CS_n} + Re_{CS_{n-1}}) \tag{18}$$

$$Re_{CX_{Avg.}} = 0.5(Re_{CX_n} + Re_{CX_{n-1}}) \tag{19}$$

The Reynolds number in the cooling channel is within the turbulent flow range; hence, the Colebrook equation [10] is used to calculate the friction factor. This equation is given by:

$$\frac{1}{\sqrt{f}} = -2.0 \log \left(\frac{e}{3.7065D} + \frac{2.5226}{Re_{CX_{Avg.}}\sqrt{f}} \right) \tag{20}$$

This implicit equation has been shown to be very closely approximated by the explicit formula [11]

$$\frac{1}{\sqrt{f}} = -2.0 \log \left[\frac{e}{3.7065D} - \frac{5.0452}{Re_{CX_{Avg.}}} \log \left(\frac{1}{2.8257} \left(\frac{e}{D} \right)^{1.1098} + \frac{5.8506}{Re_{CX_{Avg.}}^{0.8981}} \right) \right] \tag{21}$$

The correlation given by equation (21) is only valid for straight channels. To include the curvature effect, the friction factor obtained from equation (21) must be multiplied by the curvature factor given by Itō's correlation [12]:

$$\phi_{Cur.} = \left[Re_{CX_{Avg.}} \left(\frac{r_{C_n}}{R_{Cur._n}} \right)^2 \right]^{1/20} \tag{22}$$

where r_{C_n} is the hydraulic radius of cooling channel, $R_{Cur._n}$ is the radius of curvature. The curvature factor given by equation (22) is valid when $Re_{CX_{Avg.}}(\frac{r_{C_n}}{R_{Cur._n}})^2 > 6$, otherwise, $\phi_{Cur.} = 1$.

Once the friction factors are determined, the viscous pressure drop between stations $n-1$ and n is calculated using Darcy's law [13] which is given by:

$$(\Delta P_{CS_{n-1,n}})_f = \frac{f_n}{8g_c} \left(\frac{\rho_{CS_n} + \rho_{CS_{n-1}}}{d_{C_n} + d_{C_{n-1}}} \right) (V_{CS_n} + V_{CS_{n-1}})^2 \Delta S_{n-1,n} \tag{23}$$

and the momentum pressure drop is calculated via

$$(\Delta P_{CS_{n-1,n}})_M = \left(\frac{2}{(NA_C)_{n-1} + (NA_C)_n} \right) \frac{W_C^2}{g_c} \left(\frac{1}{(\rho_{CS} A_C N)_n} - \frac{1}{(\rho_{CS} A_C N)_{n-1}} \right) \tag{24}$$

An average value of variables between stations n and $n-1$ are used to improve the accuracy. The static pressure at each station is calculated based on the viscous and momentum pressure drops and is given by:

$$P_{CS_n} = P_{CS_{n-1}} - \left[(\Delta P_{CS_{n-1,n}})_f + (\Delta P_{CS_{n-1,n}})_M \right] \tag{25}$$

Once the coolant static pressure is determined, the coolant wall properties which are functions of the static coolant pressure P_{CS_n} and wall temperature, i.e.,

$$C_{p_{CW_n}}, \mu_{CW_n}, k_{CW_n}, i_{CW_n} = f(P_{CS_n}, T_{CW_n}) \tag{26}$$

are evaluated using the GASP or WASP programs. It should be noted that the wall temperature is not constant at a given station; hence, three coolant wall properties which are based on the lower, upper and side wall temperatures are determined. The reference and adiabatic wall enthalpies at the station are, respectively, calculated from the following equations [8]

$$i_{CX_n} = 0.5(i_{CS_n} + i_{CW_n}) + 0.194(i_{C0_n} - i_{CS_n}) \tag{27}$$

and

$$i_{CAW_n} = i_{CS_n} + (Pr_{CX})^{1/3}(i_{C0_n} - i_{CS_n}) \tag{28}$$

The adiabatic wall temperature is a function of the coolant static pressure and the adiabatic wall enthalpy and is evaluated using the GASP program [3]. Note that the Prandtl number in equation (26) is expressed by:

$$Pr_{CX} = \frac{C_{pCX}\mu_{CX}}{k_{CX}} \tag{29}$$

where

$$C_{pCX},\ \mu_{CX},\ k_{CX} = f(P_{CS}, i_{CX})$$

Three correlations may be used to evaluate the heat transfer coefficients in the cooling channels. The simplest one is given by the following correlation (see [8, 9]):

$$Nu = C_{C_n} Re_{CX}^{0.8} Pr_{CX}^{0.4} \tag{30}$$

Most recently, a new correlation is presented in [14, 15]. In this correlation the Nusselt number is given by:

$$\frac{Nu}{Nu_r} = C_{C_n} Re^{0.7} Pr^{0.4} \tag{31}$$

where

$$Nu_r = \psi^{-0.55}$$

$$\psi = 1 + \gamma(T_W - T_S)$$

and

$$\gamma = \left|\frac{1}{\rho}\frac{\partial \rho}{\partial T}\right|_P = \frac{1}{\rho}\frac{(\frac{\partial P}{\partial T})_\rho}{(\frac{\partial P}{\partial \rho})_T}$$

Properties for the above correlation are based on the coolant static temperature T_{CS}, and static pressure P_{CS}. Correlations described by equations (30) and (31) give inaccurate results when the coolant is liquid oxygen. A correlation, specifically for oxygen has been proposed [16]. This correlation is given by:

$$Nu = C_{C_n} Re_{CS} Pr^{0.4} \left(\frac{\overline{c_p}}{c_{pCS}}\right)^{2/3} \left(\frac{P_{Cri}}{P_{CS}}\right)^{0.2} \sqrt{\left(\frac{k_{CS}}{k_{CW}}\right)\left(\frac{\rho_{CW}}{\rho_{CS}}\right)} \tag{32}$$

where $P_{Cri} = 731.4$ psia is the critical pressure and

$$\overline{c_p} = \frac{i_{CW} - i_{CS}}{T_{CW} - T_{CS}}$$

The properties in the above correlations are calculated using the GASP program [3], or the WASP program [7] if the coolant is water. It should also be noted that there are three coolant heat transfer coefficients and adiabatic wall temperatures. They are for the top, side, and bottom walls of the cooling channel. The variable heat transfer coefficient is due to the variable wall temperature in the cooling channel. The coolant reference and adiabatic wall enthalpies are also functions of wall temperature and are larger for the surface nodes closer to the bottom of the cooling channel. The correlation factors for the heat transfer coefficient, C_{C_n}, in equations (30) and (31) are usually equal to 0.023 for most coolants. When the coolant is liquid oxygen, however, a factor of 0.0025 is used in equation (32).

The correlations given by equations (30)-(32) are for fully developed turbulent flow in a smooth and straight tube (channel). To include the effect of the entrance region, they are multiplied by the following coefficient [17]:

$$\phi_{Ent.} = 2.88 \left(\frac{\sum_{i=1}^{n} \Delta S_{i,i+1}}{d_{C_n}} \right)^{-0.325} \tag{33}$$

Other entrance effect factors for different types of cooling channel entrances reported in [17] are given by:

$$\phi_{Ent.} = \left[1 + \left(\frac{\sum_{i=1}^{n} \Delta S_{i,i+1}}{d_{C_n}} \right)^{-0.7} (T_w/T_b)^{0.1} \right] \tag{34}$$

for a 90^o bend entrance. Taylor [18] suggested the following correction factors:

$$\phi_{Ent.} = (T_W/T_b)^{[1.59/(\sum_{i=1}^{n} \Delta S_{i,i+1}/d_{C_n})]} \tag{35}$$

for straight tube and

$$\phi_{Ent.} = (T_W/T_b)^{[1.59/(\sum_{i=1}^{n} \Delta S_{i,i+1}/d_{C_n})]} \left[1 + 5/ \left(\frac{\sum_{i=1}^{n} \Delta S_{i,i+1}}{d_{C_n}} \right) \right] \tag{36}$$

for a 90^o bend entrance. The correction factor for the curvature effect is given by [19]:

$$\phi_{Cur.} = \left[Re_{CX_{Avg.}} \left(\frac{r_{C_n}}{R_{Cur.n}} \right)^2 \right]^{\pm 1/20} \tag{37}$$

where r_{C_n} is the hydraulic radius of cooling channel, $R_{Cur.n}$ is the radius of curvature, the sign (+) denotes the concave curvature and the sign (-) denotes the convex one. To incorporate the effect of surface roughness on the heat transfer coefficient, a simple empirical correlation is suggested by Norris [20]:

$$\frac{Nu}{Nu_{\text{smooth}}} = \left(\frac{f}{f_{\text{smooth}}} \right)^n \tag{38}$$

where $n = 0.68Pr^{0.215}$. For $f/f_{\text{smooth}} > 4.0$ Norris finds that the Nusselt number no longer increases with increasing roughness.

Once the heat transfer coefficients and adiabatic wall temperatures for the hot gas and coolant are evaluated, a finite difference model is used to re-evaluate the wall temperature distribution. This model has been specifically developed for three-dimensional conduction in a rocket thrust chamber and nozzle, as shown in Figure 1. Because of the symmetry of the configuration, computations are performed for only one cell (see Figure 3). Since no heat is

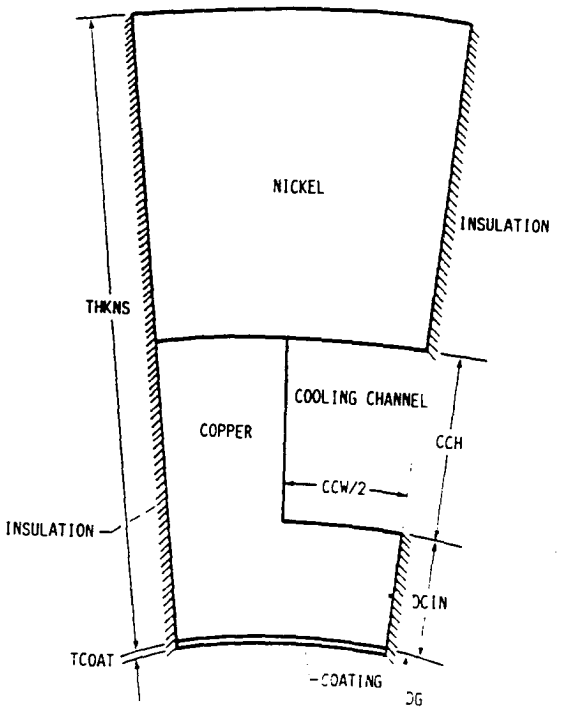

Figure 3. A Half Cooling Channel Cell.

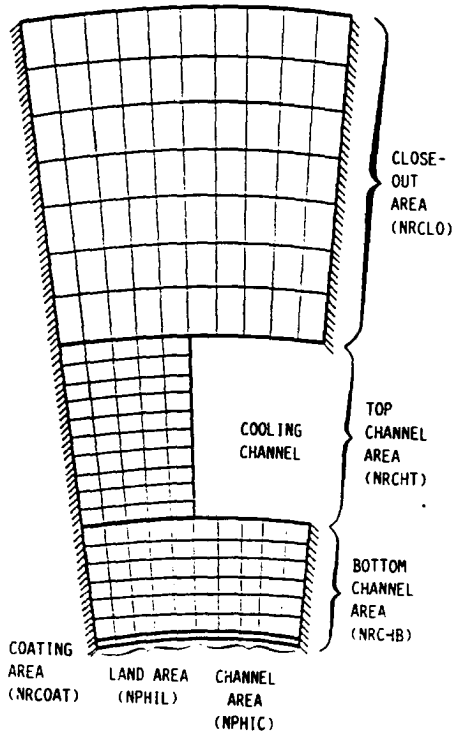

Figure 4. Finite Difference Grids Superimposed on Half of a Cooling Channel.

transferred to the two sides of the cell, they are assumed to be insulated. A finite difference grid is superimposed on the aforementioned cell as shown in Figure 4. In this program the number of nodes in the radial direction for different layers and in the circumferential direction for the land and channel area must be specified. Thus, the grid size can vary from one layer to another. Each node is connected to four neighboring nodes at the same station. It also exchanges heat with its counterpoints at two neighboring stations (i.e., stations $n+1$ and $n-1$). The finite difference equation for a node located in the middle of a material is given by

$$T^{l}_{i,j,n} = \frac{T^{l-1}_{i+1,j,n}/R_1 + T^{l-1}_{i,j-1,n}/R_2 + T^{l-1}_{i-1,j,n}/R_3 + T^{l-1}_{i,j+1,n}/R_4 + T_{i,j,n+1}/R_5 + T_{i,j,n-1}/R_6}{1/R_1 + 1/R_2 + 1/R_3 + 1/R_4 + 1/R_5 + 1/R_6} \tag{39}$$

where

$$R_1 = \frac{r\Delta\phi}{\Delta r\left(\Delta S^{n-1,n}_{i,j} + \Delta S^{n,n+1}_{i,j}\right)}\left(\frac{1}{k^{l-1}_{i,j,n}} + \frac{1}{k^{l-1}_{i+1,j,n}}\right)$$

$$R_2 = \frac{\Delta r}{(r+\frac{\Delta r}{2})\Delta\phi\left(\Delta S^{n-1,n}_{i,j} + \Delta S^{n,n+1}_{i,j}\right)}\left(\frac{1}{k^{l-1}_{i,j,n}} + \frac{1}{k^{l-1}_{i,j-1,n}}\right)$$

$$R_3 = \frac{r\Delta\phi}{\Delta r\left(\Delta S^{n-1,n}_{i,j} + \Delta S^{n,n+1}_{i,j}\right)}\left(\frac{1}{k^{l-1}_{i,j,n}} + \frac{1}{k^{l-1}_{i-1,j,n}}\right)$$

$$R_4 = \frac{\Delta r}{(r-\frac{\Delta r}{2})\Delta\phi\left(\Delta S^{n-1,n}_{i,j} + \Delta S^{n,n+1}_{i,j}\right)}\left(\frac{1}{k^{l-1}_{i,j,n}} + \frac{1}{k^{l-1}_{i,j+1,n}}\right)$$

$$R_5 = \frac{\Delta S^{n,n+1}_{i,j}}{2A_{i,j,n}}\left(\frac{1}{k^{l-1}_{i,j,n}} + \frac{1}{k_{i,j,n+1}}\right)$$

$$R_6 = \frac{\Delta S^{n-1,n}_{i,j}}{2A_{i,j,n-1}}\left(\frac{1}{k^{l-1}_{i,j,n}} + \frac{1}{k_{i,j,n-1}}\right)$$

$$A_{i,j,n} = \frac{(r\Delta\phi\Delta r)_{n+1} + (r\Delta\phi\Delta r)_n}{2}$$

and

$$A_{i,j,n-1} = \frac{(r\Delta\phi\Delta r)_n + (r\Delta\phi\Delta r)_{n-1}}{2}$$

and l is the Gauss-Siedel iteration index. Note that the above equation is a three-dimensional finite difference equation. The Gauss-Siedel iteration, however, is only performed for the nodes on the n-th station and $T_{i,j,n+1}$ and $T_{i,j,n-1}$ are kept constant during this iteration. The value of $T_{i,j,n-1}$ in equation (39) is from the recent march and $T_{i,j,n+1}$ from the previous march. The conductivity in equation (39) is a function of temperature, i.e., $k = k(T)$. Similar equations are derived for other nodes (boundary nodes and nodes at the interface between two

different materials). It should be noted that at the boundary nodes, depending on the boundary

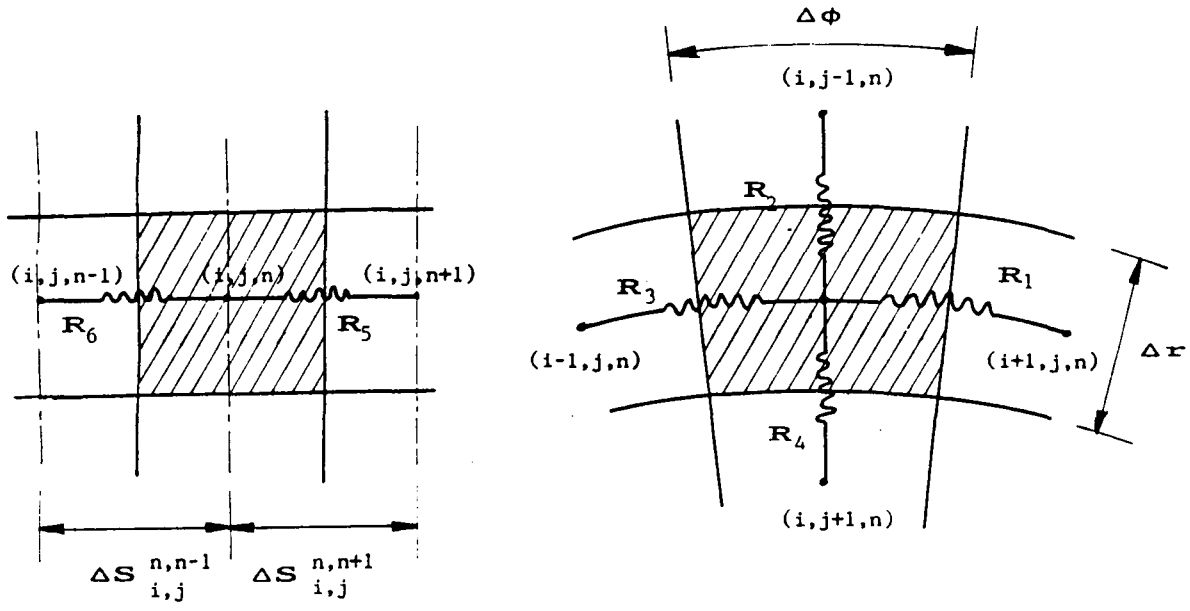

Figure 5. Resistances between a typical interior node and its adjoining nodes.

conditions, convective and radiative terms also appear in the nodal balance of energy equation. For example, for a node at the inner surface of the nozzle the finite difference equation is given by

$$T^{l}_{i,j,n} = \frac{T^{l-1}_{i+1,j,n}/R_1 + T^{l-1}_{i,j-1,n}/R_2 + T^{l-1}_{i-1,j,n}/R_3 + T_g/R_4 + T_{i,j,n+1}/R_5 + T_{i,j,n-1}/R_6 + Q_r}{1/R_1 + 1/R_2 + 1/R_3 + 1/R_4 + 1/R_5 + 1/R_6} \tag{40}$$

where

$$R_1 = \frac{2r\Delta\phi}{\Delta r\left(\Delta S^{n-1,n}_{i,j} + \Delta S^{n,n+1}_{i,j}\right)}\left(\frac{1}{k^{l-1}_{i,j,n}} + \frac{1}{k^{l-1}_{i+1,j,n}}\right)$$

$$R_2 = \frac{\Delta r}{(r+\frac{\Delta r}{2})\Delta\phi\left(\Delta S^{n-1,n}_{i,j} + \Delta S^{n,n+1}_{i,j}\right)}\left(\frac{1}{k^{l-1}_{i,j,n}} + \frac{1}{k^{l-1}_{i,j-1,n}}\right)$$

$$R_3 = \frac{2r\Delta\phi}{\Delta r\left(\Delta S^{n-1,n}_{i,j} + \Delta S^{n,n+1}_{i,j}\right)}\left(\frac{1}{k^{l-1}_{i,j,n}} + \frac{1}{k^{l-1}_{i-1,j,n}}\right)$$

$$R_4 = \frac{2}{h_g r\Delta\phi\left(\Delta S^{n-1,n}_{i,j} + \Delta S^{n,n+1}_{i,j}\right)}$$

$$R_5 = \frac{\Delta S^{n,n+1}_{i,j}}{2A_{i,j,n}}\left(\frac{1}{k^{l-1}_{i,j,n}} + \frac{1}{k_{i,j,n+1}}\right)$$

$$R_6 = \frac{\Delta S^{n-1,n}_{i,j}}{2A_{i,j,n-1}}\left(\frac{1}{k^{l-1}_{i,j,n}} + \frac{1}{k_{i,j,n-1}}\right)$$

$$A_{i,j,n} = \frac{\left[\left(r_0 + \frac{\Delta r}{4}\right)\Delta\phi\frac{\Delta r}{2}\right]_{n+1} + \left[\left(r_0 + \frac{\Delta r}{4}\right)\Delta\phi\frac{\Delta r}{2}\right]_{n}}{2}$$

$$A_{i,j,n-1} = \frac{\left[\left(r_0 + \frac{\Delta r}{4}\right)\Delta\phi\frac{\Delta r}{2}\right]_{n} + \left[\left(r_0 + \frac{\Delta r}{4}\right)\Delta\phi\frac{\Delta r}{2}\right]_{n-1}}{2}$$

Note that equation (40) is used when hot-gas-side heat transfer coefficient is known and wall heat flux is evaluated based on the temperature difference, i.e., equation (9). When wall heat flux (q_n) is known, equation (40) becomes

$$T^l_{i,j,n} = \Big[T^{l-1}_{i+1,j,n}/R_1 + T^{l-1}_{i,j-1,n}/R_2 + T^{l-1}_{i-1,j,n}/R_3 + T_{i,j,n+1}/R_5 + T_{i,j,n-1}/R_6 + q_n\Delta\phi(\Delta S^{n-1,n}_{i,j} + \Delta S^{n,n+1}_{i,j})/2 + Q_r\Big]/(1/R_1 + 1/R_2 + 1/R_3 + 1/R_5 + 1/R_6) \quad (41)$$

where q_n is wall heat flux which can be an input of the program or evaluated using equation (10). Q_r is the radiative heat transfer term which is evaluated based on the Discrete Exchange Factor (DEF) method [21, 22, 23, 24] and is given by:

$$Q_r = \frac{\Delta\phi(\Delta S^{n-1,n}_{i,j} + \Delta S^{n,n+1}_{i,j})sin\beta_n}{4\pi}\left(\sum_{l=1}^{m+2} w_{s_l}E_{s_l}\overline{DS_lS_n} + \sum_{l=1}^{m} w_{g_l}E_{g_l}\overline{DG_lS_n} - E_{s_n}\right) \quad (42)$$

E_{s_n} and E_{g_n} are surface and gas emissive powers at stations n and are related to their temperatures via

$$E_{s_n} = \epsilon\sigma\frac{2\pi r}{\sin\beta_n}T^4_{s_n}$$

$$E_{g_l} = 4K_{t_l}(1-\omega_0)\sigma\pi r^2 T^4_{g_l}$$

$\overline{DS_lS_n}$ and $\overline{DG_lS_n}$ are total exchange factors between differential surface and gas elements at station l to a surface element at station n. The total exchange factor between two elements is defined as the fraction of the radiative energy that is emitted from one element and is absorbed by the other element via direct radiation and multiple reflections and scatterings from surfaces and gas. Procedures for calculating direct and total exchange factors in rocket thrust chambers and nozzles are presented in [23] and [24]. The radiative heat transfer term, given by equation (42), evaluates the radiative energy coming to a surface node from all parts of the engine. This is done by numerical integration of the radiative energy incident on the surface at station n that is originated (emitted) from station l. The weight factors w_s and w_g are used for numerical integration of surface and gas radiation along axial direction. If the stations are equally spaced then the weight factors are the same as those of trapezoidal or Simpson methods. In the present application, however, the stations are more concentrated at the throat area and are unevenly spaced. The rectangular numerical integration method is suitable when stations are not equally spaced and the weight factors are equal to the width of each station, i.e., $(\Delta S^{n-1,n}_{i,j} + \Delta S^{n,n+1}_{i,j})/2$. It should be noted that the evaluation of exchange factors $\overline{DS_kS_n}$ and $\overline{DG_kS_n}$ involves multiple integration (see [23] and [24]) and requires significant computer time. Values of these exchange factors depend on the geometry of engine and radiative properties of combustion gases. Hence, they can be evaluated using external modules and the resulting

exchange factors stored in files for different engines. These files can then be used as inputs to the RTE. A separate computer program, namely RTE_DEF (Rocket Thermal Evaluation_Discrete Exchange Factor), has been developed for evaluation of the total exchange factors. Note that the combustion properties code given by Gordon and McBride [2] does not provide the radiative properties of combustion gases. These properties may be obtained from [25] and [26]. For example, if the fuel is RP-1, the combustion gas species mole fractions are obtained from the combustion code [5], containing 17%CO_2, 30%CO, 33%H_2O, 6%OH, 2.5%O_2, 3%H, 7%H_2 and 1.5%O. Using an integrated average value of the absorption coefficients of these species, the overall absorption coefficient is found to be $K_a = 2.5in^{-1}$.

Based on the revised wall temperature, new hot-gas and coolant wall properties, heat transfer coefficients and adiabatic wall temperatures are calculated using equations (1) through (42). Again, a new wall temperature distribution based on the most recent heat transfer coefficients and adiabatic wall temperatures is calculated using the finite difference subroutine for heat conduction within the wall. This procedure is repeated until the relative difference between the temperature distribution of two consecutive iterations becomes negligibly small. After the results for station n converge, the coolant Mach number and entropy as functions of static pressure and enthalpy ($M_{C_n}, s_{C_n} = f(P_{CS_n}, i_{CS_n})$) are evaluated using the GASP or WASP programs. Next, the coolant stagnation pressure is evaluated based on the coolant entropy and stagnation enthalpy, i.e., $P_{C0_n} = P(i_{C0_n}, s_{C_n})$. The GASP and WASP programs do not have explicit expressions for pressure in terms of entropy and enthalpy. Thus, an implicit relation for stagnation pressure (i.e., $s_{C_n} = s(P_{C0_n}, i_{C_n})$) with the secant method for solving nonlinear equations is used to determine P_{C0_n}. In the secant method, two initial guesses for the stagnation pressures were made ($P_1 = P_{C0_{n-1}} + 20$ and $P_2 = P_{C0_{n-1}} - 20$) and the corresponding entropies s_1 and s_2 were determined. The secant method's iterative equation is given by:

$$P_{k+1} = P_k - s_k \frac{P_{k-1} - P_k}{s_{k-1} - s_k} \tag{43}$$

where k is the iteration index. When equation (43) converges (the convergence criterion is $|s_k - s_{C_n}| < 0.0001$), the coolant stagnation is set equal to the latest value of P_k. Finally, the coolant stagnation temperature is determined based on the coolant stagnation pressure and enthalpy ($T_{C0_n} = T(P_{C0_n}, i_{C0_n})$).

The program then marches axially and performs similar calculations (i.e., equations (1) through (43)) for all stations. Once the results of the last station (station m) converged, the results of this march are compared to those of the previous march. If the relative differences between the results of two consecutive marches is less than the axial convergence criterion the program stops, otherwise it continues its axial marches until convergence is achieved. The effect of axial conduction can be eliminated by setting the axial convergence criterion greater than one or setting the maximum number of passes equal to one. A complete flow chart of RTE is presented in [1].

The method described here, i.e., axial marches along axial direction, has several advantages over the direct solution of a three-dimensional finite difference formulation. First, it converges very quickly. Second, it requires less memory. Third, it allows the user to control the importance of axial conduction by allowing for different convergence criterion between the axial and radial and circumferential directions. For example, in analysis of a thin-walled, radiatively-cooled, low-pressure engine, axial conduction is negligible. In this case one might set the convergence accuracy to 5% in the axial direction and 0.1% in the other directions. In

the case of a thick-walled, regeneratively-cooled, high-pressure engine, axial conduction may be significant. Thus, the accuracy in the axial direction may be set to 0.1% and 0.1% in the other directions.

Results of a Typical Run

RTE is used to determine the temperature distribution and heat transfer characteristics of a Liquid Oxygen/ Liquid Hydrogen rocket engine. The engine has the following specifications:

Fuel	LH_2
Oxidant	LO_2
Coolant	LH_2
Chamber stagnation pressure P_{GO}	1600 psi
Coolant stagnation pressure P_{CO}	2400 psi
Fuel flow rate	35.412 lb/sec
Coolant flow rate	5.059 lb/sec
Fuel/Oxidant Mixture ratio	5.9957
Coolant stagnation temperature	110 R
Number of cooling channels	100

The engine is subdivided into 29 stations. Table 1 shows dimensions of the engine and some thermal characteristics at each station (see Figure 3 for notation). Note that dimensions given in Table 1 are in inches. Also, $DCIN = 0.035$ in. remains constant along the engine. The outer surface radiates to space and its emissivity is 0.9. The thermal conductivities of wall materials, i.e., nickel and copper are functions of temperature.

The resulting wall temperature distributions for stations 1, 9, 16 and 29 are shown in Figure 6. A close examination of the temperature distributions reveals that the temperature gradient is relatively large in radial direction , especially for station 9. This may also be true for any other high pressure thrust chamber. Also, the results shown in Figure 6 can be used to optimize the cooling channel aspect ratio. For example, there is no temperature gradient at the upper section of the cooling channel in Figure 6a (station 9, throat). Hence, the cooling channel can be shorten slightly without changing the overall heat transfer to the coolant.

HOT-GAS-SIDE BOUNDARY LAYER ANALYSIS INTERFACE

The convective heat transfer coefficients and heat fluxes for the hot-gas-side of the RTE are evaluated based on a tube-like correlation [8], see equation (7). To obtain more accurate results, RTE can be linked to a nozzle flow and boundary layer analysis program. The procedure for linking RTE to TDK (Two-Dimensional Kinetics Nozzle Performance Computer Program [5]) is described in this section. A similar approach may be implemented to link RTE to other nozzle boundary layer analysis programs.

The flowchart for the iterative procedure for linking RTE to TDK is shown in Figure 7. In this approach, initially, the wall fluxes and temperatures are evaluated by running RTE under an unknown wall heat flux condition. In this run, RTE uses it internal hot-gas-side routines. The wall temperatures calculated by RTE are then used in the inputs of TDK. Using one of TDK's boundary layer modules (BLM or MABL)[5], a new wall heat flux distribution is

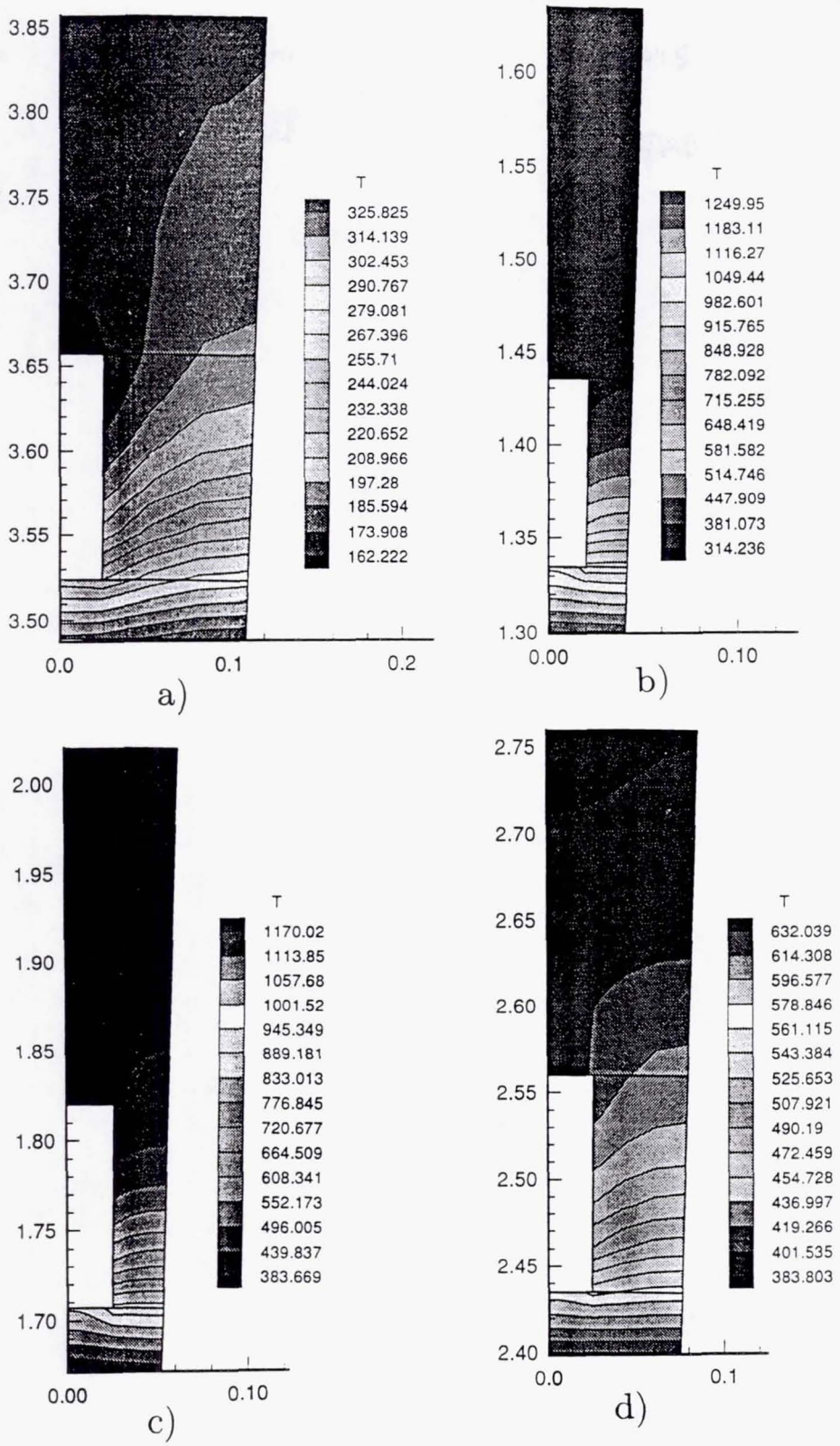

Figure 6. Temperature distribution at stations a) 1, b) 9, c) 16 and d) 29.

evaluated. The wall heat flux distribution is inserted into the RTE inputs. This time, since the hot-gas-side heat fluxes are known, RTE bypasses all hot-gas-side calculations (e.g., its CET subroutine and hot-gas-side heat transfer coefficient correlations) and calculates the wall temperature distribution. The new wall temperature distribution along the axial direction is then input to TDK and a new heat flux distribution is calculated. This iterative procedure continues until convergence is reached.

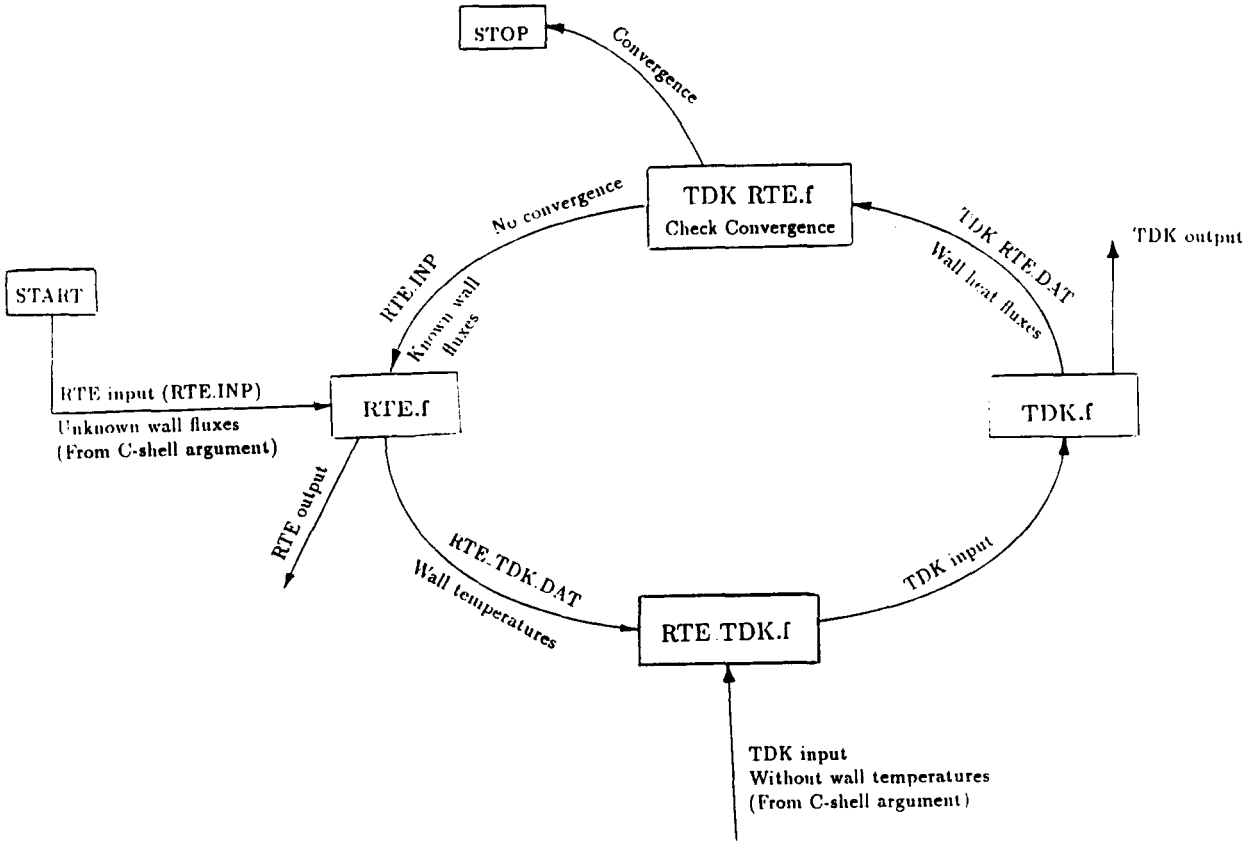

Figure 7. Flowchart of RTE-TDK Interface.

The RTE-TDK model is used to predict wall heat fluxes and temperatures of the LO/LH engine presented in the previous section. The resulting wall heat flux and temperature distributions for both RTE and RTE-TDK calculations are shown in Figures 8 and 9. As shown in these figures, the heat flux and temperature distribution when the boundary layer module is used are consistently below those calculated via hot-gas-side heat transfer coefficient, i.e., equation (5). The reduction of heat flux and temperature is due to the relaminarization of accelerating flow.

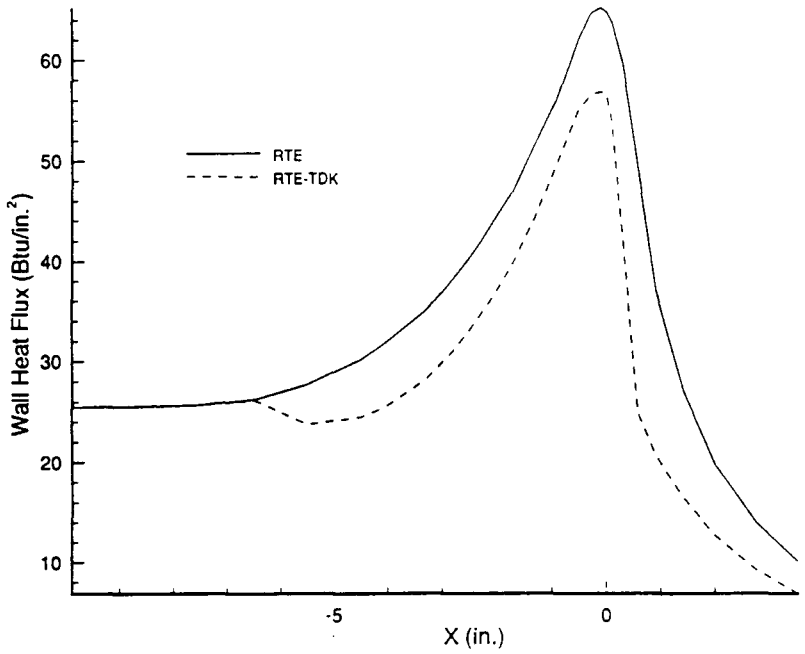

Figure 8. Wall heat fluxes for a H2 cooled engine based on RTE and RTE-TDK models.

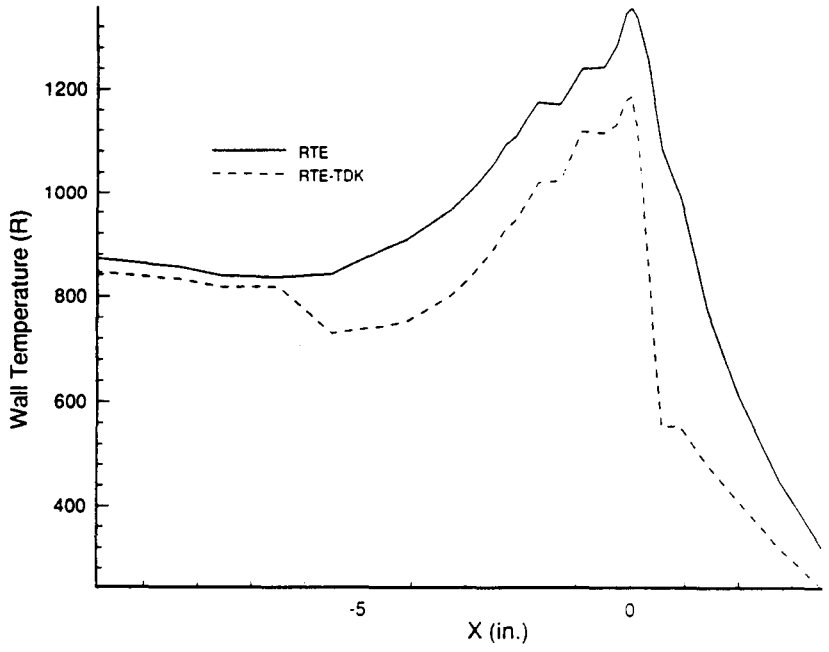

Figure 9. Wall temperatures for a H2 cooled engine based on RTE and RTE-TDK models.

Table 1: Parameters of thrust chamber and nozzle at different stations.

Station	X	DG	CCW	CCH	$THKNS$
1	3.55	6.978	0.05	0.133	0.368
2	2.75	5.898	0.05	0.123	0.358
3	2.0	4.886	0.05	0.113	0.348
4	1.4	4.076	0.05	0.104	0.339
5	0.9	3.402	0.05	0.1	0.335
6	0.559	2.942	0.04	0.1	0.335
7	0.3	2.692	0.04	0.1	0.335
8	0.1	2.610	0.04	0.1	0.335
9	0.	2.6	0.04	0.1	0.335
10	-0.1	2.608	0.04	0.1	0.335
11	-0.274	2.656	0.04	0.1	0.335
12	-0.506	2.746	0.04	0.1	0.335
13	-0.906	3.924	0.05	0.1	0.335
14	-1.306	3.092	0.05	0.1	0.335
15	-1.706	3.264	0.05	0.104	0.339
16	-1.906	3.344	0.05	0.113	0.348
17	-2.106	3.432	0.05	0.123	0.358
18	-2.306	3.516	0.05	0.125	0.36
19	-2.506	3.602	0.05	0.125	0.36
20	-2.906	3.77	0.05	0.125	0.36
21	-3.306	3.94	0.05	0.125	0.36
22	-4.106	4.236	0.05	0.125	0.36
23	-4.506	4.358	0.05	0.125	0.36
24	-5.506	4.6	0.05	0.125	0.36
25	-6.506	4.744	0.05	0.125	0.36
26	-7.572	4.8	0.05	0.125	0.36
27	-8.35	4.8	0.05	0.125	0.36
28	-9.0	4.8	0.05	0.125	0.36
29	-9.875	4.8	0.05	0.125	0.36

CONCLUDING REMARKS

The numerical model for a rocket thermal analysis code (RTE) has been discussed. This model allows temperature variation along three directions: axial, radial and circumferential. The numerical results presented show that there is a large temperature gradient in the axial direction for engines with a high chamber pressure. The resulting wall temperature distribution can be used to optimize the cooling channel aspect ratios

The RTE needs to be modified further to incorporate a wide range of cooling channel shapes and a CFD model for the cooling channel flow analysis. Efforts are presently under way to include these items in the RTE.

Acknowledgment

RTE has been developed as a result of collaborative efforts between the author and NASA Lewis Research Center. The author wishes to thank his NASA colleagues, James Giuliani,

Michael Meyer, Harold Price, Richard Quentmeyer, Elizabeth Roncace and Mary Wadel for their suggestion and helps during development of RTE.

NOMENCLATURE

A	area
C	correlation factor for heat transfer coefficient
C_p	specific heat
d	diameter
$\overline{DG_kS_n}$	total exchange factor between gas and surface differential elements
$\overline{DS_kS_n}$	total exchange factor between two surface differential elements
e	cooling channel surface roughness
E	surface and gas emissive power
f	friction factor
g_c	gravitational constant. 32.2 ft.$lb_m/lb_f.s^2$
h	heat transfer coefficient
i	enthalpy
J	work/heat proportionality factor
k	conductivity
K_t	total extinction coefficient
m	total number of axial stations
N	total number of cooling channels
P	pressure
Pr	Prandtl number
q	heat flux
Q_r	radiative heat transfer at inner surface
r	radius
$R_{Cur.}$	radius of curvature
R_n	thermal resistance
Re	Reynolds number
s	entropy
T	temperature
V	velocity
W	weight flow
w	weight factor for discrete exchange factor method
x	station position in longitudinal direction

Greek Symbols

β	angle between a vector normal to the nozzle surface and axial direction
ΔS	length of cooling channel between two stations
Δp	pressure drop
Δr	radial mesh size
$\Delta\phi$	circumferential mesh size
ϵ	convergence criteria or error limit
μ	dynamic viscosity

ρ	density
σ	Stefan-Boltzmann coefficient
ϕ	entrance and curvature effect correction factors

Subscripts

A	adiabatic
$Avg.$	average
C	coolant
$Cur.$	curvature
f	viscous or friction
G	gas
i	node i
j	node j
k	secant method iteration number
M	momentum
n	related to station n
r	radiation
S	static
s	surface
W	wall
X	reference
0	stagnation

Superscripts

j	iteration number
l	iteration number for conduction model
n	related to station n

References

[1] Naraghi, M.H.N., RTE - A Computer Code for Three-Dimensional Rocket Thermal Evaluation, Revision 2, Manhattan College Report for NASA Lewis Research Center, Grant NAG 3-892, July 1991.

[2] Gordon, S. and McBride, B. J., "Computer Program for Calculation of complex Chemical Equilibrium Compositions, Rocket Performance, Incident and Reflection Shocks, and Chapman-Jouquet Detonations," NASA SP-270, 1971.

[3] Hendricks, R. C., Baron, A. K. and Peller, I. C., "GASP - A Computer Code for Calculating the Thermodynamic and Transport Properties for Ten Fluids: Parahydrogen, Helium, Neon, Methane, Nitrogen, Carbon Monoxide, Oxygen, Fluorine, Argon, and Carbon Dioxide," NASA TN D-7808, Feb. 1975.

[4] Muss, J.A., Nguyen, T.V., and Johnson, C.W., "User's Manual for Rocket Combustor Interactive Design (ROCCID) and Analysis Compter Program," Volumes I and II, NASA Contractor Report 1087109, May 1991.

[5] Nickerson, G.R., Coats, D.E., Dang, A.L., Dunn, S.S., and Kehtarnavaz, H., "Two-Dimensional Kinetics (TDK) Nozzle Performance Computer Program," NAS8-36863, March 1989.

[6] Gordon, S., McBride, B. J. and Zeleznik, F. J., "Computer Program for Calculation of Complex Chemical Equilibrium Compositions and Applications Supplement I - Transport Properties," NASA TM-86885, Oct. 1984.

[7] Hendricks, R. C., Peller, I. C. and Baron, A. K., "WASP - A Flexible Fortran IV Computer Code for Calculating Water and Steam Properties," NASA TN D-7391, Nov. 1973.

[8] Eckert, E. R. G. and Drake, R. M., "Analysis of Heat and Mass Transfer," McGraw-Hill Book Company, 1972.

[9] Bartz, D. R., "Turbulent Boundary-Layer Heat Transfer from Rapidly Accelerating Flow of Rocket Combustion Gases and of Heated Air," Advances in Heat Transfer, pp. 2-108, 1965.

[10] Colebrook, C.F., "Turbulent Flow in Pipes with Particular Reference to the Transition Region Between the Smooth and Rough Pipe Laws," Journal of Institute of Civil Engineers, Vol. 11, pp. 133-156, 1939.

[11] Chen, N.H., "An Explicit Equation for Friction Factor in Pipe," Ind. Eng. Chem. Fundam., Vol. 18, No. 3, pp. 296-297, 1979.

[12] Itō, H., "Friction Factors for Turbulent Flow in Curved Pipes," Journal of Basic Engineering, pp. 123-134, 1959.

[13] Moody, L.F., "Friction Factors for Pipe Flow," Transactions of ASME, pp. 671-684, 1944.

[14] Hendricks, R. C., Niino, M., Kumakawa, A., Yernshenko, V. M., Yaski, L. A., Majumdar, L. A., and Mukerjee, J., "Friction Factors and Heat Transfer Coefficients for Hydrogen Systems Operating at Supercritical Pressures," Proceeding of Beijing International Symposium on Hydrogen Systems, Beijing, China, May 7-11, 1985.

[15] Kumakawa, A., Niino, M., Hendricks, R.C., Giarratano, P.J. and Arp, V.D., "Volume-Energy Parameters for Heat Transfer to Supercritical Fluids," Proceeding of the Fifteenth International Symposium of Space Technology and Science, Tokyo, pp. 389-399, 1986.

[16] Spencer, R.G. and Rousar, D.C., "Supercritical Oxygen Heat Transfer," NASA CR-135339, 1977.

[17] Niino, M., Kumakawa, A., Yatsuyanagi, N. and Suzuki, A., "Heat Transfer Characteristics of Liquid Hydrogen as a Coolant for the LO2/LH2 Rocket thrust Chamber with the Channel Wall Construction," 18Th. AIAA/SAE/ASME Joint Propulsion Conference, Cheveland, Ohio, June 21-23, 1982, AIAA paper 82-1107.

[18] Taylor, M.F.,"A Method of Predicting Heat Transfer Coefficients in the Cooling Passages of Nerva and Phoebus-2 Rocket Nozzles," NASA TM X-52437, June 1968.

[19] Owhadi, A., Bell, K.J. and Crain, B., "Forced Convection Boiling Inside Helically-Coiled Tubes," International Journal of Heat and Mass Transfer, Vol. 11. pp. 1779-1793, 1968.

[20] Norris, R.H., "Augmentation of Convection Heat and Mass Transfer." American Society of Mechanical Engineers, New York, 1971.

[21] Naraghi, M.H.N., Chung, B.T.F., and Litkouhi, B., "A Continuous Exchange Factor Method for Radiative Analysis of Enclosures with Participating Media," Journal of Heat Transfer, Trans. ASME, Vol. 110, pp. 456-462, 1988.

[22] Naraghi, M.H.N., and Kassemi, M., "Radiative Heat Transfer in Rectangular Enclosures: A Discrete Exchange Factor Solution," Journal of Heat Transfer, Trans. ASME, Vol. 111, pp. 1117-1119, 1989.

[23] Hammad, K.J., and Naraghi, M.H.N., "Exchange Factor Model for Radiative Heat Transfer Analysis in Rocket Engines," AIAA Journal of Thermophysics and Heat Transfer, Vol. 5, No. 3, pp. 327-334, 1991.

[24] Hammad, K.J., "Radiative Heat Transfer in Rocket Thrust Chambers and Nozzles," M.S. Thesis, Department of Mechanical Engineering, Manhattan College, 1989.

[25] Ludwig, C.B., Malkmus, W., Reardon, J.E., and Thomson, J.A.L., "Handbook of Infrared Radiation From Combustion Gases," NASA SP-3080, 1973.

[26] Siegel, R., and Howell, J.R., Thermal Radiation Heat Transfer, Hemisphere Publishing Corporation, 3rd Ed., 1992.

EFFECT OF TURBULENCE MODELS ON CRITICALITY CONDITIONS IN SWIRLING FLOWS

Robert E. Spall
Department of Mechanical Engineering
University of South Alabama
Mobile, Alabama

and

Thomas B. Gatski
Theoretical Flow Physics Branch
NASA Langley Research Center
Hampton, Virginia

SUMMARY

The critical state of vortex cores downstream of vortex breakdown has been studied. Base vortical flows were computed using the Reynolds-averaged, axisymmetric Navier-Stokes equations. Standard $K-\varepsilon$, RNG and second-order Reynolds stress models were employed. Results indicate that the return to supercriticality is highly dependent on the turbulence model. The $K-\varepsilon$ model predicted a rapid return of the vortex to supercritical conditions, the location of which showed little sensitivity to changes in the swirl ratio. The Reynolds stress model predicted that the vortex remains subcritical to the end of the domain for each of the swirl ratios employed, and provided results in qualitative agreement with experimental work. The RNG model produced intermediate results, with a downstream movement in the critical location with increasing swirl. Calculations for which area reductions were introduced at the exit in a subcritical flow were also performed using the Reynolds stress model. The structure of the resulting recirculation zone was altered significantly. However, when area reductions were employed within supercritical flows as predicted using the two-equation models, no significant influence on the recirculation zone was noted.

INTRODUCTION

Over the past 30 years, considerable effort has been expended toward an understanding of the mechanisms inherent in the development and evolution of longitudinal vortices. This has been motivated, in part, by the desire to control and/or disable these vortices in applications such as the aircraft-wake-vortex hazard and submarine non-acoustic stealth. Perhaps in no application are the properties of swirling flows exploited to a greater extent than in the operation of gas turbine and industrial furnace combustion chambers. Here, a region of high swirl is induced at an entrance to the combustor liner, typically through a set of swirler vanes, resulting in a region of recirculating flow. This region acts as a fluid dynamic flameholder, providing a region of low velocity within which combustion may be sustained, and recirculating hot, unburned gases to the base of the flame.

This recirculating region is known as a vortex breakdown. Although several theories have been put forth to explain the breakdown phenomena, perhaps none are more widely recognized than the early works of Squire [1] and Benjamin [2]. By choosing certain functional forms for the base vortex flow, Squire reduced the nonlinear equations of motion (inviscid, steady) to a linear disturbance equation. He subsequently solved the equation to determine conditions under which a steady perturbation to the flow could exist. This condition, in terms of a swirl ratio, was taken as a limiting condition for which breakdown could occur. Benjamin examined this phenomena from a different perspective. He considered vortex breakdown to be a finite transition between two dynamically conjugate states of flow, similar to the occurrence of a hydraulic jump in open channel flow. The two states were a *subcritical* state, which was defined as a flow which could support standing waves, and a *supercritical* state, unable to support standing waves. In this context, the work of Squire defined a critical condition marking the interface between the two states.

The criticality condition has not received much attention from those computing numerical solutions to swirling flows, and flows containing vortex breakdown in particular. Of special interest is the region downstream of the breakdown. Immediately downstream, the flow is most assuredly subcritical (c.f. Tsai and Widnall [3]). However, as the axial velocity recovers and the swirl velocity decays, the flow may return to a supercritical state at some downstream location. The consequences of the failure of a swirling flow to return to supercriticality has been discussed by Escudier and Keller [4]. In that experimental study, it was shown that the upstream influence of an exit contraction on vortex breakdown was substantially greater when the flow remained subcritical compared to a flow that reverted to supercritical (upstream of the contraction). Escudier and Keller suggest that this phenomena might have significant consequences in the imposition of accurate outflow boundary conditions.

Most swirling flows of practical interest, such as the flow within a combustor, are turbulent. For numerical calculations of turbulent swirling flows, the choice of turbulence model is of vital importance. It is well known that the standard $K-\varepsilon$ model does a poor job of predicting strongly swirling flows (c.f. Jones and Pascau [5]). One of the consequences of choosing the $K-\varepsilon$ model is that the wake region near the vortex centerline (downstream of breakdown) recovers much more rapidly than has been shown to occur in experiments. On the other hand, second-order closure models contain the physics necessary to model strongly swirling flows, and tend to do a better job of predicting the recovery of the axial velocity component (c.f. Jones and Pascau [5]).

These varying predictive capabilities have consequences in terms of the criticality of the flow. That is, one would expect the $K-\varepsilon$ model to predict a return to criticality upstream of the position predicted by second-order Reynolds stress models. This behavior has been investigated to some extent by Hogg and Leschziner [6]. However, in that work swirl ratios were such that no recirculation zone was formed when the Reynolds stress model was employed. In addition, no direct calculations of the critical condition of the flow were made. However, the critical state (based on an inviscid analysis, c.f. Hall [7]) is not difficult to compute and thus the purpose of this research is to further investigate the criticality conditions of swirling flows downstream of turbulent vortex breakdown as predicted using several different turbulence models ($K-\varepsilon$, RNG (c.f. Yakhot et al. [8]) and differential Reynolds stress). Geometries both with and without an exit restriction are employed. The relationship and consequences (if any) of the state of the flow (in terms of criticality) to the outflow restriction and turbulence model employed will be determined.

NUMERICAL PROCEDURE

The incompressible, axisymmetric Reynolds-averaged Navier-Stokes equations are solved for the swirling flow within a combustor-type geometry. Although the governing equations are solved in general curvilinear coordinates, for purposes of brevity they are presented below in cartesian tensor form. The continuity and momentum equations are given as:

$$\frac{\partial u_i}{\partial x_i} = 0 \tag{1}$$

$$\frac{\partial u_i}{\partial t} + u_j \frac{\partial u_i}{\partial x_j} = -\frac{1}{\rho}\frac{\partial p}{\partial x_i} + \frac{\mu}{\rho}\nabla^2 u_i - \frac{\partial \tau_{ij}}{\partial x_j} \tag{2}$$

respectively, where u_i is the mean velocity, ρ is the density, μ is the viscosity, p is the mean pressure and $\tau_{ij} = \overline{u'_i u'_j}$ are the Reynolds stresses.

Turbulence Models

Although the turbulence models utilized in the present study are well documented in the literature, the equations are included for completeness. When the $K-\varepsilon$ or RNG models are employed, the Boussinesq hypothesis provides an expression for the Reynolds stresses is terms of the gradients of the mean flow as:

$$-\tau_{ij} = -\frac{2}{3}\delta_{ij}K + 2\nu_t S_{ij} \tag{3}$$

where ν_t is the turbulent viscosity, K is the turbulent kinetic energy and S_{ij} is the strain rate. The turbulent viscosity is expressed in terms of K and the dissipation rate ε as:

$$\nu_t = C_\mu \frac{K^2}{\varepsilon} \tag{4}$$

Transport equations for K and ε, respectively, are written as:

$$\frac{DK}{Dt} = \frac{\partial}{\partial x_i}\left(\frac{\nu_t}{\sigma_k}\frac{\partial K}{\partial x_i}\right) + 2\nu_t S_{ij}^2 - \varepsilon \tag{5}$$

$$\frac{D\varepsilon}{Dt} = \frac{\partial}{\partial x_i}\left(\frac{\nu_t}{\sigma_\varepsilon}\frac{\partial \varepsilon}{\partial x_i}\right) + 2\nu_t C_{\varepsilon 1}\frac{\varepsilon}{K}S_{ij}^2 - C_{\varepsilon 2}\frac{\varepsilon^2}{K} - \bar{R} \tag{6}$$

In the case of the standard $K-\varepsilon$ equation $\bar{R} = 0$. For the RNG model (see Yakhot et al. [8]):

$$\bar{R} = \frac{C_\mu \eta^3 (1 - \eta/\eta_0)}{1 + \beta\eta^3}\frac{\varepsilon^2}{K} \tag{7}$$

where $\eta = SK/\varepsilon$ and $S = (2S_{ij}S_{ij})^{1/2}$.

It remains to specify the constants in the above equations. For the $K-\varepsilon$ model the standard values for boundary layer flows ($C_\mu = 0.09$, $C_{\varepsilon_1} = 1.44$, $C_{\varepsilon_2} = 1.92$, $\sigma_k = 1.0$ and

$\sigma_\varepsilon = 1.3$) have been taken. For the RNG model, theoretical analysis yields that $C_{\varepsilon 2} = 1.68$, $C_{\varepsilon 1} = 1.42$, $\sigma_k = \sigma_\varepsilon = 0.72$, $\eta_0 = 4.38$ and $\beta = 0.012$.

The Reynolds stress model involves the solution of transport equations for the individual Reynolds stresses $\overline{u'_i u'_j}$. The following equations, employing the closure assumptions of Gibson and Launder [9], and Launder [10], are solved:

$$\frac{D\overline{u'_i u'_j}}{Dt} = \frac{\partial}{\partial x_k}\left(\frac{\nu_t}{\sigma_k}\frac{\partial}{\partial x_k}\overline{u'_i u'_j}\right) + P_{ij} + \Phi_{ij} - \varepsilon_{ij} \tag{8}$$

The production term is computed as:

$$P_{ij} = -\overline{u'_i u'_k}\frac{\partial u_j}{\partial x_k} + \overline{u'_j u'_k}\frac{\partial u_i}{\partial x_k} \tag{9}$$

The pressure/strain and dissipation terms are modeled as:

$$\Phi_{ij} = -C_3\frac{\varepsilon}{K}\left(\overline{u'_i u'_j} - \frac{2}{3}\delta_{ij}K\right) - C_4\left(P_{ij} - \frac{2}{3}\delta_{ij}P\right) \tag{10}$$

$$\varepsilon_{ij} = \frac{2}{3}\delta_{ij}\varepsilon \tag{11}$$

with values $C_3 = 1.8$ and $C_4 = 0.06$ assigned to the constants.

For each model wall functions based upon the assumption of a fully developed equilibrium turbulent boundary layer are utilized in the near wall region. This approach is deemed suitable since the physics of the problem are not dominated by near wall phenomena.

Solution Procedure

The above equations were solved using the commercial code FLUENT [11]. FLUENT utilizes a pressure-based control volume technique. Second-order upwind interpolation is used to provide values of variables on cell faces. Pressure-velocity coupling is implemented using the SIMPLEC algorithm [12]. Convergence of the solution is assumed when the sum of the normalized residuals for the conservation equations is decreased to a minimum of 1.0×10^{-3}. (The residual for a given equation consists of the summation of the unbalance in the equation for each cell in the domain.) Comparisons revealed that solutions converged by an additional factor of two were virtually indistinguishable. Since the above techniques are well known and widely discussed in the literature, they will not be elaborated upon here.

Geometry and Boundary Conditions

The geometric configuration is that of a prototypical combustor. The geometry near the expansion/breakdown region is shown with the computational grid superimposed in Figure 1. The domain was discretized using 170 (axial) and 40 (radial) grid points. Grid points were clustered near the breakdown region. The length of the domain is $40h$, where h is the radius at inflow. The expansion of area ratio 4:1 takes place over a length of $3h$. Note that the i=constant lines in the

physical grid occur at constant x — this is to facilitate calculation of the flow criticality. Additional calculations were made utilizing a 114 x 27 grid. No significant changes in the solutions were noted.

At inflow, a solid body rotation of the form $w = \Omega r$ has been specified (where w represents the circumferential velocity). The value of Ω was assigned values ranging form 0.75 to 1.5. The axial velocity has been taken as uniform, that is $u = 1.0$, and the turbulence intensity was set at 10%. At the outflow boundary, zero streamwise gradient conditions were enforced. The appropriateness of these conditions is confirmed by examining the distribution of the velocity contours (as shown in the Results section) near the outflow boundary. In addition, for each calculation the Reynolds number, based on the axial velocity and duct radius at inflow, was 100,000.

Criticality Calculations

Determination of the criticality of the flow is based the solution of the following ordinary differential equation (c.f. Benjamin [2] or Hall [7]):

$$\frac{\partial^2 F_c}{\partial r^2} - \frac{1}{r}\frac{\partial F_c}{\partial r} + \left[-\frac{1}{u}\frac{\partial^2 u}{\partial r^2} + \frac{1}{ru}\frac{\partial u}{\partial r} + \frac{1}{r^3 u^2}\frac{\partial \kappa^2}{\partial r} \right] F_c = 0 \qquad (12)$$

where $\kappa = rw$ is the circulation and F_c is a quasi-cylindrical perturbation shape function. Assumptions inherent in the above equation are that the fluid is inviscid, and that the flow is steady and axisymmetric. Thus, the criticality condition, as defined by Benjamin or Hall, is concerned only with the propagation or existence of axisymmetric waves on inviscid cores. However, we shall utilize the theory to predict the ability of high Reynolds number turbulent cores to support axisymmetric waves.

The radial distributions for u and $\overline{K}$ are available at any axial location from the mean flow calculations. The above equation is solved subject to the boundary conditions $F_c = 0$ and $\frac{\partial F_c}{\partial r}$ = constant at $r = 0$. The flow is subcritical if the solution curve passes through zero in the interval $0 < r < 2h$, supercritical if the solution does not pass through zero, and critical if the solution is zero at both $r = 0$ and $r = 2h$ (where $2h$ is the duct radius). The above equation is solved utilizing a second-order accurate modified Euler technique.

RESULTS

The behavior of each of the turbulence models in predicting the location of the return to criticality of the vortex is presented first. Following this, contours of constant axial velocity are examined, and the effects of outlet restrictions on the flow are discussed.

Mean flow calculations were performed for Ω=0.75, 1.125 and 1.5, utilizing the $K-\varepsilon$, RNG and Reynolds stress turbulence models. The axial location at which the vortex returned to a supercritical state was computed by solving an ordinary differential equation, as described earlier. In each case, the vortex was supercritical upstream and subcritical immediately downstream of the breakdown location. The results for return to supercriticality are summarized in Figure 2. The $K-\varepsilon$ model predicted a return to supercritical conditions at locations considerably upstream of that predicted by the other models. In addition, and contrary to what one would expect, the $K-\varepsilon$ model predicted that the location at which the vortex returned to a supercritical state was not

affected by changes in the swirl level at inflow. Conversely, the RNG model showed an expected sensitivity to increases in swirl. That is, as the swirl level at inflow was increased, the critical location moved downstream. In the case of the Reynolds stress model, the vortex remained subcritical to the exit for all swirl levels. We note that $\Omega = 0.75$ represented the approximate minimum swirl level for which a recirculation zone was formed using the Reynolds stress model. Consequently, calculations of vortex breakdown flows using Reynolds stress models will likely involve outflow boundary conditions imposed on subcritical flows (due to practical limitations on the length of the computational domain). However, this need not be the case for the two-equation models.

Escudier and Keller [4] have shown that the shape and internal structure of the recirculation region is strongly influenced by outlet restrictions if the restriction is imposed within a subcritical flow. To examine whether or not these effects are observed in numerical calculations, results have been computed using the Reynolds stress model for area reductions of 19% and 36% with $\Omega = 1.5$. The reductions extended over $33.67h \le x \le 40h$. Results are presented in terms of axial velocity contours in Figures 3a-c for the unrestricted case, the 19% reduction, and the 36% reduction, respectively. (For purposes of clarity, the contour plots have been scaled by a factor of 3 in the radial direction. In addition, the inner-most contour levels within the bubble structure represent the level $u = -0.1$.) It is clear that the 36% area reduction has a large effect on the shape of the aft portion of the bubble near the vortex centerline. The zero axial velocity contour undercuts this portion of the bubble, in effect lifting the recirculation zone off the axis. Note however, that the forward portion of the bubble remains virtually unaffected. In addition, a strong jet-like vortex core exists downstream of the breakdown. These features are in very good agreement with those observed by Escudier and Keller [4] in their experimental work. For the 19% area reduction case, the primary effects concern the rate of recovery of the axial velocity downstream of the breakdown. The shape and internal structure of the bubble remains similar to that of the unrestricted case. This result is also consistent with the results of Escudier and Keller. We do note that the geometry of Escudier and Keller was somewhat different than that employed in this study. In their study, a solid inner cylinder was included at the inflow plane, and a step expansion rather than a gradual expansion was used. Numerical convergence problems prevented our use of that geometry. However, the structure of the recirculation region for confined flows undergoing vortex breakdown does not appear to be overly sensitive to the inlet geometry.

It is of interest that the downstream measurements by Escudier and Keller were $0.39L$ upstream of the area reduction (where L was the distance between the inlet and the reduction). Thus, it is quite possible that for their cases in which the area reductions were very large, the flow actually returned to a supercritical state upstream of the restriction (but downstream of their last data point). That is, due to continuity the mean axial flow velocity increases with the square of the area reduction; however conservation of angular momentum dictates that the swirl velocity increase in a linear manner. Thus, the ratio of swirl to axial velocity generally decreases, resulting in a possible return to supercritical conditions. In fact, the authors found that for the low swirl case ($\Omega = 0.75$) area reductions on the order of 20% did result in the flow returning to a supercritical state slightly upstream of the area reduction. However, for the high swirl cases shown in Figures 3b-c, the vortex remained in a subcritical state to the exit.

Contours of constant axial velocity for the $K-\varepsilon$ and RNG models (without exit restrictions) are shown in Figures 4a-b, respectively for the case $\Omega = 1.5$. The differences in the axial

velocity distributions downstream of the breakdown region as predicted by these models and the Reynolds stress model are quite large. The rapid increases in the axial velocity for the $K-\varepsilon$ and RNG models (accompanied by equally rapid decreases in the swirl velocity) account for the rapid return to supercriticality. In addition, the internal structures of the bubbles predicted by these two-equation models differ considerably amongst themselves, and with that produced by the Reynolds stress model. Calculations were also made for the $K-\varepsilon$ and RNG models 36% area reductions. For the sake of brevity, we show only the results from the RNG model in Figure 4c. (Recall that for the two-equation models the vortex was supercritical upstream of the restriction.) As the figure reveals, virtually no difference in the axial extent or shape of the recirculation region resulted (when compared with the case in which no restriction was employed). This further confirms the experimental results of Escudier and Keller, and highlights the extreme sensitivity of strongly swirling flows to the turbulence model employed.

CONCLUSIONS

It is clear from the results of this study that wide differences exist in the predictions of two-equation and Reynolds stress turbulence models for return to supercriticality of swirling flows downstream of vortex breakdown. The results of the Reynolds stress model are in better agreement with experimental results for swirling flows (in similar geometries) as described by Escudier and Keller [4] than results predicted using two-equation models. Thus, the study further highlights the inappropriateness of using two-equation models to predict strongly swirling flows. The suggestion by Escudier and Keller that outflow restrictions might have a drastic effect on the structure of the breakdown as predicted through numerical solutions to the equations of motion was confirmed. Results revealed that for relatively large area reductions (on the order of 36%), the structure of the recirculation region may be greatly affected. However, for lesser reductions, the shape of the recirculation zone may be very similar to that resulting from the unrestricted geometry. Consequently, it does not appear that the requirements for the specification of outflow boundary conditions need be significantly more stringent for subcritical swirling flows than for supercritical flows, or for flows without swirl. This is fortunate—the persistent nature of the subcritical flow as revealed by the experiments of Escudier and Keller [4], and as predicted by the Reynolds stress model would severely restrict the predictive capability of many engineering-type calculations.

The authors plan future work in the area of combusting flows. For these calculations, accelerations in the axial velocity due to decreases in density should considerably alter the critical state of the flow.

REFERENCES

1. Squire, H.B. "Analysis of the Vortex Breakdown Phenomenon. Part I.," Aero Dept. Imperial Coll. London, Rep. 102, 1960.

2. Benjamin, T.B., "Theory of the Vortex Breakdown Phenomena," Journal of Fluid Mechanics, Vol. 14, 1962, pp. 593-629.

3. Tsai, C-Y. and Widnall, S.E., "Examination of Group-Velocity Criterion for Breakdown of Vortex Flow in a Diverging Duct," Physics of Fluids, Vol. 23, 1980, pp. 864-870.

4. Escudier, M.P. and Keller, J.J., "Recirculation in Swirling Flow: A Manifestation of Vortex

Breakdown," AIAA Journal, Vol. 23, January 1985, pp. 111-116.

5. Jones, W.P. and Pascau, A., "Calculation of Confined Swirling Flows with a Second Moment Closure," ASME Journal of Fluids Engineering, Vol. 111, September 1989, pp. 248-255.

6. Hogg, S. and Leschziner, M.A., "Computation of Highly Swirling Confined Flow with a Reynolds Stress Turbulence Model," AIAA Journal, Vol. 27, January 1989, pp. 57-63.

7. Hall, M.G., "Vortex Breakdown," Annual Review of Fluid Mechanics, Vol. 4, 1972, pp. 195-218.

8. Yakhot, V., Orszag, S.A., Thangam, S., Gatski, T.B. and Speziale, C.G., "Development of Turbulence Models for Shear Flows by a Double Expansion Technique," Physics of Fluids A, Vol. 4, No. 7, 1992, pp. 1510-1520.

9. Gibson, M.M. and Launder, B.E., "Ground Effects on Pressure Fluctuations in the Atmospheric Boundary Layer," Journal of Fluid Mechanics, Vol. 86, 1978, pp. 491-511.

10. Launder, B.E. "Second-Moment Closure: Present... and Future?," International Journal of Heat and Fluid Flow, Vol. 10, No. 4, 1989, pp. 282-300.

11. Fluent, Inc., Lebanon, NH, Fluent Users Guide.

12. Patankar, S.V. Numerical Heat Transfer and Fluid Flow, Washington, DC: Hemisphere Publishing Corp., 1980.

ACKNOWLEDGMENTS

One of us (RES) would like to acknowledge support from the NASA JoVE program.

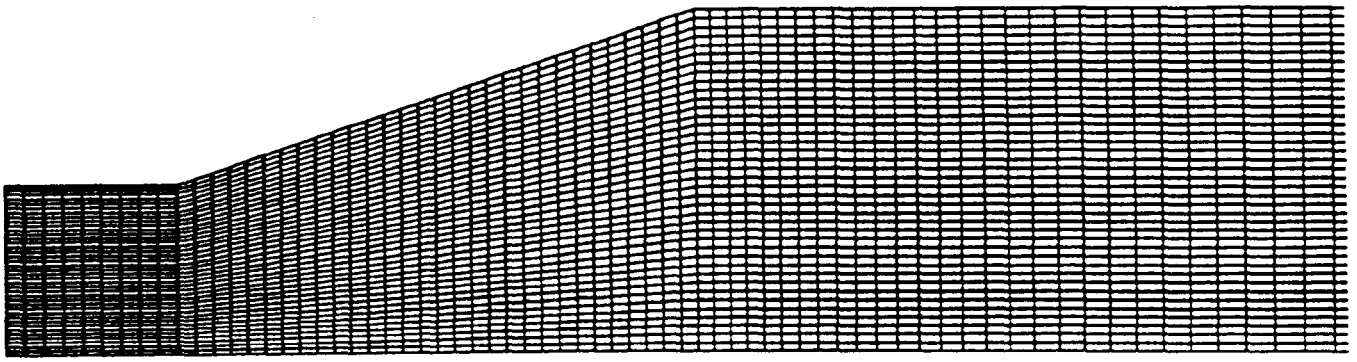

1. Computational grid in the region of vortex breakdown.

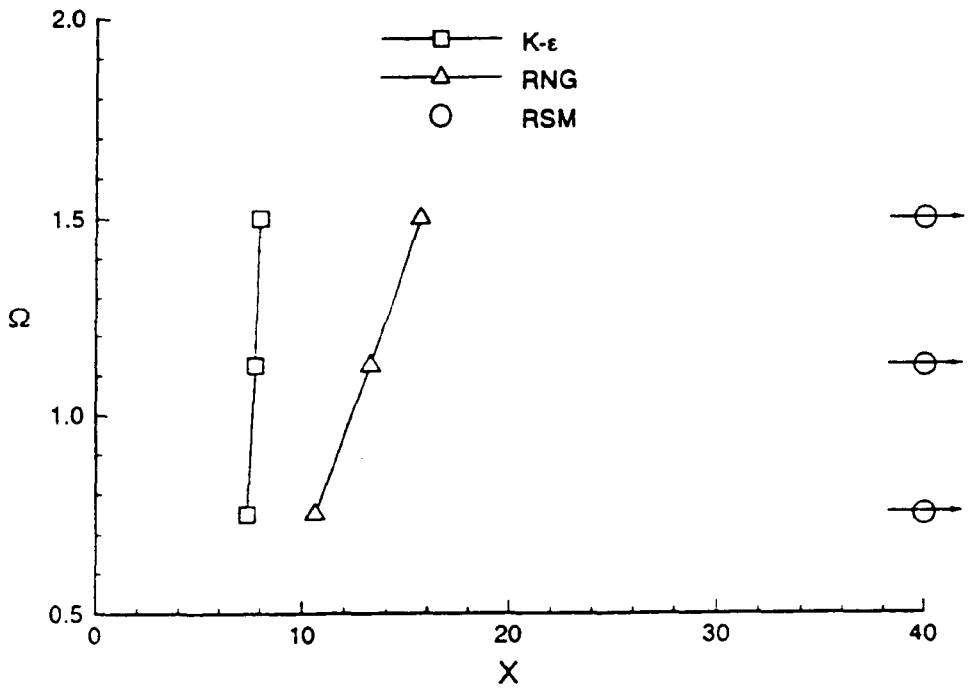

2. Location of return to supercritical conditions as predicted by $K-\varepsilon$, RNG and Reynolds stress turbulence models for strongly swirling flows.

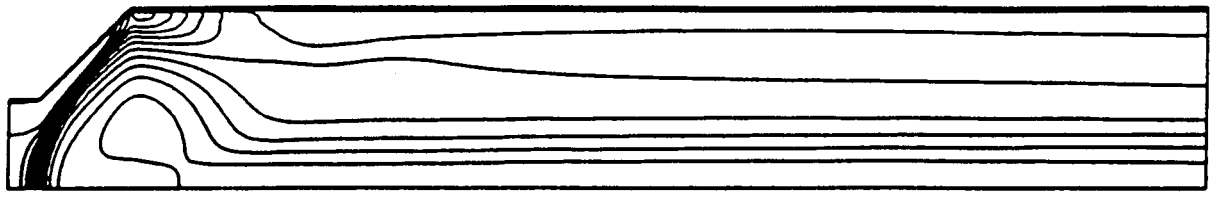

a

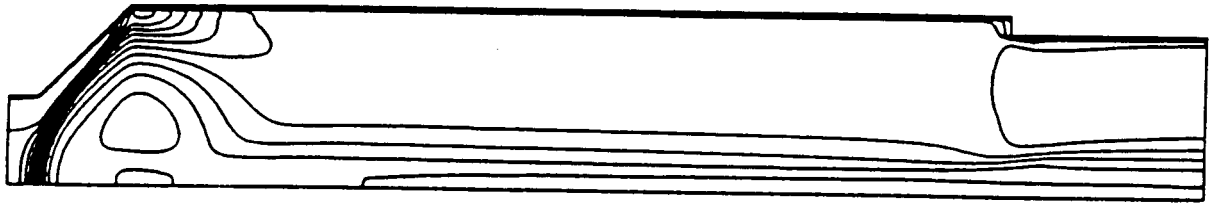

b

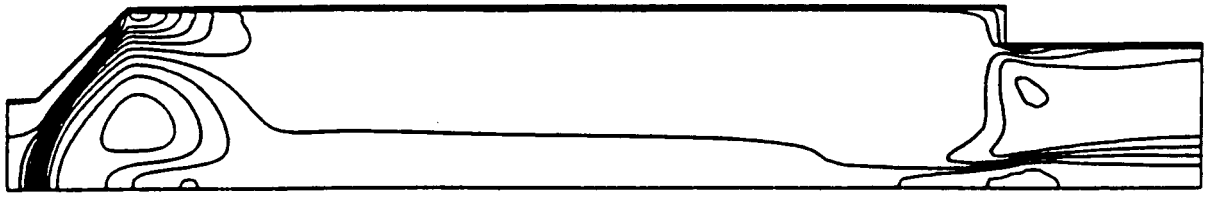

c

3. Contours of constant axial velocity; Reynolds stress model, Ω = 1.5; contour levels from - 0.1 to 1.0 in intervals of 0.1 (geometry scaled by a factor of 3 in the radial direction).
a) No outlet restriction
b) 19% area reduction
c) 36% area reduction

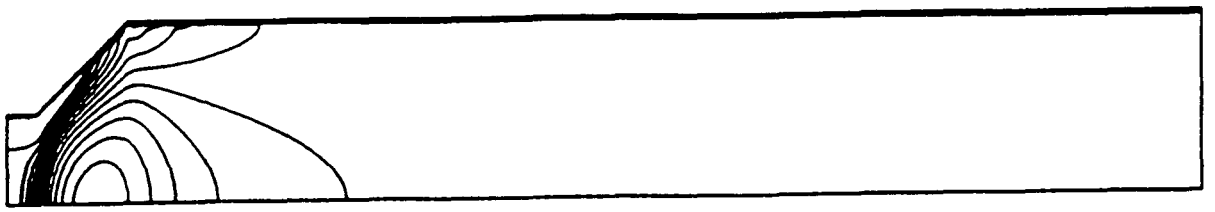

a

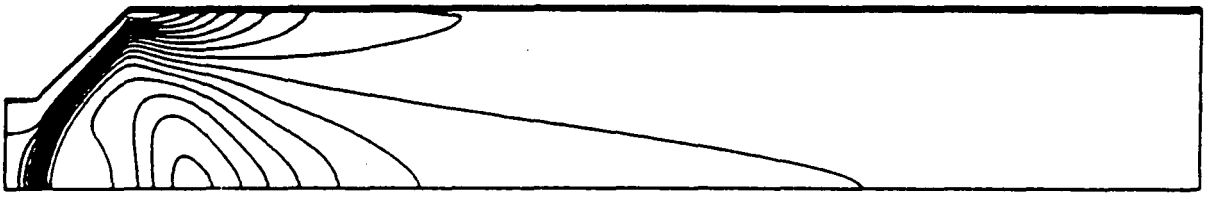

b

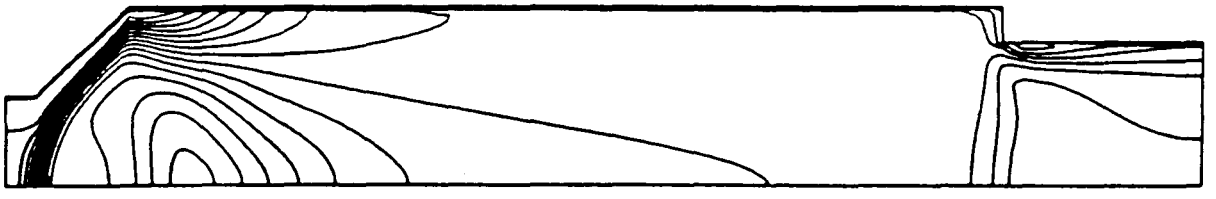

c

4. Contours of constant axial velocity; Ω = 1.5 (geometry scaled by a factor of 3 in the radial direction).
a) $K - \varepsilon$ model; contour levels from -0.2 to 1.0 in intervals of 0.1.
b) RNG model; contour levels from -0.4 to 1.0 in intervals of 0.1.
c) RNG model; 36% area reduction; contour levels from -0.4 to 1.0 in intervals of 0.1.

NUMERICAL SOLUTION OF FLUID FLOW AND HEAT TRANSFER PROBLEMS WITH SURFACE RADIATION

S. Ahuja and K. Bhatia
Engineering Mechanics Research Corporation
Troy, Michigan

SUMMARY

This paper presents a numerical scheme, based on the finite element method, to solve strongly coupled fluid flow and heat transfer problems. The surface radiation effect for gray, diffuse and isothermal surfaces is considered. A procedure for obtaining the view factors between the radiating surfaces is discussed. The overall solution strategy is verified by comparing the available results with those obtained using this approach. An analysis of a thermosyphon is undertaken and the effect of considering the surface radiation is clearly explained.

INTRODUCTION

There are many engineering applications in which a coupled analysis of fluid flow and heat transfer is desired. Among a large list of such examples, a few important ones are design of heat exchangers, cooling of electronic components, climate control and underhood analyses in automobiles, performance of industrial furnaces, heat transfer analysis in confined cavities, and, cooling and heating of buildings, etc. The fluid flow analysis generally requires solution of conservation equations of mass and momentum. Several numerical approaches are available (refs. 1 to 4) under a variety of boundary conditions. In heat transfer studies usually energy conservation involving all three modes (namely, conduction, convection and radiation) is expected. However, until recently, conduction and convection heat transfer modes were accurately accounted for while approximations were made for including the radiation analysis (ref. 5). The high nonlinearity involved in the basic theory precluded from obtaining analytical solutions and a use of ordinary numerical methods for practical problems. The availability of cheaper computer resources has caught the attention of researchers wanting to include accurate radiation analyses in their studies. This is reflected in a collection of papers included in (ref. 6) published recently.

The aim of this paper is to present a numerical methodology for analyzing fluid flow and heat transfer problems (including all three modes). A brief account of numerical solution of Navier-Stokes and continuity equations using the finite element method is presented. The assumptions involving the heat transfer via radiation include non-participating fluids and gray, diffuse surfaces based on enclosure theory (ref. 8). Solution of strongly coupled (heat transfer and fluid flow) phenomenon with natural convection is demonstrated through a couple of examples. To benchmark the developed code, a comparison with the already reported results is made. This is followed by a discussion of results in an analysis involving a study of thermosyphon (ref. 9), a passive system used for cooling of electronic components.

GOVERNING EQUATIONS

In this section, the basic equations associated with the fluid flow and heat transfer are discussed. Generally, it suffices to consider the conservation of mass, momentum, and energy in the given domain of interest. In the presence of surface radiation, additional equation representing the conservation of radiative energy must also be considered. The effect of radiative fluxes on the relevant surfaces must be reflected in the overall energy balance. In summary, the following equations must be solved to conserve mass, momentum, energy, and radiative energy:

conservation of mass:

$$\frac{\partial u_k}{\partial x_k} = 0 \tag{1}$$

conservation of momentum:

$$\rho\left[\frac{\partial u_i}{\partial t} + u_k\frac{\partial u_i}{\partial x_k}\right] = -\frac{\partial p}{\partial x_i} + \frac{\partial}{\partial x_i}\left[\mu\left(\frac{\partial u_i}{\partial x_j} + \frac{\partial u_j}{\partial x_i}\right)\right] + \rho g_i\left[1 - \beta\,(T - T_\beta)\right] \tag{2}$$

conservation of energy:

$$\rho C\left[\frac{\partial T}{\partial t} + u_k\frac{\partial T}{\partial x_k}\right] = \frac{\partial}{\partial x_j}\left(k\frac{\partial T}{\partial x_j}\right) + Q \tag{3}$$

For explanation of the symbols employed, refer to the section titled Nomenclature. It should be noted that Equations (1) through (3) are used for incompressible fluid flow with Boussinesq approximations invoked to model the natural convection phenomenon.

conservation of surface radiative energy:

$$\sum_{j=1}^{N}\left(\frac{\delta_{ij}}{\varepsilon_j} - \frac{1-\varepsilon_j}{\varepsilon_j}F_{ij}\right)q_{rj} = \sum_{j=1}^{N}\left(\delta_{ij} - F_{ij}\right)\sigma T_j^4 - \left(1 - \sum_{j=1}^{N}F_{ij}\right)\sigma T_s^4 \tag{4}$$

In deriving Equation (4), it is assumed that the surfaces are gray, diffuse and isothermal (ref. 8). The view factors, F_{ij}, between surfaces i and j, appearing in Equation (4) must be computed when attempting the solution of this equation. In the next section, a discussion on view factor calculations is undertaken.

COMPUTATION OF VIEW FACTORS

In order to compute q_r's (in Equation (4)), view factors F_{ij}, between all radiating surfaces must be available. In this section, the physical meaning of viewfactor and its calculation will be discussed. For a better understanding, i,j in the above equation can be replaced with 1 and 2. Thus, view factor, $F_{1\text{-}2}$, between two arbitrary surfaces (see Figure 1), '1' and '2' is defined as a fraction of diffuse radiant energy leaving surface '1' that arrives at surface '2'. Mathematically,

$$F_{1-2} = \frac{1}{A_1} \int_{A1} \int_{A2} \frac{\text{Cos}\,\theta_1\, \text{Cos}\,\theta_2}{\pi\, r_{12}^2}\, dA_1\, dA_2 \qquad (5)$$

where A_1 and A_2 are the areas of surfaces 1 and 2, respectively, r_{12} is the distance between the two elemental areas dA_1 and dA_2, θ_1 is the angle between the position dependent normal vector $\vec{n}$ and the line connecting dA_1 and dA_2. Angle θ_2 is defined in a similar way. It must be noted that $\text{Cos}\,\theta_1$ and $\text{Cos}\,\theta_2$ must be positive in order for the surface dA_1 and dA_2 to 'see' each other. If either of the cosines has a negative value, the corresponding view factor, $F_{dA_1-dA_2}$ should be set to zero. Such cases, in which the inactive side of the radiating face acts as an obstructer, will be termed as 'self-obstruction' cases. Also, view factor $F_{1\text{-}2}$ should be set to zero, if a third surface obstructs the view between surfaces 1 and 2.

In order to calculate view factors internally, the user must specify the radiation surfaces in terms of the finite element faces of a discretized domain. The user must also specify which of the two sides is a radiatively active side. These pieces of information can be supplied very easily via the already existing card in the NISA file of NISA/3D-FLUID. Each radiating face is taken as one radiation surface. View factors between the radiating surfaces are automatically generated by NISA/3D-FLUID taking into account self-obstruction and obstructions due to a third surface.

As can be assessed from the preceding discussion, computing view factors can result in usage of excessive computer time. To economize this computation, different techniques are used depending on whether the geometry being analyzed is 2D, 3D or axisymmetric. For example, double area integration method (ref. 8) is employed in comparison with contour integration method (ref. 8) when a 3D geometry, with radiation surfaces, is being analyzed. No special directives are required when computing view factors for axisymmetric geometries. NISA/3D-FLUID internally generates a complete 3D model (with the axis of symmetry as the X-axis [NISA/3D-FLUID]) to calculate the required view factors. Furthermore, for 2D problems, a completely different approach, called Hottel's crossed-string method (ref. 8) is employed for its computational efficiency and accuracy. Reference 8 provides more details for evaluating view factors for interested readers.

FE FORMULATION & SOLUTION PROCEDURE

The partial differential equations (Equations 1 through 3) and the radiative balance equation (Equation 4) are to be solved simultaneously to account for the fluid flow and heat transfer analyses in a given domain with specified boundary conditions. The convective terms appearing in Equations (2) and (3), simultaneous

solution of Equations (3) and (4), and arbitrary geometries encountered in most practical problems would require numerical tools for obtaining solution to coupled Equations 1 through 4. The Galerkin method in conjunction with the finite element method (ref. 8) form the basis of discretizing Equations 1 through 3. The penalty approach (ref. 3) is employed to eliminate the pressure from Equation (2) making use of Equation (1). For further details, refer to (refs. 3 and 10). The discretized form of Equations (2) and (3) can be written in matrix form as follows

$$\mathbf{[K]\ \{X\} = \{f\}} \tag{6}$$

where Kij is the "stiffness" matrix, consisting of contributions from acceleration. diffusion and pressure gradient terms of Equation (2) and acceleration and diffusion terms of Equation (3). Xj represent [U, V, W] for momentum equations and [T] in the case of energy equation. The vector fj is discussed more at length as this contains coupling terms in Equations (2), (3), and (4). For example, the vector {f} for the momentum equations is

$$- \int_{\Omega} N^I \rho g_i \beta \ (T - T_\beta)\ d\Omega + \int_{\Gamma} N^I \ (- P \delta_{ij} + \tau_{ij}\ )\ n_j\, d\Gamma \tag{7}$$

Equation (7) indicates the influence of temperature distribution on the momentum equations while convective terms (included in Kij for Equation (3)) represent a dependence of the temperature field on the velocity distribution.

Furthermore fj for the energy equation consists of the following term:

$$f_j = \int_{\Omega} N^I\ Q\, d\Omega + \int_{\Gamma} N^I\ q\, d\Gamma \tag{8}$$

where

$$q = q_a + q_c + q_r \tag{9}$$

In the above equality, q_a, q_c, and q_r refer to the applied heat flux, effect due to convection boundary conditions, and that due to radiation on the boundary , respectively. The gray-body radiative effects can be considered via q_r which is evaluated using Equation (4) for a "known" temperature distribution. It is thus evident that Equations (3) and (4) are coupled via q_r and T. Far a complete enclosure. Equation (4) can be represented in the matrix as

$$[R]\ \{q_r\} = [S]\ \{T\} \tag{10}$$

where

$$R_{ij} = \sum_{j=1}^{N} \left(\frac{\delta_{ij}}{\varepsilon_j} - \frac{1-\varepsilon_j}{\varepsilon_j} F_{ij} \right) \tag{11}$$

and

$$S_{ij} = \sum_{j=1}^{N} \left(\delta_{ij} - F_{ij} \right) \sigma T_j^3 \tag{12}$$

Ideally Equations (6) for momentum and energy equations together with the radiative balance Equation (10) must be solved simultaneously. For practical reasons (computer memory and time, and nonlinearity in Equations (6) and (10)), a sequential approach is undertaken to solve these algebraic equations. Depending on the nature of coupling (strong for flows with free convective effects and weak for flows with forced convective effects), momentum, energy, and radiative balance equations are solved. For more details, refer to (ref. 10). It has been observed that q_r (and hence T) solution may not converge or may do so slowly. An under relaxation of q_r leads to its stabilization. This is achieved as follows:

$$q_{r_*}^{i+1} = \alpha\, q_r^{i+1} + (1-\alpha)\, q_{r_*}^{i} \tag{13}$$

where α is a user-defined relaxation factor. During a calculation sequence convergence checks are performed for velocity, temperature and surface flux, q_r, distributions by evaluating the L_2 norms. The sequential calculations are performed until the L_2 norms of all the nodal variables and surface radiation fluxes fall below a user-defined tolerance.

Special Cases:

There are a few special cases which require a slight modification to the above methodology for including the gray surface radiative effects in the heat transfer analysis. These are as follows:

a) Domain with plane(s) of symmetry
b) Exchange of radiative flux through "windows" in the domain
c) Exchange of radiative flux between the domain and surroundings
d) Radiative surfaces with no thickness.

The details of these modifications are presented in (ref. 10).

ILLUSTRATIONS

The aim of the present paper is to discuss an efficient solution strategy that must be undertaken to solve coupled fluid flow and heat transfer problems in the presence of radiative energy exchange between gray surfaces in a domain of interest with specified boundary conditions. In the previous sections, the pertinent differential equations and their respective discretized forms (using the finite element method) are discussed. In this section, a discussion of the results obtained with the outlined procedure for a couple of problems is undertaken.

Example 1: Natural Convection with and without Surface Radiative Effects in a Cavity.

The validation of the developed procedure is established by solving a problem studied by Behnia et al. (ref. 11). The fluid flow due to natural convective effects in a square cavity with radiating surfaces is considered. Figure 2 shows this cavity of a characteristic dimension, L and the specified boundary conditions. The top and bottom walls are adiabatic. The left wall is maintained at a uniform hot temperature, T_h. The right wall has convective and/or radiative boundary condition. The convective heat transfer coefficient is h. The temperature of the surroundings and the ambient temperature are taken to be T_∞. All the internal surfaces of the cavity have an emissivity of 0.9 and the fluid in the cavity is air. The cavity size, L, can be chosen to get a Rayleigh number of $3x10^5$. Table 1 shows a summary of conditions under which each case is analyzed with an aim of obtaining steady state temperature and fluid flow distributions in the cavity. Due to the presence of natural convective effects, strong coupling between the fluid flow and temperature fields is expected. The cavity is discretized into a graded mesh of 44 x 36 linear quadrilateral elements. The steady state algorithm of the code is invoked. Table 2 shows the relaxation parameters employed for each of the run detailed in Table 1 and the corresponding numbers of iterations required to obtain converged solutions.

Figure 3 shows the isotherms obtained for the cases denoted as R300, EC300, and REC300. A comparison of isotherms for these cases clearly indicates the effect of surface radiation on the adiabatic walls (top and bottom), the isotherms are no longer normal to these walls. Figure 4 shows the streamlines for the cases R300, EC300, and REC300 respectively. Table 3 shows a comparison of the maximum value of stream functions obtained for these runs with those listed in Behnia et al (ref. 11). A good quantitative agreement between the results is evident. Figure 5 shows the horizontal velocity along the vertical center line for these cases. The velocity profiles shown in the figure compare well with those in Figure 7 of ref. 11.

Example 2: Analysis of a Planar Thermosyphon.

In this example, the fluid flow and temperature distributions are studied in a thermosyphon including the surface radiative effects. A thermosyphon is a device used for cooling of electronic components, heat removal systems for nuclear reactors, and having applications in solar systems (ref. 9). Since thermosyphons involve no blowing or pumping of fluids, they are less expensive and more durable (termed as passive systems) as these do not require external signals for operation. A schematic of planar thermosyphon and the assigned boundary conditions is shown in Figure 6. An analysis of fluid flow and heat transfer in a thermosyphon is presented in (ref. 9) without the surface radiation effects. These effects have been included

in the study here. All the walls are black and are considered to be radiating. By observing the radiation surfaces in Figure 6, it is evident that all the surfaces cannot "see" each other. In other words, the view factor computation, in the presence of third surface obstructions, is invoked. These computations are more complex and handled efficiently in NISA/3D-FLUID (ref. 10).

First, the results are presented for the case in which only the convective effects (due to natural convection) are considered. The same analysis is performed in (ref. 9), in which the effects of varying the Rayleigh no. and a ratio of thermal conductivities of solid to fluid are considered. Therefore for the sake of comparison, results are presented for a Rayleigh no. of 10^4 and a ratio of thermal conductivities of 1 (see (ref. 9) for more details). Figure 7 shows the stream function distribution for this case and the corresponding isotherms are shown in Figure 8. A good agreement between these results and those presented in (ref. 9) is observed.

Now, the surface radiation effects due to the surfaces shown in Figure 6 is considered. The results for this case are not presented in (ref. 9). Figures 9 and 10 show distributions of stream functions and isotherms. A comparison of isotherms shown in Figures 8 and 10 indicate a considerable difference in their distributions. A further comparison of the velocity distributions, Figure 11, at "inlet" and "outlet" of the thermosyphon show marked differences. The difference in these velocity distributions amounts to a difference of 25% in flow rate. This analysis clearly indicates that if the surface radiation heat transfer is not accounted for, inaccurate distributions of temperatures and velocities may result.

CONCLUSIONS

A numerical scheme based on the finite element method is presented for solving coupled fluid flow and heat transfer problems in the presence of surface radiation. A sequential solution of momentum, energy and, radiative energy equations is considered for efficient computer memory management and disk usage. The computed results validated the numerical procedure adopted for an analysis of coupled fluid flow and heat transfer phenomena. The results presented compared well with those reported in literature. It is shown via the results discussed in this paper that the surface radiative effects must be considered for a complete heat transfer analysis. More research is underway to extend this work to consider non-gray surfaces and eventually participating fluids.

ACKNOWLEDGMENT

The authors are thankful to Jennie Kopacki for typing the manuscript.

NOMENCLATURE

C	=	Specific Heat	q	=	Heat Flux
g	=	Gravity Force	r	=	Spatial Coordinate
k	=	Thermal Conductivity	F	=	View Factor
p	=	Pressure	t	=	Time

Q	=	Volumetric Source	α, γ, φ	=	Relaxation Parameters
R	=	Radiation Matrix, LHS	ρ	=	Density
S	=	Radiation Matrix, RHS	β	=	Coefficient of Volume Expansion
T	=	Temperature	ε	=	Surface Emissivity
u	=	Velocity	δ	=	Kronecker Delta
F	=	Forcing Function	σ	=	Stefan-Boltzmamn Constant
X	=	Generalized Vector Nodal Unknown	Ω	=	Domain
N	=	Shape Functions	Γ	=	Boundary of the Domain
ψ	=	Stream Function	τ	=	Fluid Stress

Subscripts

β	=	Reference Temperature	r	=	Radiative
j	=	Spatial Index, Surface No.	i	=	Spatial Index, Surface No.
a	=	Applied Externally	s	=	Surroundings
c	=	Convective			

Superscripts

I	=	Nodal Index	i	=	Iteration No.

REFERENCES

1. Raithby, G.D.; and Schneider, G.E.: Numerical Solution of Problems in Incompressible Fluid Flow, Treatment of the Velocity -Pressure Coupling, Num. Heat Transfer, 1979, vol. 2, pp. 417-440.
2. Patankar, S.V.: A Calculation Procedure for Two Dimensional Elliptic Situations, Num. Heat Transfer, vol. 14, 1985, pp. 409-425.
3. Reddy, J.N.: Penalty Function Methods in the Finite Element Analysis of Fluid Flow, Int. J. Num. Methods in Fluids, vol. 2, 1982, pp. 151-171.
4. Hughes, T.J.R.; Taylor, R.L.; and Levy, J.F.: A Finite Element Method for Incompressible Viscous Flows, Proceedings of the 2nd Int-Symposium on Finite Element Methods in Fluid Flow Problems, Italy, 1976.
5. Ozisik, N.M.: Radiative Transfer, Wiley, New York, 1973.
6. Thynell, S.T. et al. (Editors), Developments in Radiative Heat Transfer, HTD-vol.203, ASME, 1993.
8. Siegel, R.; and Howell, J.R.: Thermal Radiation Heat Transfer, McGraw - Hill Book Company, New York, 1981.
7. Zienkiewicz, O.C.: The Finite Element Method, McGraw-Hill Book Company, New York, 1981.
9. Clarkson, R.; and Phillips, G.: A Parametric Study of Heat Transfer within a Planar Thermosyphon. HTD-vol. 237, ASME, 1993, pp. 9-19.
10. User's Manual, NISA/3D-FLUID, 1994.
11. Behnia, M.; J.A.; and de Vahl Davis, G.: Combined Radiation and Natural Convection in a Rectangular Cavity with Transparent Wall and Containing a Non-Participating Fluid, Int. J. Num. Meth-Fluids, vol. 10, 1990, pp. 305-325.

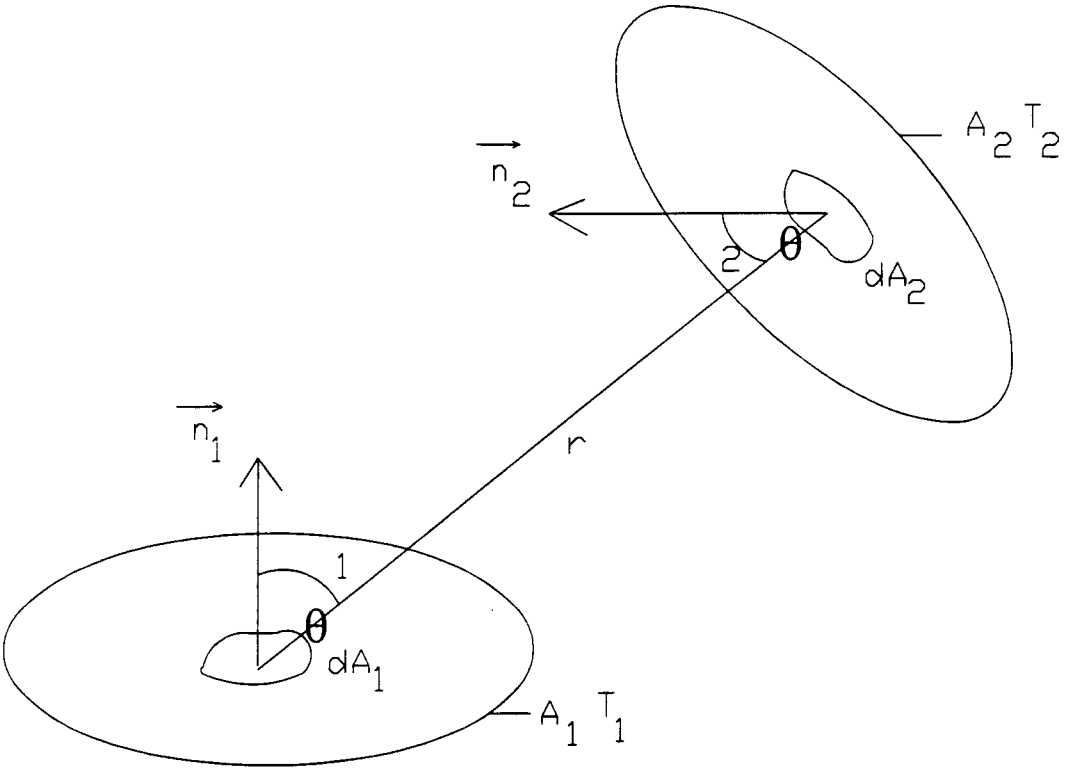

Figure 1 Definition of Terms Used in View Factor Calculations

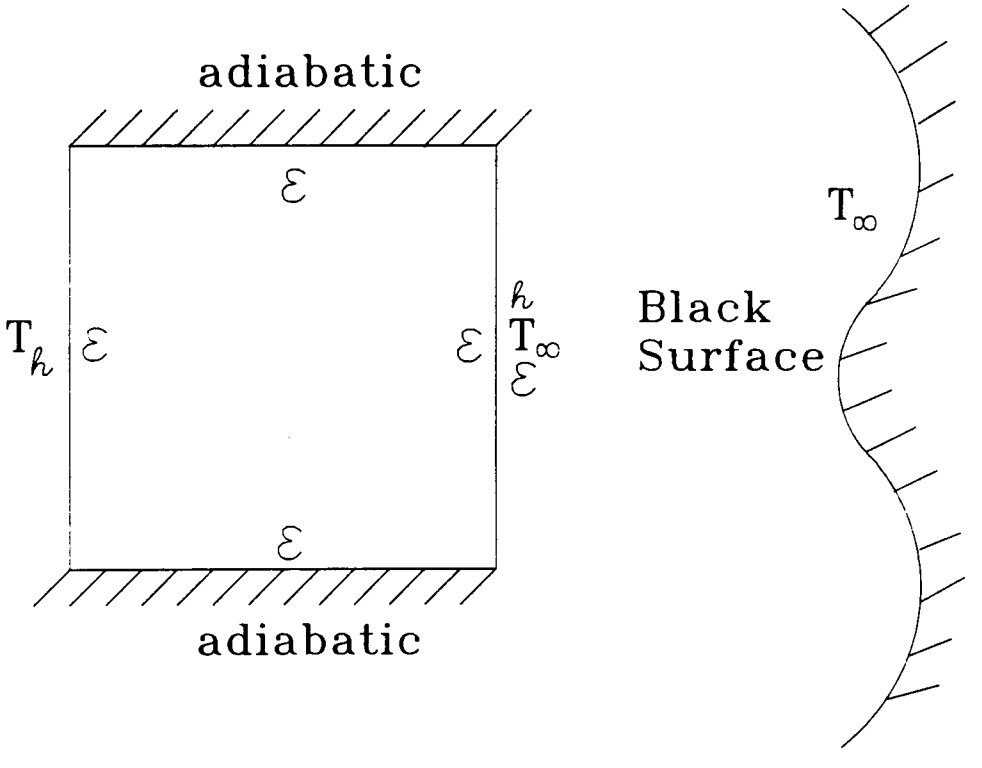

Figure 2 Schematic Diagram for Example 1

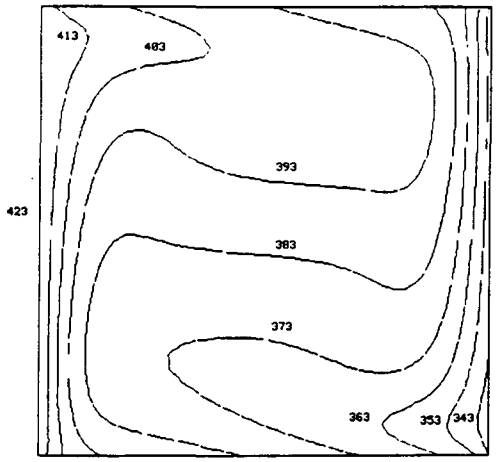

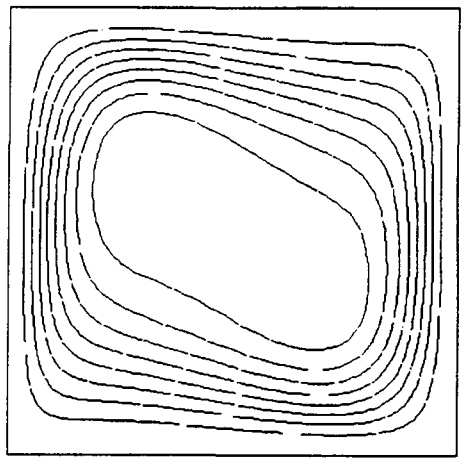

REC300

min.: -3.782×10^{-4} m^2/s max.: 0 m^2/s

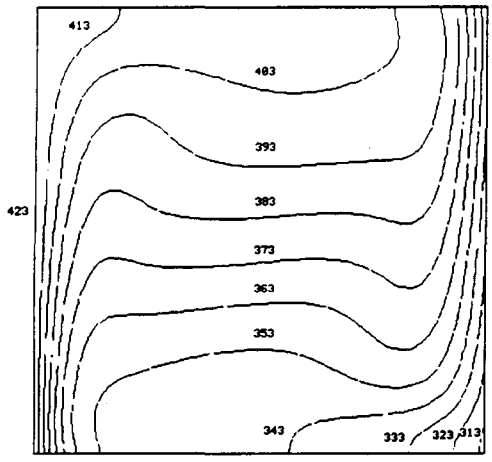

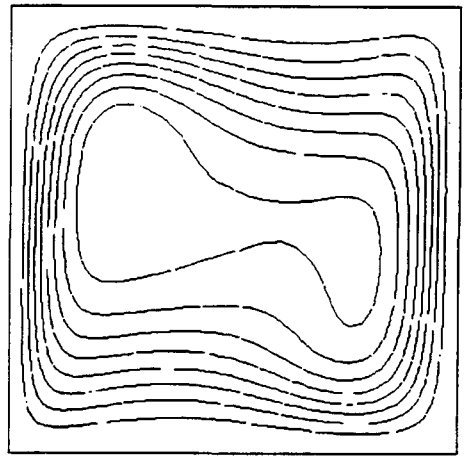

EC300

min.: -3.217×10^{-4} m^2/s max.: 0 m^2/s

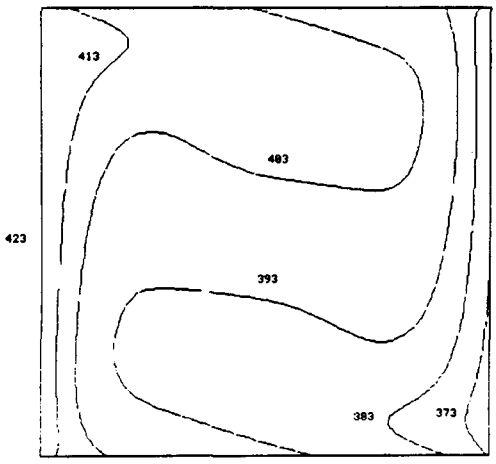

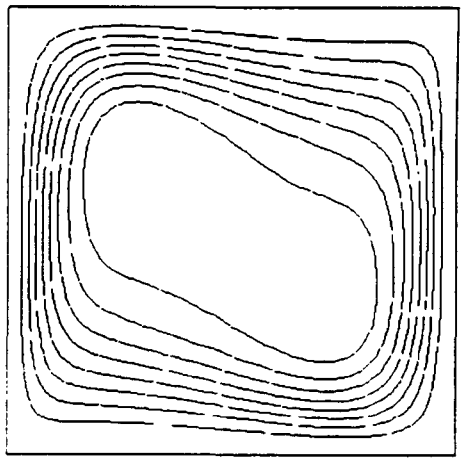

R300

min.: -3.444×10^{-4} m^2/s max.: 0 m^2/s

Figure 3 Isotherms for Runs REC300, EC300 and R300

Figure 4 Streamlines for Runs REC3000, EC3000 and R300

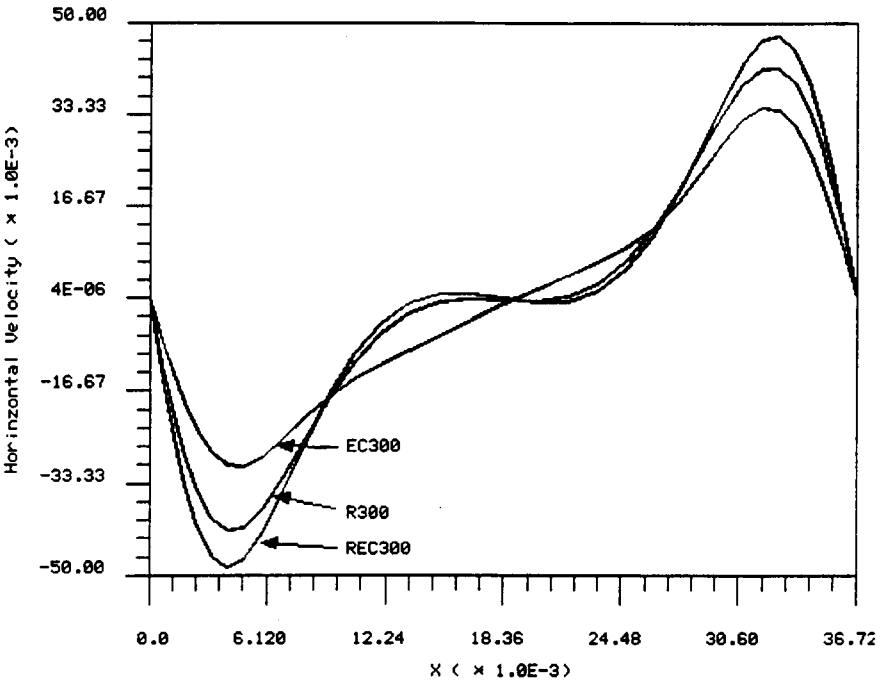

Figure 5 Horizontal Velocity Distributiuon Along the Vertical Centerline for Runs REC300, EC300 and RC300

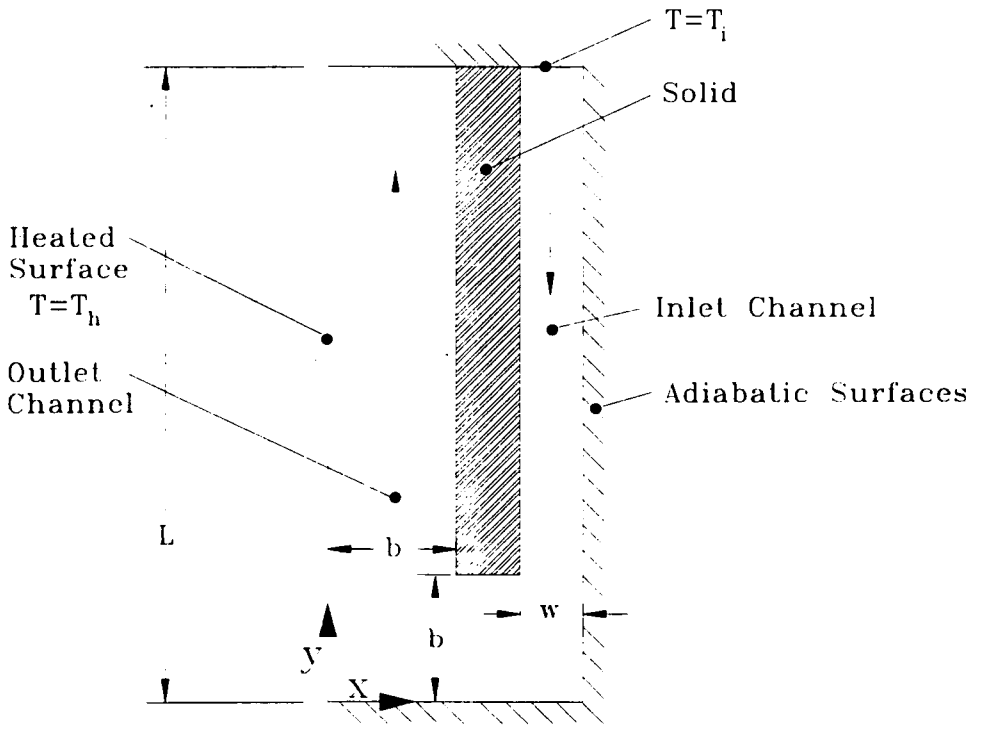

Figure 6 Schematic Diagram for Example 2 (Thermosyphon)

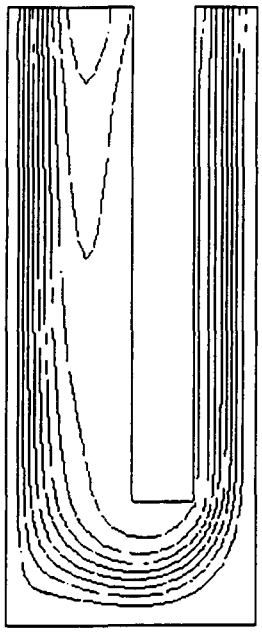

Figure 7 Streamlines for Thermosyphon (without Radiation)

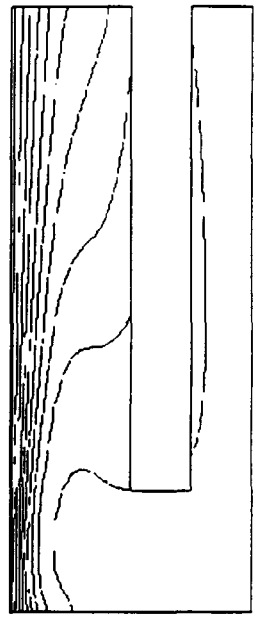

Figure 8 Isotherms for Thermosyphon (without Radiation)

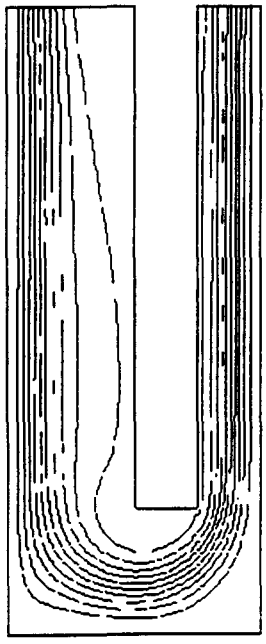

Figure 9 Streamlines for Thermosyphon (with Radiation)

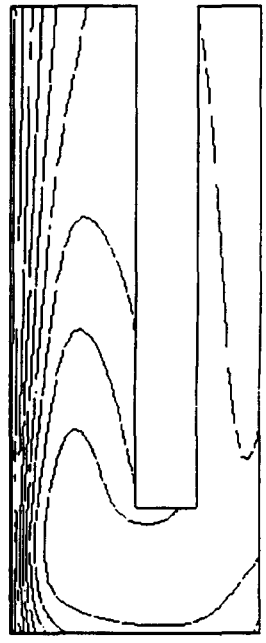

Figure 10 Isotherms for Thermosyphon (with Radiation)

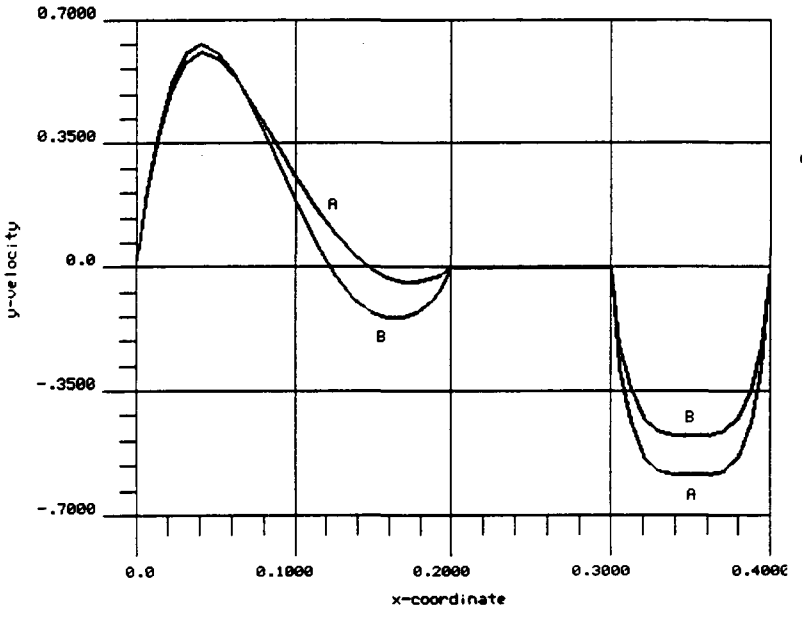

Figure 11 Inlet and Outlet Velocity Distributions for Thermosyphon

Table 1 Summary of Three Different Runs

Run	Ra	B.C. on the right wall	Surface Radiation
REC300	300,000	Convective + radiative	included
EC300	300,000	Convective	not included
R300	300,000	Radiative	included

$$Ra = Gr\,Pr = \frac{\rho^2 g \beta (T_h - T_\infty) L^3}{\mu^2} \cdot \frac{Cp\,\mu}{k}$$

Table 2 Relaxation Parameters and Number of Iterations

Run	Relaxation Parameter			No. of iterations
	Velocity α	Temperature γ	Radiative heat flux Φ	
REC300	0.04	1.0	0.1	64
EC300	0.04	1.0	0.1	40
R300	0.04	1.0	0.1	68

Table 3 Values of $|\Psi'|_{max}$ for Different Runs

Run	$\|\Psi'\|max = \frac{\|\Psi\|_{max}}{\alpha}$, $\alpha = \frac{k}{\rho C_p}$	
	Behnia et al. (ref. 11)	NISA/3D-FLUID (ref. 10)
REC300	13.04	12.94
EC300	10.93	11.01
R300	11.93	11.79

SINGLE-DROP REACTIVE EXTRACTION/EXTRACTIVE REACTION WITH FORCED CONVECTIVE DIFFUSION AND INTERPHASE MASS TRANSFER

Leonid S. Kleinman and X.B. Reed, Jr.
University of Missouri-Rolla
Rolla, Missouri

SUMMARY

An algorithm has been developed for the forced convective diffusion-reaction problem for convection inside and outside a droplet by a recirculating flow field hydrodynamically coupled at the droplet interface with an external flow field that at infinity becomes a uniform streaming flow. The concentration field inside the droplet is likewise coupled with that outside by boundary conditions at the interface. A chemical reaction can take place either inside or outside the droplet or reactions can take place in both phases.

The algorithm has been implemented and results are shown here for the case of no reaction and for the case of an external first order reaction, both for unsteady behaviour. For pure interphase mass transfer, concentration isocontours, local and average Sherwood numbers, and average droplet concentrations have been obtained as a function of the physical properties and external flow field. For mass transfer enhanced by an external reaction, in addition to the above forms of results, we present the enhancement factor, with the results now also depending upon the (dimensionless) rate of reaction.

INTRODUCTION

There are many industrial and environmental processes in which two-phase fluid-liquid systems are in use. Gases may be dispersed as bubbles in liquid phases, such as occurs in bubble columns and sparged vessels. Liquids may be dispersed in gases, such as occurs in scrubbers. And a liquid that is immiscible or partially miscible in another liquid may be dispersed in a liquid-liquid spray column extractor or reactor. The design of such systems may involve heat transfer, either intentionally or incidentally, but the widest range of applications involves mass transfer. Interphase mass transfer may proceed into or out of the dispersed phase. One (or more) chemical reaction(s) may take place in either the dispersed or the continuous phase in order to enhance the rate of mass transfer. In two-phase reactions, certain of the reactants may be transferred from one phase into the other, where the reaction takes place, and the reaction products may then be transferred back into the first phase. Reactions may also occur in both phases.

Because of the finite, generally small volume of each drop or bubble, interphase mass transfer unaccompanied by chemical reaction is inherently unsteady, regardless of the direction of mass transfer. Even if there is a reaction that admits of a steady state in the drop or bubble, unsteady behavior may nevertheless be of practical even primary importance.

The continuous phase is inevitably in motion relative to the dispersed phase, and for clean systems (containing no surface active agents), the motion in the two phases will be hydrodynamically coupled.

We undertake here for concreteness a liquid-liquid system in which a chemical reaction may take place in either or both phases. The dispersed phase is sufficiently dilute that the droplets which sediment (either falling under their weight or rising because of buoyancy) may be assumed isolated in an infinite medium, both with regard to fluid mechanics and to diffusion and reaction. The droplets are taken small enough that interfacial tension dominates shape effects and they are spherical. Although the approach we take and the methods we use do not require that that viscosity dominates flow effects and that the velocity fields have low Reynolds numbers , we consider the hydrodynamically coupled Hadamard - Rybczinsky profile for circulation within the droplet driven by an external velocity field that becomes a uniform streaming flow far from the droplet. Physical and chemical properties are assumed constant, which would be the case for dilute isothermal systems, and we thus analyze interphase mass transfer for the forced convective diffusion-reaction single-drop system. We investigate, specifically the roles of the reaction rates, as measured by appropriate Damköhler numbers, the solubility of the solute in the phases, as expressed by the linear distribution coefficient (Henry's law), the ratio of convection to diffusion, as measured by the Peclet number, and the ratio of the viscosities and that of molecular diffusivities of the two phases.

GOVERNING EQUATIONS

The dimensionless forced convective diffusion-reaction equations governing the solute concentrations in the drop ($0 \leq r \leq 1$) and the continuous ($1 \leq r < \infty$) phases, $i = 1, 2$, respectively, can be represented in the form

$$\frac{\partial c^{(i)}}{\partial t} + K_c^{(i)} \mathbf{v}^{(i)} . \nabla c^{(i)} = K_d^{(i)} \nabla^2 c^{(i)} - K_r^{(i)} c^{(i)} , \tag{1}$$

where $i = 1$ corresponds to the internal domain $0 \leq r \leq 1$, and $i = 2$ to the external one $1 \leq r < \infty$.

The dimensional partial parabolic differential equations have been rendered dimensionless using the droplet radius R as the characteristic length scale. The concentrations are measured in units of initial driving force,

$$c^{(i)} = \frac{H^{(i)} \tilde{c}^{(i)} - H \tilde{c}_\infty}{\tilde{c}_0 - H \tilde{c}_\infty}, \quad i = 1, 2 , \tag{2}$$

in which

$$H^{(i)} = \begin{cases} 1, & i = 1 \\ H, & i = 2, \end{cases} \tag{3}$$

with H the Henry's "law" distribution coefficient.

The characteristic time scale can be selected, for example, on the basis of the fastest physical or chemical process, occurring in the system, *viz.*,

$$\tau_* = \min(\tau_{\text{conv}}^{(i)} , \ \tau_{\text{diff}}^{(i)} , \ \tau_{\text{rxn}}^{(i)} , \ i = 1, 2), \tag{4}$$

in which

$$\tau_{\text{conv}}^{(i)} = \frac{R}{f^{(i)}(\mu) U_\infty}, \ \tau_{\text{diff}}^{(i)} = \frac{R^2}{D^{(i)}}, \ \tau_{\text{rxn}}^{(i)} = \frac{1}{k^{(i)}}, \ i = 1, 2 . \tag{5}$$

The diffusivities and rate constants for the first order chemical reactions are denoted by $D^{(i)}$ and $k^{(i)}$, respectively, and the K's represent different combinations of standard dimensionless parameters for different choices of τ_*, as indicated in Table 1.

Although our numerical implementation of the algorithm requires only that the velocity fields in the two phases be separable, for concreteness we have used the Hadamard - Rybczinsky solution for the convecting velocities in the dispersed and continuous phases. In this instance, the characteristic velocity in each phase, with U_∞ the freestreaming uniform flow at infinity, is taken as

$$U_*^{(i)} = f^{(i)}(\mu)\, U_\infty\,, \quad i = 1, 2\,, \tag{6}$$

in which

$$f^{(1)}(\mu) = \frac{1}{2(1+\mu)}, \quad f^{(2)}(\mu) = 1 \tag{7}$$

with the viscosity ratio

$$\mu = \mu^{(1)}/\mu^{(2)}\,. \tag{8}$$

The equations (9) are the ones used in the sequel, reflecting the selection of $\tau_{\rm diff}^{(2)}$ as the unit of time:

$$\begin{aligned} &\frac{\partial c^{(i)}}{\partial \tau} + \frac{Pe^{(2)}}{2}\cdot\left(v_r^{(i)}\frac{\partial c^{(i)}}{\partial r} - \frac{v_\lambda^{(i)}}{r}\sqrt{1-\lambda^2}\frac{\partial c^{(i)}}{\partial \lambda}\right) \\ &\quad = \frac{D^{(i)}}{D^{(2)}}\cdot\left\{\frac{1}{r^2}\frac{\partial}{\partial r}\left(r^2\frac{\partial c^{(i)}}{\partial r}\right) + \frac{1}{r^2}\frac{\partial}{\partial \lambda}\left[(1-\lambda^2)\frac{\partial c^{(i)}}{\partial \lambda}\right]\right\} \\ &\quad - Da_{II}^{(i)}\frac{D^{(i)}}{D^{(2)}}\cdot\left(c^{(i)} + \frac{H\tilde{c}_\infty}{\tilde{c}_0 - H\tilde{c}_\infty}\right)\,, \quad i = 1, 2\,, \end{aligned} \tag{9}$$

with $\lambda = \cos\vartheta$, subject to the boundary conditions at the droplet interface,

$$r = 1: \quad \begin{cases} c^{(1)} = c^{(2)} \\ H\cdot D\,\dfrac{\partial c^{(1)}}{\partial r} = \dfrac{\partial c^{(2)}}{\partial r} \end{cases} \tag{10}$$

and at the limits of the overall domain,

$$r = 0: \quad c^{(1)} < \infty \tag{11}$$

$$r \to \infty: \quad c^{(2)} \to 0 \tag{12}$$

Periodic boundary conditions in angle variable

$$\left.\frac{\partial c^{(i)}}{\partial \vartheta}\right|_{\vartheta=0,\pi} = 0, \quad i = 1, 2, \tag{13}$$

after introduction of the new independent variable λ are satisfied automatically.

The concentrations are subject to the initial conditions:

$$t = 0: \quad c^{(1)} = 1, \quad c^{(2)} = 0 \tag{14}$$

The actual direction of mass transfer may be out of or into the drop, depending upon the driving force $(\tilde{c}_0 - H\tilde{c}_\infty)$, even though the formulation of the problem suggests transfer from the droplet.

The opposite direction of mass transfer in the actual problem would lead to the appearance of the inhomogeneous part in the reaction terms in (9) (but only when the corresponding $K_r^{(i)} \neq 0$).

THE ALGORITHM

The problem is linear, and we use the Galerkin spectral method for the spatial discretization. The advantages of this method are well known [1, 2].

We express the unknown functions $c^{(i)}(\tau, \lambda, \tau)$ in a customary manner,

$$c^{(i)}(\tau, \lambda, \tau) = \sum_{m=0}^{M} c_m^{(i)}(\tau, \tau)\, P_m(\lambda), \quad i = 1, 2, \tag{15}$$

in which the $P_m(\lambda)$ are the Legendre polynomials of order m and the coefficient functions $c_m^{(i)}(\tau, \tau)$ are termed "radial functions" for brevity in the sequel.

The discretization in the radial direction is performed in somewhat different ways for the internal and external domains.

Using Equation (9) for mass transfer inside the droplet ($i = 1$), it is a simple matter to show that functions $c_m^{(1)}(\tau, \tau)$ obey the following restrictions :

$$c_l^{(1)}(\tau, \tau = 0) = 0, \quad l \neq 0 \tag{16}$$

$$\left.\frac{\partial c_l^{(1)}}{\partial \tau}\right|_{\tau=0} = 0, \quad l \neq 1 \tag{17}$$

$$\left.\begin{array}{l} c_{2k}^{(1)}(\tau, \tau) \text{ - even function of } \tau \\ c_{2k+1}^{(1)}(\tau, \tau) \text{ - odd function of } \tau \end{array}\right\} \quad k = 0, 1 \ldots \tag{18}$$

On the basis of these restrictions, the radial functions inside the droplet were approximated by a series in even Chebyshev polynomials:

$$c_m^{(1)}(\tau, \tau) = \delta_{m,0} \cdot \alpha_0(\tau) + \tau^{\kappa_m} \cdot \sum_{n=1}^{N^{(1)}} \phi_{m,n}^{(1)}(\tau)\, T_{2n-2}(\tau), \quad m = 0, 1, \ldots, M \tag{19}$$

in which the $T_p(\tau)$ are Chebyshev polynomials of the first kind of order p, and

$$\kappa_{2j} = 2, \quad j = 0, 1, \ldots \tag{20}$$

$$\kappa_1 = 1, \quad \kappa_{2j+1} = 3, \quad j = 1, 2, \ldots \tag{21}$$

Using (19) we automatically satisfy boundary condition (11), avoid the singularity at the origin of the drop, and the function $\alpha_0(\tau)$ represents the value of the concentration at the origin.

Such an expansion on the interval $0 \leq r \leq 1$ is valid as the even Chebyshev polynomials form a complete set for the type of functions considered [10].

The use of half the commonly used interval $[-1, 1]$ permits us to double the highest order of the polynomials used, leaving the number of terms in the series unaltered.

The nonuniformity of the distribution of nodes in the spectral method (their number in close proximity to the surface is higher than near the origin) matches the physics of the problem as the concentration gradient near the interface is much bigger.

For the semi-infinite external domain we implement the widely used procedure of truncating it at an appropriately large radius r_∞, far enough from the interface to make the disturbance introduced negligible. The boundary condition at infinity (12) is now imposed on this artificial boundary. It could be imposed as "hard", "soft" [12] or "behavioral" [1, 13]. We use the "hard" one,

$$r = r_\infty : \quad c^{(2)} = 0 \tag{22}$$

because it immediately results in original boundary condition (12) if $r_\infty \to \infty$.

It is necessary to realize that by doing this we are changing the physical sense of the problem. The decrease of the concentration to zero infinitely far from its source is caused physically by the spreading the species over an infinite spatial volume. After introduction of the boundary sphere at $r = r_\infty$, we model this decrease by imposing what amounts to an infinitely fast heterogeneous reaction on the artificial boundary r_∞. The only justification for this is an *a posteriori* one, *viz.*, by checking that the increase of r_∞ does not alter the solution in the vicinity of the droplet and in particular the interphase mass transfer.

Our computations have confirmed this and show that when r_∞ is chosen sufficiently large the choice of the particular type of boundary conditions mentioned above does not influence the resultant concentration distribution in regions where its value differs significantly from zero.

The domain $1 \leq r \leq r_\infty$ is mapped onto the interval $-1 \leq z \leq 1$ in such a way that the point $z = 1$ matches $r = 1$ and the point $z = -1$ matches $r = r_\infty$. Among the wide variety of possible mappings two are used more often than others, the exponential and rational ones ([1, 2]). A comparison by Grosch and Orszag [11] has shown that the latter mapping has some advantages over the former.

Specifically, we use

$$z = \frac{r - (1 + \delta)}{(1 - r)\left(1 - \frac{2\delta}{r_\infty - 1}\right) - \delta} , \tag{23}$$

where δ is the parameter representing the distance between the droplet surface and point mapped into $z = 0$. It is worth mentioning that we have also implemented the exponential mapping and could find no advantages for the rational mapping over it.

The radial functions in the external domain are expanded as

$$c_m^{(2)}(\tau, z) = \sum_{n=1}^{N^{(2)}} \phi_{m,n}^{(2)}(\tau)\, Z_n(z), \quad m = 0, 1, \ldots, M, \tag{24}$$

where the $Z_n(z)$, $n = 1, 2, \ldots, N^{(2)}$ are linear combinations of Chebyshev polynomials, each satisfying the boundary condition following from (12):

$$Z_n(z=-1)=0, \quad n=1,2,\ldots,N^{(2)}. \tag{25}$$

We take

$$\begin{aligned} Z_{2k}(z) &= T_{2k}(z)-1 \\ Z_{2k-1}(z) &= T_{2k-1}(z)+1 \end{aligned} \tag{26}$$

Thus, we reduce the system of partial differential equations for two initially unknown functions $c^{(1)}(\tau,\lambda,r)$ and $c^{(2)}(\tau,\lambda,r)$ to a larger system of ordinary differential equations in τ, for

$$\begin{aligned} &\alpha_0(\tau),\ \phi^{(1)}_{m,n_1},\ \phi^{(2)}_{m,n_2}, \quad m=0,1,\ldots,M, \\ &n_1=1,2,\ldots,N^{(1)}, \quad n_2=1,2,\ldots,N^{(2)}. \end{aligned} \tag{27}$$

The total number of these unknown functions is $1+(M+1)(N^{(1)}+N^{(2)})$.

In order to obtain equations for these functions we use the conventional Petrov – Galerkin method, i.e., the basis functions are taken as the test functions [2]. We define two inner products:

$$(f,g)^{(1)} \equiv \int_{-1}^{1} d\lambda \int_0^1 f\cdot g\,\frac{dr}{\sqrt{1-r^2}}, \tag{28}$$

$$(f,g)^{(2)} \equiv \int_{-1}^{1} d\lambda \int_{-1}^1 f\cdot g\,\frac{dz}{\sqrt{1-z^2}}. \tag{29}$$

Forming by (28) the inner product of (9) for $i=1$ with the test functions

$$P_0(\lambda)\,T_0(r),\ \ P_m(\lambda)\,r^{\kappa_m}\cdot T_{2n_1-2}(r), \quad m=0,1,\ldots,M, \quad n_1=1,2,\ldots,N^{(1)}-1, \tag{30}$$

and by (29) the inner product of (9) for $i=2$ with the test functions

$$P_m(\lambda)\,Z_{n_2}(z), \quad m=0,1,\ldots,M, \quad n_2=1,2,\ldots,N^{(2)}-1, \tag{31}$$

we obtain two vector equations

$$\mathbf{A}^{(i)}\frac{d\boldsymbol{\phi}^{(i)}}{d\tau} = (-K_c^{(i)}\,\mathbf{B}^{(i,c)} + K_d^{(i)}\,\mathbf{B}^{(i,d)} - K_r^{(i)}\,\mathbf{B}^{(i,r)})\cdot\boldsymbol{\phi}^{(i)} + K_r^{(i)}\,\mathbf{b}^{(i)}, \quad i=1,2. \tag{32}$$

Here $\mathbf{A}^{(i)}$, $\mathbf{B}^{(i,c)}$, $\mathbf{B}^{(i,d)}$, $\mathbf{B}^{(i,r)}$ are $\{1+(M+1)(N^{(i)}-1),\ 1+(M+1)N^{(i)}\}$ matrices, $\mathbf{b}^{(i)}-\{1+(M+1)N^{(i)}\}$ are the vectors of inhomogeneous terms, and $\boldsymbol{\phi}^{(i)}(\tau)-\{1+(M+1)N^{(i)}\}$ are the unknown vectors,

$$\boldsymbol{\phi}^{(1)}(\tau) = (\,\alpha_0,\ \phi^{(1)}_{0,1},\ldots\phi^{(1)}_{0,N^{(1)}},\ldots,\phi^{(1)}_{M,1},\ldots,\phi^{(1)}_{M,N^{(1)}}\,)^T, \tag{33}$$

$$\boldsymbol{\phi}^{(2)}(\tau) = (\,\phi^{(2)}_{0,1},\ldots\phi^{(2)}_{0,N^{(2)}},\ldots,\phi^{(2)}_{M,1},\ldots,\phi^{(2)}_{M,N^{(2)}}\,)^T. \tag{34}$$

The remaining $2\,(M+1)$ equations are derived from the boundary conditions (10) which are implemented by the Lanczos tau-method [1, 2, 14].

Upon substituting (19) and (24) into (10), multiplying by $P_m(\lambda)$, $m = 0, 1, \ldots, M$ and integrating λ from -1 to 1, we obtain two sets of M+1 linear algebraic equations:

$$\mathbf{Q}^{(1)} \cdot \boldsymbol{\phi}^{(1)} = \mathbf{Q}^{(2)} \cdot \boldsymbol{\phi}^{(2)}, \tag{35}$$

$$H \cdot D \cdot \mathbf{S}^{(1)} \cdot \boldsymbol{\phi}^{(1)} = \mathbf{S}^{(2)} \cdot \boldsymbol{\phi}^{(2)}, \tag{36}$$

where $\mathbf{Q}^{(i)}$, $\mathbf{S}^{(i)}$ are $\{(M+1),\ (M+1)(1+N^{(i)})\}$ matrices, $i = 1, 2$.

By expressing $\phi^{(1)}_{m,N^{(1)}}$ and $\phi^{(2)}_{m,N^{(2)}}$, $m = 0, 1, \ldots, M$, using the system (35)–(36) and substituting in the system (32), we arrive finally at the system of $1 + (M+1)(N^{(1)} + N^{(2)} - 2)$ linear ODEs:

$$\mathbf{A} \frac{d\boldsymbol{\phi}}{d\tau} = (\mathbf{B}^{(c)} + \mathbf{B}^{(d)} + \mathbf{B}^{(r)}) \cdot \boldsymbol{\phi} + \mathbf{b}. \tag{37}$$

The constant matrices $\mathbf{B}^{(c)}$, $\mathbf{B}^{(d)}$ and $\mathbf{B}^{(r)}$ correspond respectively to the convective, diffusive and reactive terms in the original equation (9), b is an $\{1 + (M+1)(N^{(1)} + N^{(2)} - 2)\}$ constant vector and $\boldsymbol{\phi}$ (τ) is the vector of unknown functions

$$\boldsymbol{\phi} \equiv (\alpha_0,\ \phi^{(1)}_{0,1}, \ldots \phi^{(1)}_{0,N^{(1)}-1},\ \phi^{(2)}_{0,1}, \ldots \phi^{(2)}_{0,N^{(2)}-1}, \ldots \phi^{(1)}_{M,1}, \ldots \phi^{(1)}_{M,N^{(1)}-1},\ \phi^{(2)}_{M,1}, \ldots \phi^{(2)}_{M,N^{(2)}-1})^T \tag{38}$$

and not simply a concatenation of vectors $\boldsymbol{\phi}^{(1)}$ and $\boldsymbol{\phi}^{(2)}$.

The matrices $\mathbf{A}$, $\mathbf{B}^{(d)}$ and $\mathbf{B}^{(r)}$ are block–diagonal. They all have M+1 nonzero square $\{N^{(1)}+N^{(2)}-2\ ,\ N^{(1)}+N^{(2)}-2)\}$ matrices on their main diagonals and their first $1+(N^{(1)}+N^{(2)}-2)$ elements in the first row and the first column are nonzero.

The matrices $\mathbf{B}^{(c)}$ that result from transforming the convective terms also have block structure with the same block sizes. However, they are no longer block-diagonal and the amount of nonzero block-diagonals depends on the velocity fields $\mathbf{v}^{(i)}$, $i = 1, 2$. The higher the degree of λ that is involved in the velocity field expressions, the greater the coupling between the radial functions of different orders will be. And the increase of the order of this coupling leads to the corresponding increase of the number of nonzero block diagonals in $\mathbf{B}^{(c)}$.

For the Hadamard – Rybczinsky field, for example, these matrices will be block-tridiagonal, and for the velocity field in [15] valid for higher Reynolds numbers, block-pentadiagonal.

The discontinuous initial conditions (14) are not appropriate for computations. Instead we used the analytical solution for the pure diffusion case (no convection, no chemical reaction) derived in [16]. The concentration distributions for very small time values were expanded over our basis functions $T_{2n-2}(\tau)$ and Z_n, $n = 1, 2, \ldots$ to initialize the computations, and the coefficients obtained were used as initial conditions for $\alpha_0(\tau)$, $\phi^{(1)}_{m,n_1}$, and $\phi^{(2)}_{m,n_2}$, $m = 0, 1, \ldots, M$, $n_1 = 1, 2, \ldots, N^{(1)} - 1$, $n_2 = 1, 2, \ldots, N^{(2)} - 1$.

For time discretization of the system (37) we use the first-order backward Euler method. Defining $\boldsymbol{\phi}^n$ as vector $\boldsymbol{\phi}$ at the n-th time step of magnitude $\Delta\tau$ and

$$\mathbf{B} = \mathbf{B}^{(c)} + \mathbf{B}^{(d)} + \mathbf{B}^{(r)}, \tag{39}$$

system (37) can be rewritten as

$$(\mathbf{A} - \Delta\tau\mathbf{B}) \cdot \Delta\boldsymbol{\phi}^{n+1} = \Delta\tau\mathbf{B} \cdot \boldsymbol{\phi}^n + \Delta\tau\mathbf{b}\,, \tag{40}$$

where

$$\Delta\phi^{n+1} = \phi^{n+1} - \phi^n . \tag{41}$$

Every time step system of linear equations (40) was solved by regular Gauss elimination (preceded by LU decomposition) with the following iterative refinement [3]. The matrix on the left side of (40) has the same structure as matrix B; as mentioned above, it is block-tridiagonal for the Hadamard-Rybczinsky velocity field. Our attempts to apply block-elimination methods (in particular, block Thomas algorithm [4]) failed presumably because block LU factorization does not involve pivoting which is essential when diagonal dominance does not occur (which is the case for high Peclet numbers).

We considered the matrix on the left side of (40) as a banded one with bandwidth $1 + 3(N^{(1)} + N^{(2)} - 2)$.

As long as this matrix depends on the time step and its factorization is a time-consuming process, only two values of the time step were used for each run. A smaller one was used for an initial time period and an another one for the subsequent time range.

The numbers of terms in series (15), (19), and (24) depend on the steepness of the concentration gradients and were different for different values of Peclet and Damköhler numbers. The maximum numbers used were $M = 87$, $N^{(1)} = 25$, $N^{(2)} = 97$.

As is well known [1, 2], an increase in the number of terms in a spectral series (especially in the series in Chebyshev polynomials) leads to very high condition numbers for the resulting system of linear equations. This was alleviated by using double precision in all computations and, as mentioned above by application of the iterative refinement to the solution obtained with the Gauss elimination procedure.

QUANTITIES OF INTEREST

The most practically interesting quantity in extraction problems is the amount of material extracted by particular instant in time. For the problem under consideration (i.e. when species are extracted from the droplet) this can be conveniently characterized by the time-dependent average dimensionless concentration of species remaining in the drop:

$$\overline{c}^{(1)} = \frac{3}{2} \cdot \int_0^1 \int_{-1}^1 r^2 c^{(1)}(\tau, \lambda, r)\, d\lambda\, dr \tag{42}$$

This quantity changes in time as a result of mass transfer out of the droplet. The local and surface average rates of this transfer are characterized by corresponding mass transfer coefficient, the quantities which when multiplied by the driving force give respective mass flux rate. The nondimensional mass transfer coefficient is usually referred to as the "Sherwood number" which is analogous to the Nusselt number in heat transfer problems.

Different kinds of Sherwood number can be introduced, depending on the driving force upon which it is based and the domain to which it is related.

For the problem of single-drop extraction, the instantaneous driving force for mass transfer is the difference between the concentration of the transferring species in the droplet and that far away from it, taking into account the step change of the concentration at the interface due to solubility,

$$F^{(\mathrm{dr})} = \overline{\tilde{c}}^{(1)} - H\tilde{c}_\infty , \tag{43}$$

where $\overline{\tilde{c}}^{(1)}$ is the dimensional average concentration of species in the droplet.

Often the Sherwood number is based on the maximum possible (or in our case, initial) driving force:

$$F_0^{(\mathrm{dr})} = \tilde{c}_0 - H\tilde{c}_\infty \,. \tag{44}$$

Here we consider only the external Sherwood number, i.e., the nondimensional rate of transfer of species from the external side of droplet surface into the external flow.

The local and average Sherwood numbers defined on the basis of maximal driving force are respectively:

$$Sh_{\mathrm{loc},0} = -2H \cdot D \left.\frac{\partial c^{(2)}}{\partial r}\right|_{r=1} \tag{45}$$

and

$$Sh_0 = -H \cdot D \int_{-1}^{1} \left.\frac{\partial c^{(2)}}{\partial r}\right|_{r=1} d\lambda \,. \tag{46}$$

Corresponding values based on instantaneous driving force are:

$$Sh_{\mathrm{loc}} = \frac{Sh_{\mathrm{loc},0}}{\overline{c}^{(1)} + \tilde{c}_\infty H / F_0^{(\mathrm{dr})}} \,, \tag{47}$$

$$Sh = \frac{Sh_0}{\overline{c}^{(1)} + \tilde{c}_\infty H / F_0^{(\mathrm{dr})}} \,. \tag{48}$$

Obviously, the chemical reaction in the external region increases the rate of the extraction, and this increase is characterized by the enhancement factor, which is the ratio of the corresponding mass transfer rates [5]:

$$E = \frac{Sh(Da_{II}^{(2)} \neq 0)}{Sh(Da_{II}^{(2)} = 0)} \tag{49}$$

COMPUTATIONAL RESULTS AND DISCUSSION

The results of the computations presented cover the following ranges of parameters:

$$0.25 \leq D \leq 4 \,,$$
$$0 \leq Pe^{(2)} \leq 500 \,,$$
$$0 \leq Da_{II}^{(2)} \leq 1000 \,,$$
$$H = \mu = 1 \,.$$

The characteristic time scale was chosen as

$$\tau_* = \tau_{\mathrm{diff}}^{(2)} \,, \tag{50}$$

which is just the Fourier number based on the diffusion coefficient of the external fluid. The times appearing on the plots are expressed in these units. The values of Peclet number Pe and Damköhler number Da presented on the plots correspond to $Pe^{(2)}$ and $Da_{II}^{(2)}$, respectively.

To illustrate qualitively the process of pure mass transfer (no reaction) from the droplet we present in Figures 1–3 the curves of constant species concentration at different times for various levels of external convection ($Pe^{(2)} = 10, 200, 500$ respectively).

The well known and intuitively expected increase of mass transfer with increasing convection is apparent.

The influence of internal circulation on the development of the mass transfer process is illustrated in Figures 4–5 where we present the isoconcentration curves for the same external Peclet number ($Pe^{(2)} = 500$) and different ratios of internal and external diffusivities ($D = 0.25$ and $D = 4.0$).

For $D = 0.25$ the internal convection is much stronger in the sense that the value of $Pe^{(1)}$ is larger. As a consequence the isoconcentration curves inside the droplet lie close to the internal streamlines, a result already obtained numerically by Johns and Beckmann [7], for the special case of mass transfer resistance solely inside the droplet. The coincidence of internal isocontours with internal streamlines also constituted the basic assumption of Kronig and Brink's model of mass transfer in a circulating drop [6]. From a simple comparison of the isocontour levels in Figures 4 and 5 alone one infers that the mass transfer from a droplet for D=4 is much more intensive than for D=0.25. The reason that the *internal* Peclet number $Pe^{(1)}$ is greater for $D = 0.25$ is not that the internal circulation is greater, for it is not ($\mu = 1$), but that the internal diffusivity is smaller. Nonetheless, it is customary for brevity to describe an increase in Peclet number as an increase in convection, rather than the more lengthy but more accurate increase of the ratio of convection to diffusion. In this usage, one may phrase the conclusion drawn from Figures 1–5 as follows: convection outside the droplet increases the rate of extraction but inside convection supresses the rate of transfer.

The influence of the external reaction rate on the concentration distribution is shown on Figures 2, 6 and 7. As could have easily been anticipated, an increase in $Da_{II}^{(2)}$ results in faster extraction and an almost immediate disappearence of extracted species outside the droplet (almost no species here for $Da_{II}^{(2)} = 100$ in Figure 7).

Figures 8 and 9 show the effect of reaction rate on the local Sherwood number. The values of $Sh_{\mathrm{loc},0}$ go to zero with time for all values of angle variable ϑ, although the distribution of Sherwood number based on the instantaneous driving force approaches a nonvanishing asymptote. An increase in the reaction rate thus results in a general increase of mass transfer and of values of the Sherwood numbers, but the temporal variation of values of local Sherwood numbers at different locations is less transparent, warranting further investigation.

Figure 10 reflects the behavior of average Sherwood number Sh in time for different values of external Peclet number $Pe^{(2)}$ for the no reaction case. The oscillations of Sh were computationally obtained by different investigators including mentioned above Johns and Beckmann's article [7] and Oliver and Chung in [9], who were solving conjugate unsteady heat trasfer problem which is mathematically analogous to the mass tranfer problem under consideration when there is no chemical reaction involved. These oscillations are caused by the internal circulation with the most detailed physical explanation given by Brignell in [8]. Consequently the period of these oscillations is smaller and the amplitute greater the higher the Peclet number is. The stronger convection also leads to a higher mass transfer rate as it creates the thinner diffusion boundary layers on the both sides of the droplet surface.

Figure 11 illustrates the influence of the rate of external chemical reaction on the average Sherwood number. The plots here confirm the made above conclusions of the increase of the rate of extraction with the increasing external convection and rate of external chemical reaction.

In more evident way this is reflected in Figure 12, where the decrease of average droplet

concentration with time is presented. From this picture we can also deduce a very important conclusion that an increase in the reaction rate over some value will not benefit the extraction results (the diffences between the average droplet concentration for $Da_{II}^{(2)}$ values of 300 and 1000 are pretty small).

Figure 13 shows the effect of reaction rates on the values and time behavior of the enhancement factor E. The oscillations here are the consequeces of the internal circulation, the same as for corresponding average Sherwood number on Figure 10. The values of E corresponding to the same reaction rate are higher for smaller $Pe^{(2)}$ (lower convection). The possible explanation for that could be that the corresponding values of $Da_I^{(2)}$ which are just the ratios of $Da_{II}^{(2)}$ and $Pe^{(2)}$ are smaller for higher $Pe^{(2)}$.

Finally, we wanted to underline that the purpose of this article was to present the developed numerical algorithm and to show what kind of results can be obtained. Our further articles will include additional results and more detailed analysis of those results as well as of the results presented in this article.

NOMENCLATURE

$\tilde{c}_0$ -dimensional value of the concentration in the origin of the droplet at $t = 0$

$\tilde{c}_\infty$ -dimensional value of the concentration at the infinity

$\tilde{c}^{(i)}$ -dimensional concentration in the i-th domain, $i = 1, 2$

$c^{(i)}$ -dimensionless concentration in the i-th domain, $i = 1, 2$

$D^{(i)}$ -molecular diffusivity of the solute in the fluid in the i-th domain, $i = 1, 2$

D -molecular diffusivities ratio, $D^{(1)}/D^{(2)}$

$Da_I^{(i)}$ -first Damköhler number in the i-th domain , $\dfrac{k^{(i)} R}{f^{(i)}(\mu) U_\infty}$, $i = 1, 2$

$Da_{II}^{(i)}$ -second Damköhler number in the i-th domain, $\dfrac{k^{(i)} R^2}{D^{(i)}}$, $i = 1, 2$

E -enhancement factor

$f^{(i)}$ -factor showing the leading viscosity ratio dependence of the velocity scale in the i-th domain, $i = 1, 2$

H -distribution coefficient

$k^{(i)}$ -chemical reaction rate constant in the i-th domain, $i = 1, 2$

M -highest order of the Legendre polynomials used in the expansion in the angular direction

$N^{(i)}$ -number of terms in the expansion of radial functions in the i-th domain , $i = 1, 2$

$Pe^{(i)}$ -Peclet number in the i-th domain, $\dfrac{2 U_\infty R}{D^{(i)}}$, $i = 1, 2$

r -dimensionless radial coordinate

R -droplet radius

t -dimensional time

$U_*^{(i)}$ -characteristic velocity scale in the i-th domain, $i = 1, 2$

U_∞ -velocity of the flow at the infinity

$\mathbf{v}^{(i)}$ -velocity field in the i-th domain nondimensionalized by the corresponding velocity scale $U_*^{(i)}$, $i = 1, 2$

ϑ -polar angle in spherical coordinate system

λ $= \cos\vartheta$

μ -molecular viscosities ratio, $\mu^{(1)}/\mu^{(2)}$

$\mu^{(i)}$ -molecular viscosity of the fluid in the i-th domain, $i = 1, 2$

τ -dimensionless time

$\tau_{\text{conv}}^{(i)}$ -convection time scale in the i-th domain, $\dfrac{R}{f^{(i)}(\mu) U_\infty}$, $i = 1, 2$

$\tau_{\text{diff}}^{(i)}$ -diffusion time scale in the i-th domain, $\dfrac{R^2}{D^{(i)}}$, $i = 1, 2$

$\tau_{\text{rxn}}^{(i)}$ -chemical reaction time scale in the i-th domain, $\dfrac{1}{k^{(i)}}$, $i = 1, 2$

REFERENCES

[1] J. P. Boyd, *Chebyshev and Fourier Spectral Methods*, Springer–Verlag, 1989.

[2] C. Canuto, M. Y. Hussaini, A. Quarteroni, *Spectral Methods in Fluid Dynamics*, Springer–Verlag, 1988.

[3] G. H. Golub and C. F. Van Loan, *Matrix Computations*, Johns Hopkins University Press, 1989.

[4] C. A. J. Fletcher, *Computational Techniques for Fluid Dynamics*, Springer–Verlag, 1988.

[5] R.B. Bird, W. E. Stewart, E. N. Lightfoot, *Transport Phenomena*, John Wiley & Sons, 1966

[6] R. R. Kronig and J. C. Brink, On the theory of extraction from falling droplets, *Appl. Sci. Res.*, **A2**, 142-155, 1950

[7] L. E. Johns, Jr and R. B Beckmann, Mechanism of dispersed-phase mass transfer in viscous, single-drop extraction systems, *A.I.Ch.E. Jl* **12**, 10-16, 1966

[8] A. S. Brignell, Solute extraction from an internally circulating spherical liquid drop, *Int. J. Heat Mass Transfer* **18**, 61-68, 1975

[9] D. L. R. Oliver, J. N. Chung, Conjugate unsteady heat transfer from a spherical droplet at low Reynolds numbers, Int. J. Heat Mass Transfer **29**, 879-887, 1986

[10] P. R. Spalart, A spectral method for external viscous flows, *Contemporary mathematics*, **28**, 315-335, 1984

[11] C. E. Grosch, S. A. Orszag, Numerical solution of problems in unbounded regions: coordinate transforms, *J. of Comput. Phys.*, **25**, 273-296, 1977

[12] B. Fornberg, A numerical study of steady viscous flow past a circular cylinder, *J. Fluid Mech.*, **98**, 819-855, 1980

[13] A. T. Patera, A spectral element method for fluid dynamics: laminar flow in a channel expansion, *J. of Comput. Phys.*, **54**, 468-488, 1984

[14] D. Gottlieb, S. A. Orszag, *Numerical Analysis of Spectral Methods*, SIAM, 1977

[15] A. E. Hamielec, A. I. Johnson, Viscous flow around fluid spheres at intermediate Reynolds numbers, *Can. J. Chem. Engng.*, **40**, 2, 41, 1962

[16] F. Cooper, Heat transfer from a sphere to an infinite medium, *Int. J. Heat Mass Transfer*, **20**, 991-993, 1977

Table 1: Coefficients in eq.(1) depending on the choice of τ_* $(i, j = 1, 2)$

τ_*	$K_c^{(i)}$	$K_d^{(i)}$	$K_r^{(i)}$
$\tau_{\text{diff}}^{(j)}$	$\frac{Pe^{(i)}}{2} \cdot \frac{D^{(i)}}{D^{(j)}}$	$\frac{D^{(i)}}{D^{(j)}}$	$Da_{II}^{(i)} \cdot \frac{D^{(i)}}{D^{(j)}}$
$\tau_{\text{conv}}^{(j)}$	$\frac{f^{(i)}(\mu)}{f^{(j)}(\mu)}$	$\frac{2}{Pe^{(i)}} \cdot \frac{f^{(i)}(\mu)}{f^{(j)}(\mu)}$	$Da_{I}^{(i)} \cdot \frac{f^{(i)}(\mu)}{f^{(j)}(\mu)}$
$\tau_{\text{rxn}}^{(j)}$	$\frac{1}{Da_{I}^{(i)}} \cdot \frac{k^{(i)}}{k^{(j)}}$	$\frac{1}{Da_{II}^{(i)}} \cdot \frac{k^{(i)}}{k^{(j)}}$	$\frac{k^{(i)}}{k^{(j)}}$

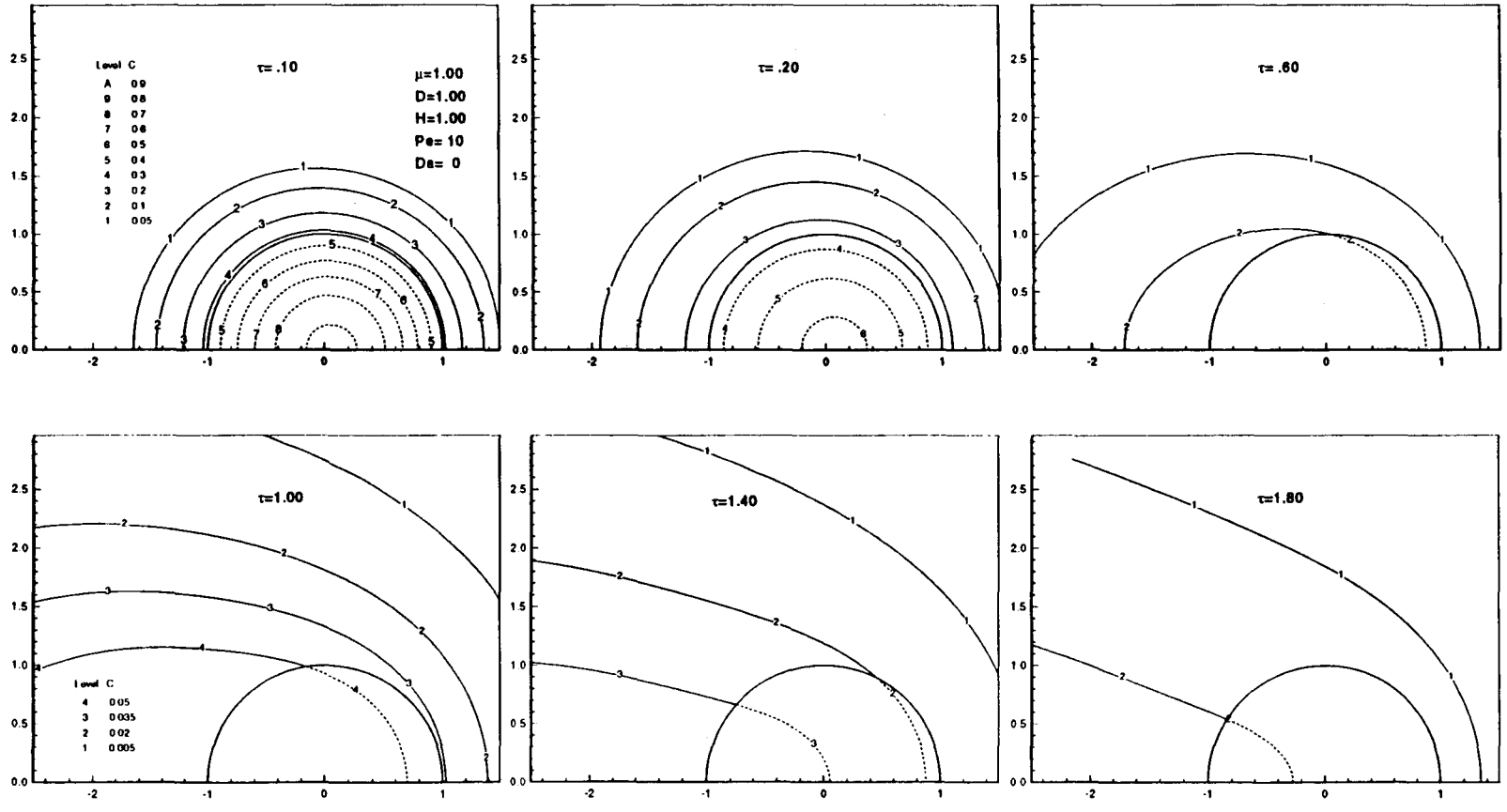

Fig. 1 Isoconcentration curves at different time moments for Pe=10

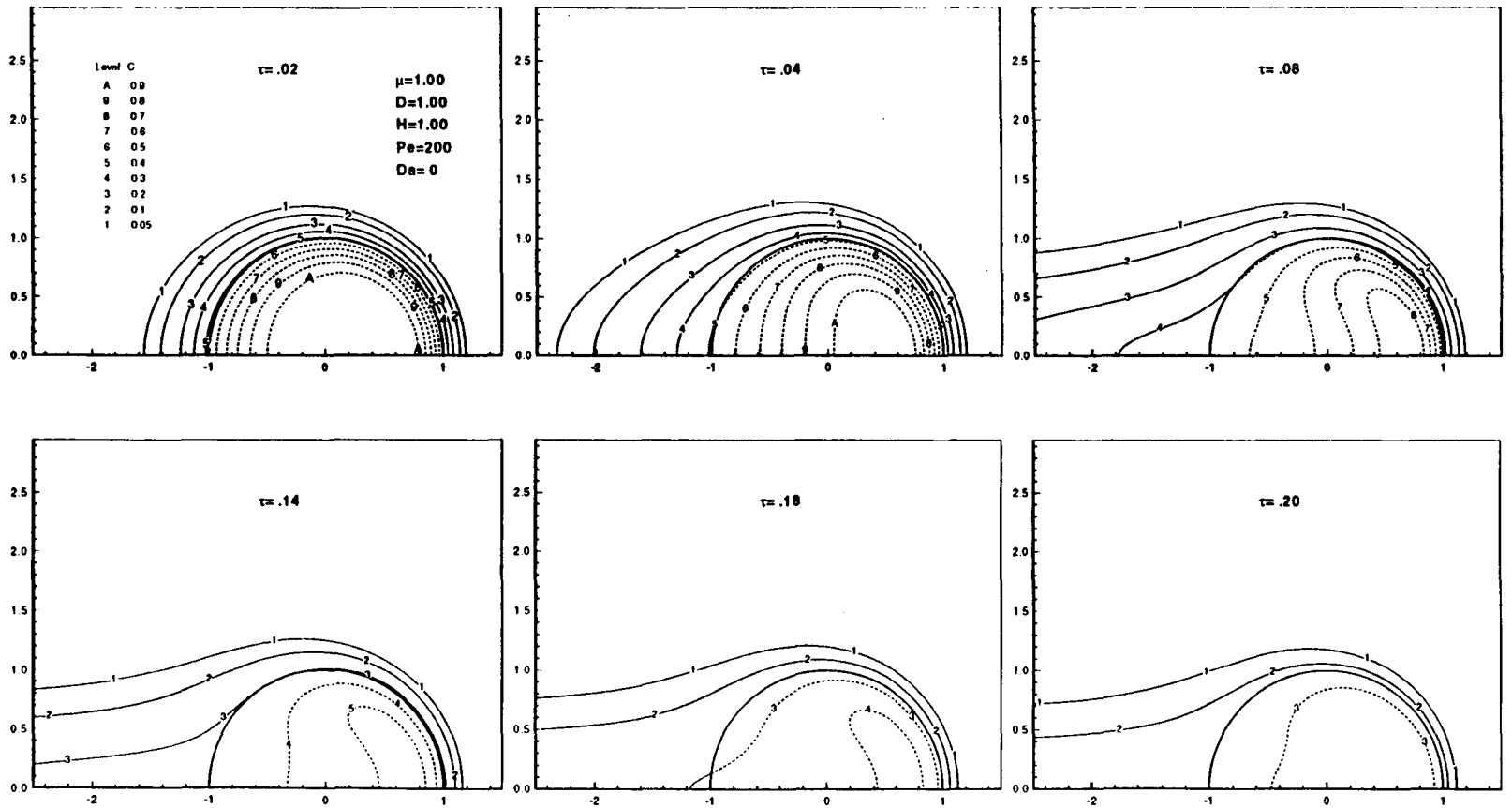

Fig. 2 Isoconcentration curves at different time moments for Pe=200

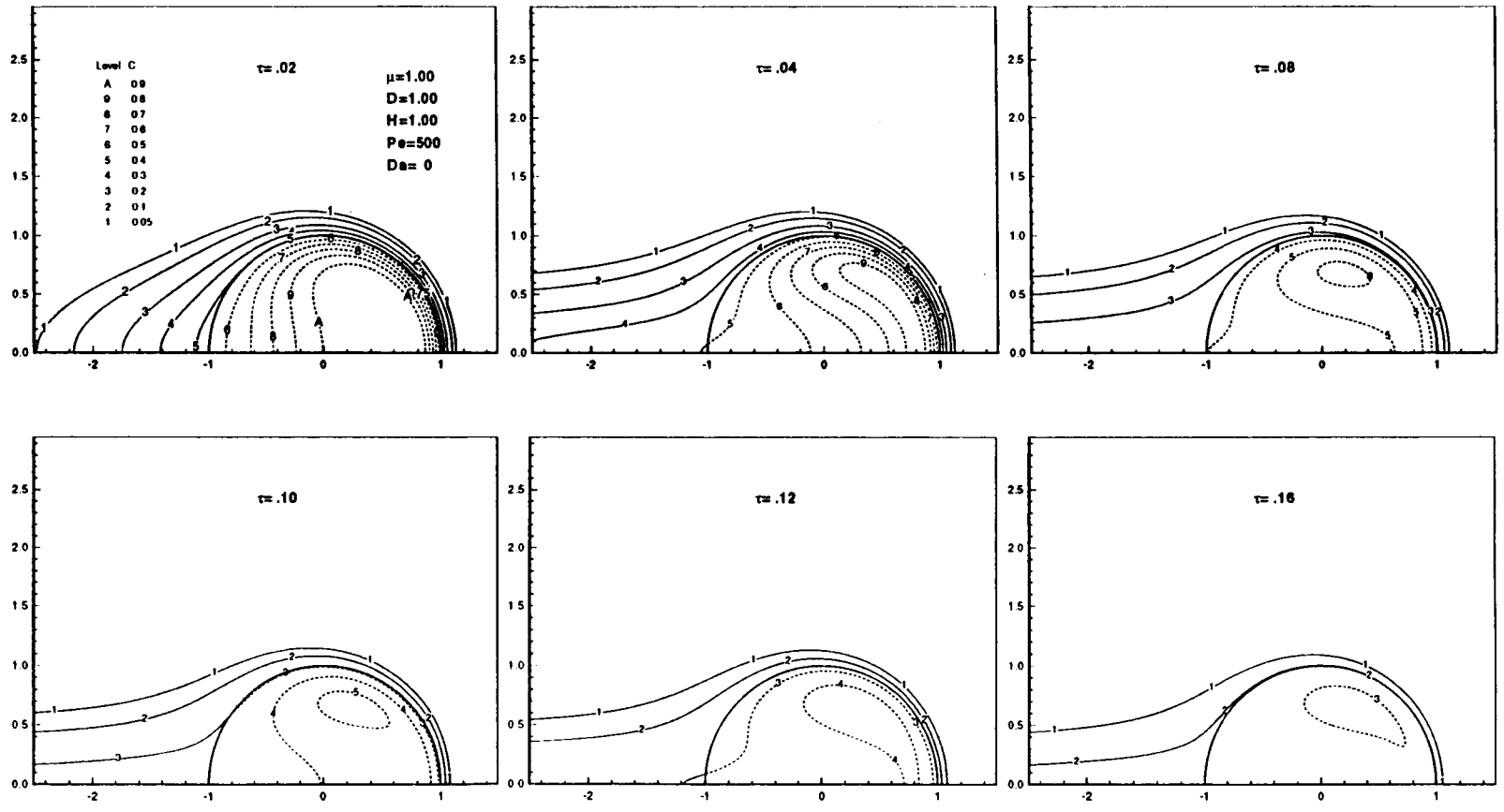

Fig. 3 Isoconcentration curves at different time moments for Pe=500

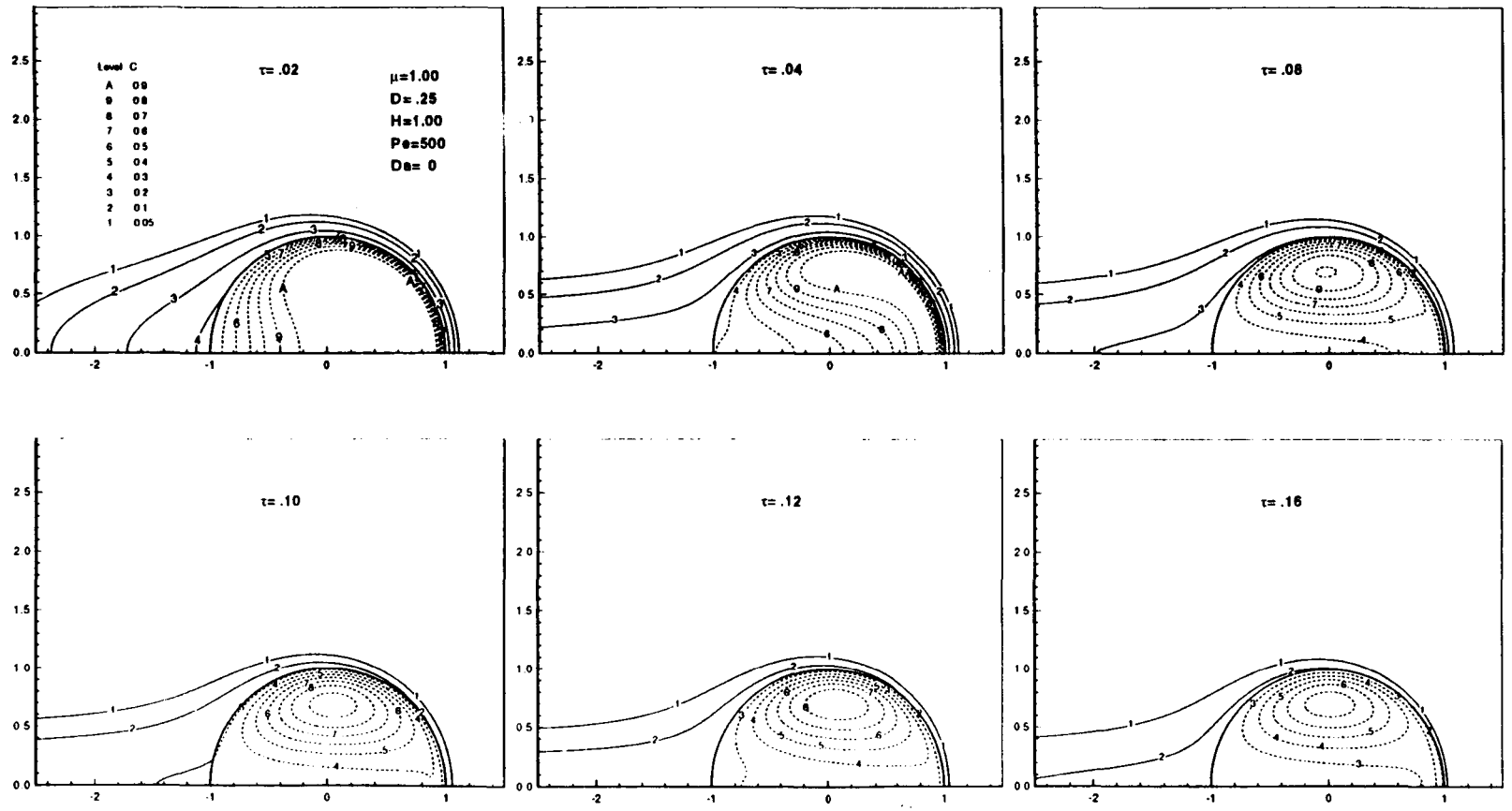

Fig. 4 Isoconcentration curves at different time moments for Pe=500 and D=.25

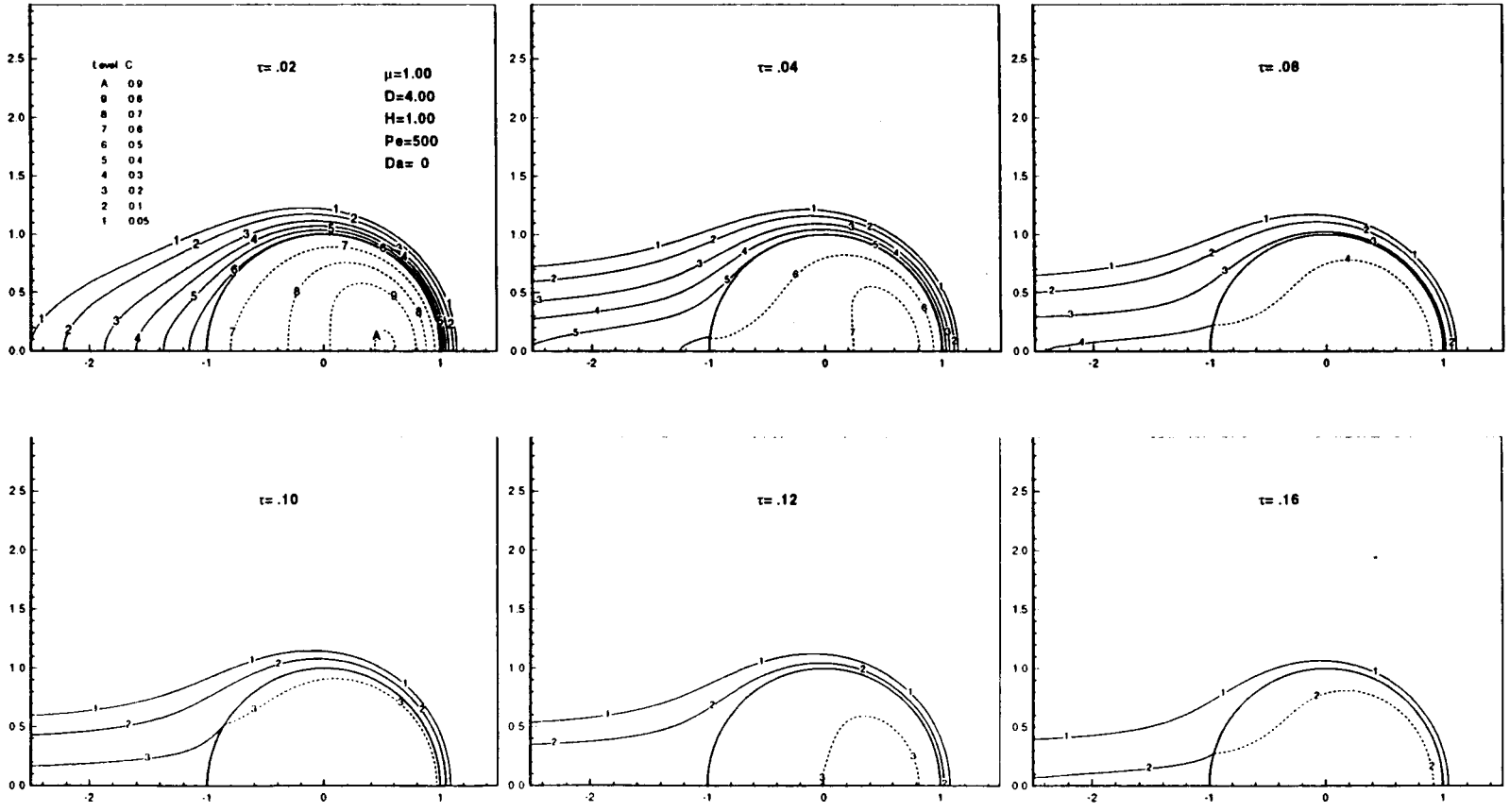

Fig. 5 Isoconcentration curves at different time moments for Pe=500 and D=4.0

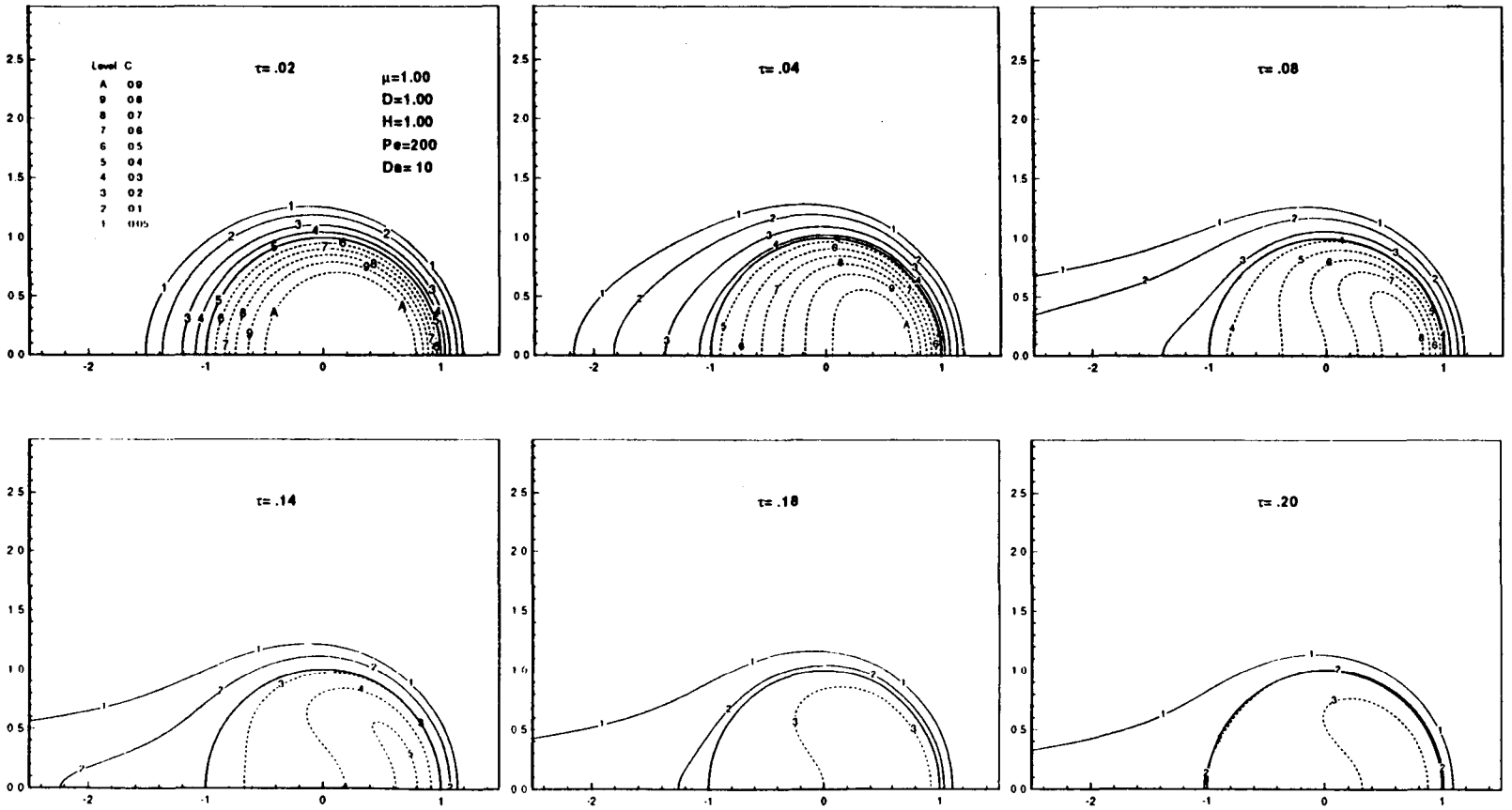

Fig. 6 Isoconcentration curves at different time moments for Pe=200 and Da=10

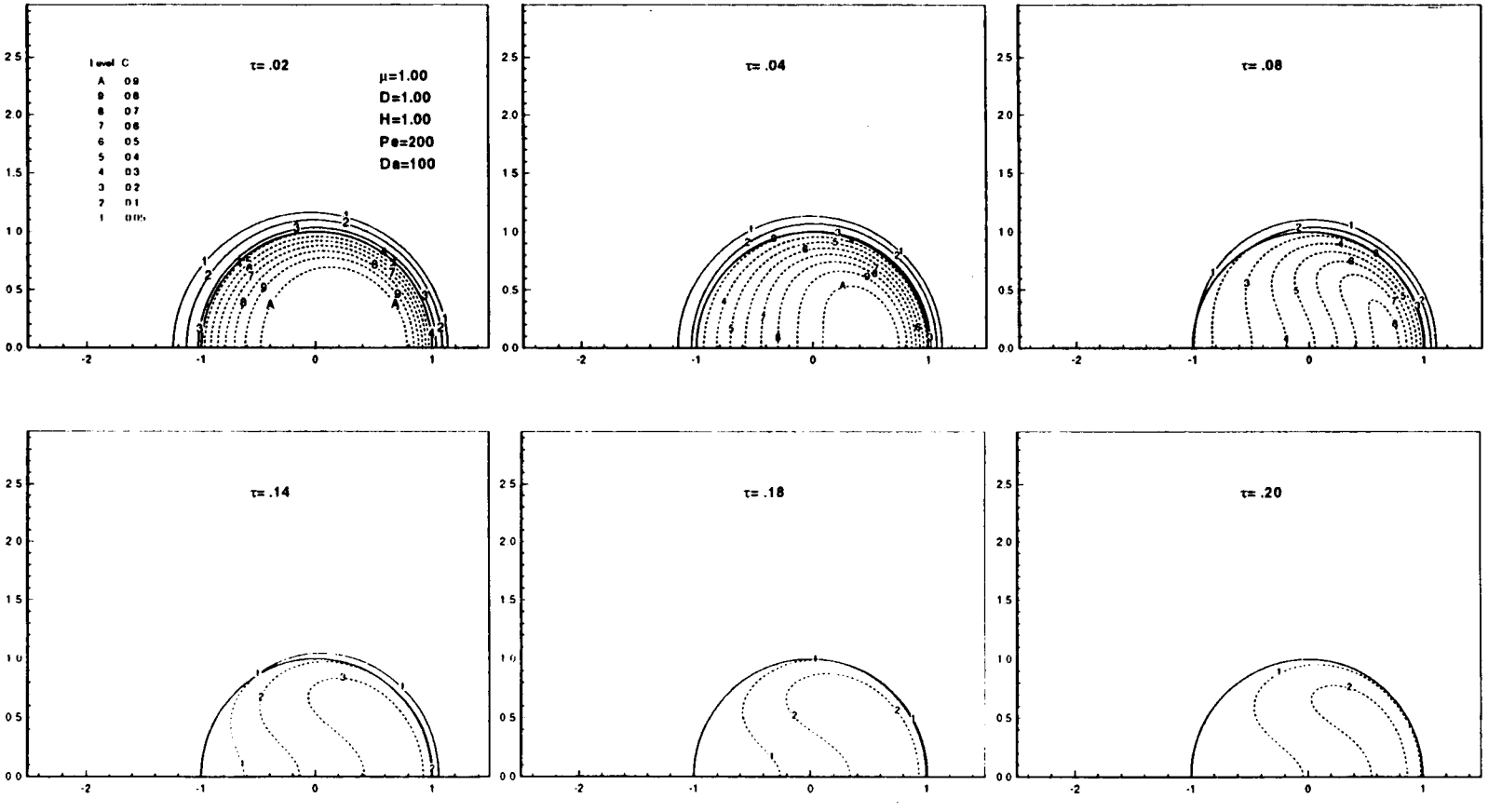

Fig. 7 Isoconcentration curves at different time moments for Pe=200 and Da=100

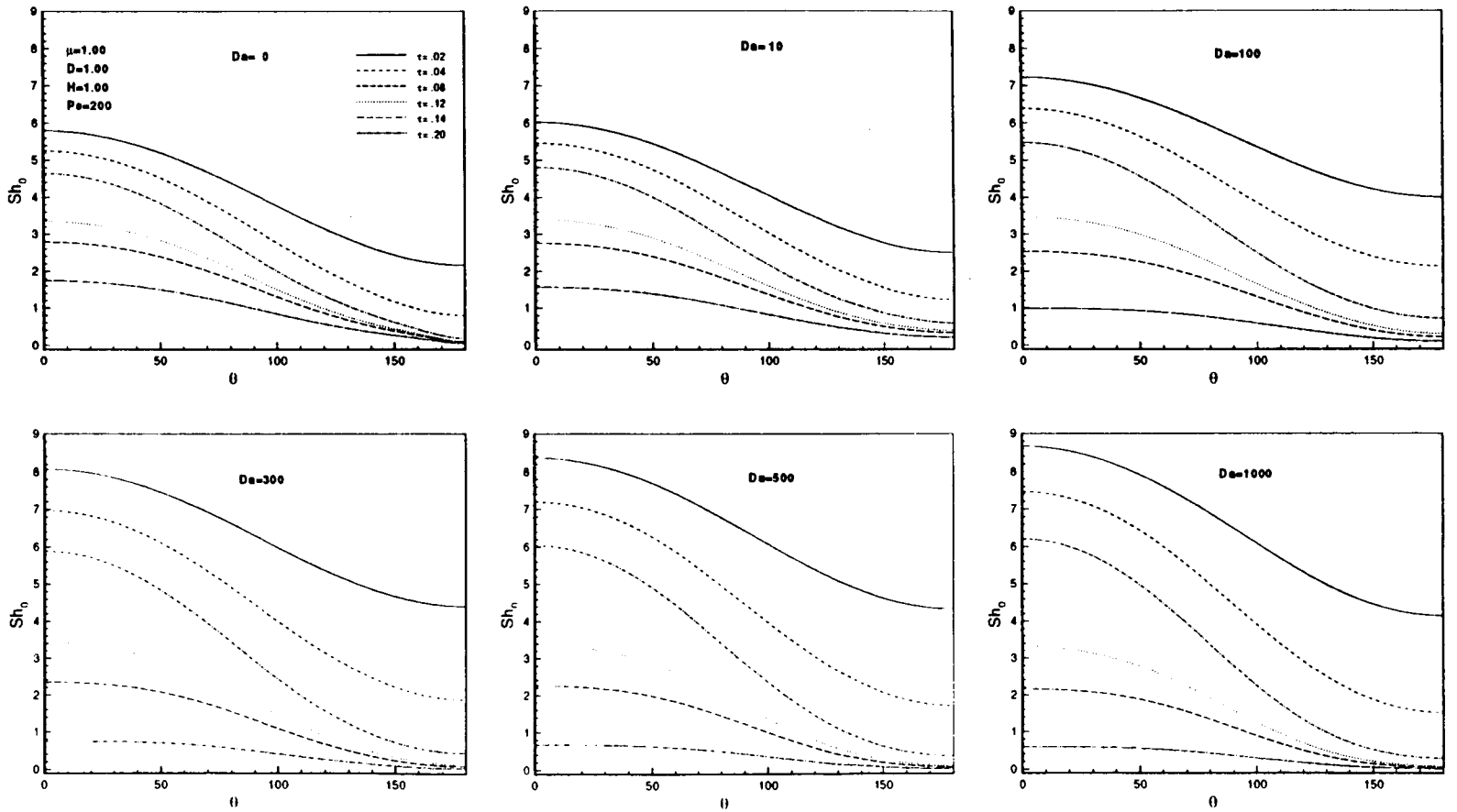

Fig. 8 Distribution of the values of local Sherwood number Sh_0 at Pe=200 for different values of Da

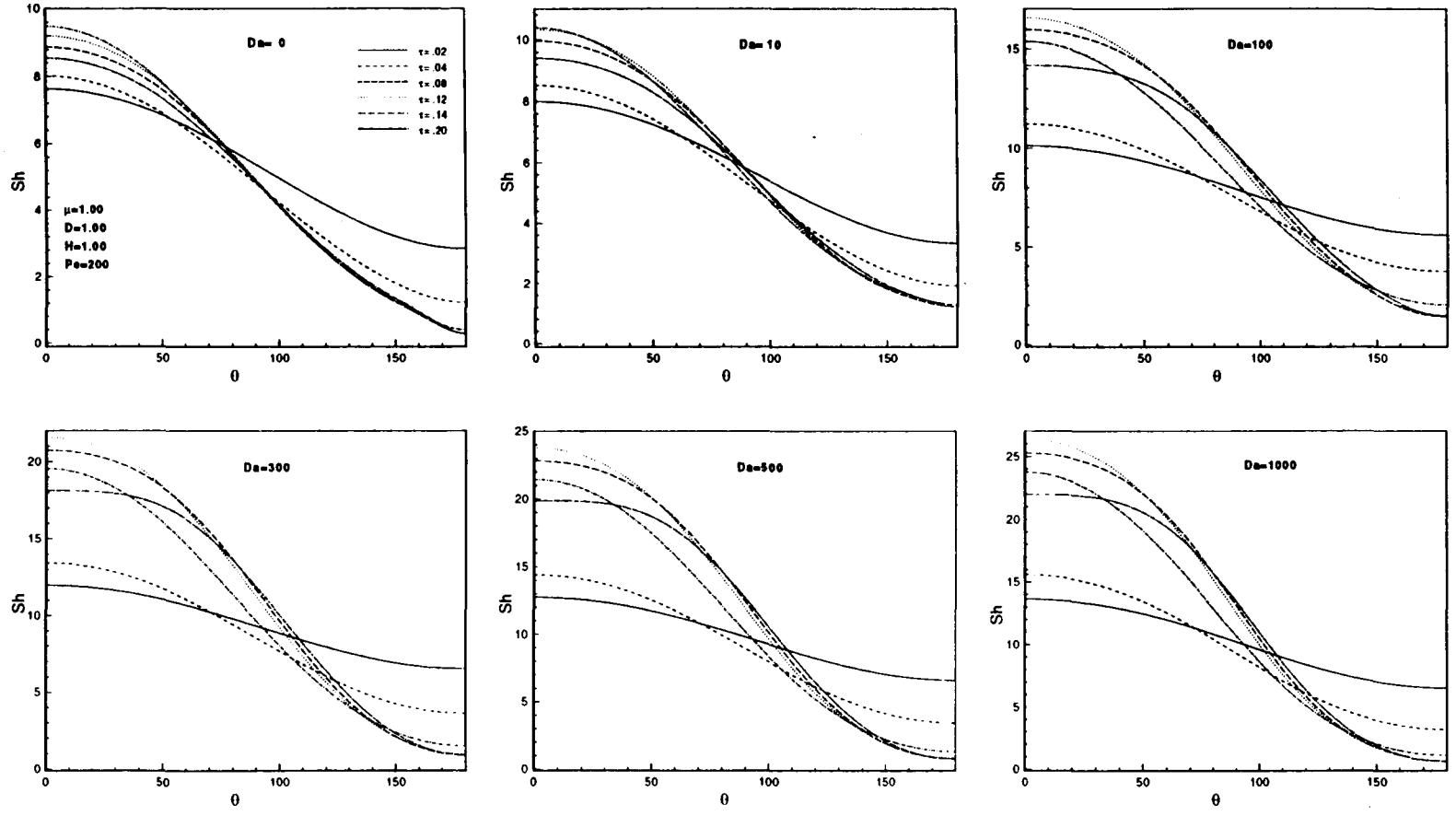

Fig. 9 Distribution of the values of local Sherwood number Sh at Pe=200 for different values of Da

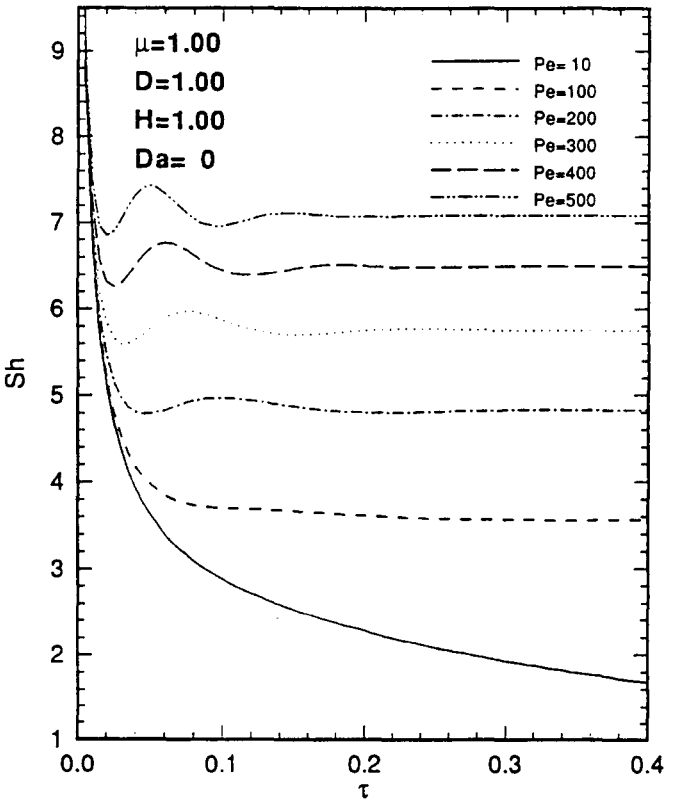

Fig. 10 Time evolution of average Sherwood number Sh for Da=0 at different values of Pe

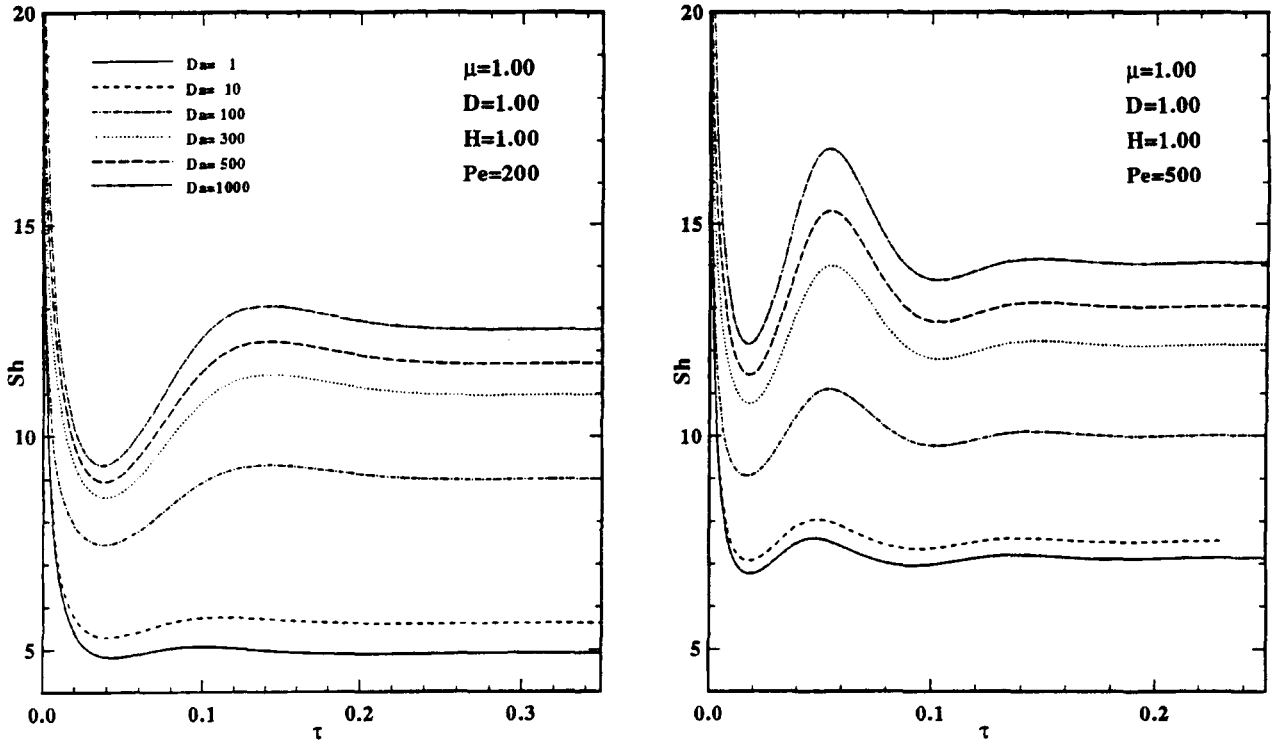

Fig. 11 Effect of reaction rate on average Sherwood number Sh for Pe=200 and Pe=500

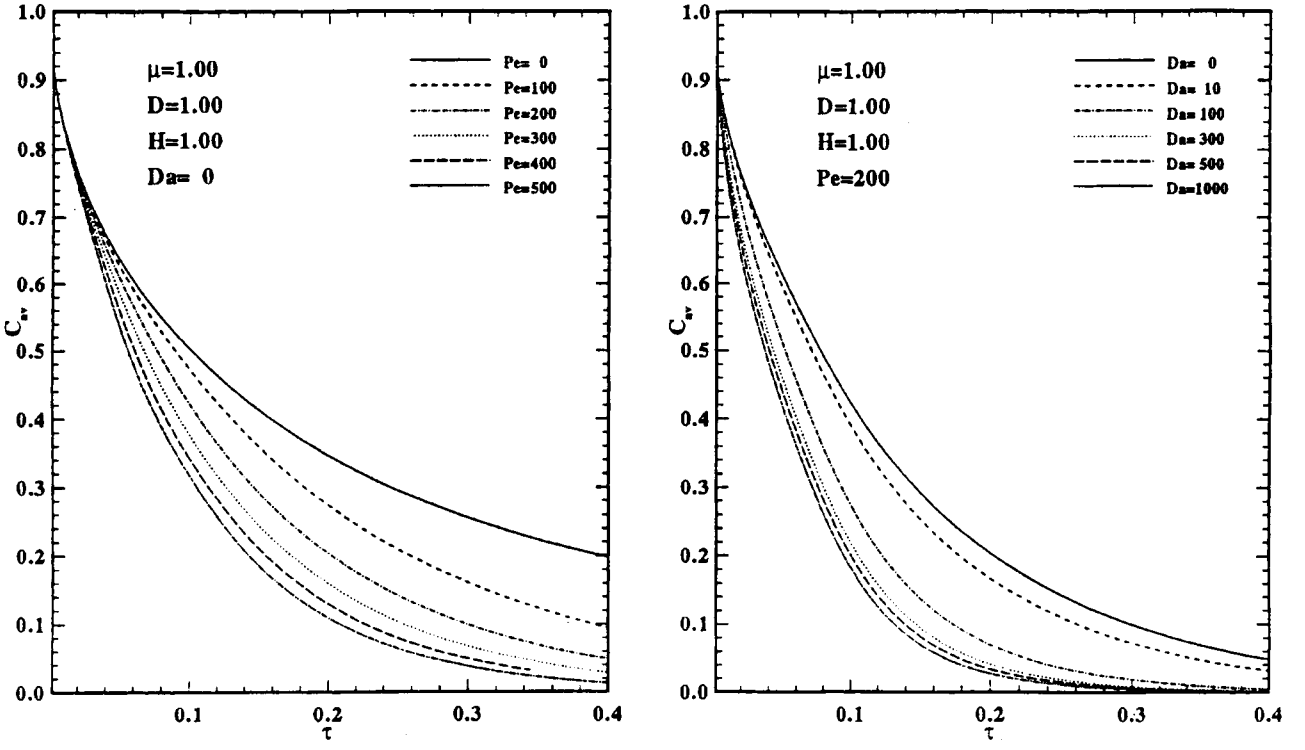

Fig. 12 Time evolution of average droplet concentration

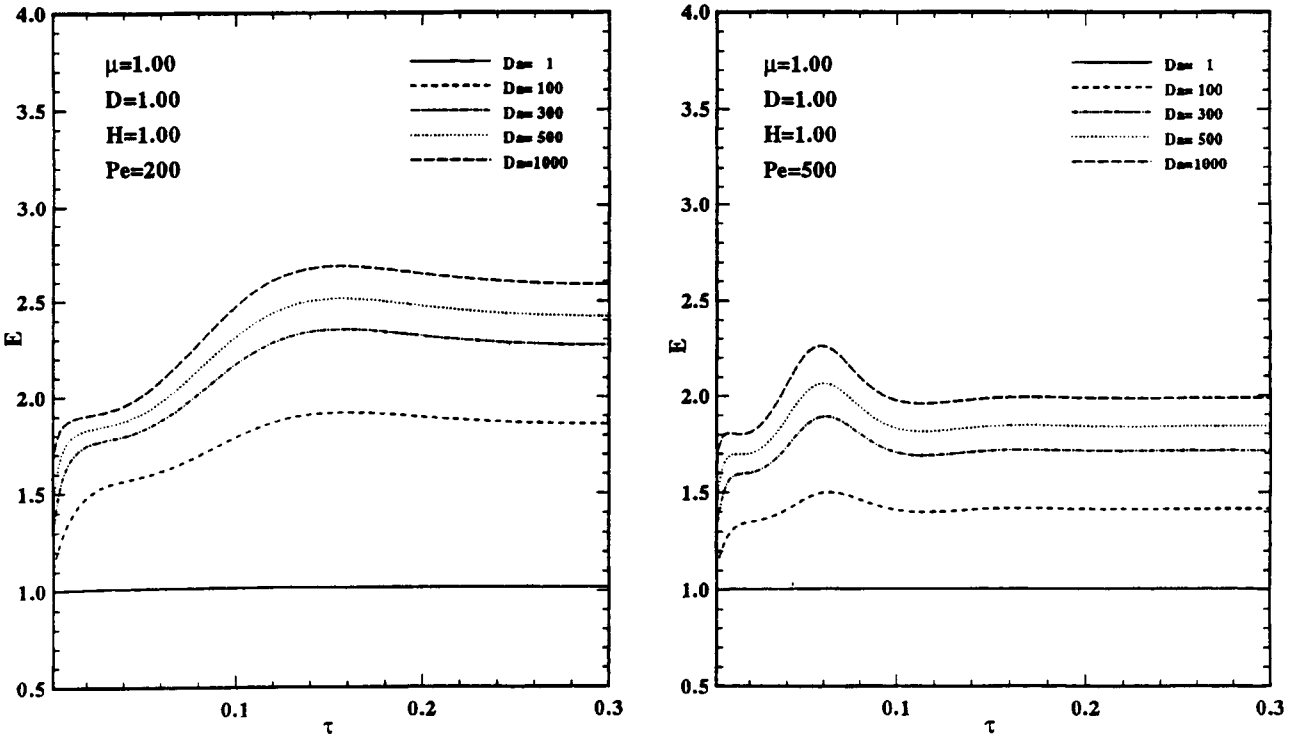

Fig. 13 Time evolution of the enhancement factor

A PROBABILSTIC MODEL OF A POROUS HEAT EXCHANGER

O.P. Agrawal and X.A. Lin
Department of Mechanical Engineering and Energy Processes
Southern Illinois University
Carbondale, Illinois

ABSTRACT

This paper presents a probabilistic one-dimensional finite element model for heat transfer processes in porous heat exchangers. The Galerkin approach is used to develop the finite element matrices. Some of the submatrices are asymmetric due to the presence of the flow term. The Neumann expansion is used to write the temperature distribution as a series of random variables, and the expectation operator is applied to obtain the mean and deviation statistics. To demonstrate the feasibility of the formulation, a one-dimensional model of heat transfer phenomenon in superfluid flow through a porous media is considered. Results of this formulation agree well with the Monte-Carlo simulations and the analytical solutions. Although the numerical experiments are confined to parametric random variables, a formulation is presented to account for the random spatial variations.

INTRODUCTION

Porous heat exchangers are key components in many engineering systems such as high performance regenerative heat exchangers, thermal energy storage systems, cryocoolers, and packed beds. Several techniques have been developed to analyze these systems. These techniques include, among others, analytical techniques, such as separation of variables [1,2], Riemann method [3] and similarity transformation [4]; semi-analytical techniques such as orthogonal collocation [5] and collocation-perturbation [6,7]; and numerical methods such as numerical integration [8], shooting and Runge-Kutta integration [9], and finite element methods [10]. In these techniques the above systems are considered as deterministic. That is, the problems are formulated in terms of mean-values of the properties neglecting variations in the mean values. Experimental measurements, however, show that the properties of the systems may vary significantly in a random fashion, especially near a low temperature. Given the stringent demand on the design of modern heat exchangers, these deterministic models may not be adequate.

Random properties can be incorporated in the above techniques using the probability theories and the theories of differential equations [11-14]. In many applications, it is difficult to solve the resulting differential equations in closed form even

when the randomness is not considered [15]. In the last 30 years, Finite Element Methods (FEMs) have successfully been applied to solve a large class of deterministic systems, and more recently, probabilistic systems. Current trends for analyzing random systems in engineering are given by Iyengar and Dash [16], Ibrahim [17], Shinozuka [18], and Benaroya and Rehak [19]. Chamis and coworkers [20, 21] have developed a general purpose finite element computer code called PICAN for probabilistic analysis of composite materials.

The numerical techniques available to solve problems consisting of random variables and functions may be broadly classified into two categories; statistical and nonstatistical. Most statistical techniques rely on numerical simulations among which Monte Carlo simulation has been widely used [22]. The nonstatistical techniques include perturbation methods [23-26], spectral decomposition methods [15, 27], and basis random variable methods [28, 29].

In addition to the FEMs, several investigators have used the Boundary Element Methods (BEMs). The random operator problems were analyzed by Ettouney et al. [30-32], and more recently by Manolis and Shaw [33]. Burczyński [34] employed the direct boundary element method to develop two distinct procedures for the treatment of random potential problems. Cheng and Lafe [35] employed the indirect boundary element method to obtain stochastic integral equations for boundary potentials and fluxes in terms of fictitious boundary sources. Other applications of the boundary element method include the first order perturbation method developed by Drewniak [36] for the analysis of heat conduction problems with random heat transfer and random heat conduction coefficient, respectively, and a procedure for the analysis of time dependent problems in the frequency domain developed by Burczyński and John [37].

The probabilistic methods discussed here, however, are largely confined to structural systems, and very little effort has been made to develop methods for porous heat exchangers. In this paper, a probabilistic one-dimensional finite element model for heat transfer process in porous heat exchangers is presented. The formulation is based on the Galerkin method, the spectral decomposition of random processes, and the Neumann expansion.

MATHEMATICAL FORMULATION

This section is divided into three parts: deterministic finite element model, probabilistic finite element models for parametric randomness and stochastic processes, and Monte-Carlo models. These models are considered next.

Deterministic Finite Element Model.- In order to develop a deterministic analytical model for the heat transfer process in fluid flow through porous media, consider the schematic of a one dimensional heat exchanger as shown in Figure 1. It is assumed that the system is stationary; that is, the system parameters are not

changing with time. Using energy balance, one can derive the following differential equations

$$k_f \frac{d^2T}{dx^2} + hs(t - T) = c\frac{dT}{dx} \tag{1}$$

$$k_s \frac{d^2t}{dx^2} + hs(T - t) = 0 \tag{2}$$

where k_f and k_s are the thermal conductivity coefficients of the fluid and the solid, h is the convective heat transfer coefficient, s is the porosity coefficient, T and t are the temperature distributions in the fluid and the solid, and the coefficient c accounts for the energy transfer due to fluid flow. In addition to these equations, the boundary conditions are also required. The formulation presented here is applicable to various boundary conditions. However, for simplicity, it is assumed that the terminal temperatures of the fluid and the solid at the two ends are prescribed. These conditions are written as

$$T(x = 0) = T_0, \quad t(x = 0) = t_0 \quad T(x = L) = T_L, \quad \text{and} \quad t(x = L) = t_L \tag{3}$$

where L is the length of the heat exchanger which is discretized into several finite elements. If N is the vector of the shape functions defined over the elements, then the temperatures T and t may be approximated as

$$T = N^T T_n \qquad \text{and} \qquad t = N^T t_n \tag{4}$$

where T_n and t_n represent the vector of the nodal temperatures of the fluid and the solid, and the superscript T represents the transpose. Observe that both solid and fluid regions have been discretized into an equal number of elements, and the same shape functions have been used for both temperature distributions. This is not necessary and a formulation that considers different numbern of elements and different shape functions is possible. Using the Galerkin approach, equations (1) and (2) may be written as

$$\int_0^L N \left[k_f \frac{d^2T}{dx^2} + hs(t - T) - c\frac{dT}{dx} \right] dx = 0 \tag{5}$$

$$\int_0^L N \left[k_s \frac{d^2t}{dx^2} + hs(T - t) \right] dx = 0 \tag{6}$$

Performing integration by parts on some terms of equations (5) and (6), and rearranging the terms, one obtains

$$E \begin{bmatrix} T_n \\ t_n \end{bmatrix} = \begin{bmatrix} b \end{bmatrix} \tag{7}$$

where E is the global coefficient matrix defined as

$$E = \begin{bmatrix} -k_f A - hsB - cC & hsB \\ hsB & -k_s A - hsB \end{bmatrix} \tag{8}$$

and vector b appears due to partial integration of some terms in Eq. (3) and the boundary conditions. Matrices A, B, and C in equation (8) are defined as

$$A = \int_0^L (\frac{dN}{dx})(\frac{dN}{dx})^T dx \tag{9}$$

$$B = \int_0^L N N^T dx \tag{10}$$

$$C = \int_0^L N(\frac{dN}{dx})^T dx \tag{11}$$

Equation (7) provides the desired deterministic finite element model. Observe that matrices A and B are symmetric positive definite finite element matrices, whereas matrix C is an asymmetric matrix. This makes matrix E asymmetric. Therefore, one should not use a symmetric simultaneous equation solver to solve equation (7).

Probabilistic Finite Element Model.- As stated earlier, two types of random behavior may appear in the system; parametric and spatial. These two random processes will be considered separately.

Parametric Randomness.- For simplicity, only k_s is considered as a random parameter. If other parameters also vary randomly, then the formulation can be extended appropriately. The random parameter k_s may be written as $k_s = k_{s0} + \epsilon$, where k_{s0} is the mean value of k_s, and ϵ represents the random variations with mean zero and standard deviation σ (i.e. $< \epsilon >= 0$, and $< \epsilon^2 >= \sigma^2$). Substituting the expression for k_s into Eq. (7), one obtains

$$[E_1 + \epsilon E_2] \begin{bmatrix} T_n \\ t_n \end{bmatrix} = b \tag{12}$$

where matrix E_1 is the same as matrix E in equation (8) except that k_s is replaced by k_{s0} and matrix E_2 is given as

$$E_2 = \begin{bmatrix} 0 & 0 \\ 0 & -A \end{bmatrix} \tag{13}$$

Observe that T_n and t_n are now vectors of random variables. Using the Neumann expansion, the temperature vector can be written as

$$\begin{bmatrix} T_n \\ t_n \end{bmatrix} = \left[I - \epsilon(E_1^{-1}E_2) + \epsilon^2(E_1^{-1}E_2)^2 - \epsilon^3(E_1^{-1}E_2)^3 + \cdots \right] E_1^{-1} b \tag{14}$$

provided that $||\epsilon(E_1^{-1}E_2)|| < 1$ is satisfied, which is reasonable for most practical systems. From equation (14), the expected value of the temperature vector is

$$< \begin{bmatrix} T_n \\ t_n \end{bmatrix} >= \left[I - < \epsilon > (E_1^{-1}E_2) + < \epsilon^2 > (E_1^{-1}E_2)^2 - < \epsilon^3 > (E_1^{-1}E_2)^3 + \cdots\right] E_1^{-1}b \tag{15}$$

where $<>$ is the expectation operator. Observe that $E_1^{-1}E_2$ is constant. Furthermore, given the probability distribution, $< \epsilon^i >$ $(i = 1, 2, \cdots,)$ can be computed numerically and in some cases analytically. Substituting these values in equation (15), the expected values of the temperatures can be obtained. Similarly, the second order characteristics of T_n and t_n can be obtained as follows:

$$< \begin{bmatrix} T_n^T & t_n^T \end{bmatrix} \begin{bmatrix} T_n \\ t_n \end{bmatrix} >=< b^T E_1^{-T} \left[I + \epsilon E_1^{-1}E_2\right]^{-T} \left[I + \epsilon E_1^{-1}E_2\right]^{-1} E_1^{-1}b > \tag{16}$$

Once again, the matrices containing ϵ in equation (16) can be expanded in Neumann series to obtain the covariance matrix for temperature distribution.

Equations (15) and (16) provide a probabilistic model for parametric randomness in k_s. A similar approach can be used for other random parameters.

Spatial Randomness.- Consider that k_s varies randomly from point to point along the length of the heat exchanger and that other properties are constant. k_s can be written as $k_s = k_{sm} + k_{sr}$, where k_{sm} represents the mean function and k_{sr} represents the stationary Gaussian process with zero mean functions and specified correlation function $R(x, u)$, which is symmetric and positive definite. Using the Karhunen-Loeve (KL) expansion, k_{sr} can be represented as [38]

$$k_{sr} = \sum_i \epsilon_i \phi_i(x) \tag{17}$$

where $\{\phi_i | i = 1, 2, \ldots\}$ is a set of orthogonal eigenfunctions of certain differential equations and ϵ_i $(i = 1, 2, \ldots)$ are uncorrelated random variables. These eigenfunctions satisfy the following integral equation

$$\lambda_i \phi_i(x) = \int_0^L R(x, u)\phi_i(u)du, \tag{18}$$

where λ_i is an eigenvalue associated with $\phi_i(x)$. Furthermore, the coefficients ϵ_i $(i = 1, \cdots, \infty)$ satisfy the following identity

$$\lambda_i \delta_{ij} =< \epsilon_i \epsilon_j >, \tag{19}$$

where $< \epsilon_i^2 >= \lambda_i$ gives measure of randomness along the $\phi_i(x)$ coordinate. One of the advantages of the series expansion is that it provides a second moment characterization of k_{sr} in terms of uncorrelated random variables.

Using Eqs. (5), (6), and (17), and following the approach presented above, one obtains

$$\begin{bmatrix} -k_f A - hsB - cC & hsB \\ hsB & -\sum \epsilon_i D_i - hsB \end{bmatrix} \begin{bmatrix} T_n \\ t_n \end{bmatrix} = \begin{bmatrix} b \end{bmatrix} \tag{20}$$

where matrix D_i is defined as

$$D_i = \int_0^L \phi_i(x)(\frac{dN}{dx})^T(\frac{dN}{dx})dx \tag{21}$$

Equation (20) is very similar to Eq. (12). Therefore, the statistical characteristics of the temperature vector $\begin{bmatrix} T_n^T & t_n^T \end{bmatrix}^T$ can be obtained using the Neumann expansion and the procedure discussed for parametric randomness.

The above discussion provides a probabilistic model when k_s represents a stochastic process. A similar approach can be used for other stochastic processes.

Monte-Carlo Method.- Monte-Carlo simulations rely on equations (12) and (20). In this technique, a random number generator is used to obtain a large set of random numbers that represent the desired probability distribution curve of the random variables. This process is repeated for each random variable. Depending on parametric or spatial randomness, equation (12) or (20) is used to obtain an equal number of sets of nodal temperatures, which are then used to obtain the statistics for the nodal temperatures. For an accurate answer, this scheme requires a large number of numerical tests. This number can be reduced using the following approach: (1) grouping the random data, (2) performing only one test for each group. and (3) using the probability information to account for other data in the group. This approach can significantly reduce the number of numerical runs for accurate results.

NUMERICAL RESULTS AND DISCUSSIONS

To validate the formulation developed here, a dilution refrigerator heat exchanger consisting of superfluid Helium II as fluid and the sintered copper as the solid was considered. The system response was obtained using this scheme and an analytical scheme. For numerical simulations, the following parameters were considered: $K_f = 7X10^4 W/(m.K)$, $K_s = 500W/(m.K)$, $h = 1200W/(m^2K)$, $c = 11.75W/(m.K)$, and $s = 0.2792m$ which are typical of this system. The value of L was taken as 10 m. For convenience, the non-dimensional temperatures of the fluid T_f and the solid t_s were defined as follows: $T_f = (T - T_0)/(T_L - T_0)$ and $t_s = (t - T_0)/(T_L - T_0)$. The following boundary conditions were taken: $T_f(0) = 0.0$, $t_s(0) = 0.8$, and $T_f(L) = t_s(L) = 1.0$. The values of k_s and h were varied to study the effects of these parameters on the temperature distribution. To study the probabilistic effects, the system statistical response was obtained using Monte-Carlo simulations, the analytical schemes, and the proposed scheme. Results of this study

are shown below.

Figure 2 compares the temperature distributions obtained using the analytical and the proposed schemes. The two results agree very well. The fluid temperature changes almost linearly due to the large conductivity of superfluid HeII. The solid media temperature decreases faster near the inlet point than inside the exchanger because of the strong convection near the inlet. Since the outlet point temperature is higher than the inlet temperature, the temperature of both fluid and solid increases after some distance. Once the temperature of the fluid and the solid become equal, convection stops and the temperature of both media increases at the same rate.

Figure 3 shows the temperature profiles of the solid and the fluid for k_s = 250, 500, 1000, 1500, and 2000 W/(m.K). It is clear that an increase in solid thermal conductivity causes the temperature of the solid to increase. This is because convection becomes less dominant at higher values of k_s. Due to large fluid thermal conductivity, the fluid temperature profile remains unchanged.

The temperature profiles for h = 600, 1200, 2400, and 12,000 W(m^2.K) are shown in figure 4. As expected, increase in convective heat transfer coefficient causes the solid temperature to decrease rapidly and merge with the fluid temperature sooner.

In this investigation, parameter h was considered as a random variable, and all other parameters were kept the same. Using a random number generator, 20,000 random sample points having 10 % variations of mean convective heat transfer coefficient with 90 % confidence were generated. These data were used in the Monte-Carlo method, the exact solution, and this scheme to predict the mean response of the temperature profile. All three schemes gave the same results. To compare the relative accuracy of the current scheme with the Monte-Carlo scheme, the percentage errors for the two schemes were computed. Results are shown in Figure 5. It can be observed that both schemes overpredict fluid temperature while they underpredict solid temperature, and the difference between the two schemes is small. However, from the formulation, it is clear that this scheme requires fewer number of computations than the Monte-Carlo scheme.

CONCLUSION

A deterministic and a probabilistic one-dimensional finite element model for heat transfer processes in porous heat exchangers has been presented. A set of numerical experiments have been performed to validate the model. This formulation leads to an asymmetric global coefficient matrix. Numerical experiments show that this scheme agrees well with the analytical and the Monte-Carlo methods. However, for mean and standard deviations, this scheme requires fewer number of computations in comparison to the Monte-Carlo scheme.

REFERENCES

1. Pust, L.: Investigation of Temperature Field in Heat Exchanger of Porous Cylindrical Board. *Int. J. Heat Mass Transfer*, vol. 20,Nov. 1977, pp. 1255-1257.

2. Yates, S.R.: An Analytical Solution For One-Dimensional Transport In Porous-Media With An Exponential Dispersion Function. *Water Resources Research*, vol.28,1992,pp. 2149-2154.

3. Montakhab, A.: Convective Heat Transfer in Porous Media. *J. Heat Transfer*, vol. 101,Aug. 1979,pp. 507-510.

4. Nakayama, A.: A Unified Similarity Transform For Free, Forced and Mixed Convection In Darcy and Non-Darcy Porous Media. *Int. J. Heat Mass Transfer*, vol. 34,1991,pp. 357-367.

5. Finlayson, B.A.: Packed-Bed Reactor Analysis by Orthogonal Collocation. *Chem. Eng. Sci.*, vol. 26, Jul. 1971, pp. 1081-1091.

6. Dixon, A.G.; and Cresswell, D.L.: Theoretical Prediction of Effective Heat Transfer Parameters in Packed Beds. *AICHE J.*, vol. 25,Jul. 1979, pp. 663-676.

7. Lin, X.A.; Guo, F.Z.; and Wang, H.: Solution to Temperature Fields of Porous Heat Exchangers. Song-Jiu Deng ed. in chief: *Heat Transfer Enhancement and Energy Conservation.* pp. 559-565, Hemisphere Publ. Corp.,1990.

8. Siegwarth, J.D.; and Radebaugh, R.: Analysis of Heat Exchangers for Dilution Refrigerators. *Rev. Sci. Instrum.*, vol. 42, Aug. 1971, pp. 1111-1119.

9. Yu, W.S., Lin, H.T., and Lu, C.S.: Universal Formulations And Comprehensive Correlations For Non-Darcy Natural-Convection And Mixed Convection In Porous-Media. Int J. Heat Mass Transfer, vol. 34, 1991, pp. 2859-2868.

10. Allen, M.B.; Ewing, R.E.; and Lu, P.: Well-Conditioned Iterative Schemes For Mixed Finite-Element Models Of Porous-Media Flows. *SIAM J on Scientific and Statistical Computing*, vol.13,1992,pp.794-814.

11. Papoulis, A.: *Probability, Random Variables, and Stochastic Processes.* McGraw-Hill, 1965.

12. Bharrucha-Reid ed.: *Probabilistic Methods in Applied Mathematics.* Academic Press, 1968.

13. Snoog, T. T.: *Random Differential Equations in Science and Engineering.* Academic Press, 1973.

14. Adomian, G.: *Stochastic Systems.* Academic Press, 1983.

15. Ghanem, R. G.; and Spanos, P. D.: *Stochastic Finite Elements: A Spectral Approach.* Springer–Verlag, 1990.

16. Iyengar, R.; and Dash, P.: Random vibration analysis of stochastic time-varying systems. *J. Sound and Vibration*, Vol.45, 1976,pp. 69-89.

17. Ibrahim, R.: Structural dynamics with parameter uncertainties. *App. Mech. Rev.*, Vol. 40, No. 3, 1987, pp. 309-328.

18. Shinozuka, M. (Editor): *Stochastic Mechanics, Vol. 1.* Department of Civil Engineering, Columbia University, 1987.

19. Benaroya, H.; and Rehak, M.: Finite element methods in probabilistic structural analysis: A selective review. *Applied Mechanics Reviews*, Vol. 41, no. 5, 1988, pp. 201-213.

20. Mase, G. T.; Murthy, P. L. N.; and Chamis, C. C.: Quantification of scatter in composite properties via probabilistic mechanics. *Composite Material Technology*, ASME Petroleum Division, PD vol. 45, 1992, pp. 71-76.

21. Liaw, D.G.; Singhal, S.N.; Murthy, P.L.N.; and Chamis, Christos C.: Quantification of uncertainties in composites. *Collection of Technical Papers*, AIAA/ASME Structures, Structural Dynamics and Materials Conference, Washington, DC, pp. 1163-1173, 1993.

22. Buslenko, N. P; Golenko, D. J.; Schreider, Y. A.; Sobol, I. M.; and Sragovich, V. G.: *The Monte Carlo Method.* Pergamon Press, Oxford, 1966.

23. Liu, W. K.; Belytschko, T; and Mani, A.: Random Field Finite Elements. *Int. J. for Numerical Methods in Engineering*, Vol. 23, 1986, pp. 1831-1845.

24. Liu, W. K.; G. Besterfield; and Belytschko, T.: Variational Approach to Probabilistic Finite Elements. *ASCE J. Engineering Mechanics*, Vol. 114, 1988, pp. 2115-2133.

25. Dias, J. B.; Nagtegaal, J. C.; and Nakazawa, S.: Iterative perturbation algorithms in probabilistic finite element analysis. In W. K. Liu and T. Belytschko, editors, *Computational Mechanics of Probabilistic and Reliability Analysis*, pp. 211-230, Elmpress International, Lausanne, 1989.

26. Kien, T. D.; and Kleiber, M.: Finite Element Analysis Based on Stochastic Hamilton Principle. *Computers and Structures*, Vol. 37,1990, pp. 893-902.

27. Spanos, P. D.; and Ghanem, R. G.: Stochastic Finite Element Expansion for Random Media. *ASCE J. Engineering Mechanics*, Vol. 115, 1989, pp. 1035-1053.

28. Lawrence, M. A.: A Basis Random Variable Approach to Stochastic Structural Analysis. University of Illinois at Urbana–Champaigne, 1986.

29. Lawrence, M. A.: Basis Random Variables in Finite Element Analysis. *Int. J. for Numerical Methods in Engineering*, Vol. 24, 1987, pp. 1849-1863.

30. Daddazio, R.; and Ettouney, M.: Boundary Element Methods in Probabilistic Acoustic Radiation Problems. *Numerical Techniques in Acoustic Radiation*, editors R. J. Bernhard and R. F. Keltie, pp. 103-108, ASME, 1989.

31. Ettouney, M.; Benaroya, H.; and Wright, H.: Probabilistic Boundary Element Method (PBEM). *Computational Mechanics of Probabilistic and Reliability Analysis*, editors W. K. Liu and T. Belytschko, pp. 141-166, Empress International, Lausanne, 1989.

32. Ettouney, M.; Benaroya, H.; and Wright, H.: Boundary Element Methods in Probabilistic Structural Analysis (PBEM). *Applied Mathematical Modeling*, Vol. 13, 1989, pp. 432-441.

33. Manolis, G. D.; and Shaw, R. P.: Wave Motion in a Random Hydroacoustic Medium Using Boundary Integrals/Elements Methods. *Engineering Analysis with Boundary Elements*, Vol. 9, 1992, pp. 61-70.

34. Burczyński, T.: The Boundary Element Method for Stochastic Potential Problems. *Applied Mathematical Modelling*, Vol. 9, 1985, pp. 189-194.

35. Cheng, A. H. -D.; and Lafe, O. E.: Boundary Element Solution for Stochastic Groundwater Flow: Random Boundary Conditions and Recharge. *Water Resources Research*, Vol. 27, 1991, pp. 231-242.

36. Drewniak, J.: Boundary Elements for Random Heat Conduction Problems. *Engineering Analysis*, Vol. 2, 1985, pp. 168-170.

37. Burczyński, T.; and John, A.: Stochastic Dynamic Analysis of Elastic and Viscoelastic Systems by Means of the Boundary Element Method. *Boundary Elements VII*, editors C. A. Brebbia and G. Maier, pp. 6/53-6/62, Springer-Verlag, Berlin, 1985.

38. H. L. Van Trees: *Detection, Estimation, and Modulation Theory, Part 1.* Wiley, 1968.

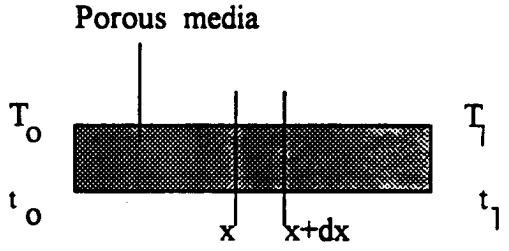

Figure 1. One dimensional porous heat exchanger

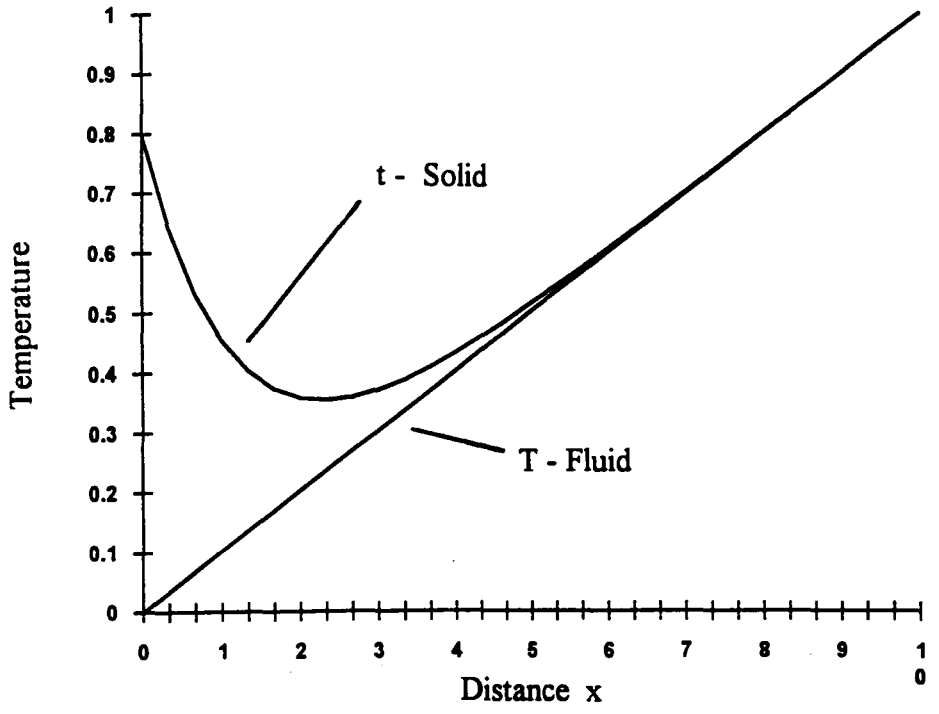

Figure 2. Temperature distribution

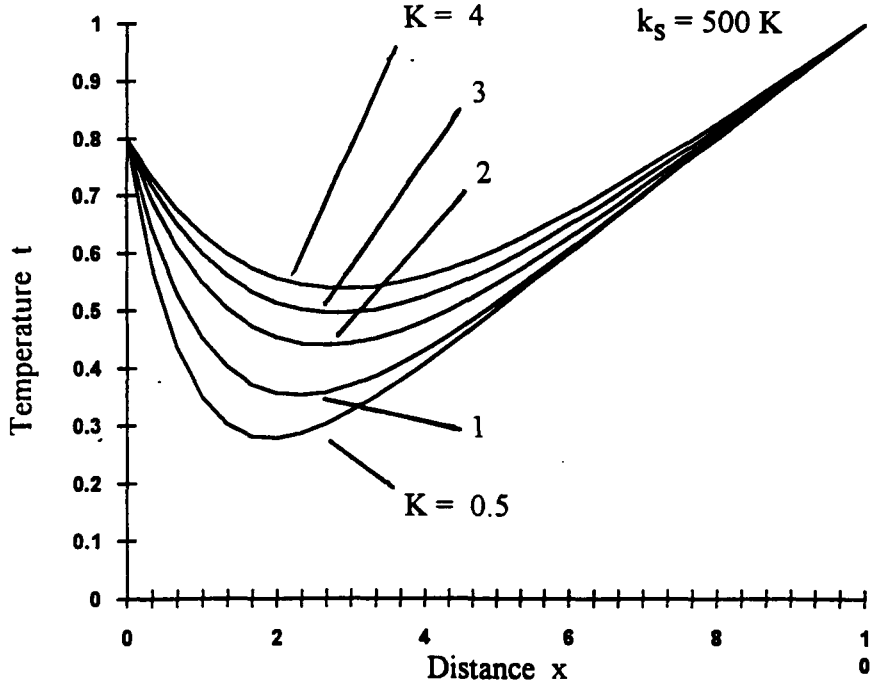

Figure 3. Effect of k_S on temperature distribution t

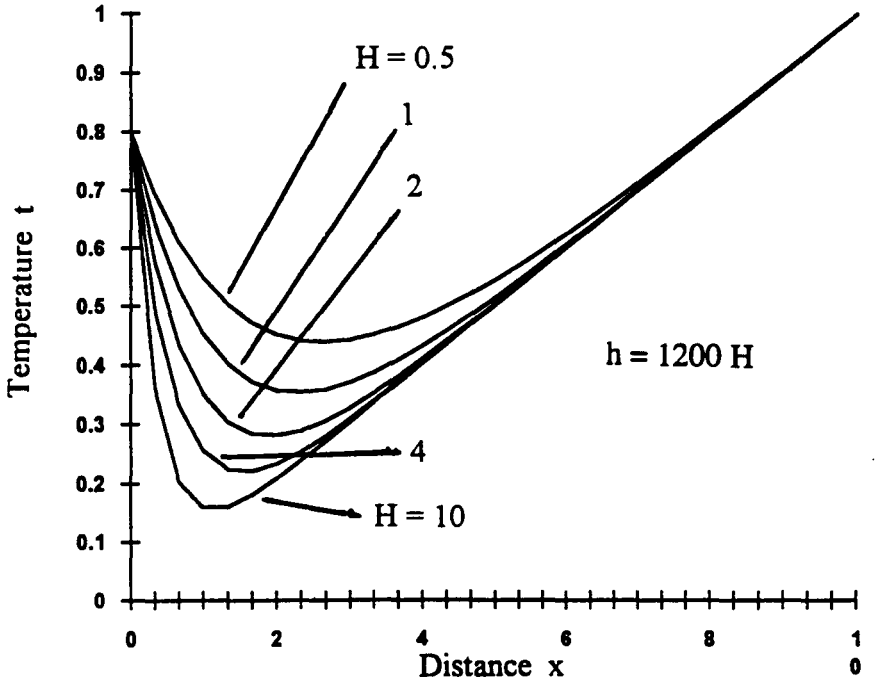

Figure 4. Effect of h on temperature distribution t

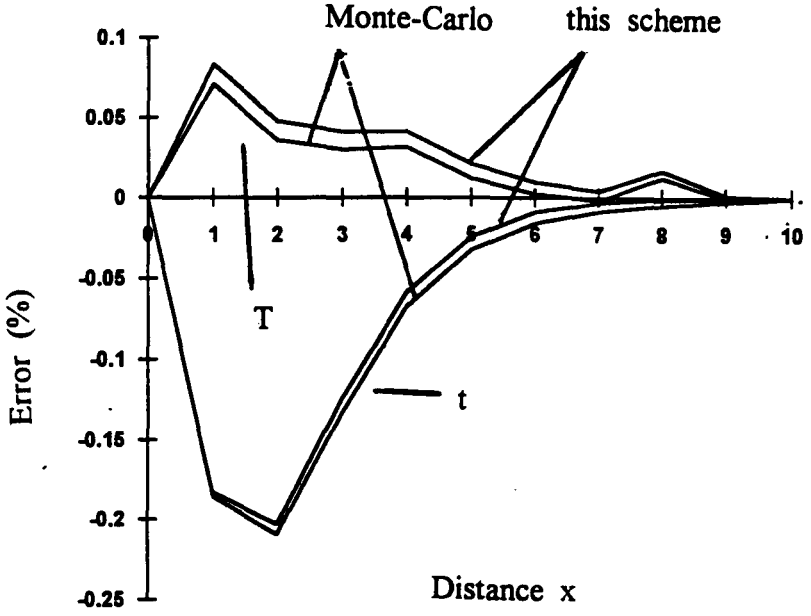

Figure 5. Error in mean values for temperatures of Monte-Carlo and this scheme

TRANSITIONAL FLOW IN THIN TUBES FOR SPACE STATION FREEDOM RADIATOR

Patrick Loney
NYMA, Inc.
Brook Park, Ohio

and

Mounir Ibrahim
Cleveland State University
Cleveland, Ohio

SUMMARY

A two dimensional finite volume method is used to predict the film coefficients in the transitional flow region (laminar to turbulent) for the radiator panel tubes. The code used to perform this analysis is CAST (Computer Aided Simulation of Turbulent Flows). The information gathered from this code is then used to augment a Sinda85 model that predicts overall performance of the radiator. A final comparison is drawn between the results generated with a Sinda85 model using the Sinda85 provided transition region heat transfer correlations and the Sinda85 model using the CAST generated data.

INTRODUCTION

Plans for the radiator for Space Station Freedom were to have several panels connected by fluid manifolds. The manifolds on either side of the radiator are connected by 12 thin tubes (1/8", 3.175 mm) per panel. (see Fig. I). Flow through the tubes is not a constant rate. It varies as a function of the position of the station as it relates to the sun. The flow in the thin radiator tubes can go from a low flow rate (laminar) to a high flow rate (turbulent). Accurate prediction of the radiator's thermal performance depends on several aspects, including the ability to predict the film coefficients of the fluid in the panel tubes. A grey area in this prediction is in the area of transition flow ($2300 < Re < 10{,}000$), especially in thin tubes. Small changes in the film coefficient can effect predictions of the radiator performance and freezing of the working fluid.

SYSTEM DESCRIPTION

A radiator panel tube has an inner diameter of 1/8", and the tube is 12' long (3.175 mm, 3.658 m). This translates to an L/D of 1150. The Sinda85 model (see Ref. I) took the entire tube into account, along with the thermal connections to the heat sink (the space environment). This allowed the model to predict the tube's fluid exit temperature.

The CAST model (see Ref. II) only modeled the tube to an L/D of 70. This allowed the flow to become fully developed and predict accurate film coefficients. A compiled table of these coefficients was then input into a second Sinda85 model. This model is an exact duplicate of the above mentioned Sinda85 model except for the differing film coefficients.

THE CAST CODE

It is assumed that the reader is familiar with the basic structure of Sinda85. No discussion will be held on the development of that model. The cast model does need some discussion. CAST is a two dimensional, finite volume fluid analysis code. After generating a grid that used an L/D of 70, the model was run for three known scenarios. The first was a laminar ($Re = 2300$) case. The predicted film coefficients were within 5% of the classic $Nu = 3.66$ correlation (see Table I and Ref. III).

Next, the geometry was changed by increasing the diameter by a factor of 10. The flow was increased to obtain a Reynold's Number of 10,000. Here, the predicted value of the film coefficient was

Table I: Laminar and Turbulent Control Cases

Re	UA (Ref III)	UA (CAST)
2300	11.9 [btu/hr/°F]	11.4
10,000 (10D)	4.25	3.57
10,000	24.0	23.5

within 10% of the classic Dittus/Boelter correlation (Nu = 0.023 * Re^.8 * Pr ^.3, see Ref. III).

Finally, the diameter of the tube was brought down to the actual value (0.125") and the model was run again at a Reynold's Number of 10,000. This time the model prediction was within 3% of the Dittus/Boelter correlation. These three results give a good deal of confidence to the ability of CAST to accuratly predict the transition flow film coefficients.

The CAST code input was now modified to run in the transition region. One point of interest was to determine that if acceleration and deceleration of the flow would effect the onset of turbulence (see Ref. IV). When the acceleration parameter K (defined beow) reached a value of 2.0e-06, laminarization becomes significant and and the heat transfer capabilities of the fluid are altered. In the case of the radiator flows, the change in the velocity rates was not great enough to have any impact. (K < 1.0e-09) In other words, the flow accelerated and decelerated at slow enough rates so as not to effect the heat transfer.

$$K = \upsilon \, (dU/dx) \, / \, U^2$$

where υ = kinematic viscosity

U = stream velocity

Another area of concern was the effect of the transient conditions would have upon the system. Sinda85 uses an implicit (backward) differencing scheme to handle its transient fluid calculations. An ideal fluid analysis code will have a long term history of each fluid element, as this may have an effect on the performance of the fluid. The CAST model was run in steady state form for a series of Reynold's numbers (see table II). A set of transient runs spanning the same range as the steady state runs was also completed. The end result being, once again, the flow rates changed slowly enough that steady state runs were accurate enough to be used to predict the transient cases. This allowed the film coefficients obtained for the transient CAST runs to be implemented in the Sinda85 model with confidence.

Table II: Reynold's Number vs. CAST Film Coefficient Calculations

Re	UA
3000	15.2 [btu/hr/°F]
4000	20.8
5000	21.4
6000	21.5
7000	23.3
8000	23.4
9000	23.5
10000	23.6

RESULTS

Figure II shows the results of the CAST model over the range 3000 < Re < 10,000. Film coefficients versus L/D and Re are presented. Film coefficients were sampled over the length of the

tube for each flow rate. The film coefficients were calculated in the following manner:

$\Delta T = (\sum Ti\ Ui) / Uave - Tw$
$q = (T1 - Tw)\ k / \Delta y$
$htc = q / \Delta T$

Where
- Ti = Incremental Axial Temperature
- Ui = Incremental Axial Velocity
- Uave = Mean velocity
- Tw = Wall (boundary) temperature
- q = Heat flux
- T1 = Temperature of increment next to the wall
- k = Thermal Conductivity
- htc = Film Coefficient

Table III shows the fully developed film coefficients obtained from CAST versus the Sinda85 film coefficients for the range of Reynold's numbers. Sinda85 uses two correlations over the area of concern, Over the range 1960 < Re 6420, Sinda85 uses Hausen's correlation:

$Nu = 0.116\ (Re^{.667} - 125)\ Pr^{.3}$

And over the range Re > 6420, Sinda85 used the Dittus/Boelter equation.

Table III was generated using the mean values for each flow rate of the film coefficients from an L/D of 50 out to an L/D of 70.

Table IV is a the final table that lists the radiator panel tube exit temperatures generated by the two Sinda85 models.

Table III: Sinda85 and CAST Film Coefficients

Re	UA (Sinda85)	UA (CAST)
3000	6.0 [btu/hr/°F]	15.2
4000	9.5	20.8
5000	12.5	21.5
6000	15.5	21.5
7000	18.0	23.3
8000	20.0	23.4
9000	22.0	23.5
10000	24.0	23.6

Table IV: Sinda85 and CAST Radiator Tube Exit Temperatures

Re	Temp (Sinda85)	Temp (CAST)
3000	-35.8 [°F]	-36.8
4000	-28.9	-29.5
5000	-29.2	-24.5
6000	-20.8	-20.9
7000	-18.2	-18.3
8000	-16.2	-16.3
9000	-14.6	-14.6
10000	-13.3	-13.2

CONCLUSIONS

A review of Table III shows that higher film coefficients are obtained using the CAST code instead of Hausen's correlation (which is empirically derived at low Reynold's numbers). The reason for the increased heat transfer can be explained by the effect of the thin tubes. Turbulent mixing boundary layers take up a larger percentage of the axial flow. This leads to more fluid mixing and enhances heat transfer.

The higher film coefficients lead to lower fluid exit temperatures, ie, the radiator becomes more effective. However, the film coefficients are only one part of the thermal network of the radiator. The overall effect is small and well within any margin of uncertainty so as not to change any conclusions of the radiator performance made by the original Sinda85 model.

A side note to the conclusions must be considered here. Had the radiator tubes been much shorter, the entry region effects would have been much greater. Figure II shows the increased UA's for at the inlet conditions and as the flow starts to develope. It is clear that there is enhanced heat transfer in this area. The overall length of the radiator panel tubes makes this insignificant but for shorter tubes, this augmented heat transfer would have had to have been considered.

RECOMENDATIONS

The particular version of the CAST code used is refered to as a High Reynold's Number (HRN) version. It is best suited for flows well above the laminar region and into turbulent. For the lower Reynold's number cases (the ones close to Re = 2300) the Low Reynold's Number (LRN) version, also known as the k-ε model could be used. The LRN could be used to verify, or modify, the HRN values.

REFERENCES

I: Sinda85 User's Manual, V2.3, Cullimore, Goble, Jensen, & Ring, 1992

II: CAST User's Manual, Peric & Scheuerer, 1989

III: Fundamentals of Heat Transfer, Incropera & De Witt,1981

IV: On the Prediction of Laminarization, Laudner & Jones, 1969

Figure I: RADIATOR

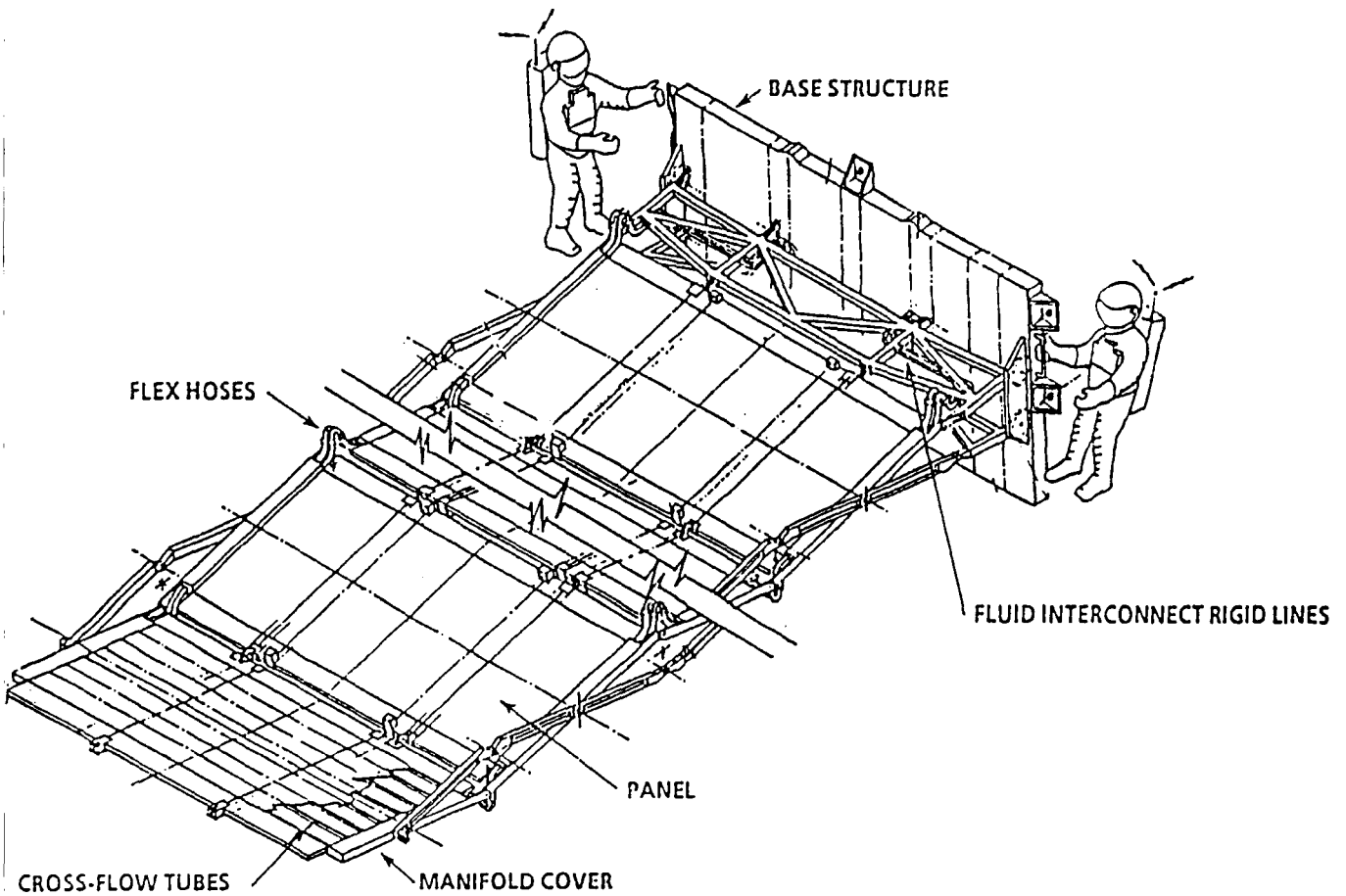

Figure II: Transition UA's vs Re and X/d

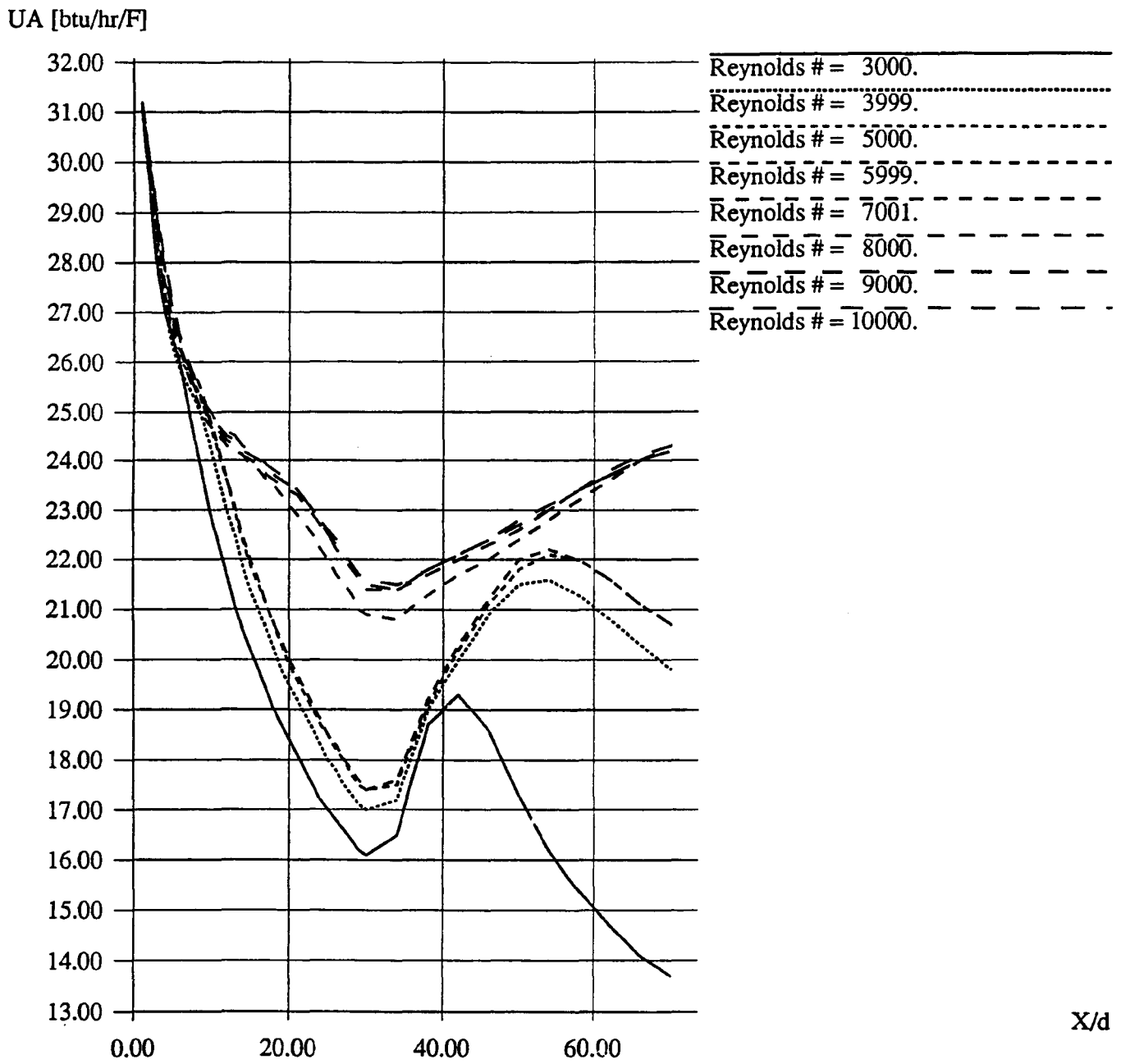

A NAVIER-STOKES BOUNDARY ELEMENT SOLVER

O. Lafe
Innovative Computing Group
OLTech Corporation
Chesterland, Ohio

D.R. Reddy
Internal Fluid Mechanics Division
NASA Lewis Research Center
Cleveland, Ohio

and

A. H-D. Cheng
Department of Civil Engineering
University of Delaware
Newark, Delaware

SUMMARY

Using global interpolation functions (GIFs), boundary element solutions are obtained for two-dimensional laminar flows. Two schemes are proposed for handling the convective terms. The first treats convection as a forcing function, and converts the flow equations to pseudo-Poisson equations. In the second scheme, some convective effect is incorporated into the fundamental solution used in constructing the pertinent integral equations. The lid-driven cavity flow is selected as the benchmark problem.

INTRODUCTION

The boundary element method (BEM) has traditionally been applied to problems governed by linear differential equations. At the core of the basic BEM computational process is the fundamental solution (also referred to as the free-space Green's function) defined as the impulse response of the governing equation to a unit action. This fundamental solution is either too difficult or impossible to derive for practical nonlinear problems. Recently, with the

introduction of the so-called *Dual Reciprocity* techniques (see *e.g., Nardini & Brebbia* [1982]; *Brebbia et al.*, [1991]; *Partridge et al.*, [1992]; *Cheng et al.*, [1993]; *Lafe* [1993]; *Lafe & Cheng* [1994]), the method is being proposed for certain classes of nonlinear problems.

Using the *Dual Reciprocity* approach, a given problem is typically decomposed into two parts - the linear and nonlinear portions. The solution to the linear portion is represented by a boundary integral whose kernel consists of the fundamental solution to the linear governing equation. The nonlinear part is represented by either 1) local bases functions (*Brebbia et al.*, [1991]); or 2) global interpolation functions (GIFS) (*Lafe* [1993]). In either case, the boundary integral expressions and interpolation functions contain coefficients whose values are to be determined by enforcing the boundary conditions. When the "direct BEM" approach is followed the unknown coefficients are in essence the unknown physical variables (velocity components, pressure, temperature) of the problem. On the other hand, using the "indirect BEM" approach, the unknown are the weights/strengths of the boundary sources/dipoles and the local/global interpolating functions. The computational intensity of the indirect approach is much less than for the direct.

In this paper, we develop a GIF-based indirect BEM code for two- dimensional steady-state incompressible Navier-Stokes equation. Test results are shown for the lid-driven cavity problem.

GOVERNING EQUATIONS

The governing equations are:

$$\frac{\partial u}{\partial x} + \frac{\partial v}{\partial y} = 0 \tag{1}$$

$$u\frac{\partial u}{\partial x} + v\frac{\partial u}{\partial y} = -\frac{1}{\rho}\frac{\partial p}{\partial x} + \frac{\mu}{\rho}\left(\frac{\partial^2 u}{\partial x^2} + \frac{\partial^2 u}{\partial y^2}\right) \tag{2}$$

$$u\frac{\partial v}{\partial x} + v\frac{\partial v}{\partial y} = -\frac{1}{\rho}\frac{\partial p}{\partial y} + \frac{\mu}{\rho}\left(\frac{\partial^2 v}{\partial x^2} + \frac{\partial^2 v}{\partial y^2}\right) \tag{3}$$

where (u, v) are the velocity components in the x and y directions respectively, p is the pressure, ρ is the density, and μ is the viscosity. Let

$$X = x/L$$

$$
\begin{aligned}
Y^{*} &= y/L \\
U^{*} &= u/\overline{v} \\
V^{*} &= v/\overline{v} \\
P &= p/\left(\rho\overline{v}^{2}\right)
\end{aligned}
$$

With these the governing equations become:

$$\frac{\partial U^{*}}{\partial X^{*}} + \frac{\partial V^{*}}{\partial Y^{*}} = 0 \tag{4}$$

$$U^{*}\frac{\partial U^{*}}{\partial X^{*}} + V^{*}\frac{\partial U^{*}}{\partial Y^{*}} = -\frac{\partial P}{\partial X^{*}} + \frac{1}{R_{e}}\left(\frac{\partial^{2}U^{*}}{\partial X^{*2}} + \frac{\partial^{2}U^{*}}{\partial Y^{*2}}\right) \tag{5}$$

$$U^{*}\frac{\partial V^{*}}{\partial X^{*}} + V^{*}\frac{\partial V^{*}}{\partial Y^{*}} = -\frac{\partial P}{\partial Y^{*}} + \frac{1}{R_{e}}\left(\frac{\partial^{2}V^{*}}{\partial X^{*2}} + \frac{\partial^{2}V^{*}}{\partial Y^{*2}}\right) \tag{6}$$

where the Reynold's Number $R_{e} = \rho\overline{v}L/\mu$.

BOUNDARY INTEGRAL EQUATIONS

In order to convert the above into boundary integral equations two approaches have been followed. In the first approach, the entire system of equations is converted into an elliptic system, with the convective term wholly embedded in the right-hand-side forcing function. There is concern about the suitability of the elliptic system to adequately represent the convective forces at moderate to high Reynold's number regimes. The second approach rectifies this through a more direct perturbation-based analysis which is more suited to capturing convective effects as the Reynold's number increases.

Approach I

The above equations are converted into an elliptic system:

$$\nabla^{2}U^{*} = F_{1} \tag{7}$$

$$\nabla^{2}V^{*} = F_{2} \tag{8}$$

$$\nabla^{2}P = F_{3} \tag{9}$$

where

$$F_{1} = R_{e}\left(U^{*}\frac{\partial U^{*}}{\partial X^{*}} + V^{*}\frac{\partial U^{*}}{\partial Y^{*}} + \frac{\partial P}{\partial X^{*}}\right)$$

$$F_2 = R_e\left(U\frac{\partial V}{\partial X} + V\frac{\partial V}{\partial Y} + \frac{\partial P}{\partial Y}\right) \tag{10}$$

$$F_3 = 2\left(\frac{\partial U}{\partial X}\frac{\partial V}{\partial Y} - \frac{\partial U}{\partial Y}\frac{\partial V}{\partial X}\right)$$

Boundary Integral Equations

The associated indirect boundary integral equations are:

$$U(X,Y) = \int_\Gamma w_1(X',Y')g(X',Y';X,Y)\,d\Gamma + \sum_k \beta_{1k}\Psi_k(X,Y) \tag{11}$$

$$V(X,Y) = \int_\Gamma w_2(X',Y')g(X',Y';X,Y)\,d\Gamma + \sum_k \beta_{2k}\Psi_k(X,Y) \tag{12}$$

$$P(X,Y) = \int_\Gamma w_3(X',Y')g(X',Y';X,Y)\,d\Gamma + \sum_k \beta_{3k}\Psi_k(X,Y) \tag{13}$$

in which

$$g = \ln\left[(X-X')^2 + (Y-Y')^2\right]$$

$$\sum_k \beta_{ik}M_k(X,Y) = F_i(X,Y) \tag{14}$$

$$\nabla^2\Psi_k(X,Y) = M_k(X,Y)$$

The functions $M_k(X,Y)$ are the interpolation functions used in representing the convective terms. If we choose

$$M_k = cos(m_k X)cos(n_k Y) \tag{15}$$

it is easily shown (*Lafe* [1993]) that

$$\Psi_k = \frac{cos(m_k X)cos(n_k Y)}{(n_k^2 + m_k^2)} \tag{16}$$

Approach II

Our aim here is to have a better incorporation of the convective effects in the driving differential operator. Let

$$U = U_0 + U_1$$

$$V = V_0 + V_1$$

$$P = P_0 + P_1$$

where (U_0, V_0, P_0) denote solutions to a convection-free flow field, while (U_1, V_1, P_1) represent the convective effects. Hence

$$\nabla^2 U_0 = 0 \tag{17}$$

$$\nabla^2 V_0 = 0 \tag{18}$$

$$\nabla^2 P_0 = 2\left[\frac{\partial U_0}{\partial X}\frac{\partial V_0}{\partial Y} - \frac{\partial U_0}{\partial Y}\frac{\partial V_0}{\partial X}\right] \tag{19}$$

while

$$\frac{1}{R_e}\nabla^2 U_1 - o_1(U_0, V_0, U_1, V_1, P_1) = f_1(U_0, V_0, P_0) + h_1(U_1, V_1) \tag{20}$$

$$\frac{1}{R_e}\nabla^2 V_1 - o_2(U_0, V_0, U_1, V_1, P_1) = f_2(U_0, V_0, P_0) + h_2(U_1, V_1) \tag{21}$$

$$\frac{1}{2}\nabla^2 P_1 - o_3(U_0, V_0, U_1, V_1, P_1) = h_3(U_1, V_1) \tag{22}$$

where

$$o_1 = U_0\frac{\partial U_1}{\partial X} + \frac{\partial U_0}{\partial X}U_1 + V_0\frac{\partial U_1}{\partial Y} + \frac{\partial U_0}{\partial Y}V_1 + \frac{\partial P_1}{\partial X}$$

$$o_2 = U_0\frac{\partial V_1}{\partial X} + \frac{\partial V_0}{\partial X}U_1 + V_0\frac{\partial V_1}{\partial Y} + \frac{\partial V_0}{\partial Y}V_1 + \frac{\partial P_1}{\partial Y}$$

$$o_3 = \frac{\partial U_0}{\partial X}\frac{\partial V_1}{\partial Y} + \frac{\partial V_0}{\partial Y}\frac{\partial U_1}{\partial X} - \frac{\partial U_0}{\partial Y}\frac{\partial V_1}{\partial X} - \frac{\partial V_0}{\partial X}\frac{\partial U_1}{\partial Y}$$

$$f_1 = U_0\frac{\partial U_0}{\partial X} + V_0\frac{\partial U_0}{\partial Y} + \frac{\partial P_0}{\partial X}$$

$$f_2 = U_0\frac{\partial V_0}{\partial X} + V_0\frac{\partial V_0}{\partial Y} + \frac{\partial P_0}{\partial Y}$$

$$h_1 = U_1\frac{\partial U_1}{\partial X} + V_1\frac{\partial U_1}{\partial Y}$$

$$h_2 = U_1\frac{\partial V_1}{\partial X} + V_1\frac{\partial V_1}{\partial Y}$$

$$h_3 = \frac{\partial U_1}{\partial X}\frac{\partial V_1}{\partial Y} - \frac{\partial U_1}{\partial Y}\frac{\partial V_1}{\partial X}$$

The external boundary conditions are imposed on (U_0, V_0, P_0). Therefore the variables (U_1, V_1, P_1) are allowed to enjoy homogeneous boundary conditions.

Boundary Integral Equations

The velocity components (U_0, V_0), which are governed by Laplace's equations, can be represented by 'pure' boundary integral equation using the fundamental solution for potential flow. However the pressure term, because of the non-zero forcing function, will include global interpolation functions.

Therefore, the indirect boundary integral equations for the convection-free variables are:

$$U_0(X,Y) = \int_\Gamma w_{01}(X',Y')g(X',Y';X,Y)\,d\Gamma \tag{23}$$

$$V_0(X,Y) = \int_\Gamma w_{02}(X',Y')g(X',Y';X,Y)\,d\Gamma \tag{24}$$

$$P_0(X,Y) = \int_\Gamma w_{03}(X',Y')g(X',Y';X,Y)\,d\Gamma + \sum_k \beta_{0k}\Psi_k(X,Y) \tag{25}$$

where (w_{01}, w_{02}, w_{03}) are fictitious sources while Ψ_k are the GIFS.

The convective effects (U_1, V_1, P_1) are represented by GIFS. For flows in simple geometries it is possible to select GIFS which automatically satisfy the required homogeneous boundary conditions.

Hence

$$U_1(X,Y) = \sum_k \beta_{1k}\Psi_k(X,Y) \tag{26}$$

$$V_1(X,Y) = \sum_k \beta_{2k}\Psi_k(X,Y) \tag{27}$$

$$P_1(X,Y) = \sum_k \beta_{3k}\Psi_k(X,Y) \tag{28}$$

in which $(\beta_{1k}, \beta_{2k}, \beta_{3k})$ are the pertinent coefficients for the GIFS. These parameters are calculated by enforcing

1. Equations (20-22) at selected collocation points within the flow region and

2. Homogeneous conditions at selected boundary points.

The chief advantage of the first approach is the simplicity and size of the global coefficient matrices, derived from the Laplace equation solver. This translates into a compact, fast, and highly efficient numerical implementation. The drawback is its iterative character since the forcing function

depends on the solution being sought. Convergence is difficult to achieve for large Reynold's number because the governing elliptic system becomes singular, and cannot adequately represent the underlying physics of the problem. The second approach, which in essence separates the convection-free flow from the main flow, allows for a more direct representation of the asymptotic limits of the Reynold's number. Furthermore, by products of higher-order terms (*i.e.*, setting $h1 = h2 = h3 = 0$, the solutions can be obtained without iteration. However, the coefficient matrix is larger and the approach involves a greater level of computational intensity.

NUMERICAL IMPLEMENTATION

Approach I

We subdivide the boundary into n_b elements. Let $N_k(\mathbf{x})$ $(k = 1, 2, \cdots n_b)$ represent the bases functions describing the distribution of w on Γ. In the examples being reported in this paper, constant bases functions are being used for the fictitious strengths w_j on the boundary. By selecting each of the n_b boundary points as successive origins of integration, the pertinent integral equations can be assembled into the system:

$$\sum_{k=1}^{n_b} a_{ik} w_k = b_i \quad i = 1, 2, \cdots, n_b \tag{29}$$

where

$$a_{ik} = \begin{cases} \int_{\Gamma_k} N_k(\mathbf{x}') g(\mathbf{x}', \mathbf{x}_i)\, d\mathbf{x}' & \mathbf{x}_i \in \Gamma_\Phi \\ \int_{\Gamma_k} N_k(\mathbf{x}') \partial g / \partial n(\mathbf{x}', \mathbf{x}_i)\, d\mathbf{x}' & \mathbf{x}_i \in \Gamma_Q \end{cases} \tag{30}$$

$$b_i = \begin{cases} \Phi(\mathbf{x}_i) - \sum_{j=1}^{n_d} \beta_j \Psi_{ij} & \mathbf{x}_i \in \Gamma_\Phi \\ \partial\Phi/\partial n(\mathbf{x}_i) - \sum_{j=1}^{n_d} \beta_j \partial\Psi_{ij}/\partial n & \mathbf{x}_i \in \Gamma_Q \end{cases} \tag{31}$$

where $\Phi = (U, V, P)$. Therefore, we have n_b equations to determine w_k $(k = 1, 2, \cdots n_b)$. Symbolically equation (29) can be written in the alternative form:

$$\mathcal{A}\mathcal{W} = \mathcal{B} \tag{32}$$

which can be inverted to give:

$$\mathcal{W} = \mathcal{A}^{-1}\mathcal{B} \tag{33}$$

The whole process boils down to the iterative solution of equations (14) and (33), with repeated updating of $\mathbf{F}$ using (10). The iterative steps are:

1. Start with a trial $\mathbf{F}$ (*i.e.*, F_i values for $i = 1, 2, \cdots n_d$).
2. Obtain β from equation (14).
3. Obtain W using equation (33).
4. Use discretized forms of the appropriate integral equations to compute Φ, $\nabla\Phi$ at all n_d points. This provides a better estimate for $\mathbf{F}$.
5. Go back to Step 2 if convergence condition is still unsatisfied.

Note that the matrix inversions in equations (14) and (33) need only be performed once, for fixed boundary problems. The vectors W and β are the quantities whose values change during the iterative process. Once convergence is reached, the discretized integral equations can be used routinely to obtain $\Phi = (U, V, P)$ or the gradient at any point $(\mathbf{x})$ of interest.

Approach II

The numerical implementation for the convection-free quantities (U_0, V_0, P_0) is similar to the one followed in Approach I, with the coefficients for the GIFS set to zero for the velocities. No iteration is required.

The convective-flow quantities are calculated through the coefficients $(\beta_{1k}, \beta_{2k}, \beta_{3k})$ whose values are obtained by solving the following coefficient matrices:

$$\sum_{k=1}^{n_T} \beta_{1k} A_{1ik} + \sum_{k=1}^{n_T} \beta_{1k} A_{2ik} + \sum_{k=1}^{n_T} \beta_{1k} A_{3ik} = F_{1i} \quad i = 1, 2, \cdots n_d \tag{34}$$

$$\sum_{k=1}^{n_T} \beta_{2k} B_{1ik} + \sum_{k=1}^{n_T} \beta_{2k} B_{2ik} + \sum_{k=1}^{n_T} \beta_{2k} B_{3ik} = F_{i2} \quad i = 1, 2, \cdots n_d \tag{35}$$

$$\sum_{k=1}^{n_T} \beta_{3k} C_{1ik} + \sum_{k=1}^{n_T} \beta_{3k} C_{2ik} + \sum_{k=1}^{n_T} \beta_{3k} C_{3ik} = F_{i3} \quad i = 1, 2, \cdots n_d \tag{36}$$

$$\sum_{k=1}^{n_T} \beta_{1k} E_{1jk} = 0 \quad j = 1, 2, \cdots n_b \tag{37}$$

$$\sum_{k=1}^{n_T} A_{1k} E_{2jk} = 0 \quad j = 1, 2, \cdots n_b \tag{38}$$

$$\sum_{k=1}^{n_T} A_{1k} E_{3jk} = 0 \quad j = 1, 2, \cdots n_b \tag{39}$$

where (if the higher order terms are neglected)

$$\begin{aligned}
A_{1ik} &= \frac{1}{R_e}\nabla^2\Psi_k(\mathbf{x}_i) - U_0(\mathbf{x}_i)\frac{\partial\Psi_k}{\partial X}(\mathbf{x}_i) - V_0(\mathbf{x}_i)\frac{\partial\Psi_k}{\partial Y}(\mathbf{x}_i) - \frac{\partial U_0}{\partial X}\Psi_k(\mathbf{x}_i) \\
A_{2ik} &= -\frac{\partial U_0}{\partial Y}(\mathbf{x}_i)\Psi_k(\mathbf{x}_i) \\
A_{3ik} &= -\frac{\partial\Psi_k}{\partial X}(\mathbf{x}_i) \\
B_{1ik} &= -\frac{\partial V_0}{\partial X}(\mathbf{x}_i)\Psi_k(\mathbf{x}_i) \\
B_{2ik} &= \frac{1}{R_e}\nabla^2\Psi_k(\mathbf{x}_i) - U_0(\mathbf{x}_i)\frac{\partial\Psi_k}{\partial X}(\mathbf{x}_i) - V_0(\mathbf{x}_i)\frac{\partial\Psi_k}{\partial Y}(\mathbf{x}_i) - \frac{\partial V_0}{\partial Y}\Psi_k(\mathbf{x}_i) \\
B_{3ik} &= -\frac{\partial\Psi_k}{\partial Y}(\mathbf{x}_i) \\
C_{1ik} &= -\frac{\partial V_0}{\partial Y}(\mathbf{x}_i)\frac{\partial\Psi_k}{\partial X}(\mathbf{x}_i) + \frac{\partial V_0}{\partial X}(\mathbf{x}_i)\frac{\partial\Psi_k}{\partial Y}(\mathbf{x}_i) \\
C_{2ik} &= -\frac{\partial U_0}{\partial X}(\mathbf{x}_i)\frac{\partial\Psi_k}{\partial Y}(\mathbf{x}_i) + \frac{\partial U_0}{\partial Y}(\mathbf{x}_i)\frac{\partial\Psi_k}{\partial X}(\mathbf{x}_i) \\
C_{3ik} &= \frac{1}{2}\nabla^2\Psi_k(\mathbf{x}_i) \\
F_{1i} &= U_0(\mathbf{x}_i)\frac{\partial U_0}{\partial X}(\mathbf{x}_i) + V_0(\mathbf{x}_i)\frac{\partial U_0}{\partial Y}(\mathbf{x}_i) + \frac{\partial P_0}{\partial X}(\mathbf{x}_i) \\
F_{2i} &= U_0(\mathbf{x}_i)\frac{\partial V_0}{\partial X}(\mathbf{x}_i) + V_0(\mathbf{x}_i)\frac{\partial V_0}{\partial Y}(\mathbf{x}_i) + \frac{\partial P_0}{\partial Y}(\mathbf{x}_i) \\
F_{3i} &= 0 \\
E_{ljk} &= \Psi_k(\mathbf{x}_j) \quad \text{if} \quad \mathbf{x}_j \in \Gamma_{\Phi_l} \\
E_{ljk} &= \frac{\partial\Psi_k}{\partial n}(\mathbf{x}_j) \quad \text{if} \quad \mathbf{x}_j \in \Gamma_{Q_l}
\end{aligned}$$

In the above $\Phi \equiv (U, V, P)$; $Q \equiv (\partial U/\partial n, \partial V/\partial n, \partial P/\partial n)$; $n_T = 3(n_b + n_d)$, and $\mathbf{x}_i \equiv (X, Y)$ for 2D flows.

TEST RESULTS

We examined the lid-driven cavity flow problem depicted in Fig. 1. A unit horizontal velocity is imposed on the lid (at $Y = 1$), while the no-slip boundary condition $U = V = 0$ is imposed on all solid walls. The boundary condition for the pressure on all walls is (*Fletcher* [1991]):

$$\frac{\partial P}{\partial n} = \frac{1}{R_e}\frac{\partial}{\partial s}\left(\frac{\partial U}{\partial Y} - \frac{\partial V}{\partial X}\right)$$

A typical convergence profile, using Approach I, is shown ($R_e = 15$) in Fig. 2. The horizontal velocity at the vertical center-line is shown in Fig. 3.

CONCLUSIONS

A boundary element code, based on the use of global interpolation functions, for solving the Navier Stokes equations have been proposed in this paper. The avoidance of any domain integration shows the enormous power of the technique. As long as the underlying physics of the problem is adequately represented in the fundamental solutions used as the kernel of the integral equations, accurate simulations can be carried out for moderate to high Reynold's number flows. Only trigonometric bases have been used to represent the nonlinear convective terms. Investigations are currently underway for employing other bases including those derived from orthogonal functions such Chebychev polynomials, wavelets, and cellular automata transforms. Three-dimensional GIF-based BEM code for internal flows are also being developed.

Acknowledgments

This investigation has been supported by NASA (Lewis Research Center) under the Contract NAS3-27019.

REFERENCES

1. Brebbia, C.A., *Two Different Approaches for Transforming Domain Integrals to the Boundary*, Mathl Comput. Modelling, Vol. 15, No. 3-5, pp. 43-58, 1991.

2. Brebbia, C.A., J.C.F. Telles, and L.C. Wrobel, **Boundary Element techniques - Theory and applications in Engineering**, Springer-Verlag, 1984.

3. Cheng, A. H-D., S. Grilli, and O. Lafe, *Dual Reciprocity Boundary Element Based on Global Interpolation Functions*, Eng. Analysis with Boundary Elements, to appear, 1994.

4. Cheng, A. H-D., and D. Ouazar, *Groundwater*, Chapter 9 in **Boundary Element Techniques in Geomechanics**, eds. G.D. Manolis and T.G. Davies, CMP/Elsevier, 1993.

5. Fletcher, C.A.J., **Computational Techniques for Fluid Dynamics**, Vol. II (pg. 391), Springer-Verlag, 1991.

6. Greenberg, M.D., **Applications of Green's Functions in Science and Engineering**, Prentice-Hall, Englewood Cliffs, New Jersey, 1971.

7. Jaswon, M.A., and G.T. Symm, *Integral Equation Methods in Potential Theory and Elastostatics*, Academic, San Diego, Calif., 1977.

8. Lafe, O., *A Dual Reciprocal Boundary element Formulation for Viscous Flows*, in Proc. NASA Fifth Annual Thermal and Fluids Analysis Workshop (NASA Conference Publication 10122), Brook Park, Aug. 16-20, 1993.

9. Lafe, O., and A. H-D. Cheng, *A Global Interpolation Function Based Boundary Element Method for Deterministic, Non-homogeneous, and Stochastic Flows in Porous Media*, Computers and Structures, To Appear, 1994.

10. Nardini, D., and C.A. Brebbia, *A New Approach to Free Vibration Analysis using Boundary Elements*, in **Boundary Element Methods in Engineering**, Proc. 4th Int. Sem., Southampton, ed. C.A. Brebbia, Springer-Verlag, 312-326, 1982.

11. Partridge, P.W., C.A. Brebbia, and L.C. Wrobel, *The Dual Reciprocity Boundary Element Method*, CMP/Elsevier, 1992.

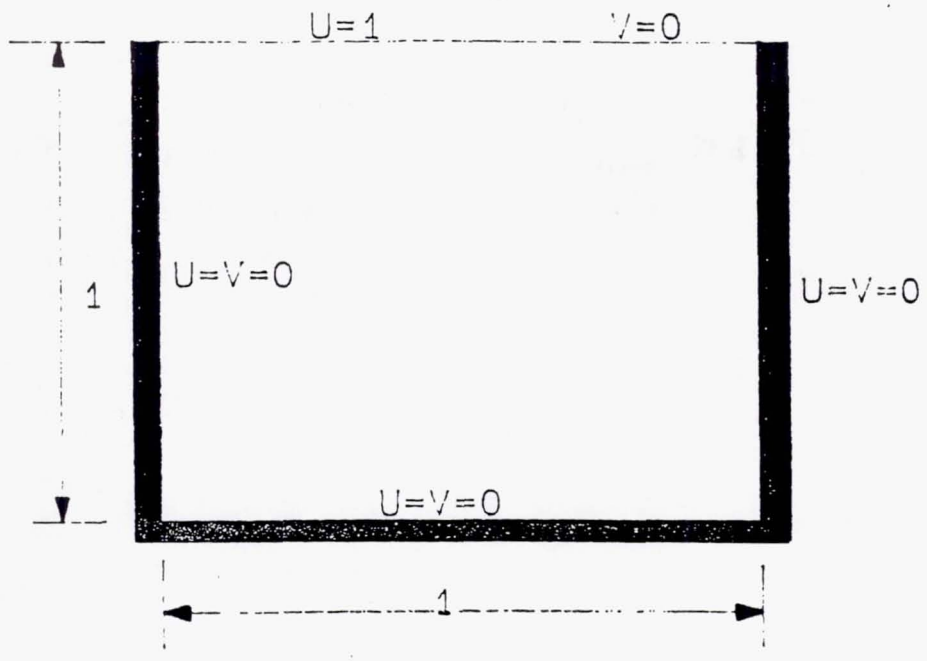

Figure 1: Lid-driven Cavity Problem

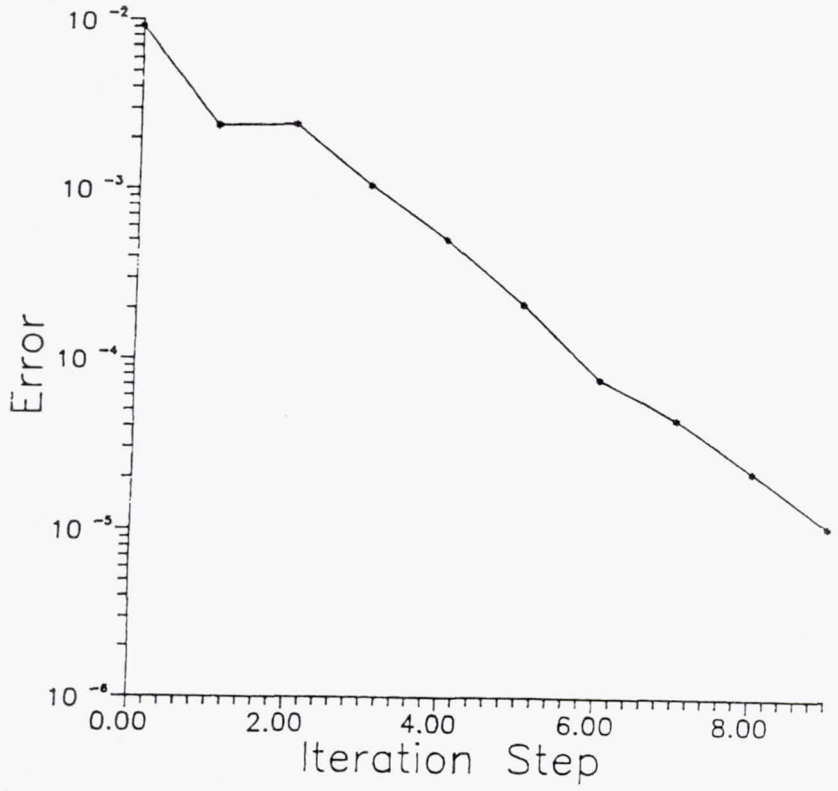

Figure 2: Typical Convergence Profile

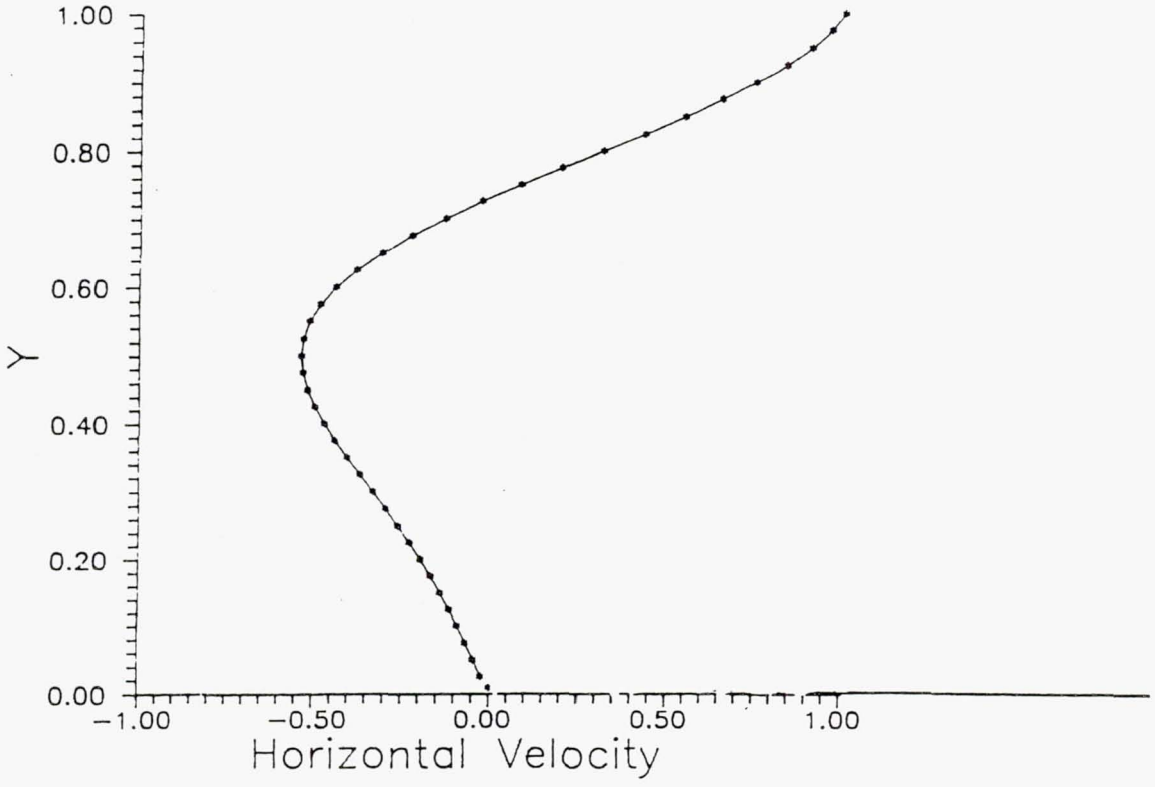

Figure 3: Horizontal Velocity at Vertical Center-Line

N95-27362

TURBULENCE BOUNDARY CONDITIONS FOR SHEAR FLOW ANALYSIS, USING THE DTNS FLOW SOLVER

M. Mizukami
NASA Lewis Research Center
Cleveland, Ohio

SUMMARY

The effects of different turbulence boundary conditions were examined for two classical flows: a turbulent plane free shear layer and a flat plate turbulent boundary layer with zero pressure gradient. The flow solver used was DTNS, an incompressible Reynolds averaged Navier-Stokes solver with k-ε turbulence modeling, developed at the U.S. Navy David Taylor Research Center. Six different combinations of turbulence boundary conditions at the inflow boundary were investigated: In case 1, 'exact' k and ε profiles were used; in case 2, the 'exact' k profile was used, and ε was extrapolated upstream; in case 3, both k and ε were extrapolated; in case 4, the turbulence intensity (I) was 1%, and the turbulent viscosity (μ_t) was equal to the laminar viscosity; in case 5, the 'exact' k profile was used and μ_t was equal to the laminar viscosity; in case 6, the I was 1%, and ε was extrapolated. Comparisons were made with experimental data, direct numerical simulation results, or theoretical predictions, as applicable. Results obtained with DTNS showed that turbulence boundary conditions can have significant impacts on the solutions, especially for the free shear layer.

INTRODUCTION

Turbulent shear flows play a major role in many aerospace and fluid dynamics applications. Wall bounded turbulent shear flows, i.e. turbulent boundary layers (TBL), are present in nearly all moderate to high speed external and internal flows. Turbulent free shear layers (FSL) are important for many applications such as flow mixers and thrust producing nozzles.

In computational fluid dynamic (CFD) analyses, the use of an appropriate boundary condition (BC) is a critical element in assuring convergence to an accurate solution. Use of inappropriate boundary conditions may cause any one or more of the following: inaccurate solutions, poor convergence, nonphysical effects, or divergence.

For turbulent flows, the k-ε turbulence model introduces two new flow properties, turbulent kinetic energy (k) and turbulent dissipation (ε), each with its corresponding transport equation which must be solved numerically by the flow solver. As for any other flow property, it would seem to be essential to assign the proper boundary conditions for k and ε, especially on the inflow boundary, where the flow enters the computational domain. However, the use of appropriate turbulence BC's is frequently underemphasized or neglected.

Ideally, the exact profiles of k and ε would be known, and they would be applied as the inflow BC, but that is usually not feasible. Experimental k profiles are sometimes available, but

often with inadequate resolution for use as a CFD BC, especially near the wall. Measurement of k requires an unsteady measurement of flow velocity, with a response time fast enough to capture the smallest turbulence time scales, preferably in 3 components to take into account turbulence anisotropy. ε is almost impossible to measure experimentally, as it is calculated from the second derivatives of mean flow properties, requiring exceedingly accurate measurements on a very fine survey grid.

Many flow solvers simply extrapolate k and ε on non-wall boundaries of the solution domain. But upstream extrapolation of turbulence properties at the inflow boundary is counter intuitive, and it has been shown to produce inaccurate results (Georgiadis and Yoder 1994). In particular, extrapolation of k and ε at the inflow appeared to inhibit the production of k near the inflow plane, resulting in locally lower turbulent viscosity. Furthermore, the eigenvalues of both k and ε transport equations are equal to the mean flow velocity, indicating that at the inflow boundary, k and ε values should be specified (Hirsch 1990).

Alternately, some turbulence properties could be assigned uniform values over the entire inflow boundary. Uniform turbulence intensity (I) and turbulent viscosity (μ_t) could be specified; k and ε values, which will vary across the boundary depending on the mean flow properties, can be derived from I and μ_t. Another possibility is to specify uniform I and turbulent length scale (L), and from these derive k and ε. However, the specified values of I and μ_t are typically arbitrary estimates. Georgiadis, Chitsomboon and Zhu (1994) examined a 2-D ejector nozzle, which includes both wall bounded and free shear flows. Specifying uniform I and μ_t at the inflow was found to match the data better than specifying I and L, or extrapolating k and ε.

In the present work, the effects of different CFD turbulence BC's are examined for two classical flows: a turbulent plane free shear layer and a flat plate turbulent boundary layer with zero pressure gradient. The flow solver used is DTNS, an incompressible Reynolds averaged Navier-Stokes solver with k-ε turbulence modeling. Different combinations of the following boundary conditions are used: 'exact' k profiles, 'exact' ε profiles, extrapolated k, extrapolated ε, uniform I, and uniform μ_t. Comparisons are made with experimental data, direct numerical simulation results, and theoretical predictions, as applicable.

METHODS

Flow Solver

DTNS is an incompressible Reynolds averaged Navier-Stokes flow solver with k-ε turbulence modeling, developed at the U.S. Navy David Taylor Research Center, primarily by Gorski (1988a, 1988b). The three versions of the code are designed to solve two dimensional (DTNS2D), axisymmetric (DTAXI) and three dimensional (DTNS3D) flows, respectively. Although the flows examined herein are two-dimensional, the three dimensional flow solver (DTNS3D) was used here, on a three dimensional grid with 5 identical grid planes in the cross stream direction, so that in the future, methods developed here could be be directly applied to three-dimensional problems of interest.

DTNS was selected for this study for two reasons. First, it is a relatively well established, general-purpose code, with a number of documented test cases with experimental comparisons, such as: cascades (Gorski 1988b), flow over a cylinder (Gorski 1988a), an NACA 0012 airfoil (Gorski 1988a), flow over a backward facing step (Gorski 1988a, Steffen 1992 & 1993) and

laminar boundary layers (Steffen 1992). This allows the present study to focus on the fluid dynamics, instead of the code development and validation. Second, it is an 'open' code, with the source code available. This allows the specialized turbulence BC's to be implemented by modifying the code. In addition, study of the source code leads to a deeper understanding of the computational procedure and the relevance of the resulting solution, which are essential to a fundamental study such as this.

The method of pseudo compressibility is used in the governing equations, so that state of the art schemes developed for compressible flows may be applied to incompressible flows. The total variation diminishing (TVD) scheme of Chakravarthy and Osher is used to discretize the convective terms of the governing equations. The discretized equations are solved implicitly using an approximate factorization method. Gorski (1988a) provides further details on the solution procedure.

The Launder and Spalding (1974) turbulence model is implemented, which is generally considered the standard high Reynolds (Re) number k-ε turbulence model. A wall function model is used, which does not require boundary layers to be resolved using large numbers of packed grid points, thus allowing complex wall bounded flows to be solved with a reasonable number of grid points, and in a reasonable amount of time. Although the profile of an attached turbulent boundary layer is assumed at the wall, the solutions have been found to be accurate even for some drastically separated flows (Steffen 1993). Even low Re k-ε models which resolve the boundary layer in detail on a fine grid, make certain empirical assumptions about the wall bounded flow characteristics. Furthermore, low Re k-ε models models are often highly grid sensitive, and can require extremely finely resolved grids packed very close to the wall to produce an accurate solution (Avva et al. 1990).

The boundary condition routines were modified to allow for different inflow conditions as follows. Mean flow velocities (**u**) are read in from a data file. k and ε may be independently specified at the boundary in two different ways: the profile may be read in from a data file, or it may be zeroeth-order extrapolated. μ_t is calculated from k and ε.

For both the wall bounded and free shear flow cases, six different combinations of k and ε BC's at the inflow boundary were investigated, as shown in table 1. In case 1, 'exact' k and ε profiles are used. In case 2, the 'exact' k profile is used, and ε is extrapolated upstream. In case 3, both k and ε are extrapolated; this is the default case for DTNS. In case 4, the I is uniformly 1%, and μ_t is equal to the laminar viscosity; k and ε values are derived from these using the following expressions. k and I are related by:

$$k = \frac{3}{2} I^2 \|\mathbf{u}\|^2 \tag{1}$$

In this turbulence model ε and μ_t are related by:

$$\mu_t = C_\mu \rho k^2 / \varepsilon \tag{2}$$

where C_μ=0.09, and the damping terms are neglected. In case 5, the 'exact' k profile is used, μ_t is equal to the laminar viscosity, and ε is calculated from (2). In case 6, the I is 1%, k is derived from I as in (1), and ε is extrapolated.

The amount of detailed turbulence information required at the inflow boundary varies from case to case. Case 1 requires both k and ε profiles; this is the most ideal case, but as discussed before, ε profiles are almost never available. Cases 2 and 5 require only k profiles; this is typically more feasible than case 1, because turbulence levels, and thus k, are often measured

experimentally. Cases 3, 4 and 6 require no detailed turbulence information at all.

Flat Plate Turbulent Boundary Layer

The flat plate TBL with zero pressure gradient is a fundamental fluid dynamic problem that has been extensively studied. Initial boundary layer flow property profiles are applied at the inflow boundary of the computational domain, the flow is propagated downstream, and the flow at a downstream station is compared with benchmark results. (figure 1)

The direct numerical simulation (DNS, not to be confused with DTNS) results of Spalart (1988) are used to provide the 'exact' inflow conditions at Re_θ = 300, and the benchmark downstream solution at Re_θ = 1410, where Re_θ is the Reynolds number based on the momentum thickness of the boundary layer and freestream velocity. When properly used, DNS is thought to be as accurate as experimental results, and it provides completely detailed information of the flowfield, including information needed to calculate k and ε, which are difficult to measure experimentally.

The grid dimensions are 100 in the streamwise direction, 40 in the vertical direction, and 5 identical planes in the cross flow direction to accommodate the 3D flow solver. The grid is packed to the wall such that at the inflow boundary y^+ is about 20. The bottom wall has a no slip boundary condition, the top 'far' wall is a slip wall, the sides are slip walls, and the outflow has a constant pressure. Convergence was typically obtained in several thousand iterations, depending on the particular case.

Turbulent Plane Free Shear Layer

The turbulent plane FSL is one of the simplest free shear layers, and it too has been extensively studied. The computational domain consists of the free shear layer mixing region only, with the upstream boundary at the trailing edge (TE) of the splitter plate (figure 6). As in the TBL, the initial profiles are applied at the upstream BC of the computational domain, the flow is propagated downstream, and the flow at a downstream station is compared with exact results.

The plane free shear layer in the McCormick's (1993) experiment is simulated, and comparisons are made with data from the extensive flow diagnostics in the mixing region. McCormick's facility consists of a fan driven wind tunnel, a contoured splitter plate, screens on one side to slow the flow, and a square test section. The flow velocity on the slower, upper side (U_1) is 4.88 m/s, and the velocity on the faster, lower side (U_2) is 8.53 m/s, giving a velocity ratio of 1 : 1.75. Just upstream splitter TE, the momentum thickness (θ) is 1.237mm on the upper / low speed side, and θ = 1.107mm on the lower / high speed side. Extensive measurements were made with triple sensor hot film probes of all three velocity components, including turbulence properties. The flow was visualized using smoke injection and laser light sheets.

The 'exact' u, k and ε profiles at the upstream boundary of the computational domain (i.e. at the splitter TE) were obtained from a separate DTNS solution to a flat plate TBL, because k and ε profiles at the splitter trailing edge were not measured experimentally. Certainly, the resulting solution of the FSL will be affected by the accuracy of the DTNS TBL solutions, but they should be sufficiently accurate for purposes of comparing with other substantially different k and ε BC's. The DNS TBL solutions discussed above could not be used for this purpose, because the Re_θ values do not correspond to those at the splitter TE.

The grid dimensions are 60 in the streamwise direction, 39 across the shear layer, and 5

identical planes in the cross flow direction to accommodate the 3D flow solver. The grid is packed such that y^+ is between 20 and 30 at the inflow boundary. The sides are slip walls, and the outflow has a constant pressure. Convergence was again typically obtained in several thousand iterations, depending on the particular case.

RESULTS

Flat Plate Turbulent Boundary Layer

Figure 2. shows the downstream development of the boundary layer momentum thicknesses (θ) for the six cases, and the TBL 1/5th power law approximate theory predictions (Kuethe & Chow 1986). Downstream distance is nondimensionalized as the Reynolds number based on the distance from the upstream plane (ΔRe_x). Cases 2 and 3 show good agreement with theory. In cases 4, 5 and 6, boundary layer development near the inflow boundary is suppressed. Surprisingly, case 1, the ideal case with all turbulence properties exactly specified, also shows slightly suppressed boundary layer development near the inflow boundary. However, downstream of the initial discrepancies, all 6 cases quickly approach the same theoretical slope.

At the inflow boundary, $\Delta Re_x = 0$ and $\Delta Re_\theta = 300$. Comparisons of u, k and ε profiles are made downstream at the $\Delta Re_x = 551000$ plane, where the approximate theory predicts that $\Delta Re_\theta = 1410$.

Figure 3a shows the 'exact' u profile, specified at the inflow boundary in all 6 cases. Figure 3b shows the u profile at the downstream plane. Although the profiles have slightly different in thicknesses, all have the about the same shape as the DNS solution.

Figure 4a show: the 'exact' inflow k profile used in cases 1,2 and 5; the k profile for I=1% used in cases 4 and 6, which is barely visible next to the vertical axis; and the k profile resulting from upstream extrapolation in case 3. Clearly, $I = 1\%$ specifies k to be much lower than it should be, and upstream extrapolation results in a k that is too high. Figure 4b shows the downstream k profiles. Despite the drastically different initial conditions, all 6 cases match the DNS solution shape surprisingly well, but again with slightly different thicknesses.

Figure 5a shows the exact ε profile used in case 1, the profiles specified in cases 4 and 5, and the profiles resulting from upstream extrapolation in cases 2, 3 and 6. Case 3, with both k and ε extrapolated upstream, gives the best prediction of the initial ε profile after case 1, but this is most likely a fortunate coincidence. Cases 2 and 6 results in ε profiles that are too low. Case 5 specifies an ε profile that is too high. The case 4 profile is not visible on the graph, because, the ε values are all near zero. Figure 5b shows the downstream ε profiles. All 6 cases fall on approximately the same curve, and overpredict ε.

Turbulent Plane Free Shear Layer

Figure 7. shows the downstream development of the shear layer momentum thicknesses (θ) for the six cases. θ is indicative of the amount of mixing taken place between the high and low speed flows, and is defined as:

$$\theta = \int \frac{(u - U_2)(U_1 - u)}{(U_2 - U_1)^2} dy \tag{3}$$

where U_1 is the mean velocity of the upper / low speed side, and U_2 is the velocity of the bottom / high speed side.

Downstream distance is nondimensionalized as the Reynolds number based on U_1 and the axial distance from the computational inflow plane (Re_x), which coincides with the trailing edge (TE) of the splitter plate. Note that near the splitter TE, θ is actually negative, due to the low speed flow from the splitter boundary layers. Cases 1, 2 and 4 show good agreement with the experimental results of McCormick & Bennett. In cases 5 and 6, shear layer development near the inflow boundary is suppressed. In case 3, the shear layer expands at an unrealistically high rate. However, the initial discrepancies in all cases except 6 do not persist far downstream, and the curves shortly approach the same slope.

Profiles of u, k and ε are plotted at three stations: $Re_x = 0$, at the splitter TE and inflow boundary; $Re_x = 28244$, and $Re_x = 290510$. The experimental data for u and k are available and plotted for the two downstream stations for comparisons.

Figure 8a shows the 'exact' u profile, used as the inflow BC in all 6 cases. Figure 8b shows the u profiles at the two downstream stations. At $Re_x = 28244$, cases 4, 5 and 6 appear to give the best agreement with data; at $Re_x = 290510$, cases 1 and 2 appear better. In case 3, the shear layer is far too thick.

Figure 9a show: the 'exact' inflow k profiles used in cases 1, 2 and 5; the k profile for I = 1% used in cases 4 and 6 which is too low to be visible on the plot; and the k profile that results from upstream extrapolation in case 3. Again, I=1% specifies k to be much lower than it should be, and upstream extrapolation results in k that is much too high. Figure 9b shows the downstream k profiles. At both stations, cases 1 and 2 give the best agreement with data, cases 4,5 and 6 underpredict k to varying extents, and case 3 drastically overpredicts k.

Figure 10a shows the 'exact' inflow ε profile used in case 1, the profiles specified in cases 4 and 5, and the profiles resulting from upstream extrapolation in cases 2, 3 and 6. Case 2 underpredicts ε, case 3 creates an unrealistically wide profile, cases 4 and 6 are close to zero and not visible on the plot, and case 5 specifies an unreasonably high spike. Downstream, since no experimental data is available for ε, it is difficult to tell which results are the most accurate, but clearly, the case 3 profile is too wide.

CONCLUSIONS

The effects of different turbulence property CFD boundary conditions were examined using the DTNS flow solver for two classical flows: a turbulent plane free shear layer (FSL) and a flat plate turbulent boundary layer (TBL) with zero pressure gradient. Six different combinations of turbulence property boundary conditions at the inflow boundary were investigated. The major observations and conclusions of the study were as follows:

1. Wall bounded turbulent shear flows appeared to be relatively insensitive to the turbulence inflow BC. Despite drastically different k and ε profiles at the inflow boundary, the mean velocity (u), k and ε profiles downstream were nearly identical, and all cases approached the same correct slope for momentum thickness development. In the near field of the

inflow boundary, cases 1, 4, 5 and 6 suppressed the boundary layer development to varying extents. Cases 2 and 3 gave the best results. Discrepancies in the initial boundary layer development slightly affected the thicknesses at downstream stations.

2. Turbulent free shear flows appear to be more sensitive to turbulence inflow BCs than the wall bounded flows. For free shear flows, all cases except 3 gave reasonably good results, but with more discrepancies between the cases than for wall bounded flows. Cases 1 and 2 gave the best results. Case 5 inhibited the initial shear layer growth, and created an unrealistic spike in the ε profile at the inflow.

3. For free shear flows, case 3 (upstream extrapolation of k and ε at the inflow boundary) gave a drastically high shear layer growth rate. Note that this is the default case for many flow solvers.

4. Overall, when both 'exact' k and ε profiles were used, cases 1 and 2 gave the best results. When only k profiles were used, case 2 was best. When no 'exact' turbulence profiles were used, cases 4 and 6 gave reasonable results.

5. Some additional factors not considered in this study were: compressibility, specifying different levels of uniform turbulence intensity, specifying different levels of uniform turbulent viscosity, and more complex flowfields.

6. The particulars of these findings may vary for different k -ε turbulence models and numerical schemes. However, it is conjectured that overall 'lessons learned' from this study are probably applicable to other flow solvers as well.

REFERENCES

Avva, R., Smith, C. and Singhal, A. Comparative study of high and low Reynolds number versions of k-ε models. AIAA 90-0246

Georgiadis, N. J., Chitsomboon, T. and Zhu, J. 1994 Modification of the two-equation turbulence model in NPARC to a Chien low Reynolds number k-ε formulation. NASA TM to be published.

Georgiadis, N. J. and Yoder, D. A. 1994 Use of Navier-Stokes methods for the calculation of high-speed nozzle flow fields. NASA TM 106551, AIAA 94-3212.

Gorski, J. J. 1988a TVD solution of the incompressible Navier-Stokes equation with an implicit multigrid scheme. in *Proceedings of the AIAA/ASME/SIAM/APS 1st National Fluid Dynamics Congress*, vol. 1, pp. 394-401.

Gorski, J. J. 1988b Incompressible cascade calculations using an upwind differenced TVD scheme. in *Advances and Applications in Computational Fluid Dynamics* (O. Baysal, ed.). ASME-FED. vol. 66, pp. 61-69.

Hirsch, C. 1990 *Numerical Computation of Internal and External Flows, Vol. 2: Computational Methods for Invscid and Viscous Flows*. pp. 344-357. John Wiley & Sons, Chichester.

Kuethe, A. M., and Chow C-Y. 1986 *Foundations of Aerodynamics*, pp. 403-408. John Wiley & Sons, New York.

Launder, B. E. and Spalding, D. B. 1974 The numerical computation of turbulent flows. *Computer Methods in Applied Mechanics and Engineering*. vol. 3, pp. 269-289.

McCormick, D. C. and Bennett, J. C. 1993 Vortical and turbulent structure of a lobed mixer free-shear layer. AIAA 93-0219.

Spalart, P. R. 1988 Direct simulation of a turbulent boundary layer up to R_θ = 1410. *J. Fluid Mech.* **187**, 61-98.

Steffen, C. J. 1992 An investigation of DTNS2D for use as an incompressible turbulence modeling test-bed. NASA TM-105593.

Steffen, C. J. 1993 A critical comparison of several low Reynolds number k-ε turbulence models for flow over a backward-facing step. NASA TM-106173, AIAA 93-1927.

Steffen, C. J. private communications

Table 1. Turbulence property boundary conditions

Case #	k	ε	I	μ_t
1	exact	exact	-	-
2	exact	extrapolated	-	-
3	extrapolated	extrapolated	-	-
4	calc. from I, **u**	calc. from k, μ_t	1%	μ_{lamin}
5	exact	calc. from k, μ_t	-	μ_{lamin}
6	calc. from I, **u**	extrapolated	1%	-

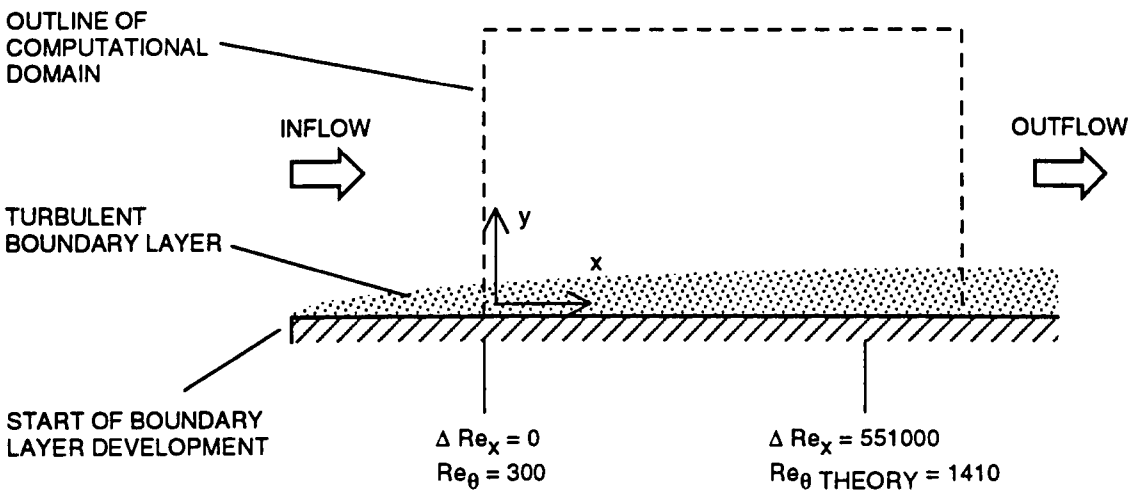

Figure 1. schematic of flat plate turbulent boundary layer (TBL) flow, and computational domain

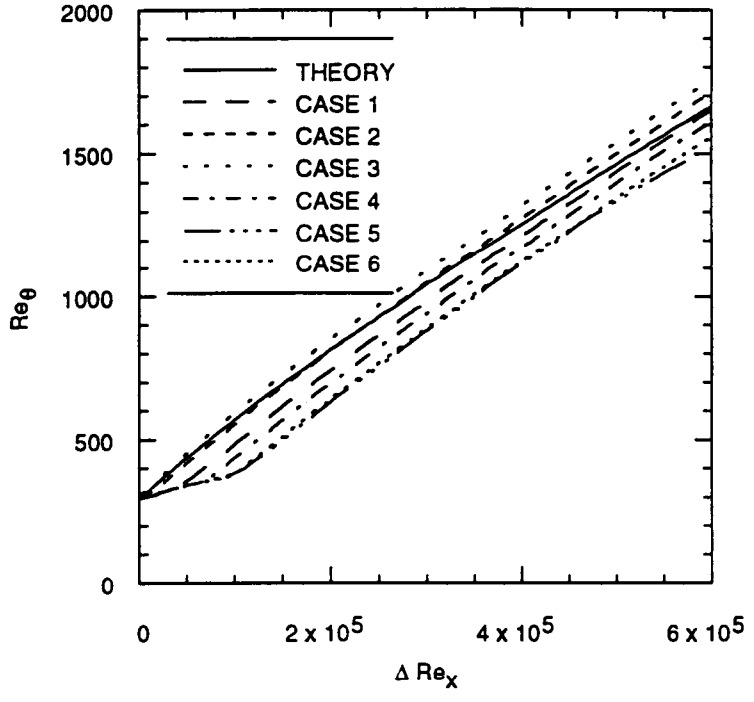

Figure 2. TBL momentum thickness development

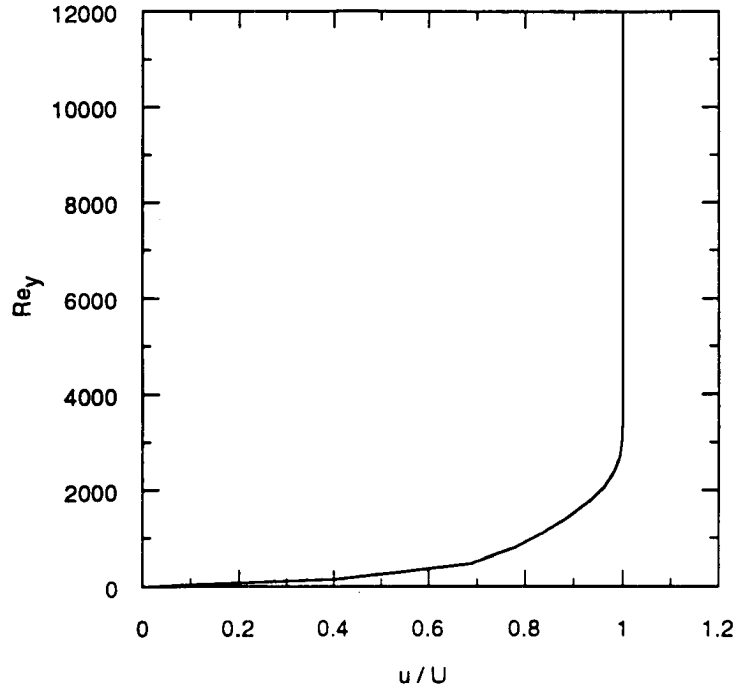

Figure 3a. TBL mean axial velocity profile at inflow boundary ($Re_\theta = 300$, $\Delta Re_x = 0$)

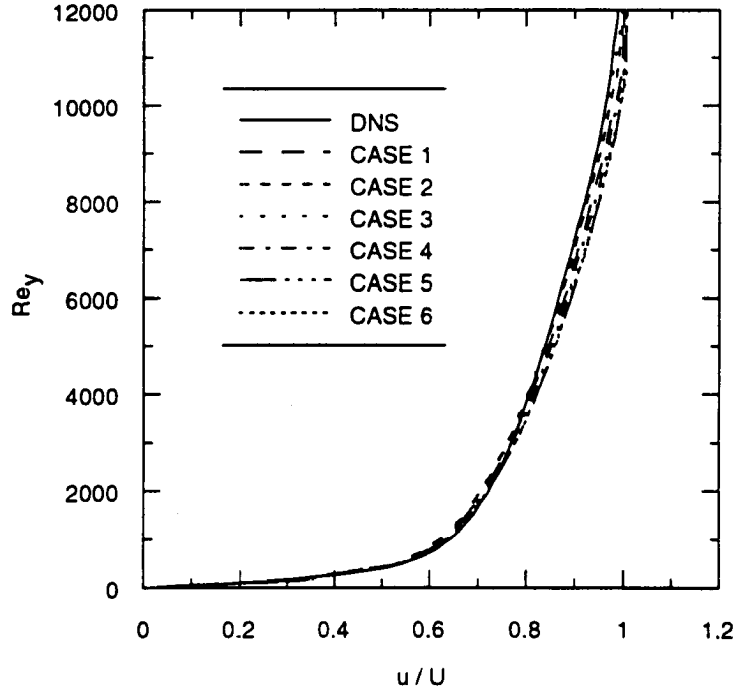

Figure 3b. TBL mean axial velocity profiles at $\Delta Re_x = 551000$

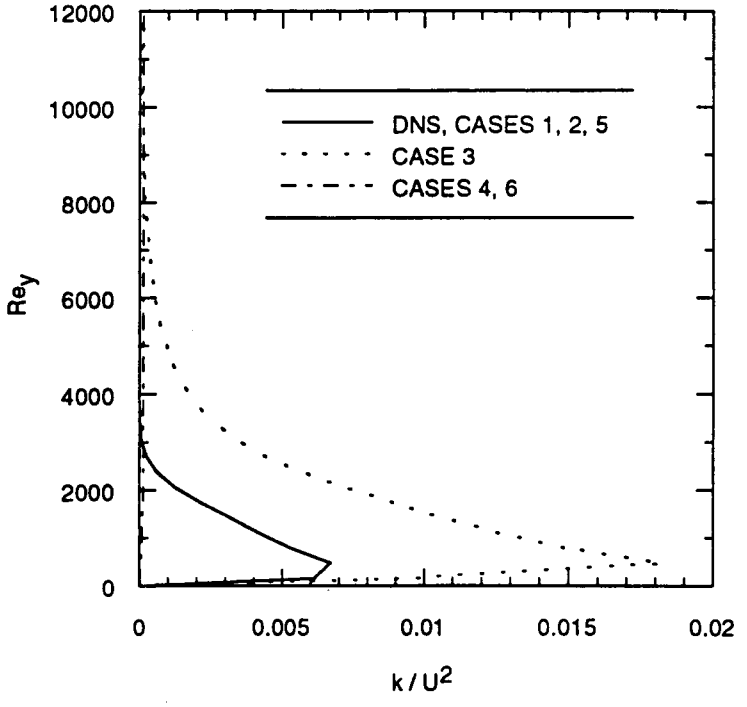

Figure 4a. TBL turbulent kinetic energy profiles at inflow boundary ($\Delta Re_x = 0$)

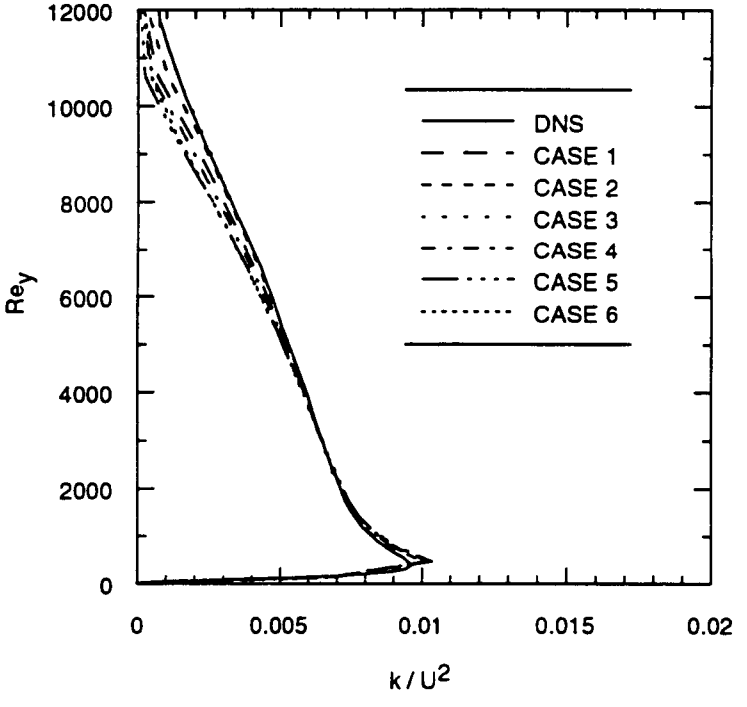

Figure 4b. TBL turbulent kinetic energy profiles at $\Delta Re_x = 551000$

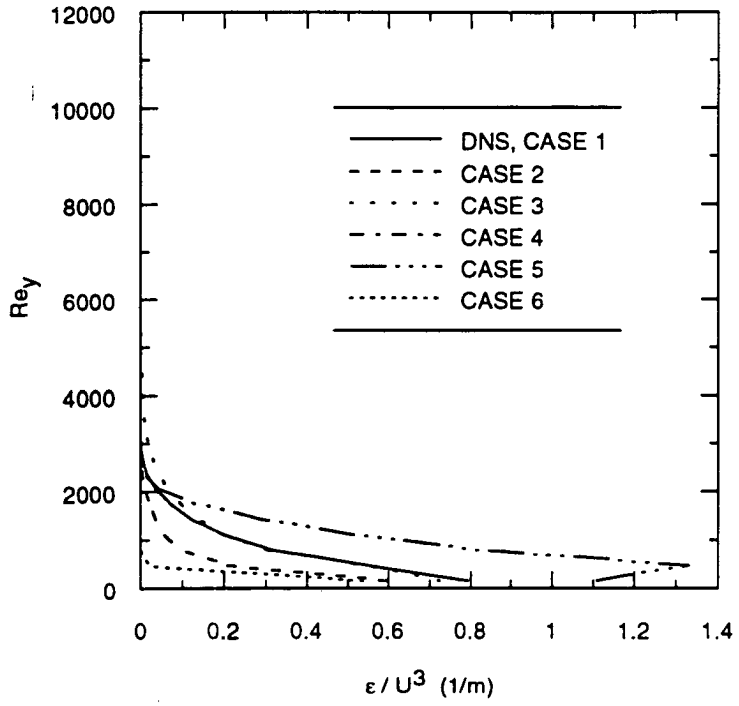

Figure 5a. TBL dissipation profiles at inflow boundary ($\Delta Re_x = 0$)

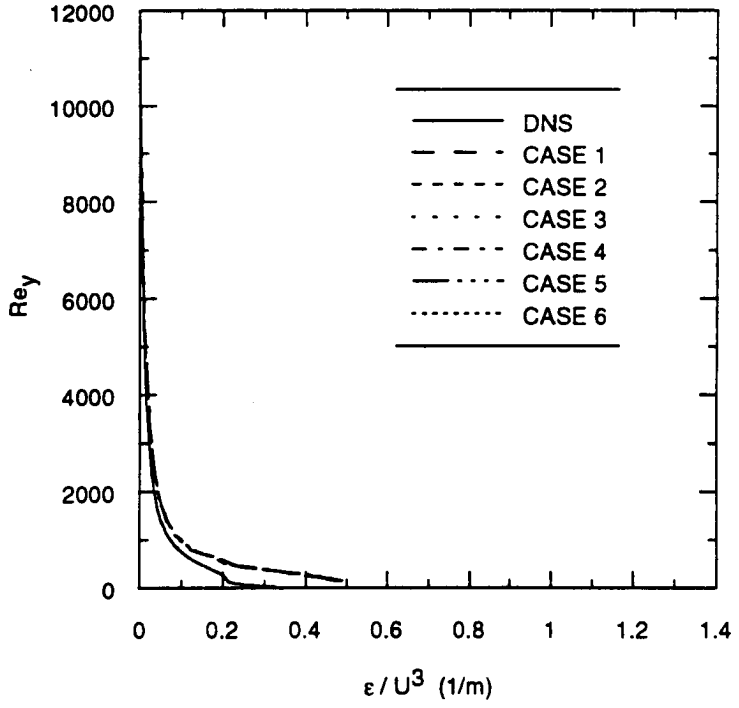

Figure 5b. TBL dissipation profiles at $\Delta Re_x = 551000$

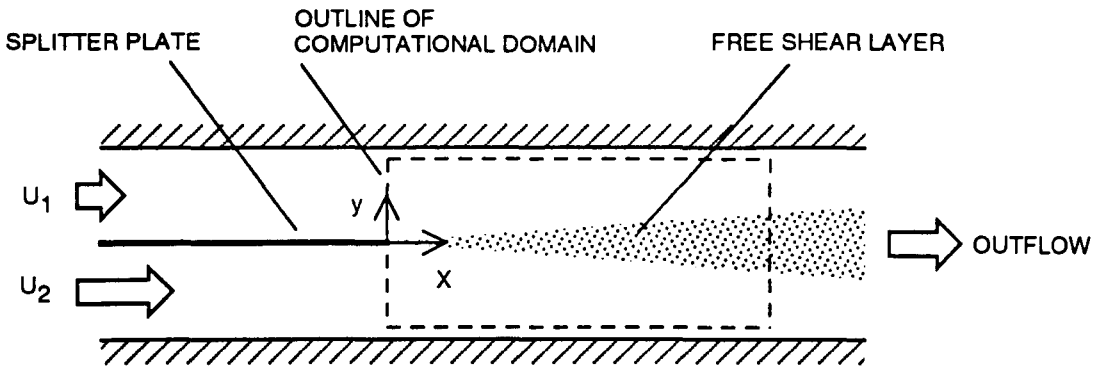

Figure 6. schematic of turbulent plane free shear layer (FSL) flow and computational domain

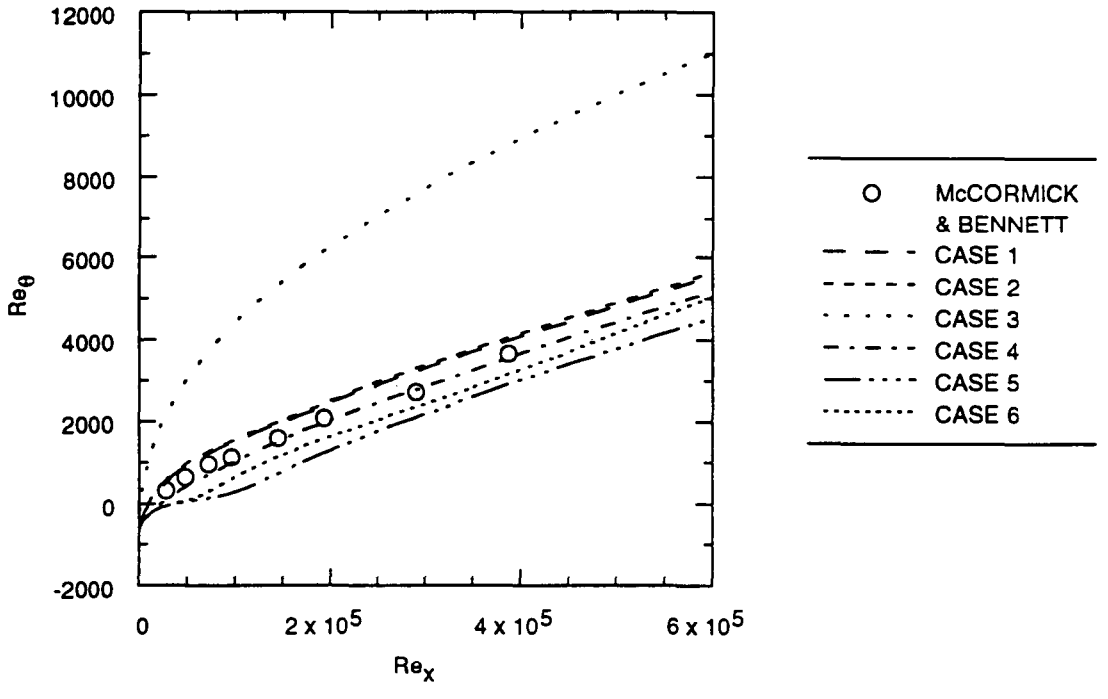

Figure 7. FSL momentum thickness development

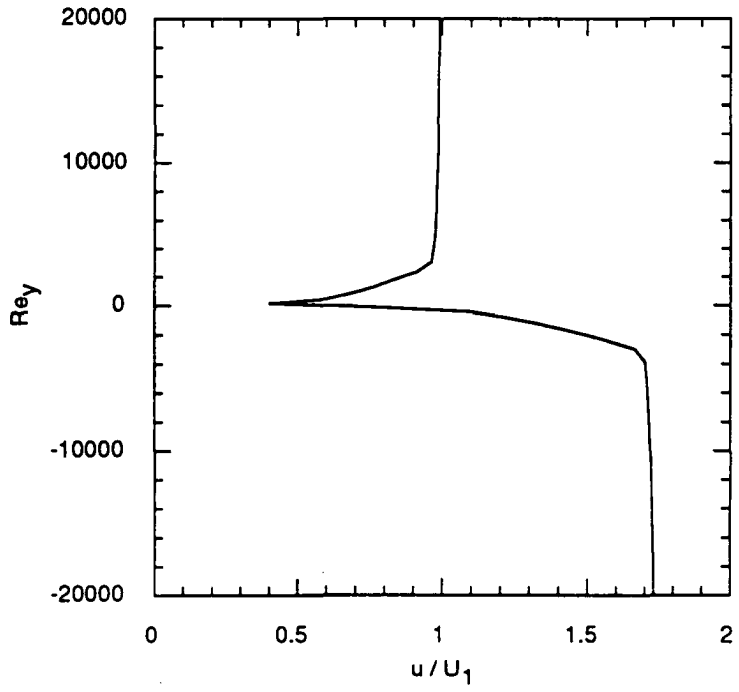

Figure 8a. FSL mean axial velocity profile at inflow boundary ($Re_x = 0$)

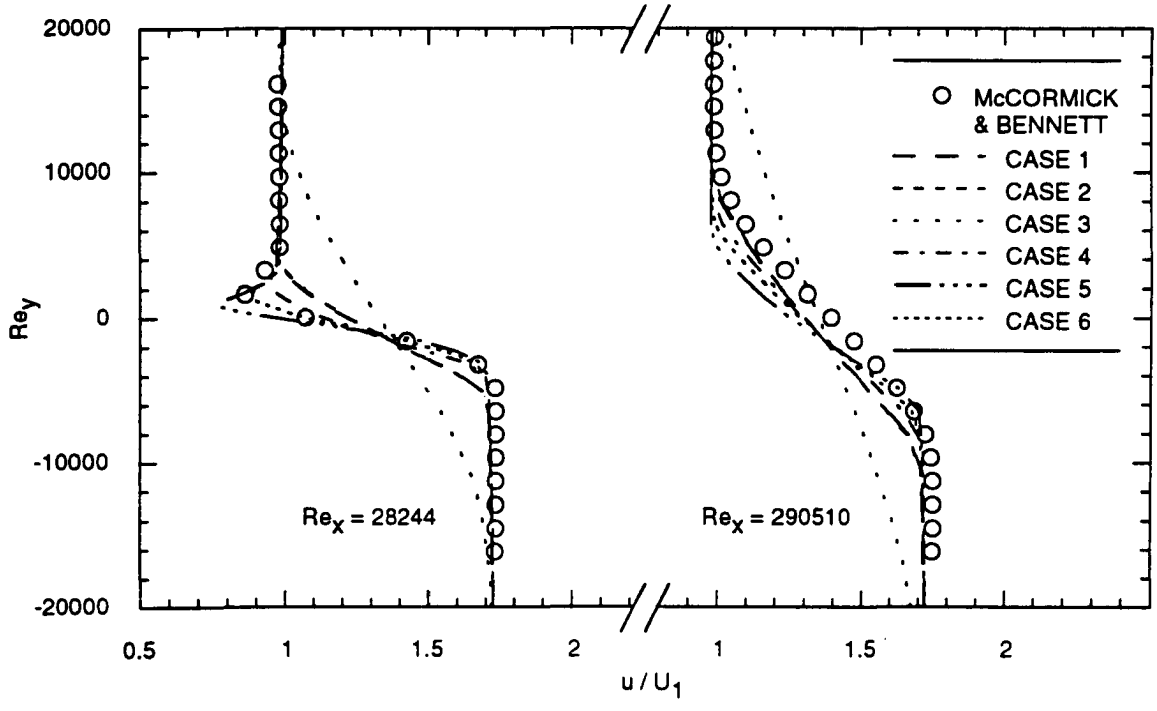

Figure 8b. FSL mean axial velocity profiles at downstream stations

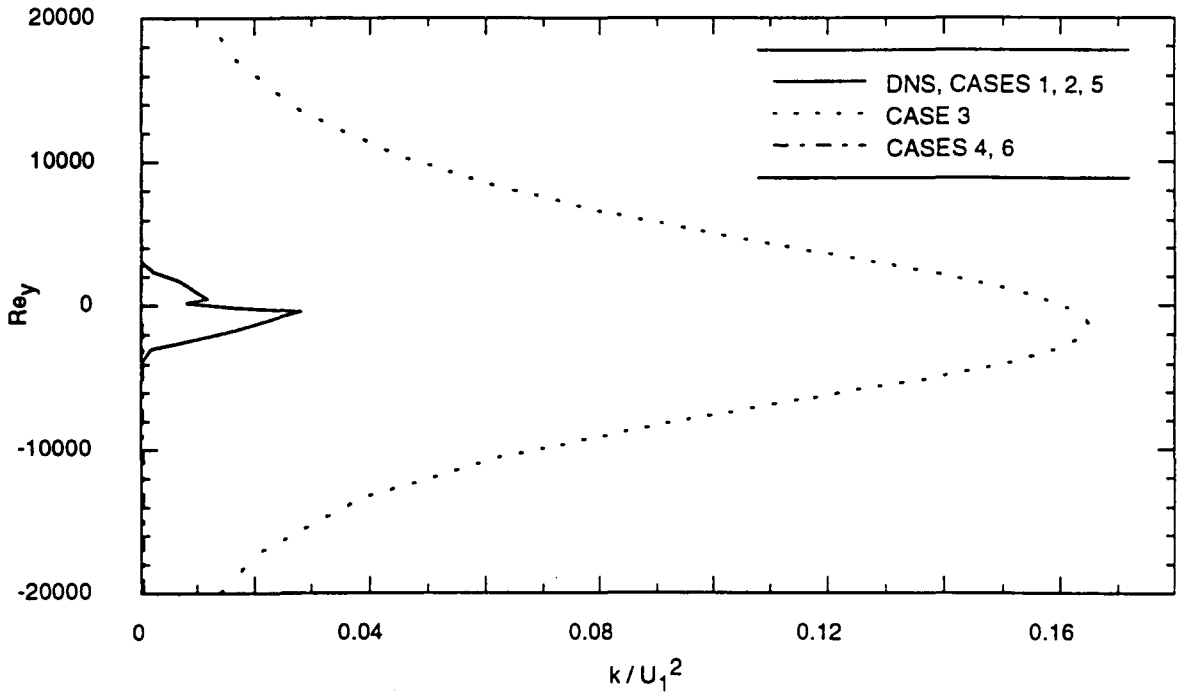

Figure 9a. FSL turbulent kinetic energy profiles at inflow boundary ($Re_x = 0$)

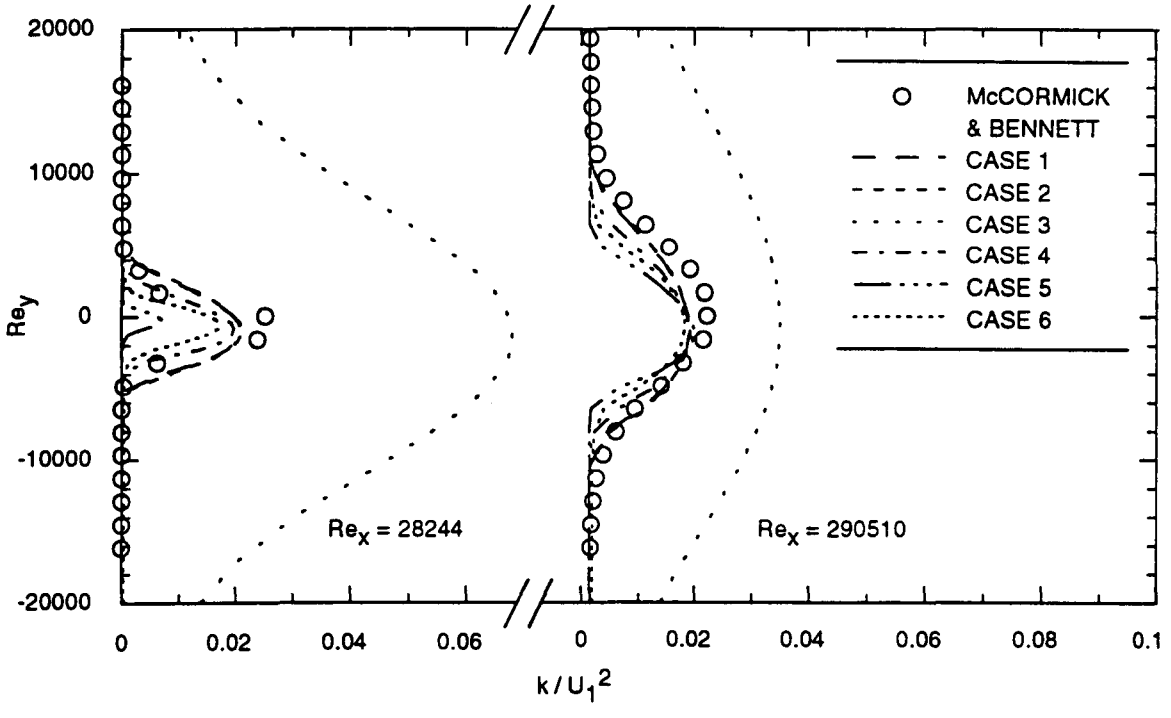

Figure 9b. FSL turbulent kinetic energy profiles at downstream stations

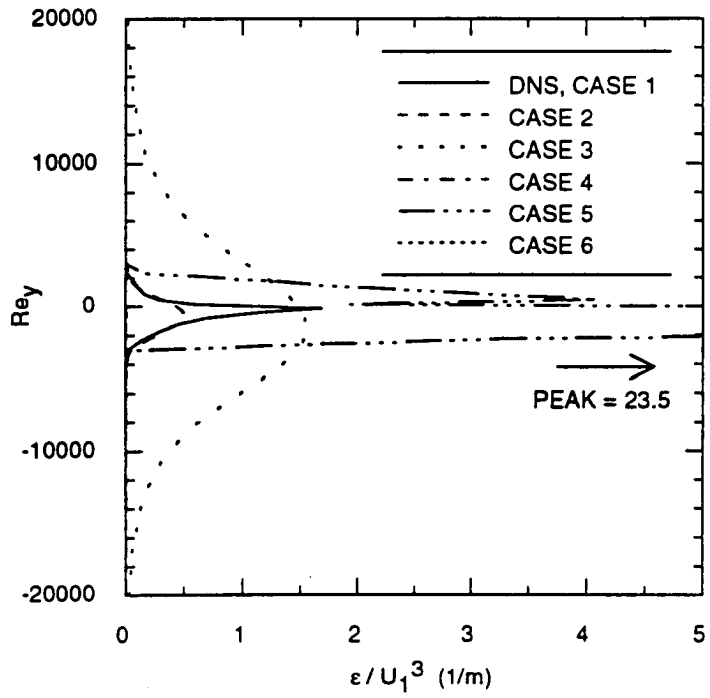

Figure 10a. FSL dissipation profiles at inflow boundary ($Re_x = 0$)

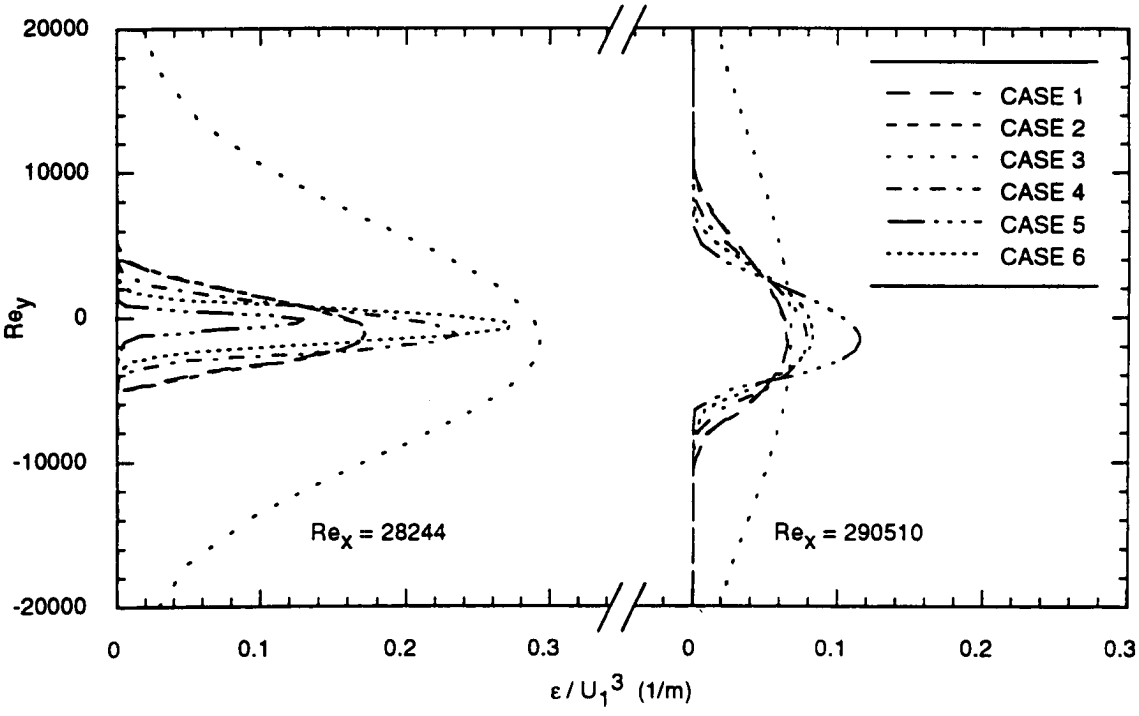

Figure 10b. FSL dissipation profiles at downstream stations

THERMAL NEUTRAL FORMAT BASED ON THE STEP TECHNOLOGY

P. Planas Almazan
Thermal Control and Life Support Division
ESTEC/ESA
Noordwijk, Netherlands

and

J.L. LeGal
Mechanical, Thermal & Energetics Division
CNES
Toulouse, France

ABSTRACT

The exchange of models is one of the most serious problems currently encountered in the practice of spacecraft thermal analysis. Essentially, the problem originates in the diversity of computing environments that are used across different sites, and the consequent proliferation of native tool formats.

Furthermore, increasing pressure to reduce the development's life cycle time has originated a growing interest in the so-called spacecraft concurrent engineering. In this context, the realisation of the interdependencies between different disciplines and the proper communication between them become critical issues.

The use of a neutral format represents a step forward in addressing these problems. Such a means of communication is adopted by consensus. A neutral format is not directly tied to any specific tool and it is kept under stringent change control. Currently, most of the groups promoting exchange formats are contributing with their experience to STEP, the Standard for Exchange of Product Model Data, which is being developed under the auspices of the International Standards Organization (ISO 10303).

This paper presents the different efforts made in Europe to provide the spacecraft thermal analysis community with a Thermal Neutral Format (TNF) based on STEP. Following an introduction with some background information, the paper presents the characteristics of the STEP standard. Later, the first efforts to produce a STEP Spacecraft Thermal Application Protocol are described. Finally, the paper presents the currently harmonised European activities that follow up and extend earlier work on the area.

ABBREVIATIONS AND TERMS

AAM	Application Activity Model
AIM	Application Interpreted Model
ARM	Application Reference Model
ANSI	American National Standards Institute
AP	Application Protocol
ASCII	American Standard Code for Information Interchange

ATS	Application Thermique Spatiale
CAD	Computer Aided Design
CAE	Computer Aided Engineering
CNES	Centre National d'Etudes Spatiales
ECLS	Environmental Control and Life Support
ESA	European Space Agency
ESARAD	ESA's radiative analysis software
ESATAN	ESA's thermal network analyser
ESTEC	ESA's European Research and Technological Centre
FE	Finite Elements
FHTS	Fluid loop extension to ESATAN
FLUOR	CNES' Radiative Analysis Software
ICETAS	Integrated Communication Environment for Thermal Analysis
IGES	Initial Graphics Exchange System
IR	Integrated Resources
ISO	International Standards Organization
SDAI	Standard Data Access Interface
SET	Standard d'Exchange et Transfert
TAS	Thermal Analysis for Space AP
STEP	ISO's Standard for Exchange of Product Model Data
TMM	Thermal Mathematical Model
TNF	Thermal Neutral Format
VDA-FS	Verband Deutschen Automobil, Flaechen Schnittstelle
YC	ESTEC's Thermal Control and Life Support Division
YCV	YC's Analysis and Verification Section

THE THERMAL NEUTRAL FORMAT

Standardisation of the analysis tools

The standardisation of analysis procedures has become an essential requirement for the organisations operating in the European Space sector, due to the complexity found in large space projects involving international consortia of companies. This standardisation has most obviously materialised in the availability of a set of *de facto* standard tools which facilitate the interaction between the different parties involved in a project. Examples are the ESABASE (ref. [1]), ESATAN (ref. [2]), FHTS (ref. [2]), THERMICA (ref. [3]) and the recently released ESARAD (ref. [4]) tools.

An important consequence of this situation is that the tool's native formats have also been adopted as the *de facto* standards for exchange and archive of thermal models. This seemed quite convenient at a time when the number of tools was small and no obvious alternative was available. However, this approach is not satisfactory any longer. In fact, the use of native formats has serious and long reaching implications, which will be reviewed in the following sections.

The problem of exchange

The exchange of thermal models is currently posing a number of serious problems to the day-to-day practice of the spacecraft thermal analysis. Essentially, the problem originates in the diversity of computing environments adopted by different organisations, and the consequent proliferation of native tool formats. The situation can be even more troublesome for those organisations needing to maintain several environments to serve different requirements or customers.

Furthermore, the organisations often invest in the development of proprietary software, which is normally intended to serve purposes not adequately covered by the standard tools. These developments contribute to enhance the companies' competitiveness, by taking advantage of in-house expertise and skills. However, most of these tools introduce new exchangeability requirements, aggravating further the problem.

The concurrent engineering issue

A state-of-the-art analysis environment cannot overlook the need to provide proper communication means between the different teams involved in the spacecraft development. Indeed, spacecraft engineering is a true multidisciplinary process, in which the information follows complicated paths and different disciplines interact in non-trivial manners.

Traditionally, each discipline's analysis has been performed in an uncoupled way, in an attempt to isolate their particularities and thus to simplify the assumptions and methods used for each of them. However, two main developments have radically changed in the last years the context in which the analysis takes place:

- the advances made in terms of computing power have allowed to perform more and more complex analysis in a shorter time. Furthermore, this evolution has enabled the development of tools that model and analyse the physical problems with fewer simplifications and restrictions.
- more and more complex missions impose requirements which cannot be achieved by performing uncoupled disciplinary analysis.

With these ideas in mind, there is an increasing trend to acknowledge the interdependencies between design and analysis and to integrate them within a tightly coupled process. This approach also encourages the concurrent analysis of several physical problems through the use of common models, procedures and tools. The final objectives are those of streamlining the flow of information and of increasing the efficiency and the capabilities of the design and analysis processes, while rationalising the resources used.

Two issues are particularly important in this context. Firstly, a good communication between the CAD world and the analysis environment has become an essential requirement. Indeed, although the flow of information between disciplines depends on several organisational issues, the initial stage is typically the acquisition of configurational data from the project source, which in general is a CAD system. Secondly, proper communication to commercial finite element (FE) packages is more and more important. The continuous evolution of these tools in the last years makes them very attractive to both managers and engineers. FE packages provide a framework which can be used to integrate individual discipline tools to yield the desired multidisciplinary analysis capability. Although finite differences remains the method of choice in spacecraft thermal analysis, the drive towards concurrent engineering is likely to foster the use of FE tools in the future.

The problem of archive

The exchangeability requirements can be extended quite naturally to the archive and retrieval of analysis models and results. After all, one can consider archiving as an exchange across time. Indeed, an archived model might not run properly when retrieved because of the evolution of the tool and the incompatibility between different versions. An extreme case, but not unlikely given the typically long duration of the space projects, would arise when the tools once used in a project are not available (or supported) any more.

A further reason making the case for stable archive means is the need to perform occasional emergency analysis campaigns to cope with spacecraft operation modes that follow unexpected events or failures. Under the urgency of these situations, costly modifications to the archived models are simply not acceptable.

The need for a neutral format

It is clear that the use of native formats as a means of exchange brings about serious problems. For instance:

- their use encourages the proliferation of tool-to-tool interfaces. Obviously this is not the most efficient way to exchange data between a given number of software packages.
- native formats are intrinsically unstable, i. e. they evolve with time. Therefore, the software interfaces that read/write native formats have to be constantly updated in order to keep up with new versions of the tools.
- the interface developers need to have a complete, updated description of the two formats being interfaced. This might be a problem if, as usual, the interface developers are not in control (at least one) of the formats. This fact increases the chances of software interfaces lagging behind the evolution of the tools, or simply being obsolete.
- organisations may have to develop different interfaces to satisfy each major customer's requirements. The extra costs incurred by this practice are frequently absorbed by the customer.

The use of a neutral format overcomes these serious problems. Such an approach is adopted by consensus as a means of exchange and archive. A neutral format does not depend on any specific tool and it is kept under stringent change control. The neutral format system consists not only of the description of the data intended to be exchanged or archived, but also of a formalism describing the means for exchange or archive and of the interfaces to other formats.

According to ref. [5], a Thermal Neutral Format (TNF) shall fulfil the following requirements:

- the TNF shall ultimately support the domain relevant to all the software tools used to perform thermal analysis.
- the interfaces in both directions (TNF to native format and vice versa) shall preserve the integrity of the information being exchanged or archived.
- the TNF shall be flexible enough to allow its extension without modification of the existing features.
- the TNF shall allow the selective treatment of the data. That is, each interface shall be able to process only the data relevant to the interface.
- the TNF shall be portable across systems and sites.

A TNF should also benefit of a large scope. Indeed, a widely spread standard formalism should be used to support the data exchanged or archived, simply because commercial CAD/CAE and FE tools are more likely to include built-in interfaces to internationally accepted standard formats. The development of a specific formalism for the TNF would not only waste efforts but also limit its immediate scope of application.

Finally, it is important to notice that were a TNF available, the development of interfaces to and from the TNF would normally be left to the tool developers themselves. This would likely give better chances to have interfaces up-to-date to the last tool versions.

Initiatives in the field of Thermal Model exchange and archive

Although the problems described in the previous sections have been around for a long time, the development of a TNF, based on a broad consensus within the European Space Industry, has not been attempted until recently. However, a number of initiatives were born with the intention to address the problems in one way or another.

As previously commented, native formats were typically exchanged between sites. The Thermal Mathematical Models (TMM) exchanged by means of ESATAN input decks are a clear example of this approach. As the need to exchange geometry-based models grew, the requirement for a new format became obvious. For that purpose, the ESABASE[4] language started to be used. Although ESABASE is basically a system engineering package, its input language provides a means to define analysis-tool-independent models. Furthermore, the ESABASE framework includes translators to several radiative and thermal packages. However, the ESABASE language depends itself on the evolution of the ESABASE software, and it has a rather limited scope.

Another ESA's initiative, ICETAS (ref. [6][7]), was not originally an effort to provide solutions to the problems of exchange and archive. Rather, it addressed the issue of integration of thermal software tools. Nevertheless, as work on ICETAS progressed these aspects became very relevant. Furthermore, the project produced a description of the complete set of data required to perform Spacecraft Thermal Analysis, as well as their interrelationships. This information is clearly very relevant to the development of a TNF.

The SET-ATS protocol

An important initiative has recently been undertaken by CNES, the French Space Agency, in order to provide a TNF based on the French standard SET. CNES have developed the "Application Thermique Spatiale" (ATS) Application Protocol to address the spacecraft thermal analysis exchange and archive requirements.

The first version of the protocol (ref. [8]) provided support for three major categories of entities:

- geometrical entities extracted from a set of primitive shapes, which are meshed and have thermo-optical properties attached to their faces. These entities can be assembled to build hierarchical models containing multiple occurrences of sub-models.
- results of calculations (processing) associated to geometric or thermal nodes.
- an entity containing the data needed to characterise the orbit.

In addition to these categories, the "neutral file header" and "neutral file summary" entities define the required additional information (origin, date of issue ...) for exchange and archive purposes.

Following a first implementation and test, a second version (ref. [9]) has extended the original protocol to improve the support for:

- orbit and kinematic extensions. Orbital data locate the satellite, considering it as a point in space (its centre of mass). Kinematics data give the attitude of the satellite and its moving parts with respect to the planet and the Sun.
- geometrical features. The set of elementary surfaces has been extended to take into account boolean operations and high-level shapes. The boolean operations (union and difference) can be used to generate complex geometry by combining elementary surfaces. High-level shapes, which have an associated type (e. g., box, cylinder ...), allow the easy manipulation of collections of elementary surfaces.
- language features such as comments, numbering and labelling, mainly introduced for man-machine interface purposes.

With this extended support, the new version aims to cover the main capabilities of the FLUOR, THERMICA ESABASE and ESARAD radiative analysis software.

The ATS protocol is based in the data and mechanisms defined in the SET Z68-300 standard, which is implemented in a large number of CAD/CAE software packages and used extensively in the European Aircraft Industry. The protocol, which covers some domain specific requirements, makes use of a subset of the generic entities available in the SET language. Moreover, some items of information, not covered by the SET standard, required the addition of new blocks and sub-blocks which can only be used by an interface that recognizes their format and semantics. Consequently, a correct SET-ATS interface will generate a SET physical file syntactically compliant to the SET standard. A standard SET interface will read these files, although it will be unable to interpret the parts of the information specific to the ATS protocol.

THE STEP STANDARD

Description of the standard

Work on communication standards between CAD/CAE systems has been under way since the beginning of the eighties, resulting in the development of several exchange formats like IGES, VDA-FS or the above mentioned SET. Currently, most of the groups promoting these exchange formats are contributing with their experience to STEP[10], the Standard for Exchange of Product Model Data, which is being developed under the auspices of the International Standards Organization (ISO 10303).

STEP was first proposed in 1984, with the intention to provide a worldwide standard supporting the complete representation of a product throughout its life cycle. STEP is different to other exchange formats in that rather than only providing rules to format a defined set of data, it is also supplying a methodology to formally describe the data and to implement the format. Furthermore, conformance testing to the standard is an integral part of STEP. From this point of view, STEP goes beyond the concept standing behind other exchange standards, by providing a standardised methodology to define application-specific product data standards. Other advantages with respect to existing standards are:

- because of the broad international consensus built around it, STEP is likely to meet the requirements set by many different applications.
- STEP establishes a separation between the logical design of the data and the physical implementation.
- the use of a formal language removes ambiguity and enables a rigorous conformance testing. Furthermore, automatic software generation from the EXPRESS specification becomes possible.

STEP consists basically of a series of components (called parts in the STEP terminology). Each of the parts are published separately, to help coping with their different degree of maturity. The main parts are:

- the EXPRESS[11] language, developed on purpose for STEP. EXPRESS is a formal information modelling language used when describing the STEP entities, with the intention to ensure consistency and avoid ambiguity.
- resource information models defining the basis for the development of application standards. The so-called Integrated Resources (IR) are in fact the basic building blocks used to define the application standards. They provide a unique representation of each element of information used within STEP. These resources can be either Generic Resources, i.e. of potential use for any type of application, or Application Resources, valid only for specific applications. The EXPRESS language is used to define the IR.
- Application Protocols (AP), which are the actual application-oriented standards that end-users will take for their exchange and integration needs. The APs are logically self-contained and complete.
- implementation methods supporting the data models provided by STEP.
- strict conformance testing procedures and tools to control and to certify compliance to STEP APs.

Therefore, the EXPRESS language is used in the definition of the Integrated Resources, from which the Application Protocols are derived (these can also use directly EXPRESS). A STEP implementation is produced when an Implementation Form is chosen. This implementation can be tested for conformance to the standard using the STEP-supplied methodology.

STEP is also to play a role in the issue of integration. Indeed, there are several possible implementation forms of the STEP standard. Today, the only implementation in place is the physical transfer file, but work is progressing in the definition of the Standard Data Access Interface (SDAI), which will introduce a software layer representing an abstract, "EXPRESS" view of the data to be transferred or stored. The SDAI will provide in practice interfaces to both relational and object STEP databases.

STEP Application Protocols

As mentioned previously, STEP provides a standardised methodology to develop protocols oriented to specific fields of application. The development of a particular AP stems from the specification of the scope and the information requirements of the AP. This is achieved by means of the Application Activity Model (AAM), which describes the processes, information flows and functional requirements of the application. The AAM helps to understand the nature of the activities and the role of the product data in the field of application. The AAM is included as an informative annex to the AP.

A more detailed Application Reference Model (ARM) specifies the information requirements and constraints of the AP, in terms of the so-called Units of Functionality. These units contain information about the entities, attributes and relationships that determine a given concept within the ARM. Although the ARM is defined by means of a formal data description language, application-specific terminology is used in this model. The ARM is also appended as an informative annex to the AP.

After the ARM is defined, the Application Interpreted Model (AIM) specify the manner in which the Integrated Resources can be used to satisfy the AP requirements. The resource constructs can be used directly, or refined depending on the application requirements.

Finally, the APs shall include the conformance requirements to be satisfied by any implementation claiming to support the AP. Such an implementation is tested by performing a conformance test based on a set of abstract test cases.

STEP and the TNF

Several fundamental STEP parts are already available either as International Standard or Draft International Standard. These parts include the EXPRESS language, the Physical File Exchange Structure, the conformance testing methodology, some Integrated Resources and some Application Protocols. A significant number of other IR and AP are being developed, with many of them close to achieve a stable state.

Certainly, the transition from current exchange standards to STEP will take some time. Nevertheless, enough progress has been achieved to appreciate the relevance of the STEP technology to the development of a TNF. Indeed, STEP is an obvious candidate for the TNF, because in addition to its intrinsic advantages as product data standard, it fulfils the basic requirements for a TNF:

- it is a neutral format that satisfies the needs for stability and tool-independence.
- its broad scope will allow immediate communication to the CAD and FE worlds.

In summary, STEP provides an excellent methodology to develop a Spacecraft Thermal Application Protocol. For the first time ever, the thermal analysis community might have the possibility to use a TNF tailored to its needs, but at the same time enjoying the character of full international standard.

DEVELOPMENT OF THE STEP THERMAL AP

CNES' STEP-ATS Application Protocol

Based on the experience gained in the production of SET-ATS, CNES undertook the development of an application protocol using the technology and methods developed for STEP (ref. [12]).

This application protocol was developed in conformance to the rules put forward in the "Guidelines document for development of STEP protocols". However, the complete process of Integration and Qualification imposed by ISO on the 10303 Parts was not followed. In particular, the Application Activity Model was not produced. On the other hand, the application protocol was developed by using, as far as possible, resources defined in ISO 10303. However, due to the fact that STEP is still in evolution, some of the required resources are not yet available in the standard. Therefore, these specific resources had to be produced in order to meet the application requirements. With these limitations in mind, the STEP protocol was defined to match the user requirements associated to the first version of the SET-ATS protocol.

The first stage of the development consisted in the specification of the information requirements in terms of units of functionality, application objects and application assertions. This stage defines the product data as viewed by the application users. The models are specified to have a tree structure including occurrences of sub-models. Any sub-model can also contain surface data representing a part of the geometry. Information related to the meshing and to the physical properties of each face is attached to the surfaces. Moreover, the protocol supports the transfer of the data needed for the orbit determination and the results of the thermal analysis. Finally, it includes the information related to the management of the exchanged models (designer, creation date, entity labels, colour for possible graphical display, grouping of entities into cells ...)

The information requirements are specified in terms of:

- Units of Functionality that allow the classification of the application objects into coherent groups such as geometry, thermo-optical properties or model structure.
- application objects such as surface type, mesh characteristics and orbit parameters. These objects are atomic elements that embody a unique application concept and contain attributes specifying the data elements of the object.
- application assertions that specify the relationships among application objects. For instance, "meshing of a Thermal_face is defined by one Mesh_characteristics", "a Mesh_characteristics applies to one Thermal_face" or "a Thermal_face has at most one Mesh_characteristics"

A graphical representation, using the EXPRESS-G notation, describes the structure and constraints of these application requirements (see Figure 1).

Following the definition of the information requirements, the Application Interpreted Model was then produced to specify the references to the STEP Integrated Resources. For each Unit of Functionality and application object, the so-called Mapping Table shows the correspondence between the information requirements and one or several AIM resource constructs.

Finally, the AIM's EXPRESS annotated listing was produced to present the complete listing of the types, entities and rules necessary to fully specify the AP.

It is important to note that the move from SET to STEP does not only represent a change in the neutral file physical format but also demands the evolution of the requirements (or at least of the way to take them into account). As a matter of fact, STEP promotes the concept of product whereas SET deals mainly with geometrical models. Although the STEP AP development process is more complex, the possible scope of the AP is much broader. Furthermore, it encourages an approach which is consistent with data representation requirements appearing in other stages of the spacecraft design.

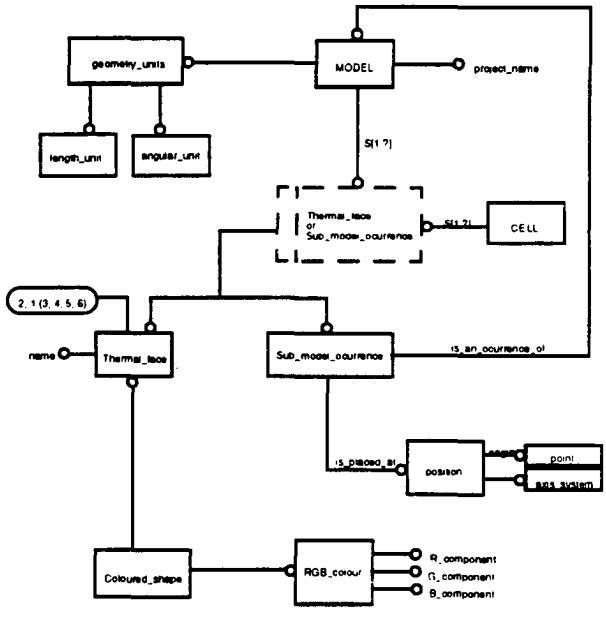

FIGURE 1. EXPRESS-G diagram presenting the information related to the Model_structure unit of functionality

The independent efforts undertaken by CNES and ESA in 1993 had similar timing and objectives, since both intended to produce a STEP Application Protocol for Spacecraft Thermal Analysis. Thus, it seemed reasonable to start a harmonisation process in order to reduce the chances of duplicating work. Furthermore, it seemed sensible to rationalise the efforts by making an efficient use of the knowledge gained by both CNES and ESA in the matter.

This harmonisation was fully achieved in early 1994 in the form of an activity to develop an Application Protocol on Thermal Analysis for Space (STEP-TAS). Previous experience coming from the STEP-ATS and the ICETAS projects was directly fed into the new project.

The harmonised work set off with the fundamental objectives of:

- merging the domain information models developed independently by CNES and ESA. Consensus in the Application Activity and Application Reference Models will result from this merge.
- extending the AIM developed by CNES to support a subset of the domain information requirements mentioned above.
- demonstrating the exchange of thermal models via STEP files. For that purpose a prototype facility is being developed to communicate FLUOR and ESARAD.

Results produced in the first stage of the harmonised effort are expected towards the end of 1994.

CONCLUSIONS

The concept of neutral file contributes in a very significant way to streamline the exchange of information, as proved by the development and use of the SET-ATS protocol. Modern product data technology, commonly associated to STEP, ensures the development of non-ambiguous domain-specific protocols which provide solutions not only to the information exchange problems but also to the integration of applications. However, the matter of successfully introducing a TNF in the spacecraft thermal analysis community remains largely a problem of consensus. Currently, a harmonised effort CNES/ESA is under way to provide a unique description of the information requirements in this domain. If an agreement is reached on the suitability of this logical description, the STEP technology is ready to produce an implementation of the TNF.

REFERENCES

[1] ESABASE User Reference Manual, ESA/ESTEC/WMA

[2] ESATAN User Manual. ESA PSS-03-105 Issue 2, November 1991

[3] THERMICA User's Guide. Matra Marconi Space. 1991

[4] ESARAD v2.1 User Manual, UM-ESARAD-024, EGT/MEC, 1993.

[5] Definition of the Common Structure of Data to Promote the Communication Between Different Thermal Software Tools. B. Desaunettes and C. Viguier, Proceedings of the 4th European Symposium on ECSS ESA SP-324, October 1991.

[6] Integrated Communication Environment for Thermal Analysis Software - Phase 2. H. P. de Koning et al., 24th ICES Conference, June 1994.

[7] ICETAS Standards Document, SID-ICETAS-
009, H. P. de Koning et al., Fokker Space & Systems, 1994.

[8] Protocole d'Application Thermique Spatiale, Association GOSET, June 1992.

[9] SET-ATS version 2 User Requirements. C. Puillet, EPSILON Ingenierie, February 1994

[10] ISO 10303-1 Product Data Representation and
Exchange - Part 1: Overview and Fundamental Principles. International Organization for Standardization.

[11] ISO 10303-11 Description Methods: the EXPRESS language reference manual. International Organization for Standardization

[12] Spacecraft Thermal Application Protocol using STEP technology, Association GOSET, December 1993

THE BENARD PROBLEM: A COMPARISON OF FINITE DIFFERENCE AND SPECTRAL COLLOCATION EIGENVALUE SOLUTIONS

J. Raymond Lee Skarda
NASA Lewis Research Center
Cleveland, Ohio

and

Frances E. McCaughan and Nessan Fitzmaurice
Case Western Reserve University
Cleveland, Ohio

Summary

The application of spectral methods, using a Chebyshev collocation scheme, to solve hydrodynamic stability problems is demonstrated on the Benard problem. Implementation of the Chebyshev collocation formulation is described. The performance of the spectral scheme is compared with that of a 2^{nd} order finite difference scheme. An exact solution to the Marangoni-Benard problem is used to evaluate the performance of both schemes. The error of the spectral scheme is at least seven orders of magnitude smaller than finite difference error for a grid resolution of N = 15 (number of points used). The performance of the spectral formulation far exceeded the performance of the finite difference formulation for this problem. The spectral scheme required only slightly more effort to set up than the 2^{nd} order finite difference scheme. This suggests that the spectral scheme may actually be faster to implement than higher order finite difference schemes.

1.0 Introduction

The theory of hydrodynamic stability has helped to explain and predict a variety of fluid flow phenomena. Recently it is being used to guide the modern computational fluid dynamicist in choosing the appropriate parameter values which are needed to simulate fluid flow behavior of interest (NASA TM-4569, 1994). Many current applications of hydrodynamic stability theory are possible because the field has benefitted greatly from the development and refinement of computational tools in addition to the existence of increasingly powerful computers. Spectral methods is one such set of tools that has been successfully applied to obtain high accuracy hydrodynamic stability results to previously intractable problems.

The purpose of this paper is to show, by example, the use of a spectral collocation formulation to solve hydrodynamic stability problems. Our discussion will be confined to the linear stability analysis which is the foundation of hydrodynamic stability theory (Lin, 1945). The linear stability problem ultimately reduces to a matrix eigenvalue problem, and the peril of the eigenvalue problem is that it requires $O(N^3)$ operations to obtain the eigenvalues where the matrix is $N \times N$. As shown herein, the high accuracy of spectral methods results in small N, therefore considerably less CPU time is required to solve for the eigenvalues when compared to finite difference methods.

The Benard problem is used to illustrate the implementation and performance of the spectral scheme. The problem is also solved using a 2nd order finite difference scheme which required slightly less time to implement. Results of the two numerical schemes are compared to the exact solution of the Marangoni-Benard problem (Pearson, 1959).

The Benard problem is described, and the governing equations and boundary conditions are developed in the following section. After a brief description of the finite difference scheme, the spectral collocation formulation is discussed. Results from both numerical schemes are then compared to an exact solution of the Marangoni-Benard problem. The spectral scheme yields results with considerably better accuracy using an order of magnitude less points than the finite difference scheme.

2.0 Description of Benard Problem & Development of Equations

A temperature difference is imposed normal to the free surface of a thin liquid layer of fluid of infinite horizontal extent and finite thickness, d, as shown in Figure 1.The initial steady state or base state of the system is one of no fluid motion, with a linear temperature profile across the layer. The velocity and temperature profiles illustrated in Figure 1 can immediately be expressed as, $U_b^* = 0$ and $T_b^* = T_{b0}^* - \beta z^*$. Using the notation of Pearson (1958) and Chandrasehkar (1981), U_b^* and T_b^* are respectively, the base flow velocity and temperature. The temperature gradient of the base state, β is defined as $\beta = -dT_b^*/dz^*$ or $\beta = \Delta T_d^*/d$ where $\Delta T_d^* = T_{b0}^* - T_{bs}^*$. The asterisk, "*" denotes dimensional quantities. The lower surface is rigid and is held at a constant temperature. The upper surface is free and exchanges heat with the environment . The free surface is assumed flat which is physically justified for many terrestrial problems. We first give the nondimensional form of the governing equations and in the next section we linearize about the base state just described in order to determine whether small disturbances to the base state will grow or decay. Specifically we are interested in the critical values of the nondimensional parameters where the change of stability occurs.

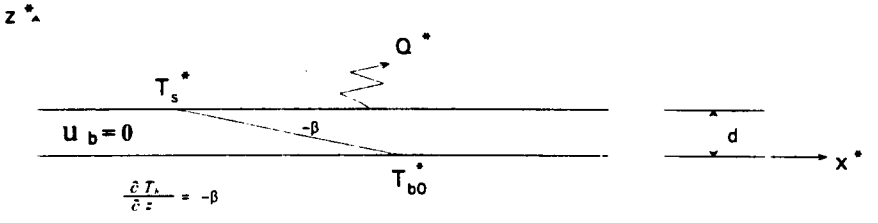

Figure 1 Base State For Thin Liquid Layer Of Infinite Extent

Nondimensional forms of mass, momentum, and energy equations for an incompressible fluid with the Boussinesq approximation are given in equations (1) through (3). The derivation of these equations with the Boussinesq approximation and constant viscosity and their subsequent nondimensionalization are well known and we refer the interested

reader to Chandrasekar (1981), and Drazin & Reid (1982) for details. All thermophysical properties are assumed constant apart from density and surface tension.

$$\bar{\nabla}\cdot\bar{U} = 0 \tag{1}$$

$$\frac{D\bar{U}}{Dt} = -\bar{\nabla}P + \hat{k}\cdot Ra\,Pr(T - T_{b0}) + Pr\,\bar{\nabla}^2\bar{U} \tag{2}$$

$$\frac{DT}{Dt} = \bar{\nabla}^2 T \tag{3}$$

$\bar{U}$, T, P, t are the velocity vector, temperature, pressure, and time respectively. The reference values used to nondimensionalize the variable; length, velocity, temperature, pressure, and time are d, κ_0^*/d, βd, $\rho_0^*\kappa_0^*/d^2$, d^2/κ_0^*, respectively. ρ_0^* is the fluid density and κ_0^* is the fluid thermal diffusivity. The subscript 0 indicates that the properties are chosen at the lower surface temperature, T_{b0}. The characteristic value of the dynamic viscosity of the fluid, μ, is denoted as μ_0^*. These reference values are consistent with those used in the buoyancy instability studies presented in Chandrasekhar (1981) and Drazin and Reid (1982), and the surface tension instability investigations of Pearson (1958) and Scriven and Sternling (1964). Two dimensionless groups appear in the momentum equation, the Prandtl number, Pr, and the Rayleigh number, Ra, which are defined as follows:

$$Pr = \frac{\mu_o}{\rho_0^*\kappa_0^*} \qquad Ra = \frac{\rho_0^*\beta d^4 \xi_0^* g_z}{\kappa_0^*\mu_0^*}.$$

ξ_0^* is the volumetric thermal expansion coefficient and g_Z is gravitational acceleration in the negative z-direction. The dot product of the unit vector in the z direction, $\hat{k}$, and the buoyancy (RaPr) term in equation (2) indicates that buoyancy only acts in the vertical direction. Therefore the Rayleigh number only occurs in the z-momentum equation.

The nondimensional boundary conditions are given by equations (4) and (5). Equations (4a,b,c), represent the no-slip conditions and impenetrable wall condition at z=0. Equation (4d) is the constant temperature condition along the wall. The normal stress boundary condition reduces to (5a) when the free surface at z=1 is assumed to be flat. Boundary condition (5b) is the heat flux balance at the free surface, where Q* is the dimensional surface heat flux to the environment and k_0^* is the fluid thermal conductivity. Equations (5c and 5d) are the tangential force balances along the free surface, in the x and y directions, respectively.

$$\text{At } z = 0; \quad \bar{U}(0) = (U_x, U_y, U_z) = 0, \quad T(0) = T_{b0} \tag{4a,b,c,d}$$

$$\text{At } z = 1; \quad U_z(1) = 0; \quad \frac{\partial T}{\partial z} + \frac{Q^*}{k_0^*\beta} = 0, \tag{5a,b}$$

$$-\left[\left(\frac{\partial U_z}{\partial x} + \frac{\partial U_x}{\partial z}\right)\hat{i} + \left(\frac{\partial U_z}{\partial y} + \frac{\partial U_y}{\partial z}\right)\hat{j}\right] = Ma\nabla_{II} T \tag{5c,d}$$

The operator, ∇_{II}, is the surface gradient defined as $\hat{i}\frac{\partial}{\partial x}+\hat{j}\frac{\partial}{\partial y}$ where, $\hat{i}$ and $\hat{j}$ are unit vectors in the x and y directions respectively. The Marangoni number, Ma, which occurs in equations (5c,d) is defined as: $Ma=\frac{\beta\, d^2\gamma_0^*}{\kappa_0^*\mu_0^*}$. The parameter, γ_0^*, is defined as $-\left.\frac{\partial\sigma^*}{\partial T^*}\right|_{T_{bs}}$, and is often referred to as the temperature variation of surface tension (Nield 1964 and Adamson 1967) or differential coefficient of surface tension change with temperature (Scriven and Sternling 1964). The surface tension, σ^*, does not appear in our equations or boundary conditions since we have assumed a flat interface. Further discussion of the nondimensionalization of the free surface boundary conditions is found in Scriven and Sternling (1964), and Koschmeider (1993).

The surface heat flux, Q^*, has to be expressed in a form that is suitable for linearizing the heat flux boundary condition, equation (5). This is accomplished by expanding Q^* about the base state surface temperature, T_{bs}^*. The first order expansion is given by equation (6). As previously noted, the base state varies only in the z-direction. Therefore, $Q^*(T_{bs})$ can be re-expressed as equation (7), using Fourier's law.

$$Q^* = Q^*(T_{bs}^*)+\left.\frac{\partial Q^*}{\partial T^*}\right|_{T_{bs}^*}\left(T^*-T_{bs}^*\right) \tag{6}$$

$$Q^*\left(T_{bs}^*\right)=k_0^*\left.\frac{\partial T^*}{\partial z^*}\right|_{z^*=d}=k_0^*\beta \tag{7}$$

Substituting equation (6) into equation (5b), using $k_0^*\beta$ in place of $Q^*\left(T_{bs}^*\right)$ and defining $h^*=\left.\frac{\partial Q^*}{\partial T^*}\right|_{T_{bs}^*}$, the heat flux boundary condition becomes:

$$\frac{\partial T}{\partial z}+1+Bi_s\left(T_s-T_{bs}\right)=0 \tag{8}$$

The dimensionless group, Bi_S, is defined as $Bi_s=\frac{h^*d}{k_0^*}$ and is referred to as either the surface Biot number (Pearson, 1958 and Nield, 1964) or the surface Nusselt number (Scriven and Sternling, 1964).

We note that the three-dimensional mass, momentum, and energy equations are given in equations (1-3), yet the boundary conditions are only specified in the z-direction. After linearizing the problem and applying some vector operations, it is shown in the next section, that the governing equations and boundary equations in the x and y directions do not affect the stability of the base state. Equations (1, 2, 3, 4 , and 5a,c,d and 8) make up the system which we will linearize in the next section.

2.1 Linearization of The Governing Equations

The dependent variables are written in terms of the following base flow and perturbation variables: $\bar{U} = \bar{u}, \quad T = T_b + \theta, \quad \Delta P = \Delta P_b + \Delta p$

After substituting for T_b and $\bar{\nabla} T_b$, the disturbance equations become:

$$\frac{\partial \bar{u}}{\partial t} = -\bar{\nabla} p + \hat{k} \cdot Ra\, Pr\, \theta + Pr\, \bar{\nabla}^2 \bar{u} \tag{9}$$

$$\frac{\partial \theta}{\partial t} - u_z = \bar{\nabla}^2 \theta \tag{10}$$

$\hat{k}$ is the unit vector in the z-direction shown in Figure 1. The curl operator is applied twice to the momentum equation, equation (9), which yields equation (11).

$$\frac{\partial(\nabla^2 \bar{u})}{\partial t} = \hat{k} \cdot Ra\, Pr\, \bar{\nabla}^2_{II} \theta + Pr\, \nabla^4 \bar{u} \tag{11}$$

The first curl operation yields the vorticity equation and eliminates the pressure terms. The second curl operation decouples the momentum equations from each other. The x and y momentum equations become uncoupled from the z-momentum and the energy equations. The z-momentum and energy equations remain coupled through the buoyancy term in equation (11), the convective term in equation (10), and the tangential boundary condition (discussed below). Furthermore, the relevant stability parameters, Ma and Ra, do not appear in either the x or y momentum equation or their associated boundary conditions. Given these considerations, equation (11) reduces to the scalar equation in u_z, equation (12).

$$\frac{\partial(\nabla^2 u_z)}{\partial t} = Ra\, Pr\, \nabla^2_{II} \theta + Pr\, \nabla^4 u_z \tag{12}$$

The boundary conditions for the perturbed variables associated with equations (10 and 12) are given by equations (13) through (14).

$$\text{At } z = 0, \qquad u_z = 0; \quad \frac{\partial u_z}{\partial z} = 0; \qquad \theta = 0 \tag{13a,b,c}$$

$$\text{At } z = 1, \qquad u_z = 0; \quad \frac{\partial \theta}{\partial z} + Bi_s \theta(1) = 0 \tag{14a,b}$$

$$-\left(\nabla^2_{II} u_z - \frac{\partial^2 u_z}{\partial z^2} \right) = Ma \nabla^2_{II} \theta \tag{14c}$$

2.2 Normal Mode Analysis

Since equations (10) and (12) are linear, we assume solutions for u_z and ϕ are of the form:

$$u_z = w(z)e^{i(\alpha_x x+\alpha_y y)+\lambda t} \quad \text{and} \quad \theta = \phi(z)e^{i(\alpha_x x+\alpha_y y)+\lambda t}$$

α_X and α_Y are the dimensionless wavenumbers in the x and y directions, and λ is the dimensionless frequency. Substituting these into equations (10) and (12) results in the following ordinary differential equations.

$$\lambda\phi(z) - D^2\phi(z) + \alpha^2\phi(z) - w(z) = 0 \tag{15}$$

$$\lambda\left(D^2w - \alpha^2 w(z)\right) = Ra\,Pr\left(D^2\phi - \alpha^2\phi\right) + Pr\left(D^4w - 2\alpha^2D^2w + \alpha^4 w(z)\right) \tag{16}$$

Where $D = \dfrac{d}{dz}$ and $\alpha^2 = \alpha_x^2 + \alpha_y^2$.

The boundary conditions at z = 0 become:

$$w(0) = 0, \quad Dw(0) = 0, \quad \phi(0) = 0. \tag{17a,b,c}$$

At z=1, the flat interface condition, heat flux condition, and tangential stress boundary condition are:

$$w(1) = 0, \quad D\phi(1) + Bi_s\phi(1) = 0, \quad D^2w = -\alpha^2 Ma\,\phi(1) \tag{18a,b,c}$$

Equations (15 through 18) are solved to determine whether the velocity and temperature disturbances grow or decay for given combinations of the relevant parameters. The relevant parameters are Ma, Ra, and α. Our problem is also referred to as a temporally developing flow problem since the disturbance growth or decay is in time. For temporally developing flows, α_X and α_Y are real and the eigenvalue, λ, is complex. If the real part of λ is positive the disturbance grows, if the real part of λ is negative the disturbance decays in time and if λ is zero, the disturbance persists unchanged in time.

3.0 Discrete Formulations

Two discrete formulations will be applied to the Benard problem, a 2nd order finite difference scheme, and a spectral collocation scheme. Irrespective of the discrete formulation the goal is construct a set of linear equations in form of the general eigenvalue problem, Ax = λBx. Once the eigenvalue problem is setup, solution mechanics are identical. If B is cheaply invertible, it usually pays to reduce the problem to a regular eigenvalue problem of the form Cx =λx, where $C = B^{-1}A$. In this study we used standard QR and QZ eigenvalue subroutines from the IMSL library to solve for the eigenvalues.

3.1 2nd Order Finite Difference Scheme

Equations (15 through 18) were discretized using a standard central difference scheme. Boundary conditions result in solving 2N-1 equations for this formulation. The discretized governing equations, equations (19) and (20), were arranged in the form $Az = \lambda Bz$, which is the generalized eigenvalue problem. Coefficients, a through g, and r are constants.

$$a w_{i-2} + b w_{i-1} + c w_i + d w_{i+1} + e w_{i+2} + r\phi_i = \lambda(f w_{i-1} + g w_i + f w_{i+1}) \quad (19)$$

$$f\phi_{i-1} + g\phi_i + f\phi_{i+1} + w_i = \lambda(\phi_i) \quad (20)$$

Here the boundary conditions for Eq (15) are applied only to the i = 0, 1, N-1, N equations and for Eq (16) only to i = 0 and i = N.

B is a nonsingular matrix so it is possible to reduce the system to a regular eigenvalue problem of the form $Cz = B^{-1}A = \lambda z$. Assuming a flat interface ensures that B is a tridiagonal matrix which can efficiently be inverted using a tridiagonal solver. The problem was discretized in terms of one fourth order equation, and one second order equation, which yields A and B matrices of rank 2N+2. Three of the six boundary conditions are Dirichlet boundary conditions which reduce the A and B matrices to rank 2N-1.

3.2 Chebyshev Collocation Spectral Scheme

The key to all spectral techniques lies in the possibility of expanding smooth functions in terms of rapidly converging sums of certain orthogonal basis functions. For example, consider any reasonable function f(x) defined in the domain $-1 \le x \le 1$ (see Canuto et. al. for a precise definition of "reasonable"). The function can be represented as a sum of Chebyshev polynomials, $T_n(x)$, of the form:

$$f(x) = \sum_{n=0}^{\infty} \hat{f}_n T_n(x) \quad (21)$$

The crucial thing is that the sum converges very rapidly if f(x) is smooth so one can truncate it at N terms and accurately represent the function with a minimal set of numbers $\{\hat{f}_n : n = 0,\ldots,N\}$. Such an expansion can be viewed as a very efficient and only slightly lossy compression technique for functions.

Pure spectral methods proceed by expanding the unknowns in terms of truncated sums of certain polynomials having excellent convergence properties (often simple combinations of Chebyshev polynomials that automatically account for any boundary conditions that must be satisfied by the function). The sums are then substituted into the differential equation and the coefficients are picked to minimize the residual. The fundamental quantities of interest in this procedure are the coefficients in the expansions of the dependent variables.

Spectral collocation methods on the other hand, concentrate directly on the physical space representation of the unknowns and as a consequence are more easily understood by the naive user. For example, in a collocation technique our hypothetical function, f(x) is not stored as $\{\hat{f}_n : n = 0,...,N\}$, but instead as $\{f_i \equiv f(x_i) : i = 0,...,N\}$. The exact correspondence between the two representations is maintained by choosing the physical space grid $\{x_i\}$ in an optimal fashion that is related to one of the Gaussian integration formulas. A typical formula of choice for Chebyshev expansions on the domain [-1,1] is the Gauss-Labatto grid, $x_i = \cos(i\pi / N)$. The spectral space and physical space representations can be interchanged with essentially no error (except perhaps for aliasing errors). Moreover, if the expansion is in terms of Chebyshev polynomials or trigonometric functions, the transformations to and from spectral space can be carried out efficiently by using Fourier Transforms (FFT's).

Solving differential equations obviously requires that the derivatives are evaluated. One method of evaluating $\{f'_i \equiv f'(x_i)\}$ is to proceed as

$$f_i \rightarrow \hat{f}_n \rightarrow \hat{f}'_n \rightarrow f'_i$$

That is, one first transforms to spectral space where a derivative is taken rapidly by using some simple properties of the basis functions. The new series produced in this fashion is then transformed back to a physical space representation. In the case of trigonometric or Chebyshev expansions, the procedure is dominated by the FFT's used in the transformations, so the total cost is $O(N \log N)$ operations.

There is a mathematically equivalent approach which uses matrix-vector multiplies to express

$$f'_i = \sum_{j=0}^{N} D_{ij} f_j \qquad (22)$$

where the elements of the derivative matrix D can be found in spectral texts such as Canuto et. al. To evaluate the derivatives on the entire grid using this method will take $O(N^2)$ operations. However, the matrix-vector multiply approach is the only one possible for eigenvalue problems where the aim is to turn the linear differential operator into the equivalent matrix operator on the discrete grid. Thus for example, the continuous equation, $\lambda f = f''$, becomes the discrete equation, $\lambda f = D^2 f$, so that in theory one simply fills and then squares the D matrix before feeding it to a standard matrix eigenvalue . In practice, the greatest programming labor is in the implementation the boundary conditions.

For the Benard problem, it is convenient to define the matrix operator

$$L = D^2 - \alpha^2 I \qquad (23)$$

where I is the identity matrix. The continuous equations, (15) and (16) then become the discrete equations, (24) and (25)

$$\Pr\left(L^2 w - \alpha^2 \mathrm{Ra}\, I\phi_j\right) = \lambda L w \tag{24}$$

$$L\phi + Iw = \lambda I\phi \tag{25}$$

and these equations can be recast into the standard form $Au = \lambda Bu$ given by equation (26).

$$\begin{bmatrix} \Pr L^2 & -\alpha^2 \mathrm{Ra}\,\Pr I \\ I & L \end{bmatrix} \begin{bmatrix} w \\ \phi \end{bmatrix} = \lambda \begin{bmatrix} L & 0 \\ 0 & I \end{bmatrix} \begin{bmatrix} w \\ \phi \end{bmatrix} \tag{26}$$

This translation of a continuous problem into a discrete one is very natural and can be carried out even more rapidly than the corresponding process for a finite difference scheme. However, this matrix eigenvalue problem as it stands does not take the boundary conditions into account. Most of the coding complexity that is present in spectral techniques (which by nature are global approximations) arises because of the need to implement boundary data (which are local point conditions).

The boundary conditions and governing equation are first mapped from the z variable in the domain [0,1] to x defined on [-1,1] by $x = 2z-1$. The mapped boundary conditions become:

At x = -1 (i=n): $$w_n = \sum_{i=0}^{N} D_{Ni} w_i = \phi_i = 0 \tag{27}$$

At x = +1 (i=0): $$w_0 = \mathrm{Bi}_s \phi_0 + \sum_{i=0}^{N} D_{0i}\phi_i = \alpha^2 \mathrm{Ma}\phi_0 \sum_{i=0}^{N} D_{0i}^2 w_i = 0 \tag{28}$$

We immediately see that $w_0 = w_N = \phi_N = 0$. The remaining equations can be used to simultaneously solve for w_1, w_{N-1}, and ϕ_0 in terms of the other w_i's and ϕ_i's as shown in equation (29). Equations (29) reveal that elements, w_1 and w_{N-1}, are coupled to the ϕ_i's through the last boundary condition in equation (28) while ϕ_0 remains uncoupled from the w_i's.

$$w_1 = \sum_{i=2}^{N-2} c_i w_i + \phi_0, \quad w_{N-1} = \sum_{i=2}^{N-2} d_i w_i + \phi_0, \quad \phi_0 = \sum_{i=1}^{N-1} e_i \phi_i \tag{29}$$

The boundary condition information is used to reduce the rank of the eigenvalue problem which is given by equation (30).

$$\sum_{j=0}^{2N+1} A_{ij} u_j = \lambda \sum_{j=0}^{2N+1} B_{ij} u_j \tag{30}$$

The first N+1 components of the vector u here corresponds to $\{w_i : i = 0,\ldots,N\}$ and the last N+1 components corresponds to $\{\phi_i : i = 0,\ldots,N\}$. Applying the six boundary conditions, we can eliminate the rows corresponding to $w_0, w_1, w_{N-1}, w_N, \phi_0$, and ϕ_N and expand equation (30) as given below.

$$A_{i1}u_1 + A_{iN-1}u_{N-1} + A_{iN+1}u_{N+1} + \sum_{\substack{j=2 \\ j\neq N-1,N,N+1}}^{2N+1} A_{ij}u_j = \lambda\left(B_{i1}u_1 + B_{iN-1}u_{N-1} + B_{iN+1}u_{N+1} + \sum_{\substack{j=2 \\ j\neq N-1,N,N+1}}^{2N+1} B_{ij}u_j \right) \tag{31}$$

where we have already used the data, $u_0 = u_N = u_{2N+1} = 0$ (which corresponds to $w_0 = w_N = \phi_N = 0$). Using the remaining boundary conditions, equations (29), take the form

$$u_1 = \sum_{j=2}^{N-2} c_j u_j = \sum_{\substack{j=2 \\ j\neq N-1,N,N+1}}^{2N} \bar{c}_j u_j, \quad u_{N-1} = \sum_{j=2}^{N-2} d_j u_j = \sum_{\substack{j=2 \\ j\neq N-1,N,N+1}}^{2N} \bar{d}_j u_j,$$
$$u_{N+1} = \sum_{j=1}^{N-1} e_j u_j = \sum_{\substack{j=2 \\ j\neq N-1,N,N+1}}^{2N} \bar{e}_j u_j \tag{32}$$

$$\text{where} \quad \bar{c}_j = \begin{cases} c_j \\ e_{j-N-3} \end{cases} \quad \& \quad \bar{d}_j = \begin{cases} d_j \\ e_{j-N-3} \end{cases} \quad \& \quad \bar{e}_j = \begin{cases} 0 & \text{if } j = 2,\ldots,N-2 \\ e_{j-N-3} & \text{if } j = N+2,\ldots,2N \end{cases} \tag{33}$$

The matrix eigenvalue problem can be rewritten as

$$\sum_{\substack{j=1 \\ j\neq N-1,N,N+1}}^{2N+1} \bar{A}_{ij}u_j = \lambda \sum_{\substack{j=1 \\ j\neq N-1,N,N+1}}^{2N+1} \bar{B}_{ij}u_j \tag{34}$$

where $\bar{A}_{ij} = A_{ij} + A_{i1}\bar{c}_j + A_{iN-1}\bar{d}_j + A_{iN+1}\bar{e}_j$ and $\bar{B}_{ij} = B_{ij} + B_{i1}\bar{c}_j + B_{iN-1}\bar{d}_j + B_{iN+1}\bar{e}_j$. The global matrix problem is finally transformed to a reduced eigenvalue problem $\tilde{A}u = \lambda\tilde{B}u$ where the matrices are $(2N-4)\times(2N-4)$ and all six boundary conditions have been incorporated into the problem.

The principle difficulty in using spectral collocation techniques for solving stability problems is the implementation of derivative boundary conditions. A condition such as $w(1) = 0$ is not a problem as all that is required is the reduction of the global matrices by eliminating one row and one column. Derivative data on the other hand, results in altering all the elements of the matrices due to the global nature of the underlying series

approximation. All data contributes to the value of the derivative at each point Nevertheless, for the Benard problem, the spectral collocation technique is only slightly more difficult to code than a second order finite difference scheme. As is observed in the subsequent results, the additional coding effort is amply rewarded.

4.0 Results

Under certain conditions, exact solutions to equations (15) through (18) have been obtained. Pearson (1958) derived an exact solution to the Marangoni-Benard problem (Ra = 0) for the case of neutral stability, $\lambda = 0$. His solution reduces to equation (35) for an insulated free surface, Bi = 0. The critical value of the Marangoni number, equation (35), versus the wavenumber is shown in Fig. 3 and is referred to as a neutral stability curve since $\lambda = 0$ for all points along the curve. For values of Ma above this curve are unstable since infinitesimal disturbances. Our objective is to use the above exact result to investigate the accuracy of the aforementioned discrete formulations, so we do not consider alternative exact or approximate solutions which exist for the general problem. The physical interpretation of these results in addition to results from other exact or approximate solutions to the Benard problem are discussed in Pearson 1958, Scriven & Sternling 1964, Smith 1966, Chandrasekhar 1981, and most of the other references cited in section 6.0. We now compare the numerical results to the exact solution.

$$Ma_c = \frac{8\alpha^2 \cosh(\alpha)(\alpha - \sinh(\alpha)\cosh(\alpha))}{\alpha^3 \cosh(\alpha) - \sinh^3(\alpha)} \tag{35}$$

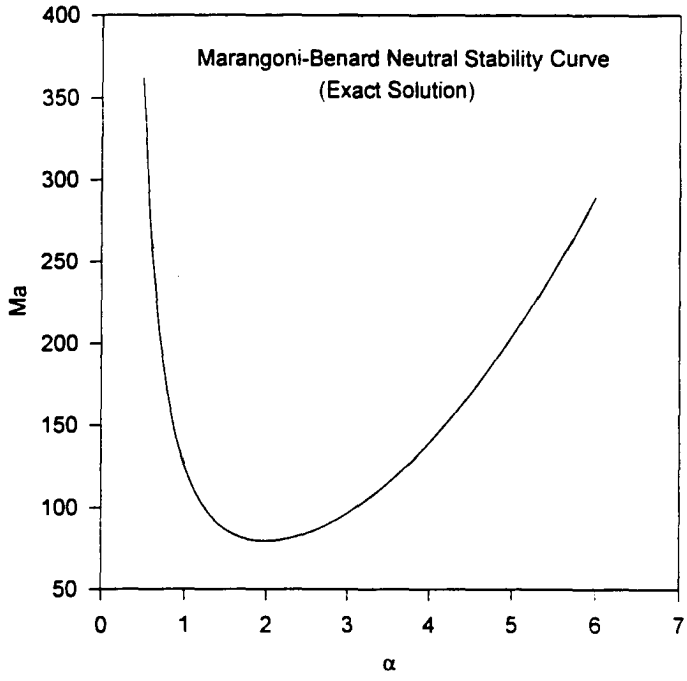

Figure 2 Marangoni-Benard Neutral Stability Curve, Exact Solution for Bi=0 (Pearson, 1958)

Neutral stability curves for the Marangoni-Benard problem which were generated using a 2nd order finite difference scheme and spectral scheme are shown in Figs. 3 and 4, respectively. The number of points across the fluid depth, N, (in the z-direction) represents the spatial resolution used to generate a given curve. In Fig. 3 the neutral stability curve converges to the exact solution as the spatial resolution increases from N = 4 to N = 100. The N = 50 and N = 100 curves are visually indistinguishable from the exact solution. Fig. 4 reveals that the neutral stability curves computed using the spectral formulation also converge to the exact solution as the spatial resolution increases. The spectrally generated neutral stability curves shown in Fig. 4 are visually identical to the exact solution for spatial resolutions as low as N = 10. In both Figs. 3 and 4, the numerically generated neutral stability curves tend to diverge from the exact solution with increasing wavenumber. It is also observed that the finite difference solution converges from above the exact solution while the spectral solution converges from below exact neutral stability curve.

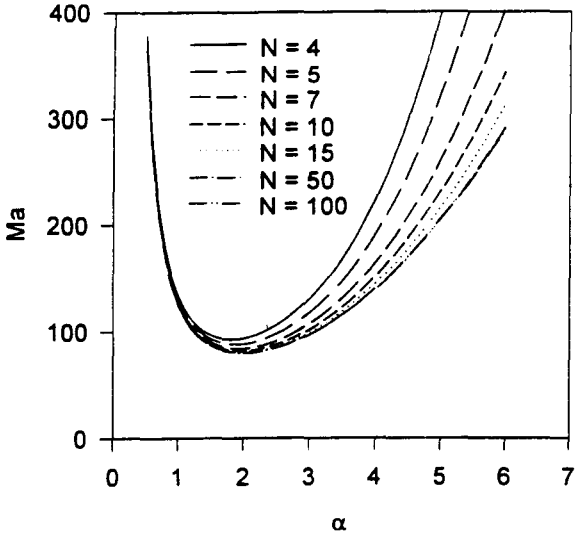

Figure 3 Marangoni-Benard Neutral Stability Curves Computed Using A 2nd Order Finite Difference Scheme. N Is The Number Points Through The Fluid Layer.

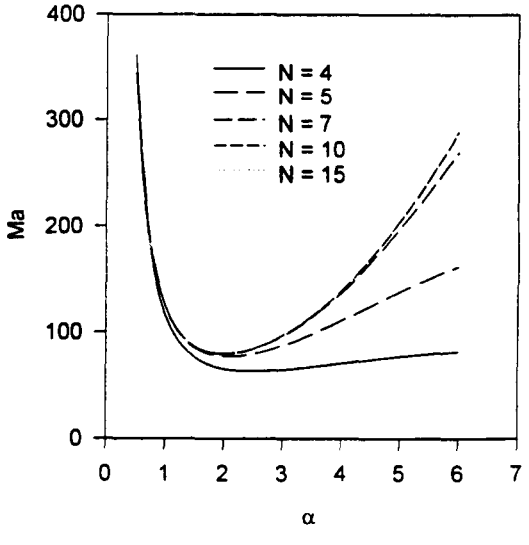

Figure 4 Marangoni Neutral Stability Curves Computed Using A Spectral Collocation Scheme. N The Number Points Through The Fluid Layer.

The error in the Marangoni number for the finite difference and spectral schemes is plotted as a function of wavenumber in Figs. 5 and 6, respectively. In both figures, error is plotted using a logarithmic scale while the wavenumber. α, is plotted with a linear scale on the abscissa. The error (ordinate) range differs between the two figures so that the error characteristics of each discrete scheme could be observed. The error is defined as $\frac{Ma_N - Ma_{exact}}{Ma_{exact}}$ where Ma_N is the Marangoni number computed from a discrete formulation for a given spatial resolution (N points) and Ma_{exact} is computed using equation (35). Both discrete schemes are observed in Figs. 1 through 4 to converge to the exact solution as the spatial resolution, N, increases. The finite difference errors for each

curve increase approximately an order of magnitude over the given wavenumber range as observed in Figure 5, while the spectral error shown in Figure 6 increases four to five orders of magnitude with wavenumber. For N greater than approximately seven. the spectral error remains considerably less than the finite difference error for the range of α considered.

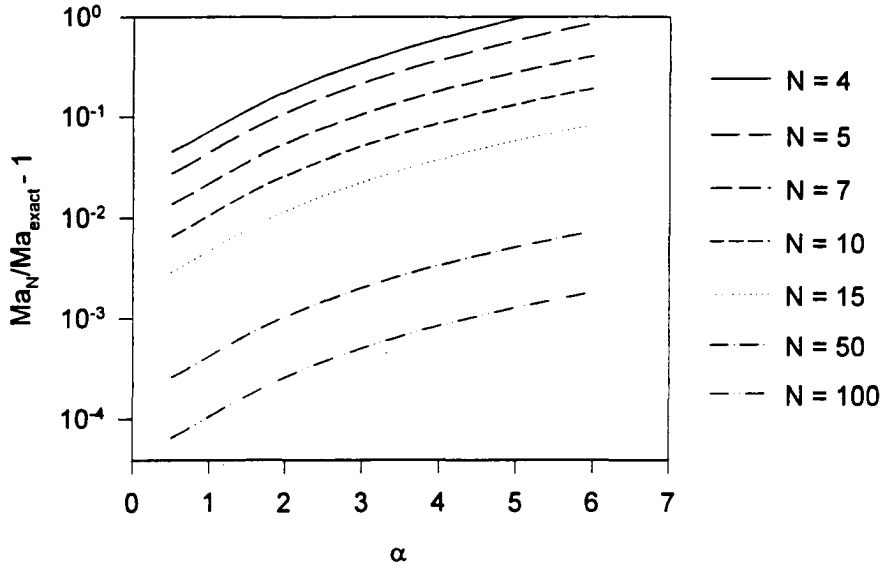

Figure 5 Marangoni Number Error vs. Wavenumber For The 2nd Order Finite Difference Solution. N Is The Number Of Points Through The Fluid Layer

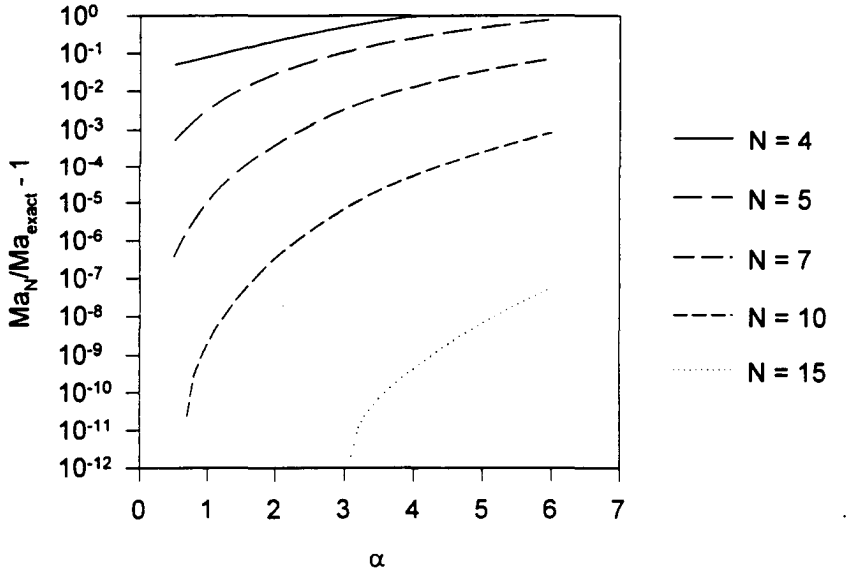

Figure 6 Marangoni Number Error vs. Wavenumber For The Spectral Collocation Scheme. N Is The Number Of Points Through The Fluid Layer

Selected error values of the two schemes for wavenumbers of 2 and 5 are tabulated in Tables 1 and 2, respectively. The errors for , $\alpha = 2$, the critical wavenumber were smaller than those of the larger wavenumber, $\alpha = 5$. In Fig. 7, the Ma error is shown on a log-log plot as function of the spatial resolution (N grid points) for both discrete formulations . Comparing Ma error values at a wavenumber of 2 and N = 10, the error for the spectral scheme is seen to be five orders of magnitude smaller than the finite difference error. Furthermore, after increasing the spatial resolution of the finite difference scheme to N = 100, still gives a spectral error **for N = 10** that is 3 orders of magnitude smaller. The reduction in error for the finite difference scheme is essentially proportional to N^2, as expected since the scheme is 2^{nd} order accurate. A slope of -2.02 was computed for the finite difference curve in Fig. 7 which is within 1% of the expected value of 2. The slope was computed from a least squares fit of the finite difference data in Table 1. The error for the spectral formulation is expected to decrease exponentially with increasing N (Boyd, 1989, Canuto et. al., 1987). However the error results in Table 2 show that the exponential rate of convergence is exceeded for this particular problem. Fig. 7 vividly illustrates that the spectral scheme results in a significant reduction in error with considerably fewer grid points than the central difference scheme for this particular problem. The spectral formulation has also been shown to out perform finite difference methods when applied to other hydrodynamic stability problems (Canuto et. al., 1987, Boyd, 1989). The exceptional performance (greater than exponential convergence) of the spectral collocation scheme for this problem was not anticipated by the authors.

Table 1 Selected Marangoni Number Errors For Wavenumber, α=2

Spatial resolution N	Finite Difference	Spectral
5	1.085×10^{-1}	2.920×10^{-2}
10	2.600×10^{-2}	3.400×10^{-7}
15	1.115×10^{-2}	4.529×10^{-11}
50	1.025×10^{-3}	
100	2.561×10^{-4}	

Table 2 Selected Marangoni Number Errors For Wavenumber, α=5

Spatial resolution N	Finite Difference	Spectral
5	5.756×10^{-1}	2.808×10^{-1}
10	1.309×10^{-1}	2.525×10^{-4}
15	5.710×10^{-2}	6.434×10^{-9}
50	5.075×10^{-3}	
100	1.268×10^{-3}	

As stated throughout, the ability to reduce the size of N is crucial to the eigenvalue problem, $A\bar{x} = \lambda B\bar{x}$. Inverting B takes $O(N^3)$ operations; the matrix multiplication of $C = B^{-1}A$ requires $O(N^3)$; and solving the regular eigenvalue problem, $C\bar{x} = \lambda\bar{x}$, requires $O(N^3)$ operations. Neglecting all other operations than those identified above, for a grid resolution of N=10, it requires appropriately 3000 operations to compute the eigenvalues while it requires $O(3 \times 10^6)$ operations for N=100. The number of iterations required to converge to Ma_c at one wavenumber is O(10), ie., the matrix eigenvalue problem is solved approximately ten times for each wavenumber.

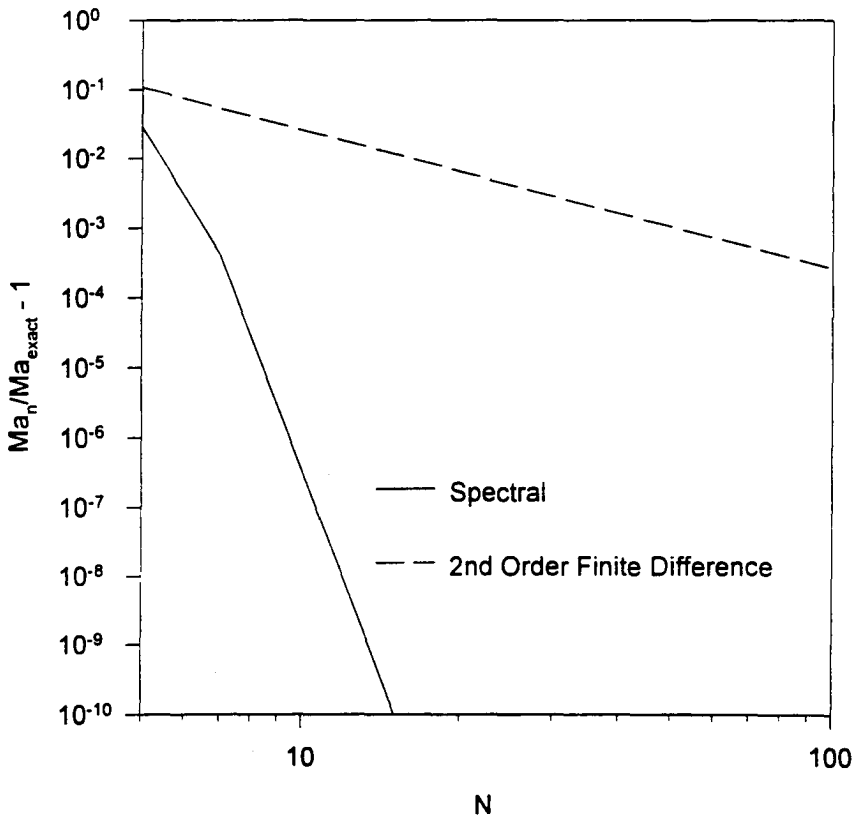

Figure 7 Error in Ma_c ($\alpha = 2$) As A Function Of The Number of Points Across The Fluid Layer, N

5.0 Concluding Remarks

A spectral scheme, the Chebyshev collocation formulation was used to perform a hydrodynamic (linear) stability analysis of the Benard problem. The problem reduces to a generalized eigenvalue problem, $Ax = \lambda Bx$, which can be reduced to a regular eigenvalue problem, $Cx = \lambda x$ by inverting B. Implementation of the spectral scheme was described. There is a bit of a learning curve that must initially be overcome to comfortably setup the spectral formulation if one has no previous experience with spectral methods. Afterwards, the spectral scheme requires only slightly more time to set up than the 2nd order finite difference scheme and is likely to be easier to program than higher order finite difference schemes. A comparison of the results from the spectral and finite difference scheme reveals that the spectral scheme out performs the finite difference scheme by a considerable margin. The error of the spectral scheme is at least three orders of magnitude smaller than the finite difference error for $N = 10$ and seven orders of magnitude smaller than finite difference error for $N = 15$.

6.0 References

Adamson, A.W., Physical Chemistry of Surfaces, John Wiley & Son's, 1967.

Boyd, J. P., Chebyshev & Fourier Spectral Methods, Springer-Verlag, New York, 1989.

Chandrasekhar, S., Hydrodynamic and Hydromagnetic Stability, Dover, New York, 1981.

Canuto, C., and M. Y. Hussaini, A. Quarteeroni, and T.A. Zang, Spectral Methods in Fluid Dynamics, Springer-Verlag, New York, 1987.

Drazin, P.G., and W.H. Reid, Hydrodynamic Stability, Cambridge University Press, 1991.

Incropera, F. P., and D. P. DeWitt, Fundamentals of Heat and Mass Transfer, John Wiley and Sons, New York, 1985.

Koschmieder, E.L., Benard Cells and Taylor Vortices, Cambridge University Press, 1993.

Legros, J.C., O. Dupont, P. Queeckers, S. Van Vaerenbergh, and D. Schwabe, "Thermohydrodynamic Instabilities and Capillary Flow," Low Gravity Fluid Dynamics and Transport Phenomena, Ed J. Koster and R. Sani, American Institute of Aeronautics and Astronautics, 1990.

Lin, C.C., The Theory of Hydrodynamic Stability, Cambridge University Press, New York, 1966

Nield, D. A., "Surface Tension and Buoyancy Effects In Cellular Convection," Journal of Fluid Mechanics, Vol. 19, 1964, pp. 341-352.

Ostrach, S., "Low-Gravity Fluid Flows," Annual Review of Fluid Mechanics, Vol 14, 1982, pp. 313-345.

Pearson, J. R. A., "On Convection Cells Induced by Surface Tension," Journal Of Fluid Mechanics, Vol. 4, 1958, pp. 489-500.

Scriven, L. E., and C. V. Sternling, "On Cellular Convection Driven By Surface-Tension Gradients: Effects Of Mean Surface Tension and Surface Viscosity," Journal Of Fluid Mechanics, Vol. 19, 1964, pp. 321-340.

Smith, K. A., "On Convective Instability Induced By Surface Tension Gradients," Journal Of Fluid Mechanics, Vol 24, 1966, pp. 401-414.

"Microgravity Science and Applications: Program Tasks and Bibliography for FY 1993," NASA TM-4569, March 1994.

SINGLE-DROP REACTIVE EXTRACTION/EXTRACTIVE REACTION WITH FORCED CONVECTIVE DIFFUSION AND INTERPHASE MASS TRANSFER

Leonid S. Kleinman and X.B. Reed, Jr.
University of Missouri-Rolla
Rolla, Missouri

SUMMARY

An algorithm has been developed for time–dependent forced convective diffusion-reaction having convection by a recirculating flow field within the drop that is hydrodynamically coupled at the interface with a convective external flow field that at infinity becomes a uniform free–streaming flow. The concentration field inside the droplet is likewise coupled with that outside by boundary conditions at the interface. A chemical reaction can take place either inside or outside the droplet, or reactions can take place in both phases.

The algorithm has been implemented, and for comparison results are shown here for the case of no reaction in either phase and for the case of an external first order reaction, both for unsteady behaviour. For pure interphase mass transfer, concentration isocontours, local and average Sherwood numbers, and average droplet concentrations have been obtained as a function of the physical properties and external flow field. For mass transfer enhanced by an external reaction, in addition to the above forms of results, we present the enhancement factor, with the results now also depending upon the (dimensionless) rate of reaction.

INTRODUCTION

There are many industrial and environmental processes in which two-phase fluid-liquid systems are in use. Gases may be dispersed as bubbles in liquid phases, such as occurs in bubble columns and sparged vessels. Liquids may be dispersed in gases, such as occurs in scrubbers and in the atmosphere. And a liquid that is immiscible or partially miscible in another liquid may be dispersed in a liquid-liquid spray column extractor or reactor. The design of such systems may involve heat transfer, either intentionally or incidentally, but the widest range of applications involves mass transfer.

Interphase mass transfer may proceed into or out of the dispersed phase. One (or more) chemical reaction(s) may take place in either the dispersed or the continuous phase in order to enhance the rate of mass transfer. In two-phase reactions, certain of the reactants may be transferred from one phase into the other, where the reaction takes place, and the reaction products may then be transferred back into the first phase. Reactions may also occur in both phases.

Because of the finite, generally small volume of each drop or bubble, interphase mass transfer unaccompanied by chemical reaction is inherently unsteady, regardless of the direction of mass transfer. Even if there is a reaction that admits of a steady state in the drop or bubble, unsteady behavior may nevertheless be of practical even primary importance.

The continuous phase is inevitably in motion relative to the dispersed phase, and for clean systems (containing for instance no surface active agents) the motion in the two phases will be hydrodynamically coupled.

The general formulation could take into account either linear or nonlinear chemical reactions in either or both phases, and it could incorporate any velocity field that can be expressed as a function of r and ϑ. Neither are variable properties excluded.

In order to demonstrate the utility of the algorithm, for concreteness we undertake the mathematical description of a liquid–liquid system in which a first order reaction takes place in the continuous phase. The dispersed phase is sufficiently dilute that the droplets which sediment (either falling under their weight or rising because of buoyancy) may be assumed isolated in an infinite medium, both with regard to fluid mechanics and to diffusion and reaction. The droplets are taken small enough that interfacial tension dominates shape effects and they are spherical. Although the approach we take and the methods we use do not require that that viscosity dominates flow effects and that the velocity fields have low Reynolds numbers, we nontheless consider the hydrodynamically coupled Hadamard - Rybczinsky profile for circulation within the droplet driven by an external velocity field that becomes a uniform streaming flow far from the droplet. Physical and chemical properties are assumed constant, which would be the case for dilute isothermal systems, and we thus analyze interphase mass transfer for the forced convective diffusion-reaction single-drop system. We investigate specifically the role of the reaction rate, as measured by an appropriate Damköhler number, the solubility of the solute in the phases, as expressed by the linear distribution coefficient (Henry's law), the ratio of convection to diffusion, as measured by the Peclet number, and the ratio of the viscosities and that of molecular diffusivities of the two phases.

GOVERNING EQUATIONS

The dimensionless forced convective diffusion-reaction equations governing the solute concentrations in the drop ($0 \leq r \leq 1$) and the continuous ($1 \leq r < \infty$) phases, $i = 1, 2$, respectively, can be represented in the form

$$\frac{\partial c^{(i)}}{\partial t} + K_c^{(i)} \mathbf{v}^{(i)} . \nabla c^{(i)} = K_d^{(i)} \nabla^2 c^{(i)} - K_r^{(i)} c^{(i)} , \tag{1}$$

where $i = 1$ corresponds to the internal domain $0 \leq r \leq 1$, and $i = 2$ to the external one $1 \leq r < \infty$.

The dimensional parabolic partial differential equations have been rendered dimensionless using the droplet radius R as the characteristic length scale. The concentrations are measured in units of the initial driving force,

$$c^{(i)} = \frac{H^{(i)} \tilde{c}^{(i)} - H \tilde{c}_\infty}{\tilde{c}_0 - H \tilde{c}_\infty}, \quad i = 1, 2 , \tag{2}$$

in which

$$H^{(i)} = \begin{cases} 1, & i = 1 \\ H, & i = 2, \end{cases} \tag{3}$$

with H the Henry's "law" distribution coefficient, and

$$t = 0 : \quad \tilde{c}^{(1)} = \tilde{c}_0, \quad \tilde{c}^{(2)} = \tilde{c}_\infty . \tag{4}$$

The characteristic time scale can be selected, for example, on the basis of the fastest physical or chemical process, occurring in the system, *viz.*,

$$\tau_* = \min(\tau_{\text{conv}}^{(i)} , \ \tau_{\text{diff}}^{(i)} , \ \tau_{\text{rxn}}^{(i)} , \ i = 1, 2), \tag{5}$$

in which

$$\tau_{\text{conv}}^{(i)} = \frac{R}{f^{(i)}(\mu)\, U_\infty}, \quad \tau_{\text{diff}}^{(i)} = \frac{R^2}{D^{(i)}}, \quad \tau_{\text{rxn}}^{(i)} = \frac{1}{k^{(i)}}, \quad i = 1,2\,. \tag{6}$$

The diffusivities and rate constants for the first order chemical reactions are denoted by $D^{(i)}$ and $k^{(i)}$, respectively, and the K's represent different combinations of standard dimensionless parameters for different choices of τ_*, as indicated in Table 1.

Although our numerical implementation of the algorithm requires only that the velocity fields in the two phases be separable, we have selected the Hadamard - Rybczinsky solution for the convecting velocities in the dispersed and continuous phases to establish connections with earlier research [7, 8, 9]. In this instance, the characteristic velocity in each phase, with U_∞ the freestreaming uniform flow at infinity, is taken as

$$U_*^{(i)} = f^{(i)}(\mu)\, U_\infty\,, \quad i = 1,2\,, \tag{7}$$

in which

$$f^{(1)}(\mu) = \frac{1}{2(1+\mu)}, \quad f^{(2)}(\mu) = 1\,, \tag{8}$$

with the viscosity ratio

$$\mu = \mu^{(1)}/\mu^{(2)}\,. \tag{9}$$

The equations (10) are the ones used in the sequel, reflecting the selection of $\tau_{\text{diff}}^{(2)}$ as the unit of time:

$$\begin{aligned} &\frac{\partial c^{(i)}}{\partial \tau} + \frac{Pe^{(2)}}{2}\cdot\left(v_r^{(i)}\frac{\partial c^{(i)}}{\partial r} - \frac{v_\lambda^{(i)}}{r}\sqrt{1-\lambda^2}\frac{\partial c^{(i)}}{\partial \lambda}\right) \\ &\qquad = \frac{D^{(i)}}{D^{(2)}}\cdot\left\{\frac{1}{r^2}\frac{\partial}{\partial r}\left(r^2\frac{\partial c^{(i)}}{\partial r}\right) + \frac{1}{r^2}\frac{\partial}{\partial \lambda}\left[(1-\lambda^2)\frac{\partial c^{(i)}}{\partial \lambda}\right]\right\} \\ &\qquad -Da_{II}^{(i)}\frac{D^{(i)}}{D^{(2)}}\cdot\left(c^{(i)} + \frac{H\tilde{c}_\infty}{\tilde{c}_0 - H\tilde{c}_\infty}\right)\,, \quad i = 1,2\,, \end{aligned} \tag{10}$$

with $\lambda = \cos\vartheta$, subject to the boundary conditions at the droplet interface,

$$r = 1: \quad \begin{cases} c^{(1)} = c^{(2)} \\ H\cdot D\,\dfrac{\partial c^{(1)}}{\partial r} = \dfrac{\partial c^{(2)}}{\partial r} \end{cases} \tag{11}$$

and at the limits of the overall domain,

$$r = 0: \quad c^{(1)} < \infty \tag{12}$$

$$r \to \infty: \quad c^{(2)} \to 0 \tag{13}$$

Periodic boundary conditions in the angle variable,

$$\left.\frac{\partial c^{(i)}}{\partial \vartheta}\right|_{\vartheta=0,\pi} = 0, \quad i = 1,2, \tag{14}$$

are satisfied automatically after introduction of the new independent variable λ.

The concentrations are subject to the initial conditions:

$$t = 0: \quad c^{(1)} = 1, \; c^{(2)} = 0 \tag{15}$$

The actual direction of mass transfer may be out of or into the drop, depending upon the driving force $(\tilde{c}_0 - H\tilde{c}_\infty)$, even though the formulation of the problem suggests transfer from the droplet.

The opposite direction of mass transfer in the actual problem would lead to the appearance of the inhomogeneous part in the reaction terms in (10) (but only when the corresponding $K_r^{(i)} \neq 0$).

THE ALGORITHM

The problem is linear, and we use the Galerkin spectral method for the spatial discretization. The advantages of this method are well known [1, 2].

Boundary conditions at the origin of the droplet (12) and at infinity (13) and the symmetry boundary conditions (15) are implemented by the Lanczos tau–method [1, 2, 14].

We express the unknown functions $c^{(i)}(\tau, \lambda, r)$ in a customary manner,

$$c^{(i)}(\tau, \lambda, r) = \sum_{m=0}^{M} c_m^{(i)}(\tau, r)\, P_m(\lambda), \quad i = 1,2, \tag{16}$$

in which the $P_m(\lambda)$ are the Legendre polynomials of order m and the unknown coefficient functions $c_m^{(i)}(\tau, r)$ are termed "radial functions" for brevity in the sequel.

The discretization in the radial direction is performed in somewhat different ways for the internal and external domains.

Using equation (10) for mass transfer inside the droplet ($i = 1$), it is a simple matter to show that functions $c_m^{(1)}(\tau, r)$ obey the following restrictions :

$$c_l^{(1)}(\tau, r = 0) = 0, \quad l \neq 0, \tag{17}$$

$$\left.\frac{\partial c_l^{(1)}}{\partial r}\right|_{r=0} = 0, \quad l \neq 1, \tag{18}$$

$$\left.\begin{array}{l} c_{2k}^{(1)}(\tau, r) \text{ - even function of } r \\ c_{2k+1}^{(1)}(\tau, r) \text{ - odd function of } r \end{array}\right\} \quad k = 0, 1 \ldots . \tag{19}$$

On the basis of these restrictions, the radial functions inside the droplet were approximated by a series in even Chebyshev polynomials:

$$c_m^{(1)}(\tau, r) = \delta_{m,0} \cdot \alpha_0(\tau) + r^{\kappa_m} \cdot \sum_{n=1}^{N^{(1)}} \phi_{m,n}^{(1)}(\tau)\, T_{2n-2}(r), \quad m = 0, 1, \ldots, M, \tag{20}$$

in which the $T_p(r)$ are Chebyshev polynomials of the first kind of order p, and

$$\kappa_{2j} = 2, \quad j = 0, 1, \ldots \tag{21}$$

$$\kappa_1 = 1, \ \kappa_{2j+1} = 3, \quad j = 1, 2, \ldots \tag{22}$$

Using (20) we automatically satisfy boundary condition (12) and avoid the singularity at the origin of the drop; the function $\alpha_0(\tau)$ represents the value of the concentration at the origin.

Such an expansion on the interval $0 \leq \tau \leq 1$ is valid as the even Chebyshev polynomials form a complete set for the type of functions considered [10].

The use of half the commonly used interval $[-1, 1]$ permits us to double the highest order of the polynomials used, leaving the number of terms in the series unaltered.

The nonuniformity of the distribution of nodes in the spectral method (their number in close proximity to the surface is higher than near the origin) matches the physics of the problem as the concentration gradient near the interface is much larger.

For the semi-infinite external domain we implement the widely used procedure of truncating it at an appropriately large radius τ_∞, far enough from the interface to make negligible the disturbance introduced by truncation. The boundary condition at infinity (13) is now imposed on this artificial boundary. It could be imposed as "hard", "soft" [12] or "behavioral" [1, 13]. We use the "hard" one,

$$\tau = \tau_\infty : \quad c^{(2)} = 0 \tag{23}$$

because it immediately results in the original boundary condition (13) if $\tau_\infty \to \infty$.

It is necessary to realize that by doing this we are changing the physical sense of the problem. The decrease to zero of the concentration infinitely far from its source is caused physically by the spreading of a finite amount of the species over an infinite spatial volume. After introduction of the boundary sphere at $\tau = \tau_\infty$, we model this decrease by imposing what amounts to an infinitely fast heterogeneous reaction on the artificial boundary τ_∞. The only justification for this is an *a posteriori* one, *viz.*, by checking that the increase of τ_∞ does not alter the solution in the vicinity of the droplet and in particular the interphase mass transfer.

Our computations have confirmed this and show that when τ_∞ is chosen sufficiently large the choice of the particular type of boundary conditions mentioned above does not influence the resultant concentration distribution in regions where its value differs significantly from zero.

The domain $1 \leq \tau \leq \tau_\infty$ is mapped onto the interval $-1 \leq z \leq 1$ in such a way that the point $z = 1$ matches $\tau = 1$ and the point $z = -1$ matches $\tau = \tau_\infty$. Among the wide variety of possible mappings two are used more often than others, the exponential and rational ones [1, 2]. A comparison by Grosch and Orszag [11] has shown that the latter mapping has some advantages over the former.

Specifically, we use

$$z = \frac{\tau - (1 + \delta)}{(1 - \tau)\left(1 - \frac{2\delta}{\tau_\infty - 1}\right) - \delta}, \tag{24}$$

where δ is the parameter representing the distance between the droplet surface and point mapped into $z = 0$. It is worth mentioning that we have also implemented the exponential mapping and could find no advantages for it over the rational mapping.

The radial functions in the external domain are expanded as

$$c_m^{(2)}(\tau, z) = \sum_{n=1}^{N^{(2)}} \phi_{m,n}^{(2)}(\tau)\, Z_n(z), \quad m = 0, 1, \ldots, M, \tag{25}$$

where the $Z_n(z)$, $n = 1, 2, \ldots, N^{(2)}$ are linear combinations of Chebyshev polynomials, each satisfying the boundary condition following from (13):

$$Z_n(z = -1) = 0, \quad n = 1, 2, \ldots, N^{(2)}. \tag{26}$$

We take

$$\begin{aligned} Z_{2k}(z) &= T_{2k}(z) - 1 \\ Z_{2k-1}(z) &= T_{2k-1}(z) + 1 \end{aligned} \tag{27}$$

Thus, we reduce the system of partial differential equations for two initially unknown functions $c^{(1)}(\tau, \lambda, \tau)$ and $c^{(2)}(\tau, \lambda, \tau)$ to a larger system of ordinary differential equations in τ, for

$$\begin{aligned} &\alpha_0(\tau),\ \phi_{m,n_1}^{(1)},\ \phi_{m,n_2}^{(2)}, \quad m = 0, 1, \ldots, M, \\ &n_1 = 1, 2, \ldots, N^{(1)}, \quad n_2 = 1, 2, \ldots, N^{(2)}. \end{aligned} \tag{28}$$

The total number of these unknown functions is $1 + (M+1)(N^{(1)} + N^{(2)})$.

In order to obtain equations for these functions we use the conventional Petrov – Galerkin method, i.e., the basis functions are taken as the test functions [2]. We define two inner products:

$$(f, g)^{(1)} \equiv \int_{-1}^{1} d\lambda \int_{0}^{1} f \cdot g \, \frac{d\tau}{\sqrt{1 - \tau^2}}, \tag{29}$$

$$(f, g)^{(2)} \equiv \int_{-1}^{1} d\lambda \int_{-1}^{1} f \cdot g \, \frac{dz}{\sqrt{1 - z^2}}. \tag{30}$$

Forming by (29) the inner product of (10) for $i = 1$ with the test functions

$$P_0(\lambda)\, T_0(\tau), \ P_m(\lambda)\, \tau^{\kappa_m} \cdot T_{2n_1 - 2}(\tau), \quad m = 0, 1, \ldots, M, \quad n_1 = 1, 2, \ldots, N^{(1)} - 1, \tag{31}$$

and by (30) the inner product of (10) for $i = 2$ with the test functions

$$P_m(\lambda)\, Z_{n_2}(z), \quad m = 0, 1, \ldots, M, \quad n_2 = 1, 2, \ldots, N^{(2)} - 1, \tag{32}$$

we obtain two vector equations

$$\mathbf{A}^{(i)} \frac{d\boldsymbol{\phi}^{(i)}}{d\tau} = (-K_c^{(i)}\, \mathbf{B}^{(i,c)} + K_d^{(i)}\, \mathbf{B}^{(i,d)} - K_\tau^{(i)}\, \mathbf{B}^{(i,\tau)}) \cdot \boldsymbol{\phi}^{(i)} + K_\tau^{(i)}\, \mathbf{b}^{(i)}, \quad i = 1, 2. \tag{33}$$

Here $\mathbf{A}^{(i)}$, $\mathbf{B}^{(i,c)}$, $\mathbf{B}^{(i,d)}$, $\mathbf{B}^{(i,\tau)}$ are $\{1 + (M+1)(N^{(i)} - 1),\ 1 + (M+1)N^{(i)}\}$ matrices, $\mathbf{b}^{(i)} - \{1 + (M+1)N^{(i)}\}$ are the vectors of inhomogeneous terms, and $\boldsymbol{\phi}^{(i)}(\tau) - \{1 + (M+1)N^{(i)}\}$ are the unknown vectors,

$$\boldsymbol{\phi}^{(1)}(\tau) = (\, \alpha_0,\ \phi_{0,1}^{(1)}, \ldots \phi_{0,N^{(1)}}^{(1)}, \ldots, \phi_{M,1}^{(1)}, \ldots, \phi_{M,N^{(1)}}^{(1)}\,)^T, \tag{34}$$

$$\phi^{(2)}(\tau) = (\phi^{(2)}_{0,1}, \ldots \phi^{(2)}_{0,N^{(2)}}, \ldots, \phi^{(2)}_{M,1}, \ldots, \phi^{(2)}_{M,N^{(2)}})^T. \tag{35}$$

The remaining 2 $(M+1)$ equations are derived from the boundary conditions (11).

Upon substituting (20) and (25) into (11), multiplying by $P_m(\lambda)$, $m = 0, 1, \ldots, M$ and integrating λ from -1 to 1, we obtain two sets of M+1 linear algebraic equations:

$$\mathbf{Q}^{(1)} . \phi^{(1)} = \mathbf{Q}^{(2)} . \phi^{(2)}, \tag{36}$$

$$H \cdot D \cdot \mathbf{S}^{(1)} . \phi^{(1)} = \mathbf{S}^{(2)} . \phi^{(2)}, \tag{37}$$

where $\mathbf{Q}^{(i)}$, $\mathbf{S}^{(i)}$ are $\{(M+1),\ (M+1)(1+N^{(i)})\}$ matrices, $i = 1, 2$.

By expressing $\phi^{(1)}_{m,N^{(1)}}$ and $\phi^{(2)}_{m,N^{(2)}}$, $m = 0, 1, \ldots, M$, using the system (36)–(37) and substituting in the system (33), we arrive finally at the system of $1 + (M+1)(N^{(1)} + N^{(2)} - 2)$ linear ODEs:

$$\mathbf{A} \frac{d\phi}{d\tau} = (\mathbf{B}^{(c)} + \mathbf{B}^{(d)} + \mathbf{B}^{(r)}) \cdot \phi \ + \mathbf{b}. \tag{38}$$

The constant matrices $\mathbf{B}^{(c)}$, $\mathbf{B}^{(d)}$ and $\mathbf{B}^{(r)}$ correspond respectively to the convective, diffusive, and reactive terms in the original equation (10), b is an $\{1 + (M+1)(N^{(1)} + N^{(2)} - 2)\}$ constant vector, and $\phi\ (\tau)$ is the vector of unknown functions

$$\phi \ \equiv (\alpha_0,\ \phi^{(1)}_{0,1}, \ldots \phi^{(1)}_{0,N^{(1)}-1},\ \phi^{(2)}_{0,1}, \ldots \phi^{(2)}_{0,N^{(2)}-1}, \ldots \phi^{(1)}_{M,1}, \ldots \phi^{(1)}_{M,N^{(1)}-1},\ \phi^{(2)}_{M,1}, \ldots \phi^{(2)}_{M,N^{(2)}-1})^T \tag{39}$$

and not simply a concatenation of vectors $\phi^{(1)}$ and $\phi^{(2)}$.

The matrices $\mathbf{A}$, $\mathbf{B}^{(d)}$ and $\mathbf{B}^{(r)}$ are block–diagonal. They all have M+1 nonzero square $\{N^{(1)}+N^{(2)}-2\ ,\ N^{(1)}+N^{(2)}-2)\}$ matrices on their main diagonals and their first $1+(N^{(1)}+N^{(2)}-2)$ elements in the first row and the first column are nonzero.

The matrices $\mathbf{B}^{(c)}$ that result from transforming the convective terms also have block structure with the same block sizes. However, they are no longer block-diagonal and the amount of nonzero block-diagonals depends on the velocity fields $\mathbf{v}^{(i)}$, $i = 1, 2$. The higher the degree of λ that is involved in the velocity field expressions, the greater will be the coupling between the radial functions of different orders. And the increase of the order of this coupling leads to a corresponding increase in the number of nonzero block diagonals in $\mathbf{B}^{(c)}$.

For the Hadamard – Rybczinsky field, for example, these matrices are block-tridiagonal, but for the velocity field in [15], valid for higher Reynolds numbers, it would be block-pentadiagonal.

The discontinuous initial conditions (15) are not appropriate for computations. Instead, we used the analytical solution for the pure diffusion case (no convection, no chemical reaction) derived in [16]. The concentration distributions for very small time values were expanded over our basis functions $T_{2n-2}(\tau)$ and Z_n, $n = 1, 2, \ldots$ to initialize the computations, and the coefficients obtained were used as initial conditions for $\alpha_0(\tau)$, $\phi^{(1)}_{m,n_1}$, and $\phi^{(2)}_{m,n_2}$, $m = 0, 1, \ldots, M$, $n_1 = 1, 2, \ldots, N^{(1)} - 1$, $n_2 = 1, 2, \ldots, N^{(2)} - 1$.

For time discretization of the system (38) we used the first-order backward Euler method. Defining ϕ^n as vector ϕ at the n-th time step of magnitude $\Delta\tau$ and

$$\mathbf{B} = \mathbf{B}^{(c)} + \mathbf{B}^{(d)} + \mathbf{B}^{(r)}, \tag{40}$$

system (38) can be rewritten as

$$(\mathbf{A} - \Delta\tau\mathbf{B})\cdot\Delta\boldsymbol{\phi}^{n+1} = \Delta\tau\mathbf{B}\cdot\boldsymbol{\phi}^{n} + \Delta\tau\mathbf{b}\,, \tag{41}$$

where

$$\Delta\boldsymbol{\phi}^{n+1} = \boldsymbol{\phi}^{n+1} - \boldsymbol{\phi}^{n}\,. \tag{42}$$

Every time step system of linear equations (41) was solved by regular Gauss elimination (preceded by LU decomposition) with the following iterative refinement [3]. The matrix on the left side of (41) has the same structure as the matrix B; as mentioned, it is block-tridiagonal for the Hadamard-Rybczinsky velocity field. Our attempts to apply block-elimination methods (in particular, the block Thomas algorithm [4]) failed, presumably because block LU factorization does not involve pivoting, which is essential when diagonal dominance does not occur (which is the case for high Peclet numbers).

We considered the matrix on the left side of (41) as a banded one with bandwidth $1 + 3\,(N^{(1)} + N^{(2)} - 2)$.

As long as this matrix depends on the time step and its factorization is a time-consuming process, only two values of the time step were used for each run. A smaller one was used for an initial time period and an another one for the subsequent time range.

The numbers of terms in series (16), (20), and (25) depend on the steepness of the concentration gradients and were different for different values of Peclet and Damköhler numbers. The maximum numbers used were $M = 87$, $N^{(1)} = 25$, $N^{(2)} = 97$.

As is well known [1, 2], an increase in the number of terms in a spectral series (especially in the series in Chebyshev polynomials) leads to very high condition numbers for the resulting system of linear equations. This was alleviated by using double precision in all computations and, as mentioned above by application of the iterative refinement to the solution obtained with the Gauss elimination procedure.

QUANTITIES OF INTEREST

The most practically interesting quantity in extraction problems is the amount of material extracted by a particular instant in time. For the problem under consideration (i.e., when species are extracted from the droplet) this can be conveniently characterized by the time-dependent average dimensionless concentration of species remaining in the drop:

$$\overline{c}^{(1)} = \frac{3}{2}\cdot\int_0^1\int_{-1}^1 r^2 c^{(1)}(\tau,\lambda,r)\,d\lambda\,dr \tag{43}$$

This quantity changes in time as a result of mass transfer out of the droplet. The local and surface average rates of this transfer are characterized by corresponding mass transfer coefficients, the quantities which when multiplied by the driving force give the respective mass transfer rate. The nondimensional mass transfer coefficient is usually referred to as the Sherwood number Sh, which is analogous to the Nusselt number in heat transfer problems.

Different kinds of Sherwood number can be introduced, depending on the driving force on which they are based and the domain to which they are related.

For the problem of single-drop extraction, the instantaneous driving force $F^{(\mathrm{dr})}$ for mass transfer is the difference between the concentration of the transferring species in the droplet and that far away from it, taking into account the step change of the concentration at the interface due to solubility,

$$F^{(\mathrm{dr})} = \overline{\tilde{c}}^{(1)} - H\tilde{c}_{\infty}\,, \tag{44}$$

where $\overline{\tilde{c}}^{(1)}$ is the dimensional average concentration of species in the droplet.

Often the Sherwood number is based on the maximum possible (in our case, initial) driving force:

$$F_0^{(\mathrm{dr})} = \tilde{c}_0 - H\tilde{c}_{\infty}\,. \tag{45}$$

Here we consider only the external Sherwood number, i.e., the nondimensional rate of transfer of species from the external side of droplet surface into the external flow.

The local and average external Sherwood numbers defined on the basis of the maximum driving force are respectively:

$$Sh_{\mathrm{loc},0} = -2H\cdot D\left.\frac{\partial c^{(1)}}{\partial r}\right|_{r=1} \tag{46}$$

and

$$Sh_0 = -H\cdot D\int_{-1}^{1}\left.\frac{\partial c^{(1)}}{\partial r}\right|_{r=1} d\lambda\,. \tag{47}$$

Corresponding values based on the instantaneous driving force are:

$$Sh_{\mathrm{loc}} = \frac{Sh_{\mathrm{loc},0}}{\overline{c}^{(1)}} \tag{48}$$

$$Sh = \frac{Sh_0}{\overline{c}^{(1)}}\,. \tag{49}$$

The chemical reaction in the external region increases the rate of the extraction, and this increase is characterized by the enhancement factor, which is the ratio of the corresponding mass transfer rates [5]:

$$E = \frac{Sh(Da_{II}^{(2)} \neq 0)}{Sh(Da_{II}^{(2)} = 0)} \tag{50}$$

COMPUTATIONAL RESULTS AND DISCUSSION

The results of the computations to be presented cover the following ranges of parameters:

$$0.25 \le D \le 4\,,$$
$$0 \le Pe^{(2)} \le 500\,,$$
$$0 \le Da_{II}^{(2)} \le 1000\,,$$
$$H = \mu = 1\,.$$

The characteristic time scale was chosen as

$$\tau_* = \tau_{\mathrm{diff}}^{(2)}\,, \tag{51}$$

which is just the Fourier number based on the diffusion coefficient of the external fluid. The times appearing on the plots are expressed in these units. The values of Peclet number Pe and Damköhler number Da presented on the plots correspond to $Pe^{(2)}$ and $Da_{II}^{(2)}$, respectively.

To illustrate qualitively the process of pure mass transfer (no reaction) from the droplet, we present in Figures 1–3 the isocontours of constant species concentration at different times for various levels of external convection ($Pe^{(2)} = 10, 200, 500$, respectively). The well known and intuitively expected increase of mass transfer with increasing convection is apparent.

The influence of internal circulation on the development of the mass transfer process is illustrated in Figures 4–5 where we present the isoconcentration contours for the same external Peclet number ($Pe^{(2)} = 500$) and different ratios of internal and external diffusivities ($D = 0.25$ and $D = 4.0$).

For $D = 0.25$ the internal convection is much stronger, in the sense that the value of $Pe^{(1)}$ is larger. As a consequence the concentration isocontours inside the droplet lie close to the internal streamlines, a result already obtained numerically by Johns and Beckmann [7] for the special case of mass transfer resistance solely inside the droplet. The coincidence of internal isocontours with internal streamlines also constituted the basic assumption of Kronig and Brink's model of mass transfer in a circulating drop [6]. From a simple comparison of the isocontour levels in Figures 4 and 5 alone one infers that the mass transfer from a droplet for D=4 is much more intense than for D=0.25. The reason that the *internal* Peclet number $Pe^{(1)}$ is greater for $D = 0.25$ is not that the internal circulation is greater, for it is not ($\mu = 1$), but that the internal diffusivity is smaller. Nonetheless, it is customary for brevity to describe an increase in Peclet number as an increase in convection, rather than the more lengthy but more accurate increase of the ratio of convection to diffusion. In this usage, one may phrase the conclusion drawn from Figures 1–5 as follows: increased convection outside the droplet increases the rate of extraction, but increased convection inside suppresses mass transfer.

The influence of the external reaction rate on the concentration distribution is shown in Figures 2, 6 and 7. As could have easily been anticipated, an increase in $Da_{II}^{(2)}$ results in faster extraction and an almost immediate disappearence of extracted species outside the droplet (almost no species present for $Da_{II}^{(2)} = 100$ in Figure 7).

Figures 8 and 9 show the effect of reaction rate on the local Sherwood number. The values of $Sh_{\mathrm{loc},0}$ go to zero with time for all values of the angle variable ϑ, although the surface distribution of Sherwood number based on the instantaneous driving force approaches a nonvanishing asymptote. An increase in the reaction rate thus results in a general increase of mass transfer and of values of the Sherwood numbers, but the temporal variation of values of local Sherwood numbers at different locations is less transparent, warranting further investigation.

Figure 10 reflects the behavior of average Sherwood number Sh in time for different values of the external Peclet number $Pe^{(2)}$ for the no-reaction case. The oscillations of Sh were obtained computationally by different investigators including Johns and Beckmann [7] and Oliver and Chung [9], who solved the conjugate unsteady heat transfer problem, which is mathematically equivalent to the mass transfer problem under consideration when there is no chemical reaction involved. These oscillations are caused by the internal circulation, with the most detailed physical explanation being given by Brignell in [8]. Consequently, the period of these oscillations is smaller and the amplitute greater the higher the Peclet number is. The stronger convection also leads to a higher mass transfer rate as it creates the thinner diffusion boundary layers on the both sides of the droplet surface.

Figure 11 illustrates the influence of the rate of external chemical reaction on the average Sherwood number. The plots confirm the conclusions made above on the increase of the rate of extraction with the increasing external convection and rate of external chemical reaction.

In a more apparent way, this is reflected in Figure 12, where the decrease of the average droplet concentration with time is shown. From this picture we can also deduce the very important conclusion that an increase in the reaction rate beyond some specific value will not benefit the extraction results (the diffences between the average droplet concentration for $Da_{II}^{(2)}$ values of 300 and 1000 are quite small).

Figure 13 shows the effect of reaction rates on the values and temporal evolution of the enhancement factor E. The oscillations here are the consequences of internal circulation, the same as for the corresponding average Sherwood number on Figure 10. The values of E corresponding to the same reaction rate are higher for smaller $Pe^{(2)}$ (lower convection). A possible explanation could be that the corresponding values of $Da_{I}^{(2)}$, which are just the ratios of $Da_{II}^{(2)}$ and $Pe^{(2)}$, are smaller for higher $Pe^{(2)}$.

In closing, we want to emphasize that the purpose of this article has been to present the numerical algorithm we have developed and to illustrate some of the kinds of results that can be obtained for this concrete situation. Our subsequent articles will include additional results for other classes of forced convective diffusion–reaction problems for single drops, as well as more detailed analyses of these and other results.

NOMENCLATURE

$\tilde{c}_0$ -dimensional value of the uniform concentration in the origin of the droplet at $t = 0$

$\tilde{c}_\infty$ -dimensional value of the concentration far from the drop

$\tilde{c}^{(i)}$ -dimensional concentration in the i-th domain, $i = 1, 2$

$c^{(i)}$ -dimensionless concentration in the i-th domain, $i = 1, 2$

$D^{(i)}$ -molecular diffusivity of the solute in the fluid in the i-th domain, $i = 1, 2$

D -molecular diffusivity ratio, $D^{(1)}/D^{(2)}$

$Da_I^{(i)}$ -first Damköhler number in the i-th domain , $\dfrac{k^{(i)} R}{f^{(i)}(\mu) U_\infty}$, $i = 1, 2$

$Da_{II}^{(i)}$ -second Damköhler number in the i-th domain, $\dfrac{k^{(i)} R^2}{D^{(i)}}$, $i = 1, 2$

E -enhancement factor, eq.(50)

$f^{(i)}$ -factor showing the viscosity ratio dependence of the velocity scale in the i-th domain, $i = 1, 2$

H -distribution coefficient (Henry "law" constant)

$k^{(i)}$ -chemical reaction rate constant in the i-th domain, $i = 1, 2$

M -highest order of the Legendre polynomials used in the expansion in the angular direction

$N^{(i)}$ -number of terms in the expansion of radial functions in the i-th domain , $i = 1, 2$

$Pe^{(i)}$ -Peclet number in the i-th domain, $\dfrac{2\, U_\infty\, f^{(i)}(\mu)\, R}{D^{(i)}}$, $i = 1, 2$

r -dimensionless radial coordinate

R -droplet radius

t -dimensional time

$U_*^{(i)}$ -characteristic velocity scale in the i-th domain, $i = 1, 2$

U_∞ -velocity of the flow at the infinity

$\mathbf{v}^{(i)}$ -velocity field in the i-th domain nondimensionalized by the corresponding velocity scale $U_*^{(i)}$, $i = 1, 2$

ϑ -polar angle in spherical coordinate system

λ $= \cos\vartheta$

μ -molecular viscosities ratio, $\mu^{(1)}/\mu^{(2)}$

$\mu^{(i)}$ -molecular viscosity of the fluid in the i-th domain, $i = 1, 2$

τ -dimensionless time

$\tau_{\text{conv}}^{(i)}$ -convection time scale in the i-th domain, $\dfrac{R}{f^{(i)}(\mu)\, U_\infty}$, $i = 1, 2$

$\tau_{\text{diff}}^{(i)}$ -diffusion time scale in the i-th domain, $\dfrac{R^2}{D^{(i)}}$, $i = 1, 2$

$\tau_{\text{rxn}}^{(i)}$ -chemical reaction time scale in the i-th domain, $\dfrac{1}{k^{(i)}}$, $i = 1, 2$

REFERENCES

[1] J. P. Boyd, *Chebyshev and Fourier Spectral Methods.* Springer–Verlag (1989).

[2] C. Canuto, M. Y. Hussaini, A. Quarteroni, *Spectral Methods in Fluid Dynamics.* Springer–Verlag (1988).

[3] G. H. Golub and C. F. Van Loan, *Matrix Computations.* Johns Hopkins University Press (1989).

[4] C. A. J. Fletcher, *Computational Techniques for Fluid Dynamics.* Springer–Verlag (1988).

[5] R.B. Bird, W. E. Stewart, E. N. Lightfoot, *Transport Phenomena.* John Wiley & Sons (1966).

[6] R. R. Kronig and J. C. Brink, On the theory of extraction from falling droplets. *Appl. Sci. Res.* **A2**, 142-155 (1950)

[7] L. E. Johns, Jr and R. B Beckmann, Mechanism of dispersed-phase mass transfer in viscous, single-drop extraction systems. *A.I.Ch.E. Jl* **12**, 10-16 (1966).

[8] A. S. Brignell, Solute extraction from an internally circulating spherical liquid drop. *Int. J. Heat Mass Transfer* **18**, 61-68 (1975).

[9] D. L. R. Oliver, J. N. Chung, Conjugate unsteady heat transfer from a spherical droplet at low Reynolds numbers. Int. J. Heat Mass Transfer **29**, 879-887 (1986).

[10] P. R. Spalart, A spectral method for external viscous flows. *Contemporary mathematics* **28**, 315-335 (1984).

[11] C. E. Grosch, S. A. Orszag, Numerical solution of problems in unbounded regions: coordinate transforms. *J. of Comput. Phys.* **25**, 273-296 (1977).

[12] B. Fornberg, A numerical study of steady viscous flow past a circular cylinder, *J. Fluid Mech.*, **98**, 819-855, 1980

[13] A. T. Patera, A spectral element method for fluid dynamics: laminar flow in a channel expansion. *J. of Comput. Phys.* **54**, 468-488 (1984).

[14] D. Gottlieb, S. A. Orszag, *Numerical Analysis of Spectral Methods.* SIAM (1977)

[15] A. E. Hamielec, A. I. Johnson, Viscous flow around fluid spheres at intermediate Reynolds numbers. *Can. J. Chem. Engng.* **40**, 2, 41 (1962).

[16] F. Cooper, Heat transfer from a sphere to an infinite medium. *Int. J. Heat Mass Transfer* **20**, 991-993 (1977).

Table 1: Coefficients in eq.(1) depending on the choice of τ_* $(i, j = 1, 2)$

τ_*	$K_c^{(i)}$	$K_d^{(i)}$	$K_r^{(i)}$
$\tau_{\text{diff}}^{(j)}$	$\frac{Pe^{(i)}}{2} \cdot \frac{D^{(i)}}{D^{(j)}}$	$\frac{D^{(i)}}{D^{(j)}}$	$Da_{II}^{(i)} \cdot \frac{D^{(i)}}{D^{(j)}}$
$\tau_{\text{conv}}^{(j)}$	$\frac{f^{(i)}(\mu)}{f^{(j)}(\mu)}$	$\frac{2}{Pe^{(i)}} \cdot \frac{f^{(i)}(\mu)}{f^{(j)}(\mu)}$	$Da_I^{(i)} \cdot \frac{f^{(i)}(\mu)}{f^{(j)}(\mu)}$
$\tau_{\text{rxn}}^{(j)}$	$\frac{1}{Da_I^{(i)}} \cdot \frac{k^{(i)}}{k^{(j)}}$	$\frac{1}{Da_{II}^{(i)}} \cdot \frac{k^{(i)}}{k^{(j)}}$	$\frac{k^{(i)}}{k^{(j)}}$

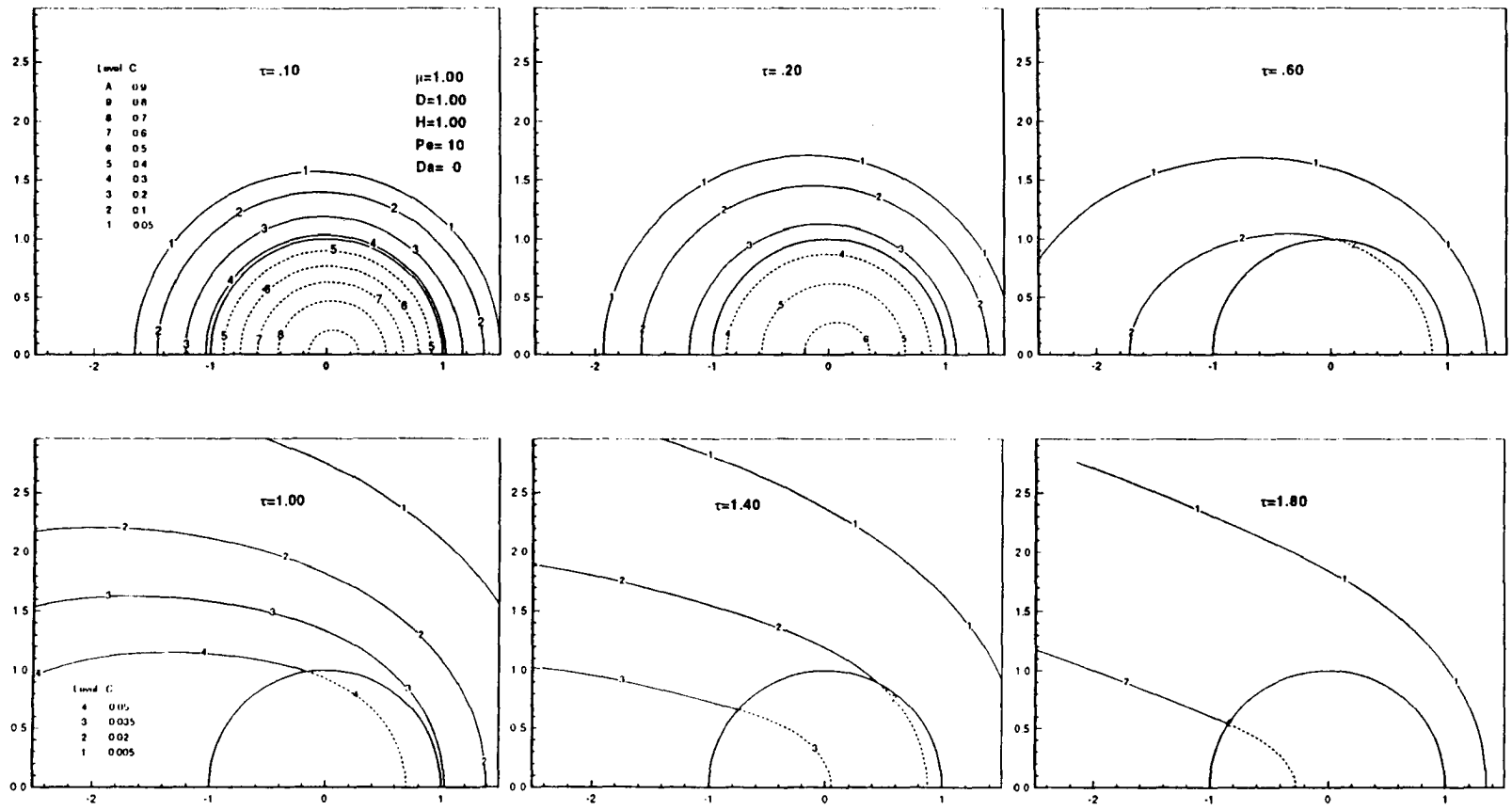

Fig. 1 Isoconcentration curves at different time moments for Pe=10

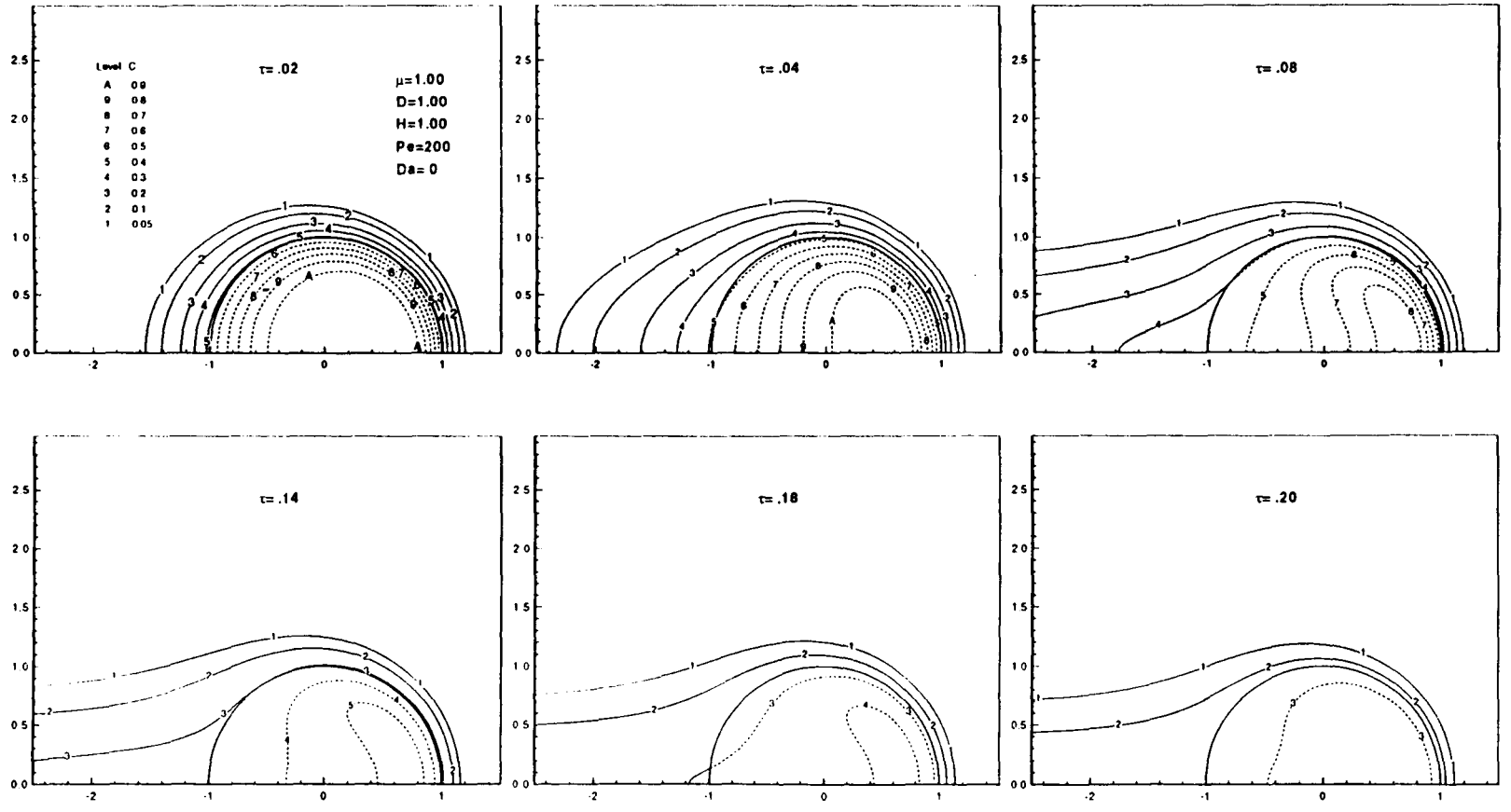

Fig. 2 Isoconcentration curves at different time moments for Pe=200

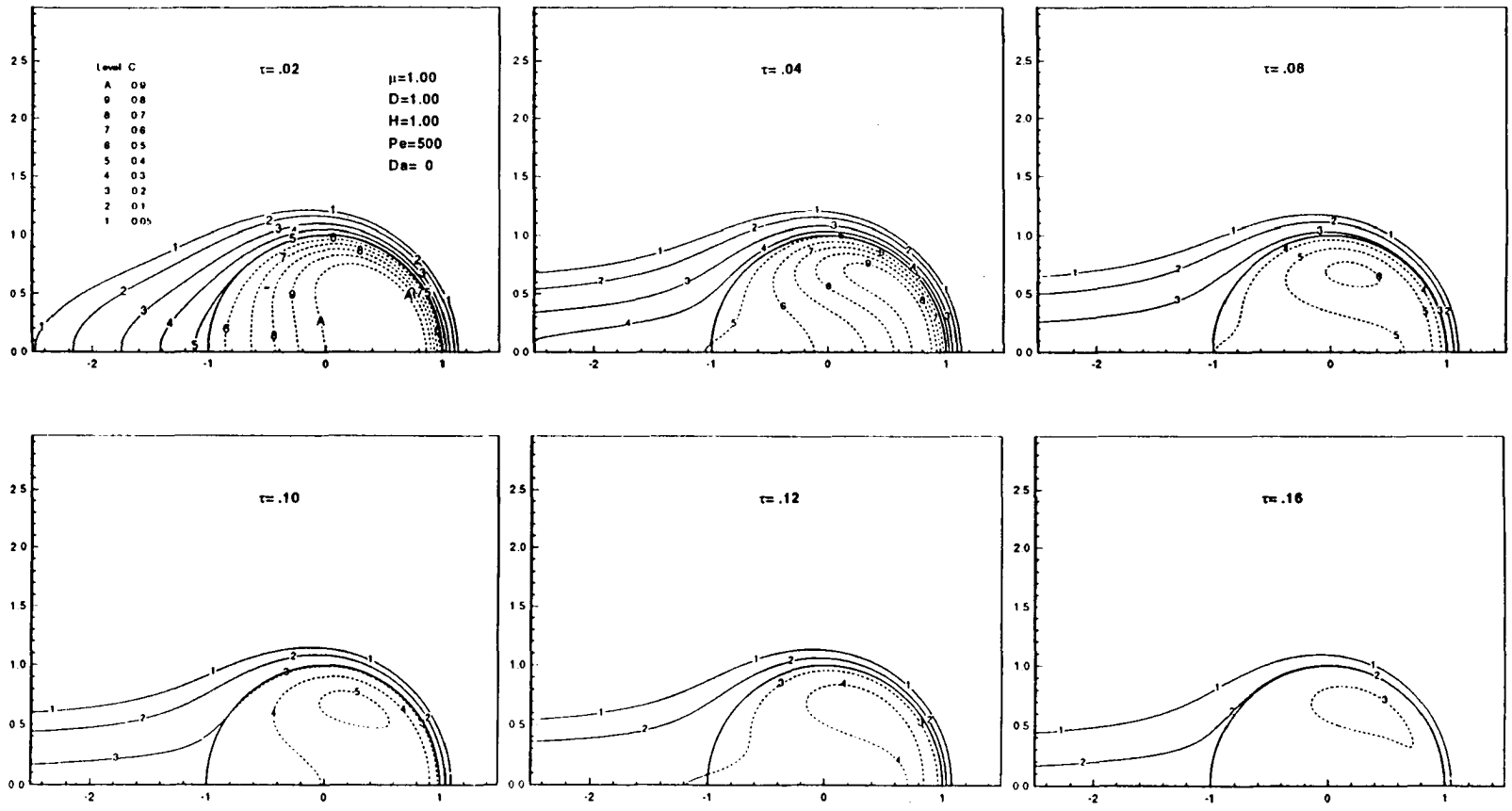

Fig. 3 Isoconcentration curves at different time moments for Pe=500

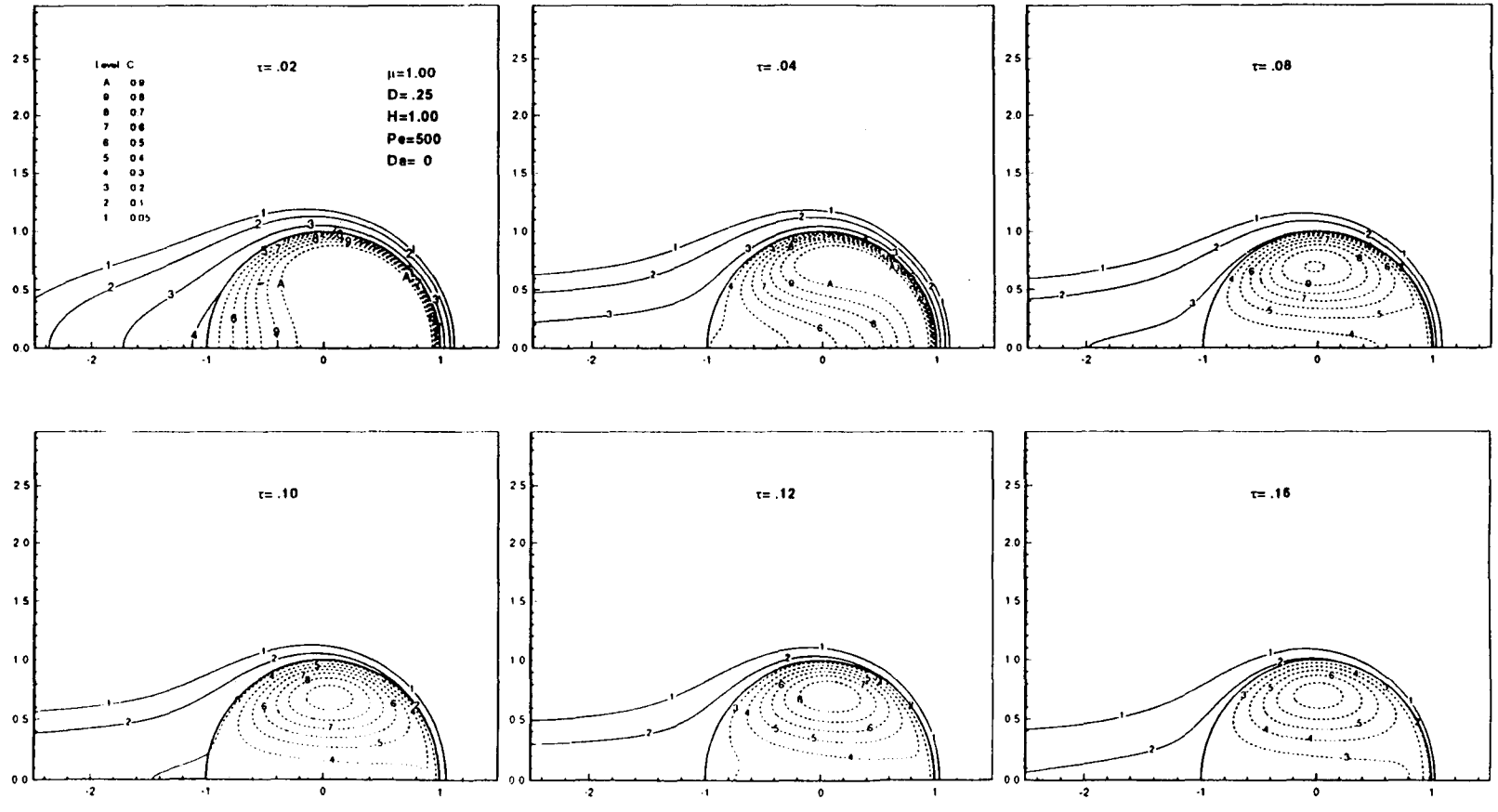

Fig. 4 Isoconcentration curves at different time moments for Pe=500 and D=.25

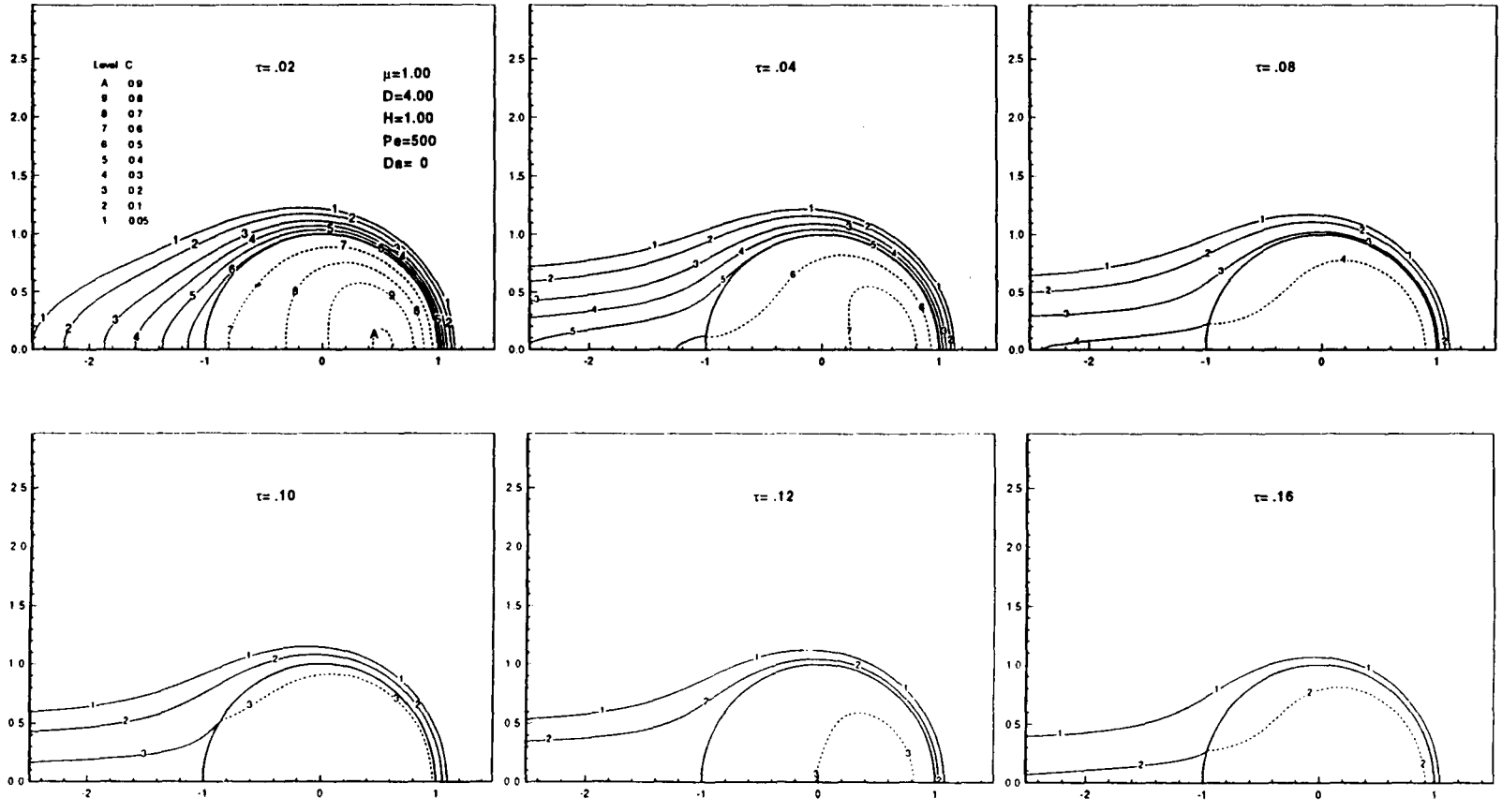

Fig. 5 Isoconcentration curves at different time moments for Pe=500 and D=4.0

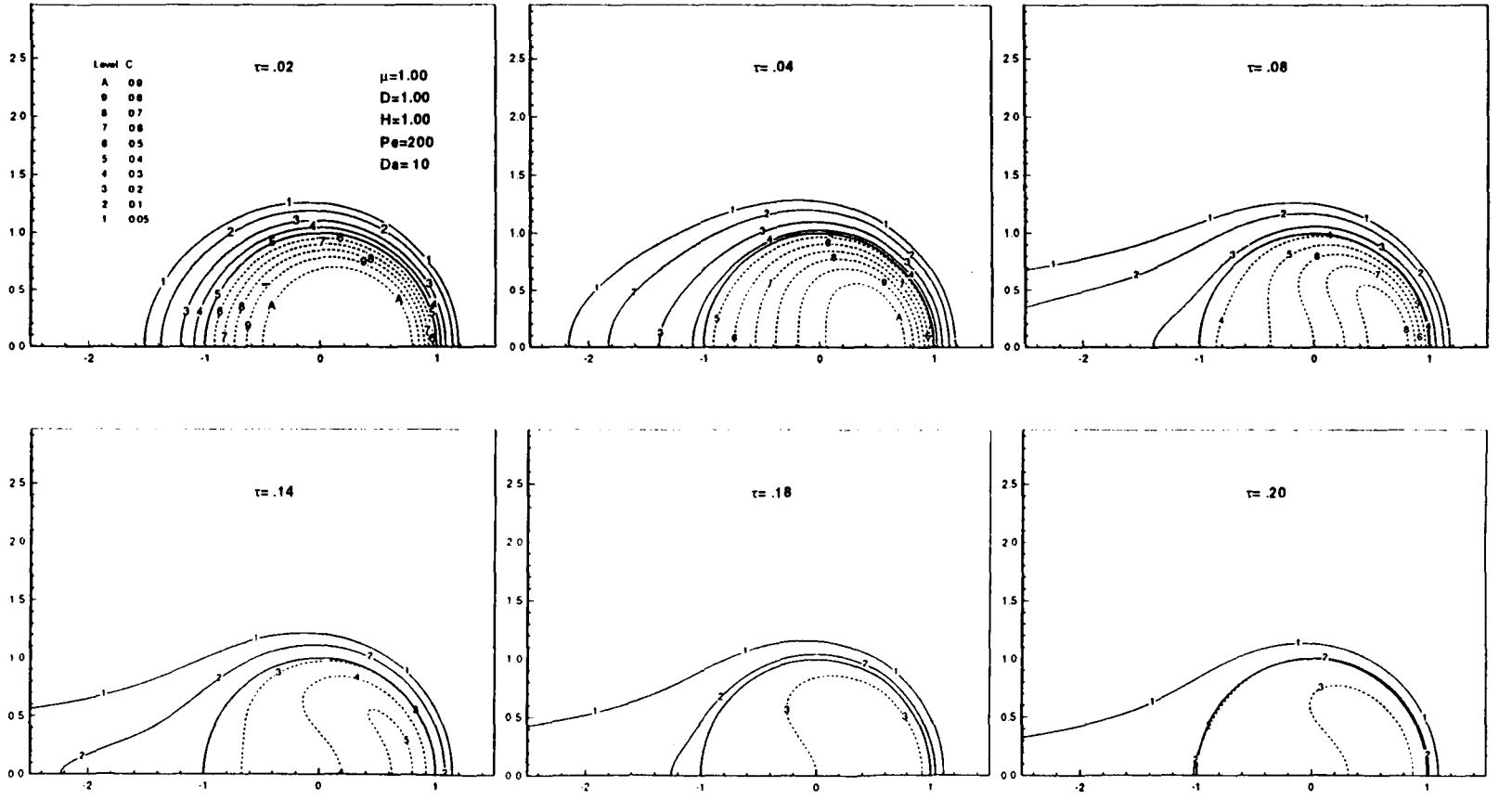

Fig. 6 Isoconcentration curves at different time moments for Pe=200 and Da=10

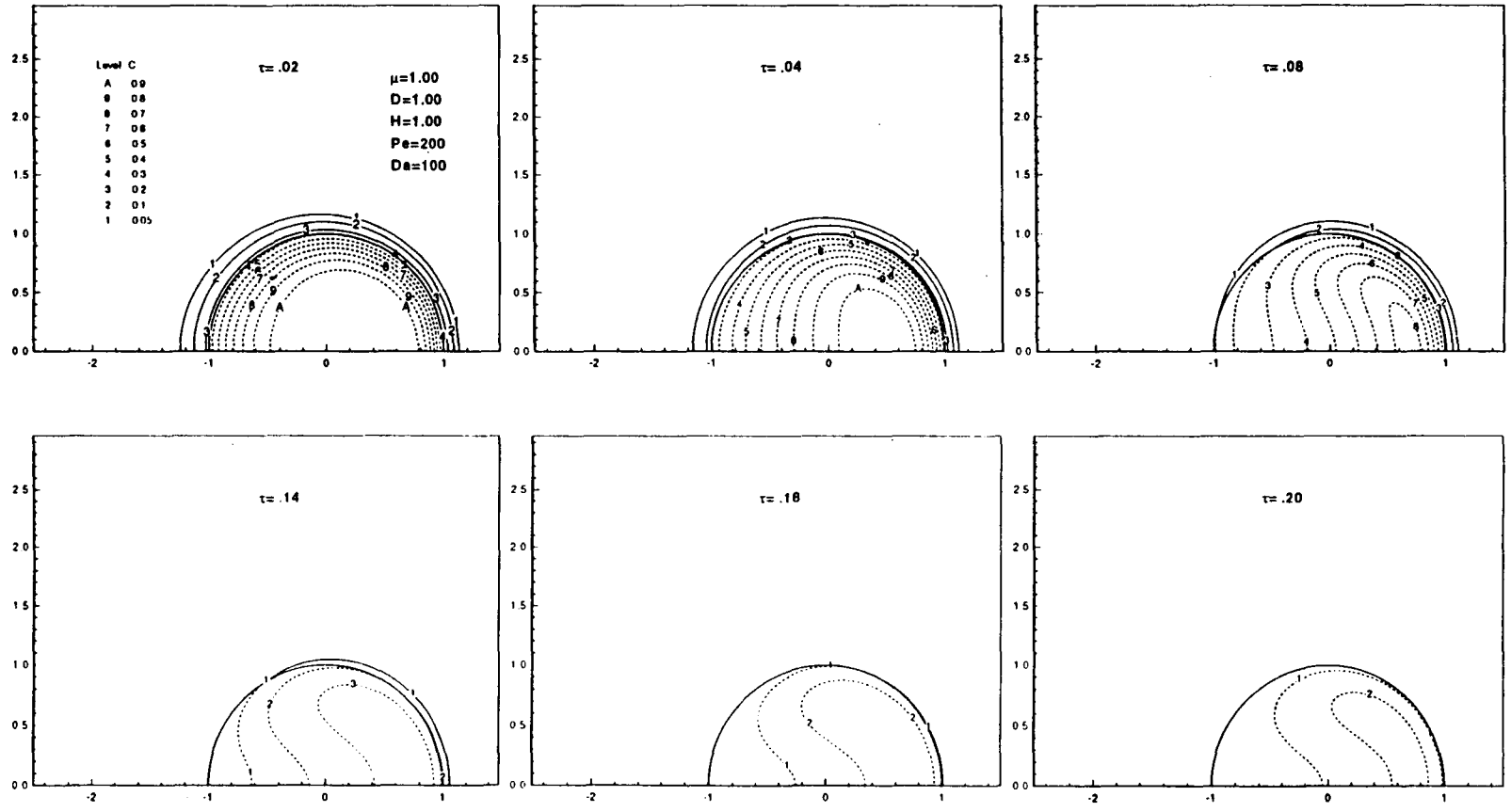

Fig. 7 Isoconcentration curves at different time moments for Pe=200 and Da=100

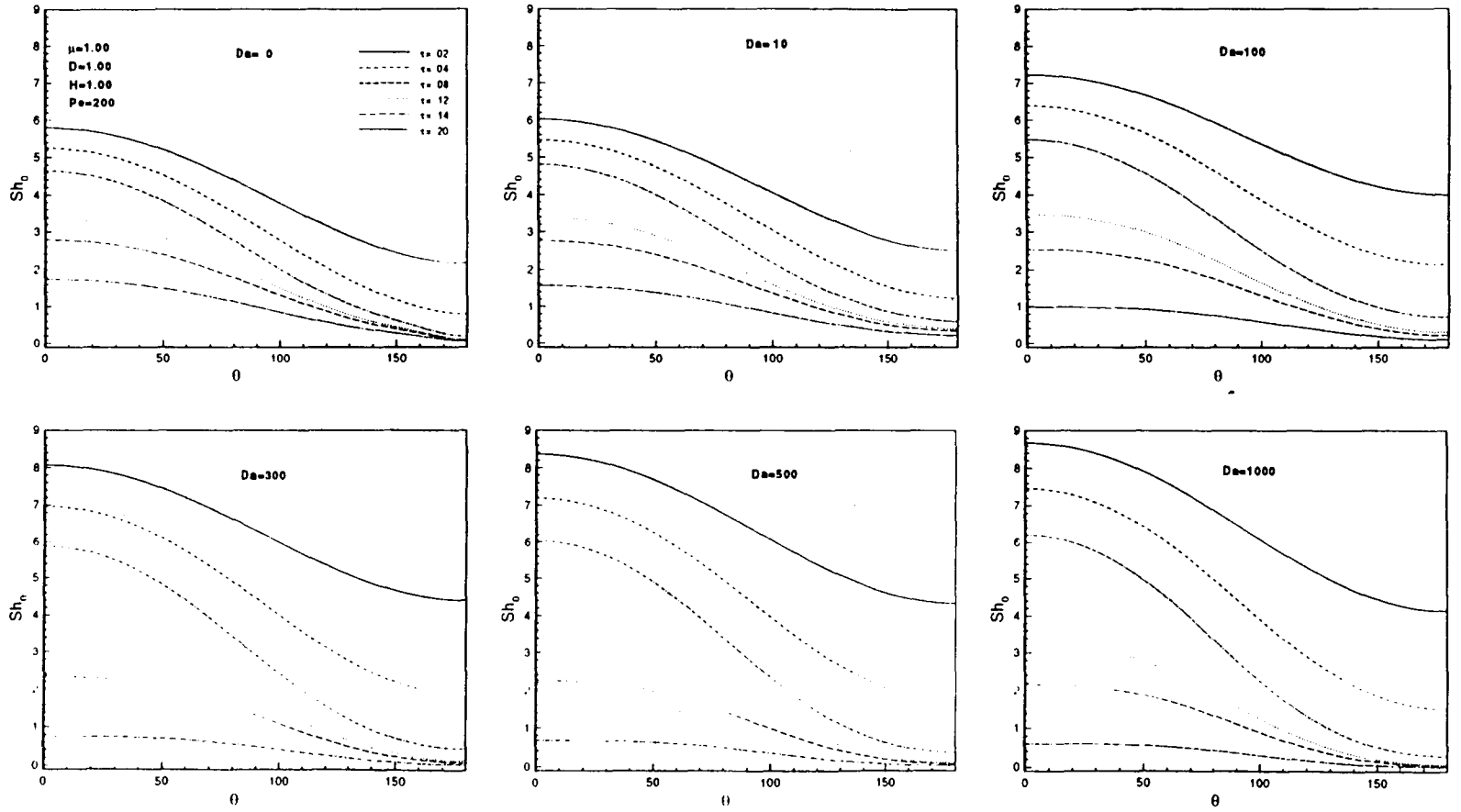

Fig. 8 Distribution of the values of local Sherwood number Sh_0 at Pe=200 for different values of Da

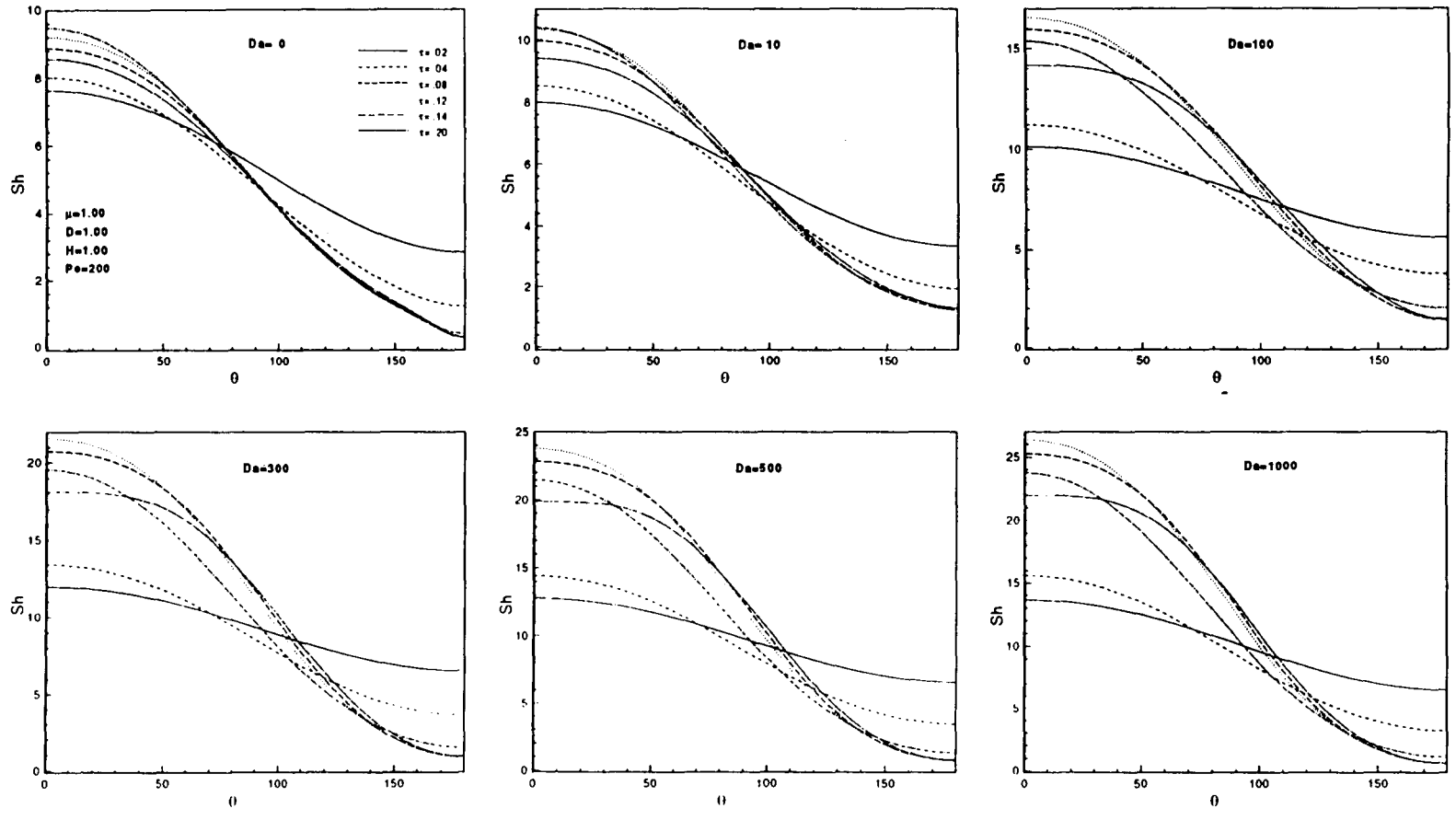

Fig. 9 Distribution of the values of local Sherwood number Sh at Pe=200 for different values of Da

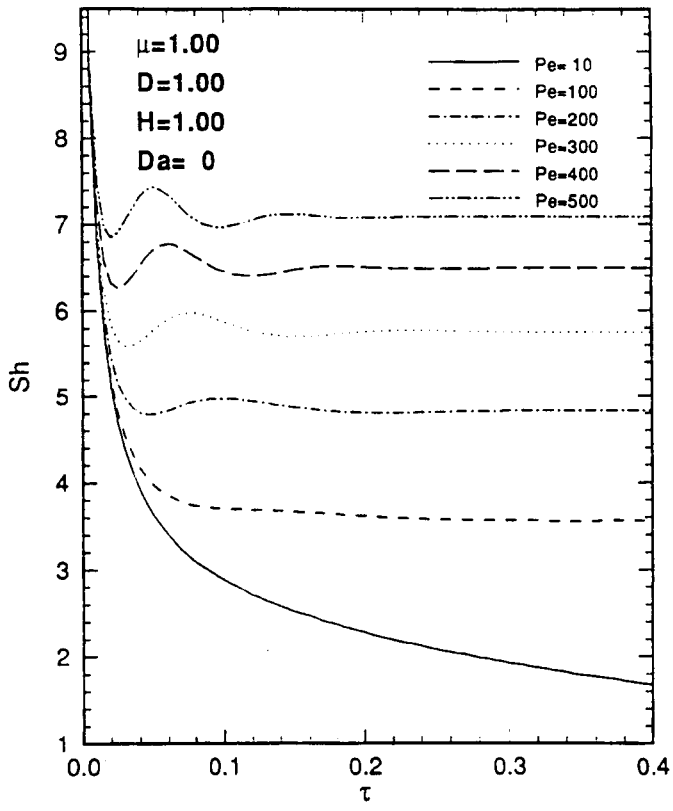

Fig. 10 Time evolution of average Sherwood number Sh for Da=0 at different values of Pe

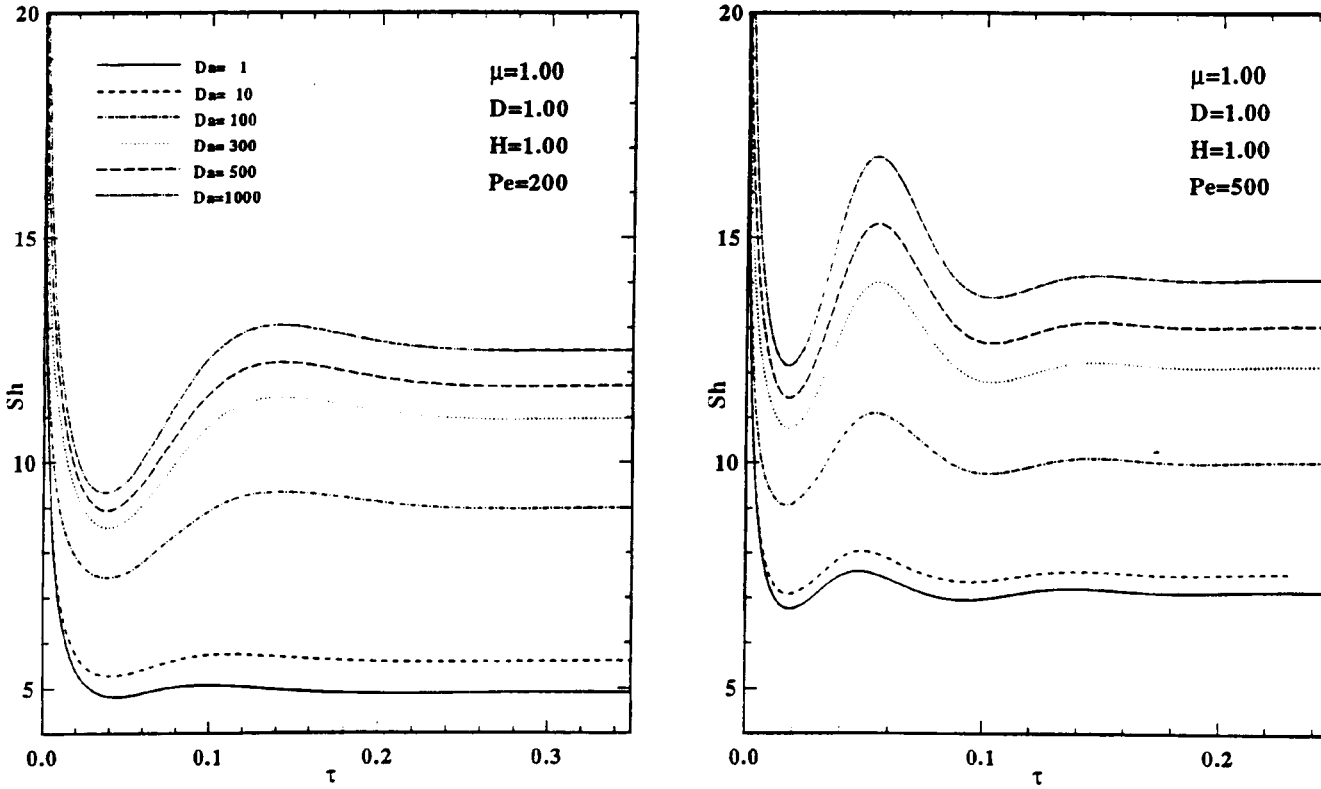

Fig. 11 Effect of reaction rate on average Sherwood number Sh for Pe=200 and Pe=500

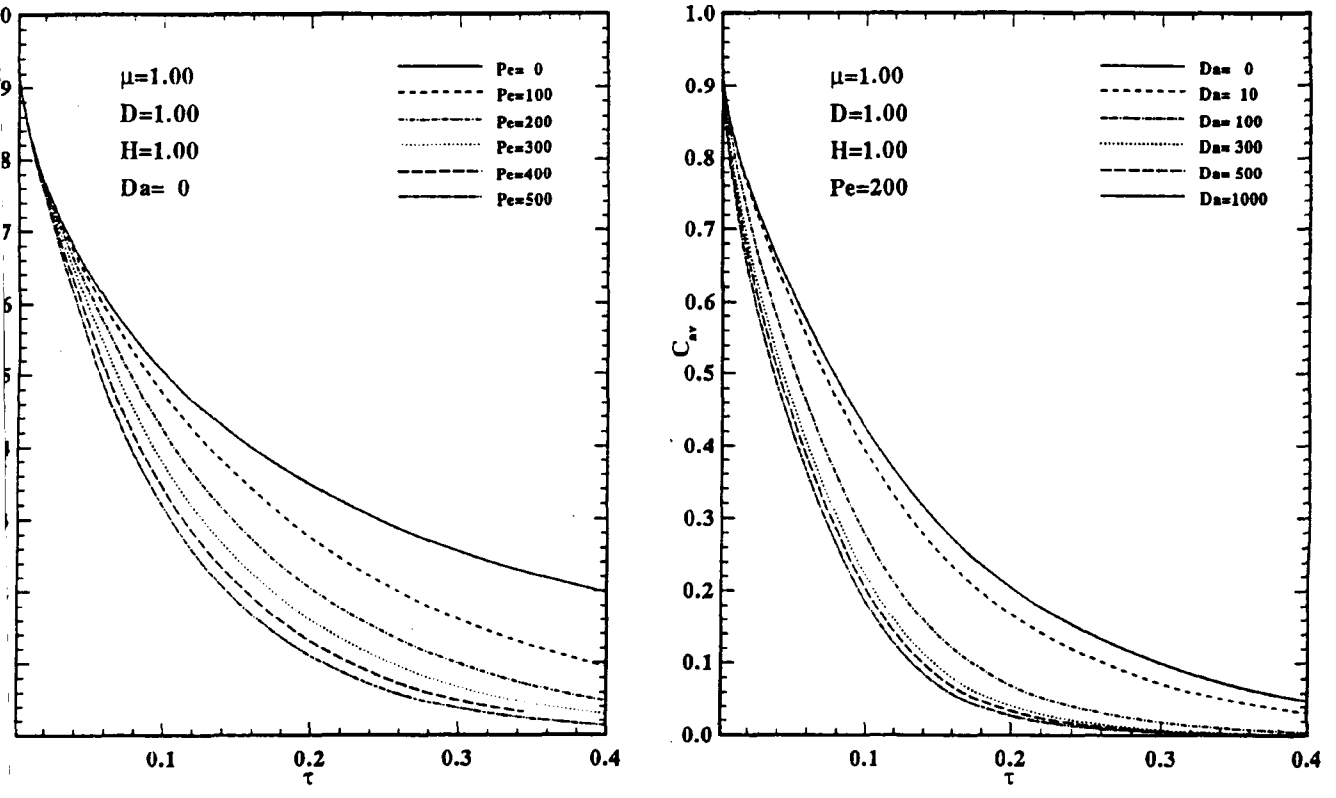

Fig. 12 Time evolution of average droplet concentration

REPORT DOCUMENTATION PAGE

Form Approved
OMB No. 0704-0188

1. AGENCY USE ONLY (*Leave blank*)	2. REPORT DATE	3. REPORT TYPE AND DATES COVERED
	January 1995	Conference Publication

4. TITLE AND SUBTITLE

Sixth Annual Thermal and Fluids Analysis Workshop

5. FUNDING NUMBERS

None

6. AUTHOR(S)

7. PERFORMING ORGANIZATION NAME(S) AND ADDRESS(ES)

National Aeronautics and Space Administration
Lewis Research Center
Cleveland, Ohio 44135–3191

8. PERFORMING ORGANIZATION REPORT NUMBER

E–9214

9. SPONSORING/MONITORING AGENCY NAME(S) AND ADDRESS(ES)

National Aeronautics and Space Administration
Washington, D.C. 20546–0001

10. SPONSORING/MONITORING AGENCY REPORT NUMBER

NASA CP–10161

11. SUPPLEMENTARY NOTES

Responsible person, Doug Darling, organization code 2710, (216) 433–8273.

12a. DISTRIBUTION/AVAILABILITY STATEMENT

Unclassified - Unlimited
Subject Categories 34 and 61

12b. DISTRIBUTION CODE

13. ABSTRACT (*Maximum 200 words*)

The Sixth Annual Thermal and Fluids Analysis Workshop was held at the Ohio Aerospace Institute, Brook Park, Ohio cosponsored by NASA Lewis Research Center and the Ohio Aerospace Institute, August 15–19. 1994. The workshop consisted of classes, vendor demonstrations, and paper sessions. The classes and vendor demonstrations provided participants with the information on widely used tools for thermal and fluids analysis. The paper sessions provided a forum for the exchange of information and ideas among thermal and fluids analysis. Paper topics included advances a uses of established thermal and fluids computer codes (such as SINDA and TRASYS) as well as unique modeling techniques and applications.

14. SUBJECT TERMS

Thermal simulation; Fluid mechanics; Computer programs

15. NUMBER OF PAGES

325

16. PRICE CODE

A14

17. SECURITY CLASSIFICATION OF REPORT	18. SECURITY CLASSIFICATION OF THIS PAGE	19. SECURITY CLASSIFICATION OF ABSTRACT	20. LIMITATION OF ABSTRA
Unclassified	Unclassified	Unclassified	